Understanding and Development of Advanced Techniques for the Processing of Single Crystal Turbine Components

Max Eric Schlienger
B.S., University of Colorado, 1979
M.S., University of Illinois, 1992

A dissertation submitted to the faculty of the
Oregon Graduate Institute of Science & Technology
in partial fulfillment of the
requirements for the degree
Doctor of Philosophy
in
Materials Science

February 1995

The dissertation "Understanding and Development of Advanced Techniques for the Processing of Single Crystal Turbine Components" by Max Eric Schlienger has been examined and approved by the following Examination Committee.

2/28/95

James T. Stanley
Dissertation Advisor

Dave G. Atteridge
Professor

Jack H. Devletian
Professor

Lemmy Meekisho
Assistant Professor

Milton R. Scholl
Assistant Professor

William E. Wood
Professor

Dr. Frank J. Zanner
Sandia National Laboratories

Acknowledgments

I wish to extend a heart felt thanks to the Rolls Royce company and to Retech Inc. for their support of this work. In particular, Alan Moulden, Ray Snider and Alan Patrick of Rolls Royce provided significant, critical and crucial discussions in regard to many of the thoughts and ideas expressed herein.

I also wish to acknowledge the support of Sandia National Laboratories and several individuals in particular. First, is Alice Kilgo of the metallography lab. Without Alice's expertise the sample preparation could not have been completed. Next I must extend my thanks to Randy Schunk of division 1511. Randy's modeling skills made the modeling segment of this work possible. In particular I would like to thank Joe Michael for sharing his expertise with BEKPs and making that section of this project possible. Joe's assistance was an honor and a pleasure.

Frank Zanner of Sandia deserves a major thanks for his continued motivational efforts on my behalf, Frank made an effort to look out for my best interests and provided the necessary kicks to keep me moving. In fact, I must acknowledge the support of the entire crew at Sandia's Liquid Metal Processing Lab, a finer group of individuals does not exist.

Hamish Fraser of OSU deserves credit for starting me along this journey and my wife janet deserves even more for traveling the tortuous path with me and providing assistance all along the way.

My parents, Max and Joan Schlienger can never be thanked enough for their life long love, support and confidence. If I can live up to their example, I will have succeeded as a parent.

Finally, I need to thank my advisor James T. Stanley. When he took me on as a student, he may not have known what he was getting into. I suspect that I may have added a gray hair or two, but Jim encouraged and motivated me the entire time and I am grateful.

Table of Contents

List of Figures

List of Tables

Abstract

Understanding and Development of Advanced Techniques for the Processing of Single Crystal Turbine Components

M. Eric Schlienger
Supervising Professor : James T. Stanley

Single crystal turbine components are experiencing an ever broadening role in today's aircraft engines and power turbines. However, in production, these single crystal parts have a number of solidification based characteristics which lead to excessive scrap. Variations in primary dendrite arm spacing can result in an uneven response to heat treatment whereas freckles and sliver grains are cause for rejection of the part. This work seeks to define the parameters responsible for such variations and to develop methods for their control.

As characterized by primary dendrite arms spacing, this work seeks to define the impact specific control parameters have on the solidification and growth of single crystal superalloy components. In pursuit of this goal, twelve test molds, each consisting of eight single crystal test bars, were produced in an industrial furnace. Each mold was poured under a controlled set of conditions. Two runs were instrumented with thermocouples to characterize the actual thermal conditions during solidification. After processing, one bar from each of the twelve molds was analyzed for dendrite spacing as a function of position along the length of the bar. Finally, a developing technology, Back-scattered Electron Kikuchi Patterns in the SEM, was evaluated to determine its effectiveness for the analysis of heat flow and interface morphology during the solidification process.

The selection of specific control parameters was guided by a review of solidification theory that takes into account the actual thermal environment expected in an industrial furnace. This analysis resulted in a new analytic solution to the growth process and pointed to a specific control strategy. A simple finite element model was

utilized to understand the effects of heat flow characteristics on the solidification environment.

It is shown that emissive cooling drives the process and insufficient understanding of it's effect is responsible for micro structural variations and solidification defects. It is further demonstrated that the heat of solidification is a significant source of heat in the process and must be considered in an optimized control scheme. Such a control scheme is demonstrated as an effective means of reducing the variation in the primary dendrite arm spacing.

Chapter 1 Introduction

In the near future (circa 5 years) today's foundry capacity will not be sufficient to meet the need for single crystal turbine blades. As the necessary equipment involves substantial lead time and capital investment, it is likely that the supply of single crystal turbine blades will be a production bottleneck for commercial jet engines. At present, the single crystal production process is far from optimized and production efficiencies may be increased significantly. One such improvement may be realized by developing an understanding of the solidification of these single crystal parts and using this understanding to design an optimized control scheme. This work seeks to determine those factors which most strongly impact the solidification and then identify process modifications suitable to counteract detrimental effects. In order to allow the identification of such factors, a multi-faceted approach is to be employed. It is the target of this work to address those gains that may be realized by improved micro-structural control during the actual growth of the blade. For reasons which will be discussed later, the production of a uniform micro structure throughout the part is the desired outcome of this work.

The production of a uniform micro structure in conjunction with an elimination of solidification defects such as freckles and sliver grains is the ultimate goal of the process development efforts that occur whenever a new part is introduced into the foundry. However, in most cases the development of the production process for a single crystal part is largely an empirical effort. Often the production process is determined through trial and error wherein the part is cast, evaluated and cast again in an iterative cycle that can be lengthy and may not produce an optimum process. Part of the difficulty resides in the working assumption that the solidification interface remains located at the baffle between the hot and cold zones of the furnace. It will be shown that such an assumption is completely erroneous and that solidification conditions such as interface position, temperature gradient, and solidification rate are all a combined function of emissive heating, cooling, withdrawal rate and the heat released upon solidification. These various phenomena are closely coupled and interact with one another to form the solidification environment. An understanding of

these interactions could provide the process metallurgist with the means to control the micro structure while eliminating defects.

As an example, a common defect is grain misorientation. Grain misorientation is a situation where the crystallographic growth direction has deviated from the vertical axis of the part. This situation in and of itself is not reason for rejecting a part, however in cases where the crystallographic orientation results in a decrease in strength for the expected loading direction, the part must be rejected. Misorientations of this type must arise from a curved solidification interface. Since the solidification interface is perpendicular to the direction of heat flow, a curvature of the solidification interface can only occur if the heat flux is not flowing in a vertical direction. If it is considered that at the baffle between the hot and the cold zone the heat flux must be flowing vertically, then it follows that misorientation in the growth direction can only occur when the solidification interface has moved away from the baffle. It will be shown that the solidification interface has a tendency to move away from the baffle as the process progresses. Further, it will be shown that this motion is a natural consequence of the process and results in misorientation and an expanding primary dendrite arm spacing.

In the past, several closed loop control techniques have been employed in an effort to reduce the variations in the parts themselves, and from one mold to the next. The most prevalent technique keeps the mold heater temperature constant as the part is withdrawn. Typically this action requires a continuous increase in the power being delivered to the mold heater. If it is assumed that the diagonal view factors are not changing, then this increase in power must be attributed to a cooler part within the hot zone of the furnace. In fact, the diagonal view factors do change, but the average temperature of the part is going down as well. The drop in the average temperature of the part necessarily implies that the liquidus position relative to the baffle is (as stated above) increasing. Although this is a closed loop control system it clearly does not directly address the growth conditions at the solidification front.

Attempts at micro structural control have been made. These attempts have sought to control the gradient and the solidification rate in such a fashion so as to eliminate constitutional undercooling thereby ensuring a planar interface. However, the processing requirements necessary to accomplish this are shown to be unobtainable using industrial equipment. As a result, the control equations used have little meaning under production conditions. The development of the criteria necessary to ensure a constant primary dendrite arm spacing leads to an equation very different from that which has been previously suggested. However, the application of a methodology for

the control of the solidification and growth process requires a thorough knowledge of the solidification conditions and those parameters which might effect them. This knowledge is one of the goals of this work.

In order to further understand the manner in which the solidification environment is effected by various furnace parameters and conditions, a finite element model has been used to predict the temperature profiles in the solidifying part as a function of the withdrawal distance. The results of this model, when contrasted to the experimental and analytic results provide an additional level of verification that the major factors have been taken into consideration. Further, since many of the parameters are difficult to vary experimentally, a finite element model provides an ideal test bed for a parametric sensitivity study. As an example, the diameter of the mold heater used in the model can be modified and the associated effect on the solidification environment may be evaluated without the need for an expensive furnace reconfiguration.

Evaluation of the various parameters that occur as a result of the modeling effort also emphasizes the differences between a laboratory and production environment. A group of test bars on a mold in a large furnace is far different than a single bar in a small device. Laboratory devices typically have very tight baffles and use refractory tubes for molds. The tight baffle helps to increase the gradient and the tube molds often have a higher operating temperature than the investment casting mold materials. These differences allow a higher gradient to be applied. These higher gradients result from lower diagonal view factors and from the ability to obtain greater superheats as a result of the mold material. In addition, mold reactions may not be considered a problem for many of the solidification studies. Unfortunately, the equipment required to mimic the industrial environment must be of comparable scale to the industrial equipment. This is a natural result of the emissive nature of the heat transfer where geometric view factors have a major impact on the heat flows. Therefore a significant and relevant advantage of this study is that all of the solidification experiments were conducted on a full size piece of industrial equipment, using production mold materials and alloys, under production conditions.

Primary dendrite arm spacing was chosen as the primary means for the evaluation of the solidification conditions. As such a computer program was developed to automate the task of measuring these spacings. Computer techniques allowed a large number of primary dendrite arm spacings to be measured and thereby improved the accuracy of the statistics. In addition, many samples were cut from each bar, thereby

allowing an accurate determination of the manner in which the primary dendrite arm spacing changes throughout the process. The dendrite statistics have been combined with thermocouple data obtained during the solidification process in order to obtain a realistic view of the solidification environment during the process. These data were then compared to the modeling results for verification. As an additional check, Back-scattered Electron Kikuchi Patterns (BEKP) in the SEM were used to evaluate the liquidus shape. This extension of the BEKP technique proved to be a valuable tool for verification of the morphology of the solidification front. The combination of these techniques provides the means for a thorough evaluation of the solidification conditions. As a result a determination could be made as to whether or not the heat of solidification could be utilized as a means of effecting the solidification process.

The utilization of the heat of solidification as an integral part of the solidification process has not been previously proposed. However, as a result of this work, it is shown that the heat of solidification can have a major impact on the ultimate solidified micro structure. As such, process modifications can be made which take advantage of this heat in such fashion as to stabilize the solidification conditions. The modifications employed were in the form of a closed loop control scheme which continuously monitored the position of the solidification interface and adjusted the withdrawal rate to attempt to maintain the solidification interface at a constant position relative to the baffle. This action resulted in a variation in the solidification rate and hence a modification in the heat flux through the part as a result of the changing heat of solidification. Such an experiment was successfully implemented and the results are discussed. As previously mentioned, the manner in which the micro structure is related to the production environment and subsequent control of the process, is via primary dendrite arm spacing and the associated theory of dendrite growth.

A series of test molds, each containing twelve test bars were cast and solidified into single crystals. The test molds were processed under a matrix of varying conditions in order to allow the effect of individual processing parameters to be evaluated. Thermocouples were installed into some of the molds to enable an analysis of the thermal conditions throughout the solidification process and to facilitate a closed loop control method which is proposed to yield a more consistent solidification structure. From ten of the test molds, one bar each was selected for sectioning and the primary dendrite arm spacing was measured along the length of the bars. The thermal and micro structural data was combined with the results of a finite element model and

BEKP study to characterize the solidification response to the various process parameters.

The micro structural results of the proposed closed loop control method are contrasted to the more traditional process methodologies and the differences in the solidification response are correlated to characteristics associated with the solidification environment.

1.1 History of Single Crystals in Jet Engines

The jet engine is a device that has had a significant impact on the manner in which we view our world. With the advent of jet travel, distances have shrunk to the point where it is no longer considered a major undertaking to travel across the country or to another continent. Since the turn of the century, air travel, made possible by the jet engine, has resulted in transit times dropping from weeks to hours. Today's large commercial jetliners are all powered by sophisticated jet engines, the enabling technology which has made long distance travel a practical reality.

A jet engine functions by compressing atmospheric gasses and mixing them with the fuel in a combustor. The heat of combustion causes the gasses in the combustor to expand. These gasses flow through several sets of rotating blades and stationary vanes wherein the rotational speed necessary to drive the turbine is derived. Older jet engines developed thrust solely from the ejection of combustion gasses out the rear of the engine, whereas newer "high bypass" designs use the torque of the engine to drive a fan which provides considerable additional thrust.

Those turbine blades which are located immediately after the combustors are subjected to extreme heat loads and rotational stresses[1]. These parts are operating in an environment where the gas temperatures can actually exceed incipient melting and the survival of these parts is only possible due to extensive gas cooling. This cooling, while providing an environment that allows the blades to survive, also reduces the efficiency of the engine. In these parts an operating temperature difference of as little as 5° has a significant effect on the efficiency and hence the operating cost of the engine. As a result, a compromise is made such that the blade operates at the highest safe temperature possible. The two predominant factors which determine this temperature are creep strength and fatigue crack growth resistance. In order to maximize the operating temperature, directionally solidified or single crystal blades may be used for this application.

In 1982, single crystal parts were first flown in commercial engines as a component in Pratt & Whitney's JT9D-7R4 engine[2]. This occurrence represents the first known use of a single crystal component in a structural application. Since that time there has been a significant expansion of the use of single crystal parts in jet turbine engines both in military and commercial applications. At present all three of the major engine producers are designing single crystal parts into their new commercial engines, the GE 90, the PW4000 and the RR Trent. Once these engines are in full production, there will not be sufficient single crystal foundry capacity to meet the projected production requirements. One potential method for meeting this challenge is through improvements in the production process.

1.1.1 Development

For many years single crystals were considered as primarily a research tool for the study of material properties. Investigations into the mechanical, electrical, magnetic, acoustic and any other material property imaginable are simplified when investigated using single crystals. Since many of these properties may be anisotropic, parameters could be determined for the various discrete orientations and then averaged over many orientations to determine the polycrystalline response. Although a useful research tool, traditional thinking did not allow the consideration of the single crystals for structural applications due to their generally acknowledged poor mechanical strength. Prior to the development of single crystal structural alloys[3] the trend in high strength parts was towards finer grains which tended to provide better creep and fatigue crack growth properties than coarser grained specimens. Clearly single crystal parts represented a step in the wrong direction!

Despite conventional wisdom, the potential of single crystal structural parts was recognized as early as 1946. While commenting on the high temperature creep rupture behavior of polycrystalline cobalt-based alloys Professor N. J. Grant wrote "since failures in these materials occur between the grains, it is most desirable to have a coarse grain resulting in the least grain boundary area. If, in addition, one could control grain orientation, then the strongest alloy would occur. However at present...control of grain orientation is an impossibility and strictly a function of probability."[4]

What was considered impossible in 1946 is now accomplished on a regular basis and the resultant parts are called Uni-Directionally Solidified, UDS or DS for short. In a DS part all of the grain boundaries are parallel and aligned with the direction of

maximum stress. This results in a part which, when in use, has relatively small stresses normal to the grain boundaries. As a result, just as Grant predicted in 1946, grain boundary associated phenomenon are far less active and such parts exhibit superior creep and fatigue crack growth properties when compared to their polycrystalline cousins. However, within an engine, in addition to the axial stresses that result from the rotation of the engine, parts are subjected to significant transverse stresses as well.[5] These transverse stresses result from the passage of combustion gasses and from various vibrations. As a result, grain boundary strengtheners such as Hafnium are used in DS alloys to prevent longitudinal splitting of the blade.

An extension of the DS process resulted in parts comprised of but a single crystallographic orientation. The complete absence of grain boundaries in these parts effectively eliminates failure modes associated with inter granular phenomenon.

Such *single crystal* parts represent the state of the art in turbine components. Though they are significantly more costly to produce than their equiaxed counterparts, these components are able to perform under conditions which are far more severe. For example, single crystal parts are typically found immediately after the combustor where temperatures and stresses are greatest. Due to their great expense, any improvement in the process or it's associated yield would be of definite value. It is intended that this work should provide such an improvement. However, to ensure that the areas for potential improvement are well understood, a review of the metallurgical considerations is in order.

Chapter 2 Metallurgical Considerations

Single crystals components have several desirable properties that translate into significant advantages for some high temperature applications[6]. These advantages bring with them some increased processing difficulties and as a result, considerably greater expense on a component basis. The advantages of single crystal components are associated with their high temperature performance characteristics whereas the added costs of these parts arise from the prevention of defects of a class which are not relevant for conventionally cast equiaxed parts. This section will provide a brief overview of the advantages of single crystals for turbine applications and of the type of defects which must be prevented.

2.1 Advantages of Single Crystals

As previously mentioned the advantages to be obtained through the utilization of single crystals are a result of the complete absence of grain boundaries and their associated phenomena[7, 8]. At engine temperatures, thermally activated failure mechanisms are of particular importance, with creep[9,10] being of greatest concern. Figure 2.1 below shows the creep properties of MAR-M200 at 1255°K and 30 ksi for (a) conventionally cast, (b) columnar grain and (c) single crystal samples[11].

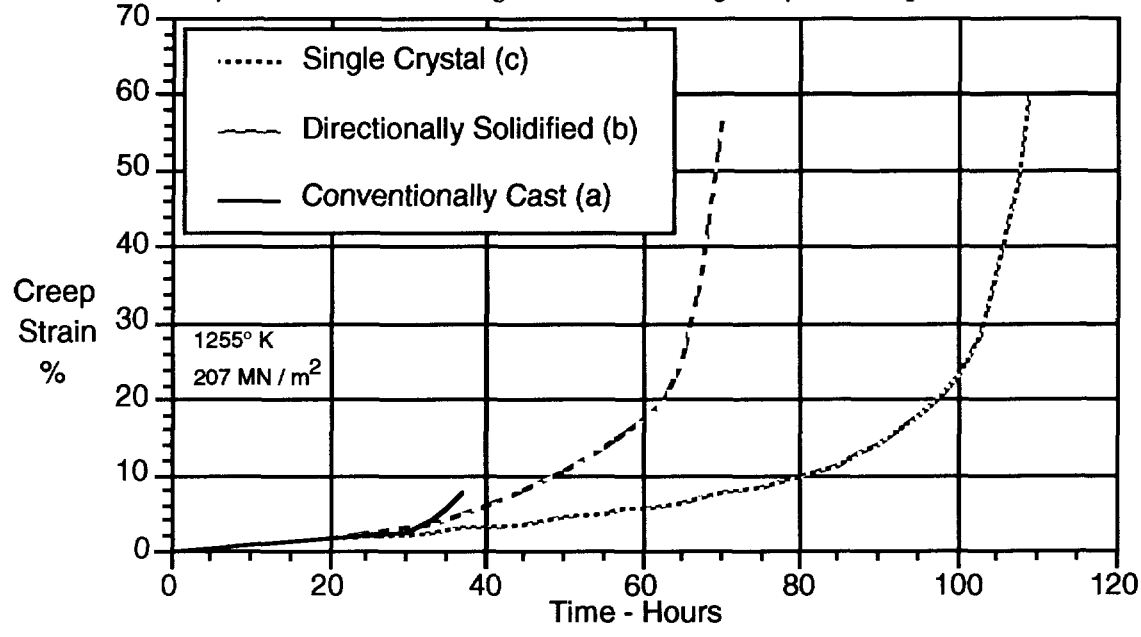

Figure 2.1
MAR-M200 Creep Characteristics

The single crystal sample (c) shows significant improvements over the other two. In sample (a), crack initiation and crack propagation along transverse grain boundaries causes the early onset of tertiary creep and subsequent failure. In the columnar grain material (b), cracks initiate on short transverse segments but cannot proceed before encountering a columnar boundary, and as a resulted there is a marked improvement[12]. With the single crystal material (c) cracks must initiate at microporosities within the material and even greater creep strength is observed. The greater high temperature creep strength of the single crystal material translates into higher temperature operations and results in higher fuel efficiencies as less bypass gas is needed to cool the parts.

The lack of grain boundaries in the single crystal material also provides significant advantages with regard to Low Cycle Fatigue[13, 14].(LCF). As in tertiary creep, crack initiation is more difficult in the single crystal material and crack propagation is unable to proceed along grain boundaries. The result is a material that has greater LCF characteristics than conventionally cast materials.

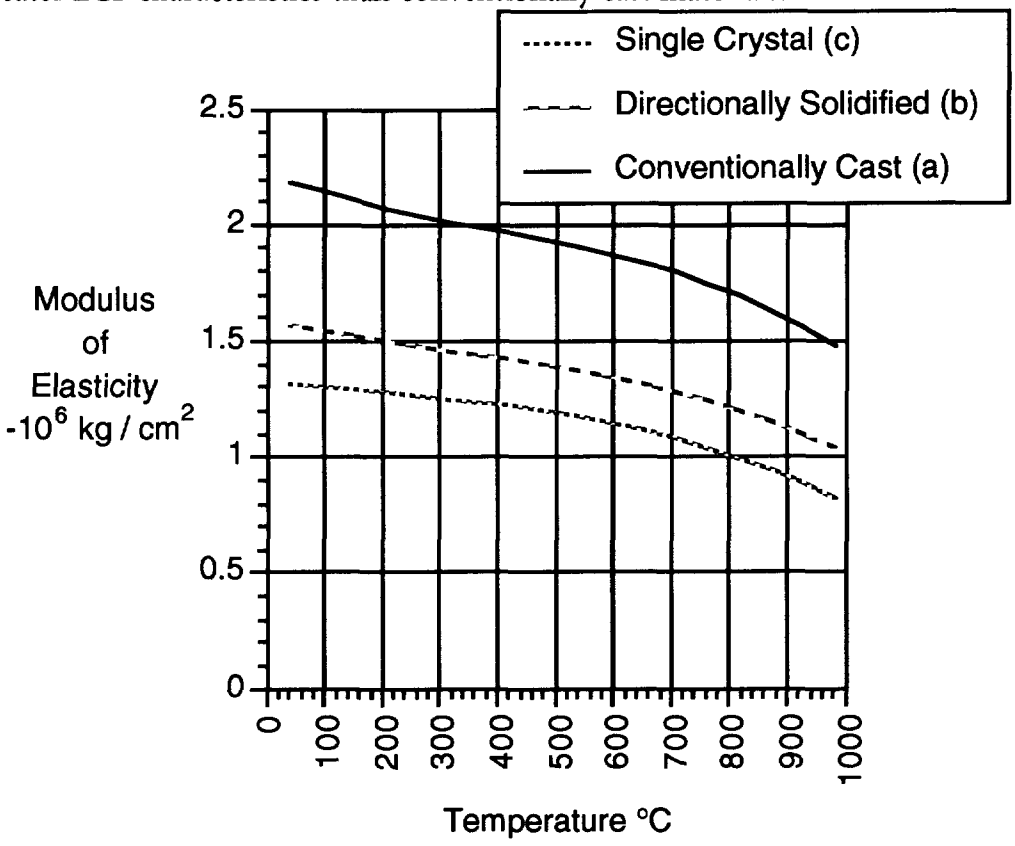

Figure 2.2
MAR-M200 Modulus of Elasticity vs. Temperature

An added advantage of the single crystal is a lower modulus of elasticity as shown in figure 2.2. This characteristic results in significantly improved thermal fatigue resistance and is another reason why single crystals are seeing increasing use for high temperature highly stressed parts.

Although single crystals have significant advantages over more conventional equiaxed parts, they may still suffer from various defects which can have disastrous effects on their properties.

2.2 Defects

All single crystal parts produced at a foundry ultimately fall into the two broad classifications of: Good Parts and Bad Parts. Bad parts are those within which some form of defect has been discovered. Defects may occur as a result of problems with the mold, such as core slippage, as a result of mechanical damage, or operator error. However in this work the concern is with those defects which may be termed solidification defects.

Solidification defects fall into three categories: Misorientation, Sliver Grains and Freckles. These defects may all occur as a result of improper furnace control during the solidification phase of the process. The implication is that these sorts of defects may be reduced through proper process control. In order to more fully appreciate the manner in which proper process control may impact the formation of these defects the mechanisms behind the formation of each of these defects will be discussed.

2.2.1 Misorientation

As previously mentioned creep life is one of the advantages obtained by using single crystal parts. For single crystal alloys, creep life is a strong function of stress orientation. As a result, a misorientation of the crystal such that the stress axis and the primary crystallographic axis do not line up, can have a drastic impact on creep properties[15]. Figure 2.3 below is an illustration of creep strength versus crystallographic orientation and illustrates this point.

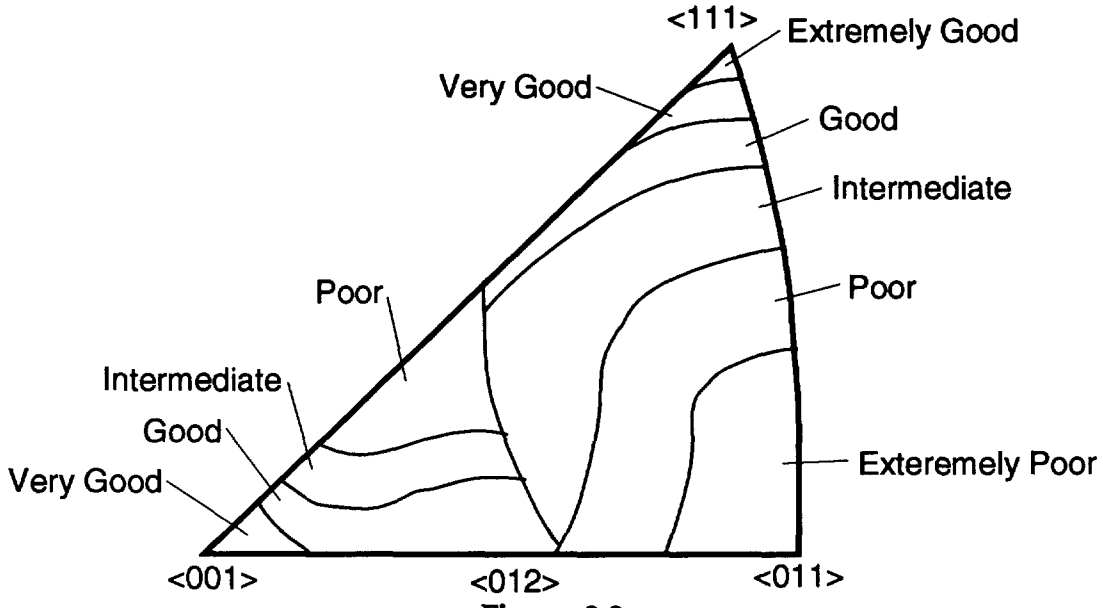

Figure 2.3
Creep Performance as a Function of Orientation

As shown above, the properties of single crystal parts can be extremely anisotropic. Therefore parts which deviate from the desired orientation (typically [001]) by more than some given angle are rejected.

The crystal selector at the bottom of the mold ensures that only a [001] orientation is present when the part begins to solidify. The propagation of this single orientation throughout the entire casting results in the single crystal component. During growth, the crystal is growing perpendicular to the solidification front, in line with the direction of heat flux. If the heat transfer is not down through the part, but is instead angled due to the position of the solidification interface within the apparatus, then the [001] crystal axis will bend away from the stress axis of the part.

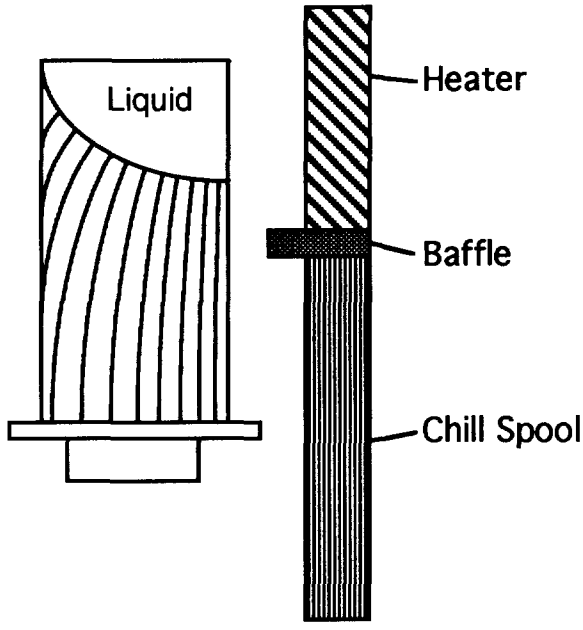

Figure 2.4
Growth Orientation at Later Stages

This type of problem typically occurs towards the later stages of solidification when the solidification interface has been pushed up into the hot zone, the mechanism behind this motion will be discussed later. This location results in a solidification interface wherein the crystals are growing toward the mold wall, and the temperature increases as the wall is approached. Grain misorientation problems could be significantly reduced by developing a control scheme that adjusts furnace parameters such that the solidification occurs only within a region of heat flow that is parallel to the stress axis of the part.

2.2.2 Sliver Grains

Sliver grains are grains of random orientation that have nucleated from the mold surface and grown into the part. As with misorientation, sliver grains are the result of a heat flux that is angled. In the case of sliver grains, the cause is typically a solidification interface that has been pushed down into the chill zone of the apparatus. When the solidification is occurring within the chill zone of the furnace (below the baffle), the heat flux is angled toward the mold wall. Contrary to the case of misorientation, the temperature decreases as the mold wall is approached and the crystal would normally try to grow away from the wall.

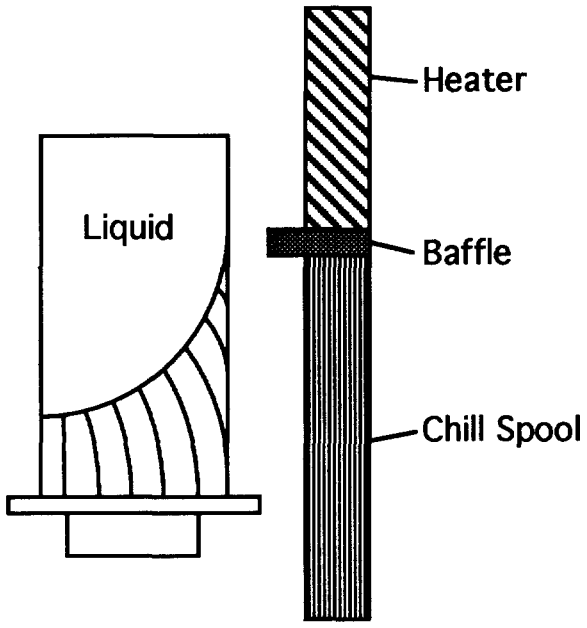

Figure 2.5
Curved Interface at Early Stages of Withdrawal

If the interface is sufficiently angled, then a condition exists which favors the nucleation of a stray grain from the mold wall. Under such conditions, the mold wall may actually become the growth substrate making random nucleation likely. A further consideration is that if the solidification interface is curved, the extent of compositional undercooling is not as great at the mold-metal boundary. This condition may result in a situation where the mold wall falls below the local liquidus; once again resulting in the nucleation of stray grains. The nucleation and growth of such a sliver grain ruins the part. Sliver grains could be significantly reduced by developing a control scheme that adjusts furnace parameters such that the solidification occurs only within a region of heat flow that is parallel to the stress axis of the part.

2.2.3 Freckles

Freckles are chains of small equiaxed grains that appear along the surface of the part. These grains are enriched in normally segregating elements. During solidification, light alloying elements such as aluminum or titanium may be rejected into the mushy interdendritic regions. The density gradient between the mushy zone and the still molten liquid can result in upward flowing jets of material from within the mushy zone into the liquid.[16] These jets break off the tips of secondary dendrite arms which are lifted up and form the basis of the freckles. Most such dendrite tips re-melt as they

are swept into areas of higher temperature. However, an upwardly curved interface can result in conditions which sweep such dendrite tips to the mold wall. It is proposed that the decrease in surface tension energy resulting from the contact with the mold wall stabilizes the broken off dendrites against the higher temperatures and allows them to survive until the solidification front has passed.

Freckles usually occur later in the process when it is proposed that the solidification zone has been pushed above the baffle and into a lower temperature gradient environment. This condition results in longer, more widely spaced dendrites. The more widely separated the primary dendrites, the deeper the mushy zone, the greater the compositional variation and the longer the secondary dendrites. The environment that favors the growth of long, widely spaced primary dendrites is therefore more favorable for the formation of buoyancy driven jets than that obtained when the primary dendrite arm spacing is small. Since primary dendrite arm spacing is a strong function of the temperature gradient at the solidification interface, freckles may be minimized by keeping the solidification gradient as high as possible.

An appropriately designed control scheme can help in minimizing freckles by keeping the gradient as high as possible. Properly configured such a system has the additional benefit of reducing misorientation and sliver grains as well.

2.3 Microstructure

The microstructure of single crystal alloys is a topic about which much has been written. For the purposes of this discussion, only those issues which may be directly effected by the solidification process need be considered. Given this caveat, the microstructural characteristic of the greatest importance is primary dendrite arm spacing.

Superalloys derive much of their strength as a result of the dispersion of fine precipitates throughout the material[17,18,19,20,21]. However, as discussed above, the composition of the crystal varies from dendrite tip to the interdendritic region. In order to achieve uniform mechanical properties through the part, the resultant part must be solution treated such that the composition is homogenized and the microstructure becomes uniform upon cooling. The length of the heat treatment is largely dependent on the time required to fully homogenize the part. The homogenization time is a direct function of the wavelength of the compositional variation, i.e. the primary dendrite arm spacing. Larger primary dendrite arm spacings

require longer heat treatments and subsequently add cost to the part. Additionally, the longer the heat treatment, the greater the likelihood that a defect may form.

As in the case of freckles, there are considerable advantages associated with higher gradients. From the microstructural standpoint, the higher gradients promote finer primary dendrite arm spacings thereby minimizing heat treatment times and the associated opportunity for the generation of defects. Here again, a control scheme that maximizes the gradients in the solidification region has some clear advantages.

2.4 Summary

The detrimental solidification artifacts discussed above are all effected by the solidification environment and hence can be controlled by properly controlling the solidification process. Fortunately, all of the above defects may be concurrently improved, a later discussion of the necessary considerations associated with the solidification process and control will deal with these matters in greater depth.

Chapter 3 Production Techniques

There are many ways of producing single crystals. In the laboratory, single crystals of alloys are usually produced as a cylinder. Crystal growth is accomplished be pulling the metal down from within a hot zone into a cold zone. The regular cylindrical shape has the advantage that it may be tightly baffled and as a result very high gradients may be imposed. Silicon and pure metals have the added advantage of solidifying at a single temperature. As a result, the solidification interface is more stable and there is no mushy zone. The lack of a mushy zone allows gradients to be smaller and the primary heat flow can be through the already formed crystal. These advantages allow such pure materials to be pulled vertically out of a molten pool of the parent alloy.

In the production of single crystal turbine blades the situation is different than either of the above cases[22]. The geometry of the blades is such that very tight baffling cannot be readily achieved. Further, in order to keep production costs down it is desirable to cast multiple parts simultaneously. Finally, since complex superalloys are typically used for these parts, significant differences between the liquidus and solidus exist and as a result gradients must be maximized. Clearly the equipment necessary to accomplish this growth must differ substantially from that used in the laboratory.

Figure 3.1. schematically illustrates the method by which single crystal components were first produced. This process is termed the "Power Down" process.

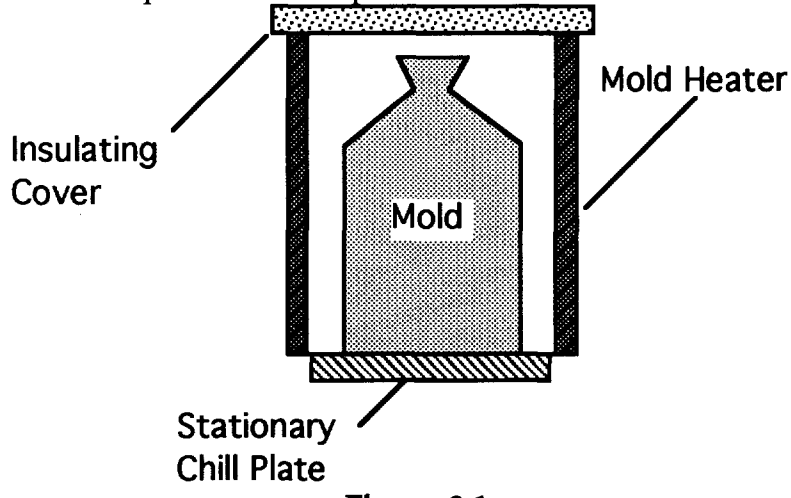

Figure 3.1
Power Down Technique

In the Power Down process, a mold, mounted on a water cooled copper chill plate, is heated in a mold heater. Once the mold has achieved a sufficiently high temperature, metal is poured into it. The metal flows down into the mold and through a crystal selector where it contacts the chill plate, beginning the solidification. This heat flow also sets up a vertical gradient through part. By lowering the mold heater power and hence the temperature of the mold environment, the emissive heat transfer into the part is reduced. In order to maintain a flux balance, the ΔT that existed prior to the reduction in temperature must be recovered. Such a recovery is achieved by the lowering of the average temperature of the mold surface. This reduction of temperature, when combined with the pre-existing temperature gradient, results in the temperature difference representing the solidification zone being swept up the part. In this fashion directional and hopefully single crystal growth is induced. This apparatus was later modified by the addition of a withdrawal mechanism. With this addition, the process became known as High Rate Solidification, otherwise known as HRS.[23]

The above described method, the HRS technique and all other methods in use today, when considered in a microstructural context, have an underlying philosophy of setting up the conditions and "letting it happen". An appropriate understanding of the process will allow the transition to a "make it happen" type of process. A review of the processes in use to day illustrates this point.

3.1 Analysis of Current Practices

As of this writing there are three production methods and one proposed method for the production of single crystal turbine components. These methods fall into two broad classes which shall be termed passive and active solidification. The passive methods rely on the characteristics of the mold and furnace to cause a solidification front to propagate through the part. The active methods pass the part through a temperature gradient wherein the solidification occurs. Each of the four methods and two classes have their advantages and disadvantages. Understanding the underlying principles associated with each methods development and assessing the 'typical' microstructure and common problems encountered in actual production is important to the establishment of a logical and effective control technology. Therefore each method will be described and evaluated in the following two subsections.

3.1.1 Passive Solidification Techniques

The two passive solidification techniques are termed Autonomous Directional Solidification and the Sulzer-MTU Process also known as Mold Integrated Heat Control. Of these only the Mold Integrated Heat Control Process is currently used in production. The Autonomous Directional Solidification technique has produced single crystals in the laboratory but has not been developed for commercial use. These techniques have two primary advantages and one significant limitation. The first advantage is mechanical simplicity. This reduced complexity translates directly into lower equipment costs. Both of these methods hold the mold static throughout the crystal growth phase, and it is the elimination of the mold withdrawal mechanism that results in a decrease in the complexity of the process. The second advantage is a decreased tendency for the growth direction to deviate from the vertical. This is a direct result of the lack of horizontal heat fluxes. However, because there is no mechanism for modifying the thermal conditions, the ever expanding thermal impedance of the previously solidified material requires that these techniques must always produce a changing primary dendrite arms spacing. This problem becomes magnified as the part sizes get larger and greater heat is released upon solidification. Beyond a certain limit it is not possible to maintain the gradient required to obtain good single crystal parts.

3.1.1.1 Mold Integrated Heat Control Process

The Mold Integrated Heat Control Process[24,25] may be successfully implemented in a standard equiax casting furnace. An equiax furnace is a piece of equipment designed to produce equiaxed fine grained turbine components. The equiax process is the manner in which the furnace is used to produce such parts. The primary difference between the HRS process and the equiax process is that the equiax process does not require a tightly controlled withdrawal mechanism or a mold heater. As a result the equipment required for the equiax process is less expensive. The relatively minor addition of a water cooled mold pedestal to such a furnace makes it suitable for the MIHC process. When compared to ADS and the active methods it is the only process that may be achieved without a mold heater in the furnace. As a result, this process is popular with investment casting foundries that do not have dedicated DS/SX furnaces. Figure 3.2 below is a schematic representation of the process.

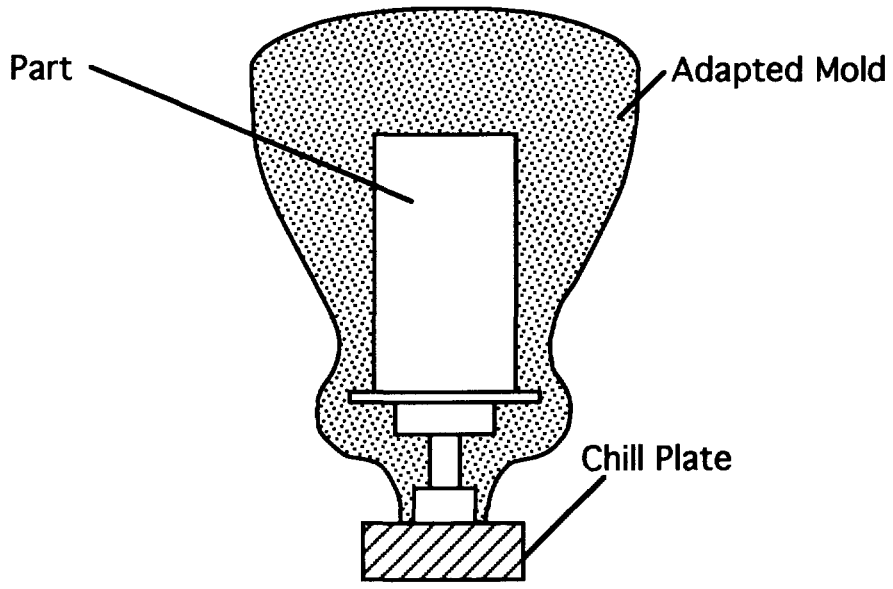

Figure 3.2
Mold Integrated Heat Control

In the MIHC process, a heavily insulated pre-heated mold is placed on a copper chill plate immediately prior to the pour. As in the equiax process, the mold must be placed in position very rapidly in order to avoid excessive cooling. This requires larger vacuum systems on the mold chamber than the other processes which have integral mold heaters. Once the mold chamber has been evacuated, the mold is rapidly traversed into the pouring position where it remains throughout the solidification portion of the cycle. Immediately after the mold has achieved its position, the metal is poured. The molten metal fills the mold and flows down through the crystal selector where the metal comes into contact with the water cooled copper chill plate thereby commencing solidification. The insulation around the mold directs the majority of the heat flow down through the part, through the selector and into the chill plate. A volume of excess metal is cast on top of the part tree to provide a heat reservoir.

Micrograph (a) Micrograph (b) Micrograph (c)

Figure 3.3
Sulzer Micrographs of MIHC Parts

The MIHC process was developed in Germany by the Sulzer corporation in conjunction with MTU. A Sulzer brochures claim that this is a high gradient process. As evidence they provide a set of three micrographs. Micrograph (a) is captioned "high temperature gradient dendrite spacing 0.35 mm." Micrograph (b) is captioned "low temperature gradient dendrite spacing 0.28 mm" and micrograph (c) is captioned "mold integrated heat control dendrite spacing 0.36 mm". Based on this evidence the process is termed a high gradient process. However since larger primary dendrite arm spacings typically result from *low* gradients it is difficult to understand how this conclusion was reached. As will be shown later, primary dendrite arm spacing *decreases* with increasing gradient. In fact, the MIHC process is a low gradient process, this result is expected merely from the limited heat transfer available down through the crystal selector and by the fact the process requires that the thermal path is continuously increasing.

Although proponents of this process claim that the crystals produced are comparable in quality to those obtained from withdrawal or active methods, such parts, when compared to active methods, exhibit greater variation in properties from root to tip. All of the heat of solidification must pass through the entire length of the previously solidified portion of the part. This ever expanding heat transfer path results in decreasing gradients throughout the solidification phase. As a result of these decreasing gradients, the primary dendrite arm spacing increases and the dendrite length increases as well. It is this change in primary dendrite arm spacing that results in the observed variation in properties. Although there is no mention in the literature, the lower gradients should result in an increase in dendrite length and hence a greater likelihood of the formation of freckles.

Ultimately for the MIHC process the main issue is not one of low gradient or high, but instead the fact the there is an ever changing gradient driving the solidification should be considered key. Under such an environment a consistent solidification structure is nearly impossible to attain.

3.1.1.2 Autonomous Directional Solidification

Autonomous Directional Solidification is a new passive technique being developed in Germany.[26] The process is similar to the Mold Integrated Heat Control Process in that the solidification occurs in a static mold. In contrast to the MIHC process an in-situ mold heater is used. The primary difference between ADS and

MIHC is that in ADS the intent is to undercool the liquid metal. Undercoolings of around 50°K are reported as typical.

In ADS, special molds with proprietary non-nucleating face coats are used. The mold heater holds the mold above the liquidus temperature of the alloy until casting is complete. Once the metal has been poured, the heaters are turned off and the metal begins to cool. A crystal selector is used at the bottom of the mold. "The isolated water cooled chill plate at the bottom of the shell mold ensures a small longitudinal temperature gradient...thus the nucleation appears at the coldest position within the foot of the turbine blade."[26] Figure 3.4 below is an illustration of the process.

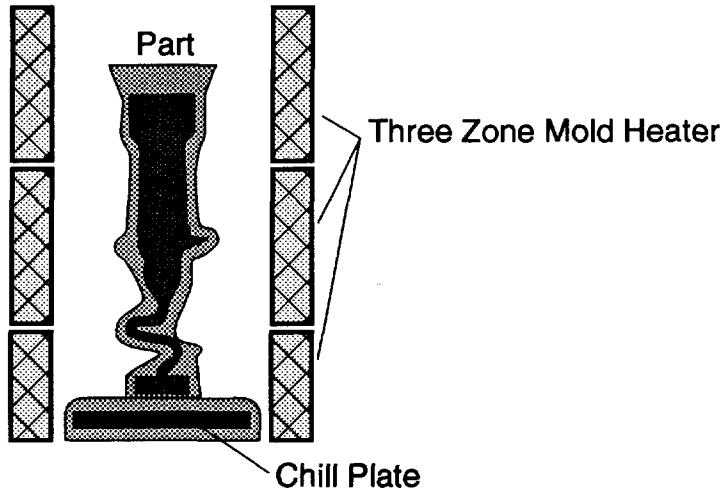

Figure 3.4
Autonomous Directional Solidification

When the metal reaches its maximum undercooling, solidification proceeds very rapidly through the selector and up through the bulk of the part. As with the MIHC process ADS boasts simplified equipment configurations. The ADS process would appear to be an improvement over the MIHC process in that heat transfer down through the part is not a limiting factor. At present however difficulties still exist in achieving the necessary degree of undercooling. The lack of non-nucleating mold materials and structural single crystal alloys that are highly undercoolable results in significant yield losses due to the nucleation of stray grains. The commercialization of this technology requires the development of different mold and alloy systems and certainly necessitates alloy cleanliness levels significantly greater than that available today. Although this process is promising, the technology must undergo significant development before it can achieve commercial success.

3.1.2 Active Solidification Techniques

The single crystal production techniques which have been termed *active*, are comprised of two processes which are currently used for production. Both techniques utilize mold heaters, baffles between a hot and cold zone, and both have a mechanism for moving the mold through a temperature gradient. The first method to be discussed, Liquid Metal Cooling, is used in Russia, whereas the High Rate Solidification Process, is used throughout the United States, Japan and much of Europe.

3.1.2.1 Liquid Metal Cooling

Liquid metal cooling is often considered a new technology from Russia. However, experiments with this technique were reported over 20 years ago by Gell, Sullivan and VerSnyder[27]. Figure 3.5 below is a representation of a typical apparatus used for this process.

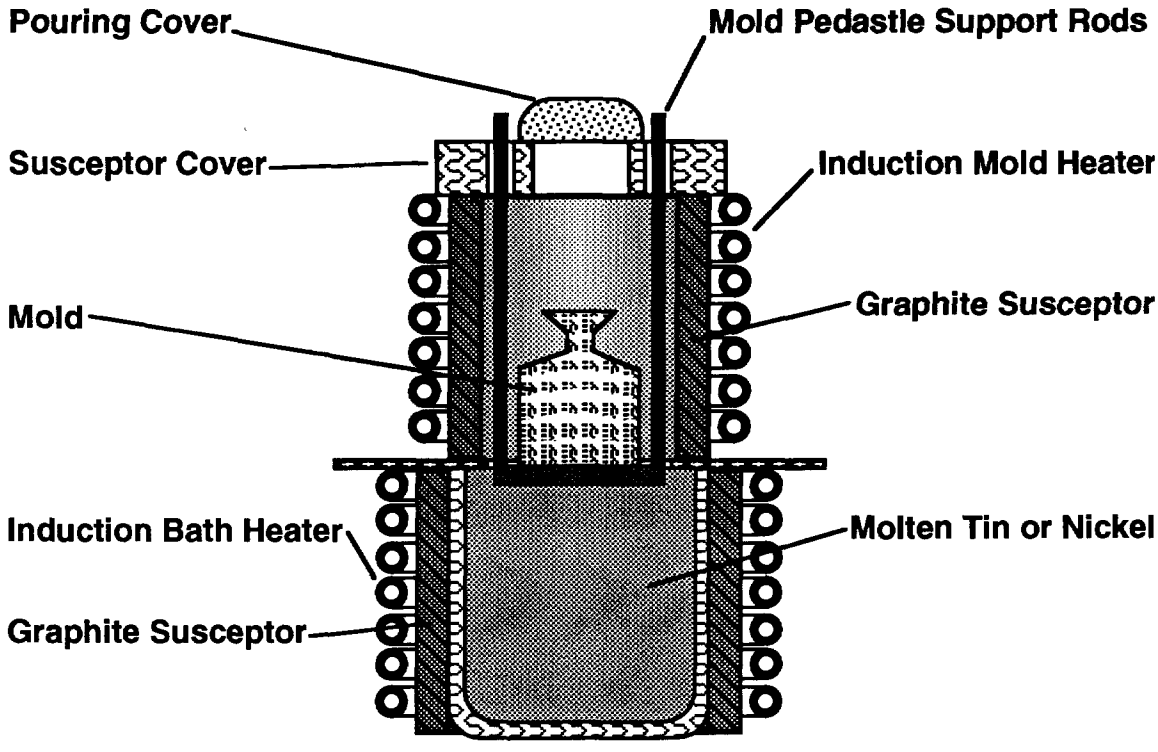

Figure 3.5
Liquid Metal Cooling

In this process the mold, which may be of a standard zirconia, is mounted on a tungsten chill plate. The chill plate is lowered until it is just immersed in a bath of molten tin. A mold heater is used to heat the mold up above the liquidus of the alloy to

be cast. A radiation baffle is placed between the liquid tin and the mold heater to insure that the tin does not overheat. Once the metal has been poured, the filled mold is gradually lowered into the molten tin bath. This action causes a solidification front to be swept through the part. The tin bath is continually stirred to prevent gradients from forming in the tin. LMC provides a very effective means of cooling the mold, however the reported gradients[28] in the metal are similar in magnitude to those found in the High Rate Solidification Process.

The gradients experienced by the parts in the LMC process are not higher than those in the HRS process because the HRS process is not cooling limited. In addition, the heat transfer out of the part is limited by conduction through the mold, not the cooling of it. So the intent of increasing the cooling is not readily realized through the use of this technique. In fact, it will be shown that excessive cooling can actually serve to *decrease* the gradient at the liquidus. The addition of liquid metal cooling therefore does not provide any significant contribution to the gradient. Liquid metal cooling does however increase the complexity of the process and introduce the additional complication of the liquid metal seeping into the mold through cracks and reacting with the part. For this reason, the molds utilized in the LMC process must be more robust, thereby further limiting the heat transfer.

The LMC process does have one distinct advantage in that the molten tin flows between the parts and as a result the parts experience uniform cooling around their entire circumference. This uniform cooling provides a flatter solidification interface than that found in the High Rate Solidification Process and crystal misorientation problems are lessened.

In the United States, LMC techniques have been abandoned in favor the High Rate Solidification Process. The liquid tin required for LMC presented an additional complication to an already complex process and provided insufficient gains to justify the expense.

3.1.2.2 High Rate Solidification Process

The High Rate Solidification Process[29] is the process that is most commonly used for the production of single crystal turbine blades. As with LMC and ADS a mold heater is used to bring the mold up to temperature. As with LMC once the part has been poured, it is pulled through an area of moderately high temperature gradient, typically between 2 and 15 °C/mm. This gradient is obtained by placing a radiation baffle between a hot zone which is kept at a temperature sufficient to keep the metal

liquid and a cold zone which is achieved with a water cooled sleeve, often termed a *chill spool.* Since the process occurs in a vacuum, the part experiences no convective cooling and in HRS the conductive cooling that occurs down through the helical starter may be neglected. For this reason, it is assumed that at the processing temperatures (1350 °C), radiation is the predominant mode of heat transfer. The parts themselves have a complex geometry which provides a complex surface area for radiation.

The outcome of this geometry is that a withdrawal profile sufficient to grow a good single crystal is a difficult empirical process at best. Not only is it possible to nucleate alternative orientations within the part, but the varying geometry can have an effect on the primary dendrite arm spacing and hence the wavelength of the compositional variations that occur during solidification. In order to ensure a homogeneous microstructure, the parts are subjected to a heat treatment after casting. The length of this heat treatment is largely determined by the greatest primary dendrite arm spacing; this spacing is in effect twice the diffusion distance necessary for homogenization. Unfortunately protracted heat treatment of the parts causes the microstructure to coarsen and increases the likelihood of the nucleation of stray grains. It is therefore desirable to produce parts with a constant fine primary dendrite arm spacing.

The HRS process is more mechanically complex than either ADS or MIHC, but less so than LMC. Unlike MIHC, it is possible to maintain a fairly uniform microstructure throughout the part and part sizes are only limited by the size of the solidification apparatus.

The HRS process has the greatest potential for crystal misorientation resulting from an angled solidification interface. The increased potential for misorientation, (>10° from <100>) is due to non-uniform circumferential heat flows that result from the presence of other parts on the mold tree. This problem has been successfully dealt with by proper mold design and production techniques, at present misorientation does not seem to be a critical concern.

Most of the single crystal parts manufactured in the world today are produced using HRS. HRS parts are superior to MIHC parts and not subject to process imposed geometry limitation. LMC appears capable of providing slightly better parts than HRS but at a cost and complexity that does not justify the process over HRS. ADS may ultimately provide a reasonable alternative to HRS but significant development efforts are still required.

For this work, attention will be focused on the HRS process although the results are equally applicable to LMC.

3.2 Equipment Configuration

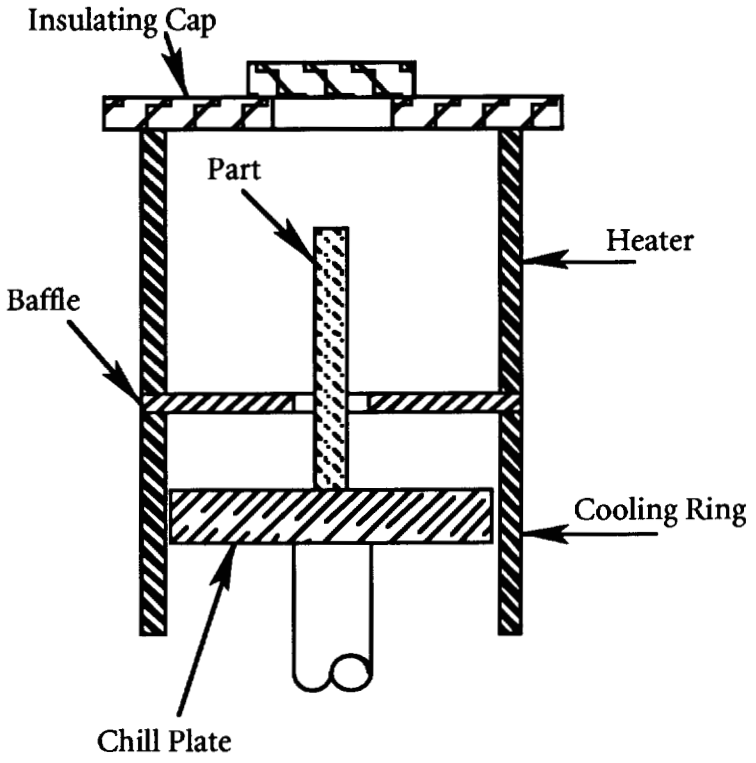

Figure 3.6
Present Day HRS Furnace Configuration

The above figure schematically illustrates the solidification section of a present day single crystal furnace utilizing the HRS technique. The mold is clamped onto the chill plate. The chill plate is initially set just below the baffle such that the mold is entirely within the heated section of the solidification hardware. Once the mold is in position the heater is energized and the mold is brought up to temperature, about 25°C above the alloy liquidus temperature. The insulating cap is opened and metal is poured into the mold. The metal is normally induction melted in a ceramic lined crucible then poured into the mold. The molten metal flows down through the mold and contacts the water cooled copper chill plate. At the bottom of the mold there is a crystal selector wherein the solidification begins. As the metal solidifies up through this section, the fastest growing crystallographic orientation is able to choke out slower growing grains and as a result, when the solidification front enters the part proper,

there is but one crystallographic orientation. It is the job of the furnace and associated control system to provide an environment where that single orientation is propagated through the entire part thus yielding a single crystal.

3.3 Control Considerations

The control of the growth of single crystal turbine blades is actually an attempt to monitor and modify the solidification environment wherein the growth of the crystal occurs. This "solidification environment" is characterized by a heat flux across the solidification interface. The "solidification interface" is that region of the system in which the metal undergoes a complete transition from a liquid to a solid phase. The heat flux through this region sets up a temperature gradient which defines the spatial dimension over which the material experiences the liquid to solid transformation. Discussion will follow which will detail the solidification phenomenon associated with the process; it is the intent of *this* section to describe the manner in which external variables are used to monitor and control the solidification environment.

Typically the manner in which the solidification front is moved through the part is primarily by means of a withdrawal process. During this process the power to the heater is controlled such that the temperature above the baffle is held constant. The temperature of the chill spool is also held constant. In this fashion a temperature gradient is established in the vicinity of the baffle. The part is withdrawn down into the furnace and as a result an area of high temperature gradient is swept up the part. The assumption is typically made that the solidification front is at the baffle and that the growth rate is equivalent to the withdrawal rate. As will be presented later, both of these assumptions are not true, however they are adequate for this discussion. It is recognized that part cross-sectional area does have an effect on the cooling and as a rule of thumb the velocity of the withdraw is often modified as a function of the cross sectional area of the part passing through the baffle.

During the withdrawal, the temperature in the heating section is typically held constant. Older techniques held the power constant, but it was found that yields were higher when the temperature was controlled. In production this results in a gradual increase of power to the heaters throughout the withdrawal. This increase in power has generally been assumed to be due to increasing diagonal view factors, however later discussions will show that geometric radiation effects play a more critical role.

This process may now be broken up into several subsystems. In its simplest form, the subsystems are: Cooling Ring control, Heater control, and Withdrawal control.

The control of the cooling ring will be discussed first as it is by far the most straightforward. The cooling ring is a large water cooled copper ring. It is fed by water which is held at a constant temperature. It requires 4180 Joules to heat a liter of water 1°C. A typical flow through a cooling ring is on the order of 120 liters/minute. As a result, 501,600 Joules per minute are required to effect a 1°C temperature rise in this flow. This number corresponds to 8.36 kW. The power necessary to keep the heater at temperature during withdrawal varies from about 10 kW at the beginning of the process to around 60 kW at the end. This corresponds to a temperature rise in the cooling ring water that varies from 1 to 7 °C. If it is assumed that the cooling water is at 30°C initially and that the hot mold is at 1400°C then the change in heat transfer as a result of the change in water temperature is less than 1%. Since the change is gradual and since other parameters such as mold thickness, instrumentation accuracy and power supply control typically have greater variability than 1%, control of the water temperature is neglected. In this case the system is run "Open loop". In other words no attempt is made to maintain the cooling ring at a constant temperature.

The Temperature Control subsystem can vary from a simple control scheme to one that is moderately complex. In its simplest form, the temperature at a fixed location within the mold heater is held constant throughout the withdrawal process. As previously mentioned, this results in a gradual increase in the heater power as the withdrawal progresses. An alternative approach is to attempt to use the mold power to keep the gradient at the solidification interface constant. However in practice, such a scheme is not feasible as there is insufficient temperature margin to affect much change before temperature limitations of the mold are encountered. Further complications arise when consideration is given to the loss of volatile alloying elements. The rate of loss of these elements increases with temperature and the total loss increases with time. The result of such a loss is that the last portion of the part to solidify may be depleted in these constituents. Clearly a control scheme that increases processing temperatures towards the later stages of the cycle will be prone to aggravated loss of volatile constituents. At present, the most prevalent practice is to hold the temperature constant.

In the most recent generation of single crystal furnaces, the mold heater is actually a pair of heaters each with its own set of control thermocouples. This is due to

the observation that even if the temperature near the baffle is held constant, the heat flux from the top portion of the mold heater may still be sufficient to overheat the mold and cause significant alloy loss. By placing two heaters into the system, the portion of the apparatus just above the baffle may be held at a constant temperature while the top portion of the system is restrained from overheating by a reduction in the heat flux. Thus the additional heat required near the baffle to overcome the cooling effect of the part that extends into the cold zone is overcome with local heating thereby avoiding excessive heating of the top of the part. However the upper heaters are still available to provide a constant temperature environment for the preheat of the mold. Typically the mold heaters are divided such that 1/3 of the total heating area is associated with the bottom heater and the remainder with the top. The control thermocouple for the top heater is often placed in the center of the top heater's zone whereas the control thermocouple for the bottom zone is placed near the baffle.

The control of these heaters can be challenging if there is a requirement to control the temperature from room temperature up to 1400°C. This is due to the change of heat transfer regimes. In a vacuum, the predominant mode of heat transfer at room temperature is conduction and the heat transfer is a linear function of ΔT. However at 1400°C the predominate mode of heat transfer is radiation and the flux is proportional to ΔT^4. As a result, the response times are significantly shorter at the higher temperatures. This response time may be considered a phase lag between the input (heating or cooling) and the output (part temperature).

The phase lag is readily visualized by imagining a sinusoidal excitation of the heater and the response of the part to that excitation. The response time of the system results in a time lag between the heater temperature and that of the part. If the excitation and response are plotted in time, the time difference between the two may be expressed as a fraction of the sinusoidal excitation cycle and readily expressed as an angular offset. This offset is termed the "phase angle". The phase angle between the excitation and the response varies with frequency and the phase angle typically increases with increasing frequency; this is a natural result of the previously mentioned time lag. Phase angles greater than 180° are unstable if the loop gain of the system is greater than unity. This may be understood by considering that at a 180° phase shift, negative feedback becomes positive and hence the system is driven unstable. A stable system therefore requires that at the frequency where the phase shift reaches 180°, the loop gain must be less than one. As a result, a responsive system has a smaller phase shift at any given frequency than a less responsive system and may therefore be

operated at higher gains thus providing tighter control. It is then immediately obvious that a system response that varies from a linear relationship to a fourth power relationship will require variable tuning parameters in the control loop if maximally tight, stable control is to be achieved throughout the temperature range.

Recent production furnaces have as many as five sets of tuning parameters to accomplish this type of control. Fortunately the system is at its most responsive in the operating region that applies during the withdrawal cycle. This allows the implementation of control loop with sufficient gain to achieve satisfactory control within the accuracy of the feedback elements (thermocouples). As a result, the temperature control of the system is readily achieved with off the shelf control packages and sufficient gain may be used to keep the system within .1% of set-point.

Withdrawal Control System

The withdrawal control system is a nested control scheme consisting of a motion control loop nested within a reference generating loop. The inner, motion control loop provides the excitation to drive the system to the value specified by the reference. The reference generator responds to operator input or alternatively to other feedback as obtained by the system.

The motion control loop is most often a servo system. Two types of loops have been used, position and velocity. Although velocity systems have been widely used, they are not well suited for this application. The deficiency of a velocity based withdrawal system arises from the very nature of the servo system itself and is a function of the feedback / response system. In a velocity loop the feedback element is a tachometer which provides a velocity signal that is compared to a reference thus generating an error signal. In its simplest form this error signal is amplified and used to generate the drive signal for the velocity actuator in the system. This type of system is termed a proportional controller.

The basic proportional control loop may be modified and an "integral" term may be added. The integral term offsets the output until the error signal becomes zero. This sort of device is termed a P I controller. By adding an additional offset when the feedback signal is changing rapidly the controller becomes a P I D controller with the D standing for derivative.

However, regardless of the type of controller used, there are periods where there is an error between the reference and the feedback signal. In a velocity loop this implies that the withdrawal mechanism is not moving at the specified velocity. The

result is a position error that accumulates with time. A turbine blade has a complex geometry containing step changes in cross section. It is desirable to produce velocity changes at these cross sectional variations such that the crystal will be allowed ample opportunity for horizontal propagation. Therefore the accumulating errors associated with a velocity loop may result in the required velocity change occuring after the geometric feature has passed.

A position loop does not have the problems of a velocity loop. In a position loop the feedback element is a position transducer and the withdrawal is accomplished with a micro-stepped position reference. Although an error is required to provide sufficient drive, this error manifests itself as a fixed, non varying position offset which is negligible when compared to the geometry of the system. This offset may be compensated for with an integral term, however in practice this is not necessary. In the position controlled scheme, the reference signal that is input by the user may still be a velocity, and typically the user will specify a distance over which this velocity may be applied. During operation, the position is recalculated at each time increment thereby avoiding round off error that might otherwise occur if a fixed step size were added to the previous position reference.

The most common withdrawal profile is nothing more than a table of velocities and the positions of the velocity transitions. This method does not take into account any additional process feedback and requires significant empirical effort. An alternative method involves utilizing additional information garnered from the process in an effort to optimize the withdrawal profile based on the real-time conditions of the system. It is a loop of this type which is the concern of this work and as such will be discussed later in more detail.

Chapter 4 Current Control Strategies

Numerous articles have been written on the proper technique for growing single crystal turbine blades. Perhaps the most prevalent control mechanism that has been proposed is expressed by the equation[30 31]:

$$k = \frac{G}{R} \tag{1}$$

Where k is a constant dependent on the alloy, G is the gradient at the solidification front and R is the growth rate. The ratio G/R is regularly used to describe the solidification environment[32]. It implies that optimum crystal growth will occur when G and R are varied in such a fashion as to keep the above relationship equal to a constant. In practice this requires measuring the gradient and solidification rate on a continuous basis. Past implementations have made the simplifying assumption that the solidification rate is equivalent to the withdrawal rate. Unfortunately this is only true in a macroscopic sense and does not take into account the effects of the rapid geometrical changes that are typical of turbine blades.

Measuring the gradient is a challenging task as it is typically achieved with an array of precisely located thermocouples. The six thermocouples with temperatures closest to the average of the liquidus and solidus temperature are then fit via a least squares algorithm[33] to a pair of cubic equations of the form:

$$x = f^3(T) \tag{2}$$

$$T = f^3(x) \tag{3}$$

Equation 3, which is an expression for the temperature of the part as a function of the distance from the base of the part, may be differentiated with respect to x to provide:

$$\left(\frac{\partial T}{\partial x}\right) = f^{3'}(x)$$

$$\left(\frac{\partial T}{\partial x}\right) = 3ax^2 + 2bx + c \tag{4}$$

Equation 4 is an expression for the gradient within the part at a location **x**. Equation 2 then is evaluated using the average of the liquidus and solidus temperature for **T**. This operation yields the approximate position of the center of the solidification zone interface. Once the position of the solidification interface is known, equation 4 may be evaluated using this location thereby obtaining the temperature gradient at the solidification interface. While evaluation of the gradient in this fashion is effective, it is also expensive. It requires a large number of high temperature thermocouples, many of which may fail and which are ultimately usable for only one run. It is therefore desirable to use the thermocouples to define a withdrawal profile which may then be "played back" for the processing of production parts.

In practice, implementing the control scheme is difficult because of the manner in which **G** and **R** are inter-related. A change in the temperature of the hot portion of the solidification apparatus also causes at least a momentary change in the solidification rate, whereas a change in the solidification rate requires that a new steady state position of the solidification interface relative to the baffle achieved. Since the gradient is highly dependent on the geometry of the solidification apparatus, any change in withdrawal rate results in a change of gradient as well. Such a situation provides a challenging control problem which is somewhat compounded by the temperature limitations that are imposed on the hot section of the solidification hardware.

The hot portion of the solidification device is limited to temperatures which are bounded on the lower end by the solidification characteristics of the alloy, and on the upper end by the working temperature of the ceramic mold material and the volatility of some of the alloying constituents. In actual practice there is very little that can be done by using the power to modify the gradient within the furnace and in most cases the mold heater is controlled to provide a relatively constant temperature above the baffle.

By holding the temperature constant, it is then possible to control a process such that **G/R** is constant. This procedure does not in general produce good parts and the reason that this is so may be seen by evaluating the basis of this control equation.

4.1 Analysis of G/R Techniques

To evaluate the basis of the **K=G/R** equation, the solidification phenomena that occur at the liquid solid interface must be examined. This examination is accomplished via the use of Fick's second law (5). However, before Fick's second law may be effectively applied, it must be transformed into a form that is applicable for the case of

a moving reference frame. Such a transformation allows the subsequent analysis to be pinned to this interface and therefore the coordinate system describes conditions at positions relative to the point of solidification. The analysis, and hence the transformation makes the simplifying assumption that the problem is that of the solidification of an infinite plane. Therefore all edge effects are eliminated and the coordinate system is reduced to a single spatial dimension, perpendicular to the solidification plane.

A further simplifying assumption is that convection and buoyancy flows are not significant. This assumption is in fact not valid[34], in production where compositional convection does occur, the finite volume of molten metal allows solute enrichment in the liquid to become a factor. However, as the intent of the discussion is merely to illustrate the theoretical basis behind a relationship that is commonly utilized, the assumption does not prove to be detrimental. The following derivations of control equations are after the work of Kurz and Fisher[35] and their work provides the primary theoretical basis for this discussion.

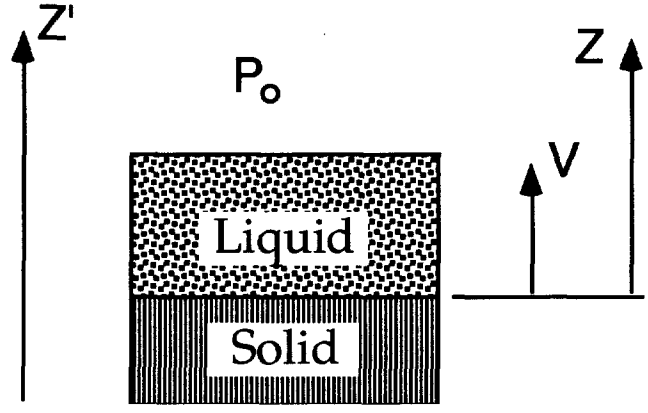

Figure 4.1
Moving Reference Frame

Figure 4.1 above illustrates the concept of the moving reference frame. Z′ is the coordinate axis of a stationary observer and the axis for the usual expression of Fick's second law (equation 5).

$$\frac{\partial^2 C}{\partial z^2} = \frac{1}{D}\frac{\partial C}{\partial t} \qquad (5)$$

The position of a stationary point, P, with respect to a stationary observer is therefore z′. The coordinate axis Z is an axis with its origin pinned to the solidification interface. The position of point P with respect to the moving axis Z may be expressed by the equation 6 in which "V" is velocity and "t" is time.:

$$z = z' - Vt \tag{6}$$

This expression (equation 6) is the necessary relationship to transform Eq. 5 into a form suitable for a moving reference frame. The first operation is to develop an expression for the left side of (5). This is accomplished below and results in equation 7:

$$\frac{\partial z}{\partial z'} = 1$$
$$\frac{\partial C}{\partial z'} = \left(\frac{\partial C}{\partial z}\right)\left(\frac{\partial z}{\partial z'}\right) = \frac{\partial C}{\partial z}$$
$$\frac{\partial^2 C}{\partial z'^2} = \frac{\partial^2 C}{\partial z^2} \tag{7}$$

The transformation expressed in (8) must next be accomplished in order to complete the expression for Fick's second law.

$$C = f(z', t) \rightarrow C = f(z(t), t) \tag{8}$$

Using the chain rule it is possible to write:

$$\frac{dC}{dt} = \frac{\partial C}{\partial z}\frac{dz}{dt} + \frac{\partial C}{\partial t} \tag{9}$$

and from (6):

$$\frac{dz}{dt} = -V \tag{10}$$

The combination of (7), (9) and (10) allows Fick's second law to be re-written as:

$$\frac{\partial^2 C}{\partial z^2} = \frac{-V}{D}\left(\frac{\partial C}{\partial z} + \frac{\partial C}{\partial t}\right) \tag{11}$$

Consideration of equation 11 above yields the realization that in the steady state case of interest, the concentration at any given point relative to the axis Z is invariant with time and therefore the proper expression for this instance of Fick's second law is:

$$\frac{\partial^2 C}{\partial z^2} - \frac{V}{D}\frac{\partial C}{\partial z} = 0 \qquad (12)$$

Equation 12 is the appropriate expression for Fick's second law. Equations of this form have well characterized solutions and are most easily solved through the use of a trial solution.[36] In order to solve this equation, a trial solution is assumed such that the concentration C in advance of the interface will be of the form:

$$C = e^{bz} \qquad (13)$$

The trail solution is only valid if, after differentiation, the roots of b from the trial solution are real. Substituting the expression for C of (13) into (12) then yields:

$$b^2 e^{bz} + \frac{Vb}{D} e^{bz} = 0$$

$$b = 0, b = -\frac{V}{D} \qquad (14)$$

Since the roots for b are real the trial solution is valid. By inspection only one of the values for b in (14) above provides any information and so the solution for (12) may be written:

$$C = A + Be^{-\left(\frac{Vz}{D}\right)} \qquad (15)$$

To evaluate the boundary conditions which will yield a complete solution of (15), a further simplification is made. For the purposes of this analysis it is assumed that the diffusion of solute in the solid material is very slow when compared to the solidification rate and the liquid diffusion rate. In fact, the difference in the solute diffusion rates of the liquid to the solid is typically on the order of 3 to 4 orders of magnitude and therefore for the purpose of this analysis it may be assumed that there is no compositional variation in the solid past the initial transient. With this

assumption in mind, the solution is therefore only valid for positive values of z, that is to say, within the liquid.

In order to obtain the complete solution, **A** and **B** in (15) must be evaluated. This is achieved by examination of the boundary conditions. The left hand side of figure 4.2 depicts a section of a phase diagram representing eutectic solidification. For a liquid of nominal composition C_0, steady state solidification must ultimately produce a solid of the same composition. By inspection of the phase diagram, a solid of composition C_0 must be forming from a liquid of composition C_0/k. There is then a boundary layer in advance of the interface into which solute is being rejected such that ultimately, at the solidification interface itself the composition of the liquid is C_0/k. This situation is described schematically in the diagram on the right hand side of figure 4.2.

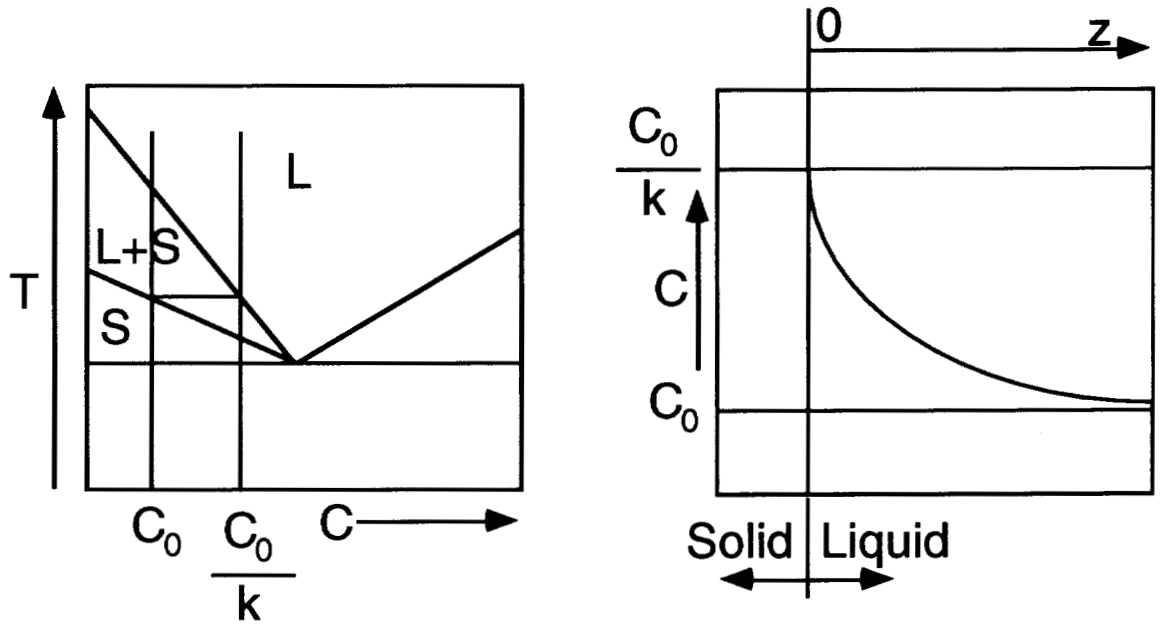

Figure 4.2
Eutectic Solidification

Evaluation of the boundary conditions is therefore straightforward. At $z = \infty$, the composition of the liquid must be C_0, whereas as previously described, the composition of the liquid at $z = 0$ is C_0/k. The complete expression for the composition of the liquid as a function of the distance away from the solidification interface may be written:

$$C = C_0 + \left(\frac{C_0}{k} - C_0\right)e^{-\left(\frac{Vz}{D}\right)} \tag{16}$$

Equation 16 implies that there is an exponentially decreasing composition gradient in advance of the solidification interface. If the liquidus temperature is linearly decreasing with composition as shown in figure 4.3, then the liquidus temperature of the alloy within the diffusion boundary layer is as shown in figure 4.3 by the line labeled T_L.

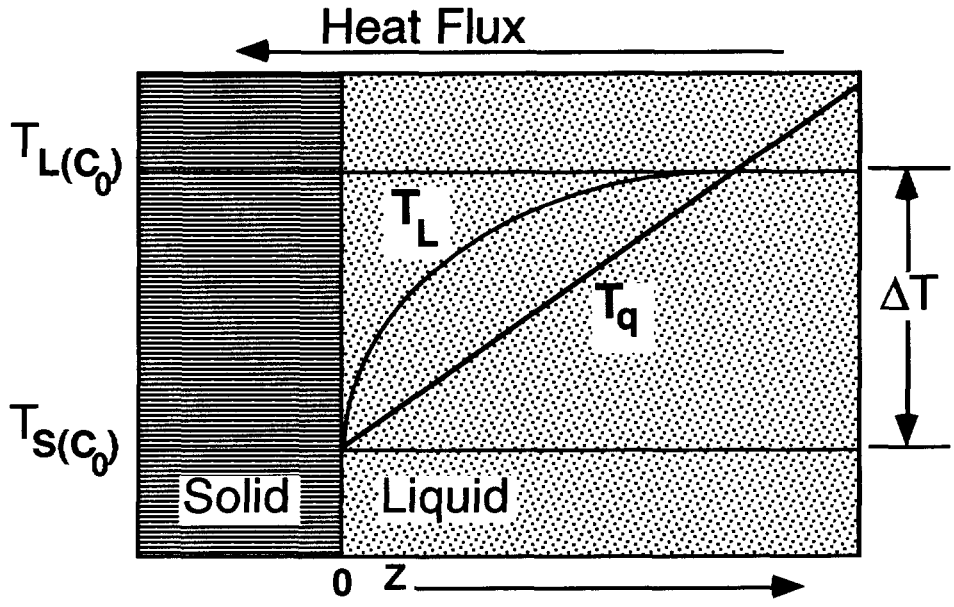

Figure 4.3
Constitutional Undercooling

For solidification to occur, heat must be extracted from the system. In the case of the growth of single crystals as described, the heat flux is in the -z direction. Although in the actual furnace environment the heat flux through the part may have horizontal components, the dendritic growth is still perpendicular to the heat flow. As the expressions for the concentration are pinned to the interface, z is in fact a coordinate axis which is perpendicular to that interface and therefore for the purpose of this analysis the macroscopic direction of the heat flux may be ignored. The heat flux that is passing through the part is in part a function of the thermal conductivity of the material. Since the alloy has a finite thermal conductivity, this flux creates a gradient in the material through which it flows. The temperature gradient that results from the heat removal in the system is illustrated by the line T_q and shown in figure 4.3. The slope of Tq is the temperature gradient in the region of the solidification

interface and is a function of the solidification environment. From figure 4.3 it may be seen that for the liquid in advance of the solidification front, the liquidus temperature, due to the compositional variation, may increase more rapidly than the liquid metal temperature increase that occurs as a result of the temperature gradient. This situation results in a region of liquid metal which is undercooled with respect to the local liquidus temperature in front of the solidification interface. This phenomena is termed constitutional undercooling. Convex perturbations of the solid / liquid interface into the molten metal can extend rapidly under these conditions. This extension occurs because the perturbation is growing into a region where the interface is increasingly undercooled with respect to the local liquidus temperature. Therefore in order to ensure that the planar interface remains stable, the temperature gradient in the region of the solidification front must be sufficiently high to preclude any constitutional undercooling.

In order to evaluate the temperature gradient which must be maintained to preclude interface instabilities that are a result of constitutional undercooling, it is first necessary to obtain an expression for the liquidus temperature in advance of the interface. From figure 4.3, the temperature of the liquidus as a function of composition has the form:

$$T_L(c) = m_c c + T_0 \tag{17}$$

and by inspection m_c must be:

$$m_c = \frac{T_L - T_s}{\frac{C_0}{k} - C_0} = \frac{\Delta T}{\frac{C_0}{k} - C_0} \tag{18}$$

In addition, T_0 from (17) may be solved for by substituting m_c from (18) into (17) and solving with $T = T_L$ and $c = C_0$. This operation leaves an expression for T_0 of:

$$T_0 = T_L - \left(\frac{\Delta T}{\frac{C_0}{k} - C_0} \right) \tag{19}$$

Combining (18) and (19) into (17) provides the solution that:

$$T = \left(\frac{\Delta T}{\frac{C_0}{k} - C_0} \right) c + T_L - \left(\frac{\Delta T C_0}{\frac{C_0}{k} - C_0} \right) \quad (20)$$

Recalling that (16) is an expression for the composition of the liquid in advance of the interface, equation 16 may be substituted into (20) in place of the variable c. Performing this substitution and simplifying produces an expression for the liquidus temperature in advance of the interface as a function of distance. This expression is shown in (21).

$$T_L = T_{L(C_o)} - \Delta T e^{-\left(\frac{Vz}{D}\right)} \quad (21)$$

The expression for the temperature of the molten metal in advance of the interface is a function of the gradient and easily written as:

$$T_q = T_{S(C_o)} + Gz \quad (22)$$

Equation 21 is an expression for the liquidus temperature in advance of the solidification interface as a function z and equation 22 is an expression for the liquid metal temperature in front of the interface as a function of the temperature gradient G and the distance from the interface z. Equation 23, which is the difference between (21) and (22), therefore describes the undercooling of the liquid metal as a function of the distance in advance of the interface.

$$T_U = \Delta T\left(1 - e^{-\left(\frac{Vz}{D}\right)}\right) - Gz \quad (23)$$

It is reasonable to argue that if there is no position in advance of the interface where the liquid metal is undercooled, then a planar interface will be stable. If (23) is differentiated the result is Eq. 24. Equation 24 represents the slope of the undercooling function; if at all times this slope is less than zero, then none of the liquid will be undercooled.

$$\frac{dT_U}{dz} = \frac{\Delta T V}{D} e^{-\left(\frac{Vz}{D}\right)} - G \quad (24)$$

The exponential in (24) has its maximum value at z = 0. It may therefore be written that the condition for the stability of a planar interface is:

$$G \geq \frac{\Delta T V}{D} \tag{25}$$

This necessarily neglects the fact that the suppression of the melting point that occurs due to the curvature of an interface can have a local stabilizing effect that will allow some perturbations to exist[37]. This aspect will be reviewed shortly; however it will be shown that for practical processing conditions, such perturbations are not significant.

Equation 25 may be re-written into (26) by combining the alloy dependent values of ΔT and D into a single constant K. The result, equation 26, is in fact the same as Equation 1 with the only difference being that the interface velocity V has been used instead of the solidification rate R.

$$K = \frac{G}{V} \tag{26}$$

Equation 26 does in fact represent a valid criterion for planar interface stability in a eutectic alloy. Unfortunately, when physical values are used for evaluation of the equation, the gradients required for stability are unobtainably high. Figure 4.4 is an example of the gradient required to insure a planar solidification in an Aluminum alloy with 2.5 atomic percent copper.

$$\left.\begin{aligned} D_L &= .003 \frac{mm^2}{s} \\ \Delta T &= 100^\circ K \\ V &= .085 \frac{mm}{s} \end{aligned}\right\} G \approx 2800 \frac{^\circ K}{mm}$$

Figure 4.4
Gradient Calculation

Clearly gradients of this magnitude are not readily achievable in most equipment that is available for the commercial production of single crystal turbine blades.

As it is apparent that a planar interface does not represent a reasonable morphology for the solidification front, it has been proposed that the solidification environment be controlled such that the dimensions of the dendrites are maintained at

a length roughly equivalent to the diffusion boundary layer thickness. The rationale behind such a strategy is based largely upon the desire to keep the dendrites as short as possible. The above conditions which produce short dendrites are typified by small local solidification times. This environment provides little opportunity for horizontal growth. As a result, shorter dendrites are spaced closer together and hence an environment that produces shorter dendrites provides a finer microstructure. Given that there is a composition gradient in advance of the solidification interface, it may be said that to a gross approximation the shortest dendrite that could be obtained can be no shorter than the diffusion boundary layer thickness.

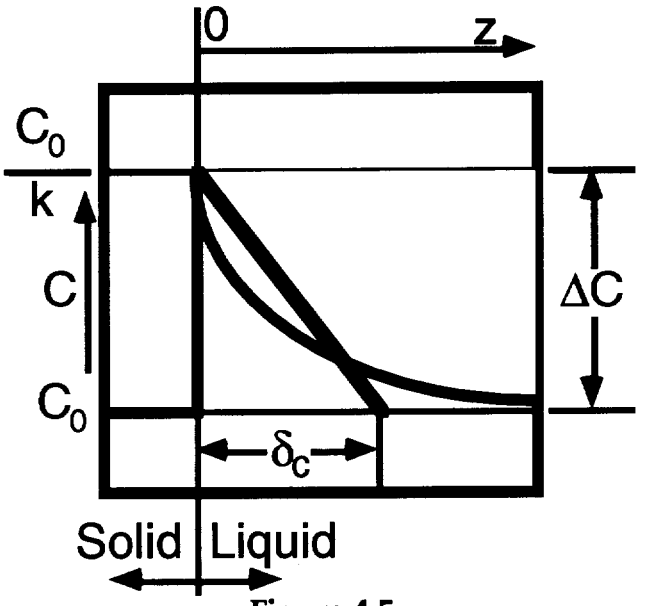

Figure 4.5
Diffusion Boundary Layer

As shown in figure 4.5, assume that an equivalent diffusion boundary layer thickness δ_c is chosen such it has a constant concentration gradient and the same total solute content as the infinite layer. Placing the expressions for the solute content equal to one another yields (27) and (28) below and evaluation of equation (28) results in (29) which is an expression for the equivalent boundary layer thickness.

$$\frac{\Delta C \delta_c}{2} = \Delta C \int_0^\infty e^{-\left(\frac{Vz}{D}\right)} dz \qquad (27)$$

$$\frac{\Delta C \delta_c}{2} = - \frac{\Delta C D}{V} e^{-\left(\frac{Vz}{D}\right)} \Big|_0^{\infty} \tag{28}$$

$$\delta_c = \frac{2D}{V} \tag{29}$$

If the assumption is made that the dendrite tips are at the liquidus temperature and that the roots are at the solidus temperature of the alloy, then the gradient may be expressed as:

$$G = \frac{\Delta T}{\delta_c} \tag{30}$$

Substituting in the result from (25) yields:

$$G = \frac{V \Delta T}{2D} \tag{31}$$

which is but a factor of 2 different than the planar interface solution of (25). Evaluating (31) with the same physical parameters as before requires a gradient in the neighborhood of 1400°K/mm, which again represents a somewhat challenging proposition. If a more reasonable gradient typical of production equipment where used to evaluate (31) the results are not acceptable. For example if a gradient of 10°K/mm were assumed, a typical part would require 36 hours to produce. Similar parts are regularly produced in today's production equipment in about 1.5 hours.

Given that G/R control schemes are based on the assumption that the solidification can take place in an environment where the dimension of the diffusion boundary layer is significant when compared to the dendrite length, it is unlikely that any such scheme may be implemented in a production environment. It is necessary then to re-evaluate the purpose behind an automated control scheme for the production of single crystal turbine blades. Such re-evaluation leads to the conclusion that, in any sort of present day production equipment, a planar interface cannot be stable in a eutectic alloy. Since the solidification interface is by its very nature unstable, stability arguments are unsuitable as the basis of a control scheme. A more productive

approach is to evaluate the phenomena behind the resultant microstructure. A possible result of such an approach is to try to develop a control methodology that would result in a constant primary dendrite arm spacing.

4.2 Dendrite Formation

In order to design a control scheme that would keep the primary dendrite arm spacing constant it is necessary to briefly consider the underlying phenomena associated with dendrite formation.

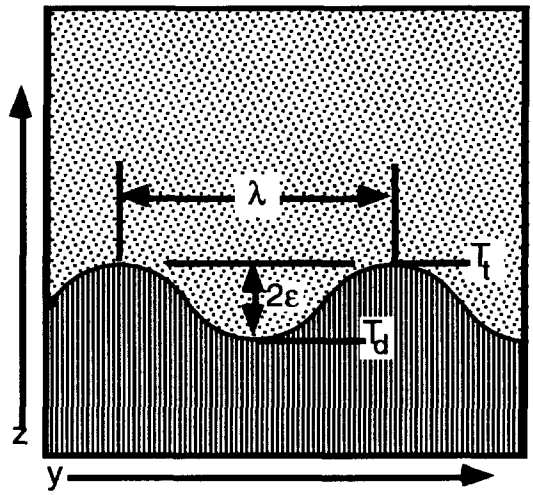

Figure 4.6
Interface Perturbations

Consider a solidification interface as illustrated in Figure 4.6. This interface experiences a sinusoidal perturbation of wavelength λ along y and magnitude ε such that the deviation of the interface in z, away from its mean location may be expressed as:

$$z = \varepsilon \sin\left(\frac{2\pi}{\lambda} y\right) \tag{32}$$

As established previously, for all DS or single crystal alloys being processed in a readily achievable environment, the liquid in advance of the interface must be constitutionally undercooled. If the perturbation is to be stable, then the temperature difference that occurs between the tip of the perturbation and the depression of the perturbation must be offset by the energy required to generate the additional interfacial length necessary to form the perturbations and by the change in the

liquidus temperature that occurs as a result of the composition gradient. This is expressed in (33) as:

$$T_t - T_d = m(C_t - C_d) - \Gamma(K_t - K_d) \quad (33)$$

Where T_t is the tip temperature, T_d is the depression temperature, m is the slope of the liquidus curve as a function of composition, C_t is the composition of the liquid at the tip, C_d is the composition of the liquid at the depression, Γ is the Gibbs-Thompson coefficient whose product with curvature expresses the change in the local melting temperature as a result of that curvature, K_t is curvature of the tip and K_d is the curvature of the depression.

If the temperature gradient in the vicinity of the interface is expressed as G, then the temperature difference T_t - T_d may be expressed as $2\varepsilon G$, where 2ε is the tip to depression distance in z. In a similar fashion, since there is a composition gradient G_C, the change in the melting temperature that results from the composition gradient C_t - C_d may be expressed as $2\varepsilon G_C$. Thus allowing (33) to be re-written as:

$$2\varepsilon G = m2\varepsilon G_C - \Gamma(K_t - K_d) \quad (34)$$

The curvature terms K_t and K_d, may be evaluated by taking the second derivative of (32) yielding:

$$\frac{\partial^2 z}{\partial y^2} = \frac{4\pi^2\varepsilon}{\lambda^2}\sin\left(\frac{2\pi}{\lambda}y\right) \quad (35)$$

As the expression chosen for the perturbation is a sine wave, the curvature should be evaluated at $\lambda/4$ and $3\lambda/4$ since this is where the maximum curvature occurs. The curvature may therefore be expressed as:

$$\left.\frac{\partial^2 z}{\partial y^2}\right|_{\frac{\lambda}{4},\frac{3\lambda}{4}} = K_t = -K_d = \frac{4\pi^2\varepsilon}{\lambda^2} \quad (36)$$

With the expression for the curvature from (36), equation 34 may be expressed as:

$$2\varepsilon G = m2\varepsilon G_C - \Gamma\frac{8\pi^2\varepsilon}{\lambda^2} \tag{37}$$

and so the wavelength of the stable perturbation is:

$$\lambda = 2\pi\sqrt{\frac{\Gamma}{mG_C - G}} \tag{38}$$

Considering equation 38 and recalling the previously described arguments for planar interface stability, the temperature gradient that results as a function of the heat flux is much smaller than the slope of the liquidus so it is reasonable to assume that:

$$mG_c \rangle\rangle G \tag{39}$$

and as a result G may be neglected. Further, since the scale of the perturbations under consideration are small, the composition gradient at the interface may be assumed to be linear. The gradient of the liquidus temperature at the solidification interface is therefore equivalent to the slope of the liquidus curve at the interface. This value was derived as the criterion for planar interface stability and was described in (25) and may be expressed as:

$$mG_C = \frac{\Delta TV}{D} \tag{40}$$

Equations 39 and 40 allow the expression for the wavelength of the perturbation to be expressed as:

$$\lambda = 2\pi\sqrt{\frac{D\Gamma}{V\Delta T}} \tag{41}$$

Although equation 41 expresses the wavelength of a stable perturbation, it does not express the primary dendrite arm spacing. It is instead a measure of probable curvature within the solidification environment. If the dendrite envelope is said to be

approximated by an ellipse as shown in figure 4.7, and the dendrites are assumed to be hexagonal in nature, then an expression for the primary dendrite arm spacing may be obtained.

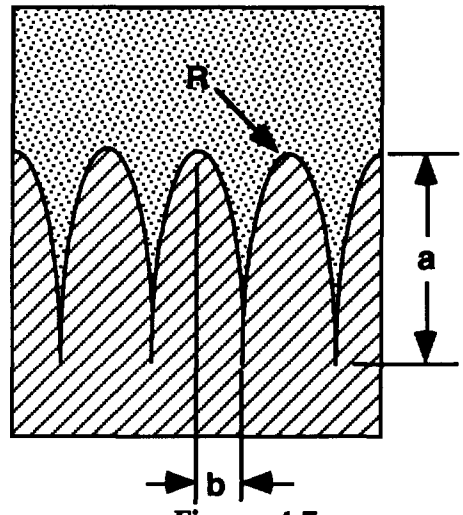

Figure 4.7
Dendrite Shape

The elliptical dendrite structure shown in Figure 4.7 has a tip radius which may be characterized by the equation:

$$R = \frac{b^2}{a} \tag{42}$$

If the dendrites grow rapidly to the extent available as a result of constitutional undercooling, then the dendrite length may be expressed as:

$$a = \frac{\Delta T}{G} \tag{43}$$

In order to form a complete solid it is necessary to allow the dendrite bases to assume a configuration that is ultimately hexagonal in cross-section. This is illustrated in figure 4.8. So while the primary dendrite arm spacing is the distance between the centers of the hexagons, the dimension b must be used to express the geometry for the ellipse. The need to use a slice through b arises from the realization that a slice through the hexagon in such a fashion describes the dimension of greatest curvature. As a result,

the primary dendrite arm spacing is not **2b** as implied in figure 4.7, rather it is something less as illustrated in figure 4.8.

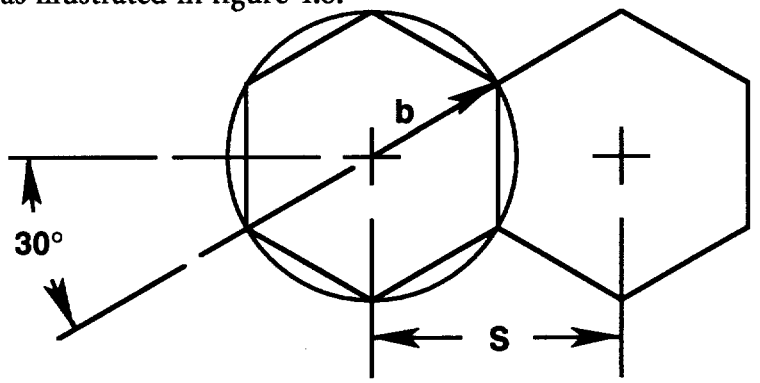

Figure 4.8
Hexagonal Dendrites

Referring to figure 4.8, the primary dendrite arm spacing S may be related to **b** by the expression:

$$\frac{S}{2} = b\cos(30°)$$

$$b = \frac{S}{2\cos(30°)}$$

$$b = .58\,S \qquad (44)$$

This result (44) when combined with (42), which is the expression for the dendrite length, allows the expression for the tip radius (44) to be re-written as:

$$R = \frac{.33S^2G}{\Delta T} \qquad (45)$$

Langer and Müller-Krumbhaar[38] have shown that the dendrite tip radius will become the shortest wavelength which would cause the dendrite tip to undergo morphological instability. It has been shown that to a first approximation the wavelength of the stable perturbation at the solidification interface may be used as a valid expression for **R**. It is therefore possible to combine (45) with the expression for the wavelength of the stable perturbation at the interface (41) to arrive at:

$$2\pi\sqrt{\frac{D\Gamma}{V\Delta T}} = \frac{.33S^2G}{\Delta T} \qquad (46)$$

which may be written as an approximate expression for the primary dendrite arm spacing S as:

$$S^2 = \frac{18.85(D\Gamma\Delta T)^{.5}}{GV^{.5}}$$

$$S = \frac{4.34(D\Gamma\Delta T)^{.25}}{G^{.5}V^{.25}} \quad (47)$$

A more rigorous solution includes the partition constant k in the denominator[39], but as the concern here is primarily with the form of the solution with regard to G and V, (47) is adequate. The form of (47) has been verified experimentally[40] and the expression is generally written:

$$\lambda_p = K_p G^{-.5} V^{-.25} \quad (48)$$

where λ_p is the primary dendrite arm spacing and K_p is a correlation constant which is based upon the solidification characteristics of the alloy and usually empirically determined.

4.3 Development of an Optimized Control Scheme

It is assumed that the optimum production method for single crystal parts would involve a control scheme that was able to keep the primary dendrite arm spacing as constant as possible throughout the part. Given that this is the case, then for control purposes the result expressed in (47) may be further reduced to the expression:

$$K = G^2 V \quad (49)$$

where the constant K takes into account the primary dendrite arm spacing as well as all of the solidification characteristics of the alloy. At present commercial producers of single crystal parts do not utilize such a relationship for the basis of any control scheme.

The most common method utilized for the production of single crystal parts is to have the susceptor operate at a constant temperature and to withdraw the part from the hot zone into the cold zone at a constant rate. The velocity is often varied in an attempt to optimize the crystal growth through various geometric features of the part. However the location at which this velocity change occurs is based on the underlying assumption that the solidification is occurring at the baffle. This assumption is

erroneous and may be seen to be at the root of the difficulty that occurs in optimizing a part production profile.

Although equation (49) would appear to be a superior relationship upon which to base a control scheme, there remains the previously mentioned problem with respect to the control of the gradient. Variations in susceptor temperature have been tried, and are used in production, however in general such schemes have not taken the radiation effects fully into account. Equation 50 shows that the heat transfer from a hot body to a cooler one is proportional to the temperature difference between the two bodies raised to the forth power.

$$R \propto (T_2 - T_1)^4 \qquad (50)$$

When considered within the context of the solidification apparatus, the portion of the mold within the cooling area is capable of dissipating significantly more heat per unit area than a similar area in the hot zone is able to absorb.

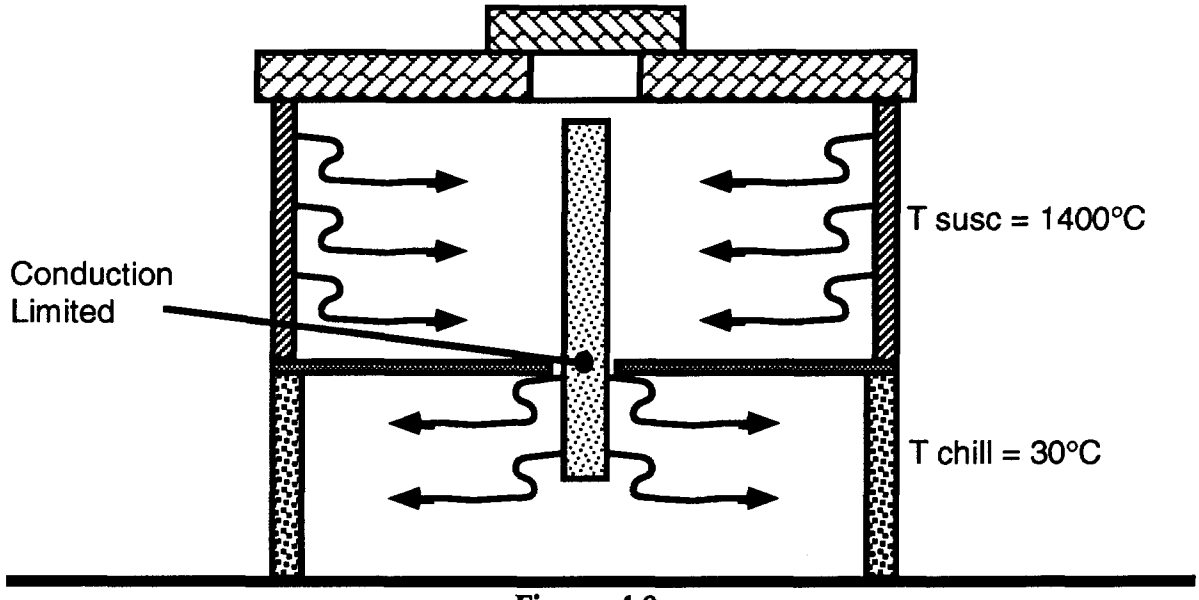

Figure 4.9
Heat Transfer

Figure 4.9 schematically illustrates the solidification apparatus. If the metal has a liquidus temperature of 1370°, then the temperature difference available to serve as a driving force for the heat flux into the part is very much smaller than that available for the cooling of the part. If the heat flux through the part is significantly greater than the heat that is liberated on freezing of the molten metal, then it is possible to regard the problem as being in a steady state. If a steady state is assumed, then the heat flux out of the portion of part that is below the baffle must be equivalent to that going into

the upper portion. Due to the nature of the emissive heat transfer, this condition is going to require a significant ΔT be available above the baffle. If it is considered that the temperature difference between the liquidus temperature and the hot wall is not particularly large, clearly the position on the part where the temperature of the bar is at the liquidus must be some distance above the baffle. Further, the location of the liquidus with respect to the baffle must vary as a function of the relative amounts of surface area exposed above and below the baffle. Since the liquidus location is a function of exposed surface areas and the ratio of the surface areas is a function of the distance that the part has been withdrawn, the liquidus position within the bar may be said to be a non-linear function of the position of the part within the solidification apparatus. In addition, since heat is being transferred from the hot zone, down through the bar and into the cold portion of the device, there must be a vertical heat flux and temperature gradient through the part.

The heat flux into or out of the part is a function of the temperature difference between the part and the heating/cooling wall. Since there is a temperature gradient along the part, the heat flux into the part must also vary. Therefore the maximum heat fluxes per unit area occur immediately on either side of the baffle. Similarly the heat flux through the part itself must have a maximum at the center of the baffle. Since temperature gradient may be said to be the product of the heat flux and the thermal conductivity, the temperature gradient within the part is at a maximum at the baffle. It follows that the magnitude of the temperature gradient experienced through any section of the part must then be a function of the distance that particular section is away from the baffle. In addition as the part is withdrawn, the total area available for heat input is continually decreasing such that the maximum heat flux through the part, and hence the gradient will also decrease with time. So therefore, as the part is withdrawn through the solidification apparatus, the solidification interface moves up the part and into regions of decreasing gradient. This situation results in an increase in the primary dendrite arm spacing as the process progresses.

In addition to the increase in primary DAS, since the gradient is decreasing the mushy zone or dendrite length must be increasing as well. Following (43), the thickness of the mushy zone may be expressed as:

$$L_m = \frac{T_L - T_S}{G} \qquad (51)$$

Where L_m is the thickness of the mushy zone, T_L is the liquidus temperature, T_S is the temperature of the solidus and G is the temperature gradient at the solidification interface. Although the solidification interface is moving up the part with respect to the baffle, the change in the withdrawal rate due to this motion is not significant. As a result, the approximation that the solidification rate is equal to the withdrawal rate is valid. It may then be said that the local solidification time is expressed by the relationship:

$$t_s = \frac{L_M}{V}$$

$$t_s = \frac{T_L - T_S}{GV} \tag{52}$$

This result (52) makes clear that not only is the primary dendrite arm spacing increasing, but so is the local solidification time. This implies that the amount of time available for solute redistribution will be increasing if the part is processed at a constant withdrawal rate. In fact, in production macro-segregation defects such as freckles are more prone to appear towards the later stages of process. This is the result that is expected from the above discussion.

Further examination of (52) reveals that the product GV is the cooling rate and is typically described as:

$$\dot{T} = GV \tag{53}$$

Re-writing the results of (48) and (53) yields:

$$\dot{T} = \frac{K_p^4}{\lambda_p^4 G} \tag{54}$$

which is an expression for the cooling rate as a function of the primary dendrite arm spacing and the gradient. If (54) is combined with (52), the expression for the local solidification time becomes:

$$t_s = \frac{\lambda^4 G(T_L - T_S)}{K_p^4} \tag{55}$$

Equation (55) illustrates clearly that the primary dendrite arm spacing is strongly related to the local solidification time and hence the amount of segregation. This result

does not initially seem to agree with the published work of Heubner, Köhler and Prinz[41] whose data indicate that "...reduced segregation can only be achieved at the cost of significant extension of the diffusion distance, here characterized by the dendrite arm spacing.". Their experimental work however is concerned with the amount of micro-segregation and in fact their results indicate that although a 19% greater DAS results in significantly improved homogeneity in the as cast part, the heat treatment time must be increased 150% in order to achieve a similar concentration profile after annealing. From a production standpoint, a small primary dendrite arm spacing is more desirable than reduced micro-segregation.

In production, the consideration that the steady state location of the solidification interface, the magnitude of the maximum temperature gradient and the temperature gradient at the solidification interface are all a function of the withdrawal position and part geometry is not properly taken into account. That the solidification interface is generally considered to be at the baffle leads to improper attempts at micro-structural control; in general the velocity modification used to effect a change occurs after the solidification front has passed the feature in question. As a first step towards easing the optimization of the withdrawal profile, an expression for the position of the solidification interface as a function of withdrawal distance is desirable.

The solution to this problem is achieved by setting up a flux balance into and out of the part. Since the temperature is a function of the heat flux down through the part and the heat flux into the part is a function of the temperature of the part, a closed form of the solution does not seem likely. Therefore a finite element model will be used to verify that in fact the ratio of surface areas is driving the solidification behavior.

To actually achieve a control scheme as expressed in (49), requires that the system be driven away from the previously expressed condition of flux balance. This would allow the position of the solidification interface to be moved closer to the baffle and into an area of increased gradient. Such an action may be accomplished by an increase in the solidification rate and implies that the heat released as a result of solidification must be of sufficient magnitude to account for the difference in heat necessary to allow the interface to move closer to the baffle. It must be experimentally verified that the position of the solidification interface can be moved from its steady state position to a location of higher gradient by increasing the withdrawal rate. It is predicted that in order to keep the solidification interface at a constant position relative to the baffle, the velocity must increase as the ratio of the exposed surface areas.

Given the verification that the withdrawal velocity required to maintain the solidification interface at a constant position relative to the baffle is in fact proportional to the ratio of the surface areas above and below the baffle, then controlling the withdrawal rate in the described fashion provides a means of characterizing the ratio of the surface areas of a complex part. A surface area profile of this sort, when coupled with the previously described numerical analysis should allow the calculation of that component of the heat flux which is a result of the solidification. This data, in conjunction with the surface area ratio profile should allow the calculation of a velocity profile that satisfies the conditions required to keep the primary dendrite arm spacing relatively constant. Hence the information that is achieved by holding the solidification interface at a constant position relative to the baffle throughout the withdrawal process should provide the information required to allow an optimized profile such that the expression of (49) may be achieved. Once parts are produced, primary dendrite arm spacings will be used to determine the value of the method.

A method of producing single crystal parts as has been described should be achievable in production. The development of a system which utilizes the underlying conditions responsible for the solidification as the basis for a control scheme should result in less microstructural variation. It is further expected that grain and macro segregation defects would be reduced. Such a control scheme has the potential of reducing months of process development time and many thousands of dollars worth of parts down to a single test run and some post processing time on a computer. It is the intent of this work to determine whether or not such a scheme is in fact feasible.

Chapter 5 Research Overview

It is the intent of this work to provide the necessary basis for further optimization of the commercial single crystal process. Single crystal test bars will be grown in a state of the art production furnace. These test bars will be grown under varying conditions including furnace temperatures, furnace configuration and withdrawal rate. Each test bar will then be sectioned and etched to allow a determination of the primary dendrite arm spacing and how this spacing is changing throughout the solidification and growth process. From these data, an assessment of the impact of geometrical view factors on the solidification conditions will be made. Additional data regarding furnace gradients and the effect such gradients have on the solidification process will be discussed. Data from instrumented molds will allow the assessment of the actual solidification environment within the part. A computer model will be used to predict the position of the solidification interface and associated gradient as a function of withdrawal position. A scanning electron microscope (SEM) technique which may be used to determine crystallographic orientations will be utilized to determine a pool profile from a solidified bar. This technique, termed Backscattered Electron Kikuchi Patterns (BEKP), can measure grain orientations with regard to a surface. Since the crystal grows against the heat flux, the crystal is always perpendicular to the solidification interface. Therefore, a map of crystallographic orientations taken from a transverse slice may be used to determine the morphology of the solidification interface that existed as solidification occurred. Finally, a test bar will be grown under conditions where the gradient is maximized by continuously determining the location of the solidification interface and positioning it at the baffle. This can only be accomplished if the heat of solidification is able to provide enough of a contribution to the total heat flux in order to overcome the emissive flux. This test will verify whether or not the heat of solidification is of sufficient magnitude to allow its utilization as a heat source within the process.

Chapter 6 Experimental Setup

These experiments were conducted as part of a new furnace evaluation program conducted by Rolls Royce. It was the intent of this program to contrast the solidification performance of furnaces produced by different manufacturers. The test matrix utilized for the Rolls Royce evaluation proved ideal for this study. In support of this work, Rolls Royce was kind enough to provide a single crystal test bar from the same location from each of 12 cluster molds in the furnace study. Each test bar cluster is the result of a full scale single crystal production cycle and as such each bar is worth a considerable amount..

6.1 Equipment Configuration

The furnace utilized for the production of the test bars was manufactured by Retech Inc. of Ukiah, California. This furnace is a standard two chamber design utilizing two 3000 Hz induction power supplies manufactured by Inductotherm Corp. of Rancocas New Jersey. One power supply is used for melting the metal; the other is used to control the temperature of the hot zone of the furnace. The furnace hot zone is actually two independent inductively heated graphite susceptors. These susceptors pre-heat the mold and drive the gradient necessary for the growth of single crystal parts. Figure 6.1 is a schematic illustration of the furnace used for these experiments. The furnace is constructed as two main chambers with an *Isolation Valve* between them. The top chamber, termed the *Melt Chamber*, is where melting and solidification take place. The lower chamber referred to as the *Mold Chamber* may be isolated from the *Melt Chamber*, and is used for the loading and unloading of molds. It is configured such that these operations may occur while maintaining the *Melt Chamber* under vacuum. The *Bar Feeder* is used to load the billet that is to be melted into the *Tilt-Pour Melt Box* and as with the *Mold Chamber*, vacuum isolation is provided. Once a billet has been loaded, the *Tilt-Pour Melt Box* is rotated to a vertical position for the actual melting operation. While in this position, the melt may be viewed by an *Optical Pyrometer* thus providing a means for closed loop temperature control. It should be noted that the temperature as sensed by the *Optical Pyrometer* may be inaccurate due to the build up of metallic film on the viewport. As a result, a *Thermocouple Assembly* is included for periodic verification and calibration of the pyrometer. When the

Thermocouple Assembly is used, the *Tilt-Pour Melt Box* is rotated away from vertical to allow the insertion of the thermocouple, but not so far as to impede the view of the pyrometer.

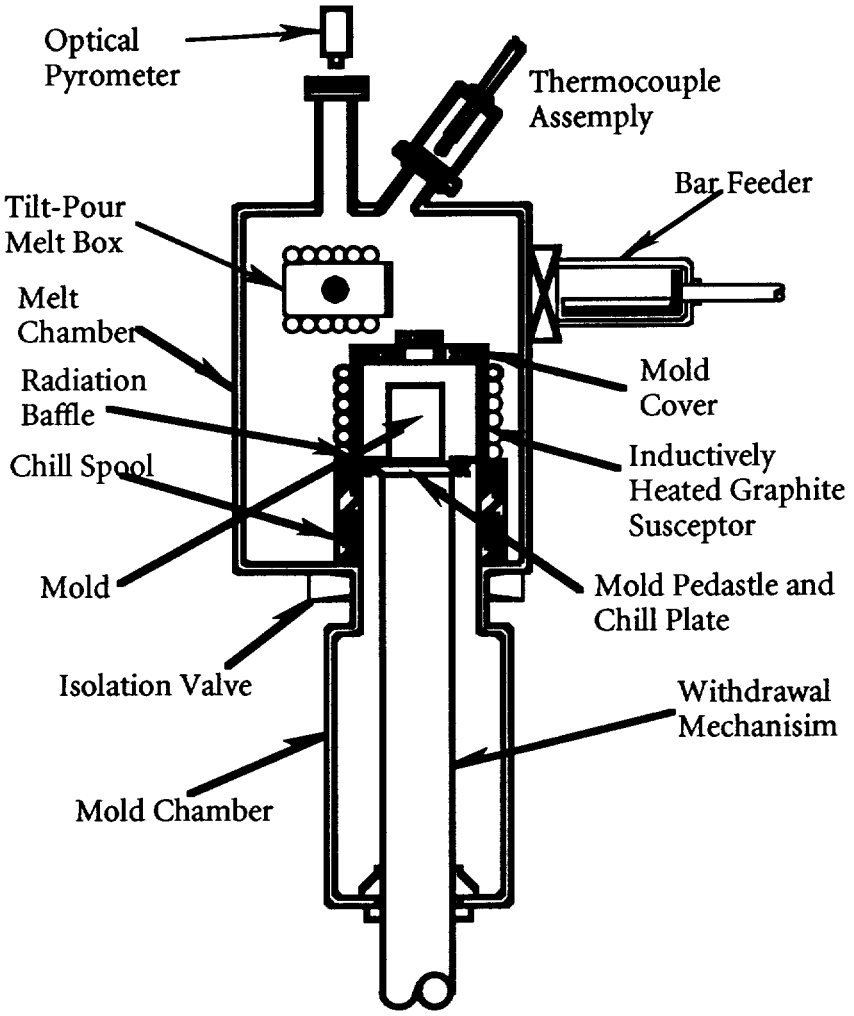

Figure 6.1
Single Crystal Furnace Configuration

Once the appropriate melt temperature has been reached the *Mold Cover* is removed from the *Inductively Heated Graphite Susceptor* and the *Tilt-Pour Melt Box* is rotated such that the metal is poured from the crucible contained within the melt box through the hole in the *Mold Cover* and into the *Mold*. Once the metal has been poured into the Mold, the solidification cycle is initiated by a *Chill Plate*, which is a water cooled copper plate upon which the molten metal impinges during the pour. Immediately above the Chill Plate is a helical crystal selector which assures only a single crystallographic orientation grows up into the solidifying part. After a brief hold time

to allow the crystal growth to start, the *Withdrawal Mechanism* is actuated. This action lowers the *Mold* and in so doing subjects the solidifying part to a vertical temperature gradient. This gradient is a result of the area above the *Radiation Baffle* being heated to above the liquidus temperature of the metal by the *Inductively Heated Graphite Susceptor* while the area below the baffle is kept cool by the *Chill Spool.* The two zone susceptor design allows a high heat flux to be generated just above the *Radiation Baffle* where heat losses are the greatest while maintaining lower fluxes at the top of the mold where heat losses are at a minimum. This design allows for maximum gradients, without overheating the mold. As the mold is lowered, the solidification interface is caused to sweep upward through the part. Table 3.1 is a summary of a typical part production cycle.

Table 6.1 Single Crystal Process Sequence

1). Obtain proper furnace vacuum.	2). Close mold chamber isolation valve.
3). Vent mold chamber to atmosphere.	4). Load mold onto mold pedestal .
5). Close mold chamber and evacuate.	6). Open isolation valve.
7). Raise mold into position.	8). Begin mold pre-heat.
9). Wait until mold is at temperature.	10). Load billet into bar feeder.
11). Evacuate bar feeder.	12). Rotate crucible to horizontal.
13). Load billet into crucible.	14). Rotate crucible to vertical.
15). Begin melting billet.	16). Wait for pour temperature.
17). Pour metal.	18). Begin part Withdrawal.

The furnace was designed to readily accept different Chill Spools. In support of this work, Rolls Royce purchased and Retech manufactured both standard and specially designed chill spools.

As was discussed in §4.3, during the early portion of the crystal growth, there is a lack of radiating area below the baffle. This condition could result in a situation wherein the solidification interface is driven significant distances below the baffle. Since the maximum gradient occurs at the baffle and gradients decrease as the distance from the baffle increases, this movement of the solidification interface results in a lowering of the gradients around this interface. Lower gradients translate into wider dendrite arm spacings as expressed in (48).

$$\lambda_p = K_p G^{-.5} V^{-.25} \tag{56}$$

Assuming that little or no conductive heat transfer occurs down through the crystal selector, then the implication is that during the initial portion of the crystal growth the primary dendrite arm spacing must be large until sufficient radiating area has moved below the baffle to allow the solidification interface to move up into areas of higher gradient. In order to address this initial lack of cooling a method of increasing the heat transfer was sought. The proposed solution is termed a shaped chill spool and is shown in figure 6.2 along with the traditional design.

Chill spools are typically made of copper and are water cooled. They serve as a radiation sink for heat escaping that portion of the mold which has an emissive view of the chill spool. As is apparent from figure 6.2, the primary difference between the shaped chill spool and the traditional design lies in an angled section at the top.

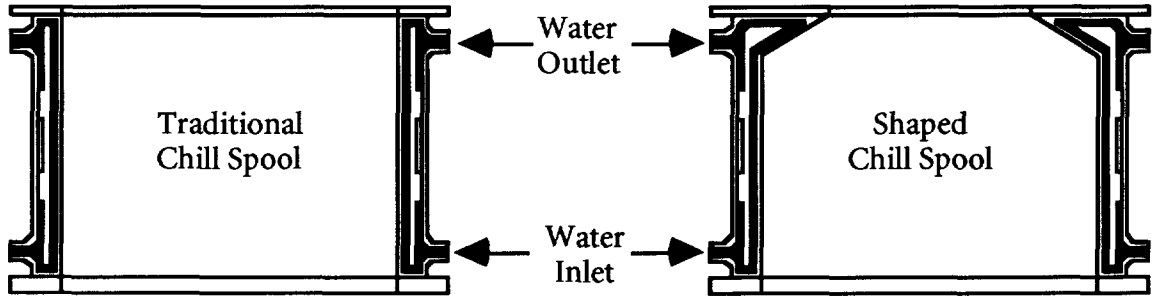

Figure 6.2
Shaped Chill Spool Concept

This angled section has a three potential advantages over the traditional design. The first advantage lies in the fact that the portion of a mold that is just below the radiation baffle "sees" a larger cooling surface as a result of the angle. This larger area translates into a lower heat flux per unit area of cooling surface, thereby lowering the effective surface temperature of the chill spool. Emissive heat transfer is related to the difference between the temperature of the mold, T_m and the temperature of the chill spool T_s by the equation:

$$Q \propto \left(T_m - T_s\right)^4 \tag{57}$$

Clearly small differences in the chill spool temperature T_s can have a significant impact on the cooling imparted to the mold. It is intended that the angled section of the shaped chill spool shall lower the heat flux per unit area of chill spool surface sufficiently to provide an increase in the heat transfer from the mold. It should be noted that a similar conductive effect occurs at the internal chill spool / cooling water

boundary where the increased surface area also enhances the conductive heat transfer from the chill spool to the cooling water.

The second potential advantage associated with the shaped chill spool configuration occurs as a result of increased view factors from the mold to the chill spool. This is shown in Figure 6.3 which illustrates how the angled section of the shaped chill spool (right side) allows a given surface element of the mold to "see" a greater area of cooling surface. Although emissive energy leaves normal to the hot surface, a mold is anything but flat. This lack of a flat surface, which is inherent in present day mold making technologies, results in emissive energy leaving the mold at all angles. Therefore techniques which allow a greater percentage of the mold to experience good cooling should improve the heat transfer. Contrasting the shaped spool on the left to the traditional spool on the right shows that a greater area of the mold should experience cooling as a result of the shaped chill spool.

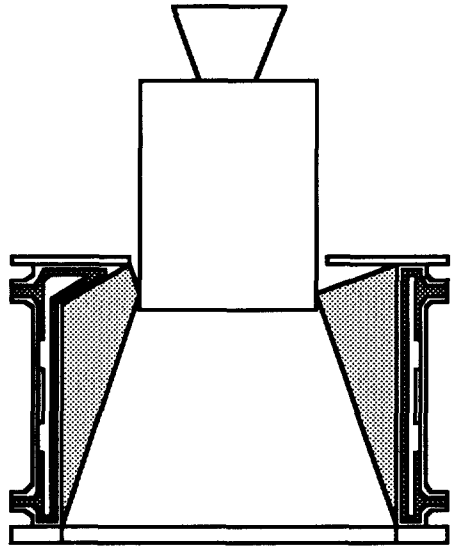

Figure 6.3
Chill Spool View Factors

The third potential advantage is associated with the reflection and re-radiation of the heat from the mold. In order for a chill spool to be maximally effective it must be clean and free of contaminants which could impede the heat conduction capabilities of the copper. However the vacuum furnace environment has some partial pressure of metal vapor present throughout most of the process. The cold copper chill spool is an ideal condensation site for such vapor and as a result slowly builds up a coating of condensed metal. This condensed metal layer resembles soot and is a very poor conductor of heat. When appreciable amounts of this deposit form, the performance

of the chill spool is adversely impacted. It is therefore necessary to periodically clean the inner surface of the chill spool in order to maintain its capacity as an emissive heat sink. If the chill spool surface is rough, cleaning is difficult and optimum performance may not be regained. However, very smooth surfaces do not perform well and it is proposed that they are too reflective and as a result significant amounts of heat are reflected back to the part.

A similar phenomenon is proposed in the case where the chill spool is dirty. In this case, although no energy is being reflected, the coating begins to heat up and some of the heat may then be re-radiated back to the mold.

If a shaped chill spool is used both of these concerns are readily addressed. This is illustrated in Figure 6.4. Contrary to the case of the traditional chill spool design, the shaped chill spool does not reflect energy directly back to the mold. Rather when using the shaped chill spool, energy is reflected downward into the lower section of the chill spool. This transfers energy away from the portion of the mold just below the baffle and as a result helps maintain higher gradients than could be achieved with traditional designs.

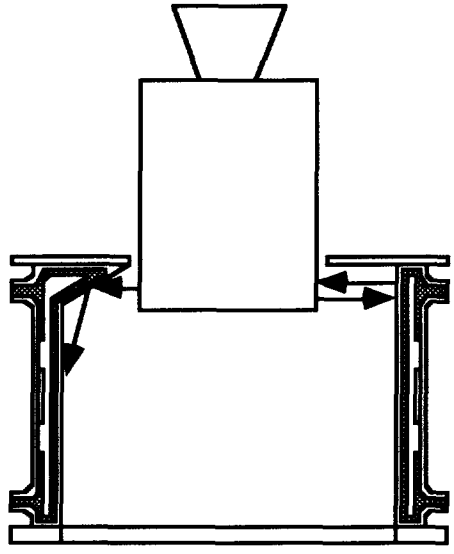

Figure 6.4
Reflection and Re-Radiation

As the chill spool becomes covered with metal vapor and the surface coating begins to experience heating, the primary direction of re-radiation from the chill spool will be angled away from the hottest part of the mold. As a result, this design should also have performance advantages as low conductivity coatings form on the chill spool surface.

In order to evaluate whether or not the shaped chill spool provides the predicted advantages over conventional designs, 50% of the trials were conducted using the shaped design and 50% were conducted using a straight chill spool. A complete outline of the parameters used in the experiments may be found in §6.4.

6.2 Test Bar Configuration

The eight test bars used for this work were each from location 2 in a mold cluster comprised of a total of eight bars. These test bar clusters were provided by Rolls Royce and are their standard test bar mold configuration. Several advanced proprietary aspects of the Rolls Royce process were incorporated into these molds and as such photographs and detailed schematic descriptions are not provided. However, the proprietary aspects of these molds have no effect on the solidification behavior being studied in this work and as such their omission is of little consequence. The bars produced are 12.5 millimeters in diameter and varied from 135 millimeters to 180 millimeters in length. The molds were identical and variations in test bar length are primarily the result of the simultaneous testing of the tilt pour system during these trials. Each bar had a base reservoir which allowed the molten metal to contact the chill plate directly. Immediately above the base reservoir was positioned a helical crystal selector which terminated at the base of the test bar itself. Each of these test bar molds was fed from a centrally located pour cup which facilitated the pouring operation and provided a molten metal head for proper mold fill. Figure 6.5 is a horizontal illustration of the configuration for a single bar.

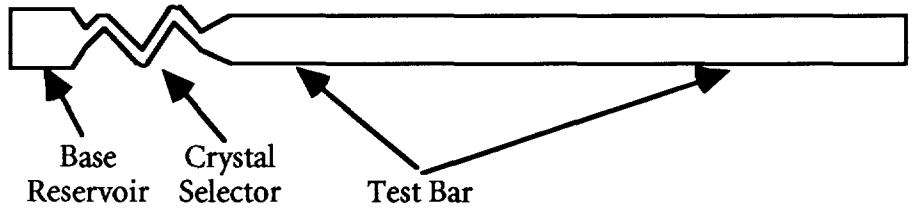

Figure 6.5
Single Crystal Test Bar
Scale = 1/2

The alloy used for these tests is CMSX-4, a widely used single crystal alloy produced by Cannon Muskegon Corp. Table 6.2 provides the composition of this alloy as well as some of the other first and second generation single crystal alloys presently in use. Personal communications indicate that some users of this alloy have experienced

occasional difficulty in obtaining a uniform heat treatment response. Such difficulty has been attributed to a variation in primary dendrite arm spacing and an associated variation in the resultant diffusion distance between the cores of primary dendrites. This variation results in a condition wherein the optimum heat treatment cycle varies across the length of the part. As such, a mechanism for obtaining a more uniform microstructure in the as-cast condition would be of value.

Table 6.2 Single Crystal Alloy Compositions

Alloy	Cr	Co	Mo	W	Ta	V	Nb	Re	Al	Ti	Hf	Ni
PWA 1480	10	5	-	4	12	-	-	-	5.0	1.5	-	BAL
René N-4	9	8	2	6	4	-	.5	-	3.7	4.2	-	BAL
SRR 99	8	5	-	10	3	-	-	-	5.5	2.2	-	BAL
RR 2000	10	15	3	-	-	1	-	-	5.5	4.0	-	BAL
AM1	8	6	2	6	9	-	-	-	5.2	1.2	-	BAL
AM3	8	6	2	5	4	-	-	-	6.0	2.0	-	BAL
CMSX-2	8	5	.6	8	6	-	-	-	5.6	1.0	-	BAL
CMSX-3	8	5	.6	8	6	-	-	-	5.6	1.0	.1	BAL
CMSX-6	10	5	3	-	2	-	-	-	4.8	4.7	.1	BAL
AF 56	12	8	2	4	5	-	-	-	3.4	4.2	-	BAL
CMSX-4	6.5	9	.6	6	6.5	-	-	3	5.6	1.0	.1	BAL
PWA 1484	5	10	2	6	9	-	-	3	5.6	-	.1	BAL
SC 180	5	10	2	5	8.5	-	-	3	5.2	1.0	.1	BAL
MC2	8	5	2	8	6	-	-	-	5.0	1.5	-	BAL

6.3 Standard Process

The term *Standard Process* is perhaps a misnomer when applied to the production of single crystal turbine blades. Each foundry has their own set of process parameters which they believe will produce the best parts at the highest yield. Figure 6.6 illustrates a typical turbine blade as it might look immediately after mold break-out.

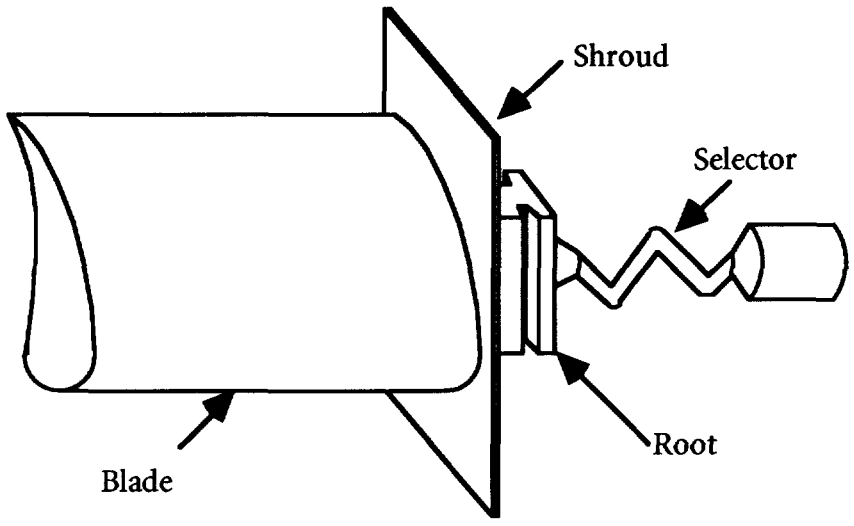

Figure 6.6
Jet Engine Turbine Blade Example

As may be seen from the illustration, the geometry of the parts being produced provides some challenges for the growth of single crystals. Once the crystal has propagated up through the selector, it must grow laterally to fill the root. In a similar fashion, after growing through the root, the crystal must spread out through the shroud. If instead of a blade, a vein is being produced, then the situation is further complicated by the presence of a top shroud and mounting tip. Some foundries make an effort to decrease the withdrawal velocity as the solidification interface encounters the various cross sectional changes. In many such cases, it has been assumed that the solidification interface is at the location of the baffle. However it is the assertion of this work that, in the steady state, the location of the solidification interface is a function of the radiating areas above and below the baffle. This is illustrated by the use of a simple finite element model developed for this work. This model is intended only to illustrate the effect that the ratio of surface areas above and below the baffle can have on the steady state location of the solidification interface. The model is discussed in detail in the process modeling section of this document.

6.4 Parameter Factor Space

Several factors in the experiment were varied to determine their effect on the solidification process. These variables are: Mold heater temperature, Withdrawal velocity, Chill spool shape, and Control mode. Rolls Royce determined the values and variables which they felt were most likely to provide the most useful information.

These parameters and the values used for the casting trials are shown in Table 6.3. The factor space is graphically illustrated in Figure 6.7.

Table 6.3 Test Bar Factor Space

Sample ID	Pour Temp	Zone 1 Temp	Zone 2 Temp	Withdraw Velocity	Chill Spool Type
A	1550°C	1550°C	1550°C	5.6 mm/min	Std.
W	1500°C	1475°C	1475°C	4.0 mm/min	Std.
Y	1500°C	1500°C	1550°C	5.8 mm/min	Std.
Z	1500°C	1550°C	1550°C	4.0 mm/min	Std.
1	1500°C	1500°C	1550°C	Closed Loop	Shaped
2	1500°C	1475°C	1475°C	Closed Loop	Shaped
3	1500°C	1475°C	1475°C	4.0 mm/min	Shaped
4	1510°C	1475°C	1475°C	Closed Loop	Shaped
5	1500°C	1475°C	1475°C	4.0 mm/min	Shaped
6	1500°C	1475°C	1475°C	4.0 mm/min	Shaped

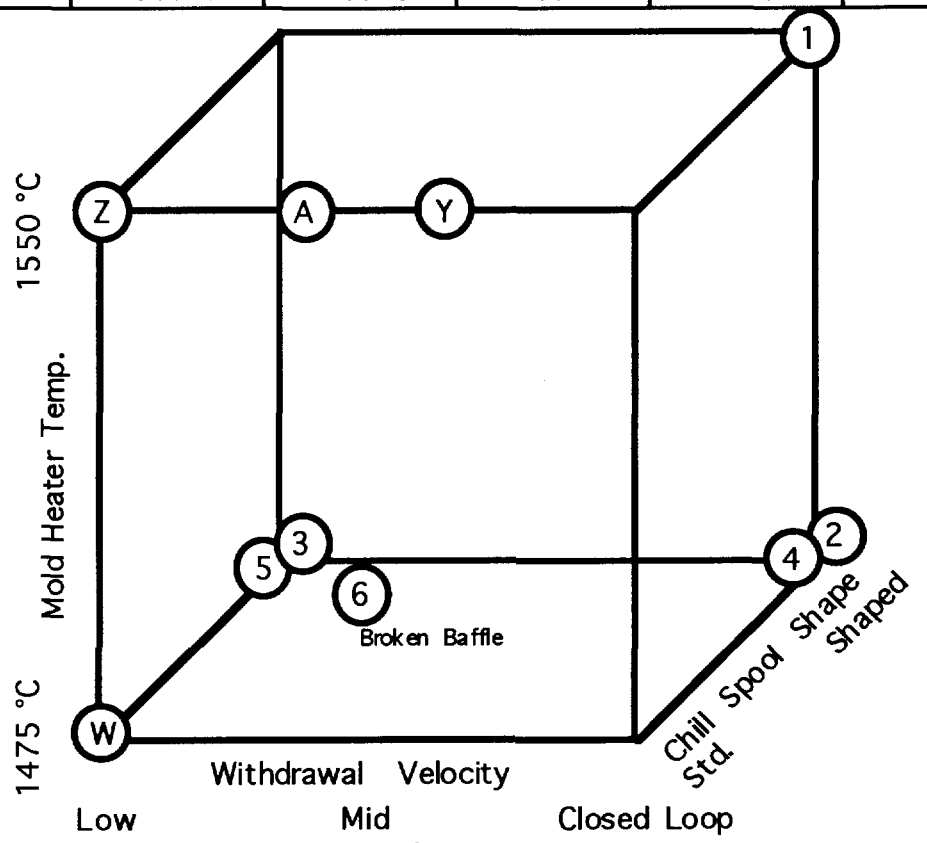

Figure 6.7
Experimental Factor Space

Chapter 7 Process Modeling

As a means of gaining greater insights into the process, a finite element model which calculates the steady state temperatures in the test bar as a function of withdrawal position has been developed. A finite element solution was selected because the series of equations necessary to solve the problem analytically proved to be excessively challenging. The model is based on code that was developed at Sandia National Laboratories in Albuquerque specifically for emissive view factor and heat transfer problems of this nature. The code called "Coyote" was written by Dave Gartling of Division 1511. In operation, part geometry's and an enclosure are specified along with the physical properties, emissivities and temperature (if applicable) of the various components. Proprietary meshing algorithms are employed and the solution is solved via a finite element method.

7.1 Model Overview

The model is configured to track the heat distribution along the test bar as a function of the withdrawal distance. This also allows the determination of the location of the solidification interface as a function of withdrawal distance as well as the temperature gradient around that interface. The model is of a simple heat flow only design and does not take into account the dependency of temperature on the various thermal conductivities. Steady state is assumed and as a result the heat of solidification is eliminated from the model. Convective heat flows in the liquid are also not considered. Further simplification occurs as a result of the axi-symmetric nature of the problem.

Figure 7.1 is an illustration of the problem is to be solved. It is the contention of this work that as the withdrawal distance "D" is increased, the solidification interface will move up the bar and become more curved. It is also expected that the gradient at the solidification interface will *decrease* as the withdrawal distance increases. It is this factor which drives the assertion that current processes should be modified to take into account the impact of the changing view factors.

7.2 Boundary Conditions & Parameters

From Figure 7.1 it may be seen that the simplified problem consists of a 6.5 mm diameter metal core which is sheathed in an 3.0 mm thick alumina mold. The system is

axi-symmetric and as such the center boundary may be assumed to be perfectly insulating, that is to say, no heat flux flows across it. The top and bottom of the mold have been defined as emissive *only* boundaries.

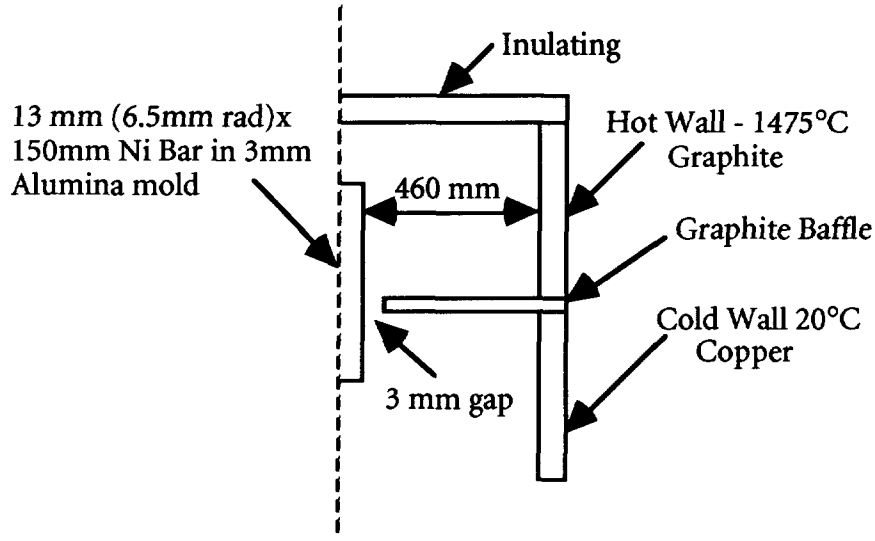

Figure 7.1
Axi Symmetric Model Configuration

The assumption of emissive ends is very good for the top boundary since this is in fact close to the actual situation. The assumption of an emissive bottom however is not as well justified. The difficulty lies in the fact that at small withdrawal distances the crystal selector conducts heat when the model would have only emissive flux. The conductive heat flow through the crystal selector is in addition to the heat flow due to radiation. In order to estimate the heat flux through the selector consider a hypothetical case.

The crystal selector has an effective thermal length of 130 mm which is comprised of 2.5 revolutions of a 6.5 mm radius spiral over 30 mm of length. The selector is approximately 1.2 mm in diameter yielding a cross section of 1.13 mm^2. The thermal impedance of the selector may be determined in units of °K/ Watt from (58) where Z_T is the thermal impedance, k_T is the thermal conductivity, L is the length of the heat conductor, and A is the cross sectional area.

$$Z_T = \frac{L}{A\,\kappa_T}\ \frac{°K}{W} \qquad (58)$$

Assuming that the conductivity is that of Ni, then the thermal impedance of the selector is calculated to be 1263 °K / Watt. This contrasts to a total impedance for

the test bar of 39 °K/ Watt. It should further be noted that the 3 mm mold (although having a thermal conductivity that is only 20% that of the metal), because of its large surface area and small thickness has a total thermal impedance of .022 °K / Watt. Clearly, the thermal impedance of the crystal selector is large in contrast to the rest of the system. Given that the susceptor temperature is 1748 °K and assuming that the test bar is at that temperature, then with a 300 °K sink, the absolute maximum heat which could flow through the crystal selector is 1.1 Watts (Figure 7.2A).

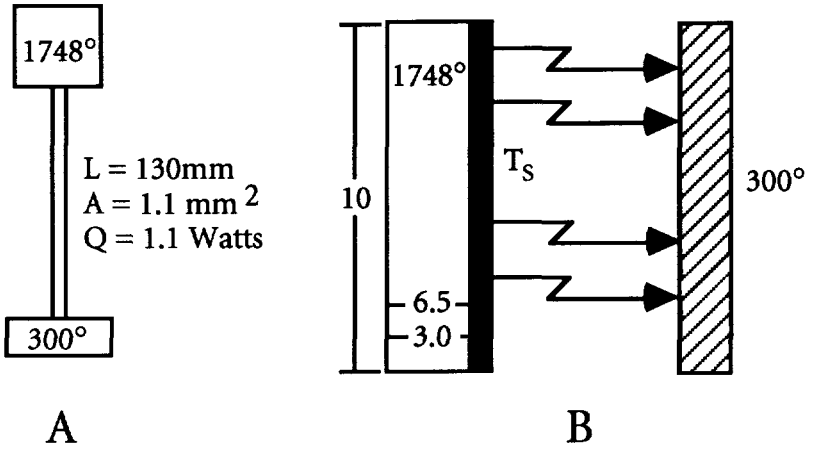

Figure 7.2
Crystal Selector Heat Flux

It may be readily shown that the heat flux through the crystal selector is small when compared to the total flux. As an example, assume that the test bar has been withdrawn 10 mm, the mold emissivity is .4, the view factor is calculated to be .26, and the inner wall of the mold is at 1748 °K as in Figure 7.2B, then in order to solve for the heat flux, the surface temperature T_S must first be determined. This is accomplished by balancing the conductive and emissive heat fluxes at the mold surface as shown in (59). Where ε is the emissivity, ν is the view factor, k is the Stefan Boltzman constant and the other constants are defined above.

$$\frac{(1740 - T_s)A\,\kappa_T}{L} = \varepsilon\,\nu k A(T_s - 300)^4 \qquad (59)$$

Solving for T_S and then plotting the ratio of the conductive heat transfer down through the crystal selector to the total heat output yields the plot in Figure 7.3. From this plot it is evident that early in the withdrawal cycle conduction dominates. This is

of course necessary in order to start solidification. However, by half way into the withdrawal of the part, the contribution of the crystal selector has fallen to near 1%.

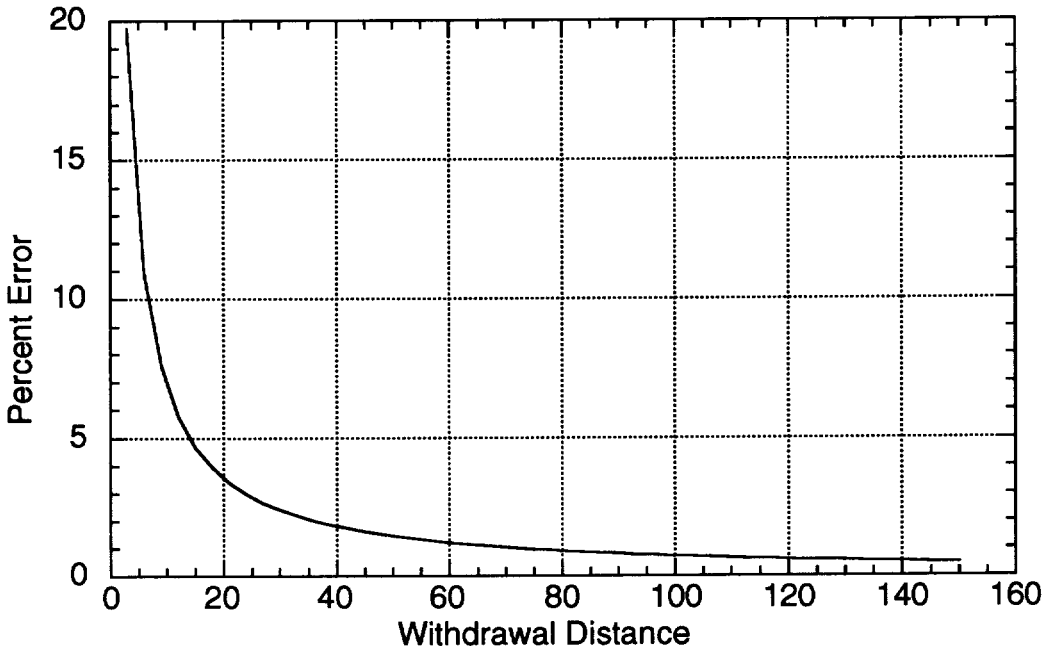

Figure 7.3
Conductive heat vs. Total Heat

Since the interest is in the later stages of the process it has been assumed that the errors introduced by the omission of the conductive heat transfer through the crystal selector are minimal. This is an extremely conservative estimation. Typically the emissive heat flows will be reducing the temperature at the top of the selector by many hundreds of degrees at small withdrawal distances. As a result, the conductive heat flux will be attenuating rapidly as the withdrawal distance increases. This reduces the actual contribution of crystal selector to the total heat flux and further justifies the removal of the crystal selector from the model.

Chapter 8 Analytic Techniques

Each of the eight test bars used in this study was transversely sliced into multiple sections, then polished and etched to reveal the dendrite structure. This procedure was intended to reveal the spacing and morphology of primary dendrites. Once a clear view of the primary dendrites was achieved, optical micrographs were taken of each slice. These micrographs were acquired using a video camera attached to the microscope and then stored to a magneto-optical disk. The micrographs were then processed by a computer program written specifically for this work. The program automated the task of measuring the primary dendrite arms spacing and determining the standard deviation in the measurement. A total of 271 samples from eight test bars were processed in this fashion.

After the primary dendrite statistics were determined, several samples were examined in the SEM using Backscattered Electron Kikuchi Patterns (BEKP) to determine the primary dendrite orientation as a function of position along the bar. The intent of this study was to determine if the shape of the solidification interface was changing. Of particular interest was the assessment as to whether or not variations in the growth direction with respect to the vertical axis could be attributed to a curvature of the solidification interface which might result as a consequence of the interface location being pushed above the baffle. Such a result would provide confirmation of the mechanism behind misorientation in the growth direction of the crystal. The SEM analysis consisted of the acquisition of Backscattered Electron Kikuchi Patterns across the sample. These images were stored to magneto-optical disk and allow an accurate determination of the dendrite growth direction. AS BEKP has not previously been used to determine liquidus shape from solidified transverse slices, this study also explores the use of BEKP as an effective tool for solidification studies.

8.1 Sample Preparation

8.1.1 Test Bar Sectioning

A Buehler™ cut-off saw was employed to section each of the test bars. The saw was of the abrasive variety and the blade left a consistent kerf (or cut width) of 3.3 millimeters. The kerf was determined by cutting approximately 1/2 way through a kerf sample, comprised of a 25 millimeter square bar of alloy 718. The width of the kerf was

then measured at the top, front and back of the kerf sample. This technique had the advantage of eliminating pinching and allowed easy kerf measurement through the use of a micrometer. Additional cuts on the kerf sample were made throughout the bar sectioning process. These additional cuts insured that the blade thickness did not vary as the blade was consumed. A total of 32 kerf measurement cuts were made throughout the sectioning process. No significant variations in kerf thickness were observed thus resulting in the assumption of a constant kerf. The test bars were jigged up such that the saw cut through the bars at an angle of 90° to the nominal dendrite growth direction. An error analysis was completed in order to ascertain the criticality of the angle of cut to the dendrite statistics.

Errors in the primary dendrite arm spacing measurement that result as a function of inaccuracies in the cutting angle will tend to increase the primary dendrite arm spacing. This occurs since as the cutting angle approaches the growth direction, fewer dendrites are intersected for a given surface area of the cutting plane. This situation is illustrated in figure 8.1.

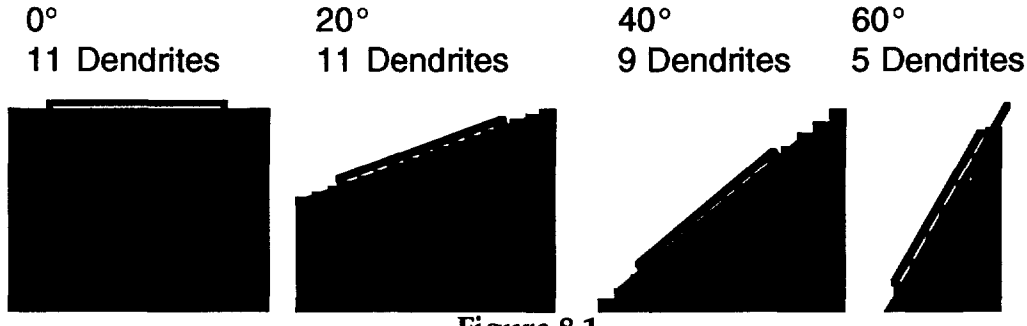

Figure 8.1
Effect of Cutting Angle on the Number of Dendrites Intersected

From the diagram it is clear that as the deviation from a 90° cut increases, the number of dendrites which intersect the given area of the cutting plane will decrease. This decrease in the apparent number of dendrites within the sampling area results in an apparent *increase* in the primary dendrite arm spacing. It should be noted this phenomenon occurs along the axis of misalignment only and that the spacing in the direction orthogonal to the misalignment direction is not effected. In a good crystal, the dendrites line up as if on a grid. This alignment is due to the cubic nature of the material and results in an alignment of secondary dendrite arms. As a result, cutting errors are greater when the misalignment direction is 45° from the secondary dendrite arm direction. In such a situation the expansion of the primary dendrite arm spacing is evenly distributed along both secondary directions. If it is assumed that a 1% error in

the primary dendrite arms spacing must be maintained, then the maximum error in the cutting angle may be readily calculated. This is shown in figure 8.2.

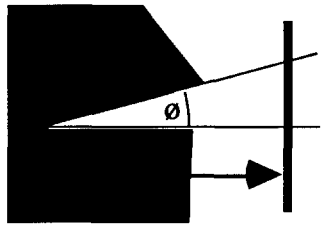

$$\text{ø} = \cos^{-1}\left(\frac{1}{1.1}\right) = 24.6°$$

Figure 8.2
Calculation of Angular Error for 1% PDAS Error

In figure 8.2 the thick vertical lines are primary dendrite cores. and μ represents the primary dendrite arm spacing. The angle ø is the angle necessary to generate a 1% expansion in the distance between the two primary dendrites cores. As is shown in the figure, the angle required to generate a 1% error in the primary dendrite arm spacing is on the order of 24°. The cutting fixture provided accuracy to within about 2° and as such the error in the primary dendrite arm spacing measurement as generated by the cutting operation should be no greater than .06%.

The test bars were cut from the bottom of the test bar up towards the top and set aside and arranged in the order cut. Earlier test bars showed a greater variability in the thickness of the samples cut. As experience was obtained a gauging technique evolved which allowed relatively constant sample thicknesses to be obtained. On the average the samples ended up being about 3 mm thick. This sample thickness when combined with the blade width resulted in a sample being taken about every 6 mm of test bar length. After each test bar was fully sectioned, the slices were marked using an arc discharge pen. The identification marks were placed on the unsupported side of the cut. This made the supported side of the cut the one used for analysis. This approach insured that surface anomalies resulting from any motion of the slice during the later stages of the cutting operation did not work their way into the analysis. Once the slices were labeled, the thickness of each slice was carefully measured. The slice thickness measurements were then combined with the blade thickness measurement to generate a table of locations along the bar versus sample identifier. This data may be found in Appendix F

8.1.2 Grind, Polish and Etch

The measured test samples were divided by thickness into approximately 10 groups. Of these groups one group was comprised of samples that had a thickness which was unique. These samples required individual polishing. The remaining samples were in groups of similar thickness. As many as 40 samples at a time were affixed to a six inch platen with double stick tape. The samples were first ground to insure that they were of a uniform thickness and had parallel faces. Once ground, the samples were then polished and etched. The etchant used was a Marbles etch which was found to be effective at bringing out the dendritic structure of the as cast alloy. This etch is primarily a staining etch and resulted in dark staining of the interdendritic region. The most difficult aspect of this procedure was the removal of the tape which proved quite tenacious.

8.2 Dendrite Density

The main focus of this work is a survey of the solidification environment associated with a commercial single crystal furnace as a function various furnace and operating parameters. Although some invasive thermocouple trials were conducted, primary dendrite arm spacings are a more revealing measure of the quality of the part as well as the variability and parametric sensitivity of the process. It then follows that the primary data associated with this study are the surveys of primary dendrite arm spacing along the length of the 8 test bars utilized for this work.

8.2.1 Optical Microscopy

The microscope used to generate the digital optical micrographs from which the dendrite statistics were obtained is located in the metallography lab at Sandia National Laboratories. Fred Greulich of Sandia was kind enough to provide access to this piece of equipment and as such played a facilitating role in the completion of this work. Figure 8.3 is a block diagram of the system used to obtain the digital images.

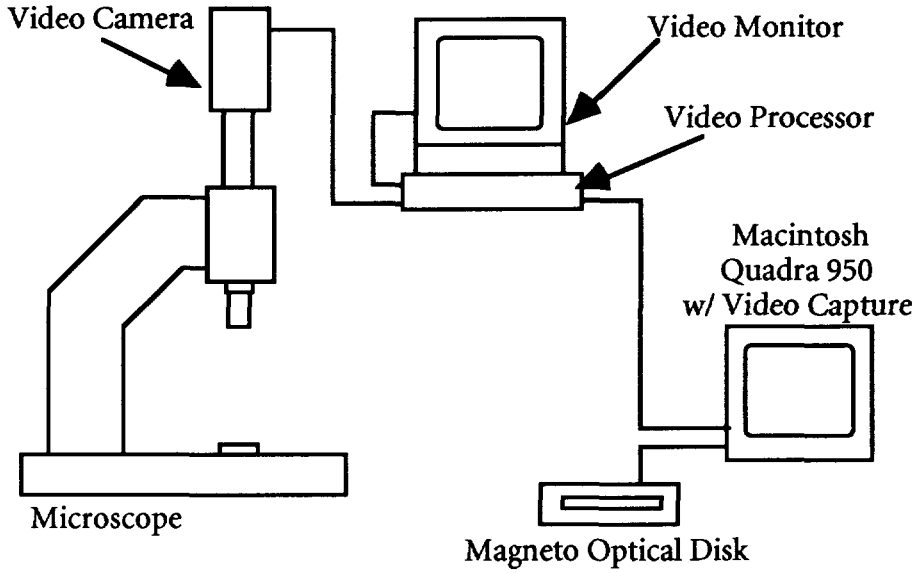

Figure 8.3
Optical Microscope

A specimen placed on the stage of this microscope is viewed with a video camera and monitor. The microscope is also configured with several different light sources. The micrographs obtained for this study were all acquired while utilizing a half wave filter to enhance the contrast of specimen. A video processor was also in line between the camera and monitor to provide brightness and contrast control of the video image. Subsequent to the video processor the video signal was spilt with one signal being fed to a nine inch video monitor placed beside the microscope. This monitor was utilized for focus and the adjustment of brightness and contrast. The signal was additionally fed to a Rasterops video capture board within a Macintosh™ Quadra 950 computer. An Adobe Photoshop™ plug in allowed photoshop to access this board directly. The video image was contiguously displayed on the Quadra's 17 inch monitor. When an appropriate image was achieved, the frame was grabbed from within Photoshop and stored to a Magneto-optical disk as 8 bits per pixel. The file format of the stored image was an Apple™ standard PICT and required about 250 kilobytes of disk space.

A glass slide was employed as the primary substrate for the samples. Upon this slide was placed a small round ball of clay. The sample to be viewed was then placed upon the ball of clay and the whole assembly was then put into a small press. This is shown in figure 8.4.

This method of sample preparation assured that the surface of the sample would be completely flat within the microscopes field of view. This action was required for although the microscope had sufficient depth of field to accommodate slight misalignments, the half wave filter was not so forgiving. If the sample was not flat, the half wave filter would cause the image to have a varying brightness from side to side. So in order to ensure that the brightness and contrast of the image were invariant, the above described technique was employed.

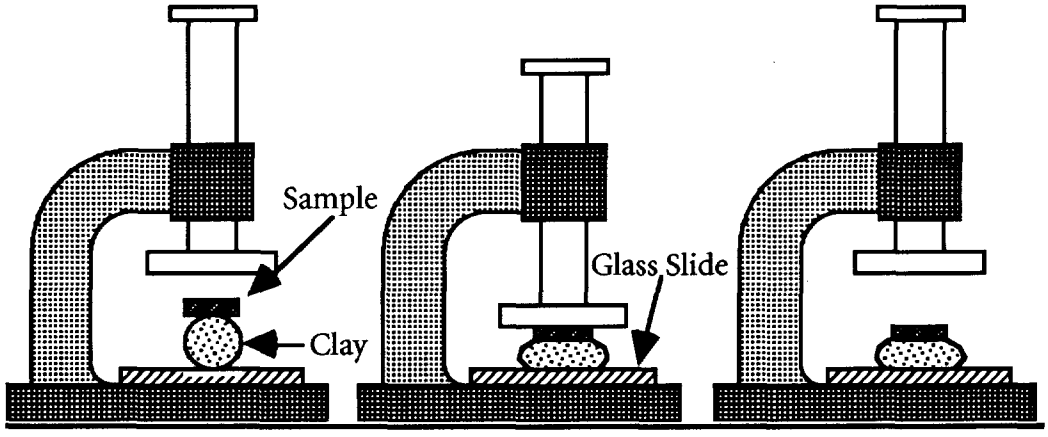

Figure 8.4
Sample Press to Assure Flatness

The magnification on the microscope was set at twelve for some sample sets and sixteen for others. This was the microscope setting only and did not take into account the video train. When taken to the Macintosh™ screen the actual magnifications turned out to be 45 and 60 respectively. The final image on the screen was 225 mm x 170 mm. To ensure proper calibration a calibration procedure was employed. At the beginning of each session on the microscope, an image was taken of a 2 mm scale. These calibration images were stored to disk and utilized as part of the setup for all subsequent analysis.

The optical images were taken at the center at the center of the test bar. There may be some error in the location and as a result some errors in the primary dendrite arm spacing measurements may have been introduced. The error in image location stems from the requirement that the magnification remain fixed in order to maintain a known calibration of the magnification. This translates into an error in the primary arm spacing because the dendrites are spaced a bit closer together near the edge of the part. The 12.7 millimeter in diameter test bar samples had a total surface area of 127

mm^2 and at the microscope magnification of 12.5 yielded an image area of 5.2 mm x 3.9 mm for a total area of 20.3 mm^2 or 16%. At a magnification of 16 the sample size was 3.9 mm x 2.9 mm for a total area of 11.4 mm^2 or 9%.

The magnification was chosen to be as high as possible while still maintaining a statistically significant number of dendrites. The high magnification gives better dendrite definition thus easing the task of locating dendrite cores in software. Lower magnification images were reviewed, and it was found that neither the spacing nor the standard deviation in the spacing experienced any significant change as long as greater than 30 dendrites were evaluated. As a result, in consideration of the software task associated with counting dendrites and determining their statistics, the magnification was kept high.

The magnifications chosen resulted in greater than 30 dendrites appearing within the sampling area of each micrograph. The number of dendrites appearing in any given micrograph range from a high of around 180 under high gradient solidification and a magnification of 12.5, to a low of around 30 in the case where single crystal growth was beginning to break down and the magnification was set at 16.

8.2.2 Dendrite Counting Software

In order to accurately determine the dendrite statistics, a computer program was written to process the digital images and determine the location of the dendrite cores. Once these locations were established, it became a simple matter to ascertain the dendrite statistics. The digital images were stored as a 640 x 480 array of 8 bit gray scale pixels. These images were read into memory and stored as 16 bit integer numbers for ease of processing. The value of the individual pixels represented the brightness of the image. As there was a sharp demarcation in brightness between the dendritic and interdendritic regions it was not difficult to differentiate between the two types of material.

The alloy used in the test bars is cubic in nature. The cubic structure is very apparent in the cross-sectional micrographs of the test bars. In many of the test bars, the primary dendrites are aligned into fairly regular arrays. If rectangular sampling areas are used, this even alignment of primary dendrites, when couples with the dendrite spacing calculation, brings up the possibility of aliasing. This is illustrated in figure 8.5.

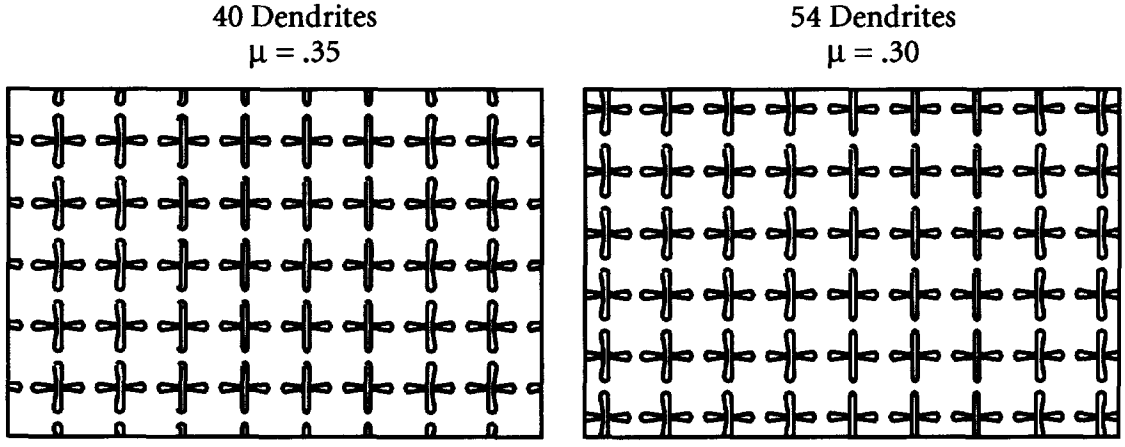

Figure 8.5
Dendrite Aliasing

The cubic nature of the material raises the probability that the boundaries of the sampling area are not exactly equivalent to an integral number of dendrite spacings. The result of this situation is realized by envisioning a rectangular area sliding across a regular array of dendrites. At some point, a new column of dendrites will slide into the sampling area. However, if a column does not simultaneously slide out the other side, then the number of dendrites within the sampling area has increased. This occurs despite the fact that the test sample maintains a constant dendrite spacing. The same possibility occurs in the case of vertical displacement of the sampling area. Figure 8.5 shows a worst case scenario that can occur with a diagonal displacement. Since the primary dendrite spacing is not actually changing, the problem might initially seem more imagined than real. The complication arises as a result of the dendrite spacing calculation within the software.

When writing the software to determine dendrite statistics, the question of how to determine the spacing of primary dendrite arms needed to be addressed. Initially, the calculation involved finding the four nearest neighbors for each dendrite, determining the distance between them and then averaging the readings. In order to be certain that the nearest neighbor of each dendrite used was in fact present within the image (and not off screen), this method required that only a subset of the image be used. For regular arrays of dendrites this method worked very well and was not subject to errors due to aliasing. However, in those instances where irregularities in the spacing occurred, such irregularities imposed a disproportionate impact on the results. Further, the results were not self consistent. If the spacing calculated in this fashion is

used to generate a regular array of dendrites, then the solution is easily checked by the application of the original sample space to this array. Completing this action reveals that the number of dendrites within the sample space has not remained constant. As this method does not produce self consistent results, it was rejected in favor of a different method.

The method which was finally used to calculate the primary dendrite arm spacing allocates each dendrite counted an equivalent area of image. As the crystal is cubic, the area allocated to each dendrite is assumed to be in the shape of a square. Since each dendrite is allocated a square area, then if the dendrites were in a regular array the distance between them would be the square root of the allocated area. This method was implemented by first selecting a circular sample area. The selection of a circular sample area eliminates problems that could be induced due to aliasing. The sample area chosen is 464 pixels in diameter (D) and is in the center of the image. The diameter of the circle is then converted into microns using the image scale factor (S). The number of dendrites within this circle (N) is determined and the area of the circle (A) is calculated. The primary dendrite arms spacing μ, is then calculated using equation 60.

$$\mu = \sqrt{\frac{\pi(D\,S)^2}{4N}} \tag{60}$$

Unlike the previously described method for determining primary dendrite arm spacings, this method yields self consistent results.

The accuracy of either method for determining the spacing is dependent upon getting the appropriate scaling into the software. This is accomplished by reading in one of the previously described images of the two millimeter scale and then graphically pulling a line along the two millimeter distance. Once the line has been defined, the true length of the line in microns (2000) is entered. The computer calculates the length of the line on the screen in pixels and arrives at a scaling factor. Scale factors of around 8 microns per pixels were typical.

The counting software was written under the assumption the vertical and horizontal axes on the computer screen would correspond to the <001> directions of the secondary dendrite arms. This was not a requirement, but allowed significant simplification of the dendrite recognition routine.

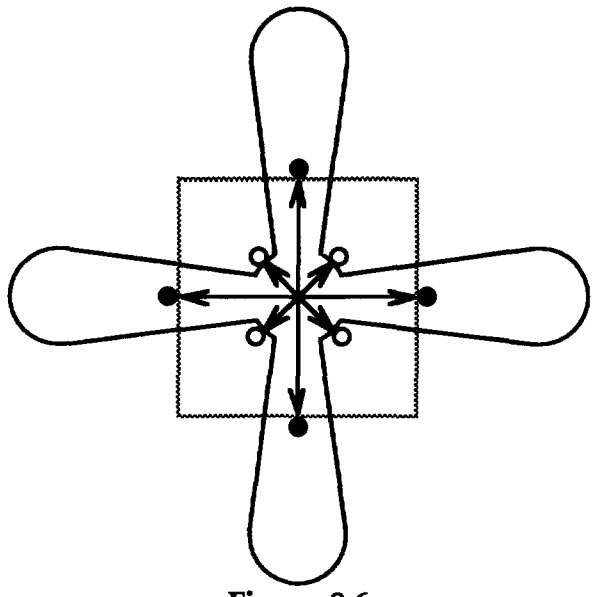

Figure 8.6
Dendrite Location Algorithm

Figure 8.6 is an illustration of a primary dendrite which will be used to describe the dendrite counting software. The program begins at the left side of the image, 8 pixels down from the top and scans the rows of pixels sequentially from left to right until the eighth row from the bottom. This captures the upper and lower bound of the sample circle and ensures that there is sufficient image above and below the sample circle for the discrimination of a dendrite which may exist at the outer boundary of the circle. The software checks to see if the pixel currently addressed is within the sample circle, if it is not, the next pixel is checked. If the current pixel is within the sample circle then the image is interrogated at four points, each located a fixed displacement along the directions of the secondary arms. These points are shown in figure 8.6 as filled circles and are located at the points where the horizontal and vertical arrows impinge on the dashed square. The size of the dashed square is an adjustable parameter and may be entered by the user or alternatively automatically determined by the software from a sample dendrite from within the screen image. If any of these four points possesses a brightness that is less than the brightness threshold for a dendrite, the program steps to the next pixel in the row. If all four points are brighter than the dendrite brightness level, then the software scans from the left point to the right and from the top point to the bottom. If at any time during these scans a pixel is detected with a brightness level that is lower than the dendrite brightness threshold, the program steps to the next pixel in the row. After the above procedure has occurred,

the software then proceeds to verify if the location is a dendrite core. To accomplish this the program begins at the current pixel and tests outward at four points at angles 45° between the secondary arm directions. These point are indicated in figure 8.6 as open circles. The distance from the current pixel to these points is an adjustable parameter and may be entered by the user or automatically determined by the software. If all of these four points are of a brightness that is lower than the interdentritic brightness threshold, then the current pixel is considered to be near the core of a dendrite.

Once a potential dendrite location has been identified, four diagonal scans are made and the distance from the center dendritic material to the interdendritic boundary is determined for each scan. From these four distances an average distance is calculated. The average distance is then subtracted from the actual distances and each of these four results are squared and then summed together. If the current pixel is considered to be the center of the dendrite core, then the resultant number is a measure of the asymmetry of the dendrite.

The location of the current pixel is then compared to any dendrites which may have been found previously. If the dendrite core as specified by the current pixel is within twice the primary search distance (twice the length of a side of the dashed rectangle of figure 8.6), of a dendrite which was found previously, then the two are considered to be the same dendrite. In such a situation, the asymmetry of the dendrites at the two core locations are compared and the location and asymmetry value of the core location with the lowest asymmetry is retained within the list of found dendrites.

After the computer has found all locations which match the selection criteria of a dendrite core the user is then able to add or subtract additional location. This feature proved useful, but in general, the errors made by the computer were on the order of one to two percent of the total count.

Once all dendrite locations are identified, the statistics are calculated. The primary dendrite arm spacing is determined as previously described. In addition the standard deviation in the primary dendrite arms spacing is also calculated. In order to calculate the standard deviation, the four nearest neighbors of each dendrite within a reduced sample area are determined. These spacings are then contrasted to the previously obtained primary dendrite arm spacing and a standard deviation is then calculated.

The statistics are added to the image along with a micron bar and sample identifier. The image is then saved to disk. Additionally, the statistics are written to a

tab delimited text file for subsequent processing by a spreadsheet or graphing program.

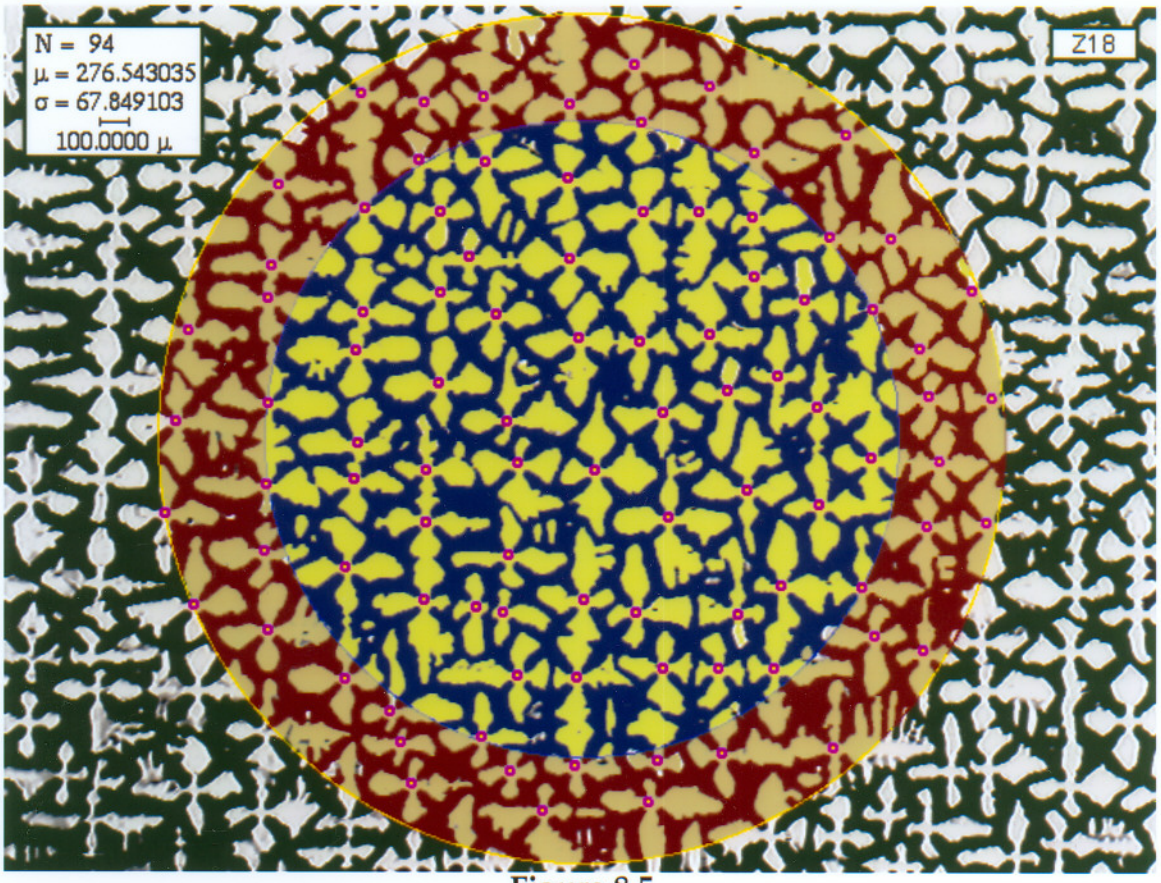

Figure 8.5
Dendrite Counting Example

Figure 8.5 is an example of one of the files generated by this program. The figure is displayed at 68% of the size used for the analysis. False color has been added to ease the explanation. In the figure, primary dendrites appear in white or mustard. The interdendritic regions in red, purple or black. Dendrites which appear on the black background are not used for the calculation. The yellow circle which bounds the mustard colored dendrites represents the sample area used for the determination of the primary dendrite arms spacing and encompasses those dendrites which reside on both red and purple backgrounds. The mustard colored dendrites within the center purple region are those used for the determination of the standard deviation in the primary dendrite arms spacing. The small magenta circles with the yellow center indicate the core of a primary dendrite as determined by the software.

8.3 Growth Orientation

A brief assessment of the changing heat transfer environment which occurs within the system makes it apparent that the solidification interface is not normally located at the baffle. From this statement it may then be inferred that solidification is occurring under conditions where the heat flux is not traveling in the same direction throughout the cross section of the test bar. This is illustrated in figure 8.8.

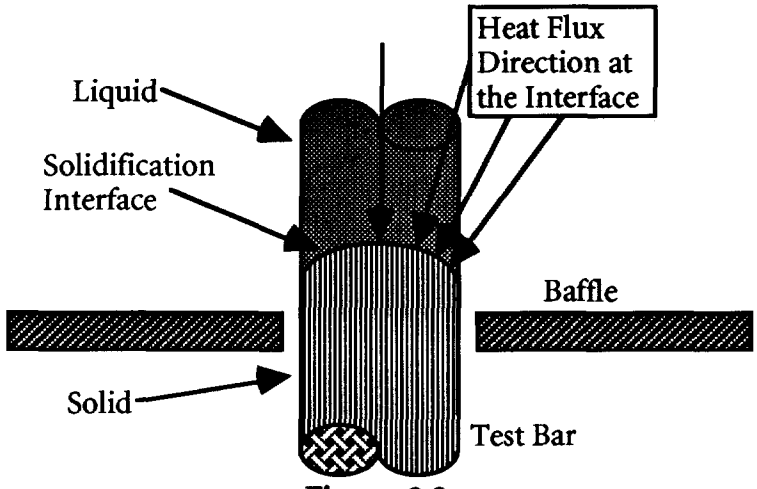

Figure 8.8
Curvature of Solidification Interface

Figure 8.8 shows what happens to the shape of the solidification interface as it is pushed above the baffle. The driving force behind this push is the high heat flux out of the portion of the mold below the baffle. The result is that the interface ends up being located in an area where significant heat flux from the susceptor into the mold is present. So while the heat flux at the geometrical center of the bar may in fact be axial, the radial component introduced by the flux from the susceptor drives the interface to a curved morphology. Since dendrites grow in the opposite direction of the heat flux, if the interface is not at the baffle, then one would expect to observe a change in the dendrite growth direction from the center to the edge of the test bar. The magnitude of this change would be a function of the distance of the interface from the baffle and as such should increase as the withdrawal process progresses.

In order to verify this phenomenon, Back-Scattered Electron Kikuchi Patterns were acquired. This technique, which may be used to determine crystallographic orientation is described in the following section.

8.3.1 Back-Scattered Electron Kikuchi Patterns

A Back-Scattered Electron Kikuchi Pattern (BEKP) is a diffraction phenomenon which may be observed within a Scanning Electron Microscope (SEM). The addition of this capability to a standard SEM is relatively inexpensive and as a result, the technique is seeing an ever increasing degree of interest.

Kikuchi patterns were first reported in 1928 by S. Kikuchi[42]. While studying electron diffraction using thin films of mica, Kikuchi found that in addition to the Laue spots, there appeared a background structure on his film as well. The structure reported by Kikuchi consisted of parallel lines, initially termed *excess* or *defect* lines, and later to be called Kikuchi lines. Kikuchi lines are explained by assuming that scattered electrons diffusing through the crystal are scattered by Bragg planes.

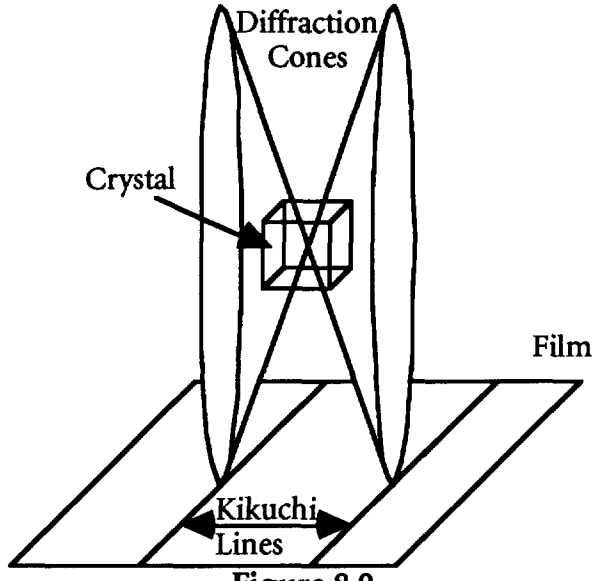

Figure 8.9
Kikuchi Patterns

The scattered electrons form cones of radiation. A film placed such that it intersects these cones will show their traces. The cones are sufficiently flat to cause the traces to look like lines. The lines come in pairs for example (100) and (-100) and may be readily indexed as to their planes of origin.

In 1953, Alam, Blackman and Pashley[43] reported on High Angle Kikuchi Patterns. Although previously described by Meibom and Rupp[44] in 1933 and by Boersch[45] in 1937, the paper by Alam, Blackman and Pashley is the first definitive study of the phenomenon. Alam et al describe a series of experiments wherein energies from 6 to 50 keV and scattering angles from 0° to 164° are examined. The experiments were conducted on crystals with a sodium chloride structure and results were related

to elastic scattering cross-section. In order to accomplish the study a special device was fabricated that would allow the complete investigation of the chosen parameter space. This device is shown in figure 8.10.

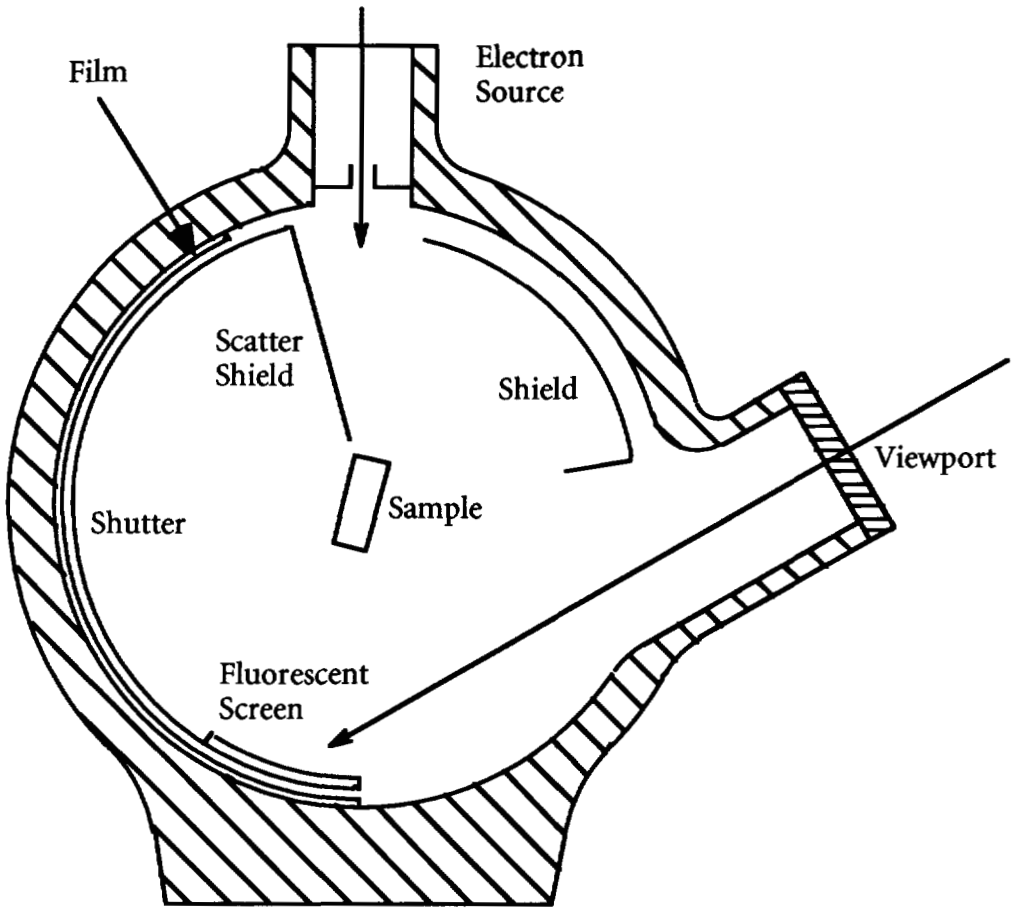

Figure 8.10
Alam Apparatus

During operation an electron source at the top of the device would direct a stream of electrons at a crystal located in the center of the apparatus. A fluorescent screen placed on the back of the shutter was viewed through the viewport to enable proper alignment of the crystal. During exposure of the film, the fluorescent screen was covered by a shield in order to prevent it from fogging the film. A scatter shield was also attached to the shutter to avoid film fogging by electrons which were scattered by the shutter. The shutter configuration allowed varying exposure times for different areas of film.

The intent of this original work was purely the investigation and explanation of an observed phenomenon. Experiments with this device as conducted and

documented by Alam, Blackman and Pashley form the basis for all future work. However it was not until 1973 when Venables and Harland[46] proposed using the phenomenon in the SEM as a way of gathering crystallographic information that high angle Kikuchi patterns became anything more than a curiosity.

The phenomenon originally termed "High Angle Kikuchi Patterns" is today a technique used within the SEM and called BEKP, BKP, EBSD, or BKDP for Backscattered Electron Kikuchi Patterns, Backscattered Kikuchi Patterns, Electron Back-Scattered Diffraction Patterns and Backscattered Kikuchi Diffraction Patterns respectively. BEKP has four primary uses. The first is determination of crystal structure, symmetry and point group[47,48],. The second use of BEKP is orientation analysis [49,50] which is the most common use of the technique. Originally used for the determination of the orientation of a single crystal, the technique has been extended to automatic texture determination[51,52,53,54] of an entire sheet and the associated generation of texture maps. A third use of BEKP is the study of deformation. In this instance, BEKP is proposed as a method for the study of plastic strain[55,56]. Although possible, image quality has made this use difficult. The final use is a technique which is still under development and that is application of BEKP to phase identification in the SEM[57,58]. This application has the potential of turning an SEM into a machine for the accurate determination of crystallographic phase. This last use, if realized will significantly increase the importance of BEKP as an analytical tool. As such, BEKP could achieve widespread usage as the number of SEMs where this technique could be of benefit is very large. In summary, BEKP is a relatively new technique and its uses are just being understood. It holds the potential of bringing significant new capabilities to SEM labs.

The microscope used for this work was a JEOL 6400. The detector was designed by Joe Michael of Sandia National Laboratories in Albuquerque NM. Figure 8.11 is an illustration of the equipment used for these determinations. In operation the sample to be analyzed is placed upon a stage which has been rotated 70.5° from the horizontal. The usual motion of the stage is retained in order to allow access to the complete sample. (When determining the location of various areas on the sample it must be remembered that the sample is tilted and one axis appears very much fore-shortened.) The electron beam impinges on the crystal and a cone of diffracted backscattered electrons are emitted from the surface. The emitted electrons then impinge upon a phosphor screen which has been placed at a precise distance from the sample. The phosphor screen is attached to a fiber optic reducing bundle. This bundle of optical

fibers has been extruded down form the original phosphor size of approximately 2.5 inches by 2.5 inches to around one inch in diameter. This reduction acts as an image

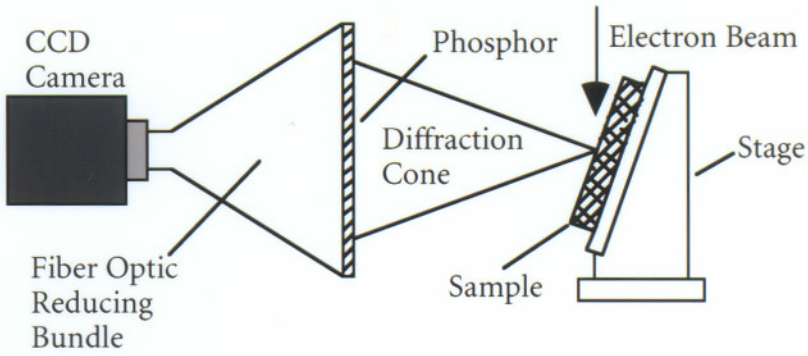

Figure 8.9
Hardware Configuration for BEKP Acquisition

intensifier allowing a larger area of phosphor to be used to generate the image. The fiber optic reducing bundle is then fed into a CCD camera. The CCD camera is connected to a Macintosh™ IIfx computer running Adobe Photoshop. The resultant backscattered electron Kikuchi pattern is viewed in real time on the Macintosh™ computer screen.

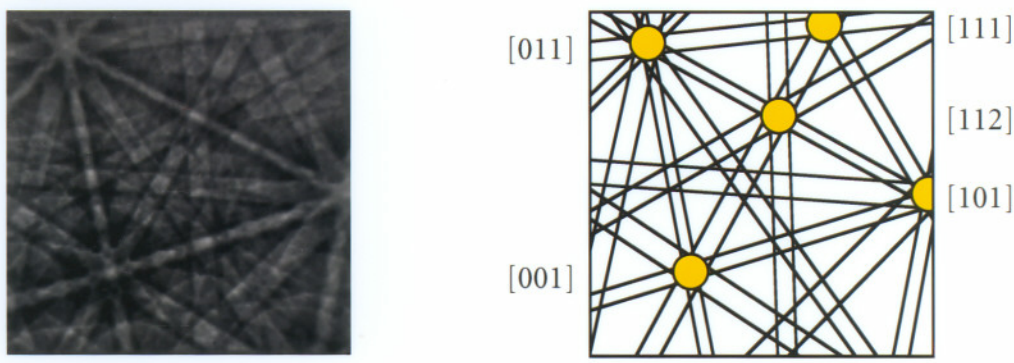

Figure 8.10
Cubic BEKP Image and Indexing

Before an actual BEKP image is acquired, a *flat field* image is first obtained. This image, which is taken under an even illumination obtained by scanning the beam, contains no diffraction information but does show up defects in the phosphor, the fiber optic reducing bundle and pixelation effects which may occur due to the discrete nature of the optical fibers.

Once a flat field has been obtained, the sample is moved until the desired area of the sample is in view on the SEM monitor. The area is centered and the beam scan is

stopped. This sets up the single electron beam needed to obtain the BEKP. If the image on the computer screen is appropriate, the software is instructed to store that image.

After acquisition, the BEKP image is divided by the flat field image. This action results in a removal of image artifacts that may occur as a result of the image train and yields a very high quality image. The final image is stored as an 8 bit per pixel gray scale bit map, figure 8.12 is an example.

As may be seen from the figure, the technique yields a high quality diffraction pattern which is easily indexed. However, due to the geometry of the setup, the center of the image is not the center of the diffraction pattern. As a result, a calibration must be performed to determine the pattern center. There are several methods for accomplishing this. Randle[59] describes a method using a pair of wires placed in front of the phosphor screen and the use of a silicon calibration crystal. Venables[60] describes a method using steel balls. At Sandia, the Silicon crystal calibration method is used.

The calibration procedure begins by obtaining a silicon crystal cleaved to reveal a [001] surface normal. This crystal is placed on the stage such that it lies parallel to the surface of the stage and such that [011] is the horizontal axis (out of the page). Figure 8.13 illustrates the geometry.

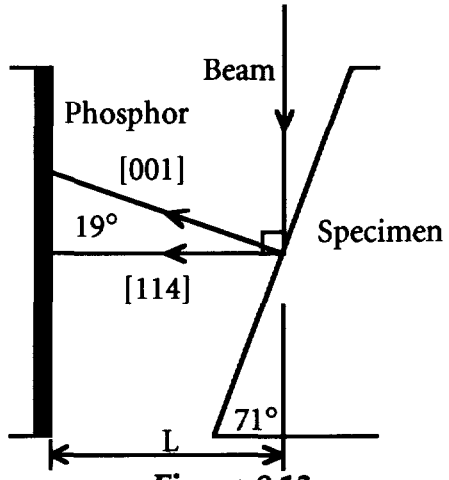

Figure 8.13
BEKP Calibration

From the figure it may be seen that, for a properly oriented silicon calibration crystal, the [114] zone axis will appear at the center of the screen. Further the [001] will be located at a distance corresponding to 19° away. If the specimen to film distance L is known, then the angle may be checked and the position on the screen which corresponds to the sample normal may be identified. Once the location of the pattern center has been ascertained then, given an indexed pattern and L, the orientation may

be readily calculated. It is important to note that for all angular measurements, the position of the pattern center must be known, otherwise calculations cannot be made.

For this work, BEKP will be used to determine the dendrite orientations across the sample. Since dendrites grow perpendicular to the heat flow it is hoped that this technique will allow the shape of the liquidus to be determined. Such determinations will provide additional evidence of the operative heat flow mechanisms. This technique for the determination of the molten pool shape that existed during solidification is a new application of the BEKP process. It allows pool shape determinations from a thin transverse slice. With proper equipment such measurements could be made automatically. The technique allows the assembly of an entire 3 - D solidification pattern by surveying successive slices. It should also prove very useful for solidification studies of large ingots. At present, such studies require longitudinal sections which are very expensive. Due to the lower material costs, BEKP would allow access to a greater variety of solidification conditions for study.

Chapter 9 Results of Casting Trials

The casting trials were conducted at Retech Inc. in Ukiah CA on a furnace belonging to Rolls Royce. A total of 12 test bar molds were cast and directionally solidified into single crystals. After cropping the test bars ranged from 140 to 180 mm in length. The mold contained a helical crystal selector and was configured to sit atop a 150 mm diameter water cooled copper chill plate. Each mold contained a total of 8 test bars. Figure 9.1 is an approximate diagram of the mold configuration.

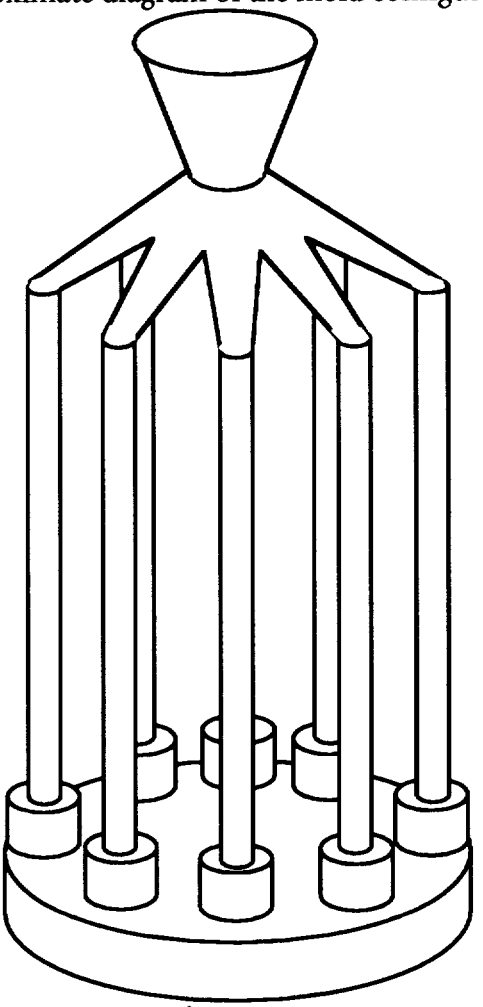

Figure 9.1
Mold Example

The twelve molds were broken down into two categories. The first group of six molds was processed in a straight sided chill spool whereas the second group was processed using a shaped design. The two different chill spool design were described in

section 6 and are illustrated in Figure 6.2 - 6.4. The furnace supported a multiple zone susceptor and different susceptor temperatures were tried. Some variations in withdrawal speed were also experimented with. Table 9.1 shows the conditions of the twelve melts.

Table 9.1 Process Data for Single Crystal Molds

Identity	Melt Temp °C	Zone 1 Temp °C	Zone 2 Temp °C	Velocity mm / min	Chill Spool Shape
A	1550	1500	1550	5.6	Standard
V	1550	1550	1550	4	Standard
W	1500	1475	1475	4	Standard
X	1475	1500	1500	8	Standard
Y	1500	1500	1500	5.8	Standard
Z	1500	1550	1550	4	Standard
1	1500	1500	1550	Auto	Shaped
2	1500	1475	1475	Auto	Shaped
3	1500	1475	1475	4	Shaped
4	*1510*	*1475*	*1475*	Auto	*Shaped*
5	1500	1475	1475	4	Shaped
6	*1500*	*1475*	*1475*	*4*	*Shaped*

The test bars listed in bold face type were selected for transverse sectioning to allow determination of the primary dendrite arms spacings. This aspect is covered in depth in the section on primary dendrite arm spacing. The test bars which are listed in *underlined italic* (4 & 6) are the test bars into which thermocouples have been placed. The velocities marked as auto were those tests during which an attempt was made to control the solidification interface location.

Thermocouples were placed within one of the molds on each of the respective trees during the two instrumented melts. This was accomplished by actually building miniature thermocouple wells into the mold such that the thermocouple bead was located at the center of the bar. Not all of the thermocouples survived the process and as a result data was gathered from a total of 11 thermocouples during melt 4 and from 8 thermocouples during melt 6. The thermocouple data was acquired at 1 Hz throughout the process. This data sample rate resulted in approximately 3000 readings per thermocouple per experiment. The experiments were conducted under two

different modes of withdrawal. During run number 6, the mold was withdrawn at a constant velocity of 4 mm per minute. During run number 4 the velocity was varied in an effort to maintain the solidification interface at the baffle.

9.1 Constant Velocity Withdrawal

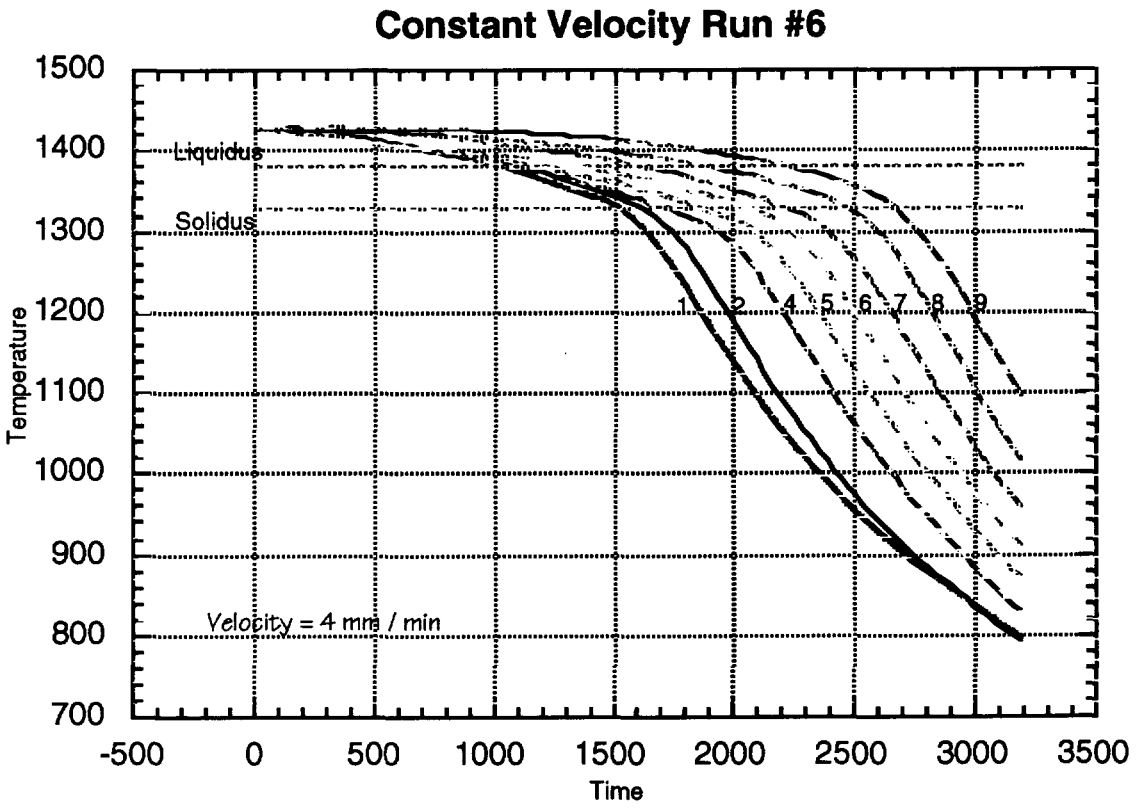

Figure 9.2
Constant Velocity Temperature Profiles

After the constant speed run was complete (run 6), it was discovered that the baffle had been broken when the mold was raised into position. As a result, this run is representative of a furnace without a baffle separating the hot and cold zone. Figure 9.2 is a scatter plot of temperature versus time for the thermocouples placed into the mold during melt #6. The two horizontal lines represent the liquidus and solidus temperatures and are placed on the graph for convenience.

This data is to be analyzed in an effort to predict the primary dendrite arm spacing for the test bars. The first step is the verification of the thermocouple locations. This is accomplished by calculating the temperature difference between adjacent thermocouples during the process. When the average position of the thermocouple

passes from the hot to the cold zone, the temperature difference will peak. This occurs because the baffle location is the location of highest temperature gradient. Since the baffle location is also the "zero" position in the furnace, the withdrawal distance may be considered a location on the mold. These temperature differences are fitted to a fifth order polynomial in the form of $\Delta T = f(x)$, where x is the withdrawal position. A fifth order polynomial was chosen because it allowed a good fit across the temperature peaks. The first derivative of the peak equations was then set equal to zero and solved. This method had the effect of utilizing a least squares minimization for the determination of the peak location. Figure 9.3 is a plot of the temperature differences obtained in this fashion.

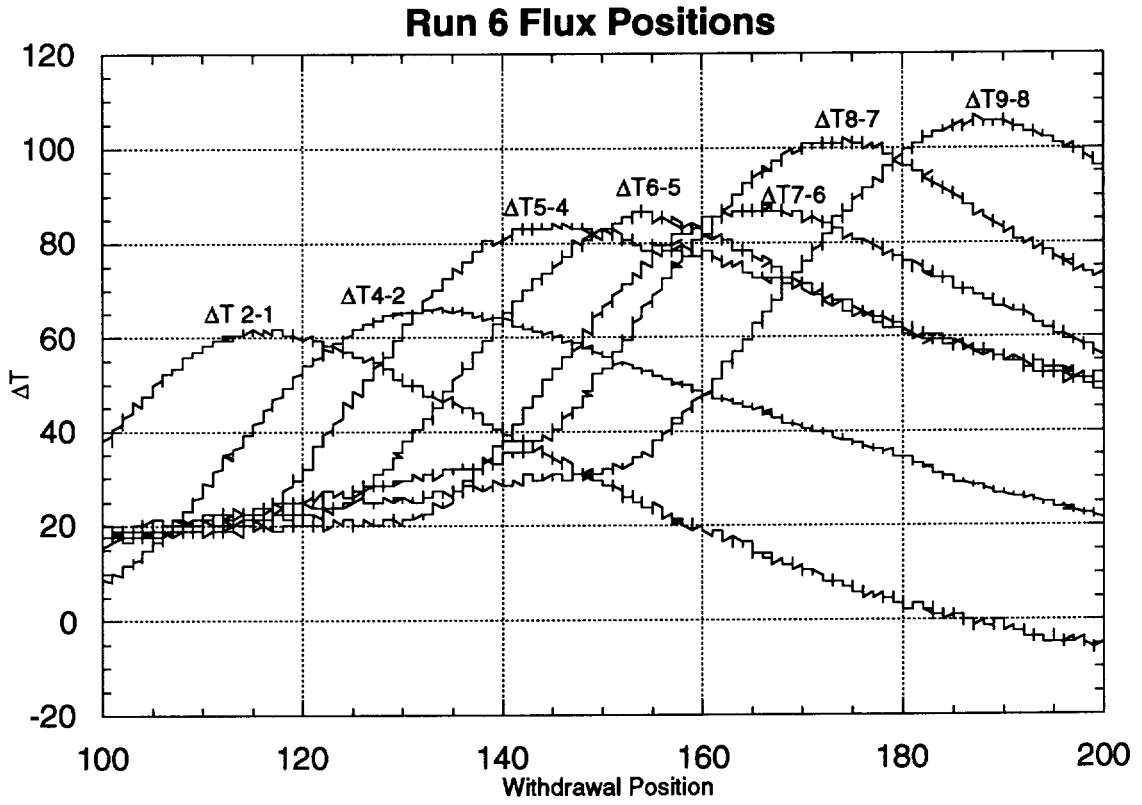

Figure 9.3
ΔT Between Adjacent Thermocouples vs. Withdrawal Position

This operation was conducted for each pair of adjacent thermocouples and a peak location was determined. For the case of run #6, this resulted in peak locations for seven thermocouple pairs. It should be noted that thermocouple #3 was bad and as a result the distance between thermocouple 2 and thermocouple 4 is twice the typical distance. This larger distance is responsible for the higher ΔT associated with these thermocouples and evidenced in the figure. Once the peak locations were determined,

a set of equations may be written such that the peaks are located precisely between the two thermocouples. This results in a set of equations as shown in figure 9.4.

Figure 9.4 is the matrix expression for a set of *n* equations in *n* unknowns. The temperature differences only yield n - 1 equations and so an additional equation must be generated. For this work an equation of the form: $x_n - x_1 = L$ was used where the x's are the thermocouple locations and L is the total length of the thermocouple array. The solution of this series of equations provides a set of thermocouple locations that are corrected for errors in the location and angle of placement.

$$\begin{bmatrix} .5 & .5 & 0 & 0 & \dots & 0 \\ 0 & .5 & .5 & 0 & \dots & 0 \\ 0 & 0 & .5 & .5 & \dots & 0 \\ n\ rows & & & & & \end{bmatrix} \begin{bmatrix} x_1 \\ x_2 \\ x_3 \\ x_n \end{bmatrix} = \begin{bmatrix} Peak_1 \\ Peak_2 \\ Peak_3 \\ Peak_n \end{bmatrix}$$

Figure 9.4
Array Notation for N Equations in N Unknowns

Once the thermocouple locations have been verified, a plot of temperature gradient at the solidification interface vs. position along the bar may be generated.

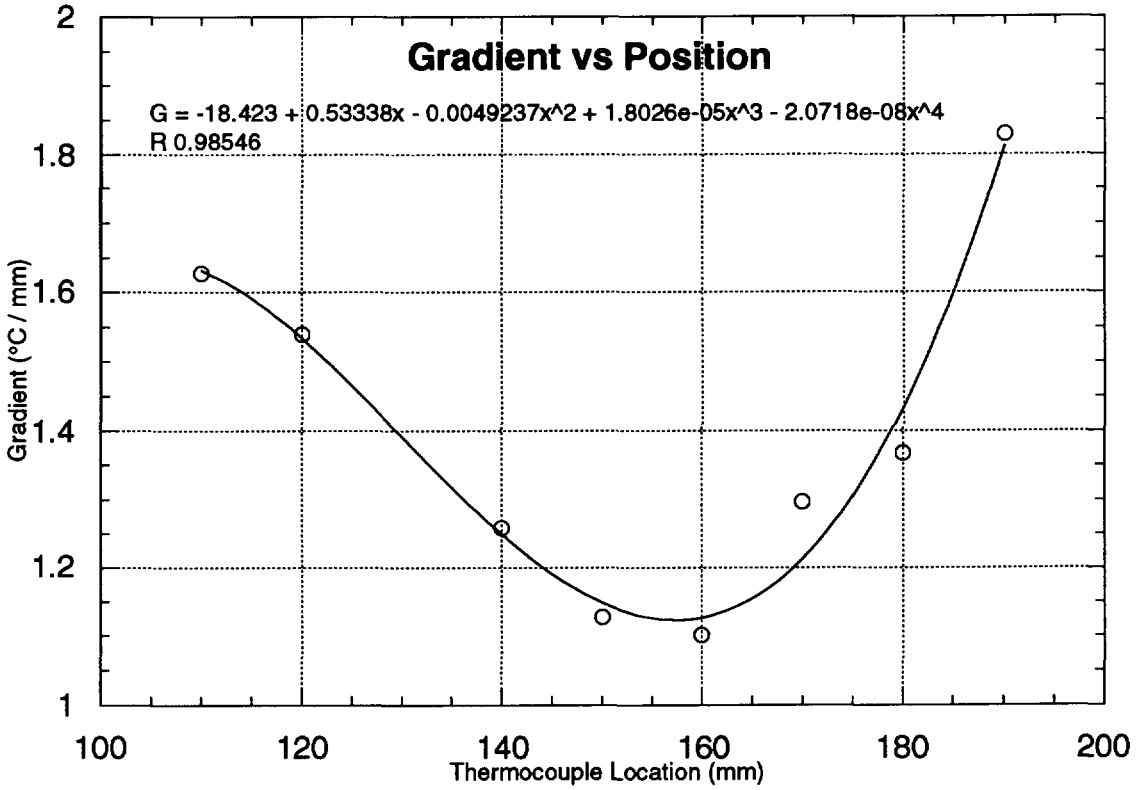

Figure 9.5
Gradient vs. Thermocouple Location

Figure 9.5 is the plot of gradients for the various thermocouple locations as the solidification front passed. The data has been fit to a fourth order polynomial in order to allow an expression for primary dendrite arm spacing to be derived. The assumption of a fourth order polynomial is based upon the emissive nature of the heat flux into and out of the part. The rationale is that since the gradient is changing as a function of withdrawal distance, and the withdrawal distance is effecting the relative ratio of emissive heating and cooling, then emissive heat flux must be impacting the gradient. It should be noted that during the course of this analysis it was verified that the primary dendrite arms spacing is a function of the conditions at the dendrite tip and as a result liquidus positions and gradients are used in this analysis.

In addition to the gradient information, the liquidus, solidus and average interface locations were also determined. Plots of these locations may be found in figure 9.6.

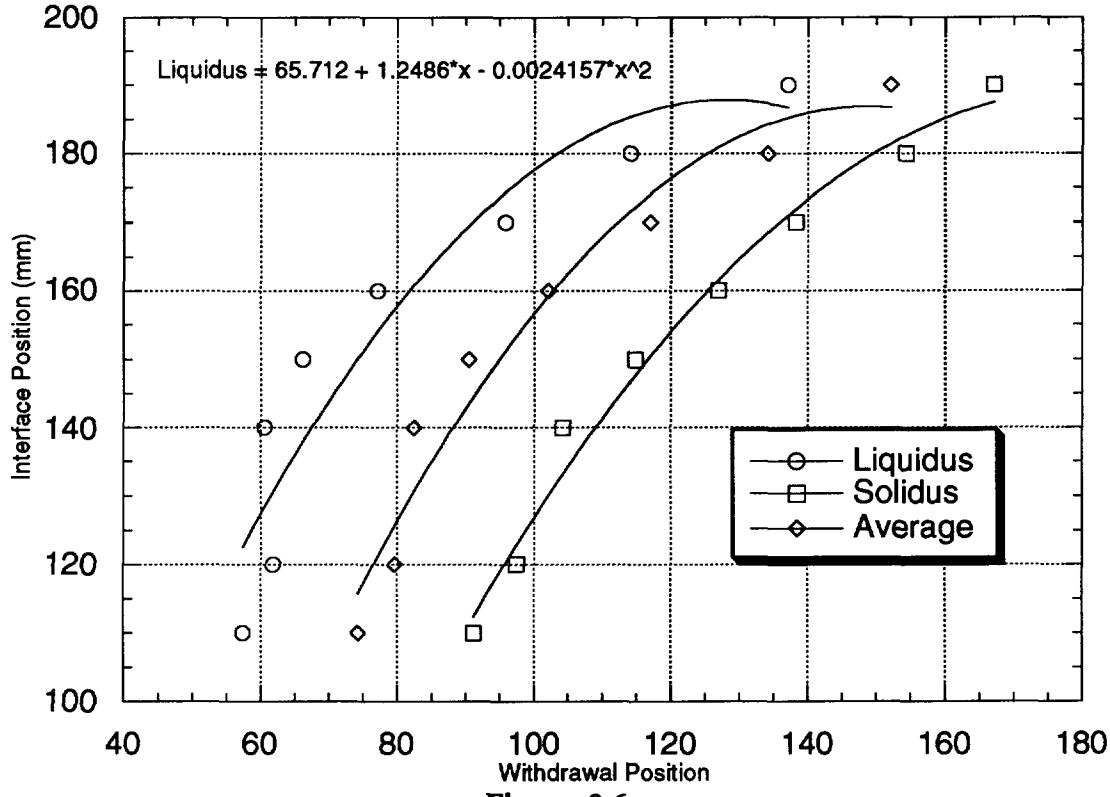

Figure 9.6
Interface Position vs. Withdrawal Distance

The data was fit to second order curves in order to minimize errors. In order to calculate the primary dendrite arm spacing, a solidification rate must be determined. This is achieved by first determining an equation for the interface location and then taking the derivative. When higher order curves where utilized, the derivative was quite irregular. This was the result of the function mapping tightly to the data. The curvature required to achieve the tight mapping resulted in irregular derivatives. The irregularity in the expression for the solidification rate caused the ultimate results to vary widely from the expected values.

To determine the solidification rate, let L represent the interface location and x the withdrawal position, then the each of the above curves represents a function of the form:

$$L = f(x) \tag{61}$$

In this case the equation for the location of the liquidus position as a function of withdrawal distance is written in (62).

$$L = 65.712 + 1.2486x - 0.0024157x^2 \tag{62}$$

From this expression it is desired to obtain a solidification velocity. In order to accomplish this the initial expression for the location of the liquidus as a function of withdrawal distance must be transformed into a change in interface position with time. As such it may be said that:

$$\left(\frac{\partial L}{\partial t}\right) = \left(\frac{dL}{dx}\right)\left(\frac{dx}{dt}\right) \tag{63}$$

In other words, the interface velocity may be expressed as the product of the first derivative of the equation for Position as a function of Withdrawal Distance and of the withdrawal velocity. Under constant velocity the withdrawal position x is simply:

$$x = v\,t$$

$$\frac{dx}{dt} = .0667 \tag{64}$$

The velocity is 4 mm / min or .0667 mm / sec. Evaluating the equation for the liquidus position in the manner described results in an expression for the liquidus velocity as a function of time.

$$\frac{dL}{dt} = .08324 - 3.2209 * 10^{-4} t \tag{65}$$

Before the primary dendrite arm spacing may be calculated, the expression for the gradient must be transformed. The gradient expression is in terms of thermocouple location and must be in terms of time like the solidification rate equation. Note however that the x_is in the equation are in fact the same as the L of equation (62) and further, from (64) x may be expressed in t. From figure 9.5 equation (66) is the 4th order polynomial for the gradient. This equation may be transformed into the appropriate form by first substituting the withdrawal vs. time function(64) into the liquidus location expression (62).

$$G = -18.423 + 0.53338x_i - 0.0049237x_i^{\,2} + 1.8026 * 10^{-5} x_i^{\,3} - 2.0718 * 10^{-8} x_i^{\,4} \tag{66}$$

The resulting expression for L as a function of t may be substituted into (66), the equation for gradient as a function of bar location, thereby yielding an equation for gradient as a function of time. By inspection the result is a very large equation. As such Mathematica™ by Wolfram Research was used for this set of evaluations and all subsequent manipulations. The Mathematica™ program and its results are included in Appendix A.

Once expressions for the gradient and the solidification rate as a function of the location along the bar have been determined, a plot of primary dendrite arm spacing vs. $1 / (G^{.5} * R^{.25})$ may be obtained. Figure 9.7 is such a plot.

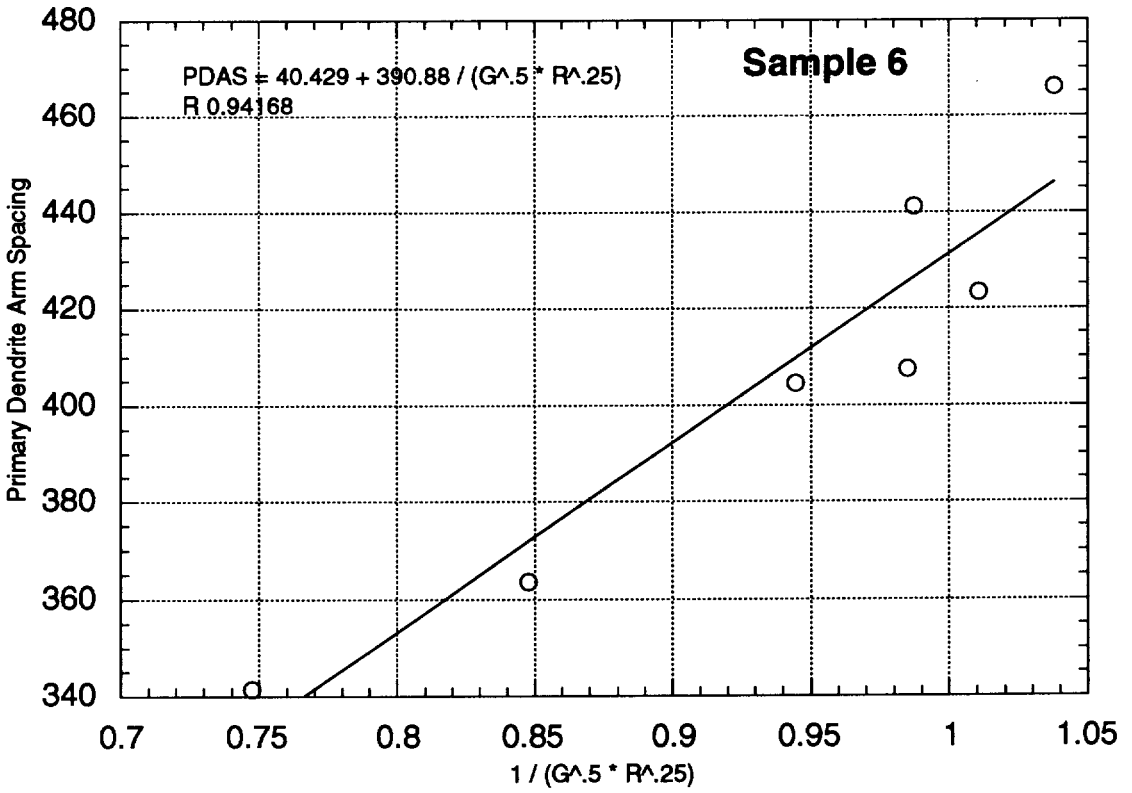

Figure 9.7
PDAS vs. $1 / (G^{.5} R^{.25})$

This plot was generated by calculating $(G^{.5} * R^{.25})$ at the positions along the bar at which primary dendrite arm spacing measurements were made. The results of these calculations were then paired up with the associated dendrite arm spacings and plotted. It has been reported[61] that superalloys exhibit a linear relationship between the primary dendrite arm spacing and the factor $1 / (G^{.5} R^{.25})$. Therefore the data were fit to a linear equation. For this set of data, the resultant equation that describes this relationship is:

$$PDAS = 40.43 + \frac{390.88}{\left(G^{.5}\ R^{.25}\right)} \tag{67}$$

Utilizing this expression, a series of ($G^{.5} * R^{.25}$) were calculated at positions along the test bar. For this particular experiment, only 90 mm of bar was ultimately instrumented and as a result that was the extent of the data generated. The various values of ($G^{.5} * R^{.25}$) were then evaluated in (67) and plotted against the associated bar location yielding a plot of primary dendrite arm spacing as a function of position along the bar. On to this plot the actual primary dendrite arm spacing measurements were added: Figure 9.8 is the result of this operation.

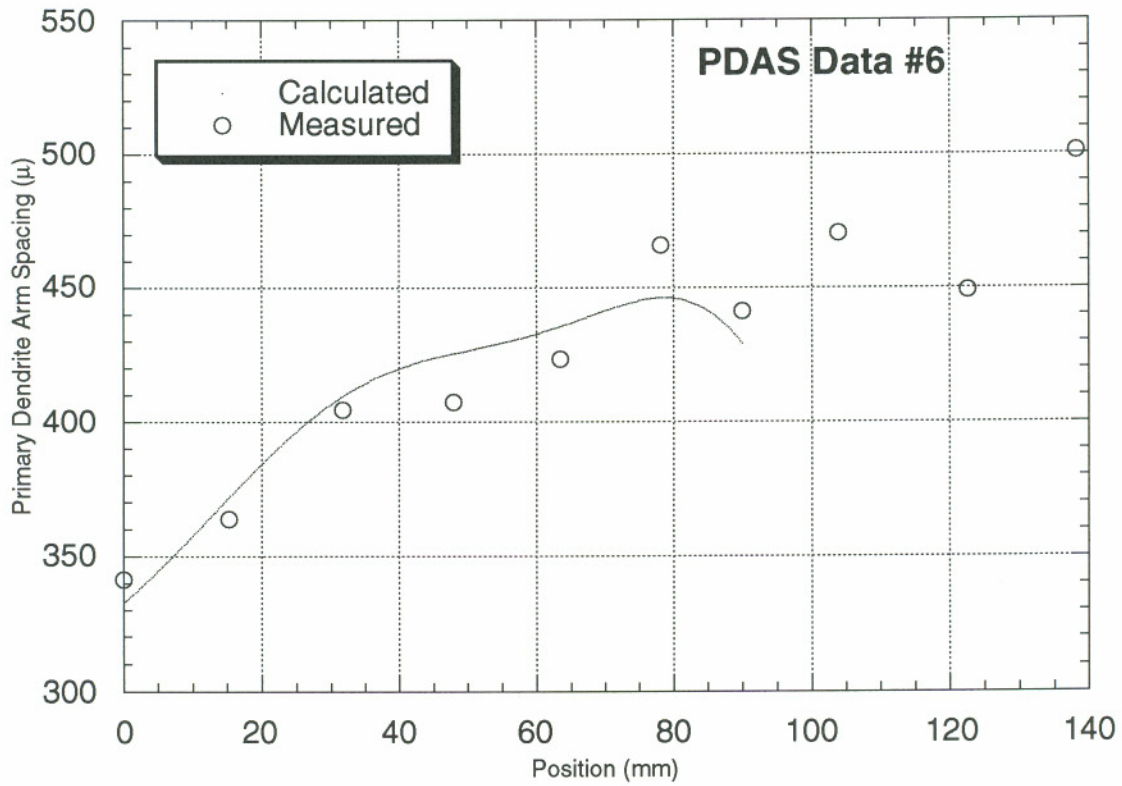

Figure 9.8
Calculated and Measured PDAS

As may be seen from the figure, the fit is fairly good. The turn down at the end of the calculated PDAS curve is due to the behavior of the fitting function as it is evaluated towards the end of the data.

The lack of an effective baffle is evident in the low gradients, as seen in figure 9.5. It is also evident in the location of solidification zone relative to the baffle as shown in Figure 9.9.

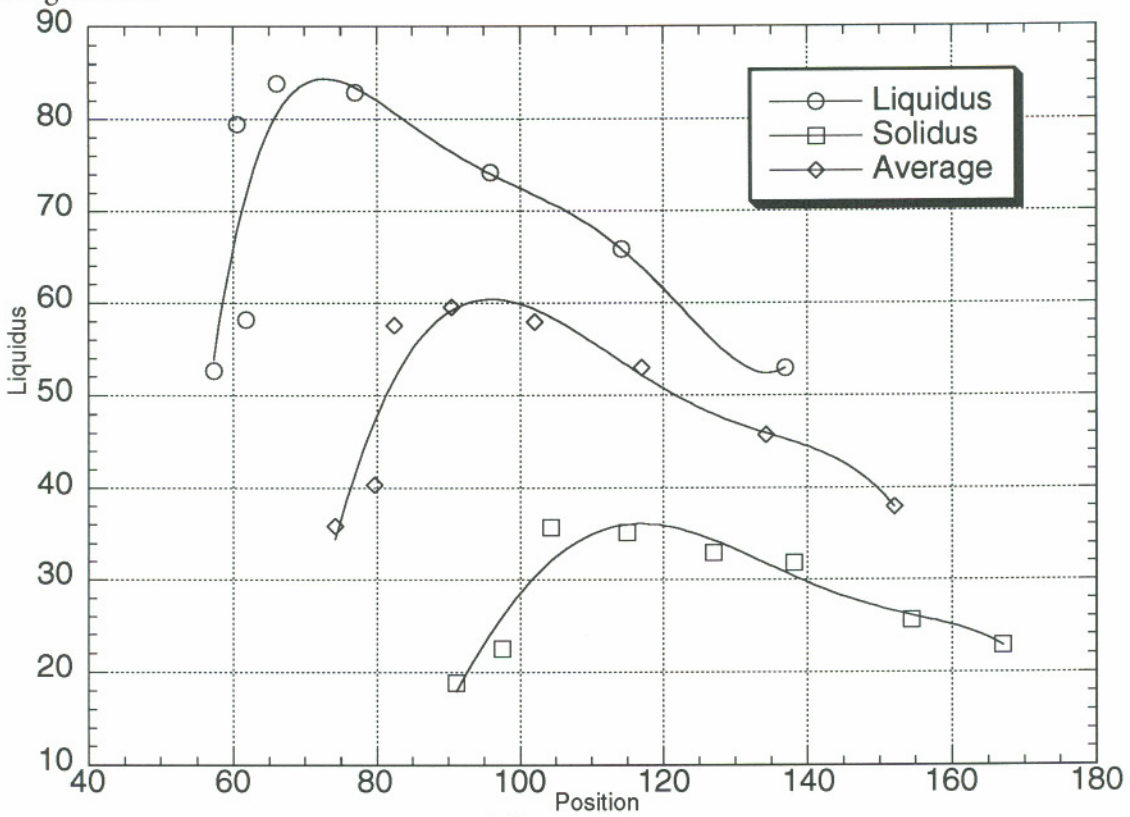

Figure 9.9

Liquidus Positions Relative to the Baffle vs. Withdrawal Distance

The damaged baffle allowed substantial emissive heat loss from portions of the mold that would normally not *see* a cold surface. This had the effect of reducing the heat flux down through the part by allowing much of the mold a simultaneous view of the hot susceptor and the cold chill spool. However despite the low gradients, the effect on the primary dendrite arm spacing is not as great as might be expected. The gradients for this run were typically around 1.3°C / mm whereas for other runs a value of 8°C/mm was obtained. This represents a factor of about 6. It would be expected from (67) that such a gradient difference would result in a factor of 2.4 in dendrite spacing between the cases, however such is not the case. Clearly for this configuration the increase in the gradient across the solidification zone does not necessarily change the gradient at the liquidus. This may in fact be seen in the data for run #4. As will also be seen in the analysis of run #4, the function relating PDAS to $(G^{.5} * R^{.25})$ is also different despite the fact that both runs used the same alloy from the same heat.

9.2 Gradient Controlled Withdrawal

The intent of this experiment was to determine whether or not a positive impact on the solidification microstructure could be achieved by utilizing a control scheme which kept the solidification interface at the baffle. It was decided that the solidification interface would be that position along the mold at which the temperature was half way between the liquidus and solidus temperature. In order to maintain the interface at a fixed location, the thermocouple temperatures along with their associated location along the part, were fit to a pair of cubic polynomials. This technique is described in chapter four and allows the calculation of the gradient at the solidification interface. The location of that interface is also readily obtainable.

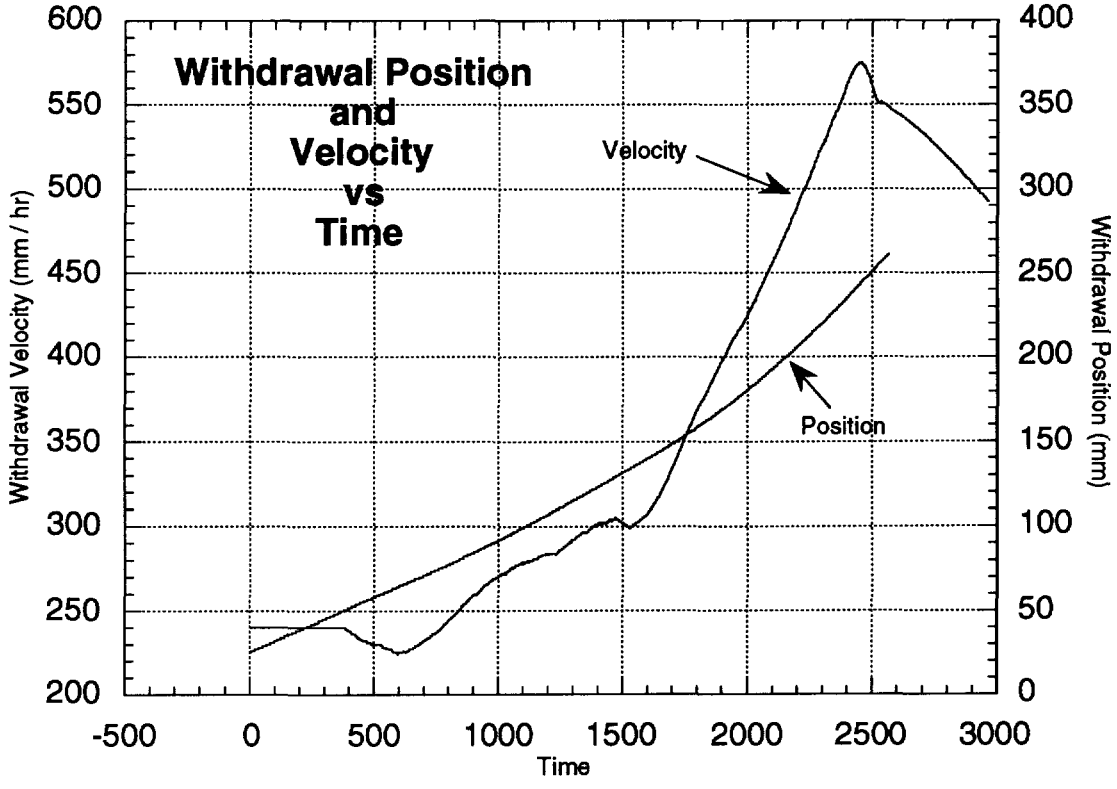

Figure 9.10
Withdrawal Position and Velocity vs. Time

Under the gradient control scheme, the withdrawal speed is modified in such a fashion as to attempt to maintain the solidification interface at the baffle. In this manner the dendrite growth would be occurring under conditions of maximum gradient. This mode of operation was accomplished and the withdrawal velocity exhibited a strong tendency to continuously increase as shown in figure 9.10. These traces were seen as verification that the ratio of emissive surface area above and below

the baffle does in fact have a significant effect on the cooling. During the first portion of the process, the control algorithm was improperly tuned and as a result the controller was not responding properly. This problem was rectified at about t = 1600, and as may be seen from the plot the velocity response changed.

Figure 9.11 is a plot of the liquidus and solidus position relative to the baffle. It is interesting to note that the change in the velocity response allowed the controller to move the solidification interface back towards the baffle. As will be seen later in this discussion, the desired effect on the solidification structure was also achieved.

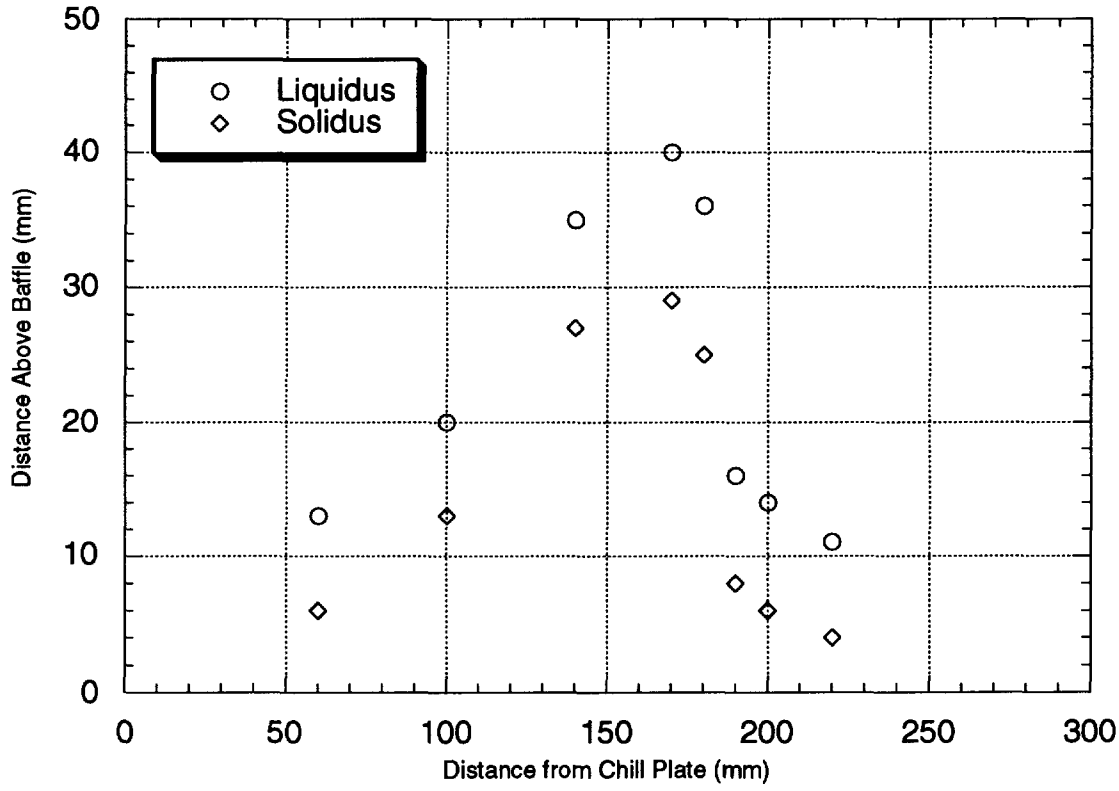

Figure 9.11
Interface Position Relative to the Baffle vs. Distance

In order to compare the measured vs. predicted primary dendrite arms spacings the procedure outlined in the previous section on the constant velocity was repeated. The first plot, that of the thermocouple temperatures vs. time, makes quite clear the much higher gradients that were present during this experiment (figure 9.12). The wider thermocouple spacing along the mold is also evident. Of particular note is the manner in which the gradient at the liquidus and solidus are *different.* Figure 9.13 is a plot of the gradient around the thermocouples as the liquidus and solidus temperatures passed. Significantly better correlation's with measured dendrite

arms spacing are achieved when the characteristics at the liquidus are used for the prediction of primary dendrite arm spacings. Specifically these characteristics are the gradient and the solidification rate. Typically, the gradient is measured by a straight line approximation. On figure 9.12 this would be analogous to drawing a line between the locations where a given thermocouple temperature trace intersects the liquidus and solidus lines. The slope of such a line would be the gradient. For this experiment, the method described in section 4, wherein an expression for the temperature as a function of position, was utilized. The first derivative of this equation was evaluated at the interface location in order to determine a gradient. This method was used as it provided continuous results which could then be utilized in a control algorithm.

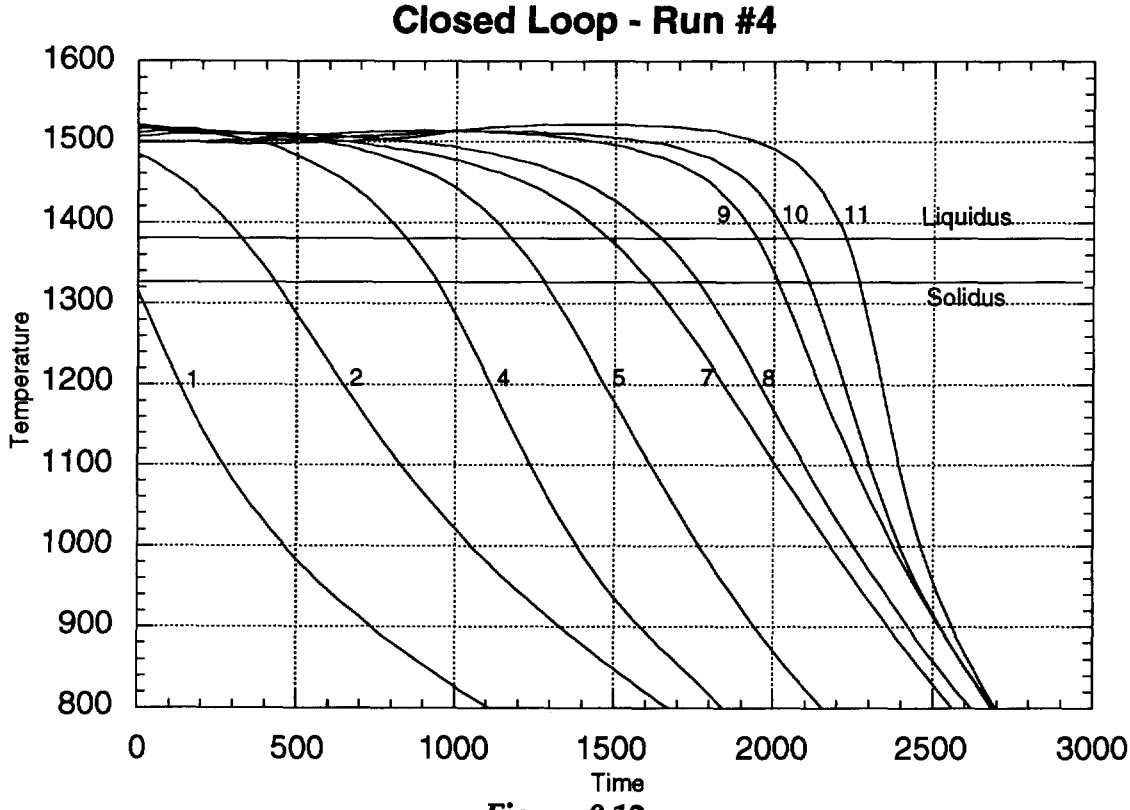

Figure 9.12
Thermocouple Temperatures vs. Time

Both methods of determining gradient, yield about the same results. Both methods are incorrect when it comes to the prediction of microstructure. As may be seen in figure 9.13, significant differences exist between the gradient at the liquidus and the gradient at the solidus. Although the shapes of the curves are very similar, the linear fit of primary dendrite arm spacing to $1 / (G^{.5} R^{.25})$ shows less scatter when the

characteristics of the liquidus are utilized in calculations. This result should not be unexpected as the mathematics describing the dendrite arm spacing are based on the conditions at the dendrite tip.

Another aspect of note in figure 9.13 is that the location of the lowest gradient corresponds to the point where the interface is the farthest away from the baffle. As predicted, the temperature gradient at the solidification interface does decrease as the interface moves away from the baffle. Further, the fact that changes in the withdrawal speed may be used to move the gradient location implies that the heat of solidification comprises a significant portion of the heat flow at temperatures near the solidus. This conclusion follows from the observation that an increase in withdrawal speed both moves the solidification interface closer to the baffle and increases the solidification rate. However, as the part is withdrawn, the change in emissive surface areas should move the interface *away* from the baffle. Motion of the interface towards the baffle can only occur as a result of increased heat flux, and the only source of additional heat is the heat of solidification. Therefore, this result confirms the prediction that the heat of solidification may be used as an internal heat source for the control of single crystal solidification conditions.

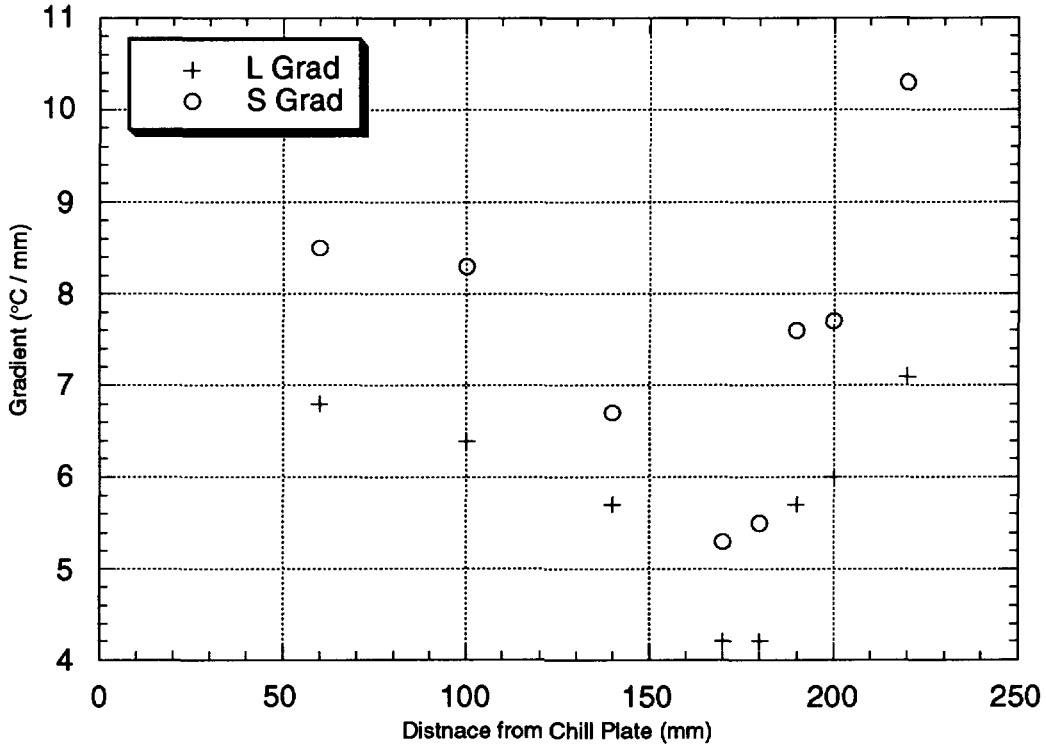

Figure 9.13
Liquidus and Solidus Gradient vs. Distance from Chill Plate

Figure 9.13 when combined with the velocity data also indicates that the higher the velocity the greater the difference in the gradient between the liquidus and the solidus. This too is evidence that significant heat of solidification is being released. Since that heat must come out between the liquidus and the solidus, if the heat of solidification is considered as a source, then the heat flux associated with this source may be expected to increase as a function of distance from the dendrite tip. Such a variation in flux would result in increasing gradients as one moves away from the liquidus and towards the solidus.

As with the constant withdrawal velocity experiment the Δt between thermocouples was plotted as a function of withdrawal distance in order to verify the thermocouple locations. This plot may be found in figure 9.14.

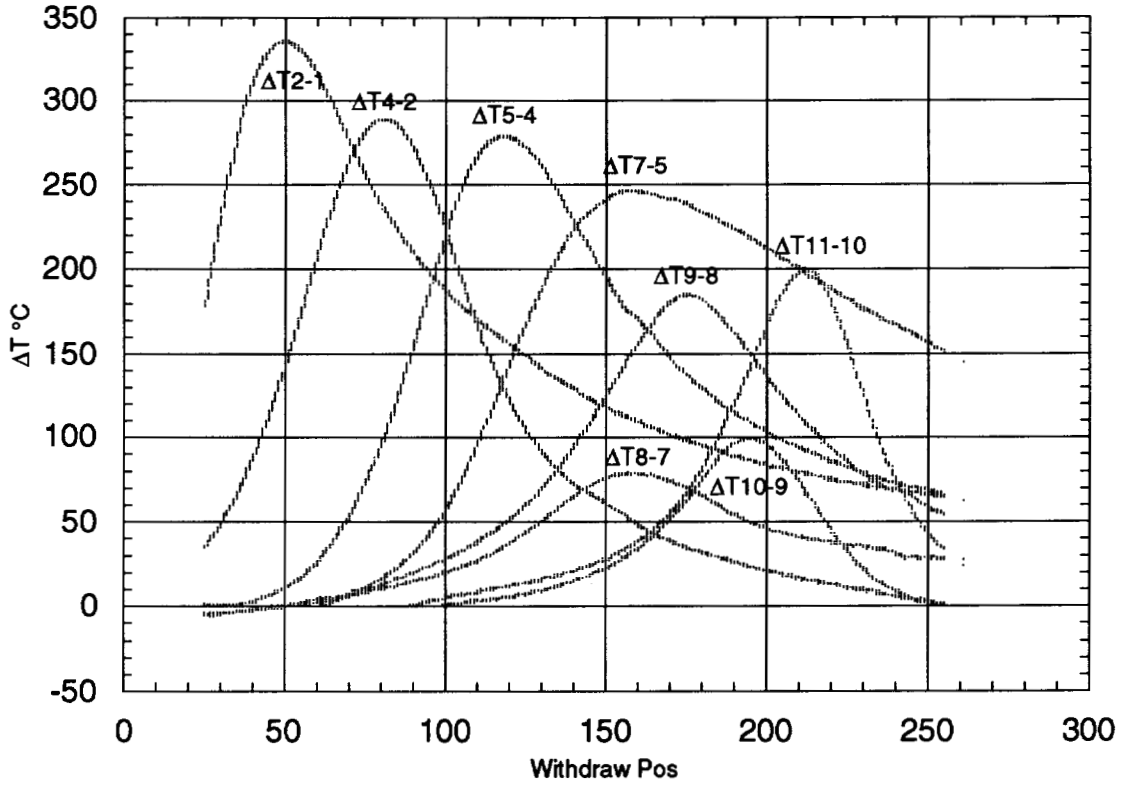

Figure 9.14
ΔT Between Thermocouples vs. Withdrawal Position

As before, the peaks correspond to the thermocouple location. In addition, although not used, the relative height of the peaks corresponds to the distance between the thermocouples. The locations of the peaks were determined by fitting a fifth order polynomial across the top, setting the derivative equal to zero and solving. These peak locations were then used to generate a set of nine equations with nine unknowns and

subsequently solved simultaneously using Mathematica™ in order to determine the thermocouple locations.

Once the thermocouple locations were verified, a plot of the gradient vs. the thermocouple location (or distance from the chill plate) was produced. This plot is shown in figure 9.15. Since a continuous equation for gradient as function of thermocouple location was desired, a polynomial fit of the data was obtained. An eighth order polynomial was required in order to get the function to plunge deep enough. With only eight data points, an eight order fit would normally cause a least squares algorithm to oscillate wildly as the curve passed through each point. In order to prevent this occurrence, the fitting algorithm was constrained by the addition of several additional points. The location of these points was determined by linearly interpolating between existing points. The resultant fit is not unreasonable.

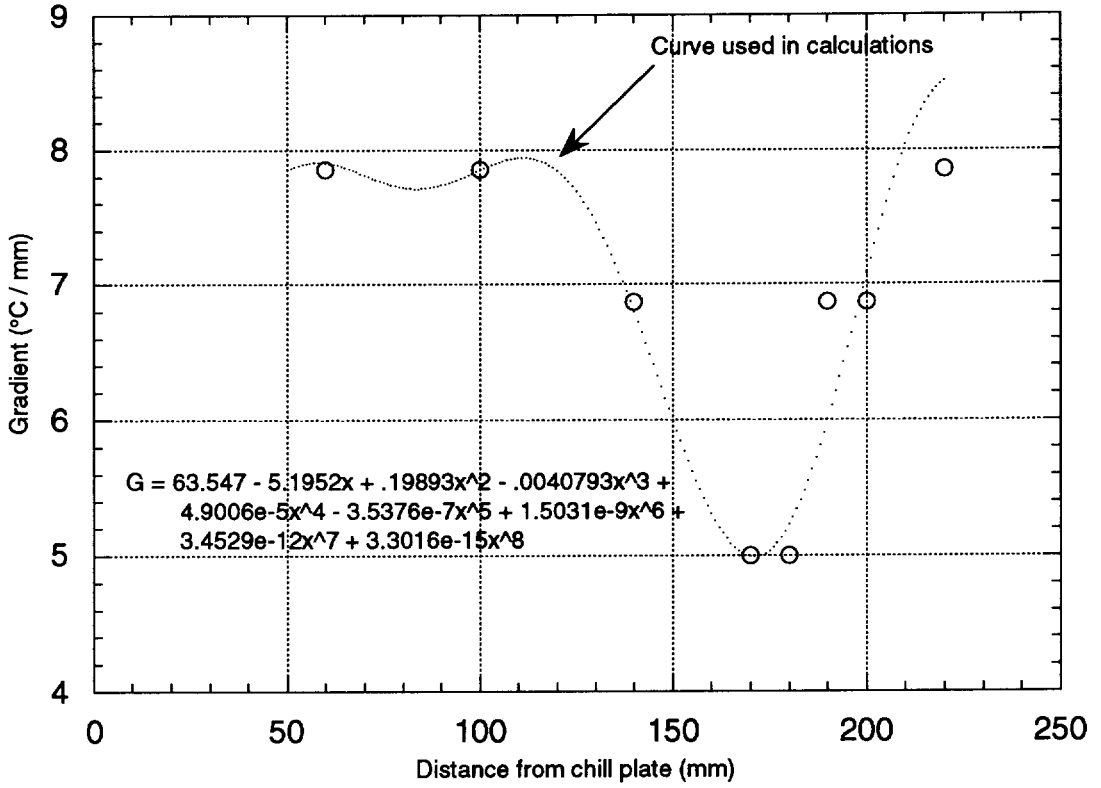

Figure 9.15
Gradient vs. Thermocouple Location

Once an expression for the gradient has been established, the next step is to determine an expression for the solidification rate. As expressed in (63), this relationship may be developed by multiplying the first derivative of the expression for liquidus position as a function of thermocouple location by the expression for velocity.

It might initially seem more straightforward to plot the times when the liquidus temperature passed the various thermocouples, fit the data and then calculate the derivative. This does works when the velocity is constant, but figures 9.11 and 9.13 illustrate the very significant effect that the velocity can have on the solidification environment. If the derivative of the expression for the liquidus position vs. time is taken in an effort to arrive at an expression for the solidification rate, then due to the relatively coarse resolution of the temperature information, a significant quantity of structure is lost. This loss of structure is avoided by utilizing the full amount of velocity data available in the experimental data stream.

To determine the solidification rate, the thermocouple location is plotted against the withdrawal distance at which the thermocouple was at the liquidus temperature. The resultant plot expresses the relationship between liquidus location and the position of the withdrawal mechanism. Figure 9.16 is such a plot for the gradient controlled experiment.

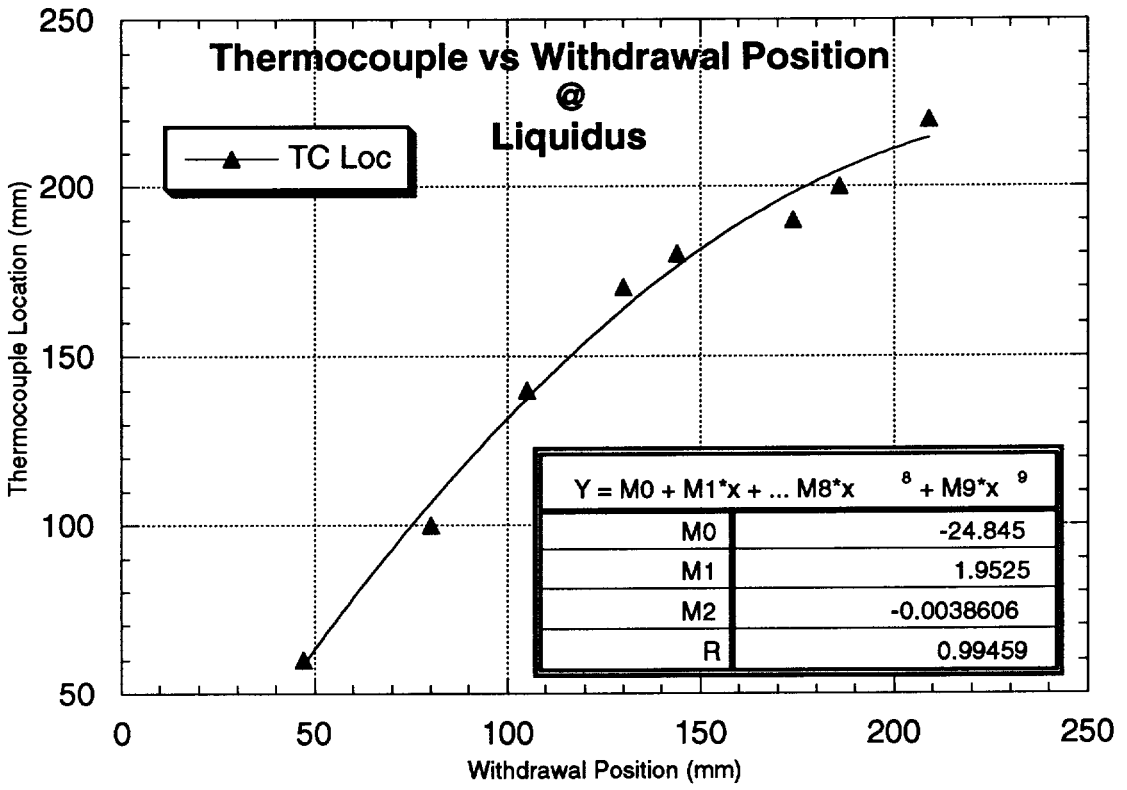

Figure 9.16
Thermocouple Location vs. Withdrawal Position

A second order polynomial is generated from the data. From the figure it may be seen that this provides a reasonable fit.

Next the velocity data is plotted against time. Since the velocity was recorded and since it is by definition the first derivative of the withdrawal position it may be readily used in the determination of the solidification velocity. As previously mentioned, changes in the withdrawal velocity appear to have a marked effect on the solidification environment. Therefore an effort has been made to maintain as much of the structure in the data as possible. Further the large quantity of data available (about 3000 points) allowed a high order fit to be used quit effectively. In this instance, a ninth order polynomial was required to fit the data in order to generate an appropriate expression for the withdrawal velocity vs. time. This curve corresponds to the derivative of a tenth order polynomial of position. Such a polynomial could not have been generated for the solidification velocity without interpolating points and the structure of the withdrawal velocity would have made it difficult to accomplish this in a correct fashion. A higher order fit may have been better but a ninth order fit was the limit of KaleidaGraph™ and turned out to be adequate. The data for the withdrawal velocity and the associated ninth order polynomial are shown in figure 9.17.

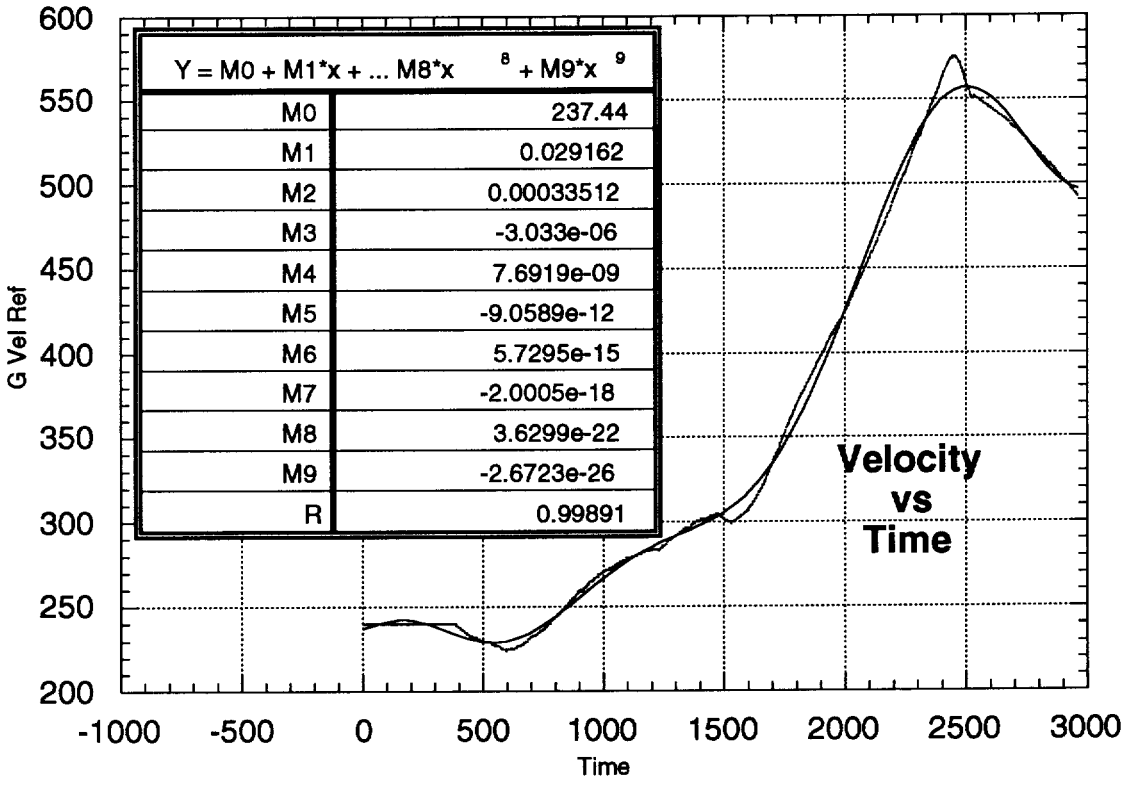

Figure 9.17
Withdrawal Velocity vs. Time

The equations derived from the plots of the gradient at the liquidus, the position of the liquidus and the withdrawal velocity may now be combined into an expression for the primary dendrite arm spacing. This is accomplished using Mathematica™ to generate a continuous expression for the primary dendrite arm spacing as a function of the distance along the test bar. The final equation is offset in order to accommodate the material that was cropped off as the test bars were removed from the mold tree. The Mathematica™ notebook that was used for this may be found in Appendix B. As was the case in the constant velocity experiment, Mathematica™ was used to generate a table of $1 / (G^{.5} R^{.25})$ at the different locations along test bar where primary dendrite arm measurements were made. The measured primary dendrite arms spacings were then plotted against the calculated values of $1 / (G^{.5} R^{.25})$ and the results were then plotted. Figure 9.18 is the result. As previously discussed, the data were fit to a linear relationship. From the figure it may be seen that although there is some scatter, a linear has high correlation.

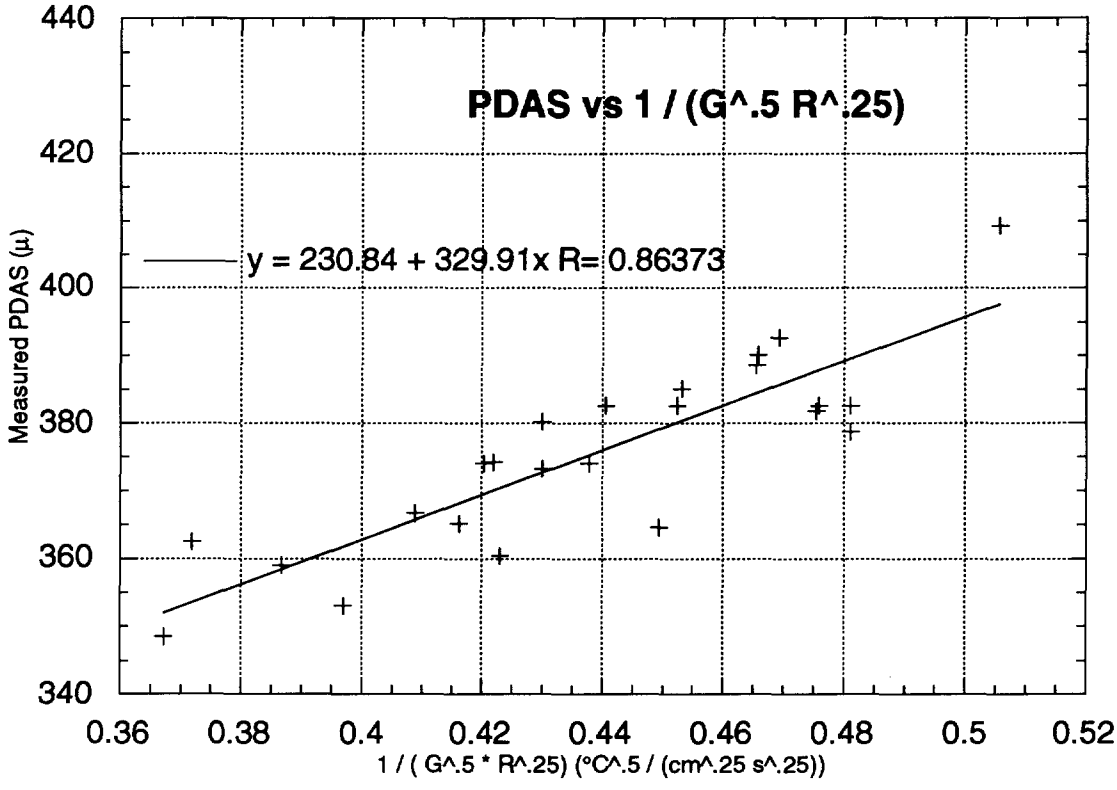

Figure 9.18
Measured PDAS vs. $1 / (G^{.5} R^{.25})$

The resultant equation for the primary dendrite arm spacing (68) is:

$$PDAS = 230.84 + \frac{329.91}{\left(G^{.5}\, R^{.25}\right)} \tag{68}$$

Values of 1 / ($G^{.5}$ $R^{.25}$) were generated every .25 mm for the 120 mm length of test bar length over which thermocouple data was available. The resultant values were substituted into (68) in order to generate a set of predicted primary dendrite arm spacings as a function of distance along the bar. These predicted data points and the measurements of the primary dendrite arms spacing were then plotted against the associated location along the test bar. Figure 9.19 is the resultant plot. These results are quite exciting in that the effect of the variation in the withdrawal velocity seems quite clear.

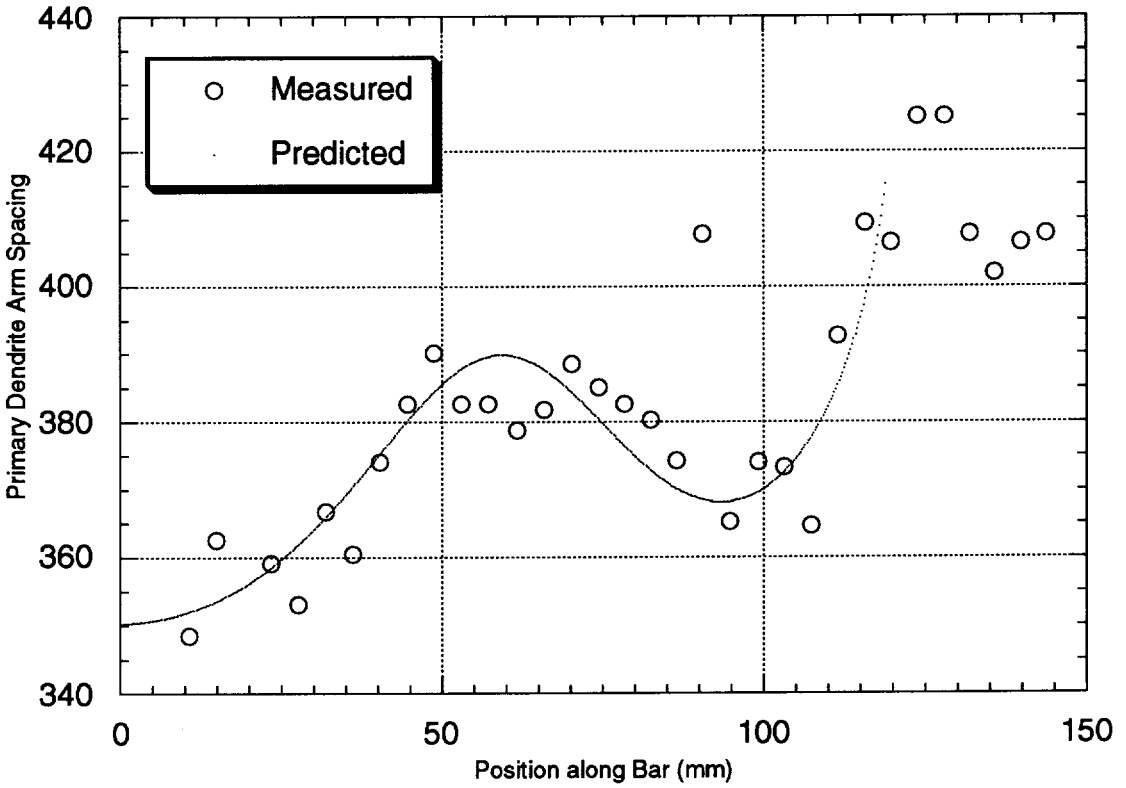

Figure 9.19
Measured and Predicted Primary Dendrite Arm Spacing vs. Position

The peak in the primary dendrite arm spacing which occurs at approximately 50 mm is also the point at which the withdrawal rate began to suddenly increase. This

action was quite clearly able to bring the liquidus position into an area of higher gradient. The controller was set to attempt to maintain the solidification interface at 7 mm above the baffle and as may be seen from figure 9.11 was just achieving this goal when the thermocouple array progressed beyond usefulness.

Once there were no longer sufficient thermocouples above the liquidus, the control algorithm was unable to accurately locate the solidification interface and the velocity output dropped back. This action corresponds to the location where the primary dendrite arm spacing takes an abrupt upturn and, due to a lack of thermocouple data, also represents the limit of prediction.

The abrupt increase in the primary dendrite arm spacing is probably due to a sudden change in heat flux which results from the lack of continuous acceleration of the withdrawal mechanism. During the prior portion of the process a continuous acceleration of the withdrawal velocity provided an ever increasing heat flux to compensate for the increased cooling that results from an expanding emissive radiator. The rapid change in the withdrawal velocity decreases the heat flux associated with the solidification process. This action drops the gradient, and growth slows down as the liquidus and solidus move farther apart. The combination of lower gradient and arrested growth results in an increase in the primary dendrite arms spacing. However, once a new equilibrium configuration is established, the PDAS drops back to a more stable value. This growth behavior is born out by evaluating the last nine PDAS measurements within figure 9.19.

From this data it is evident that changes in withdrawal velocity should be made smoothly in order to avoid overshoot. In particular, sudden decreases must be avoided. A sudden decrease in velocity can precipitate short term increases in the primary dendrite arms spacing. Commensurate with this increase in PDAS is an increased dendrite length. Longer dendrites increase the likelihood of convection jets and the associated probability of freckles. Therefore sudden changes in the withdrawal velocity, or step changes in the withdrawal position can result in the formation of freckles.

An analogous situation could occur as a result of a rapid increase in part cross section passing the baffle. Such an occurrence implies a rapid change in emissive surface area below the baffle and therefore an associated increase in emissive cooling. This increase in cooling forces the solidification interface up and away from the baffle resulting in a transient that drives the liquidus into an area of decreased gradient at an increased solidification rate. Once a new equilibrium configuration has been established

the growth slows down and due to the lower gradient, the PDAS increases. However, the closed loop control method utilized in this work could mitigate such effects.

The experimental method employed in this experiment could be used to profile a test part as part of a production setup. The velocity could be automatically adjusted to keep the liquidus near the baffle. As shown, such an action would provide any necessary additional heat as a result of solidification. This is in contrast to the "open loop" case where the additional heat occurs because the solidification zone has been pushed up high enough to allow sufficient emissive heat to enter the part below the solidus where the ΔT is higher. Once an instrumented test part has been produced, a plot of primary dendrite arm spacings could be generated. Examination of this plot would provide a rough idea as to whether or not solidification defects are likely. Further the resultant velocity trace could be used as a template for the processing of future parts.

9.3 Comparison of Results

When the results of the two instrumented runs are compared, the results do not correlate very well. Work by Pollock and Murphy[62], showed a reasonable correlation from run to run over a similar range of conditions. The results of these experiments provide distinct data sets. The difference may lie in the very different furnace conditions that existed as a result of the broken baffle in the constant velocity run. The data from the two runs is combined in figure 9.20.

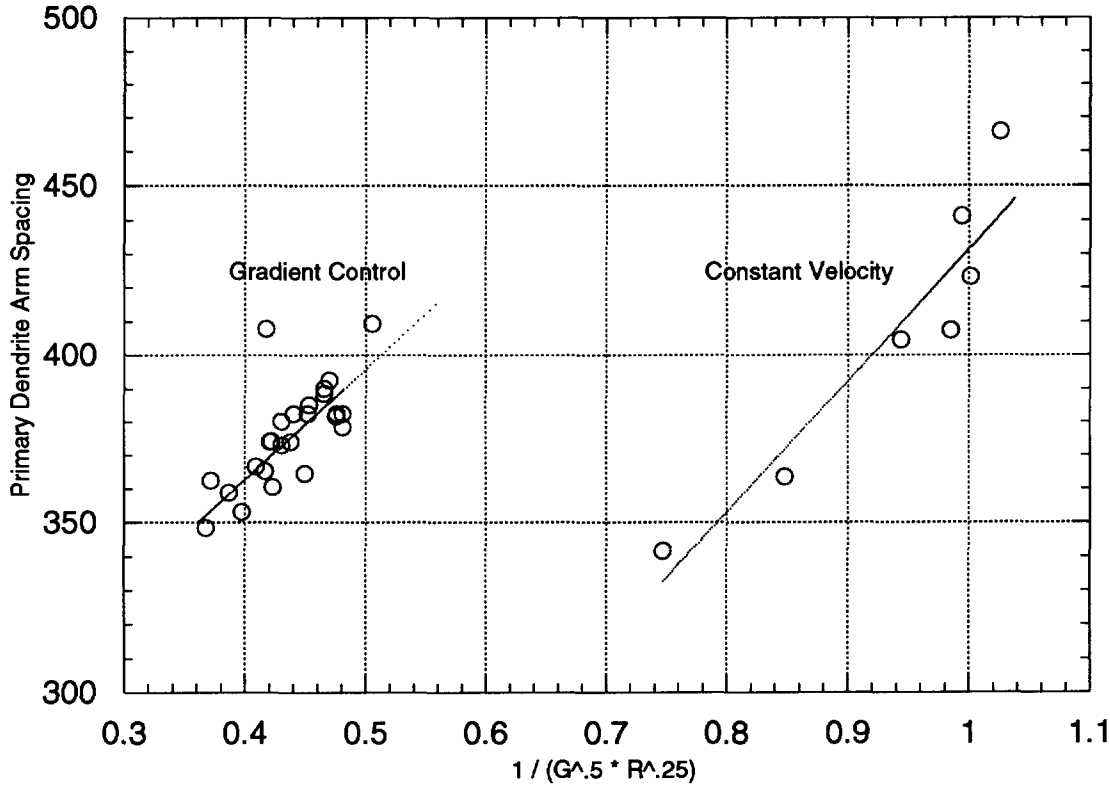

Figure 9.20
Comparison of Constant Velocity and Gradient Control Data

From the figure it is evident that the data falls into two distinct populations. Any attempt to plot a line through the two populations would result in a solution that would not allow a successful calculation of primary dendrite arms spacings. However the slopes of the two lines are similar and most of the variation occurs within the y intercept. This implies that although the magnitude of the effect engendered by a change in $1 / (G^{.5} R^{.25})$ is roughly constant for a given alloy, the absolute magnitude of the microstructural response is additionally governed by another factor. The observed behavior seems to imply some sort of memory of previous conditions. Pollock

and Murphy had comparable initial solidification conditions for all experiments and as a result obtained data which could be fit to a single curve. On the other hand, when the initial solidification conditions varied greatly, distinctly different data populations emerged. It is unfortunate that additional tests are not immediately available as it is difficult to draw conclusions from only two test runs. However, an analysis of the situation suggests that the initial cooling rate is a likely source for this divergence in populations.

The rate at which the material cools as it comes out of the crystal selector and expands into the part may be expressed as:

$$\dot{T}_i = G_i R_i \tag{69a}$$

Which states that the initial cooling rate is equal to the product of the initial gradient and the initial solidification velocity. Slower cooling rates allow the eutectic reaction to proceed further by providing more time for the diffusional rejection of excess solute from the solidified material. This situation results in a solid composition which moves closer to the eutectic composition with increasing local solidification times. This then lowers the *effective* solidus temperature and increases the composition gradient in advance of the interface. If subsequent solidification were dependent on the cooling rate at which the growth substrate was formed, then an equation for primary dendrite arm spacing could be written:

$$PDAS = K\left[\dot{T}_i + \frac{1}{\left(G^{.5} R^{.25}\right)}\right] \tag{69b}$$

If the measured primary dendrite arms spacings are plotted against the factor inside the brackets of (69b), then figure 9.20 is the result for both runs combined. It should be noted that the values used for T_i were the first measured gradient and the initial withdrawal velocity. These numbers were 16.5 °C / cm for constant velocity and 87 °C / cm for gradient control. Both withdrawals started at .006667 cm / sec. These figures yield initial cooling rates of .11 °C / sec and .58 °C / sec respectively. As may be seen from the figure, if the cooling rate is used to specify the initial conditions, the two populations close up into a single data set. This is an extremely interesting result and is clearly an area where more work is required. The resultant linear fit yields nearly identical results in the case of the constant velocity experiment (with the broken baffle). However, for the gradient control experiment the curve is a little bit different. In order to verify whether or not the new curve fit still describes the measured

primary dendrite arm spacing the results of the new curve have been plotted against the measured data. This plot may be found in figure 9.22. The equation used to convert the 1 / ($G^{.5}$ $R^{.25}$) factor into primary dendrite arms spacings was extracted from figure 9.21 and is written:

$$PDAS = -19.83 + 393.6\left[T_i + \frac{1}{G^{.5} R^{.25}}\right] \tag{70}$$

This equation (70) allows the successful prediction of the primary dendrite arm spacing from the gradient and solidification rate data for both experimental runs.

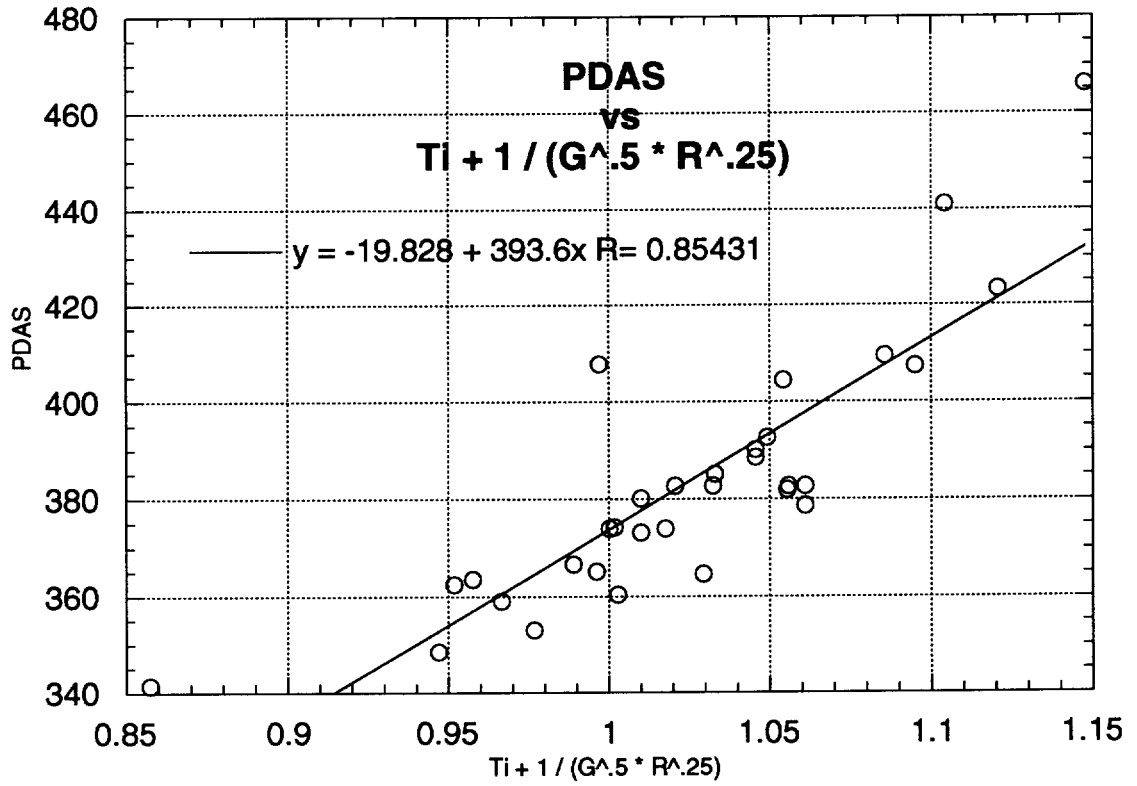

Figure 9.21

Combined PDAS Measurements vs. T_i + 1 / ($G^{.5}$ $R^{.25}$)

It is of interest to note that although the slope or K obtained by Pollock and Murphy is considerably different (207 as opposed to 393), the Y intercept does in fact appear to be equal to the product of K and the initial cooling rate.

It would seem as if there is some evidence that for this type of single crystal growth process, the initial conditions have the capability of effecting the solidification

behavior of the entire part. If such were proved to be the case, then a very significant refinement of the microstructure could be accomplished. This would be achieved by starting the solidification process at very low cooling rates. Once a substrate has been formed, the solidification response of the system would then be defined as well. By initiating the solidification at a low cooling rate, the resultant growth behavior would provide a finer PDAS at lower gradients and growth rates than that which could be obtained for parts started at higher cooling rates.

There is some evidence in the industry of an empirical understanding of this phenomenon. Many foundries have a "hold time after pour" in order to let the crystal establish itself. This is exactly as it sounds. After pouring the mold, the part is allowed to sit for some predetermined amount of time before the withdrawal is started. Such an action would provide a low cooling rate environment for the establishment of the growth substrate. The result would be a part that was easier to grow under limited gradient conditions. Conversely, a high initial cooling rate could result in a part with a very large primary dendrite arm spacings and as a result a higher incidence of freckles would result.

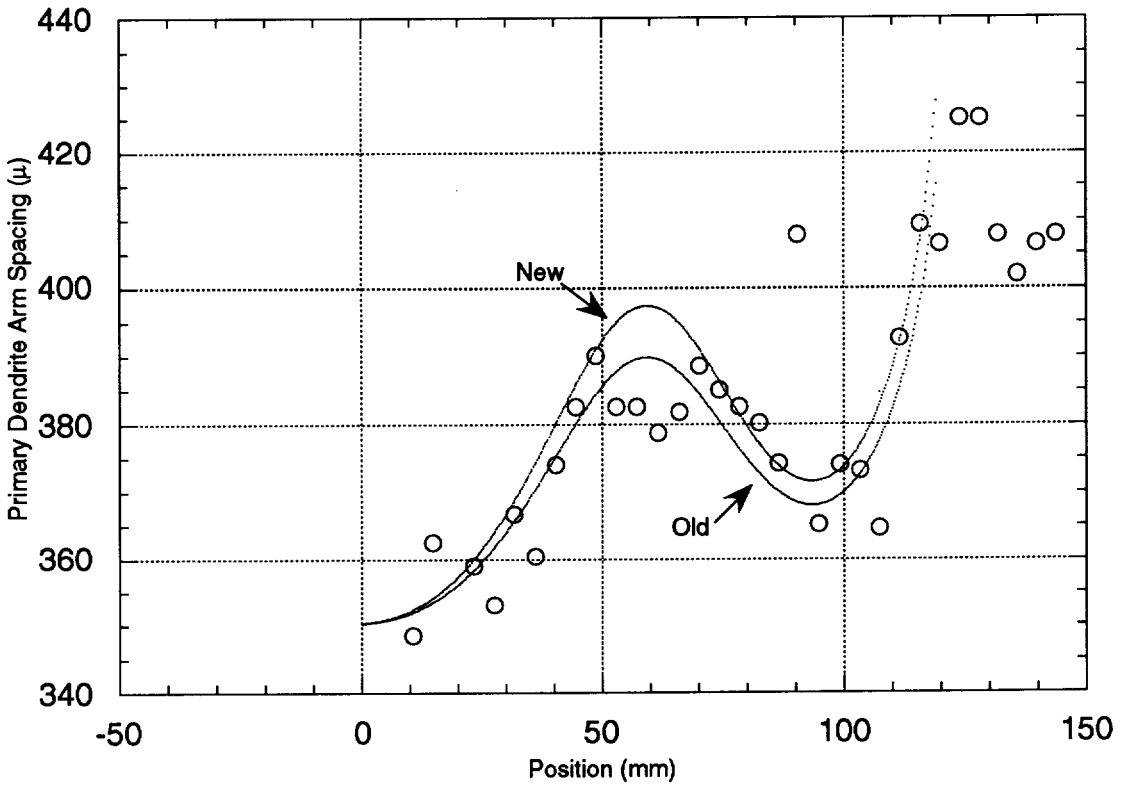

Figure 9.22
Modified Data Fit

Verification of this behavior would have an additional impact on such items as the length of the crystal selector as well as the chill spool configuration of the furnace. Quite clearly some additional work is warranted.

Chapter 10 Model Predictions

The modeling results verified the prediction that the solidification interface would be moving up the bar as the withdrawal progressed. This is also the result that was obtained from the gradient controlled set of thermocouple data. For this evaluation, the model was run at five different withdrawal distances and the temperatures were plotted. Each position was plotted first with a complete temperature range and then at an expanded scale and magnification in order to more fully observe the solidification region. These plots may be found in appendix C and are summarized below.

During early stages of withdrawal, the model predicts that the solidification interface will be located below the baffle. As the withdrawal continues the interface is seen moving up closer to and finally past the baffle. With continued withdrawal motion the solidification interface is shown above and moving away from the baffle at an ever increasing rate. The model predicts that the test bar will be fully solidified after 75% of the part has been pulled down through the baffle.

Although more data points would have been desirable, the necessary computer resources were not available for more than this limited data set. Nonetheless, the data obtained does allow enough analysis to ascertain whether or not the predictions are reasonable. Table 10.1 below is a table of the data extracted from the runs. No data is provide for run five since the bar turned out to be fully solidified for that set of conditions.

Table 10.1 Table of Model Data

Simulation Number	Withdrawal Distance	Gradient at Interface	Interface Position
1	3.3	22.86	-.54
2	7.21	24.29	1.13
3	10.88	18.8	2.22
4	13.53	9.72	5.19
5	16.47	-	-

The data derived from the modeling was manipulated in order to obtain some insight into the primary dendrite arm spacing that theory would predict from the model results. First the gradient vs. withdrawal distance information was fit to a third order polynomial. The third order curve provided an absolute fit for the limited data. Equation (71) is the resulting equation of the curve where the resultant gradient G is given in units of °C / cm and the withdrawal distance x is also in cm.

$$G = 17.3243 + 2.13865\,x - .120437\,x^2 - .00585142\,x^3 \quad (71)$$

Since the equation for the primary dendrite arms spacing (69), requires a solidification rate, it will be necessary to bring a velocity into the equation. If the product of a withdrawal velocity v and time t is substituted in (71) the resulting equation (72) is the time dependent form.

$$G = 17.3243 + 2.13865(vt) - .120437(vt)^2 - .00585142(vt)^3 \quad (72)$$

In a similar fashion, when the data for the location of the solidification interface (X_I), is fit to a third order polynomial the result is equation (73).

$$X_I = -6.09044 + 3.59936\,x - .325584\,x^2 + .0144189\,x^3 \quad (73)$$

Once again by substituting $v\,t$ for x, the time dependent form is realized (74).

$$X_I = -6.09044 + 3.59936(vt) - .325584(vt)^2 + .0144189(vt)^3 \quad (74)$$

This equation (74) is an expression for the gradient location as a function of the withdrawal velocity v and time t. The solidification rate may be assumed to be the first derivative with time of the interface position and so it may be expressed as (75).

$$\frac{dX_I}{dt} = 3.59935\,v - 0.65116\,v^2t + 0.043256\,v^3t^2 \quad (75)$$

When Eq. (72) and Eq. (75) are substituted into (69) an expression for the primary dendrite arm spacing is realized. Figure 10.2 is a plot of this result with the withdrawal velocity set at 24 cm/hr.

As may be seen from the figure, the primary dendrite arm spacings as modeled vary from about 140μ to 200μ. These spacings are about 1/2 of the values actually measured during the dendrite analysis. When it is considered that no heat of fusion has been taken into account, these results are very good. If one considers the heat flows in the problem and assuming a thermal conductivity of .9 W/ cm °K, a latent heat of fusion of 297 Joules / gm and a .65 cm bar radius then with a gradient of 20°C /cm the heat flowing through the part as a result of the gradient is 23.9 watts . However at 24 cm / hr solidification rate the heat being released as a result of the solidification is 20.5 watts.

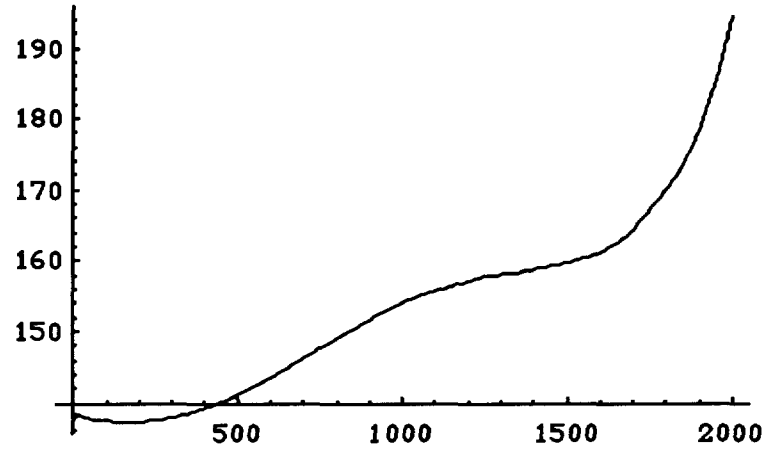

Figure 10.1
Modeled Primary Dendrite Arm Spacing

The fact that the heat of solidification is comparable to the steady state heat flows implies that heat of solidification is to a very large extent driving the heat flow from the top of the part during the solidification process. The result of this situation should be an effective lowering of the gradient at the dendrite tip. This reduction occurs because the heat flux which is primarily responsible for the establishment of the gradient is being generated below the tip. It is therefore to be expected that actual primary dendrite arm spacings will be larger than the calculation suggests.

As an example, if the heat flux at the tip is 25% of the total then the plot of the primary dendrite arm spacings becomes as shown in Figure 10.2

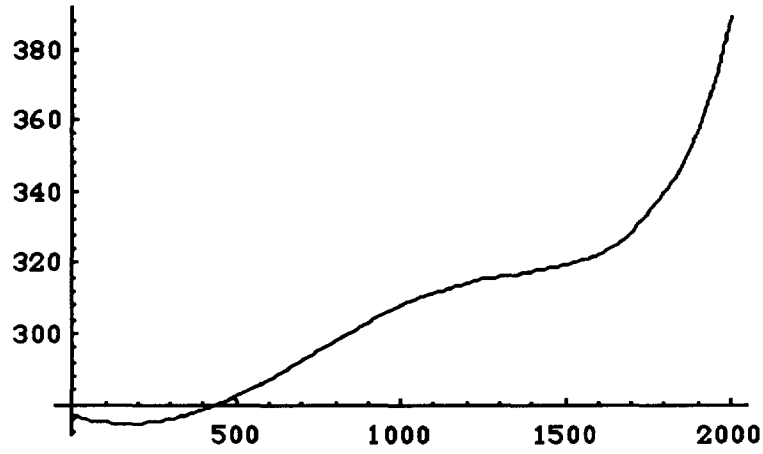

Figure 10.2
Dendrite Arm Spacing with Reduced Heat at the Tip

As may be seen from the figure, such a modification brings the primary dendrite arm spacing more in line with observed values.

It should be noted that the gradients predicted by the model are lower than those measured experimentally. This is probably due to the lack of a crystal selector in the model. An omission that if rectified would further increase the dominance of the cooling in determining the solidification characteristics. These results indicate quite clearly that, as a result of the large emissive heat drop which exists below the baffle, the solidification process is driven by the cooling.

The mathematical verification of the process being dominated by the cooling that occurs below the baffle is not surprising. It does however point to a potential optimization in the process which to date has not been incorporated. The results indicate that the continuously expanding, high ΔT emissive heat sink drives the interface up and away from the baffle. Since the highest gradients occur at the baffle, the interface is driven into areas of ever decreasing gradient. If the susceptor temperature could be increased as more cooling area is moved below the baffle, then the solidification interface could be held at a relatively constant position. Unfortunately the temperature cannot be raised without risk of overheating the mold. Even if it could be raised some, due to the necessity of keeping the metal above the baffle liquid, the temperature difference between the mold and the chill spool will always be very much greater than that between the mold and the susceptor. It is then clear that increasing the heat flux into the tip of the part in an effort to overcome increased cooling capacity is not a viable solution. However, limiting the cooling below the baffle should be feasible. Figure 10.3 is an illustration of the proposed modification.

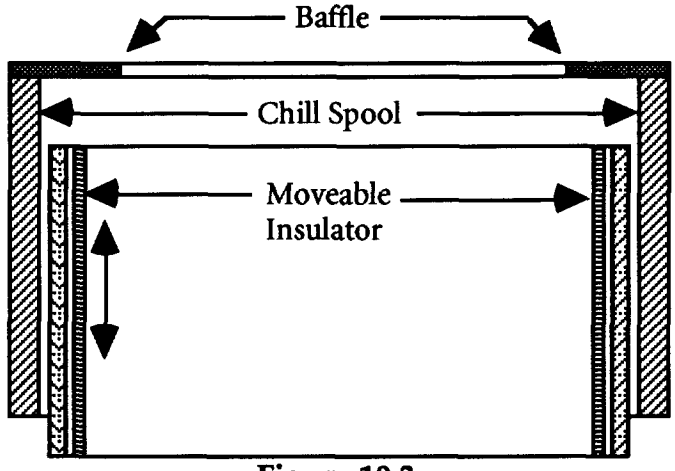

Figure 10.3
Chill Spool Modification

This chill spool design incorporates a movable insulated reflector or alternatively a resistive heater between the mold and the chill spool. The reflector would be adjusted during the process in order to limit the heat being removed from that portion of the part which is below the baffle. Initially, the reflector would be pulled out of the way in order to allow a full view of the chill spool. As the withdrawal process proceeds and more radiating area is moved below the baffle, the reflector would be raised, thereby lowering the view factor. In this fashion, the cooling could be limited such that the solidification interface remained in the vicinity of the baffle.

The technique is easily extended to the control of the heat removed. By modifying the cooling aperture an effective and nearly instantaneous change may be made at the solidification interface. If this is contrasted to the traditional method of changing the withdrawal velocity, the advantages are obvious. Typically, an attempt is made to slow down the solidification when the cross section undergoes a sudden increase. Conventional wisdom holds that such an action will allow the crystal to spread sidewise. If however, the heat of solidification is a major contributor to the total heat flow down through the part, then the effect of a withdrawal slow down is not necessarily the action which conventional wisdom holds to be true. Consider, if the solidification velocity were reduced, then a heat source immediately below the dendrite tips would also be reduced. From the vantage point of the dendrite tip this would look like a sudden cooling which would result in higher gradients and the continuation of growth. In fact the growth of the crystal is a process in equilibrium. The location of the solidification interface is that location at which the emissive heat flux and heat of

solidification balance the emissive heat removed. The net result of a slow down in the withdrawal velocity is a decrease in the contribution of heat of fusion. Such a decrease in heat flux results in a momentary increase in the solidification velocity while the solidification interface is seeking a new equilibrium position at a distance further away from the baffle. If however a cooling aperture is applied the result is different.

If a cooling aperture were installed in the system, then if the aperture were closed down, thus lowering the cooling, the interface would be driven down towards the baffle. A simultaneous decrease in speed could be used to offset the downward trend of the interface. The net result of these actions is a situation where the solidification rate can in fact be controlled. The realization of this type of control is significant.

Another interesting outcome of the model is the verification that the baffle is conducting a significant amount of energy from the hot zone into the cold. From the simulations it may be seen that the baffle attains temperatures comparable to the solidification temperatures and that the gradient through it is similar to that of the part as well. As the experience of the constant velocity thermocouple run demonstrated, the baffle (or lack thereof) has a very pronounced effect. The significant flux that is passing through the baffle, even when it is properly configured, must be diminishing its effectiveness. The model then verifies the potential advantage of a baffle that is designed to be a more effective heat shield than those designs which are currently in use.

Chapter 11 Primary Dendrite Arm Spacing

The survey of primary dendrite arm spacings was conducted in order to gain insight into the various furnace parameters and their effect on the solidified microstructure. A fortunate outcome of section 9 was the realization of an equation describing the primary dendrite arm spacing across a wide range of conditions. This equation is repeated below for convenience:

$$PDAS = -19.83 + 393.6\left[T_i + \frac{1}{G^{.5} R^{.25}}\right] \tag{76}$$

It is assumed that for the experiments where the baffle was intact the initial cooling rate is the same and as such the value for T_i is assumed to be .58. This is very close to the value of .534 which may be derived from the work of Pollock and Murphy. It is also the value determined in run #4 with an intact baffle. As a result, this equation may be used to determine the factor $1 / (G^{.5} R^{.25})$. As an additional item of reference Table 9.1 has been duplicated as well:

Table 11.1 Process Data for Single Crystal Molds

Identity	Melt Temp °C	Zone 1 Temp °C	Zone 2 Temp °C	Velocity mm / min	Chill Spool Shape
A	1550	1500	1550	5.6	Standard
V	1550	1550	1550	4	Standard
W	1500	1475	1475	4	Standard
X	1475	1500	1500	8	Standard
Y	1500	1500	1500	5.8	Standard
Z	1500	1550	1550	4	Standard
1	1500	1500	1550	Auto	Shaped
2	1500	1475	1475	Auto	Shaped
3	1500	1475	1475	4	Shaped
4	*1510*	*1475*	*1475*	Auto	*Shaped*
5	1500	1475	1475	40	Shaped
6	*1500*	*1475*	*1475*	*4*	*Shaped*

The data allows the evaluation of the effects of susceptor temperature, withdrawal rate and chill spool design. In addition, the effect of geometric view factors may be assessed .Plots of primary dendrite arm spacing vs. bar position for each of the ten test bars surveyed may be found in Appendix G. It should be noted that after the sectioning operation but prior to the marking operation sample A was dropped. Many pieces bounced and rolled about the floor in a very effective mixing operation. As a consequence very little may be said about this sample.

11.1 Effect of Susceptor Temperature

In order to assess the effect of susceptor temperature on the PDAS, experiments W and Z were compared as were 1 & 2. In each pair of experiments, the only difference between two was a change in the susceptor temperature. The resultant primary dendrite arms spacings are plotted in figure 11.1. Recall that samples Z and 1 were processed at a susceptor temperature of 1550 °C whereas samples W and 2 were processed at 1475°C. As may be seen in the figure, the results are quite striking. In both cases the test bars which were processed at the higher temperatures yielded a finer primary dendrite arms spacing. The curvature seen in samples 1 and 2 is similar to that seen in sample 4 and is apparently associated with the closed loop gradient control method.

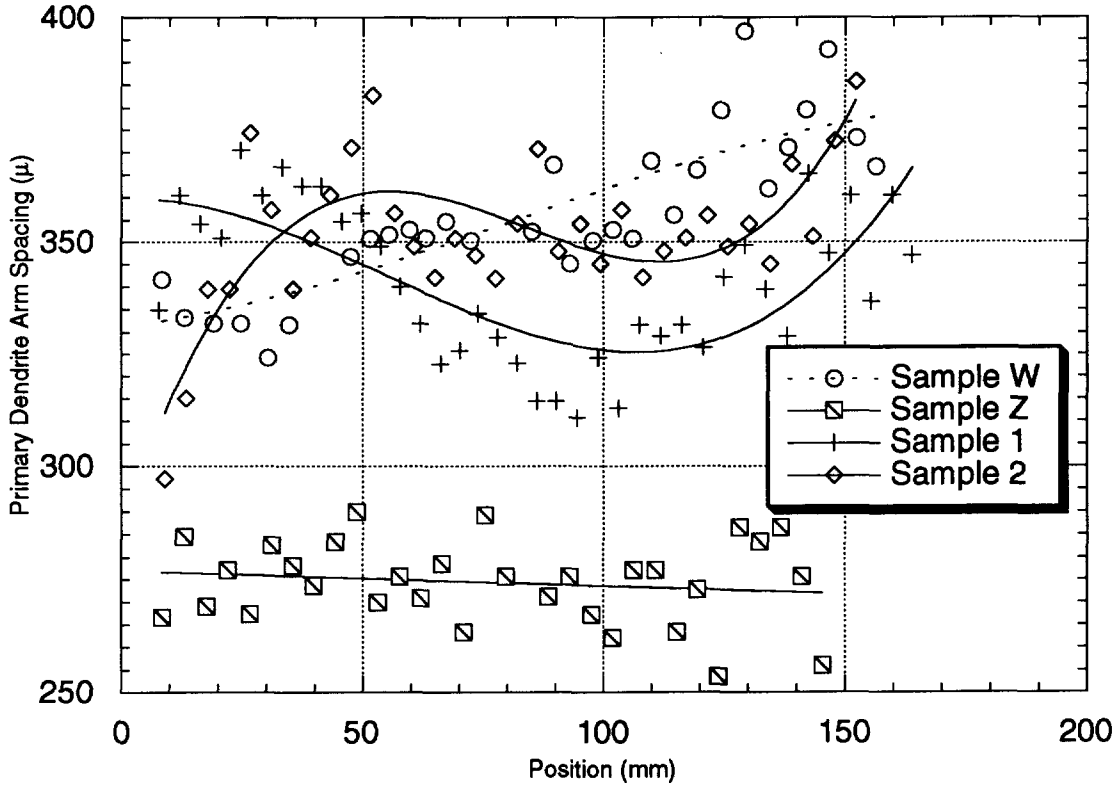

Figure 11.1
Effect of Susceptor Temperature

This result is not unexpected. Higher susceptor temperature provide a more "headroom" in the process and as a result the emissive heat transfer at locations above the solidus is enhanced. The additional heat flow has the effect of pushing the liquidus down towards the baffle into a higher gradient environment. This results in a finer primary dendrite arms spacing than similar parts processed at a lower susceptor

temperature. However as previously stated, there exists the very real possibly of overheating the mold and creating adverse reactions if the susceptor temperature is raised too high. Therefore as a potential process modification, higher susceptor temperatures are limited by the service temperature of the mold.

The very large difference between sample W and sample Z when contrasted to the difference between sample 1 and sample 2 is probably a result of the different chill spool arrangements and will be discussed in section 11.2

11.2 Effect of Chill Spool Shape

The different chill spool arrangements utilized presented the greatest surprise in this work. As previously discussed, a shaped chill spool was developed in order to increase the heat transfer immediately below the baffle. Such behavior would have the necessary result of increasing the gradient at the baffle. It was presumed that an increased gradient at the baffle would additionally provide an environment where the gradient at the solidification interface was increased as well. However the process modeling effort provided indications that this might not be the case.

The model indicated that the process was driven by the cooling below the baffle and in the modeling section it was suggested that a heat shield be placed between the part and the chill spool in order to prevent emissive cooling from overpowering the solidification process. Based on the modeling result, the implementation of a *more* effective cooling design should serve to drive the liquidus away from the baffle and up into a lower gradient environment. As a result, a more effective chill spool should increase the primary dendrite arm spacing thereby having an effect exactly opposite of that which was intended. The microstructural results indicate that the goal of designing a more effective cooling mechanism was realized. As expected this manifests itself as an increase in the primary dendrite arm spacing.

This result holds true for all of the parts cast. The greatest effect is seen in those parts solidified with a shaped baffle but at a constant withdrawal rate. These parts all show a significant geometrical effect as a result of the more efficient cooling. This effect will be discussed in more detail in section 11.3.

A contrast of the effect of the shaped chill spool vs. the conventional cylindrical design is most effectively seen by contrasting sample W and sample 5 (Figure 11.2). These samples were solidified under identical susceptor temperatures and withdrawal rates. Further they were processed in identical molds and with identical alloys. The only difference was in the chill spool configuration. From the figure it may be seen that

sample 5, the one processed with the shaped chill spool, shows a greater increase in primary dendrite arm spacing as solidification progresses. This may be interpreted as meaning that for a given amount of positioned mold below the baffle, the heat extraction is greater for the shaped chill spool. As previously described, this more effective heat extraction drives the liquidus position into positions of lower gradient and thereby results in greater primary dendrite arm spacings.

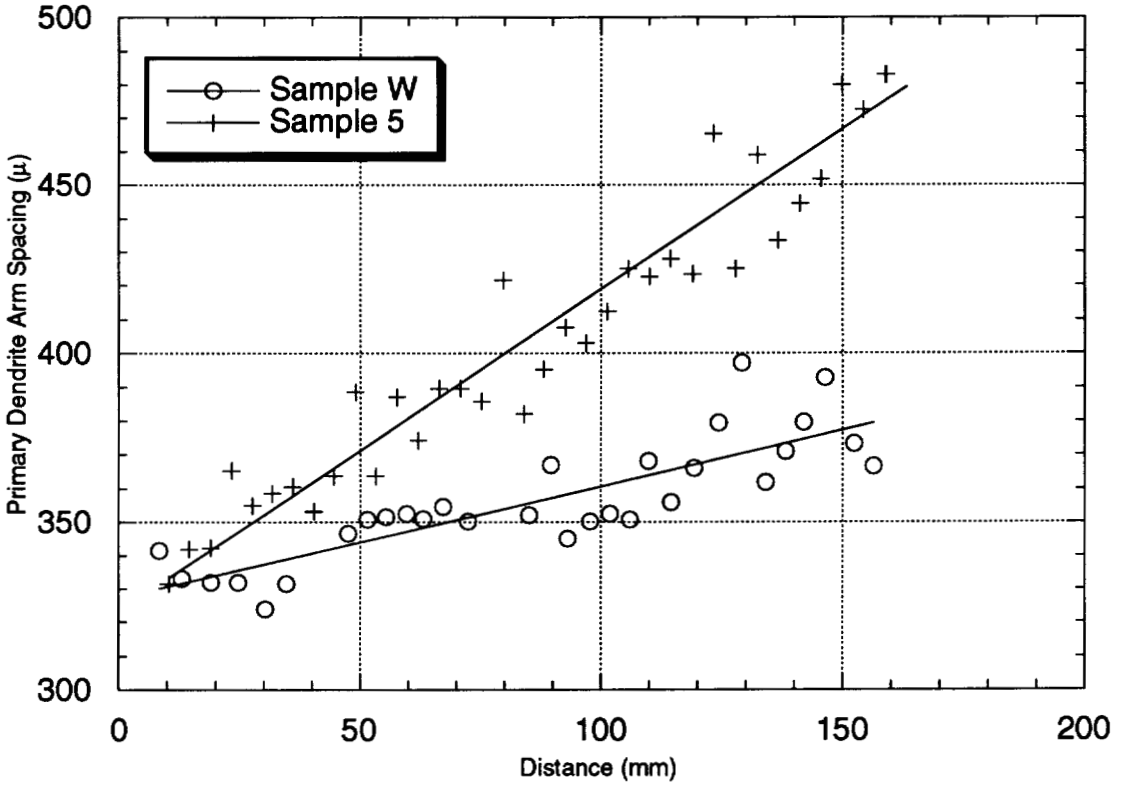

Figure 11.2
Comparison of Samples W & 5

This effect of the chill spool is readily apparent for all runs other than those which were conducted under gradient control. A comparison of the PDAS results of samples 3,5 and 6 to those of samples W, Y and Z (plots may be found in appendix 20) reveals that the behavior found in figure 11.2 is consistent.

In summary a shaped chill spool may be effectively employed to increase the cooling capacity of the cold zone of a commercial single crystal furnace and in so doing result in an adverse contribution to product quality.

11.3 Effect of Geometrical View Factors

From figure 11.2 it may be seen that the primary dendrite arms spacing showed a continual increase throughout the process. Such an increase must be due to a decrease in the gradient, a decrease in the solidification rate or a combination of the two. Since the process is being conducted at a constant withdrawal rate, and the gradient has a significantly greater impact on PDAS than does the solidification rate, it is likely that the change is due to a decrease in gradient. This concept is further strengthened by the realization that in light of the more effective cooling that is proposed to occur as a consequence of additional surface area being exposed beneath the baffle, any observed change in the solidification rate should manifest itself as an increase resulting from the interface being pushed upwards. Clearly then a change in the gradient at the liquidus must be primarily responsible for the increase in the primary dendrite arm spacing. Assuming that this is in fact the situation, equation (70) may be re-written into an expression which is proportional to the gradient:

(77)
$$G R^{.5} = \left(\frac{393.6}{PDAS - 211.5} \right)^2$$

The measured primary dendrite arm spacing at each location along the test bar may be used to evaluate this expression as a function of position. The result may then be plotted (Figure 11.3). If the solidification rate is relatively constant, then a change in position along the bar may be said to represent a commensurate change in the withdrawal distance. Since the withdrawal distance is in effect the amount of mold below the baffle, then at a constant solidification rate, the distance along the bar is proportional to the radiating area below the baffle as well. Figure 11.3 would then seem to imply that the gradient is directly related to the radiation that occurs below the baffle.

Such a proposition makes sense in that as the heat removed below the baffle increases, more heat must be introduced above the baffle to offset the effect. This can only occur if the liquidus position is driven upward thereby exposing more "cool" bar to emissive heat input. With heat being introduced along the entire length of the portion of the bar that is above the baffle, (albeit at a decreasing rate as one moves away from the baffle), the gradient must be decreasing as the distance from the baffle increases.

The linear nature of the curve in figure 11.3 implies that the surface area dominates the effect. The implication is that if a more constant primary dendrite arm spacing is desired, this may be accomplished by limiting the effective cooling area below the baffle. Such limiting may be accomplished by a heat shield. As described previously, the heat shield would be a movable device that would limit the amount of cooling surface seen by that portion of the mold which is below the baffle. This device would in effect allow the cooling surface to be kept constant thereby resulting in a more uniform solidification structure. In addition it would provide the ability to truly modulate the heat flow as section variations occurred.

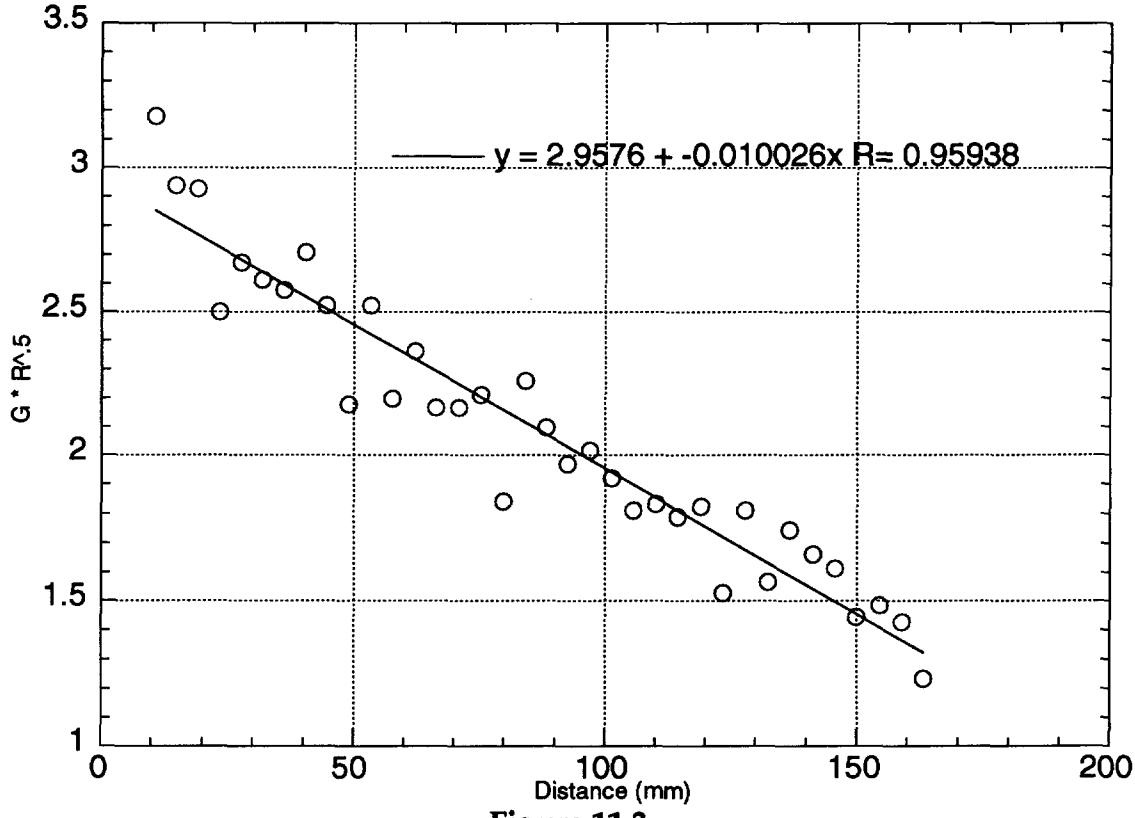

Figure 11.3
Gradient as a Function of Bar Position

As predicted, the solidification is to a very large degree driven by the surface area available for cooling. This same effect is seen when the more conventional baffle is used as exemplified by Sample W in Figure 11.2. It is of interest to note that the addition of more heat above the baffle, as may be accomplished through an increase in the susceptor temperature or as the result of increased solidification rate, reduces the geometrical effect.

11.4 Effect of Withdrawal Velocity

The results indicate that, in general, a higher solidification rate tends to refine the primary dendrite arm spacing. This is evidenced by the response of the system under gradient control conditions as well as the constant velocity experiments. By contrasting samples Y & Z, the effect of a higher withdrawal velocity may be quantified. Recall the expression for primary dendrite arm spacing:

$$\lambda \propto \frac{1}{\left(G^{.5} R^{.25}\right)} \tag{78}$$

If the withdrawal rate is very close to the growth rate, then if it is assumed that similar susceptor temperatures yield comparable gradients as a function of withdrawal distance, then the withdrawal velocity should relate to the PDAS through the above equation (78).

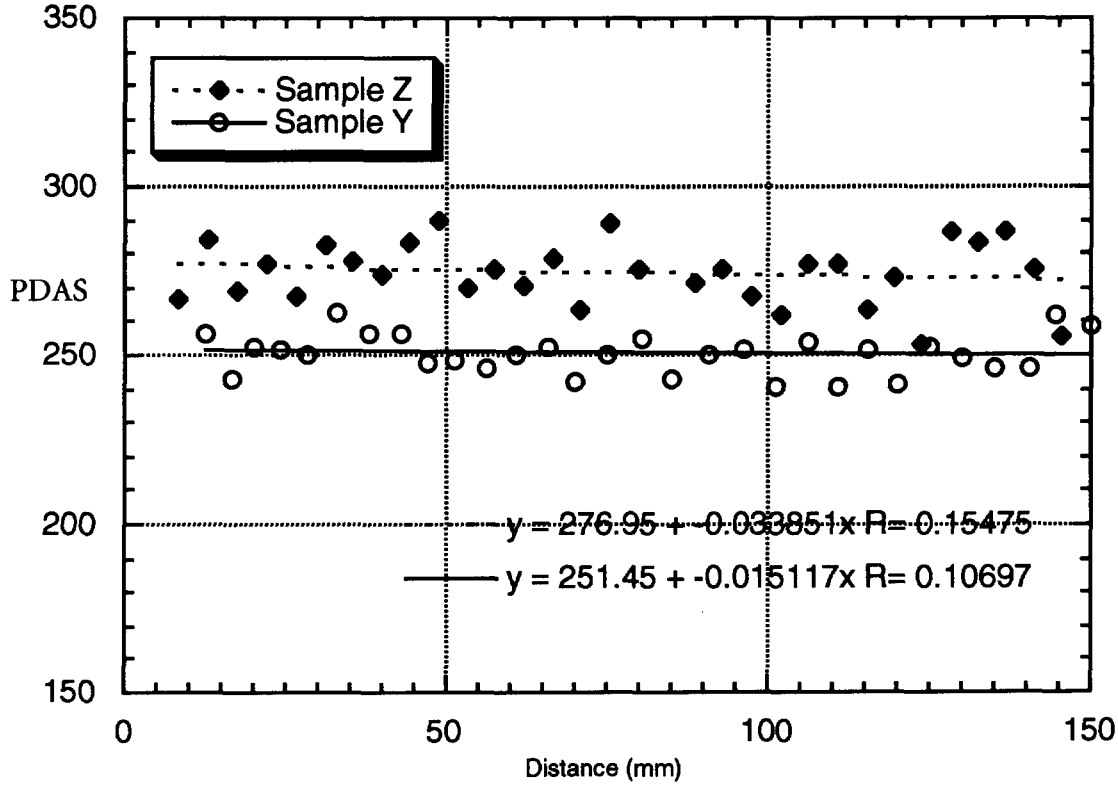

Figure 11.4
Comparison of PDAS for Sample Y and Sample Z

Figure 11.4 is a plot of the PDAS data from samples Y and Z. The data has been fit to a linear curve in order to allow an average value to be determined. Substituting x = 75 (1/2 length) in to the equations for Y and Z yields PDAS values of 250.31 and 274.41 respectively. If equation (78) were re-written for the solidification rate the result would be

$$R = \frac{K}{G^2 \lambda^4} \tag{79}$$

Utilizing the data for Z of R = 4 mm / min and λ = 274.4, it may be determined that:

$$\frac{K}{G^2} = R\lambda^4 \Rightarrow \quad \frac{K}{G^2} = 4(274.4)^4$$

$$\frac{K}{G^2} = 2.2678x10^{10} \tag{80}$$

So therefore, if the relationship is valid, it could be written that:

$$\lambda = \left(\frac{K}{G^2}\right)^{.25}\left(\frac{1}{R^{.25}}\right)$$

$$\lambda = \left(\frac{388}{R^{.25}}\right) \tag{81}$$

By substituting in the withdrawal rates of 4 mm / min and 5.8 mm / min, primary dendrite arms spacings for Z and Y are calculated to be 274 and 250 respectively. This is a very strong indication that once a steady state solidification has been established, the solidification velocity tends towards the value of the withdrawal velocity. This is only strictly true when the susceptor temperature is sufficiently high to overcome the geometrical effects. Such a condition existed during the processing of Y & Z and as such it may be said that for the thermal conditions associated with these parts, the solidification rate is effectively approximated by the withdrawal.

For the parts processed at lower temperatures or with the shaped chill spool, the geometric factors were driving the liquidus into areas of lower gradient and as such, the solidification velocity would have had to vary.

Although a high solidification rate provides a smaller primary dendrite arm spacing, a higher withdrawal rate does not always translate into a higher solidification rate. If the withdrawal rate is set too high, then the liquidus may be pulled below the baffle. In such cases, the solidification region becomes a heat source, with emissive cooling on both sides. In the region above the solidification zone this has the effect of reversing the gradient. Such a reversal would cause a break down in the single crystal growth.

It seems likely that many production process are operated at withdrawal velocities significantly below those which could be obtained. High initial velocities result in insufficient emissive cooling area to support the high velocity and single crystal growth could break down in the method described above. As a result slower velocities are used. If however the withdrawal rate was gradually increased throughout the process, the gradient control results indicate an improvement could be achieved.

11.5 Effect of Gradient Control

The primary goal of this work was the verification of potential techniques for the real time - closed loop control of the primary dendrite arm spacing. The primary dendrite arm spacing measurements provide evidence this goal was in fact achieved. When the primary dendrite arm spacing from samples 1, 2 and 4 are compared to those of sample 3, 5 & 6 clear differences are obvious. Figure 11.5 is a comparison of samples 2 & 5 which clearly illustrate the variation in the primary dendrite arm spacing which may be typically observed as a result of the gradient controlled and constant velocity processing methods.

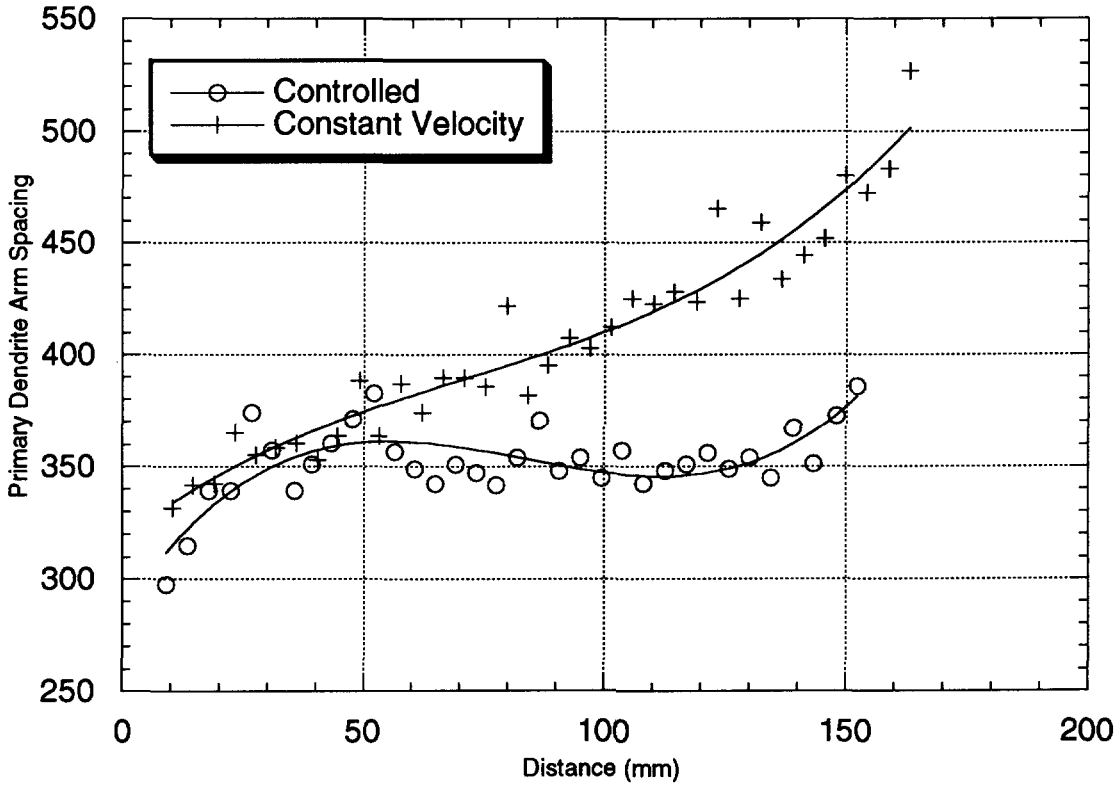

Figure 11.5
The Effect of Control Mode on PDAS

As may be seen from the figure, sample 2, (the gradient controlled sample), does not exhibit the same tendency towards an ever increasing primary dendrite arm spacing that is apparent in sample 5(the constant velocity sample). The regulation of the primary dendrite arms spacing observed in sample 2 is due to the gradient control methodology which had the effect of continuously accelerating the withdrawal velocity

as the process progressed. This acceleration is the control action required to maintain the gradient at a constant location relative to the baffle. A consequence of such acceleration is that the solidification velocity must also be increasing. The increased solidification rate provides the heat necessary to overcome the increase in emissive heat loss that occurs as a function of the expanding radiator surface below the baffle. The net result is that under this control mode, the variation in the primary dendrite arms spacing is reduced. It should be noted that the curvature at the ends of the "controlled" curve is probably due to the length of the thermocouple array which did not encompass the full length of the test bars.

The closed loop control mode described is based upon the calculation of the location of a particular temperature on the part and the subsequent control action required to place that location at or near the baffle. The control action employed is a modification of the withdrawal velocity. A drawback of the system is that it requires a method of sensing the temperature as a function of position along the part be employed. As such the technique is of use in the development of an optimized withdrawal profile for a part, but not as a production technique.

Optical pyrometer manufacturers have reported that alumina is transparent to long wave infra red radiation. If such is the case ,then an optical pyrometer at the baffle could be used to sense the part temperature at that location. The withdrawal velocity could then be modified to control that temperature at the desired value. Fiber optics and a liquid nitrogen cooled sensor could be used to interrogate the system at very long wavelengths with the result being that the actual metal temperature would be sensed. Such a system could be readily implemented into a production process. Although further investigations along these lines are necessary, there exists the strong possibility of a closed loop method of microstructural control that would be suitable for daily production.

Chapter 12 Growth Orientation

A potential advantage that may be realized through the control of the interface position is the realization of a more consistent growth direction. Many single crystal parts may be seen to have growth direction that changes as the process progresses, with the result being that <001> moves away from alignment with the vertical axis. This change in the growth direction is due to heat fluxes in the solidification region which have a horizontal component. Since the dendrites grow in an opposite direction to the heat flux, the non-vertical heat flux causes the growth direction to tilt away from the vertical. It is typically observed that the degree of tilt increases with withdrawal distance. As previously discussed, the interface position also changes as a function of withdrawal distance and is seen to move up the bar with increased withdrawal.

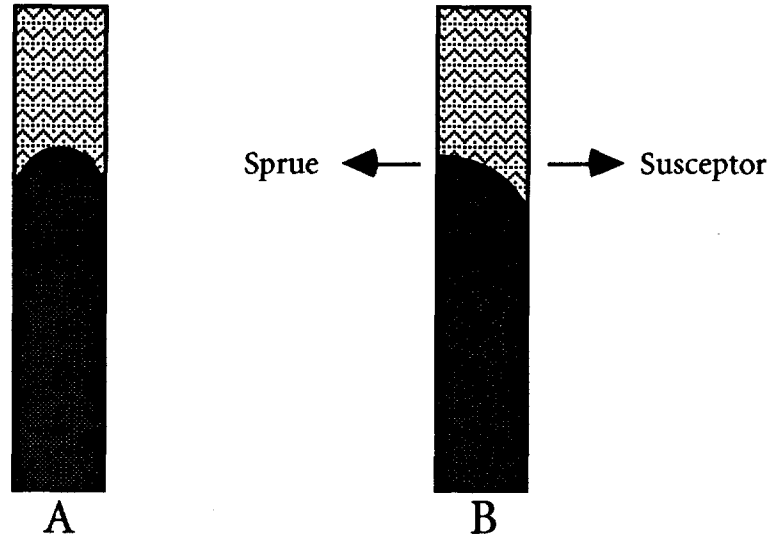

Figure 12.1
Interface Morphology

The solidification interface is pushed up (relative to the baffle) because of the increased cooling efficiency. Since any heat that enters the mold must arrive from outside the mold as a result of emissive heating, the outside of the part sees a higher temperature than the center. The heat must eventually leave the part at some distance below the interface and therefore the flux lines must curve downward. This vertical downturn of the horizontal emissive heat flux results in a curved solidification interface. This is shown in figure 12.1A. However, the example shown in 12.1A is an

idealized example and assumes a radially invariant heat flux. The presence of multiple parts on a tree and a center sprue, greatly reduces the incident radiation flux seen by some sides of the various parts on the tree. Such uneven heat flow can result in a situation where the side of the part away from the heat source receives no additional heat and as a result is subjected to vertical fluxes only. However, the opposite side of the part where emissive heating is occurring could have a significant horizontal component of heat flow. The net result is an asymmetric solidification interface as shown in figure 12.1B.

The curvature is largely due to the heat entering that area of the part that encompasses the solidification region and it is the combination of the emissive heat and the heat of solidification which results in the hotter periphery of the part. It then follows that the degree of curvature is directly related to the amount of emissive heat incident upon the solidification zone. As such, lower gradients expand the area that is effected and result in a greater degree of curvature at the interface.

Using the BEKP technique described in section 8.3, two disks from sample 5 were surveyed to see if a change could be detected in the shape of the solidification interface. The disks were mounted and loaded into the SEM. BEKPs were acquired at the positions indicated in Figure 12.2

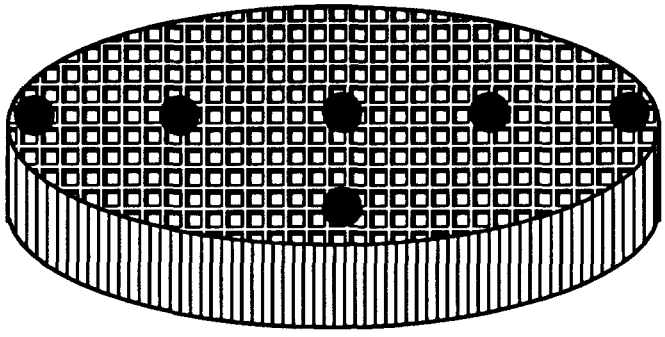

Figure 12.2
BEKP Test Positions

The configuration of the mounting fixture and the 70° tilt of the sample result in a situation where it is very easy to scan across the sample and remain in calibration but more difficult to maintain calibration while scanning up and down. Since the twofold intent of the experiment was to see if the technique was feasible and if the interface was becoming more curved as solidification progressed, this test array was deemed adequate. Future planned experiments will test the technique across a 22 inch diameter Electro-Slag Re-melt (ESR) ingot.

A trial was conducted using slices as etched for the optical micrographs. It was decided that the measurements would be taken at the dendrite cores. However, the combination of 70° tilt view and lack of experience with dendritic single crystal samples induced some difficulty in the determination of dendrite core locations. The samples were then re-etched. This re-etching provided a better view of dendrite cores in the SEM, but left a film that smeared the diffraction pattern. Nonetheless, diffraction patterns were observed from slice 2-32 at locations 1, 3 and 5. These patterns revealed that the location of the [0 0 1] pole on the diffraction pattern was shifting. Slices 5-10 and 5-33 were then re-polished and etched using the original Marbles etch. With the experience gained, the determination of dendrite cores became trivial.

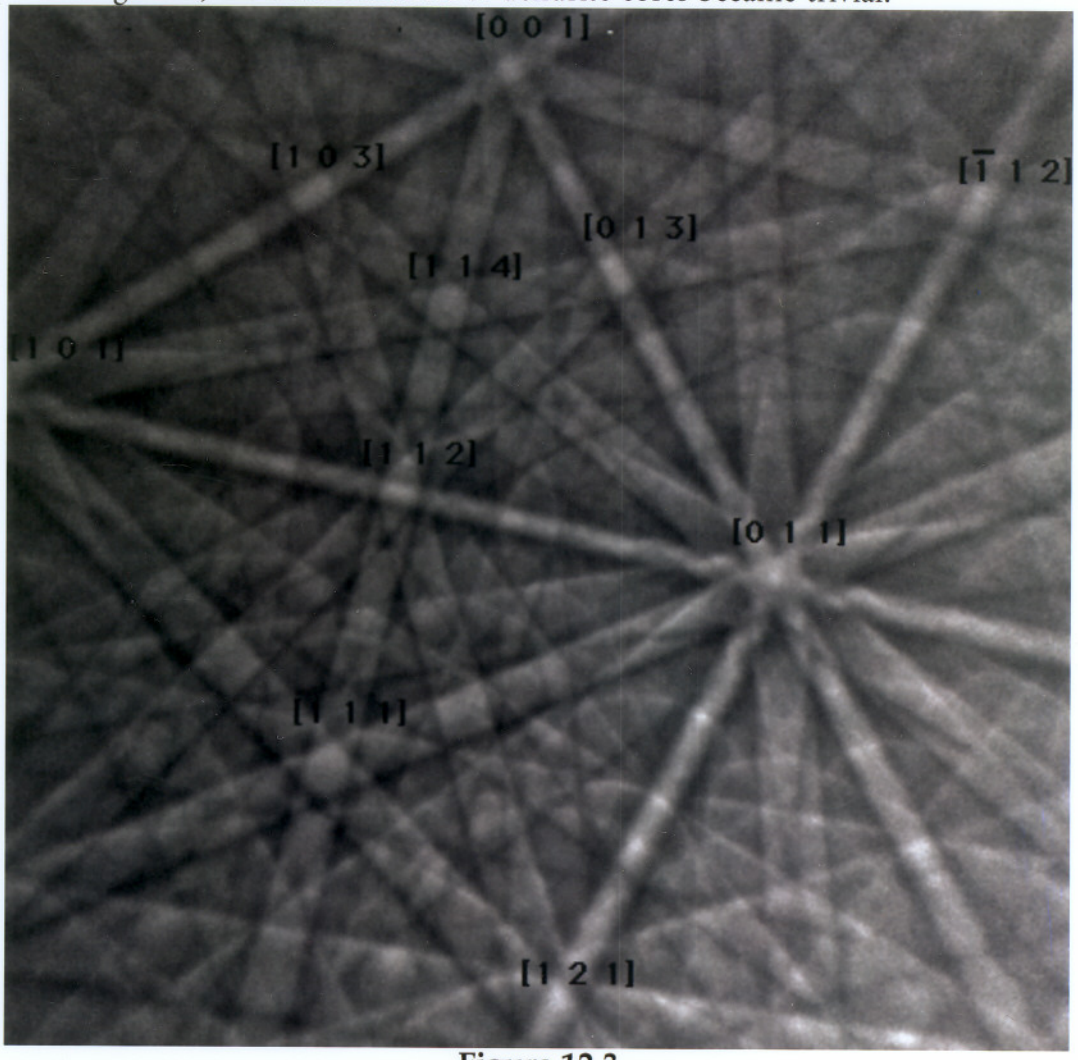

Figure 12.3
Typical BEKP Image (5-33 : 3)

Figure 12.3 is a typical BEKP pattern as obtained from slices 5-10 and 5-33. This pattern has actually been cropped to fit on the page. The patterns found in appendix G have been reduced to allow a view of the entire pattern. Figure 12.3 has also been partially indexed for convenience. It should be remembered that the center of the image is not the center of the pattern nor are either of them the sample normal.

The center of the pattern resides at (194,194) referenced to the upper right hand corner of the complete image. The camera length was 271 mm and the accelerating voltage was 30KV. With this information and an indexed pattern, it is possible to calculate the sample normal.

For the experiment, diffraction patterns were acquired at the locations shown in Figure 12.2. As the diffraction patterns were stored, the positions of the [0 0 1] zone axis were recorded. Table 12.1 are these values.

Table 12.1 Pixel Coordinates of [0 0 1]

Slice	Location	Pixel Row	Pixel Column
5-10	1	319	99
5-10	2	318	99
5-10	3	320	102
5-10	4	321	99
5-10	5	322	102
5-10	6	318	99
5-33	1	303	95
5-33	2	304	90
5-33	3	305	95
5-33	4	309	87
5-33	5	311	93
5-33	6	306	92

By inspection it may be seen that there is more variation in the location of the [0 0 1] in slice 5-33 than there is in slice 5-10. Once the images have been stored to magneto-optical disk, they are ready to be analyzed.

The images are analyzed by a program that runs on a Macintosh™ computer. The locations of known zones are entered along with the image center, camera length and accelerating voltage. The program then calculates the direction of the sample

normal. As an example, the surface normal at the center of slice 5-33 is [.0228, -.0208,.99905], this is 2.5° off of [0 0 1]. Slice 5-33 showed a total difference of 3.7° and an asymmetric change in angle with position. Slice 5-10 showed a total maximum shift of .65° symmetric about the center. Slice 5-10 was oriented 1.4° off of [0 0 1].

The absolute values of orientation are not provided as they have no meaning. The cutting fixture used for the slices was not accurate to much better than 2°-5°. It is therefore likely that the surface is slightly skewed from the orientation necessary for a true transverse slice. So while the absolute orientations are not well known the relative changes in orientation necessary to verify a change in curvature of the solidification front may be determined to within the accuracy of the technique which is about .5°.

We may then conclude that early in the melt the interface is essentially flat with a variation across the slice of .65°. This tends to change slightly as the interface is pushed away from the baffle until toward the end of the withdrawal when the variation across the part had risen to 3.7°. This amount of variation is probably of no consequence, but geometry's more complex than the round bars used for this study will certainly experience a greater degree of curvature. These results indicate that it is likely that the closed loop control mode proposed in this work will also tend towards lowering the degree of curvature of the primary growth axis.

It should be noted that the curvatures measured correlate well with the modeling results.

Chapter 13 Conclusion

In summary, the following conclusions have been reached:

- The process is dominated by the cooling.
- At constant withdrawal rates the interface moves up and away from the baffle as more cooling area is exposed below the baffle.
- As the solidification interface moves up and away from the baffle, the temperature gradients around the solidification interface decrease.
- As the solidification interface moves away from the baffle, the interface becomes curved.
- The low gradients which occur later in the process provide an environment where freckles are more likely to form.
- The heat of solidification is a significant portion of the total heat flux down through the part.
- The heat of solidification may be used to modify the solidification environment.
- Closed loop microstructural control is feasible.
- Backscattered Electron Kikuchi Patterns may be used on solidified specimens to measure the shape of the solidification interface.

The intent of this work has been to broaden the understanding of the industrial process for the growth of single crystal turbine components. The available literature and control techniques most typically applied, seemed to be at odds with the inherent process characteristics. This situation implied a need for a comprehensive examination of the single crystal process as it is found in industry. The desired outcome being a sufficiently enhanced understanding to allow optimization of the process. At the outset, it was determined that the proof would have to be in the metal. As such, primary dendrite arm spacing was determined to be the best measure of the process.

In order to obtain good statistics from a given sample, many primary dendrite arm spacing measurements were required. Further, in order to accurately track the primary dendrite arm spacing along the bar many samples had to be measured. It was

the intent of this work to examine the variation in primary dendrite arm spacing in greater detail than previous work. To this end a computer program was written to automatically determine the average primary dendrite arm spacing for each sample.

The primary dendrite arm spacings were measured along ten test bars which were processed under a variety of operating conditions. Three of these test bars were operated under a closed loop control scheme which sought to maintain the position of the solidification interface relative to the baffle. Two test bars were processed such that in-situ thermocouples provided continuous temperature readings along the test bars as the solidification occurred. These data provided significant insights into the solidification conditions. Among other things, the data showed that the solidification interface was moving up and away from the baffle as the withdrawal progressed. This conclusion was reached by comparing the thermocouple positions to the withdrawal position and determining the location of the solidification interface. This work was facilitated by the development of an analytical technique which utilized the temperature difference between adjacent thermocouples to determine the actual thermocouple locations.

The motion of the solidification interface is attributed to the enhanced cooling that occurs as result of the increasing surface area below that baffle. In order to verify this conclusion a finite element model was used to calculate the equilibrium positions of the solidification interface. The model verified that the process is dominated by the cooling. In addition, the model led to the conclusion that greater control over the process could be realized by controlling the cooling. It is suggested that an aperture be used to limit the view factor of the chill spool. Such a device would allow the cooling to be kept relatively constant thereby avoiding the process variations induced by an ever expanding emissive radiator. An attempt to increase the cooling and hence the gradient via a shaped chill spool further verified that the process is dominated by the cooling. Since the trials with the shaped chill spool resulted in greater detrimental cooling effects, enhanced cooling is not a positive addition. Any modification of the cold zone should involve a reduction or stabilization of the cooling through the later stages of the process, although enhanced cooling at the beginning could be beneficial.

Observation of the test bars indicated a slight variation in the growth direction. In order for such a variation to occur, the solidification interface must be curved. The model indicated that this could occur, but since the model was a single bar axi-symmetric case, the extent of the curvature was undervalued. In order to determine the actual shape of the solidification interface, backscattered electron Kikuchi patterns

in the scanning electron microscope were utilized. This work demonstrated that the backscattered electron Kikuchi pattern technique could be used to ascertain steady state liquidus profiles from solidified transverse sections. The backscattered electron Kikuchi pattern work also showed that the interface curvature becomes more pronounced as the interface position moves away from the baffle. This realization provides confirmation of the conclusion that grain misorientation may be largely eliminated by taking actions to keep the solidification interface close to the baffle.

The thermocouple data, primary dendrite arm spacing data and modeling results demonstrate that the gradient at the liquidus decreases as the liquidus position moves away from the baffle. Since the gradient is the dominant factor in determining the primary dendrite arm spacing, the motion of the interface away from the baffle is also responsible for the observed increase in primary dendrite arm spacing. Further, since lower gradients result in longer dendrites, the lower gradients that result from the interface motion may also set up the conditions for convection jets which may cause freckles. This then leads to the conclusion that micro structural variations in the form of expanding primary dendrite arm spacing and defects in the form of grain misorientations and freckles are a result of excessive cooling which pushes the solidification interface up into areas of lower gradient.

Closed loop control trials, where the interface location was held near the baffle, resulted in a stabilization of the primary dendrite arm spacing and demonstrated that the heat of solidification could be used to offset the effect of enhanced cooling that occurs due to increased emissive surface area below the baffle. The closed loop technique which utilized third order least squares fits to obtain the magnitude of the temperature gradient around the solidification interface and also the location of the interface was shown to be an effective method for generating a withdrawal profile. It also provides sufficient data to allow an assessment of the effectiveness of the cooling which would be suitable for post processing into a further optimized withdrawal profile. The constant acceleration of the withdrawal velocity which was the response of this control technique to the changing thermal conditions further demonstrates the dominance of the cooling in the process. It also illustrates the fashion in which the heat of solidification may be used to modify the solidification environment. This conclusion, when coupled with the demonstrated ability to control the micro structure in a closed loop fashion are critical results.

While contrasting primary dendrite arm spacing results to thermocouple data it was discovered that the primary dendrite arm spacing data from two separate runs

and one run reported in the literature did not fit the same curve. Although the data from the literature would not be expected to match (a different alloy was used), the data from the two runs in this study should have been the same. It was observed that the two populations could be fit to the same relationship if the y intercept of the linear curve of primary dendrite arm spacing to ($G^{-.5}$ $R^{-.25}$) was based upon the initial cooling rate. It is conjectured that the lower the initial cooling rate, then the greater the time available for solid state diffusion and the further the eutectic reaction can proceed. This effectively lowers the solidus temperature of the substrate and extends the zone of constitutional undercooling. This relationship may be expressed as:

$$PDAS = K\left[\dot{T}_i + \frac{1}{\left(G^{.5}\, R^{.25}\right)}\right] \tag{82}$$

As may be seen, a change in the cooling rate impacts the y intercept of this equation. Slower initial cooling rates result in a finer primary dendrite arm spacing for a given combination of G and R. This equation fits all of the available data and explains the empirical practice of allowing a hold time after pour for the crystal to establish itself.

It was additionally shown that higher susceptor temperature results in a finer micro structure and that the associated solidification conditions do not lead to the variation in primary dendrite arm spacing that is typical of lower susceptor temperature operations. This result is further evidence that the process is often over cooled. It also is evidence of the process improvements that could be achieved through the development of higher temperature mold materials and face coats.

This work, its conclusions, and the process and equipment modifications which have been identified should allow much of the empiricism associated with the process to be eliminated. Although the methods utilized are somewhat diverse, these results could not have been obtained without the full range of experiments. Each of the varied aspects of this work, the primary dendrite arm spacing study, thermocouple data, closed loop tests, finite element model, parametric experiments and backscattered electron Kikuchi pattern studies provided necessary cross checks and additional insights which could not have been otherwise obtained.

Chapter 14 Future Work

As with any study of this sort, there seems to be more questions at the end than there were at the beginning. One particularly intriguing area of future work is a experimental program to determine whether the observed relationship:

$$PDAS = K\left[\dot{T}_i + \frac{1}{\left(G^{.5} R^{.25}\right)}\right] \tag{83}$$

holds up under a more rigorous study. The implied result that the solidification microstructure may retain a significant dependency on the initial solidification conditions has far reaching implications for the processing of single crystal parts and could represent a useful extension to the theory of eutectic solidification. Such a study would include the processing of multiple test bars under identical conditions but with different initial cooling rates. The study would likely also include processing several test bars at different gradients and rates but with the same initial cooling rate. A primary dendrite arm spacing survey would then be used to evaluate the results.

Further development of the BEKP technique for measuring the morphology of the molten pool as it existed during solidification is also clearly warranted. This technique is almost certainly valid as it is simply a logical extension of existing technology. Nonetheless, it is a hitherto for unrealized capability that should be of considerable value in solidification studies since the volume of material needed to investigate a pool profile is greatly reduced. Significant savings will also be realized in expenses associated with cutting and polishing since the total sample area is reduced to a single thin transverse strip. At the time of this writing, a transverse section of 8 inch vacuum arc re-melt furnace ingot is being processed to determine the shape of the molten pool that was in existence during solidification. As a result, the verification of this technique is well under way.

In order to verify that the process observations that occurred as a result of this study are universally true, several production turbine components should be evaluated. Back-scattered electron Kikuchi patterns and dendrite surveys would provide the necessary information to determine if the solidification interface was

moving a significant distance from the baffle. Of greater interest would be the determination of the primary dendrite arm spacing and the morphology of the solidification interface (using BEKP) when evaluated at positions along the part which contain freckles. This work could provide definitive information regarding the solidification conditions responsible for the formation of freckles.

Instrumented closed loop control trials on industrial parts would be of use in assuring whether or not techniques designed to control the liquidus position using the simple geometry of test bars may be readily extended. Further work may also be done in determining if withdrawal profiles may be optimized as a result of post processing the data.

Finally several equipment modifications are indicated and should be tried. First among these modifications is the implementation of an aperture in front of the chill spool. This device would be used to limit and stabilize the emissive cooling that occurs below the baffle such that the degree of emissive cooling does not continuously increase as the withdrawal progresses. This device would prevent the solidification interface from being pushed above the baffle and in so doing maintain a higher gradient, and a flatter interface while eliminating those conditions responsible for the formation of freckles.

The second modification is the evaluation of a low frequency pyrometer as a permanent feedback element. Such a device should be able to *see* through the ceramic mold and read the metal temperature directly. This would allow the direct measurement of the metal temperature and provide the capability of running all production under a closed loop scheme designed to directly control the microstructure.

When combined, these two equipment modifications allow precise, real time microstructural control of single crystal parts. As this work has shown, microstructural control is feasible; the next step is industrial implementation.

Appendix A...PDAS Calc., Sample 6

(The expressions used within this Mathematica™ Notebook were extracted from the thermocouple data for run #6. The data were plotted and then fit to polynomials using a least squares algorithm *)*

(Expression for the Liquidus Location. *)*

$$\text{LiquidusPos} = 65.712 + 1.2486\,x - 0.0024157\,x^2$$

(Expression for the liquidus position as a function of time. *)*

$$\text{LiqPosT} = -49.469 + .28962\,t - .0001213\,t^2 + 1.8638\,10^{-8}\,t^3$$

(Solidification velocity is the 1st derivative. *)*

$$\text{SolVel} = 0.1\ D[\text{LiqPosT},t]$$

(Expression for the gradient as a function of test bar location. *)*

$$\text{theGrad} = 3.8927 - 0.17956\,xi + 0.0052339\,xi^2 - 6.9038\,10^{-05}\,xi^3 + 4.5442\,10^{-07}\,xi^4 - 1.5322\,10^{-09}\,xi^5 + 2.4854\,10^{-12}\,xi^6 - 1.483\,10^{-15}\,xi^7$$

(Substitute in the expression for test bar location as a function of time. *)*

$$\text{GradvsTime} = (10 * \text{theGrad}) /. xi \to \text{LiqPosT}$$

(Calculate the gradient - solidification rate term *)*

$$\text{InverseGR} = 1.0 / (\text{GradvsTime}^{.5}\ \text{SolVel}^{.25})$$

(Generate an Equation for PDAS vs. time. *)*

$$\text{Spacing} = -19.83 + 393.6\,(.11 + \text{InverseGR}))$$

(Specify the equation for time as a function of liquidus position. *)*

$$\text{theTime} = 143.30 + 7.3177\,x - .056433\,x^2 + 0.00035272\,x^3$$

(Convert PDAS vs. Time into an expression for location along the bar. *)*

$$\text{TheSpacing} = \text{Spacing} /. t \to \text{theTime}$$

```
(* Adjust for test bar cut off *)
        PDAS          =   TheSpacing /. x-> theLoc + 115;

(* Plot various results *)
        Plot[LiqPosT,{t,750,3000}]
        Plot[SolVel,{t,750,3000}]
        Plot[GradvsTime,{t,750,3000}]
        Plot[PDAS,{theLoc,0,90}]

(* Calculate a table of 1/G^.5 * R^.25 at dendrite  measurement locations *)
        N[InverseGR /.theLoc->{0,15.27,31.83,47.97,63.52,78.14,90.8}]

(* Generate a table of PDAS vs. position for valid TC Span *)
        Table[{theLoc,TheSpacing },{theLoc,0,90,.25}]
```

Appendix B...PDAS Calc., Sample 4

```
(* Gradient as function of TC position *)
    G          = 63.547 - 5.1952 xi + 0.19893 xi^2 - 0.0040793 xi^3 +
                 4.9006 10^-05 xi^4 - 3.5376 10^-07 xi^5 + 1.5031 10^-09 xi^6 -
                 3.4529 10^-12 xi^7 + 3.3016 10^-15 xi^8

(* Liquidus position as function withdrawal *)
    Liquidus   = -24.845 + 1.9525 x - 0.0038606 x^2

(* Withdrawal Velocity as function of position *)
    WithdrVel  = -0.18573 + 0.02516 x - 0.0009834 x^2 + 1.9824 10^-05 x^3 -
                 2.2926 10^-07 x^4 + 1.5898 10^-09 x^5 - 6.598 10^-12 x^6 +
                 1.5546 10^-14 x^7 - 1.7899 10^-17 x^8 + 6.2513 10^-21 x^9

(* Solidification velocity as f(x) *)
    SolVel     = .1 * D[Liquidus,x] * WithdrVel

(* Gradient as a f(x) *)
    Gofx       = (10 G) /. xi->Liquidus

(* PDAS as f(x) *)
    theSpacing = -19.83 + 393.6 (.58 + 1.0 / (Gof^.5 SolVel^.25))

(* x as f(bar location) *)
    TheWDPos   = -4.9571 + 1.147 xi - 0.0056659 xi^2 + 2.2637 10^-05 xi^3

(* PDAS as f(bar location) *)
    spac2      = theSpacing /. x->TheWDPos;

(* PDAS offset for cut off from tree *)
    spac3      = spac2 /. xi->(dist + 113);

(* Plot PDAS vs. bar location *)
    Plot[spac3,{dist,0,110},GridLines->Automatic]
```

```
(* Table of locations and spacings *)
        Table[{dist,spac3},{dist,0,150,.25}]
```

Appendix C...Modeling Results

The following ten pages are the results of the modeling runs. These represent five test cases in which the part has been moved relative to the baffle. The first case has most of the part above the baffle. Successive runs move the part downward until at the final case ,most of the part is below the baffle. Only those elements with a temperature within the solidification band are colored.

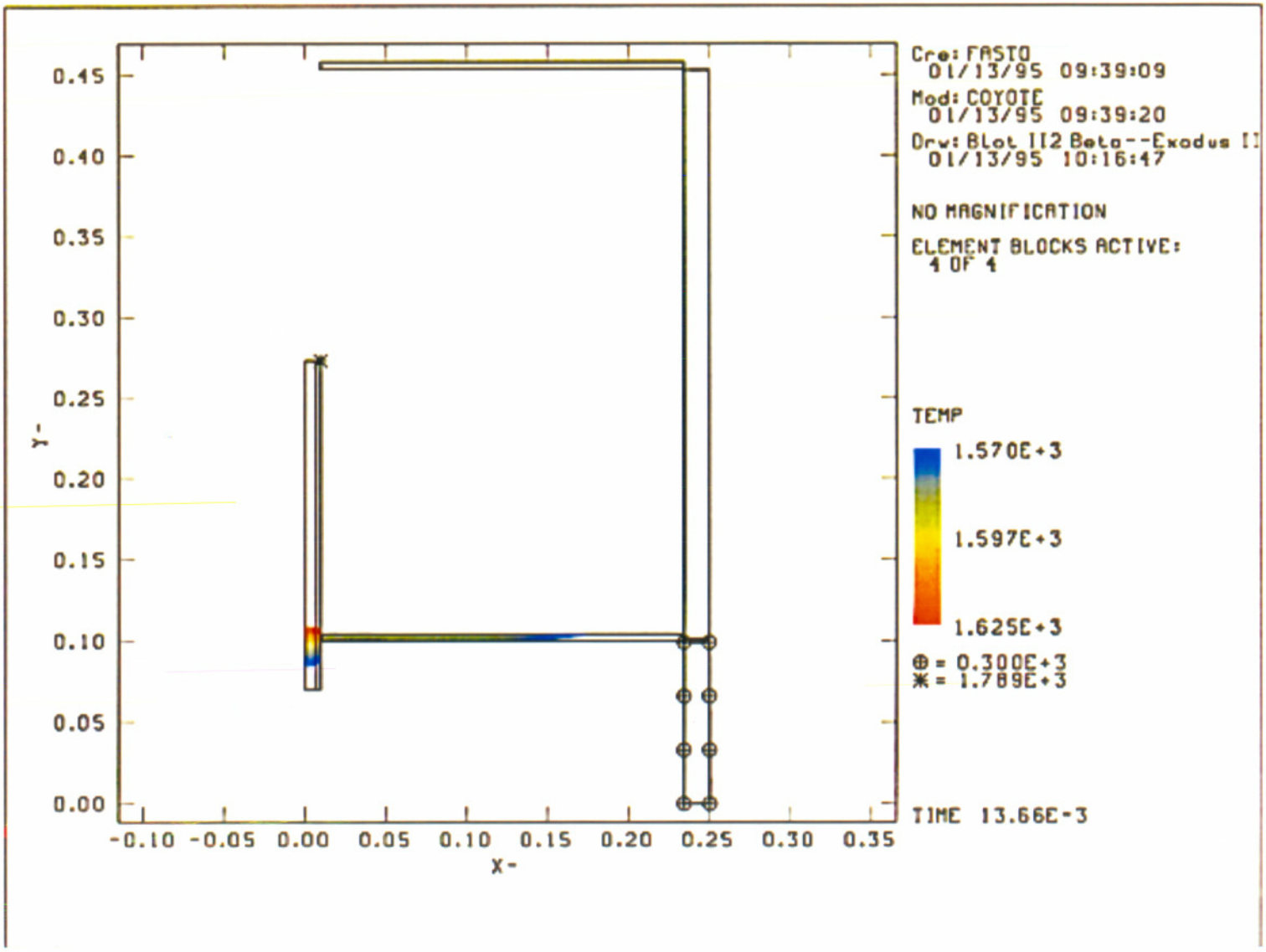

15 Percent Withdrawal

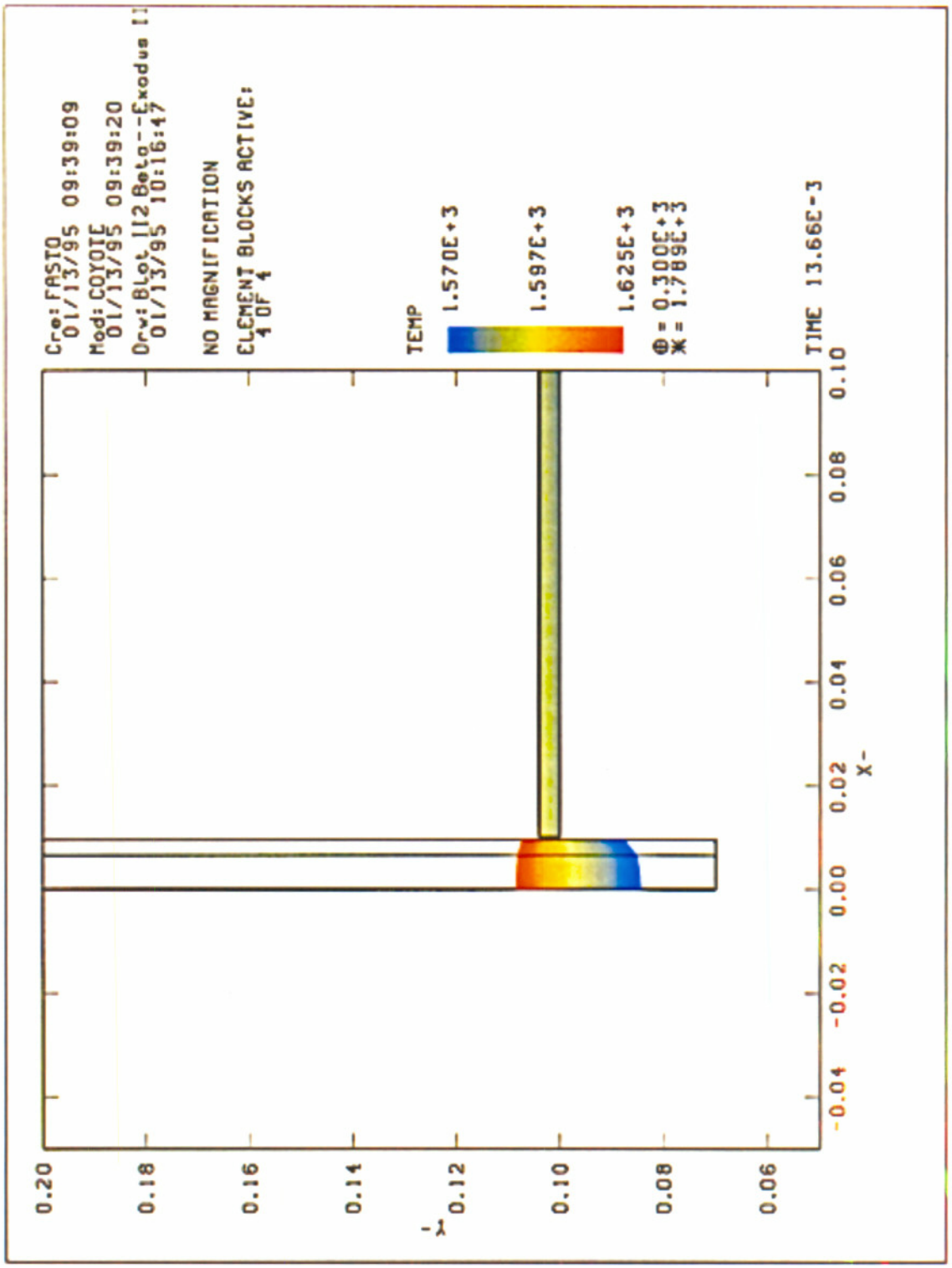

15 Percent Withdrawal - Expanded View

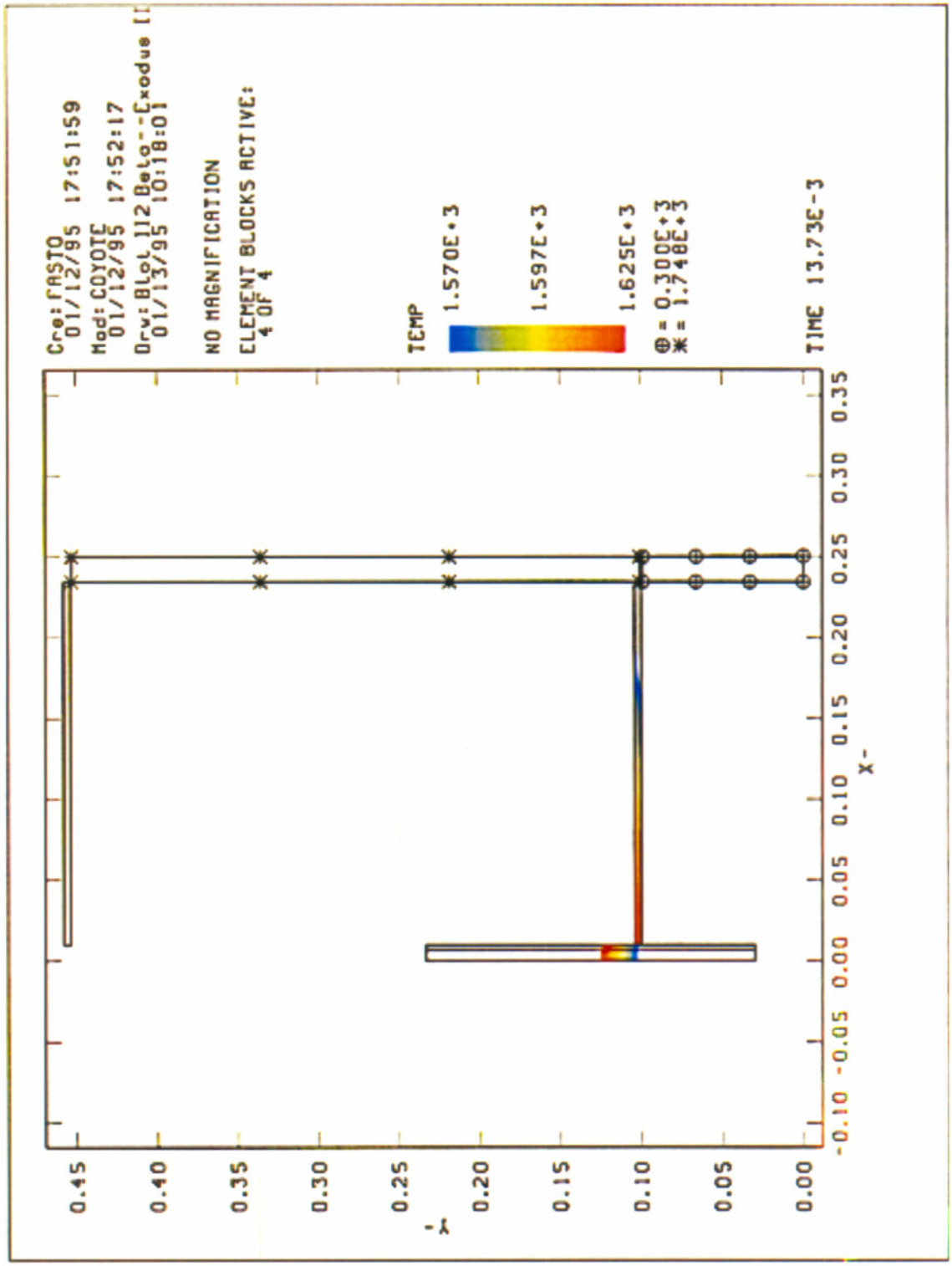

35 Percent Withdrawal

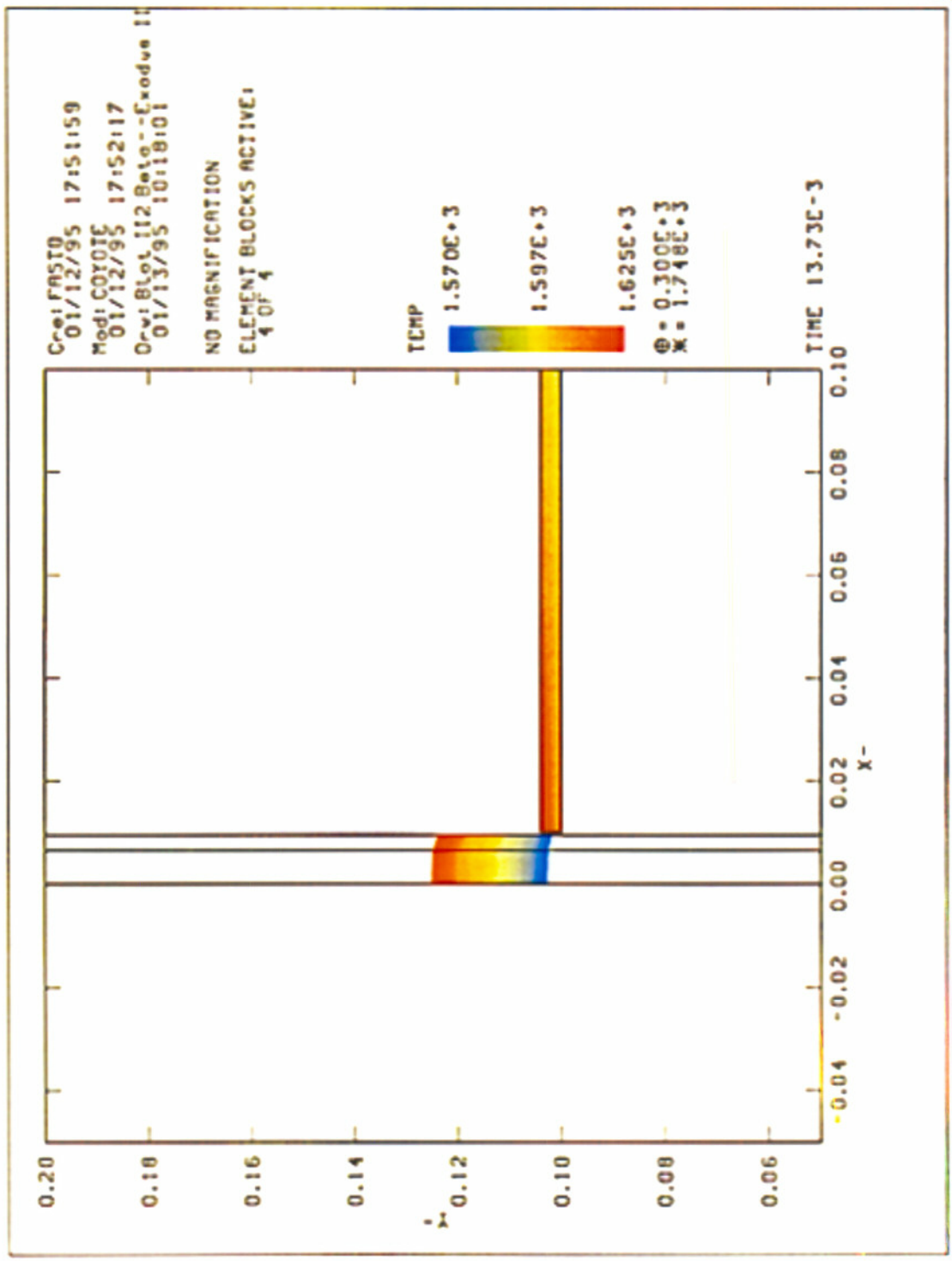

35 Percent Withdrawal - Expanded View

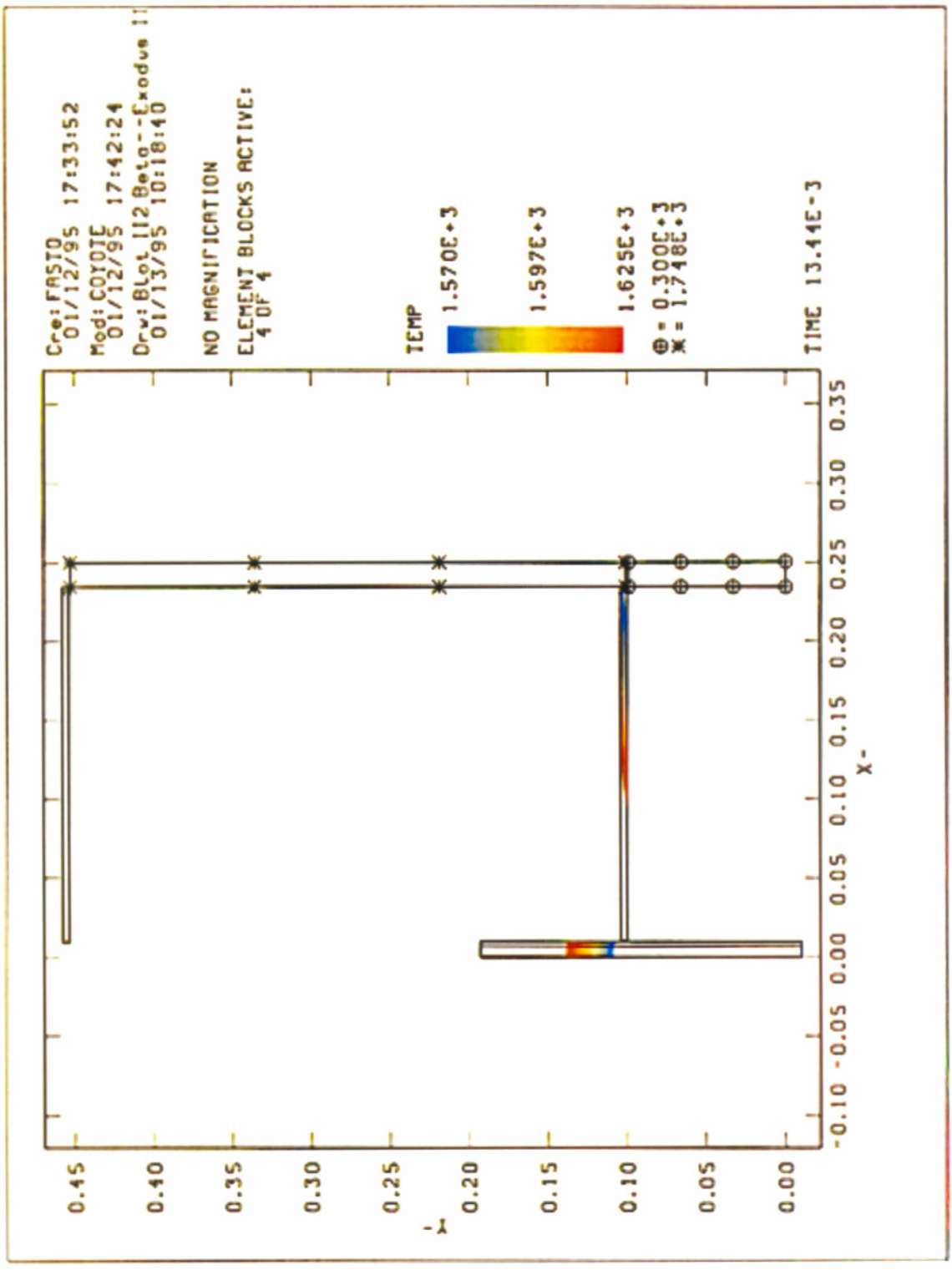

55 Percent Withdrawal

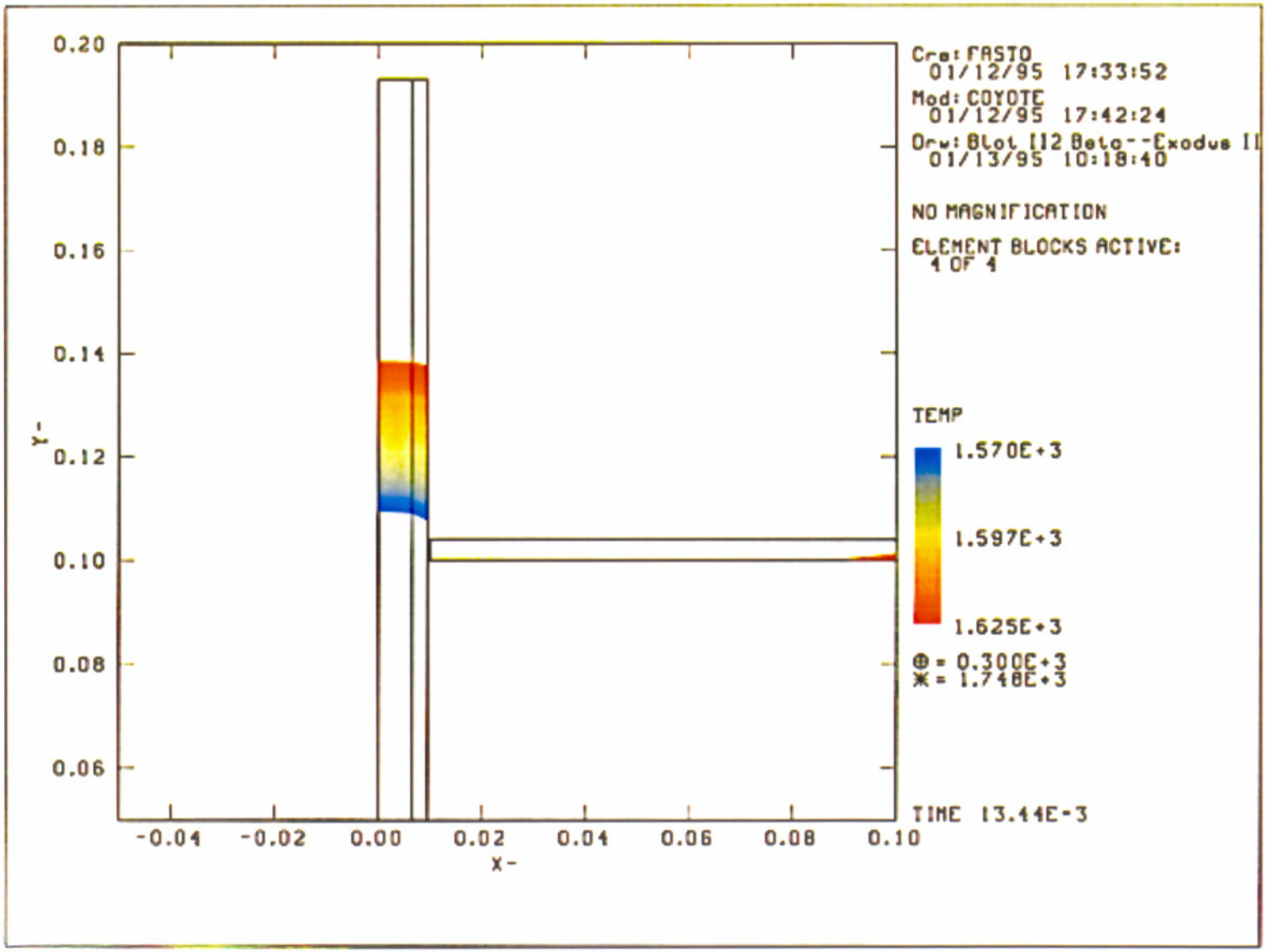

55 Percent Withdrawal - Expanded View

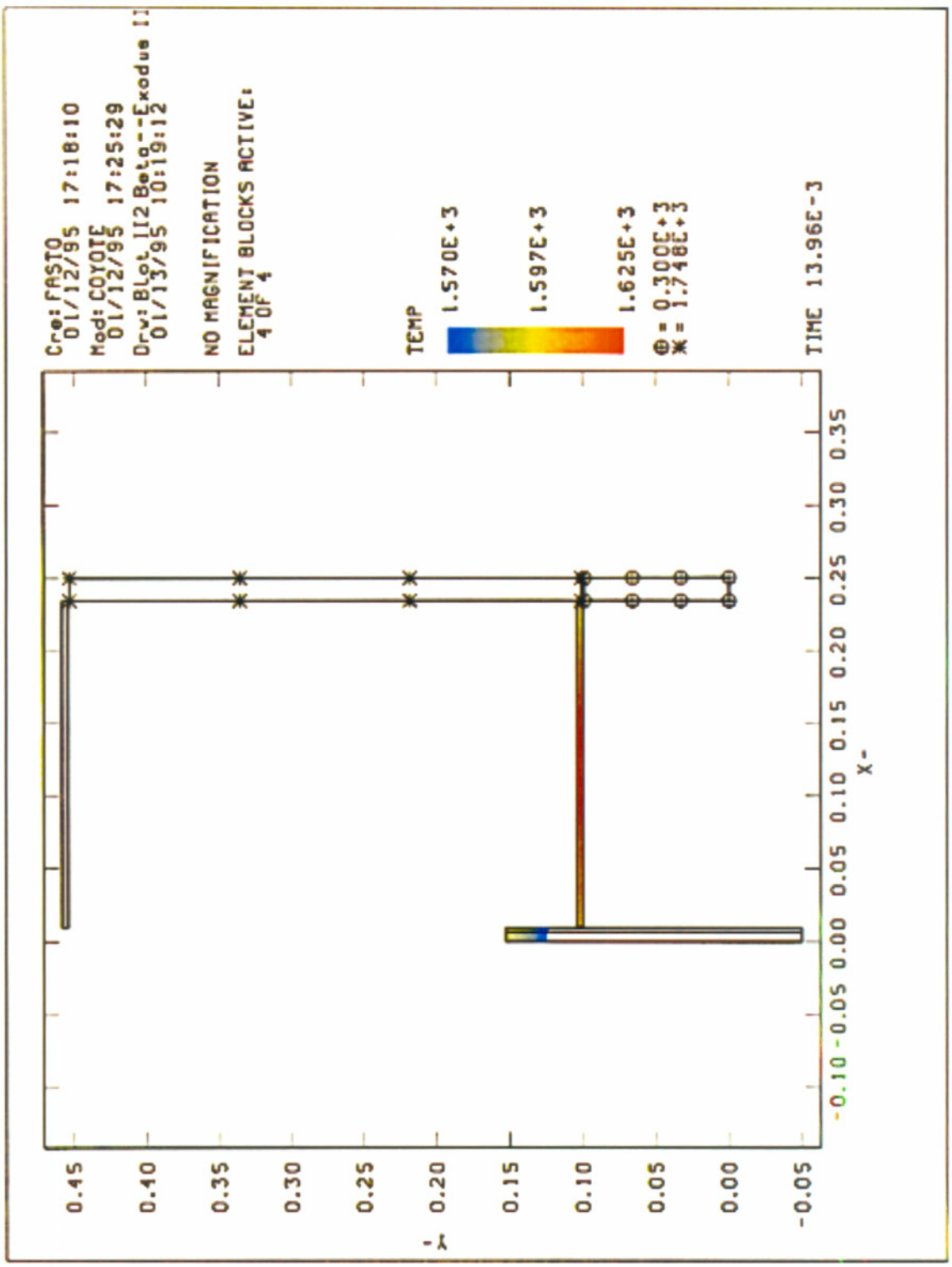

65 Percent Withdrawal

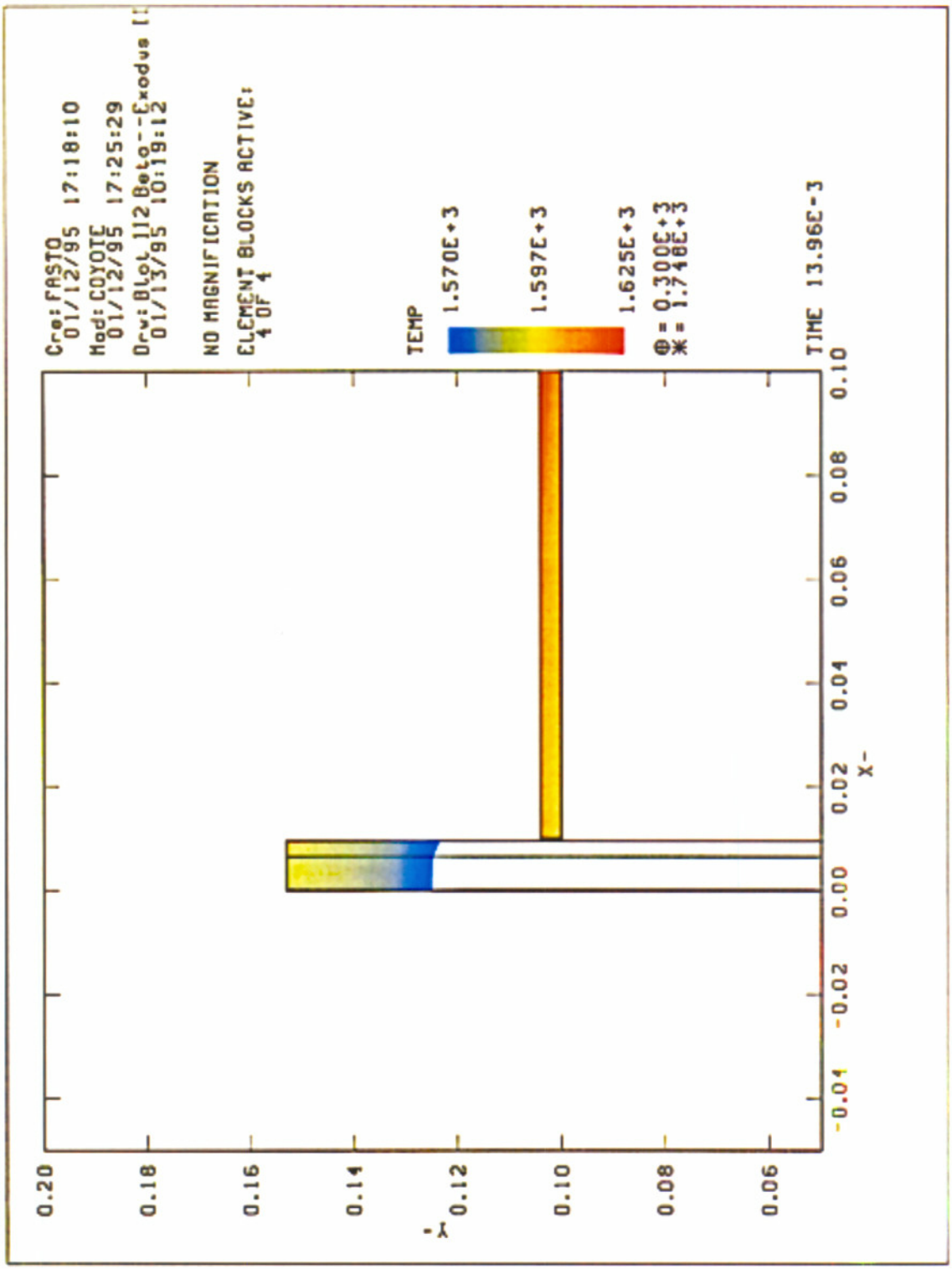

65 Percent Withdrawal - Expanded View

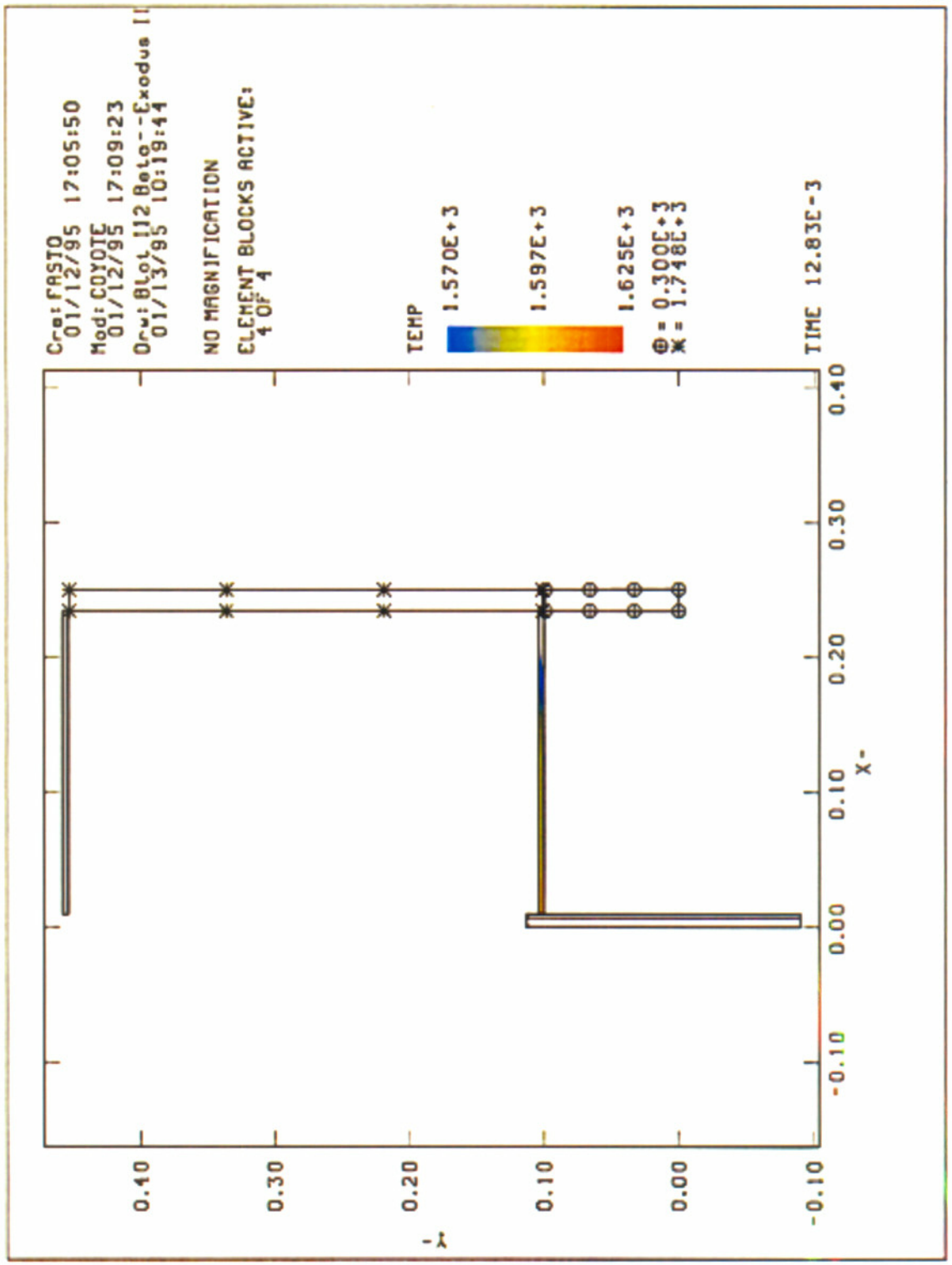

90 Percent Withdrawal

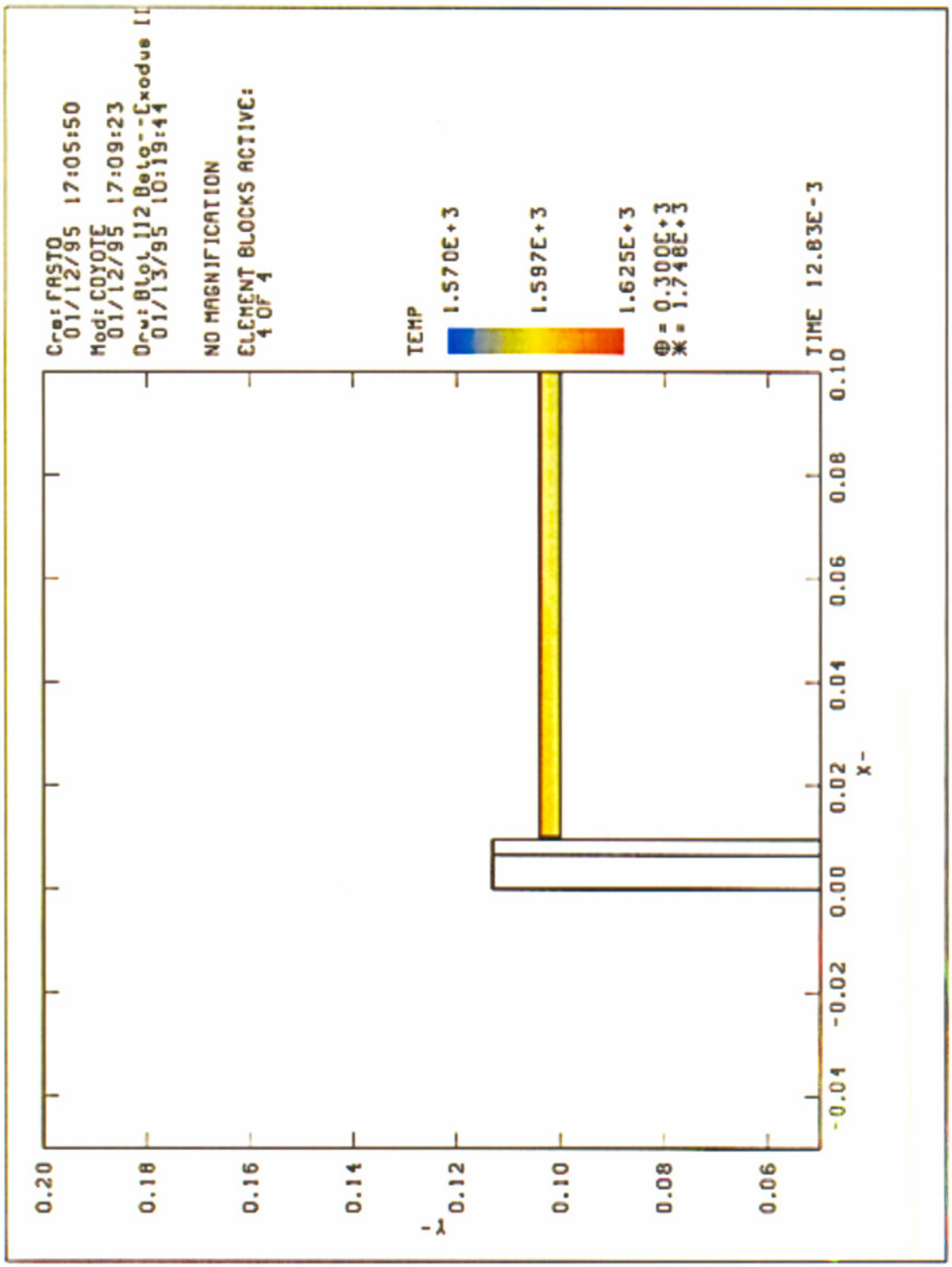

90 Percent Withdrawal - Expanded View

Appendix D...Dendrite Counting Code

The following pages are the source code for the dendrite counting software used in this work. The first section is source code, the next is #include files and the last is a resource dump.

D.1 Source Code

Each source code file starts at the beginning of a new subsection at the top of a page.

D.1.1 Dendrites.c

```
#define __MAIN__
#include "Dendrites.h"
#undef  __MAIN__


unsigned short* GetDataFromPICT(PicHandle thePicture,short
*rows,short *columns);
void    DrawPixels(unsigned short *theData,short rows,short columns);

void main(void)
{
    Handle          theMenuBar;
    EventRecord     theEvent;
    Point           thePoint;

    InitGraf(&qd.thePort);
    InitFonts();
    FlushEvents(everyEvent, 0);
    InitWindows();
    InitMenus();
    TEInit();
    InitDialogs(0L);
    InitCursor();
    PrOpen();
    hPrtRec = (THPrint)NewHandle(sizeof(TPrint));
    PrintDefault(hPrtRec);
    theCenters = (DendriteCenter*)new(DendriteCenter);
    theCenters->DoInit(UNDEFINED);


    mouseRgn    = NewRgn();
    quitFlag    = false;
    changed         = false;
    selectFlag      = false;
    rectVis         = false;
    validWindow     = false;
```

```
    multiPlot         = false;
    pointsFlag        = false;
    delPointsFlag     = false;
    learnFlag         = false;
    autoFlag      = false;
    theTypes[0]       = 'PICT';
    colorScheme       = 1;
    theMenuBar        = GetNewMBar(128);
    theWindow         = (WindowPtr)0L;


    SetMenuBar(theMenuBar);
    DrawMenuBar();
    AddResMenu(GetMHandle(APPLE_MENU),'DRVR');

    theWindow         = ((WindowPtr)0L);


    DoMenu(((long)FILE_MENU << 16) | OPEN_ITEM);

    GetMouse(&thePoint);
    LocalToGlobal(&thePoint);
    SetRectRgn(mouseRgn,thePoint.h - 4, thePoint.v-4, thePoint.h + 4,
thePoint.v + 4);



    while(!quitFlag){
        if(WaitNextEvent(everyEvent,&theEvent,updateRate,mouseRgn)){
            DoEvent(&theEvent);
        }
    }
    DisposHandle(theMenuBar);
    PrClose();
    DisposeRgn(mouseRgn);
    FlushEvents(everyEvent,0);
    theCenters->DoClose();
}
```

D.1.2 DendriteCenter.c

```
#include "Dendrites.h"
#include "GrabBitData.h"
#include "Eric'sLib.h"

Boolean TestPoint(unsigned short *theDataPtr,short rectRad,short
diagDist,short rowLength);
void    ExpandScale(unsigned short *theData,short rows,short columns);
double  CenterThePoint(unsigned short *theDataPtr,short columns);

void    DendriteCenter::ReInit(void)
{
    recordType      = UNDEFINED;
    thePicture      = (PicHandle)0L;
    pointCount      = 0;
    span            = 10000;

    infoFlag    = false;

    line1.start.x   = 0.0;
    line1.start.y   = 0.0;
    line1.end.x  = 0.0;
    line1.end.y  = 0.0;

    line2.start.x   = 0.0;
    line2.start.y   = 0.0;
    line2.end.x  = 0.0;
    line2.end.y  = 0.0;

    center.x    = 0.0;
    center.y    = 0.0;

    angle           = 0.0;

    next            = (DendriteCenter*)0L;
}


void    DendriteCenter::DoInit(short type)
{
    recordType      = type;
    thePicture      = (PicHandle)0L;
    dHorizAuto      = 4;
    dDiagonalAuto   = 4;
    span            = 10000;
    distance    = 100.0;
    pointCount      = 0;
    area            = 0;
    scale           = 0.0;
    infoFlag    = false;

    line1.start.x   = 0.0;
    line1.start.y   = 0.0;
```

```
    line1.end.x  = 0.0;
    line1.end.y  = 0.0;

    line2.start.x    = 0.0;
    line2.start.y    = 0.0;
    line2.end.x  = 0.0;
    line2.end.y  = 0.0;

    center.x     = 0.0;
    center.y     = 0.0;

    angle            = 0.0;

    next             = (DendriteCenter*)0L;
}


void    DendriteCenter::NewLine(void)
{
    if(next == (DendriteCenter*)0L){
        next = (DendriteCenter*)new(DendriteCenter);
        next->DoInit(LINES);
        next->DefineLine(&line1);
        next->DefineLine(&line2);
        next->DoCalculations();
        next->recordType = LINES;
    } else {
        next->NewLine();
    }
}

void    DendriteCenter::NewPoint(Point thePoint,short theSpan)
{
    if(next == (DendriteCenter*)0L){
        next = (DendriteCenter*)new(DendriteCenter);
        next->DoInit(POINT);
        next->thePoint = thePoint;
        next->span = theSpan;
        next->DrawPoint();
    } else {
        next->NewPoint(thePoint,theSpan);
    }
}


void    DendriteCenter::DefineLine(FLine* theLine)
{
    Point   thePoint,startPoint,endPoint;

    while(!Button())
        ;
    GetMouse(&startPoint);
    while(Button())
        ;
    endPoint = startPoint;
    MoveTo(startPoint.h,startPoint.v);
    PenMode(srcXor);
```

```
    LineTo(endPoint.h,endPoint.v);
    while(!Button()){
        GetMouse(&thePoint);
        if(!EqualPt(thePoint,endPoint)){
            LineTo(startPoint.h,startPoint.v);
            endPoint = thePoint;
            LineTo(endPoint.h,endPoint.v);
        }
    }
    while(Button())
        ;
    theLine->start.x = startPoint.h;
    theLine->start.y = startPoint.v;
    theLine->end.x    = endPoint.h;
    theLine->end.y    = endPoint.v;
}

void    DendriteCenter::DoCalculations(void)
{
    double  deltaX,deltaY;

    deltaY          = line1.end.y - line1.start.y;
    deltaX          = line1.end.x - line1.start.x;
    line1.angle     = atan2(deltaY,deltaX);
    line1.slope     = deltaY / deltaX;
    line1.intercept = line1.end.y - line1.slope * line1.end.x;

    deltaY          = line2.end.y - line2.start.y;
    deltaX          = line2.end.x - line2.start.x;
    line2.angle     = atan2(deltaY,deltaX);
    line2.slope     = deltaY / deltaX;
    line2.intercept = line2.end.y - line2.slope * line2.end.x;

    center.x    = (line2.intercept - line1.intercept) / (line1.slope -
line2.slope);
    center.y    = line1.slope * center.x + line1.intercept;
    angle           = fabs(fmod(line2.angle - line1.angle,.5 * pi));
    if(angle > (.25 * pi))
        angle = .5 * pi - angle;
}


void    DendriteCenter::WriteElements(short fileRef,short numElements)
{
    long    inOutCount;
    short   iErr;

    if(next == (DendriteCenter*)0L){
        inOutCount  = sizeof(short);
        iErr        = FSWrite(fileRef,&inOutCount,(Ptr)&numElements);
    } else {
        next->WriteElements(fileRef,numElements);
    }

    inOutCount  = sizeof(FLine);
    iErr        = FSWrite(fileRef,&inOutCount,(Ptr)&line1);
    inOutCount  = sizeof(FLine);
```

```
    iErr        = FSWrite(fileRef,&inOutCount,(Ptr)&line2);
    inOutCount  = sizeof(FPoint);
    iErr        = FSWrite(fileRef,&inOutCount,(Ptr)&center);
    inOutCount  = sizeof(double);
    iErr        = FSWrite(fileRef,&inOutCount,(Ptr)&angle);
}

void    DendriteCenter::ReadElements(short fileRef,short numElements)
{
    long    inOutCount;
    short   iErr;

    if(numElements < 0){
        inOutCount  = sizeof(short);
        iErr        = FSRead(fileRef,&inOutCount,(Ptr)&numElements);
        if(numElements <= 0)
            return;
    }

    numElements--;

    inOutCount  = sizeof(FLine);
    iErr        = FSRead(fileRef,&inOutCount,(Ptr)&line1);
    inOutCount  = sizeof(FLine);
    iErr        = FSRead(fileRef,&inOutCount,(Ptr)&line2);
    inOutCount  = sizeof(FPoint);
    iErr        = FSRead(fileRef,&inOutCount,(Ptr)&center);
    inOutCount  = sizeof(double);
    iErr        = FSRead(fileRef,&inOutCount,(Ptr)&angle);

    if(numElements > 0){
        next = (DendriteCenter*)new(DendriteCenter);
        next->DoInit(UNDEFINED);
        next->ReadElements(fileRef,numElements);
    }
}



short   DendriteCenter::CountPoints(void)
{
    short   count;

    if(next == (DendriteCenter*)0L){
        if(recordType == POINT){
            return (1);
        } else {
            return(0);
        }
    }

    count = next->CountPoints();

    if(recordType == POINT){
        count++;
    }
```

```
    return (count);
}

void    DendriteCenter::DrawElements(void)
{
    RGBColor yellow,white,black,blue;
    short       x,y;
    Rect        centerRect;

    yellow.red      = 65535;
    yellow.green = 65535;
    yellow.blue     = 0;
    black.red       = 0;
    black.green     = 0;
    black.blue      = 0;
    white.red       = 65535;
    white.green     = 65535;
    white.blue      = 65535;
    blue.red    = 16000;
    blue.green      = 16000;
    blue.blue       = 65535;


    switch(recordType){
        case CIRCLE:
            centerRect   = circleRect;
            x            = (centerRect.right - centerRect.left) >> 3;
            InsetRect(&centerRect,x,x);
            DrawPicture(thePicture,&(*thePicture)->picFrame);
            RGBForeColor(&yellow);
            FrameOval(&circleRect);
            RGBForeColor(&blue);
            FrameOval(&centerRect);
            break;

        case LINES:
            SetRect(&centerRect,-3,-3,3,3);
            x = (short)(center.x + .5);
            y = (short)(center.y + .5);
            OffsetRect(&centerRect,x,y);
            RGBForeColor(&black);
            RGBBackColor(&white);
            EraseOval(&centerRect);
            InsetRect(&centerRect,1,1);
            PaintOval(&centerRect);
            InsetRect(&centerRect,1,1);
            EraseOval(&centerRect);
            break;

        case POINT:
            DrawPoint();
            break;

        default:
            SysBeep(30);
            break;
    }
```

```
    if(next != (DendriteCenter*)0L){
        next->DrawElements();
    }
}


void    DendriteCenter::DoClose(void)
{
    Handle  thePicture;
    if(recordType == CIRCLE){
        thePicture      = *((Handle*)(&line2));
        DisposeHandle(thePicture);
    }

    if(next != (DendriteCenter*)0L){
        next->DoClose();
    }
    delete(this);
}


void    DendriteCenter::AddCircle(RectwindowRect,PicHandle thePic)
{
    short       dh,dv,ch,cv;

    if(recordType != UNDEFINED){
        return;
    }

    recordType      = CIRCLE;
    thePicture      = thePic;

    dh          = windowRect.right - windowRect.left;
    dv          = windowRect.bottom - windowRect.top;
    ch          = (windowRect.right + windowRect.left) >> 1;
    cv          = (windowRect.bottom + windowRect.top) >> 1;

    circleRect.left  = 0;
    circleRect.top   = 0;
    if(dh > dv){
        circleRect.bottom = dv - 8;
        circleRect.right = dv - 8;
    } else {
        circleRect.bottom = dh - 8;
        circleRect.right = dh - 8;
    }

    dh          = (circleRect.right + circleRect.left) >> 1;
    dv          = (circleRect.bottom + circleRect.top) >> 1;
    ch          -= dh;
    cv          -= dv;

    OffsetRect(&circleRect,ch,cv);
}
```

```
void    DendriteCenter::DrawPoint(void)
{
    Rect theRect;
    RGBColor yellow,white,black,cyan,blue,magenta;

    yellow.red      = 65535;
    yellow.green = 65535;
    yellow.blue     = 0;
    black.red       = 0;
    black.green     = 0;
    black.blue      = 0;
    white.red       = 65535;
    white.green     = 65535;
    white.blue      = 65535;
    cyan.red    = 0;
    cyan.green      = 65535;
    cyan.blue       = 65535;
    blue.red    = 0;
    blue.green      = 0;
    blue.blue       = 65535;
    magenta.red     = 65535;
    magenta.green   = 0;
    magenta.blue = 65535;

    SetRect(&theRect,-3,-3,3,3);
    OffsetRect(&theRect,thePoint.h,thePoint.v);
    EraseOval(&theRect);
    RGBForeColor(&magenta);
    PaintOval(&theRect);
    InsetRect(&theRect,2,2);
    RGBForeColor(&yellow);
    PaintOval(&theRect);
//  RGBBackColor(&yellow);

//  EraseOval(&theRect);
//  InsetRect(&theRect,1,1);

//  InsetRect(&theRect,1,1);
//  if(span == 0){
//      RGBBackColor(&blue);
//  } else {
//      RGBBackColor(&cyan);
//  }
//  EraseOval(&theRect);
    RGBBackColor(&white);
    RGBForeColor(&black);
}

void    DendriteCenter::AutoSearch(short rectRad,short diagRad)
{
    unsigned short   *theData,*theDataPtr;
    short            rows,columns,i,j;
    long             cx,cy,rad2,dx,dy,theRad2;
    Point            thePoint;
    double           span;

    cx          = (circleRect.left + circleRect.right) >> 1;
```

```
    cy          = (circleRect.top + circleRect.bottom) >> 1;
    rad2        = circleRect.right - cx;
    rad2        = rad2 * rad2;

    theData = GetDataFromPICT(thePicture,&rows,&columns);
    // ExpandScale(theData,rows,columns);
    theDataPtr  = theData;
    for(j = 0 ; j < rows ; j++){
        if(j < circleRect.top || j > circleRect.bottom){
            theDataPtr += columns;
        } else {
            for(i = 0 ; i < columns ; i++){
                if(i >= circleRect.left && i <= circleRect.right){
                    dx      = cx - (long)i;
                    dy      = cy - (long)j;
                    theRad2 = dx * dx + dy * dy;
                    if(theRad2 <= rad2){

    if(TestPoint(theDataPtr,rectRad,diagRad,columns)){
                                span        =
CenterThePoint(theDataPtr,columns);
                                thePoint.h  = i;
                                thePoint.v  = j;
                                if(!FoundPoint(thePoint,2 *
rectRad,span)){
                                    NewPoint(thePoint,span);
                                }
                            }
                        }
                    }
                    theDataPtr++;
                }
            }
    }
    DisposePtr((Ptr)theData);
}

void        DendriteCenter::DoSmartScan(Point thisPoint)
{
    short
    rows,columns,l1,l2,l3,l4,whiteScan,blackScan,theSelect;
    unsigned short *theData,*thePointPtr,*theDataPtr;
    RGBColor    theColor;
    GrafPtr         oldPort;
    Boolean         quit;
    DialogPtr       theDialog;

    theData     = GetDataFromPICT(thePicture,&rows,&columns);

    theColor.red    = 0;
    theColor.blue   = 65535;
    theColor.green  = 0;
    RGBForeColor(&theColor);
    MoveTo(thisPoint.h - 10,thisPoint.v);
    Line(20,0);
    MoveTo(thisPoint.h,thisPoint.v - 10);
    Line(0,20);
```

```
    theColor.red     = 0;
    theColor.blue    = 0;
    theColor.green   = 0;
    RGBForeColor(&theColor);

    thePointPtr = theData + (long)thisPoint.v * columns +
(long)thisPoint.h;

    l1 = l2 = l3 = l4 = -1;
    theDataPtr = thePointPtr;
    while(*theDataPtr <= WHITE_VALUE){
        theDataPtr--;
        l1++;
    }

    theDataPtr = thePointPtr;
    while(*theDataPtr <= WHITE_VALUE){
        theDataPtr++;
        l2++;
    }

    theDataPtr = thePointPtr;
    while(*theDataPtr <= WHITE_VALUE){
        theDataPtr -= columns;
        l3++;
    }

    theDataPtr = thePointPtr;
    while(*theDataPtr <= WHITE_VALUE){
        theDataPtr += columns;
        l4++;
    }

    whiteScan = l1;
    if(l2 < whiteScan){
        whiteScan = l2;
    }
    if(l3 < whiteScan){
        whiteScan = l3;
    }
    if(l4 < whiteScan){
        whiteScan = l4;
    }

    l1 = l2 = l3 = l4 = 0;
    theDataPtr = thePointPtr;
    while(*theDataPtr <= BLACK_VALUE){
        theDataPtr -= (columns + 1);
        l1++;
    }

    theDataPtr = thePointPtr;
    while(*theDataPtr <= BLACK_VALUE){
        theDataPtr += (columns + 1);
        l2++;
    }
```

```
    theDataPtr = thePointPtr;
    while(*theDataPtr <= BLACK_VALUE){
        theDataPtr -= (columns - 1);
        l3++;
    }

    theDataPtr = thePointPtr;
    while(*theDataPtr <= BLACK_VALUE){
        theDataPtr += (columns - 1);
        l4++;
    }
    blackScan = l1;
    if(l2 > blackScan){
        blackScan = l2;
    }
    if(l3 > blackScan){
        blackScan = l3;
    }
    if(l3 > blackScan){
        blackScan = l3;
    }

    DisposePtr((Ptr)theData);

    GetPort(&oldPort);
    theDialog = GetNewDialog(130,0L,(WindowPtr)-1L);
    SetPort(theDialog);
    SetShortItemText(theDialog,3,whiteScan,"%3d");
    SetShortItemText(theDialog,4,blackScan,"%3d");
    quit = false;
    while(!quit){
        ModalDialog((ModalFilterUPP)0L,&theSelect);
        switch(theSelect){
            case 1:
                quit            = true;
                break;
            case 2:
                quit            = true;
                dHorizAuto      = whiteScan;
                dDiagonalAuto   = blackScan;
                break;
            default:
                break;
        }
    }
    SetPort(oldPort);
    DisposDialog(theDialog);


    AutoSearch(whiteScan,blackScan);
}


Boolean DendriteCenter::FoundPoint(Point testPoint,short hDist,double
theDif)
{
    if(recordType == POINT){
```

```
        if(abs(testPoint.h - thePoint.h) <= hDist){
            if(abs(testPoint.v - thePoint.v) <= hDist){
                if(theDif < span){
                    thePoint = testPoint;
                    span     = theDif;
                }
                return true;
            }
        }
    }

    if(next == (DendriteCenter*)0L){
        return false;
    }

    return(next->FoundPoint(testPoint,hDist,theDif));
}

void        DendriteCenter::RemovePoints(void)
{
    DendriteCenter *oldNext;

    if(next != (DendriteCenter*)0L){
        next->RemovePoints();
        if(next->recordType == POINT){
            oldNext = next;
            next = next->next;
            delete(oldNext);
        }
    }
    return;
}

void        DendriteCenter::ConfigAuto(WindowPtr theWindow)
{
    DialogPtr       theDialog;
    short           theSelect,hVal,dVal;
    Rect            theRect;
    GrafPtr         oldPort;
    Boolean         quit,done;
    ControlHandle   theOKButton,whichCtl;
    EventRecord     theEvent;
    WindowPtr       whichWin;

    GetPort(&oldPort);
    theDialog = GetNewDialog(129,0L,(WindowPtr)-1L);
    SetPort(theDialog);
    SetShortItemText(theDialog,3,dHorizAuto,"%3d");
    SetShortItemText(theDialog,4,dDiagonalAuto,"%3d");
    SelIText(theDialog,3,0,32767);
    quit    = false;
    if(thePicture == (PicHandle)0L){
        DisableControl(theDialog,5);
    } else {
        EnableControl(theDialog,5);
    }
```

```
    while(!quit){
        ModalDialog((ModalFilterUPP)0L,&theSelect);
        switch(theSelect){
            case 1:
                dHorizAuto      = GetShortItem(theDialog,3);
                dDiagonalAuto   = GetShortItem(theDialog,4);
                quit            = true;
                break;
            case 2:
                quit            = true;
                break;
            case 5:
                while(StillDown())
                    ;
                hVal    = GetShortItem(theDialog,3);
                dVal    = GetShortItem(theDialog,4);
                SetPort(theWindow);
                SelectWindow(theWindow);
                InvalRect(&theWindow->portRect);
                RemovePoints();
                BeginUpdate(theWindow);
                theCenters->DrawElements();
                EndUpdate(theWindow);
                AutoSearch(hVal,dVal);
                BeginUpdate(theWindow);
                theCenters->DrawElements();
                EndUpdate(theWindow);
                theRect = theWindow->portRect;
                OffsetRect(&theRect,-10,-10);
                theRect.top  = theRect.bottom - 20;
                theRect.left = theRect.right - 70;
                theOKButton     =
NewControl(theWindow,&theRect,"\pOK",true,0,0,1,pushButProc,0L);
                done = false;

                while(!done){

    if(WaitNextEvent(mDownMask,&theEvent,10L,(RgnHandle)0L)){
        theSelect = FindWindow(theEvent.where,&whichWin);
        if(theSelect == inContent){
            GlobalToLocal(&theEvent.where);
            if(FindControl(theEvent.where,whichWin,&whichCtl) ==
inButton){
            if(TrackControl(whichCtl,theEvent.where,0L) == inButton) {
                                    done = true;
                                }
                            }
                        }
                    }
                }

                DisposeControl(theOKButton);
                InvalRect(&theRect);
                BeginUpdate(theWindow);
                theCenters->DrawElements();
                EndUpdate(theWindow);
                SelectWindow(theDialog);
```

```
                SetPort(theDialog);
                break;

            default:
                break;
        }
    }
    SetPort(oldPort);
    DisposDialog(theDialog);
}

void        DendriteCenter::EnterScale(void)
{
    DialogPtr       theDialog;
    short           theSelect;
    GrafPtr         oldPort;
    Boolean         quit;
    Point           testPoint1,testPoint2,lastPoint;
    double          x,y,scaleVal;

    theDialog = GetNewDialog(131,0L,(WindowPtr)-1L);
    GetPort(&oldPort);
    SetPort(theDialog);
    SetDoubleItemText(theDialog,4,distance,"%8.7f");
    SetDoubleItemText(theDialog,5,scale,"%8.7f");
    scaleVal = scale;
    quit        = false;

    while(!quit){
        ModalDialog((ModalFilterUPP)0L,&theSelect);
        switch(theSelect){
            case 1:
                scale   = GetDoubleItem(theDialog,5);
                quit    = true;
                scale   = scaleVal;
                break;
            case 2:
                quit    = true;
                break;
            case 3:
                SetCursor(*GetCursor(2));
                SelectWindow(oldPort);
                SetPort(oldPort);
                BeginUpdate(theWindow);
                DrawElements();
                EndUpdate(theWindow);


                while(Button())
                    ;
                while(!Button()){
                    GetMouse(&testPoint1);
                }
                while(Button())
                    ;
                MoveTo(testPoint1.h,testPoint1.v);
                PenMode(srcXor);
```

```
                    GetMouse(&testPoint2);
                    lastPoint = testPoint2;
                    LineTo(testPoint2.h,testPoint2.v);
                    while(!Button()){
                        GetMouse(&testPoint2);
                        if(!EqualPt(lastPoint,testPoint2)){
                            LineTo(testPoint1.h,testPoint1.v);
                            LineTo(testPoint2.h,testPoint2.v);
                            lastPoint = testPoint2;
                        }
                    }
                    LineTo(testPoint1.h,testPoint1.v);
                    PenNormal();
                    while(Button())
                        ;
                    scaleVal = GetDoubleItem(theDialog,4);
                    x           = testPoint1.h - testPoint2.h;
                    y           = testPoint1.v - testPoint2.v;
                    scaleVal /= sqrt(x * x + y * y);
                    SelectWindow(theDialog);
                    SetPort(theDialog);
                    SetDoubleItemText(theDialog,5,scaleVal,"%8.7f");
                    break;
                default:
                    break;
            }
        }

        SetPort(oldPort);
        DisposDialog(theDialog);
}


void        DendriteCenter::DisplayStatics(void)
{
    DialogPtr       theDialog;
    short           theSelect,number;
    GrafPtr         oldPort;
    Boolean         quit;
    double          sumOfSqrs,screenRad,pixelArea,pixelSpacing;

    GetPort(&oldPort);
    theDialog = GetNewDialog(132,0L,(WindowPtr)-1L);
    SetPort(theDialog);

    screenRad       = (double)(circleRect.right - circleRect.left) *
.5;
    pixelArea       = 3.141592654 * screenRad * screenRad;
    pointCount      = (double)CountPoints();
    pixelSpacing = sqrt(pixelArea / pointCount);
    spacing         = pixelSpacing * scale;
    area            = pixelArea * scale * scale;

    CalcStandardD(this,(Rect*)0L,pixelSpacing,&sumOfSqrs,&number);
    standardD       = sqrt(sumOfSqrs / ((double)number - 1)) * scale;

    SetDoubleItemText(theDialog,2,area,"%8.7f");
```

```
    SetDoubleItemText(theDialog,3,pointCount,"%8.7f");
    SetDoubleItemText(theDialog,4,spacing,"%8.7f");
    SetDoubleItemText(theDialog,5,standardD,"%8.7f");
    quit = false;

    while(!quit){
        ModalDialog((ModalFilterUPP)0L,&theSelect);
        switch(theSelect){
            case 1:
                quit        = true;
                infoFlag= true;
                break;
            default:
                break;
        }
    }

    SetPort(oldPort);
    DisposDialog(theDialog);
}
```

```
DendriteCenter*     DendriteCenter::DoPointRemove(void)
{
    DendriteCenter* retval;

    if(next != (DendriteCenter*)0L){
        next = next->DoPointRemove();
    }
    if(recordType == POINT){
        retval = next;
        delete(this);
        return retval;
    } else {
        return((DendriteCenter*)this);
    }
}

void        DendriteCenter::DeletePoint(Point testPoint)
{
    Rect    redrawRect;
    DendriteCenter *oldNext;
    if(next == (DendriteCenter*)0L){
        return;
    }

    if(next->recordType == POINT){
        if(abs(next->thePoint.h - testPoint.h) < 3 && abs(next-
>thePoint.v - testPoint.v) < 3){
            SetRect(&redrawRect,-5,-5,5,5);
            OffsetRect(&redrawRect,next->thePoint.h,next->thePoint.v);
            InvalRect(&redrawRect);
```

```
            oldNext = next;
            next = next->next;
            delete(oldNext);
            return;
        }
    }
    next->DeletePoint(testPoint);
}

void        DendriteCenter::Find4Nearest(PointtestLoc,double
    *distArray)
{
    short   i;
    double  x,y,dist,*dataPtr;

    if(recordType == POINT && !EqualPt(testLoc,thePoint)){
        x       = testLoc.h - thePoint.h;
        y       = testLoc.v - thePoint.v;
        dist    = x * x + y * y;
        dataPtr = distArray;
        for(i = 0 ; i < 4 ; i++){
            if(dist < *dataPtr){
                x           = *dataPtr;
                *dataPtr= dist;
                dist        = x;
            }
            dataPtr++;
        }
    }
    if(next != (DendriteCenter*)0L){
        next->Find4Nearest(testLoc,distArray);
    }
}


//  static FSSpec   theFileInfo;
//  static short refNum;
//  long            length;

void        DendriteCenter::CalcStandardD(DendriteCenter *top,Rect*
    theRect,double theMean,double *sum,short *number)
{
    Rect        theBounds;
    short       amount,i;
    double      distArray[4],value;
//  short       iErr;

    if(recordType == CIRCLE){
        theBounds       = circleRect;
        amount          = (circleRect.right - circleRect.left) >> 3;
        *sum            = 0.0;
        *number         = 0.0;
        InsetRect(&theBounds,amount,amount);
//  iErr = FSMakeFSSpec(0,0,"\pSpacings.txt",&theFileInfo);
//  iErr = FSpDelete(&theFileInfo);
//  iErr = FSpCreate(&theFileInfo,'ERIC','TEXT',0);
//  iErr = FSpOpenDF(&theFileInfo,fsRdWrPerm,&refNum);
```

```
        if(next != (DendriteCenter*)0L){
            next->CalcStandardD(this,&theBounds,theMean,sum,number);
        }
//  iErr = FSClose(refNum);
//  iErr = FlushVol(0L,theFileInfo.vRefNum);
        return;
    } else if(recordType == POINT){
        if(PtInRect(thePoint,theRect)){
            for(i = 0 ; i < 4 ; i++){
                distArray[i] = 40000.0;
            }
            top->Find4Nearest(thePoint,distArray);
            for(i = 0 ; i < 4 ; i++){
                value    = sqrt(distArray[i]);
//  length   = sprintf(theText,"%7.6f\r",value);
//  iErr     = FSWrite(refNum,&length,(Ptr)theText);
                value    -= theMean;
                value    *= value;
                *sum     += value;
            }
            *number += 4;
        }
    }
    if(next != (DendriteCenter*)0L){
        next->CalcStandardD(top,theRect,theMean,sum,number);
    }
}

void        DendriteCenter::AddInfo(void)
{

    char    theText[256];
    Rect    theRect;
    short   num,left;

    if(infoFlag){
        SetRect(&theRect,10,10,110,85);
        EraseRect(&theRect);
        PenSize(2,2);
        FrameRect(&theRect);
        PenSize(1,1);
        TextFont(symbol);
        TextSize(14);
        num = pointCount;
        sprintf(theText,"N = %3d",num);
        c2pstr(theText);
        MoveTo(16,26);
        DrawString((unsigned char*)theText);
        sprintf(theText,"m = %7.6f",spacing);
        c2pstr(theText);
        MoveTo(16,42);
        DrawString((unsigned char*)theText);
        sprintf(theText,"s = %7.6f",standardD);
        c2pstr(theText);
        MoveTo(16,58);
        DrawString((unsigned char*)theText);
```

```
        num = (short)(.5 + distance / scale);
        left = (theRect.right + theRect.left - num) >> 1;
        MoveTo(left,62);
        Line(0,4);
        Move(0,-2);
        Line(num,0);
        Move(0,-2);
        Line(0,4);
        sprintf(theText,"%5.4f m",distance);
        c2pstr(theText);
        left = (theRect.right + theRect.left - StringWidth((unsigned
char*)theText)) >> 1;
        MoveTo(left,80);
        DrawString((unsigned char*)theText);


        SetRect(&theRect,580,10,630,30);
        EraseRect(&theRect);
        PenSize(2,2);
        FrameRect(&theRect);
        PenSize(1,1);
        TextFont(helvetica);
        TextSize(14);
        left = (theRect.right + theRect.left - StringWidth((unsigned
char*)theFileName)) / 2;
        MoveTo(left,theRect.bottom - 5);
        DrawString((unsigned char*)theFileName);

        TextFont(systemFont);
        TextSize(12);

    }
}
```

```
Boolean TestPoint(unsigned short *theDataPtr,short rectRad,short
diagDist,short rowLength)
{
    unsigned short *right,*left,*up,*down;
    short           columnOffset;

    left    = theDataPtr - rectRad;
    if(*left > WHITE_VALUE){
        return false;
    }

    right   = theDataPtr + rectRad;
    if(*right > WHITE_VALUE){
        return false;
    }

    columnOffset = rectRad * rowLength;
```

```
    up      = theDataPtr - columnOffset;
    if(*up > WHITE_VALUE){
        return false;
    }

    down    = theDataPtr + columnOffset;
    if(*down > WHITE_VALUE){
        return false;
    }
//
    while(left <= right){
        if(*left > WHITE_VALUE){
            return false;
        }
        left++;
    }

    left = up;
    while(left <= down){
        if(*left > WHITE_VALUE){
            return false;
        }
        left += rowLength;
    }
//

    up = theDataPtr - diagDist * (rowLength + 1);

    if(*up < BLACK_VALUE){
        return false;
    }

    up += (diagDist + diagDist);
    if(*up < BLACK_VALUE){
        return false;
    }

    down = theDataPtr + diagDist * (rowLength - 1);
    if(*down < BLACK_VALUE){
        return false;
    }

    down += (diagDist + diagDist);
    if(*down < BLACK_VALUE){
        return false;
    }

    return true;
}

void    ExpandScale(unsigned short *theData,short rows,short columns)
{
    long            arrayLength;
    unsigned short *theDataPtr,*endPtr;
    short           minValue,maxValue;
    double          scale,value;
```

```
    arrayLength = (long)rows * (long)columns;
    maxValue= 0;
    minValue     = 255;
    theDataPtr   = theData;
    endPtr       = theData + arrayLength;

    while(theDataPtr < endPtr){
        if(*theDataPtr < minValue){
            minValue = *theDataPtr;
        }
        theDataPtr++;
    }
    theDataPtr   = theData;
    while(theDataPtr < endPtr){
        *theDataPtr -= minValue;
        if(*theDataPtr > maxValue){
            maxValue = *theDataPtr;
        }
        theDataPtr++;
    }
    scale = 255.0 / (double)maxValue;

    theDataPtr   = theData;
    while(theDataPtr < endPtr){
        value        = .5 + (double)*theDataPtr * scale;
        *theDataPtr = (unsigned short)value;
        theDataPtr++;
    }
}

double CenterThePoint(unsigned short *theDataPtr,short columns)
{
    short            d1,d2,d3,d4;
    unsigned short   *theDataLoc,*startPtr;
    double           rmsValue,aveValue;

    startPtr= theDataPtr;

    d1           = 0;
    theDataLoc   = startPtr;
    while(*theDataLoc < BLACK_VALUE){
        d1++;
        theDataLoc -= (columns + 1);
    }


    d2           = 0;
    theDataLoc   = startPtr;
    while(*theDataLoc < BLACK_VALUE){
        d2++;
        theDataLoc -= (columns - 1);
    }


    d3           = 0;
    theDataLoc   = startPtr;
```

```
    while(*theDataLoc < BLACK_VALUE){
        d3++;
        theDataLoc += (columns + 1);
    }

    d4          = 0;
    theDataLoc  = startPtr;
    while(*theDataLoc < BLACK_VALUE){
        d4++;
        theDataLoc += (columns - 1);
    }

    aveValue    = (double)(d1 + d2 + d3 + d4) * .25;
    rmsValue =   (d1 - aveValue) * (d1 - aveValue);
    rmsValue +=  ((d2 - aveValue) * (d2 - aveValue));
    rmsValue +=  ((d3 - aveValue) * (d3 - aveValue));
    rmsValue +=  ((d4 - aveValue) * (d4 - aveValue));
    return(rmsValue);
}
```

D.1.3 DoEvents.c

```
#include "Dendrites.h"

void     DoEvent(EventRecord* theEvent)
{
     short              theWindowCode;
     WindowPtr          thisWindow;
     long               menuInfo;
     GrafPtr            thePort;
     char               theKey,theText[128];
     Rect               theRect;
     GrafPtr            theCurrentPort;
     RGBColor     theColor;

     theWindowCode = FindWindow(theEvent->where,&thisWindow);

     switch(theEvent->what){
          case osEvt:
               if((theEvent->message & 0xFF000000) == 0xFA000000){  //
not mouse moved
                    SetRectRgn(mouseRgn,theEvent->where.h - 1,theEvent-
>where.v - 1,theEvent->where.h + 1,theEvent->where.v + 1);
                    GlobalToLocal(&theEvent->where);
                    if(thisWindow == theWindow && theWindow !=
(WindowPtr)0L){
                         if(PtInRect(theEvent->where,&thisWindow-
>portRect)){
                              GetCPixel(theEvent->where.h,theEvent-
>where.v,&theColor);
                              theColor.red /= 257;
                              theColor.red = 255 - theColor.red;
                              TextFont(monaco);
                              TextSize(9);
                              SetRect(&theRect,2,2,52,14);
                              sprintf(theText,"%3d %3d",theEvent-
>where.h,theEvent->where.v);
                              sprintf(theText,"%3d ",theColor.red);
                              c2pstr(theText);
                              EraseRect(&theRect);
                              MoveTo(4,12);
                              DrawString((unsigned char*)theText);
                              if(cursorID != 2){
                                   SetCursor(*GetCursor(2));
                                   cursorID = 2;
                              }
                         } else {
                              if(cursorID != 0){
                                   InitCursor();
                                   cursorID = 0;
                              }
                         }
                    }
               }
               if(thisWindow != (WindowPtr)0L){
```

```
                if((theEvent->message & 0x01000000) == 0x01000000){
                    if((theEvent->message & 0x00000001) != 0){
                        SetPort(thisWindow);
                        updateRate   = 3L;
                        SetRect(&theRect,2,2,4,4);
                        InvalRect(&theRect);
                    } else {
                        updateRate   = 30L;
                    }
                }
            }
            break;

        case updateEvt:
            SetPort(theWindow);
            BeginUpdate(theWindow);
            theCenters->DrawElements();
            theCenters->AddInfo();
            EndUpdate(theWindow);
            break;
        case keyDown:
            theKey = theEvent->message & charCodeMask;
            if((theEvent->modifiers & cmdKey) != 0){
                menuInfo = MenuKey(theKey);
                DoMenu(menuInfo);
            }
            break;

        case mouseDown:
            switch(theWindowCode){
                case inMenuBar:
                    menuInfo = MenuSelect(theEvent->where);
                    DoMenu(menuInfo);
                    break;
                case inGoAway:
                    if(TrackGoAway(thisWindow,theEvent->where)){
                        DoMenu(((long)FILE_MENU << 16) | CLOSE_ITEM);
                    }
                    break;
                case inDrag:
                    GetWMgrPort(&thePort);
                    DragWindow(thisWindow,theEvent->where,&thePort-
>portRect);
                    break;
                case inContent:
                    if(pointsFlag){
                        GlobalToLocal(&theEvent->where);
                        theCenters->NewPoint(theEvent->where,0);
                        return;
                    }
                    if(delPointsFlag){
                        GlobalToLocal(&theEvent->where);
                        theCenters->DeletePoint(theEvent->where);
                        return;
                    }
                    if(learnFlag){
                        GlobalToLocal(&theEvent->where);
```

```
                        theCenters->DoSmartScan(theEvent->where);
                        return;
                    }
                    break;
                default:
                    break;
            }
            break;

        default:
            break;
    }
}
```

D.1.4 DoMenu.c

```
#include "Dendrites.h"
#include "Eric'sLib.h"
#include "string.h"

void    DoInfoSave(char* fileName);
void    RecordData(StandardFileReply reply);
void    PostCommand(char theKey);
void    ScreenUpdate(void);
void    SavePict(StandardFileReply reply,PicHandle thePicture);

void    DoMenu(long menuData)
{
    short                           iErr,fileRefNum,wdRefNum;
    long                            size;
    SFTypeList                      theTypes;
    static StandardFileReply theReply;
    Handle                          thePicture;
    Rect                            theRect;
    FInfo                           fndrInfo;
    PicHandle                       dataPict;

    switch(HiWord(menuData)){
        case FILE_MENU:
            switch(LoWord(menuData)){
                case IMPORT_ITEM:
                    theTypes[0] = 'PICT';
                    StandardGetFile(0L,1,theTypes,&theReply);
                    if(!theReply.sfGood)
                        break;
                    iErr =
FSpOpenDF(&(theReply.sfFile),fsRdWrPerm,&fileRefNum);
                    if(iErr != 0){
                        sprintf(theText,"Problem opening file. File
Error %d",iErr);
                        c2pstr(theText);
                        ParamText((unsigned
char*)theText,"\p","\p","\p");
                        StopAlert(GENERIC_ALERT,0L);
                        break;
                    }
                    iErr = GetEOF(fileRefNum,&size);
                    if(iErr != 0){
                        sprintf(theText,"Problem reading EOF. File
Error %d",iErr);
                        c2pstr(theText);
                        ParamText((unsigned
char*)theText,"\p","\p","\p");
                        StopAlert(GENERIC_ALERT,0L);
                        iErr = FSClose(fileRefNum);
                        break;
                    }
                    size -= 512;
                    iErr = SetFPos(fileRefNum,fsFromStart,512);
```

```
                    if(iErr != 0){
                        sprintf(theText,"Problem positioning file.
File Error %d",iErr);
                        c2pstr(theText);
                        ParamText((unsigned
char*)theText,"\p","\p","\p");
                        StopAlert(GENERIC_ALERT,0L);
                        iErr = FSClose(fileRefNum);
                        break;
                    }
                    thePicture = NewHandle(size);
                    HLock(thePicture);
                    iErr =
FSRead(fileRefNum,&size,(Ptr)(*thePicture));
                    HUnlock(thePicture);
                    if(iErr != 0){
                        sprintf(theText,"Problem reading file. File
Error %d",iErr);
                        c2pstr(theText);
                        ParamText((unsigned
char*)theText,"\p","\p","\p");
                        StopAlert(GENERIC_ALERT,0L);
                        iErr = FSClose(fileRefNum);
                        break;
                    }
                    iErr = FSClose(fileRefNum);
                    iErr =
OpenWD(theReply.sfFile.vRefNum,theReply.sfFile.parID,0L,&wdRefNum);

                    p2cstr(theReply.sfFile.name);
                    strcpy(theFileName,(char*)theReply.sfFile.name);
                    c2pstr((char*)theReply.sfFile.name);
                    c2pstr(theFileName);

                    iErr = GetFInfo
(theReply.sfFile.name,wdRefNum,&fndrInfo);
                    fndrInfo.fdType = 'P$$T';
                    iErr = SetFInfo
(theReply.sfFile.name,wdRefNum,&fndrInfo);
                    iErr = CloseWD(wdRefNum);
                    theRect      = (*((PicHandle)(thePicture)))-
>picFrame;
                    OffsetRect(&theRect,0,40);
                    theWindow    = NewCWindow(0L,&theRect,"\pAbel
Inversion",true,4,(WindowPtr)-1L,true,0L);
                    SetPort(theWindow);
                    theCenters->AddCircle(theWindow-
>portRect,(PicHandle)thePicture);

        //          theData =
GetDataFromPICT((PicHandle)thePicture,&rows,&columns);
        //          if(theData != (unsigned short*)0L){
        //              DrawPixels(theData,rows,columns);
        //              while(!Button())
        //                  ;
        //              DisposePtr((Ptr)theData);
        //          }
```

```
                    EnableItem(GetMHandle(FILE_MENU),CLOSE_ITEM);
                    EnableItem(GetMHandle(FILE_MENU),SAVE_AS);
                    DisableItem(GetMHandle(FILE_MENU),OPEN_ITEM);
                    DisableItem(GetMHandle(FILE_MENU),IMPORT_ITEM);
                    EnableItem(GetMHandle(TOOL_MENU),0);

    EnableItem(GetMHandle(TOOL_MENU),ENTER_DENDRITES_ITEM);

    EnableItem(GetMHandle(TOOL_MENU),DELETE_DENDRITES_ITEM);
                    EnableItem(GetMHandle(TOOL_MENU),SMART_SCAN);

    EnableItem(GetMHandle(TOOL_MENU),REMOVE_ALL_DENDRITES);

    EnableItem(GetMHandle(TOOL_MENU),ENTER_SCALE_ITEM);

    DisableItem(GetMHandle(TOOL_MENU),ADD_STATS_ITEM);

                    ScreenUpdate();

                    if(autoFlag){
                        PostCommand('a');
                    }
                    break;
                case SAVE_AS:
                    dataPict = OpenPicture(&(*theCenters-
>thePicture)->picFrame);
                    theCenters->DrawElements();
                    theCenters->AddInfo();
                    ClosePicture();
                    SavePict(theReply,dataPict);
                    KillPicture(dataPict);
                    break;
                case CLOSE_ITEM:
                    theCenters->RemovePoints();
                    DisposHandle(thePicture);
                    theCenters->ReInit();
                    DisposeWindow(theWindow);
                    DoMenu(TOOL_MENU << 16 + REMOVE_ALL_DENDRITES);
                    DisableItem(GetMHandle(FILE_MENU),CLOSE_ITEM);
                    DisableItem(GetMHandle(FILE_MENU),SAVE);
                    DisableItem(GetMHandle(FILE_MENU),SAVE_AS);
                    DisableItem(GetMHandle(TOOL_MENU),0);
                    EnableItem(GetMHandle(FILE_MENU),OPEN_ITEM);
                    EnableItem(GetMHandle(FILE_MENU),IMPORT_ITEM);
                    delPointsFlag           = false;
                    pointsFlag              = false;
                    learnFlag               = false;
                    theCenters->infoFlag = false;

    CheckItem(GetMHandle(TOOL_MENU),ENTER_DENDRITES_ITEM,pointsFlag);

    CheckItem(GetMHandle(TOOL_MENU),DELETE_DENDRITES_ITEM,delPointsFlag
);

    CheckItem(GetMHandle(TOOL_MENU),SMART_SCAN,learnFlag);
                    if(autoFlag){
                        PostCommand('n');
```

```
                    }
                    break;
                case RESTORE_PICTS_ITEM:
                    theTypes[0] = 'P$$T';
                    StandardGetFile(0L,1,theTypes,&theReply);
                    if(!theReply.sfGood)
                        break;
                    iErr =
OpenWD(theReply.sfFile.vRefNum,theReply.sfFile.parID,0L,&wdRefNum);
                    iErr = GetFInfo
(theReply.sfFile.name,wdRefNum,&fndrInfo);
                    fndrInfo.fdType = 'PICT';
                    iErr = SetFInfo
(theReply.sfFile.name,wdRefNum,&fndrInfo);
                    iErr = CloseWD(wdRefNum);
                    PostCommand('f');
                    break;

                case QUIT_ITEM:
                    theCenters->DoClose();
                    quitFlag = true;
                    break;
                default:
                    break;
            }
            break;
        case EDIT_MENU:
            switch(LoWord(menuData)){
                case REFRESH_ITEM:
                    InvalRect(&theWindow->portRect);
                    break;
                case AUTO_CYCLE_ITEM:
                    autoFlag = !autoFlag;

    CheckItem(GetMHandle(EDIT_MENU),AUTO_CYCLE_ITEM,autoFlag);
                    break;
                default:
                    break;
            }
            break;

        case TOOL_MENU:
            switch(LoWord(menuData)){
                case ENTER_DENDRITES_ITEM:
                    delPointsFlag    = false;
                    learnFlag        = false;
                    pointsFlag       = !pointsFlag;

    CheckItem(GetMHandle(TOOL_MENU),ENTER_DENDRITES_ITEM,pointsFlag);

    CheckItem(GetMHandle(TOOL_MENU),DELETE_DENDRITES_ITEM,delPointsFlag
);

    CheckItem(GetMHandle(TOOL_MENU),SMART_SCAN,learnFlag);
                    break;
                case DELETE_DENDRITES_ITEM:
                    delPointsFlag    = !delPointsFlag;
```

```
                    pointsFlag      = false;
                    learnFlag       = false;

    CheckItem(GetMHandle(TOOL_MENU),ENTER_DENDRITES_ITEM,pointsFlag);

    CheckItem(GetMHandle(TOOL_MENU),DELETE_DENDRITES_ITEM,delPointsFlag
);

    CheckItem(GetMHandle(TOOL_MENU),SMART_SCAN,learnFlag);
                    break;
                case SMART_SCAN:
                    delPointsFlag   = false;
                    pointsFlag      = false;
                    learnFlag       = !learnFlag;

    CheckItem(GetMHandle(TOOL_MENU),ENTER_DENDRITES_ITEM,pointsFlag);

    CheckItem(GetMHandle(TOOL_MENU),DELETE_DENDRITES_ITEM,delPointsFlag
);

    CheckItem(GetMHandle(TOOL_MENU),SMART_SCAN,learnFlag);
                    break;
                case REMOVE_ALL_DENDRITES:
                    delPointsFlag   = false;
                    pointsFlag      = false;
                    learnFlag       = false;

    CheckItem(GetMHandle(TOOL_MENU),ENTER_DENDRITES_ITEM,pointsFlag);

    CheckItem(GetMHandle(TOOL_MENU),DELETE_DENDRITES_ITEM,delPointsFlag
);

    CheckItem(GetMHandle(TOOL_MENU),SMART_SCAN,learnFlag);
                    theCenters->RemovePoints();
                    InvalRect(&theWindow->portRect);
                    break;
                case CONFIG_AUTO_SCAN:
                    theCenters->ConfigAuto(theWindow);
                    InvalRect(&theWindow->portRect);
                    EnableItem(GetMHandle(TOOL_MENU),AUTO_SCAN);
                    delPointsFlag   = false;
                    pointsFlag      = false;
                    learnFlag       = false;

    CheckItem(GetMHandle(TOOL_MENU),ENTER_DENDRITES_ITEM,pointsFlag);

    CheckItem(GetMHandle(TOOL_MENU),DELETE_DENDRITES_ITEM,delPointsFlag
);

    CheckItem(GetMHandle(TOOL_MENU),SMART_SCAN,learnFlag);
                    break;
                case AUTO_SCAN:
                    theCenters->AutoSearch(theCenters-
>dHorizAuto,theCenters->dDiagonalAuto);
                    InvalRect(&theWindow->portRect);
                    delPointsFlag   = false;
                    pointsFlag      = false;
```

```
                    learnFlag        = false;

    CheckItem(GetMHandle(TOOL_MENU),ENTER_DENDRITES_ITEM,pointsFlag);

    CheckItem(GetMHandle(TOOL_MENU),DELETE_DENDRITES_ITEM,delPointsFlag
);

    CheckItem(GetMHandle(TOOL_MENU),SMART_SCAN,learnFlag);

                    break;
                case ENTER_SCALE_ITEM:
                    theCenters->EnterScale();

    EnableItem(GetMHandle(TOOL_MENU),VIEW_STATISTICS_ITEM);
                    delPointsFlag    = false;
                    pointsFlag       = false;
                    learnFlag        = false;

    CheckItem(GetMHandle(TOOL_MENU),ENTER_DENDRITES_ITEM,pointsFlag);

    CheckItem(GetMHandle(TOOL_MENU),DELETE_DENDRITES_ITEM,delPointsFlag
);

    CheckItem(GetMHandle(TOOL_MENU),SMART_SCAN,learnFlag);
                    break;
                case VIEW_STATISTICS_ITEM:
                    theCenters->DisplayStatics();
                    delPointsFlag    = false;
                    pointsFlag       = false;
                    learnFlag        = false;

    CheckItem(GetMHandle(TOOL_MENU),ENTER_DENDRITES_ITEM,pointsFlag);

    CheckItem(GetMHandle(TOOL_MENU),DELETE_DENDRITES_ITEM,delPointsFlag
);

    CheckItem(GetMHandle(TOOL_MENU),SMART_SCAN,learnFlag);
                    EnableItem(GetMHandle(TOOL_MENU),ADD_STATS_ITEM);

    EnableItem(GetMHandle(EDIT_MENU),AUTO_CYCLE_ITEM);
                    PostCommand('r');  // Screen Refresh
                    if(autoFlag){
                        PostCommand('d');
                    }
                    break;
                case ADD_STATS_ITEM:
                    delPointsFlag    = false;
                    pointsFlag       = false;
                    learnFlag        = false;

    CheckItem(GetMHandle(TOOL_MENU),ENTER_DENDRITES_ITEM,pointsFlag);

    CheckItem(GetMHandle(TOOL_MENU),DELETE_DENDRITES_ITEM,delPointsFlag
);

    CheckItem(GetMHandle(TOOL_MENU),SMART_SCAN,learnFlag);
```

```
    DisableItem(GetMHandle(TOOL_MENU),ADD_STATS_ITEM);
                    RecordData(theReply);

                    if(autoFlag){
                        PostCommand('w');// Close Window
                    }
                    break;
                default:
                    break;
            }
            break;

        default:
            break;
    }
    HiliteMenu(0);
}

void    RecordData(StandardFileReply reply)
{
    DialogPtr   theDialog;
    short       type,theSelect,iErr;
    Handle      theHandle;
    Rect        theRect;
    GrafPtr     oldPort;
    Boolean     quit;
    FSSpec      theFileInfo;
    short       refNum;
    long        length;
    char        text2[256],text3[256];

    GetPort(&oldPort);
    theDialog = GetNewDialog(133,0L,(WindowPtr)-1L);
    SetPort(theDialog);

    SetDoubleItemText(theDialog,3,theCenters->area,"%8.7f");
    SetDoubleItemText(theDialog,4,theCenters->pointCount,"%8.7f");
    SetDoubleItemText(theDialog,5,theCenters->spacing,"%8.7f");
    SetDoubleItemText(theDialog,6,theCenters->standardD,"%8.7f");
    SelIText(theDialog,7,0,32767);
    quit = false;

    while(!quit){
        ModalDialog((ModalFilterUPP)0L,&theSelect);
        switch(theSelect){
            case 1:
                GetDItem(theDialog,7,&type,&theHandle,&theRect);
                GetIText(theHandle,(unsigned char*)text2);
                p2cstr((unsigned char*)text2);

                iErr =
FSMakeFSSpec(0,0L,"\pSampleStats",&theFileInfo);
                iErr = FSpOpenDF(&theFileInfo,fsRdWrPerm,&refNum);
                if(iErr == fnfErr){
                    iErr = FSpCreate(&theFileInfo,'ERIC','TEXT',0);
```

```
                    iErr =
FSpOpenDF(&theFileInfo,fsRdWrPerm,&refNum);
                }
                iErr     = SetFPos(refNum,fsFromLEOF,0L);
                if(iErr != 0){
                    SysBeep(30);
                    SysBeep(30);
                    SysBeep(30);
                    SysBeep(30);
                    SysBeep(30);
                }
                p2cstr(reply.sfFile.name);
                strcpy(text3,(char*)reply.sfFile.name);
                length   =
sprintf(theText,"%8.6f\t%8.6f\t%8.6f\t%8.6f\t"theCenters->area,

                theCenters->pointCount,

                theCenters->spacing,

                theCenters->standardD);
                strcat(text3,"\t");
                strcat(text3,theText);
                strcpy(theText,text3);
                strcat(theText,text2);
                strcat(theText,"\r");
                length   = strlen(theText);
                iErr     = FSWrite(refNum,&length,(Ptr)theText);
                if(iErr != 0){
                    SysBeep(30);
                    SysBeep(30);
                    SysBeep(30);
                    SysBeep(30);
                    SysBeep(30);
                }
                iErr     = FSClose(refNum);
                iErr     = FlushVol(0L,theFileInfo.vRefNum);

                DoInfoSave(text2);
                quit         = true;
                break;

            case 2:
                quit = true;
                break;

            default:
                break;
        }
    }
    DisposDialog(theDialog);
    SetPort(oldPort);
}

void    PostCommand(char theKey)
{
    EvQElPtr qElPtr;
```

```
    long        eventMsg;
    short       iErr;

    eventMsg    = 0x0000FF00 + theKey;
    iErr        = PostEvent(keyDown,eventMsg);
    iErr        = PPostEvent(keyDown,eventMsg,&qElPtr);
    qElPtr->evtQModifiers = cmdKey;
}


void    DoInfoSave(char* fileName)
{
    ;
}


void    ScreenUpdate(void)
{
    long        time;
    EventRecord theEvent;

    time = TickCount() + 30;

    while(time > TickCount()){
        if(WaitNextEvent(everyEvent,&theEvent,15L,0L)){
            DoEvent(&theEvent);
        }
    }
}

void    SavePict(StandardFileReply reply,PicHandle thePicture)
{
    char    theName[256];
    short   fRefNum,iErr,i,fileHeader[256];
    long    lByteCnt;
    Ptr     thePictData;

    p2cstr(reply.sfFile.name);
    strcpy(theName,"zz_");
    strcat(theName,(char*)reply.sfFile.name);
    strcat(theName,".dnt");
    c2pstr(theName);

    StandardPutFile("\pFileName:",(unsigned char*)theName,&reply);
    if(!reply.sfGood)
        return;
    if(reply.sfReplacing){
        iErr = FSpDelete(&reply.sfFile);
    }
    for(i = 0 ; i < 256 ; i++){
        fileHeader[i] = 0;
    }
    iErr        =
FSpCreate(&reply.sfFile,'DNDR','P$$T',reply.sfScript);
    iErr        = FSpOpenDF(&reply.sfFile,fsWrPerm,&fRefNum);
    lByteCnt = 512;
```

```
    iErr          = FSWrite(fRefNum,&lByteCnt,(Ptr)fileHeader);
    lByteCnt      = GetHandleSize((Handle)thePicture);
    HLock((Handle)thePicture);
    thePictData   = *(Handle)thePicture;
    iErr          = FSWrite(fRefNum,&lByteCnt,thePictData);
    iErr          = FSClose(fRefNum);
    iErr          = FlushVol("\p",reply.sfFile.vRefNum);
    HUnlock((Handle)thePicture);
}
```

D.1.5 Eric'sLib.c

```
#include "Eric'sLib.h"


void DoInits()
{
    InitGraf(&qd.thePort);
    InitFonts();
    FlushEvents(everyEvent, 0);
    InitWindows();
    InitMenus();
    TEInit();
    InitDialogs(0L);
    InitCursor();
}

void    SetShortItemText(DialogPtrtheDialog,short theItem,short
theValue,char *theFmt)
{
    Handle  theHandle;
    char    theText[256];
    short   type;
    Rect    theRect;

    GetDItem(theDialog,theItem,&type,&theHandle,&theRect);
    type &= 0x007F;
    if(type == 8 || type == 16){
        sprintf(theText,theFmt,theValue);
        c2pstr(theText);
        SetIText(theHandle,(unsigned char*)theText);
    }
}

short   GetShortItem(DialogPtr   theDialog,short theItem)
{
    Handle  theHandle;
    char    theText[256];
    short   type,value;
    Rect    theRect;

    GetDItem(theDialog,theItem,&type,&theHandle,&theRect);
    if(type == 8 || type == 16){
        GetIText(theHandle,(unsigned char*)theText);
        p2cstr((unsigned char*)theText);
        value = atoi(theText);
        return(value);
    }
    return(-1);
}

void    SetDoubleItemText(DialogPtr  theDialog,short theItem,double
theValue,char *theFmt)
{
```

```
    Handle   theHandle;
    char     theText[256];
    short    type;
    Rect     theRect;

    GetDItem(theDialog,theItem,&type,&theHandle,&theRect);
    type &= 0x007F;
    if(type == 8 || type == 16){
        sprintf(theText,theFmt,theValue);
        c2pstr(theText);
        SetIText(theHandle,(unsigned char*)theText);
    }
}

double   GetDoubleItem(DialogPtr  theDialog,short theItem)
{
    Handle   theHandle;
    char     theText[256];
    short    type,value;
    Rect     theRect;

    GetDItem(theDialog,theItem,&type,&theHandle,&theRect);
    if(type == 8 || type == 16){
        GetIText(theHandle,(unsigned char*)theText);
        p2cstr((unsigned char*)theText);
        value = atof(theText);
        return(value);
    }
    return(-1);
}

void     EnableControl(DialogPtr  theDialog,short theItem)
{
    Handle   theHandle;
    short    type;
    Rect     theRect;

    GetDItem(theDialog,theItem,&type,&theHandle,&theRect);
    if(type >= 4 && type <= 6){
        HiliteControl((ControlHandle)theHandle,0);
    }
}

void     DisableControl(DialogPtr theDialog,short theItem)
{
    Handle   theHandle;
    short    type;
    Rect     theRect;

    GetDItem(theDialog,theItem,&type,&theHandle,&theRect);
    if(type >= 4 && type <= 6){
        HiliteControl((ControlHandle)theHandle,255);
    }
}
```

D.1.6 GrabBitData.c

```
#include "GrabBitData.h"

unsigned short* GetDataFromPICT(PicHandle thePicture,short
*rows,short *columns)
{
    unsigned short      *theData,*theDataPtr;
    Handle              imageData;
    short               *opcodeInfo;
    Size                numPixels,lBytesFree,bytesNeeded;
    long                i;
    Ptr                 theCharData;

    HLock((Handle)thePicture);    /* Lock down the picture so it
doesn't move */
    opcodeInfo   = (short*)&(*thePicture)->picFrame;
    opcodeInfo   += (sizeof(Rect) >> 1);

    while(*opcodeInfo != 0x00FF){
        switch(*opcodeInfo){
            case 0x0011:          /* Version Number */
                opcodeInfo += 2;
                break;

            case 0x0C00:          /* Header Info */
                opcodeInfo += 13;
                break;

            case 0x0001:          /* Clip Region */
                opcodeInfo += (*(++opcodeInfo) >> 1); /* offset by
region size + opcode */
                break;

            /*  NOTE: The PackedBitsRect opcode is documented as
having a data structure as
                defined above in the PackedBitsInfo structure.
However, the data does not
                align unless opcodeInfo is decremented. In other words
there is an undocumented
                four byte shift in the data. */

            case 0x0098:          /* PackedBitsRect*/
                lBytesFree   = CompactMem(1000000L);
                opcodeInfo--;                          /* Note the
decrement */
                imageData    =
GetTheData((PackedBitsInfoPtr)opcodeInfo,&numPixels,rows,columns);
                HUnlock((Handle)thePicture);      /* Unlock to help
pack mem */

                if(imageData == (Handle)0L){
                    return((unsigned short*)0L);
                }
```

```
                bytesNeeded = numPixels * sizeof(short);  /* Pack
the memory */
                lBytesFree   = CompactMem(bytesNeeded);
                theData = (unsigned short*)NewPtr(bytesNeeded);  /*
Get the mem for array of shorts */
                if(theData == (unsigned short*)0L || MemError() !=
noErr){
                    DisposeHandle(imageData);
                    return((unsigned short*)0L);
                }

                HLock(imageData);                                /* lock
down bytewise bitmap */
                theCharData = *imageData;
                theDataPtr   = theData;
                for(i = 1 ; i <= numPixels ; i++){
                    *(theDataPtr++) = ((unsigned
short)(*(theCharData++))) & 0X00FF;
                }

                HUnlock(imageData);
                DisposeHandle(imageData);                        /* Get
rid of bytwise bitmap */
                return(theData);                                 /* return
array of shorts */
                 break;

            case 0x001C:
            case 0x001E:
                opcodeInfo++;
                break;

            default:                        /* OOPS */
                SysBeep(30);
                if(!DoOtherOPCODE(&opcodeInfo)){
                    HUnlock((Handle)thePicture);  /* OPCODE not
recognized */
                    return(0L);
                }
                break;
        }
    }
    HUnlock((Handle)thePicture);                                 /*
shouldn't ever get to here */
    return (unsigned short*)0L;
}


Handle GetTheData(PackedBitsInfoPtr theDataInfo,long* dataSize,short
*rows,short *columns)
{
    long                size;
    Handle              theData;
    Ptr                 theDestPtr,theSrcPtr;
    short
    rowBytes,*theDataBlock,numColors,i,lengthValue;
    ColorSpec           *theColorArray;
```

```
    theDataBlock = (short*)theDataInfo;
    numColors        = theDataBlock[28];                    /* Avoids
struct aligment problems */
    theColorArray    = (ColorSpec*)&theDataBlock[29]; /* Avoids
struct aligment problems */

    if( theDataInfo->thePixMap.packType  != 0 ||  /* Try to trap
wrong type of pictures */
        theDataInfo->thePixMap.pixelType != 0 ||
        theDataInfo->thePixMap.pixelSize != 8 ||
        theDataInfo->thePixMap.cmpCount  != 1 ||
        theDataInfo->thePixMap.cmpSize   != 8 ||
        numColors                            != 255){

        *dataSize = 0;
        return((Handle)0L);
    }

    *rows        = theDataInfo->thePixMap.bounds.bottom - theDataInfo-
>thePixMap.bounds.top;
    *columns = theDataInfo->thePixMap.bounds.right - theDataInfo-
>thePixMap.bounds.left;
    rowBytes = theDataInfo->thePixMap.rowBytes & 0x7FFF; /* High bit is
a flag bit...Mask it. */
    size         = (long)(*rows) * rowBytes;                  /*
Calculate image size */
    theData      = NewHandle(size);                           /*
get data as a handle so we can pack mem */
    if(theData == (Handle)0L || MemError() != noErr){     /* Trap
the error if insufficient memory */
        *dataSize = 0;
        return((Handle)0L);
    }

    HLock(theData);                                           /* Lock
down handle so we can use pointer */
    theDestPtr   = *theData;                                  /* Get
ptr to data */
    theSrcPtr    = (Ptr)&theColorArray[256];                  /*
Address at end of colorTable (avoids alignment problems) */
    theSrcPtr    += 18;                                       /* Rect +
Rect + short (avoids alignment problems) */

    if(rowBytes > 250){                                       /* Take
care of length word */
        lengthValue = 2;
    } else {
        lengthValue = 1;
    }

    for(i = 1 ; i <= *rows ; i++){                       /* Unpack the
rows */
        theSrcPtr += lengthValue;                        /* skip line
length word or can't unpack*/
        UnpackBits(&theSrcPtr,&theDestPtr,rowBytes);/* Use O.S.
Unpacking routine */
```

```
    }
    HUnlock(theData);                                   /* Unlock the
handle */
    *dataSize = size;                                   /* Return the
byte count*/

    return(theData);

}

void    SetGrayPixel(short h,short v,unsigned short value)
{
    RGBColor theColor;

    theColor.red    = 65535 - 257 * value;
    theColor.green  = theColor.red;
    theColor.blue   = theColor.red;
    SetCPixel(h,v,&theColor);
}

void            DrawPixels(unsigned short *theData,short rows,short
columns)
{
    short h,v;

    for(v = 0 ; v < rows ; v++){
        for(h = 0 ; h < columns ; h++){
            SetGrayPixel(h,v,*theData);
            theData++;
        }
    }
}

Boolean DoOtherOPCODE(short **opcodeInfo)
{
    short theOPCODE;

    theOPCODE =  **opcodeInfo;

    if(theOPCODE >= 0x0030 && theOPCODE <= 0x0037){
        *opcodeInfo += 5;
        return true;
    }

    if(theOPCODE >= 0x0038 && theOPCODE <= 0x003F){
        (*opcodeInfo)++;
        return true;
    }

    if(theOPCODE >= 0x0040 && theOPCODE <= 0x0047){
        *opcodeInfo += 5;
        return true;
    }

    if(theOPCODE >= 0x0048 && theOPCODE <= 0x004F){
        (*opcodeInfo)++;
        return true;
```

```
    }

    if(theOPCODE >= 0x0050 && theOPCODE <= 0x0057){
        *opcodeInfo += 5;
        return true;
    }

    if(theOPCODE >= 0x0058 && theOPCODE <= 0x005F){
        (*opcodeInfo)++;
        return true;
    }

    if(theOPCODE >= 0x0060 && theOPCODE <= 0x0067){
        *opcodeInfo += 7;
        return true;
    }

    if(theOPCODE >= 0x0068 && theOPCODE <= 0x006F){
        *opcodeInfo += 3;
        return true;
    }

    switch(theOPCODE){

        case 0x0000:
            (*opcodeInfo)++;
            return true;
            break;

        case 0x0003:
        case 0x0005:
        case 0x0008:
        case 0x000D:
            *opcodeInfo += 2;
            return true;
            break;

        case 0x0006:
        case 0x0007:
        case 0x000B:
        case 0x000C:
        case 0x000E:
        case 0x000F:
            *opcodeInfo += 3;
            return true;
            break;

        case 0x0002:
        case 0x0009:
        case 0x000A:
        case 0x0010:
            *opcodeInfo += 5;
            return true;
            break;
    }
    return false;
}
```

D.2 #include Files

These files are the include files referenced from within the source code files of section D.1.

D.2.1 Dendrites.h

```
/*   Dendrites.h   */

#include <stdio.h>
#include <math.h>
#include <stdlib.h>
#include <Printing.h>
#ifdef  __MAIN__
    #define VARLOC
#else
    #define VARLOC   extern
#endif

#include "DendriteCenter.h"

VARLOC   Boolean
    quitFlag,changed,selectFlag,rectVis,autoFlag;
VARLOC   Boolean
    refreshFlag,validWindow,bitMapFlag,multiPlot,pointsFlag,delPointsFl
ag,learnFlag;
VARLOC   WindowPtr            theWindow;
VARLOC   FSSpec               theFile;
VARLOC   SFTypeList           theTypes;
VARLOC   short                fileRefNum,colorScheme;
VARLOC   char                 theText[256],cursorID,theFileName[80];
VARLOC   Ptr                  theData,oldData;
VARLOC   long                 dataSize,updateRate;
VARLOC   RgnHandle            mouseRgn;
VARLOC   Rect                 selectRect;
VARLOC   CGrafPort            offScreenCPort,*offScreenCPortPtr;
VARLOC   Ptr                  pixMapAddr;
VARLOC   THPrint              hPrtRec;
VARLOC   DendriteCenter*      theCenters;


void     main(void);
void     DoEvent(EventRecord* theEvent);
void     DoMenu(long menuData);

#define  GENERIC_ALERT 128


enum     {                          // Menus
             APPLE_MENU = 128,
             FILE_MENU,
             EDIT_MENU,
             TOOL_MENU
         };

enum     {                          // File Menu Items
```

```
        OPEN_ITEM = 1,
        IMPORT_ITEM,
        CLOSE_ITEM,
        RESTORE_PICTS_ITEM,
        FILE_DUMMY_1,
        SAVE,
        SAVE_AS,
        FILE_DUMMY_2,
        PAGE_SETUP_ITEM,
        PRINT_ITEM,
        FILE_DUMMY_3,
        QUIT_ITEM
    };

enum    {                           // Edit Menu
        UNDO_ITEM = 1,
        EDIT_DIVIDER_1,
        CUT_ITEM,
        COPY_ITEM,
        PASTE_ITEM,
        CLEAR_ITEM,
        EDIT_DIVIDER_2,
        REFRESH_ITEM,
        AUTO_CYCLE_ITEM
    };


enum    {                           // Tool Menu Items;
        ENTER_DENDRITES_ITEM = 1,
        DELETE_DENDRITES_ITEM,
        SMART_SCAN,
        REMOVE_ALL_DENDRITES,
        TOOL_DIVIDER_1,
        CONFIG_AUTO_SCAN,
        AUTO_SCAN,
        TOOL_DIVIDER_2,
        ENTER_SCALE_ITEM,
        VIEW_STATISTICS_ITEM,
        ADD_STATS_ITEM
    };
```

```
/*   DendriteCenter.h   */

#define pi 3.141592654

typedef struct FPoint{
    double  x;
    double  y;
}FPoint;

typedef struct FLine{
    FPoint   start;
    FPoint   end;
    double   angle;
    double   slope;
    double   intercept;
}FLine;

class DendriteCenter{
    public:
    PicHandle        thePicture;
    Rect             circleRect;
    Point            thePoint;
    short            dHorizAuto;
    short            dDiagonalAuto;
    short            recordType;
    short            span;
    FLine            line1;
    FLine            line2;
    FPoint           center;
    double           area;
    double           angle;
    double           scale;
    double           spacing;
    double           distance;
    double           pointCount;
    double           standardD;
    Boolean          infoFlag;
    DendriteCenter*  next;

    void                DoInit(short type);
    void                NewLine(void);
    void                NewPoint(Point thePoint,short theSpan);
    void                DoClose(void);
    void                DefineLine(FLine* theLine);
    void                DoCalculations(void);
    short               CountPoints(void);
    void                WriteElements(short fileRef,short
numElements);
    void                ReadElements(short fileRef,short
numElements);
    void                AddCircle(Rect   theRect,PicHandle
thePicture);
    void                DrawElements(void);
    void                DrawPoint(void);
    void                AutoSearch(short dist,short diagDist);
    void                RemovePoints(void);
    void                DeletePoint(Point thePoint);
```

```
    void                DoSmartScan(Point thePoint);
    DendriteCenter*     DoPointRemove(void);
    Boolean             FoundPoint(Point thePoint,short hDist,double
span);
    void                ConfigAuto(WindowPtr theWindow);
    void                EnterScale(void);
    void                DisplayStatics(void);
    void                CalcStandardD(DendriteCenter *top,Rect*
    theRect,double theMean,double *sum,short *number);
    void                Find4Nearest(Point   testLoc,double
    *distArray);
    void                AddInfo(void);
    void                ReInit(void);
};


#define WHITE_VALUE  128
#define BLACK_VALUE  200

enum {
        UNDEFINED,
        CIRCLE,
        LINES,
        POINT
        };
```

D.2.2 Eric'sLib.h

```
/*   Eric'sLib.h   */

#include <stdio.h>
#include <stdlib.h>

void     DoInits(void);


void     SetShortItemText(DialogPtr theDialog,short theItem,short
theValue,char *theFmt);
short    GetShortItem(DialogPtr   theDialog,short theItem);
void     SetDoubleItemText(DialogPtr  theDialog,short theItem,double
theValue,char *theFmt);
double   GetDoubleItem(DialogPtr  theDialog,short theItem);
void     EnableControl(DialogPtr  theControl,short theItem);
void     DisableControl(DialogPtr theControl,short theItem);
```

D.2.3 GrabBitData.h

```
/*   GrabBitData.h   */

/*****************************************************************/
/*                    Application Notes                          */


/*  The routines contained herein will work for 8 bit grey scale images
only.    */
/*  In general the user need only call GetDataFromPICT to obtain the
image        */
/*  data. The GetDataFromPICT function scans the picture and responds
to those*/
/*  opcodes typical for this type of picture...it may be necessary to
add a    */
/*  few more depending on the image capture software. The 8 bit data is
         */
/*  converted into 16 bit words and pointer to an array is returned to
the user.*/
/*  In the event of insufficient memory, the routine returns a 0 for
the Ptr.*/
/*  The DrawPixels routine can be used to display the data if desired.
             */
/*
                    */
/*  NOTE:    GetDataFromPICT returns a Ptr which must be disposed of
using the    */
/*           the DisposePtr Toolbox call. Failure to do so once you no
longer   */
/*           need the data will result in a somewhat less than
gracefull        */
/*           termination.... ie. a crash.
                 */
/*
                    */
/*****************************************************************
*********/

/*****************************************************************
*********/
/*                                  PackedBitsInfo
                    */
/*
                    */
/*       The PackedBitsInfo structure is used to decode PICT opcode
0x0098.      */
/*  It is used to obtain information about the image and to generate
the          */
/*  offset into the picture data.
                 */
/*
                    */
/*****************************************************************
*********/
```

```
typedef struct PackedBitsInfo{
        PixMap      thePixMap;       /* NOTE: compiler struct
alignment can cause problems here */
        short       ctSeed;
        short       ctFlags;
        short       ctSize;
        ColorSpec   theColors[256]; /* NOTE: compiler struct
alignment can cause problems here */
        Rect        srcRect;     /* NOTE: compiler struct alignment
can cause problems here */
        Rect        destRect;        /* NOTE: compiler struct
alignment can cause problems here */
        short       mode;
        short       dataStart;
}PackedBitsInfo,*PackedBitsInfoPtr;

/*****************************************************************
*********/
/*                                  GetDataFromPICT
                    */
/*
                    */
/*  theData = GetDataFromPICT(thePicture,&rows,&columns);
            */
/*
                    */
/*      This routine returns a pointer of type unsigned short*. Within
this    */
/*  data block the routine will return the intensity data. The routine
also        */
/*  returns the number of rows and columns in the image. In the event
of an   */
/*  error a Ptr address of '0' is returned.
                */
/*
                    */
/*****************************************************************
*********/
unsigned short* GetDataFromPICT(PicHandle thePicture,short *rows,short
*columns);

/*****************************************************************
*********/
/*                                  GetTheData
                    */
/*
                    */
/*  theHandle = GetTheData(opcodeInfo,&dataSize,&rows,&columns);
            */
/*
                    */
/*      This routine returns a Handle to a byte array which was
extracted from   */
/*  the picture. GetDataFromPICT calls this routine and converts the
byte array   */
/*  into a unsigned short array. This routine returns the number of
pixels, the  */
```

```
/*  number of rows and the number of columns. In the event of an error
the          */
/*  routine returns a Handle value of '0'.
                */
/*
                */
/*********************************************************************
*********/
Handle  GetTheData(PackedBitsInfoPtr opcodeInfo,long *dataSize,short
*rows,short *columns);

/*********************************************************************
*********/
/*                                        DrawPixels
                */
/*
                */
/*  DrawPixels(theData,rows,columns);
                */
/*
                */
/*      The DrawPixels routine takes a Ptr to an array of unsigned
shorts and   */
/*  the number of rows and columns and draws the bit data to the
screen. This */
/*  routine is good for verification. It calls SetGrayPixel to generate
the     */
/*  colors for the pixels.
                */
/*
                */
/*********************************************************************
*********/
void    DrawPixels(unsigned short *theData,short rows,short columns);

/*********************************************************************
*********/
/*                                    SetGrayPixel
                */
/*
                */
/*  SetGrayPixel(h,v,value);
                */
/*
                */
/*      The SetGrayPixel routine takes horizontal and vertical pixel
                */
/*  coordinates and a short value in the range 0 <= value <= 255 and
sets the*/
/*  pixel at the coordinates to a gray value.
                */
/*
                */
/*********************************************************************
*********/
void    SetGrayPixel(short h,short v,unsigned short value);
```

```
/*************************************************************************
*********/
/*                                    DoOtherOPCODE
                    */
/*
                    */
/*  if(!DoOtherOPCODE &opcodeInfo){
                    */
/*
                    */
/*      The DoOtherOPCODE routine is invoked whenever an unexpeted
OPCODE is    */
/*  encountered. If the OPCODE is recognized by the routine, the opcode
Ptr      */
/*  is incremented the proper amount to allow processing to continue
and the */
/*  function return TRUE. If the OPCODE is not recognized, the Ptr is
not      */
/*  altered and the function returns FALSE.
                */
/*
                    */
/*  NOTE: Not all picture opcodes are included
                */
/*
                    */
/*************************************************************************
*********/
Boolean DoOtherOPCODE(short **opcodeInfo);
```

D.3 Resources

The following is the DeRez dump for the resources used for this program. A new resource file may be assembled by utilizing this data as the input for the Rez tool in MPW.

DeRez Dendrites.rsrc

```
data 'MENU' (128) {
    $"0080 0000 0000 0000 0000 FFFF FFFB 0114"          /*
.Ä........ˇˇˇ•.. */
    $"1241 626F 7574 2074 6869 7320 7072 6F67"          /* .About
this prog */
    $"7261 6D00 0000 0001 2D00 0000 0000"               /* ram.....-
..... */
};

data 'MENU' (129)
{
    $"0081 0000 0000 0000 0000 FFFF F017 0446"
    $"696C 6507 4F70 656E 2E2E 2E00 4F00 0009"
    $"496D 706F 7274 2E2E 2E00 4E00 0005 436C"
    $"6F73 6500 5700 0010 5265 7374 6F72 6520"
    $"5049 4354 732E 2E2E 0046 0000 012D 0000"
    $"0000 0753 6176 652E 2E2E 0053 0000 0A53"
    $"6176 6520 4173 2E2E 2E00 0000 0001 2D00"
    $"0000 000D 5061 6765 2053 6574 7570 2E2E"
    $"2E00 0000 0008 5072 696E 742E 2E2E 0050"
    $"0000 012D 0000 0000 0451 7569 7400 5100"
    $"0000"
};

data 'MENU' (130) {
    $"0082 0000 0000 0000 0000 FFFF FD01 0445"
    $"6469 7404 556E 646F 005A 0000 012D 0000"
    $"0000 0343 7574 0000 0000 0443 6F70 7900"
    $"0000 0005 5061 7374 6500 0000 0005 436C"
    $"6561 7200 0000 0001 2D00 0000 0007 5265"
    $"6672 6573 6800 5200 000A 4175 746F 2043"
    $"7963 6C65 0000 0000 00"
};

data 'MENU' (131) {
    $"0083 0000 0000 0000 0000 FFFF F041 0554"
    $"6F6F 6C73 0941 6464 2050 6F69 6E74 002B"
    $"0000 0C44 656C 6574 6520 506F 696E 7400"
    $"2D00 000B 4C65 6172 6E65 6420 4164 6400"
    $"2A00 0011 5265 6D6F 7665 2041 6C6C 2050"
    $"6F69 6E74 7300 4B00 0001 2D00 0000 0016"
    $"436F 6E66 6967 7572 6520 4175 746F 2053"
    $"6361 6E2E 2E2E 0000 0000 0941 7574 6F20"
    $"5363 616E 0041 0000 012D 0000 0000 0E45"
    $"6E74 6572 2053 6361 6C65 2E2E 2E00 0000"
    $"0012 5669 6577 2053 7461 7469 7374 6963"
    $"732E 2E2E 004C 0000 0A53 6176 6520 5374"
    $"6174 7300 4400 0000"
```

```
};

data 'MBAR' (128) {
    $"0004 0080 0081 0082 0083"
};

data 'ALRT' (128) {
    $"0028 0028 0087 01BE 0080 5555"
};

data 'DITL' (128) {
    $"0001 0000 0000 0008 0048 004D 0182 8802"
    $"5E30 0000 0000 0040 0008 0054 0042 0406"
    $"4275 7474 6F6E"

data 'DITL' (129) {
    $"0007 0000 0000 0088 0010 009C 004A 0402"
    $"4F4B 0000 0000 0088 00E8 009C 0122 0406"
    $"4361 6E63 656C 0000 0000 0018 00A4 0028"
    $"00C1 1000 0000 0000 0038 00A4 0048 00C1"
    $"1000 0000 0000 00B0 0010 00C4 0067 0409"
    $"5465 7374 2053 6361 6E6C 0000 0000 0018"
    $"0018 004B 00A1 882B 486F 7269 7A6F 6E74"
    $"616C 2044 6973 7461 6E63 653A 0D0D 2020"
    $"2044 6961 676F 6E61 6C20 4469 7374 616E"
    $"6365 3A20 0000 0000 0018 00C8 004A 012E"
    $"8820 5069 7865 6C73 2074 6F20 626C 6163"
    $"6B0D 0D50 6978 656C 7320 746F 2062 6C61"
    $"636B 0000 0000 0050 0058 00D2 00DA C002"
    $"0080"};

data 'DITL' (130) {
    $"0004 0000 0000 0050 0048 0064 0082 0402"
    $"4F4B 0000 0000 0070 0020 0085 00AB 0413"
    $"436F 7079 2074 6F20 4175 746F 2053 6574"
    $"7570 2E00 0000 0000 0010 0098 0020 00C1"
    $"880B 5374 6174 6963 2054 6578 744C 0000"
    $"0000 0030 0098 0040 00C1 880B 5374 6174"
    $"6963 2054 6578 744C 0000 0000 0010 0018"
    $"0043 0095 8827 486F 7269 7A6F 6E74 616C"
    $"204C 656E 6774 683A 0D0D 2020 2044 6961"
    $"676F 6E61 6C20 4C65 6E67 7468 3A00"
};

data 'DITL' (131) {
    $"0006 0000 0000 0080 0028 0094 0062 0402"
    $"4F4B 0000 0000 0080 00C0 0094 00FA 0406"
    $"4361 6E63 656C 0000 0000 0010 0018 0024"
    $"007D 040B 456E 7465 7220 5363 616C 6500"
    $"0000 0000 0038 00A8 004A 00FA 1000 0000"
    $"0000 0058 00A8 006A 00FA 0800 0000 0000"
    $"0038 0010 006F 00A5 8831 4D65 6173 7572"
    $"6564 2064 6973 7461 6E63 6520 6973 3A0D"
    $"0D20 2020 2043 616C 6375 6C61 7465 6420"
    $"7363 616C 6520 6973 3A0D 0D12 0000 0000"
    $"0038 0100 006D 0142 8812 6D69 6372 6F6E"
    $"730D 0DB5 202F 2070 6978 656C"
```

```
};


data 'DITL' (132) {
    $"0006 0000 0000 0098 0010 00AC 004A 0402"
    $"4F4B 0000 0000 0010 00C8 0020 0113 8800"
    $"0000 0000 0030 00C8 0040 0113 8800 0000"
    $"0000 0050 00C8 0060 0113 8800 0000 0000"
    $"0070 00C8 0080 0113 8800 0000 0000 0010"
    $"0010 0084 00BF 8878 2020 2020 2020 2020"
    $"2020 2020 2020 2020 2020 2020 2053 616D"
    $"706C 6520 4172 6561 3A0D 0D20 2020 2020"
    $"2020 4E75 6D62 6572 206F 6620 4465 6E64"
    $"7269 7465 733A 0D0D 5072 696D 6172 7920"
    $"4465 6E64 7269 7465 2053 7061 6369 6E67"
    $"3A0D 0D20 2020 2020 2020 2020 2053 7461"
    $"6E64 6172 6420 4465 7669 6174 696F 6E3A"
    $"0000 0000 0010 0120 0084 013D 880B B55E"
    $"320D 0D0D 0DB5 0D0D B500"};

data 'DITL' (133) {
    $"0007 0000 0000 00B0 0010 00C4 004A 0402"
    $"4F4B 0000 0000 00B0 0098 00C4 00D2 0406"
    $"4361 6E63 656C 0000 0000 0010 00A8 0020"
    $"00F3 880B 5374 6174 6963 2054 6578 7420"
    $"0000 0000 0030 00A8 0040 00F3 880B 5374"
    $"6174 6963 2054 6578 7462 0000 0000 0050"
    $"00A8 0060 00F3 880B 5374 6174 6963 2054"
    $"6578 7420 0000 0000 0070 00A8 0080 00F3"
    $"880B 5374 6174 6963 2054 6578 7464 0000"
    $"0000 0090 00A8 00A0 00F3 900B 5374 6174"
    $"6963 2054 6578 7420 0000 0000 0010 0010"
    $"00A4 00A1 8883 2020 2020 2020 2020 2020"
    $"2020 2020 2020 2020 2020 2020 2020 2020"
    $"2041 7265 613A 0D0D 4E75 6D62 6572 206F"
    $"6620 4465 6E64 7269 7465 733A 0D0D 2020"
    $"2020 2020 2020 5072 696D 6172 7920 5370"
    $"6163 696E 673A 0D0D 2020 2053 7461 6E64"
    $"6172 6420 4465 7669 6174 696F 6E3A 0D0D"
    $"2020 2020 2053 616D 706C 6520 4964 656E"
    $"7469 6669 6572 3A0D 0D00"
};

data 'DLOG' (129, "Auto Scan Parameters") {
    $"0028 0028 010A 015D 0000 0100 0100 0000"
    $"0000 0081 1441 7574 6F20 5363 616E 2050"
    $"6172 616D 6574 6572 73"};

data 'DLOG' (130, "Dendrite info") {
    $"002F 000B 00C4 00E0 0005 0100 0100 0000"
    $"0000 0082 0D44 656E 6472 6974 6520 496E"
    $"666F"
};

data 'DLOG' (131, "Enter Scale") {
    $"0029 0025 00CB 016A 0001 0100 0100 0000"
```

```
    $"0000 0083 00"
};


data 'DLOG' (132, "Display Statistics") {
    $"0028 0028 00DA 0174 0000 0100 0100 0000"
    $"0000 0084 0A53 7461 7469 7374 6963 73"
};

data 'DLOG' (133, "Enter Sample Info") {
    $"0028 0028 00F2 012E 0000 0100 0100 0000"
    $"0000 0085 0F57 7269 7465 2054 6578 7420"
    $"496E 666F"
};

data 'PICT' (128) {
    $"0A0C 0070 0036 00F2 00B8 0011 02FF 0C00"
    $"FFFF FFFF 0036 0000 0070 0000 00B8 0000"
    $"00F2 0000 0000 0000 00A0 0082 0001 000A"
    $"0070 0036 00F2 00B8 0007 0000 0000 0009"
    $"3049 883A B59C F039 0022 00A9 0070 0000"
    $"0009 FFFF FFFF FFFF FFFF 0023 0000 00A0"
    $"00C4 00A1 00C0 024F 2525 4453 4944 4943"
    $"543A 5F63 760D 7573 6572 6469 6374 202F"
    $"5F63 7620 6B6E 6F77 6E20 6E6F 7420 6375"
    $"7272 656E 7464 6963 7420 2F62 7520 6B6E"
    $"6F77 6E20 616E 647B 6275 7D7B 7361 7665"
    $"7D69 6665 6C73 650D 7573 6572 6469 6374"
    $"202F 5F63 7620 6B6E 6F77 6E20 6E6F 7420"
    $"6475 7020 7B75 7365 7264 6963 7420 2F5F"
    $"6376 2032 3020 6469 6374 2070 7574 7D69"
    $"660D 5F63 7620 6265 6769 6E0D 2F62 6466"
    $"7B62 696E 6420 6465 667D 6269 6E64 2064"
    $"6566 0D2F 7365 7463 6D79 6B63 6F6C 6F72"
    $"2077 6865 7265 7B2F 7365 7463 6D79 6B63"
    $"6F6C 6F72 2067 6574 202F 6376 636D 796B"
    $"2065 7863 6820 6465 667D 7B2F 6376 636D"
    $"796B 7B31 2073 7562 2034 2031 2072 6F6C"
    $"6C20 337B 3320 696E 6465 7820 6164 6420"
    $"6E65 6720 6475 7020 3020 6C74 7B70 6F70"
    $"2030 7D69 6620 3320 3120 726F 6C6C 7D72"
    $"6570 6561 7420 7365 7472 6762 636F 6C6F"
    $"7220 706F 707D 6264 6620 7D69 6665 6C73"
    $"650D 2F73 7467 7B63 6620 6361 202F 6373"
    $"206C 6F61 6420 7365 7473 6372 6565 6E20"
    $"7365 7467 7261 797D 6264 660D 2F73 7472"
    $"6762 7B63 6620 6361 202F 6373 206C 6F61"
    $"6420 7365 7473 6372 6565 6E20 7365 7472"
    $"6762 636F 6C6F 727D 6264 660D 2F73 7463"
    $"6D79 6B7B 6366 2063 6120 2F63 7320 6C6F"
    $"6164 2073 6574 7363 7265 656E 2063 7663"
    $"6D79 6B7D 6264 660D 2F6D 696E 317B 6475"
    $"7020 3020 6571 7B70 6F70 2031 7D69 667D"
    $"6264 660D 6375 7272 656E 7473 6372 6565"
    $"6E2F 6373 2065 7863 6820 6465 662F 6361"
    $"2065 7863 6820 6465 662F 6366 2065 7863"
```

```
$"6820 6465 660D 656E 640D 6375 7272 656E"
$"7464 6963 7420 2F62 6E20 6B6E 6F77 6E20"
$"616E 647B 626E 7D7B 7265 7374 6F72 657D"
$"6966 656C 7365 0D00 00A0 00BF 00A0 008C"
$"00A0 008C 00A1 0064 00A0 6472 7732 0009"
$"0078 003F 00E8 00AF C000 0000 8000 0000"
$"0101 0000 0000 0000 0000 0000 FFFF FFFF"
$"FFFF 0001 1401 0800 0000 0000 0000 0000"
$"000D 0078 C000 0070 8000 00AA 0000 0070"
$"8000 00AA 0000 003F 0000 00B7 4000 003F"
$"0000 00B7 4000 0070 4000 00E8 8000 0070"
$"4000 00E8 8000 007D 8000 00B7 4000 007D"
$"8000 00B7 4000 00AF 0000 00AA 4000 00AF"
$"0000 00AA 4000 007D 8000 0078 C000 007D"
$"8000 0078 C000 0070 8000 0009 5350 4320"
$"5350 4320 0022 0078 0070 0000 00A0 00BE"
$"0009 0000 0000 0000 0000 0071 003E 0078"
$"003F 00E8 00AF 0078 0070 00AA 0070 00AA"
$"003F 00B7 003F 00B7 0070 00E8 0070 00E8"
$"007D 00B7 007D 00B7 00AF 00AA 00AF 00AA"
$"007D 0078 007D 0078 0070 00A0 00BF 0009"
$"5350 4320 5350 4320 0023 0000 00A0 00A0"
$"00A0 00A5 000A 0000 0000 0000 0000 0084"
$"000A 0000 0000 0000 0000 0007 0001 0001"
$"0009 FFFF FFFF FFFF FFFF 0023 0032 0023"
$"CF00 0023 000D 0023 3100 0023 0031 0023"
$"0D00 0023 00CF 0023 3200 0023 00F3 0023"
$"CE00 0023 00CE 0023 F300 00A0 00A1 00A0"
$"008C 00A1 0064 0064 6472 7732 0007 0071"
$"0070 0079 0077 0000 8000 8000 0000 0101"
$"0000 0000 0000 0000 0000 FFFF FFFF FFFF"
$"0001 1401 088F 0000 0001 0014 000C 0003"
$"0002 0000 005A 0001 0000 0002 0000 0003"
$"000C 0000 0000 0000 0070 0070 007A 0077"
$"8000 0000 0000 8000 0000 FFA6 0009 0000"
$"0000 0000 0000 0061 0071 0070 0083 0080"
$"010E 005A 0009 FFFF FFFF FFFF FFFF 0068"
$"010E 005A 00A1 0064 0064 6472 7732 0007"
$"0071 0077 0079 007D 0000 0000 8000 8000"
$"0101 0000 0000 0000 0000 0000 FFFF FFFF"
$"FFFF 0001 1401 08FF 0000 0001 0014 000C"
$"0003 0002 0000 005A 0001 0000 0002 0000"
$"0003 000C 0000 0000 0000 0070 0076 007A"
$"007E 8000 8000 0000 0000 0168 005A 0009"
$"0000 0000 0000 0000 0061 0071 0070 0083"
$"007E 0168 005A 0009 FFFF FFFF FFFF FFFF"
$"0068 0000 005A 00A0 008D 00A0 008C 00A1"
$"0064 0064 6472 7732 0007 00B0 0037 00B7"
$"003F A000 4000 3DB7 C000 0101 0000 0000"
$"0000 0000 0000 FFFF FFFF FFFF 0001 1401"
$"08FF 0000 0001 0014 000C 0003 0002 0000"
$"005A 0001 0000 0002 0000 0003 000C 0000"
$"0000 0000 00B0 0036 00B7 0040 2000 C000"
$"BDB7 4000 FFA6 FFA6 0009 0000 0000 0000"
$"0000 0061 00A8 0037 00B8 0049 00B4 005A"
$"0009 FFFF FFFF FFFF FFFF 0068 00B4 005A"
$"00A1 0064 0064 6472 7732 0007 00AA 0037"
```

```
$"00B0 003F 0249 4000 A000 C000 0101 0000"
$"0000 0000 0000 0000 FFFF FFFF FFFF 0001"
$"1401 08FF 0000 0001 0014 000C 0003 0002"
$"0000 005A 0001 0000 0002 0000 0003 000C"
$"0000 0000 0000 00A9 0036 00B1 0040 8249"
$"C000 2000 4000 010E 005A 0009 0000 0000"
$"0000 0000 0061 00AA 0037 00B8 0049 010E"
$"005A 0009 FFFF FFFF FFFF FFFF 0068 010E"
$"005A 00A0 008D 00A0 008C 00A1 0064 0064"
$"6472 7732 0007 00AA 00AE 00B0 00B7 76D2"
$"8000 E95D 0000 0101 0000 0000 0000 0000"
$"0000 FFFF FFFF FFFF 0001 1401 08FF 0000"
$"0001 0014 000C 0003 0002 0000 005A 0001"
$"0000 0002 0000 0003 000C 0000 0000 0000"
$"00A9 00AE 00B1 00B7 F6D2 0000 695D 8000"
$"005A FFA6 0009 0000 0000 0000 0000 0061"
$"00AA 00A4 00B8 00B8 0000 005A 0009 FFFF"
$"FFFF FFFF FFFF 0068 0000 005A 00A1 0064"
$"0064 6472 7732 0007 00B0 00AE 00B7 00B7"
$"E95D 8000 5BE8 0000 0101 0000 0000 0000"
$"0000 0000 FFFF FFFF FFFF 0001 1401 08FF"
$"0000 0001 0014 000C 0003 0002 0000 005A"
$"0001 0000 0002 0000 0003 000C 0000 0000"
$"0000 00B0 00AE 00B7 00B7 695D 0000 DBE8"
$"8000 005A 005A 0009 0000 0000 0000 0000"
$"0061 00A8 00A4 00B8 00B8 005A 005A 0009"
$"FFFF FFFF FFFF FFFF 0068 005A 005A 00A0"
$"008D 00A0 008C 00A1 0064 0064 6472 7732"
$"0007 00E8 0070 00F0 0076 0000 396F 8000"
$"D6DB 0101 0000 0000 0000 0000 0000 FFFF"
$"FFFF FFFF 0001 1401 08FF 0000 0001 0014"
$"000C 0003 0002 0000 005A 0001 0000 0002"
$"0000 0003 000C 0000 0000 0000 00E7 006F"
$"00F1 0077 8000 B96F 0000 56DB 00B4 005A"
$"0009 0000 0000 0000 0000 0061 00DF 0070"
$"00F1 007E 00B4 005A 0009 FFFF FFFF FFFF"
$"FFFF 0068 00B4 005A 00A1 0064 0064 6472"
$"7732 0007 00E8 0076 00F0 007D 0000 D6DB"
$"8000 7447 0101 0000 0000 0000 0000 0000"
$"FFFF FFFF FFFF 0001 1401 08FF 0000 0001"
$"0014 000C 0003 0002 0000 005A 0001 0000"
$"0002 0000 0003 000C 0000 0000 0000 00E7"
$"0076 00F1 007D 8000 56DB 0000 F447 00B4"
$"FFA6 0009 0000 0000 0000 0000 0061 00DF"
$"006E 00F1 007E 005A 005A 0009 FFFF FFFF"
$"FFFF FFFF 0068 005A 005A 00A0 008D 00A0"
$"008D 00A1 0064 0060 6472 7732 0003 00AC"
$"0076 00B5 00B6 8000 0000 0000 8000 0101"
$"0000 0000 0000 0000 0000 FFFF FFFF FFFF"
$"0001 1401 08FF 0000 0002 00B0 00B6 00B0"
$"0077 C000 0000 C000 8000 0001 0014 000C"
$"0003 0002 0000 005A 0001 0000 0002 0000"
$"0003 000C 0000 0000 00A0 00AB 0061 00A5"
$"00AA 00BD 00C2 FF92 0028 0022 00B0 00AB"
$"CC00 00A0 00AD 00A1 0064 0060 6472 7732"
$"0003 00A0 0066 00B1 0077 4000 C000 4000"
$"C000 0101 0000 0000 0000 0000 0000 FFFF"
```

```
$"FFFF FFFF 0001 1401 08FF 0000 0001 00B0"
$"0077 00A1 0068 C000 4000 C000 4000 0001"
$"0014 000C 0003 0002 0000 005A 0001 0000"
$"0002 0000 0003 000C 0000 0000 00A0 00AA"
$"0061 0096 005C 00AE 0074 0073 0028 0023"
$"F9F9 00A0 00AD 00A0 008D 00A1 0064 0006"
$"6472 7732 0044 00A0 0083 00FF"
```

Appendix E...Dendrite Micrographs

The micrographs on the following pages are the source for the dendrite statistics. They have been processed by the debnrite counting software and as such the sample rings may be seen as well as the circular marks used to identify those dendrites (or features) which have been counted by the software.

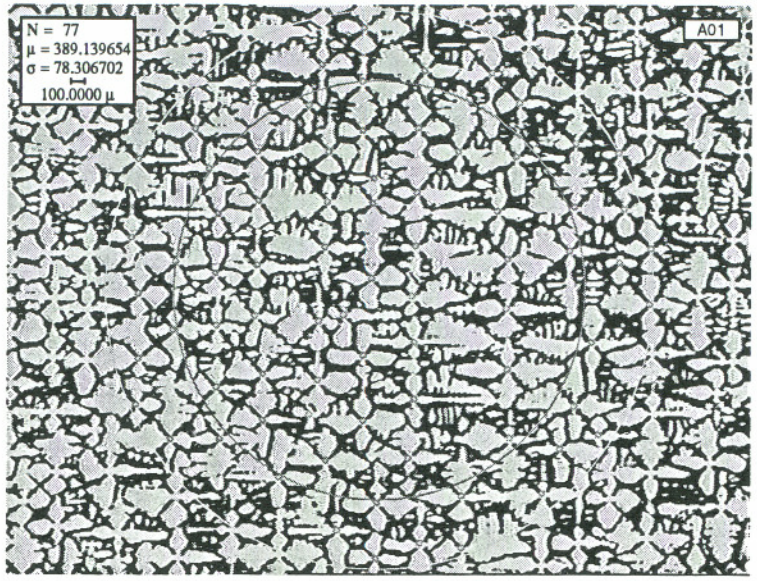
N = 77
μ = 389.139654
σ = 78.306702
100.0000 μ
A01

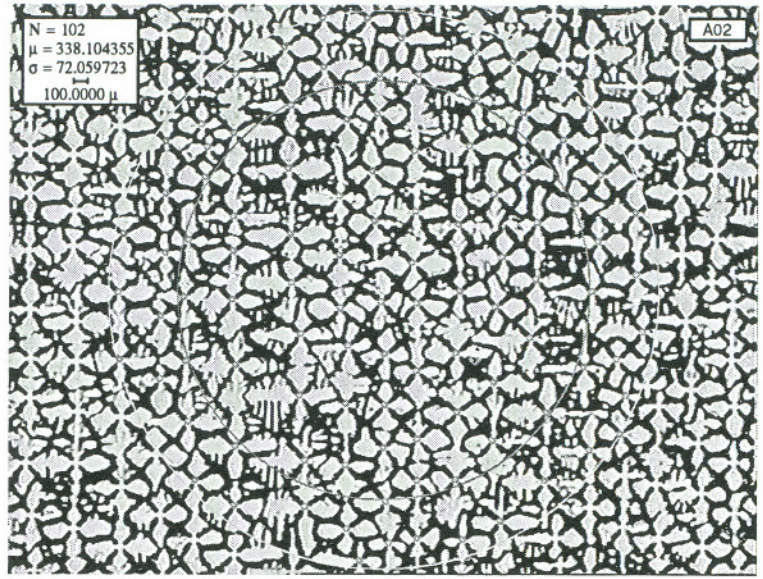
N = 102
μ = 338.104355
σ = 72.059723
100.0000 μ
A02

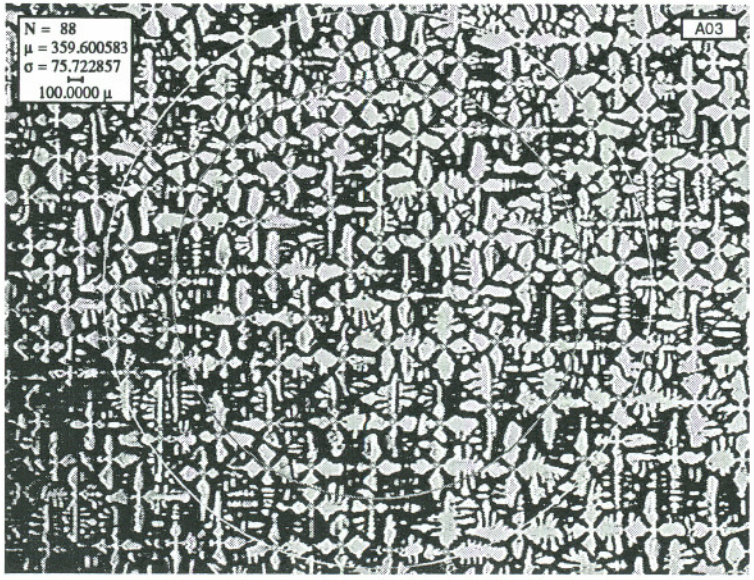
N = 88
μ = 359.600583
σ = 75.722857
100.0000 μ
A03


N = 108
μ = 328.578372
σ = 65.731589
100.0000 μ
A04

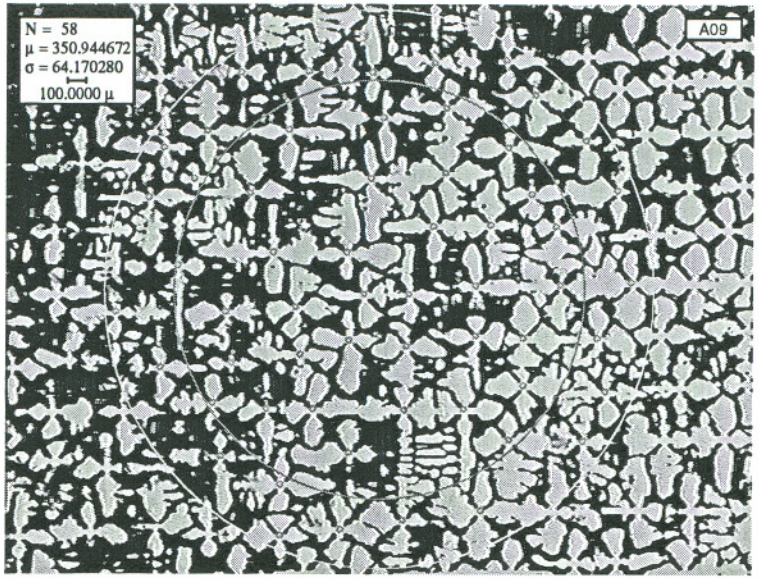
N = 58
μ = 350.944672
σ = 64.170280
100.0000 μ
A09


N = 69
μ = 411.076535
σ = 85.564558
100.0000 μ
A10

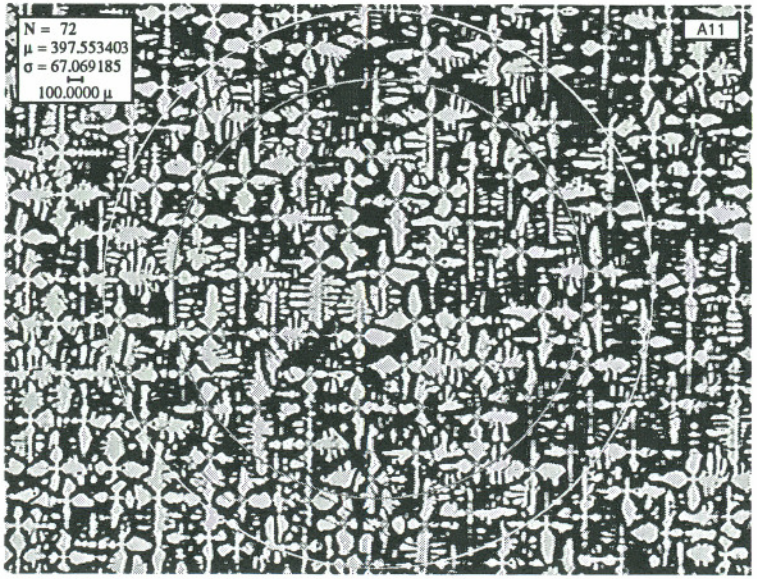
N = 72
μ = 397.553403
σ = 67.069185
100.0000 μ
A11

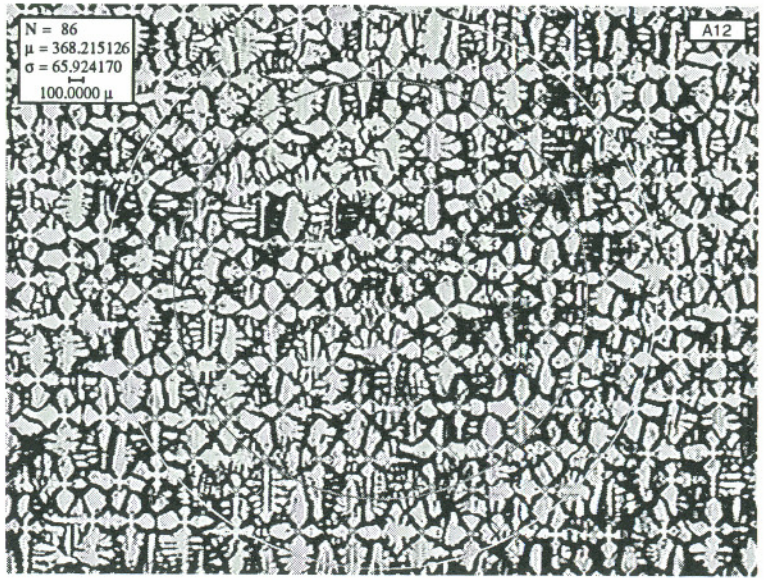
N = 86
μ = 368.215126
σ = 65.924170
100.0000 μ
A12

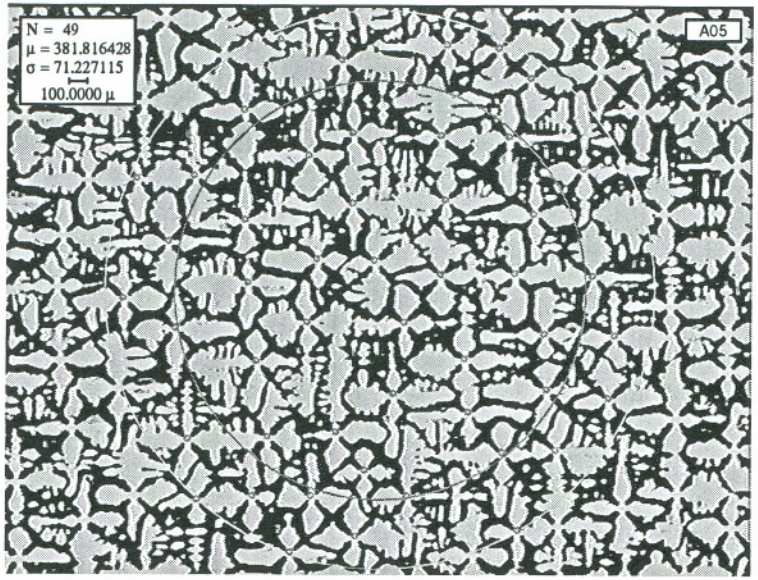
N = 49
μ = 381.816428
σ = 71.227115
100.0000 μ
A05


N = 81
μ = 379.406462
σ = 66.853660
100.0000 μ
A06

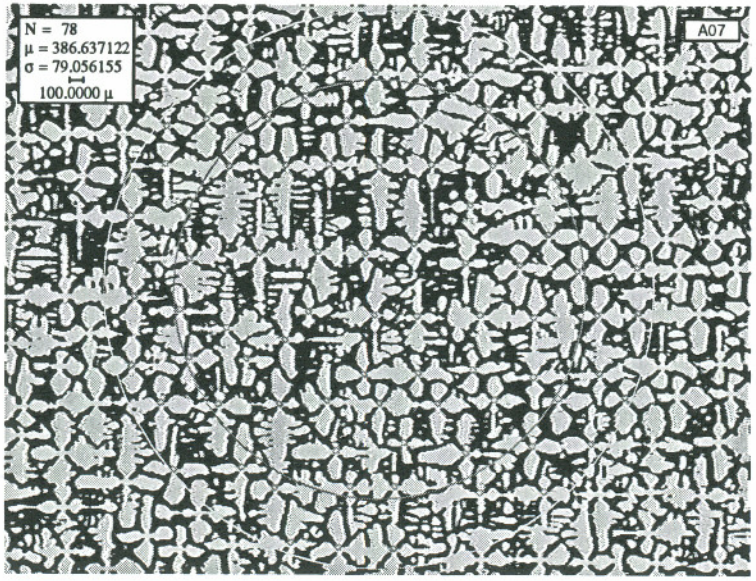
N = 78
μ = 386.637122
σ = 79.056155
100.0000 μ
A07

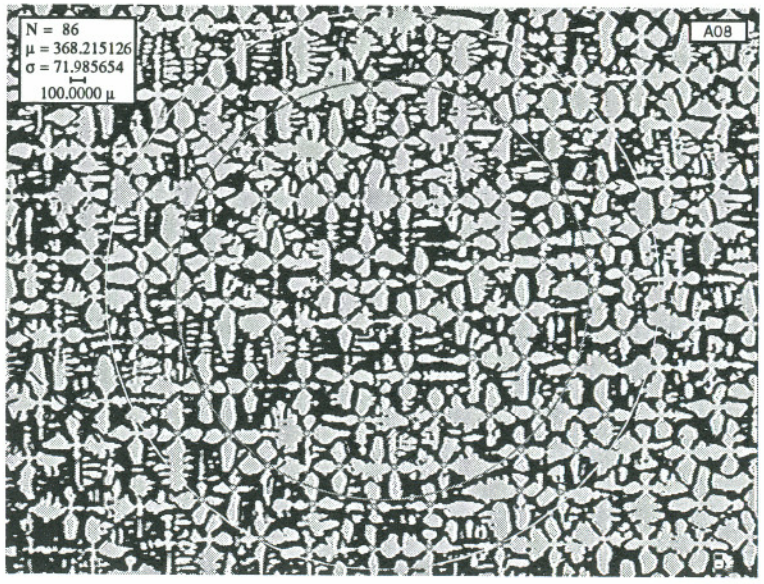
N = 86
μ = 368.215126
σ = 71.985654
100.0000 μ
A08


A14
N = 84
μ = 372.572853
σ = 68.444689
100.0000 μ

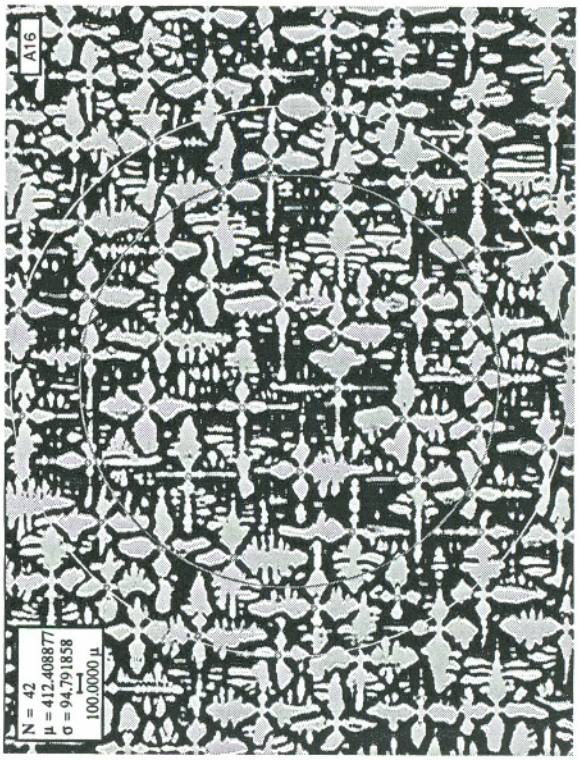
A16
N = 42
μ = 412.408877
σ = 94.791858
100.0000 μ


A13
N = 81
μ = 379.409623
σ = 73.475772
100.0000 μ

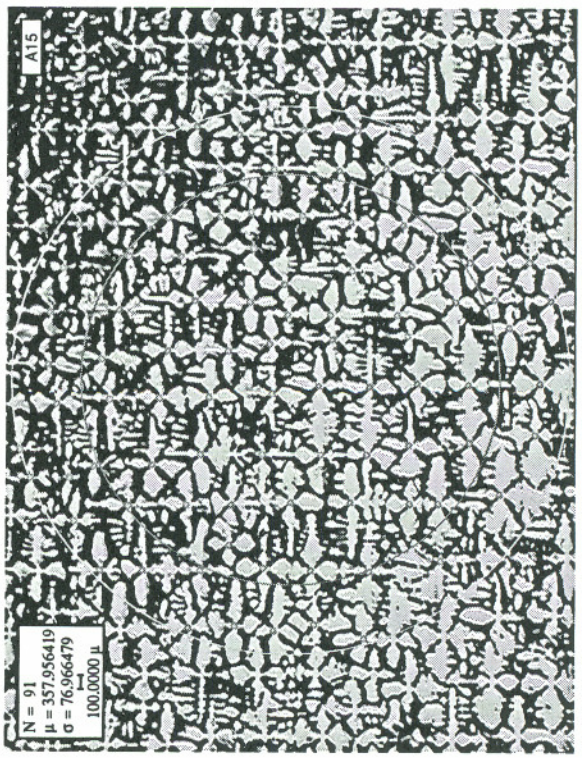
A15
N = 91
μ = 357.956419
σ = 76.966479
100.0000 μ


N = 65
μ = 423.536218
σ = 75.044028
100.0000 μ
A17

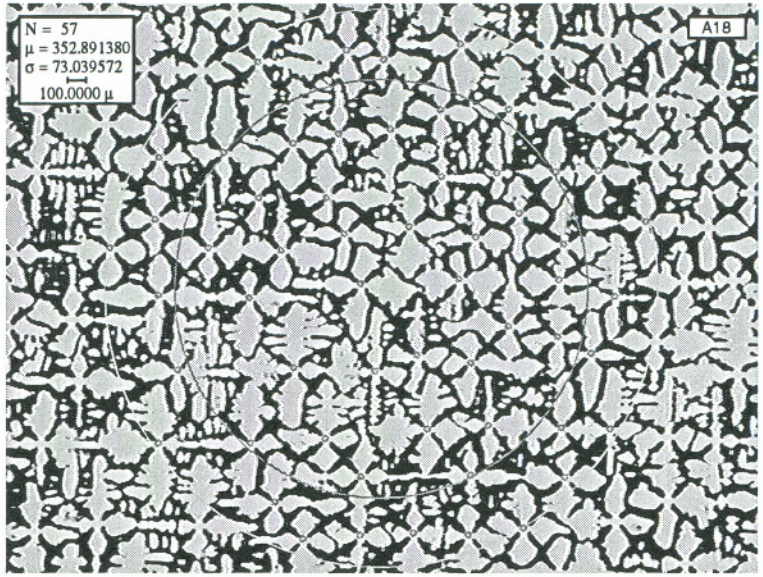
N = 57
μ = 352.891380
σ = 73.039572
100.0000 μ
A18

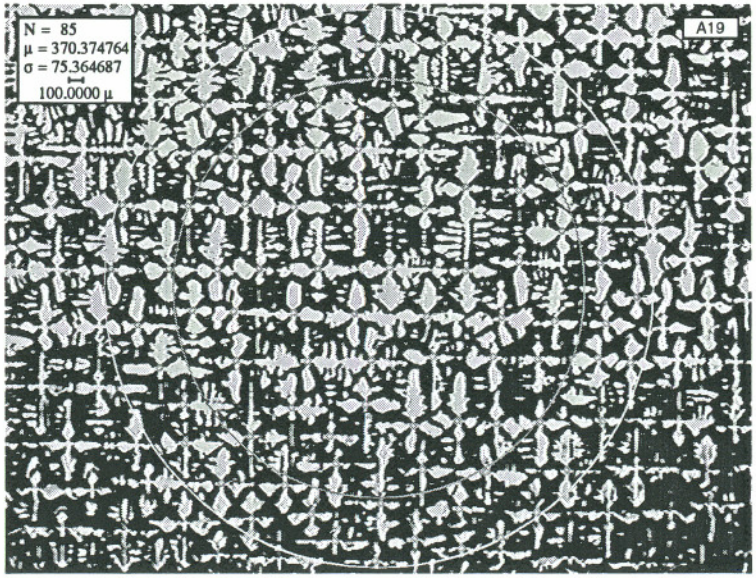
N = 85
μ = 370.374764
σ = 75.364687
100.0000 μ
A19

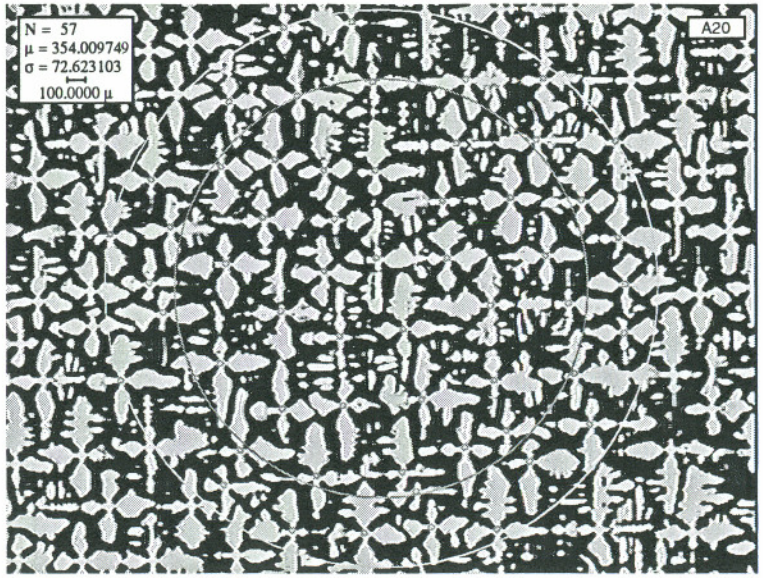
N = 57
μ = 354.009749
σ = 72.623103
100.0000 μ
A20

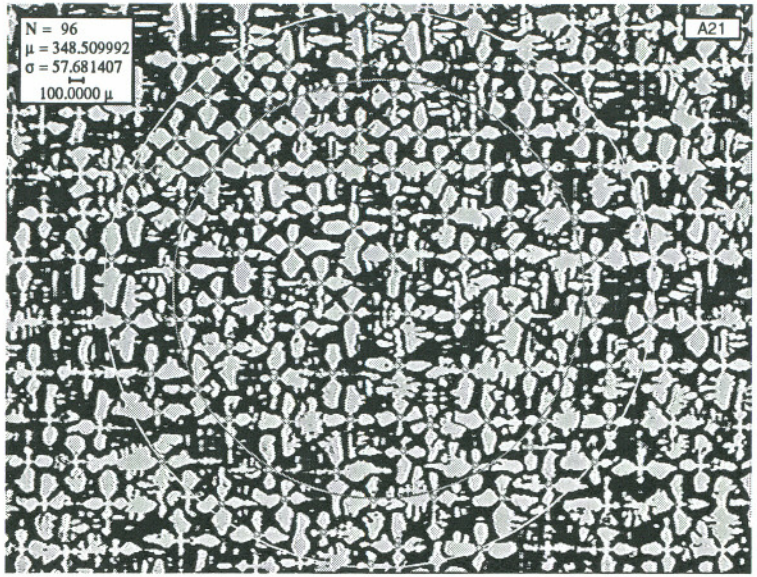
N = 96
μ = 348.509992
σ = 57.681407
100.0000 μ
A21

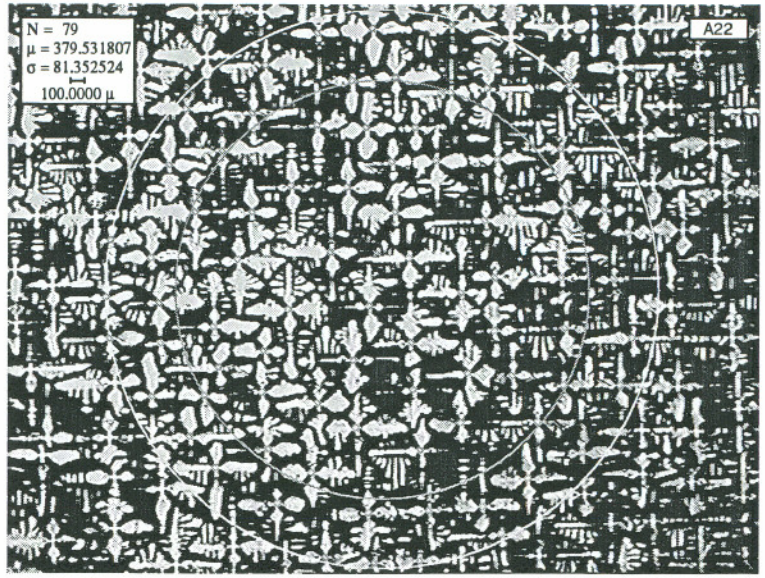
N = 79
μ = 379.531807
σ = 81.352524
100.0000 μ
A22

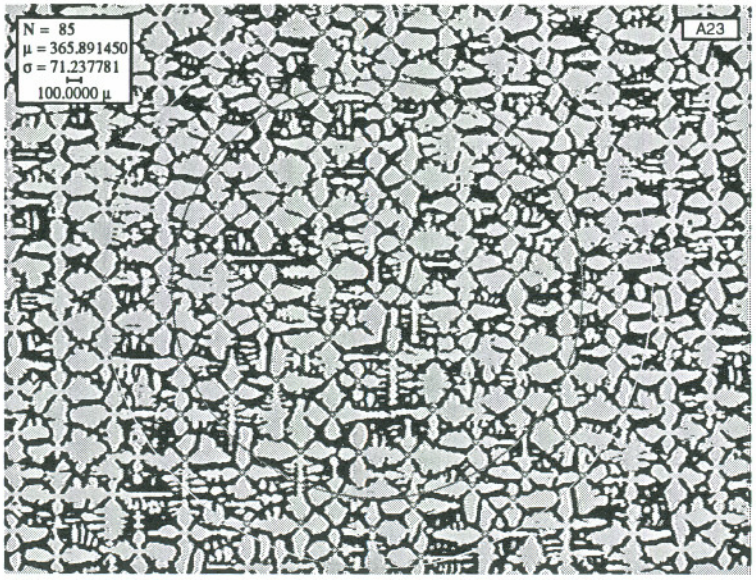
N = 85
μ = 365.891450
σ = 71.237781
100.0000 μ
A23

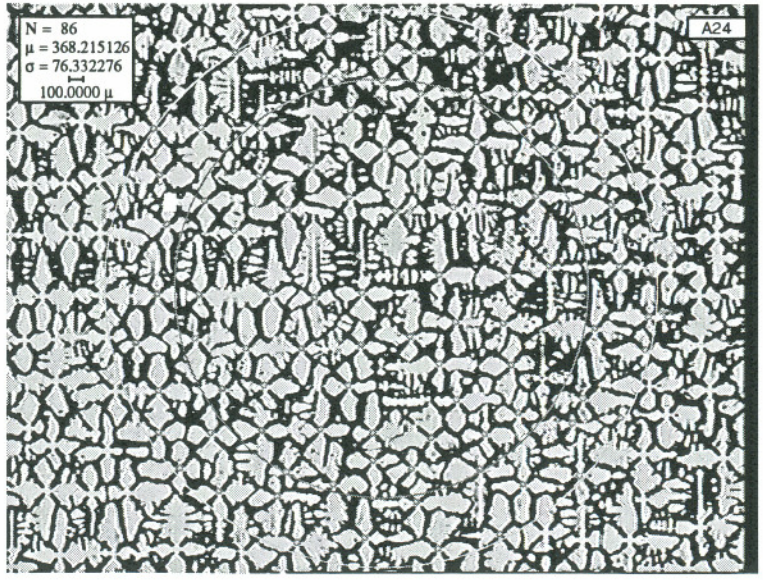
N = 86
μ = 368.215126
σ = 76.332276
100.0000 μ
A24

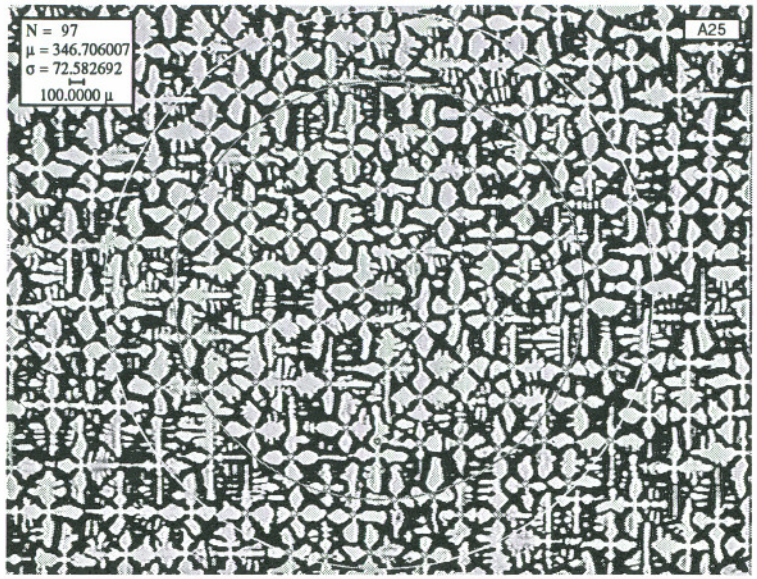
N = 97
μ = 346.706007
σ = 72.582692
100.0000 μ
A25

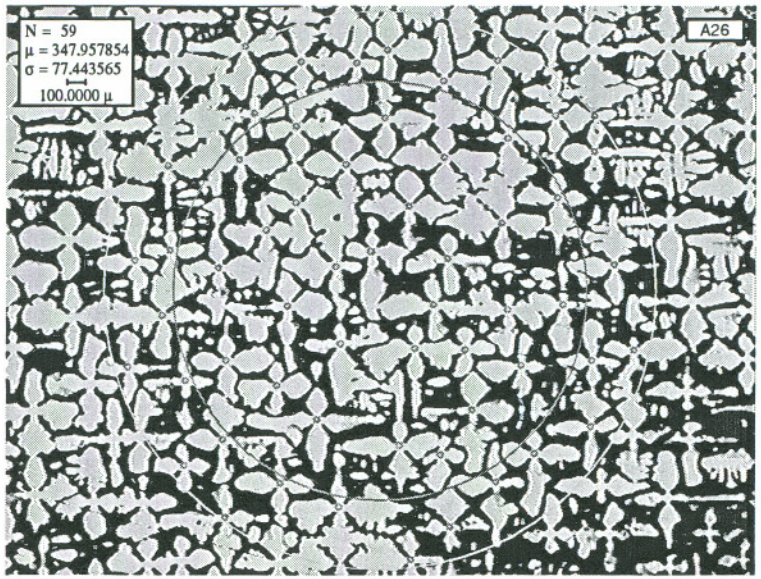
N = 59
μ = 347.957854
σ = 77.443565
100.0000 μ
A26

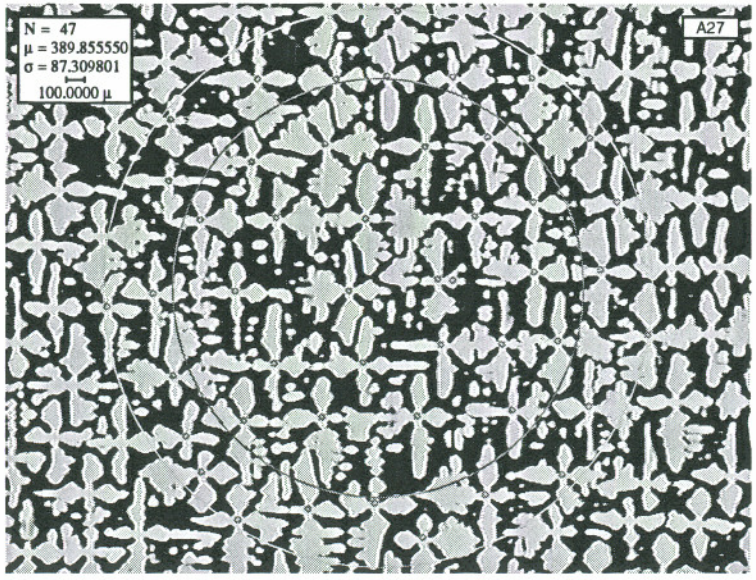
N = 47
μ = 389.855550
σ = 87.309801
100.0000 μ
A27

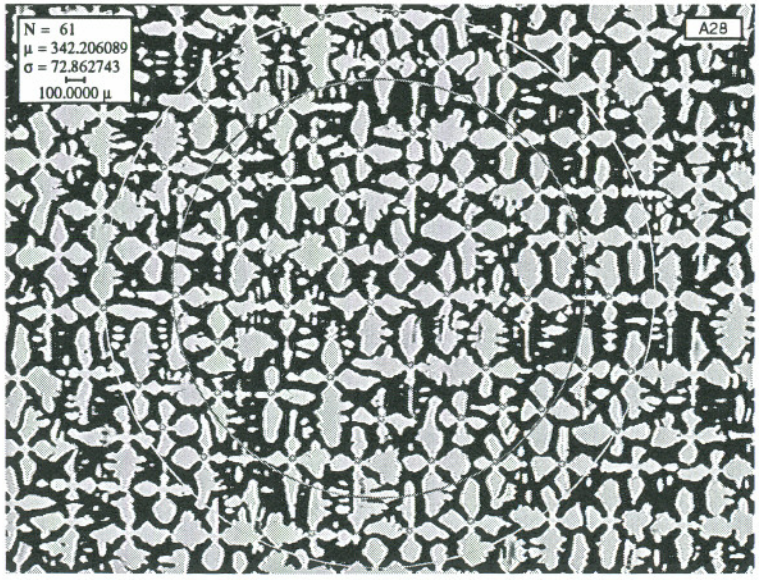
N = 61
μ = 342.206089
σ = 72.862743
100.0000 μ
A28

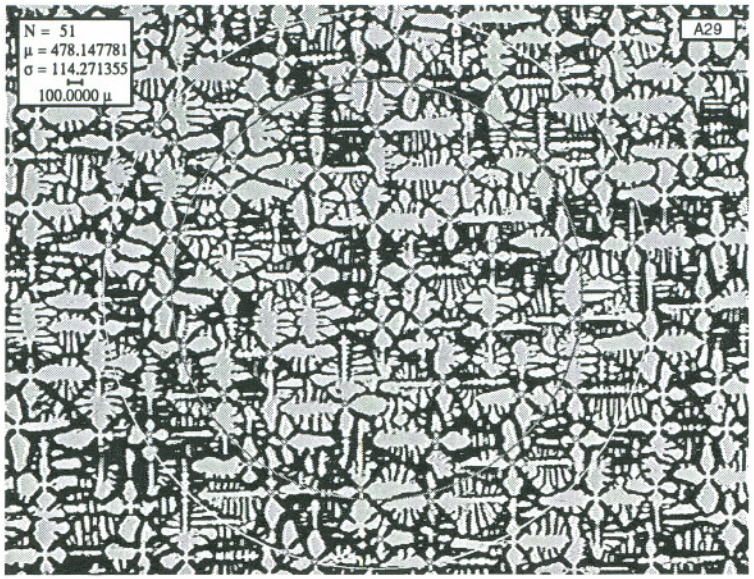
N = 51
μ = 478.147781
σ = 114.271355
100.0000 μ
A29

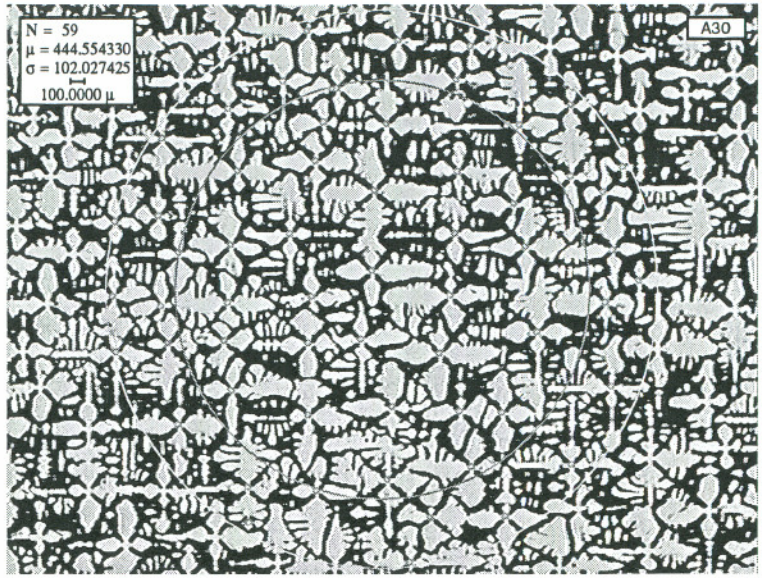
N = 59
μ = 444.554330
σ = 102.027425
100.0000 μ
A30

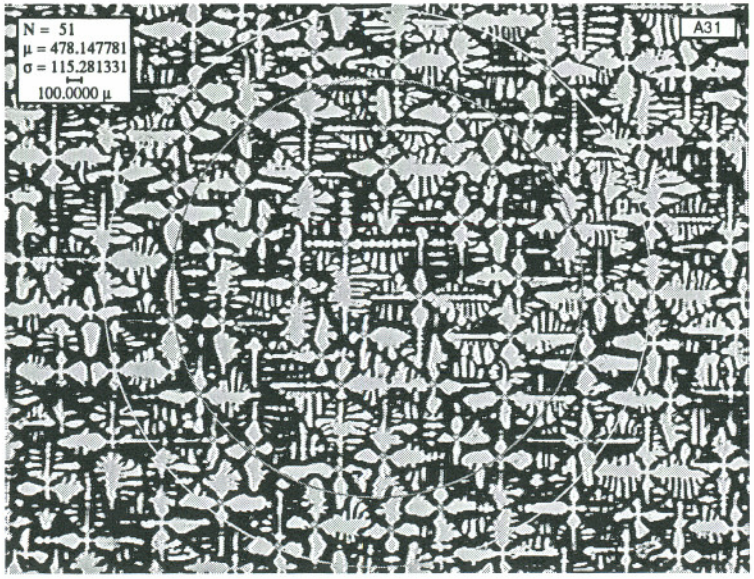
N = 51
μ = 478.147781
σ = 115.281331
100.0000 μ
A31

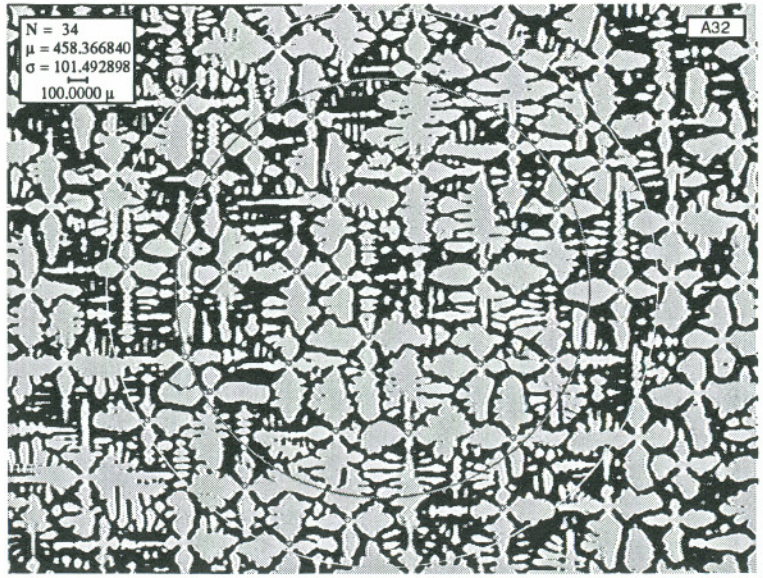
N = 34
μ = 458.366840
σ = 101.492898
100.0000 μ
A32

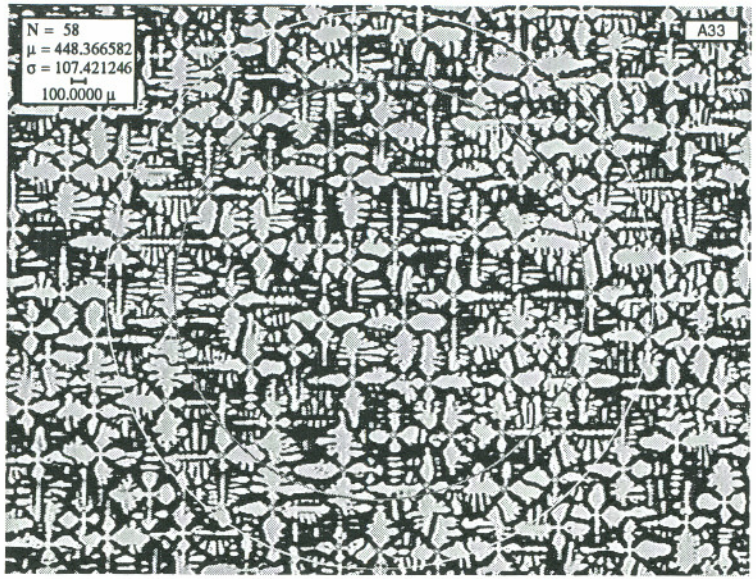
N = 58
μ = 448.366582
σ = 107.421246
100.0000 μ
A33

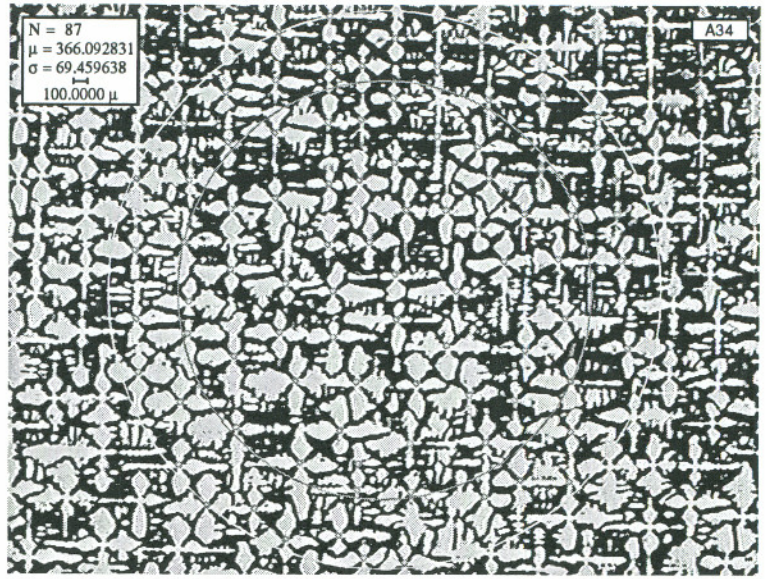
N = 87
μ = 366.092831
σ = 69.459638
100.0000 μ
A34

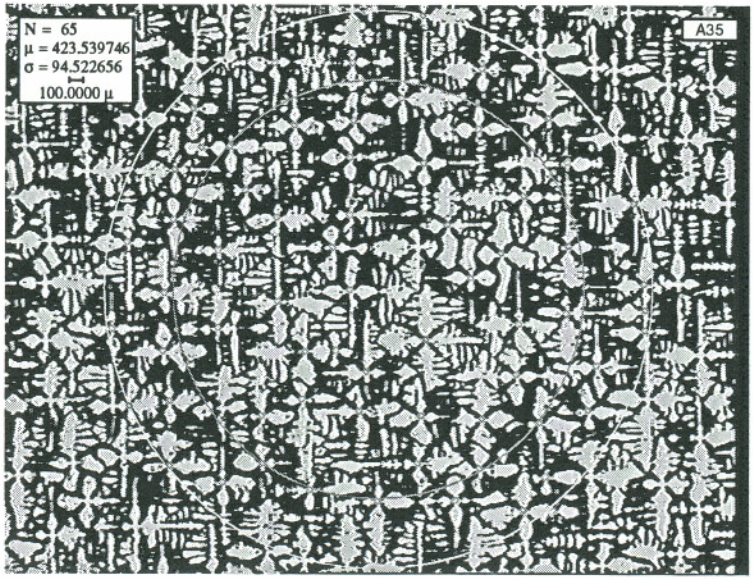
N = 65
μ = 423.539746
σ = 94.522656
100.0000 μ
A35

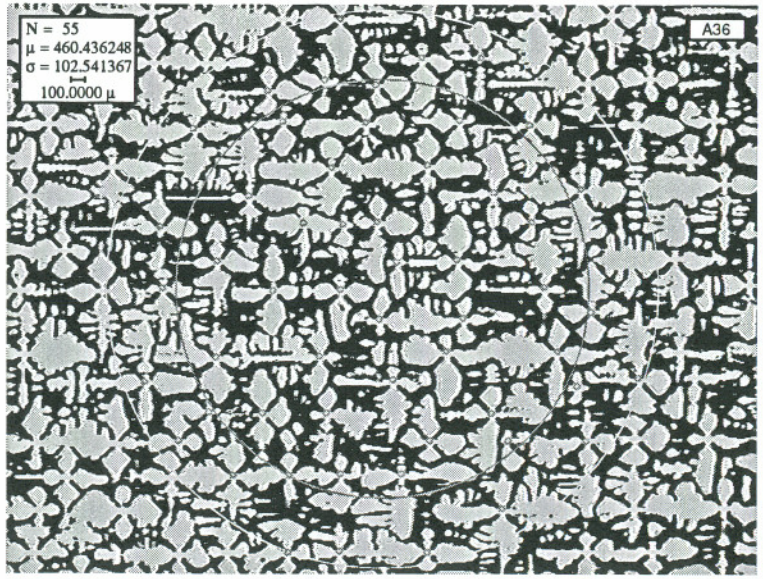
N = 55
μ = 460.436248
σ = 102.541367
100.0000 μ
A36


A37
N = 31
μ = 480.033784
σ = 110.416343
100.0000 μ

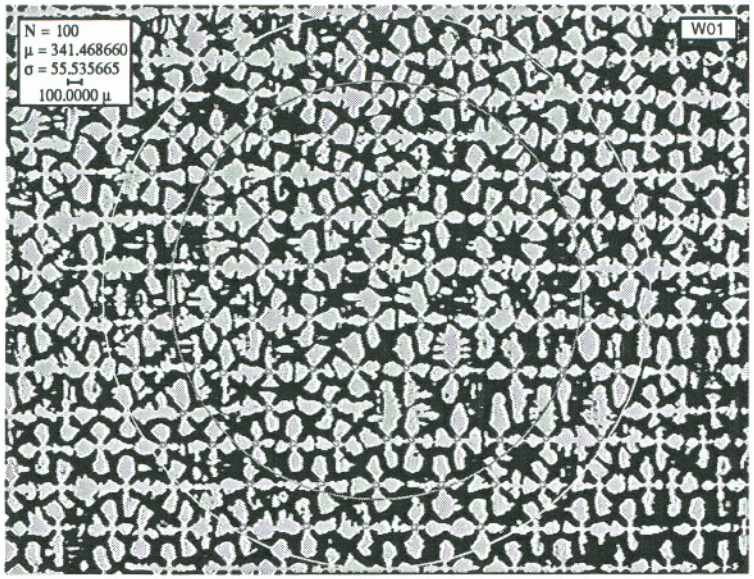
N = 100
μ = 341.468660
σ = 55.535665
100.0000 μ
W01

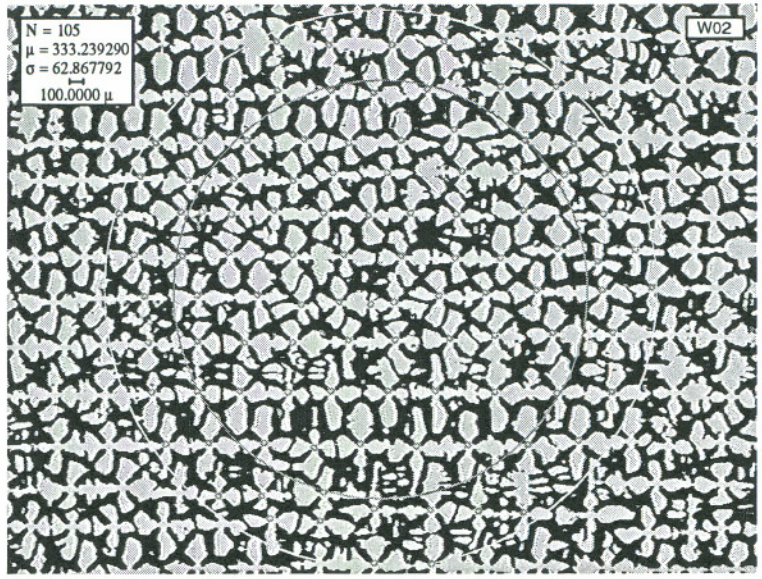
N = 105
μ = 333.239290
σ = 62.867792
100.0000 μ
W02

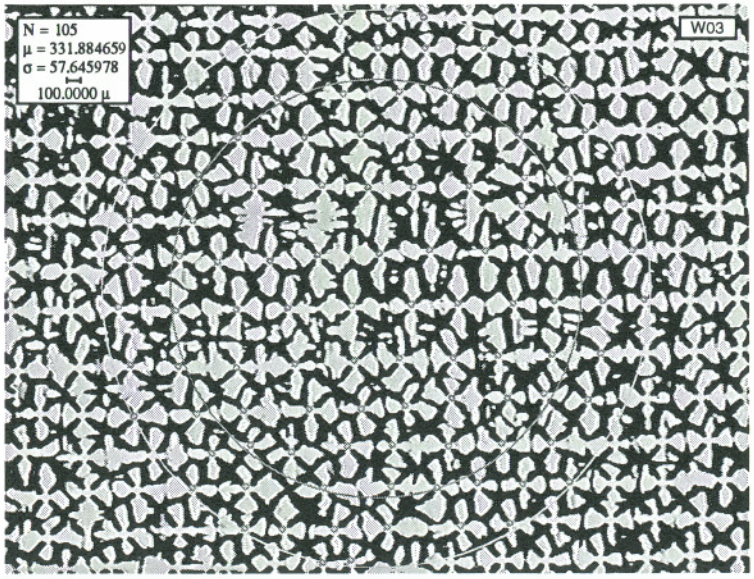
N = 105
μ = 331.884659
σ = 57.645978
100.0000 μ
W03

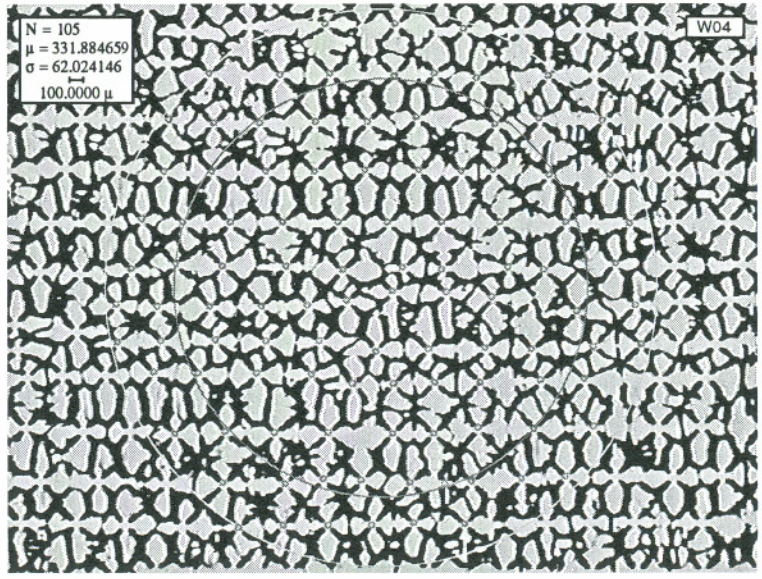
N = 105
μ = 331.884659
σ = 62.024146
100.0000 μ
W04

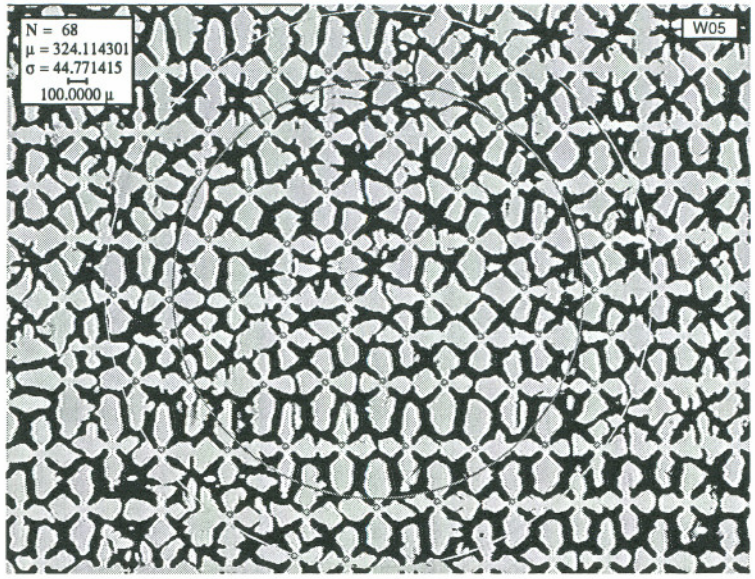
N = 68
μ = 324.114301
σ = 44.771415
100.0000 μ
W05

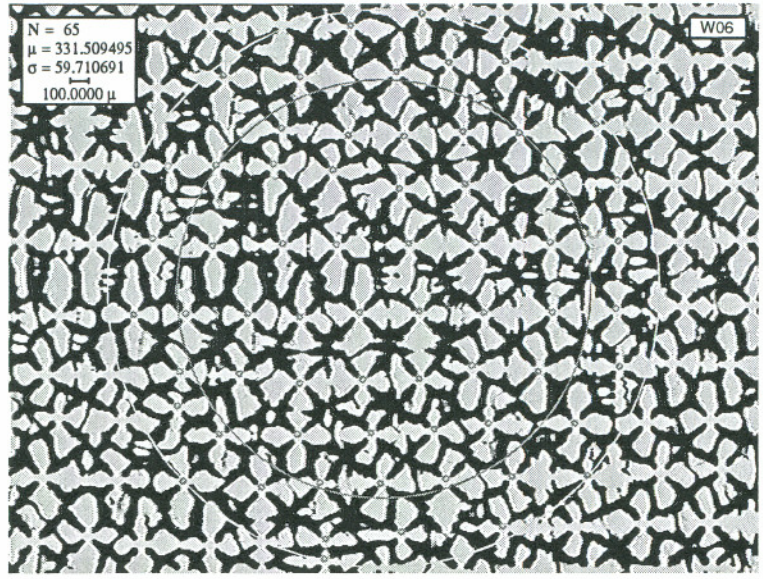
N = 65
μ = 331.509495
σ = 59.710691
100.0000 μ
W06

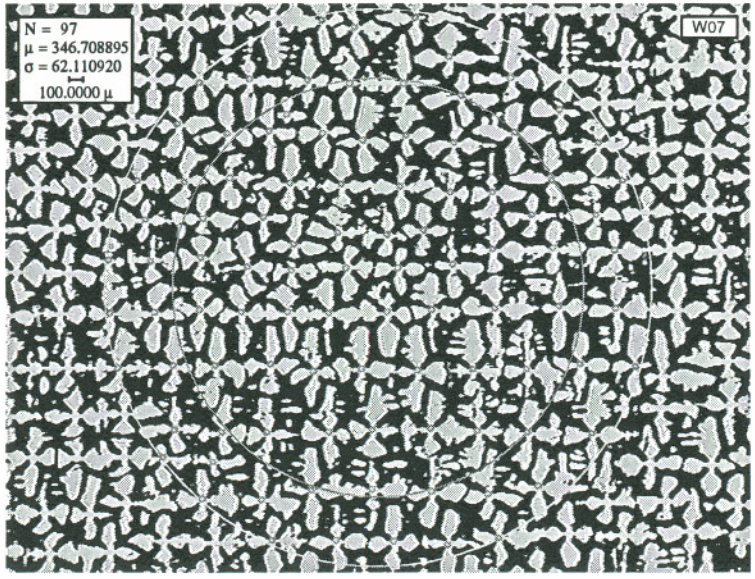
N = 97
μ = 346.708895
σ = 62.110920
100.0000 μ
W07


N = 94
μ = 350.766332
σ = 65.793224
100.0000 μ
W08

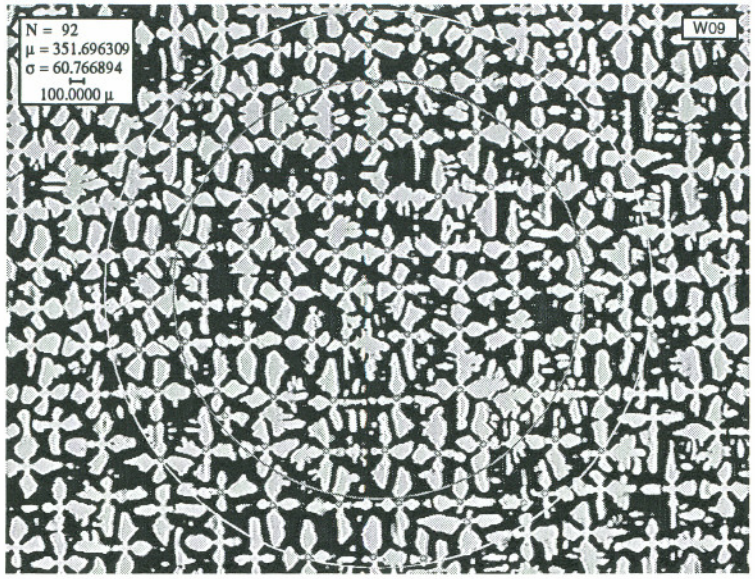
N = 92
μ = 351.696309
σ = 60.766894
100.0000 μ
W09

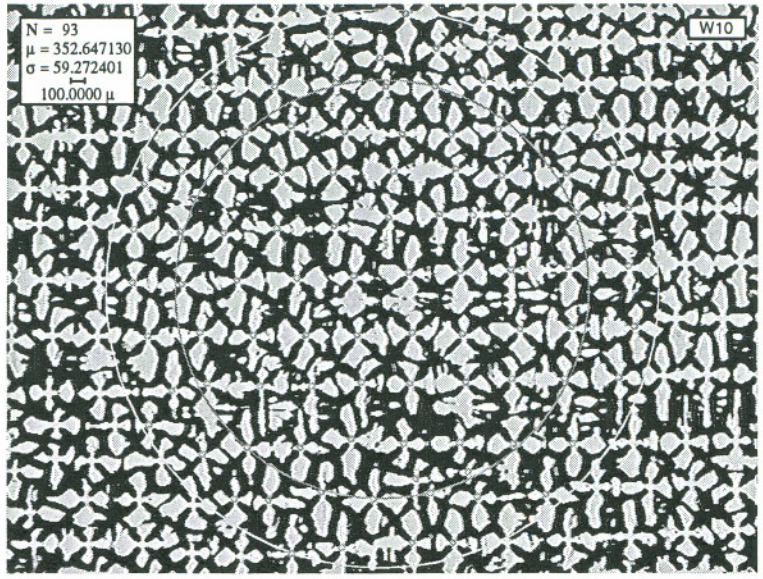
N = 93
μ = 352.647130
σ = 59.272401
100.0000 μ
W10

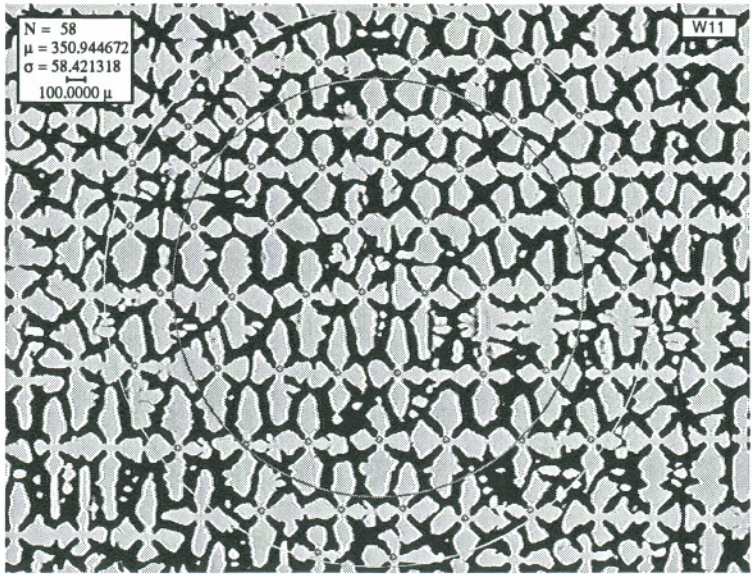
N = 58
μ = 350.944672
σ = 58.421318
100.0000 μ
W11

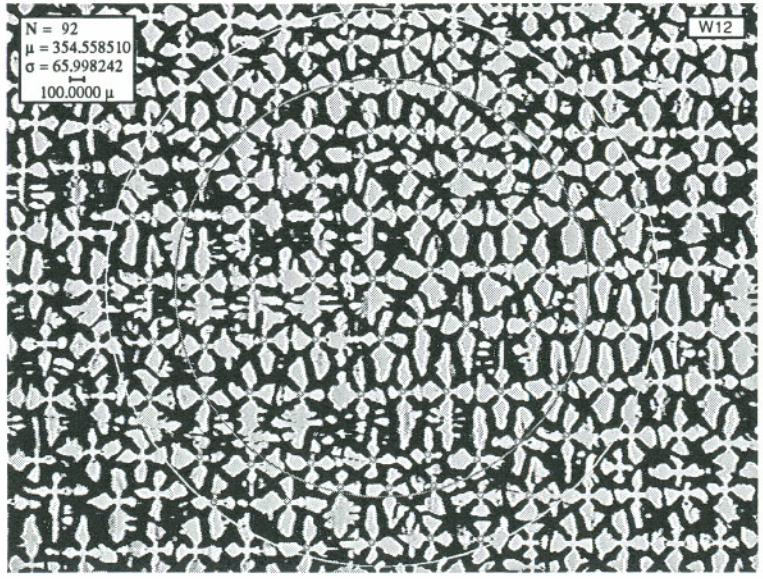
N = 92
μ = 354.558510
σ = 65.998242
100.0000 μ
W12

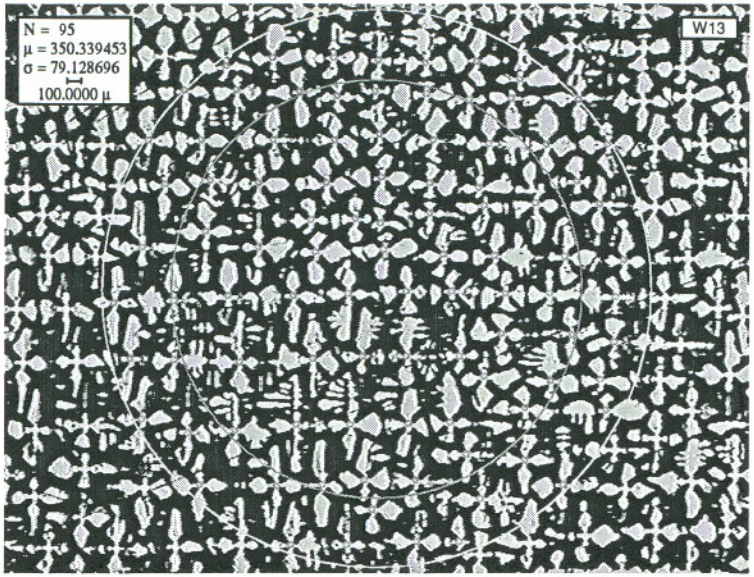
N = 95
μ = 350.339453
σ = 79.128696
100.0000 μ
W13

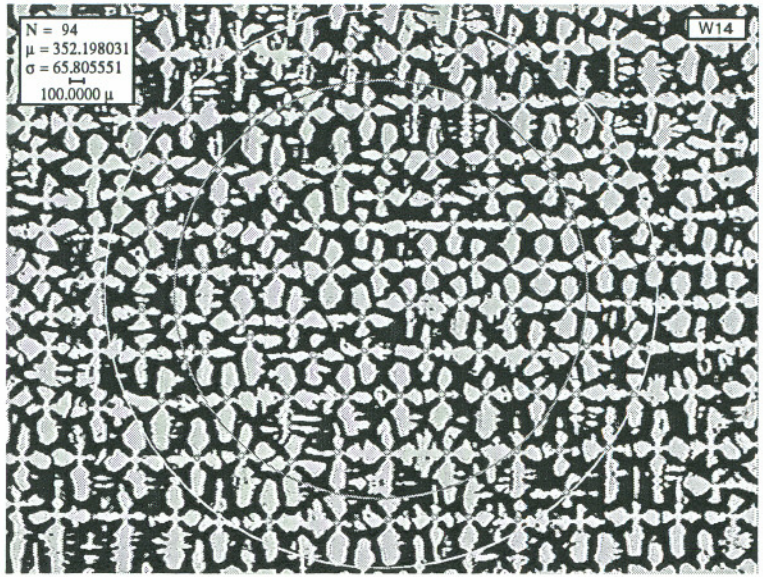
N = 94
μ = 352.198031
σ = 65.805551
100.0000 μ
W14

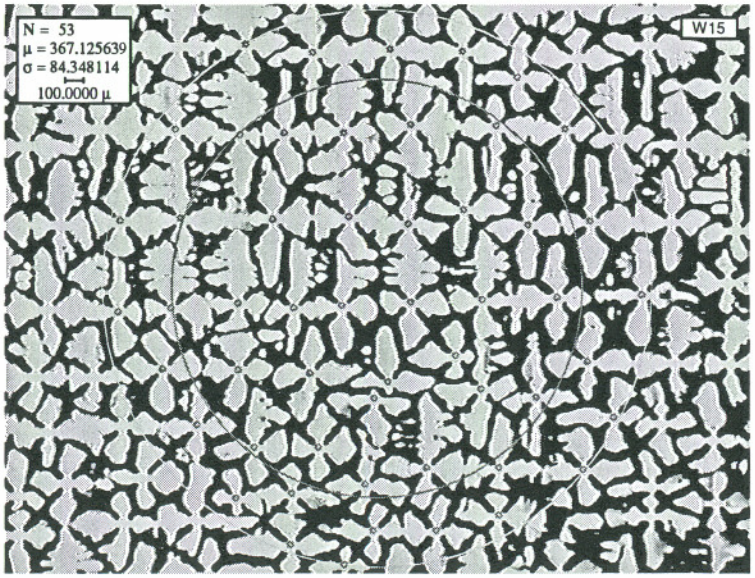
N = 53
μ = 367.125639
σ = 84.348114
100.0000 μ
W15

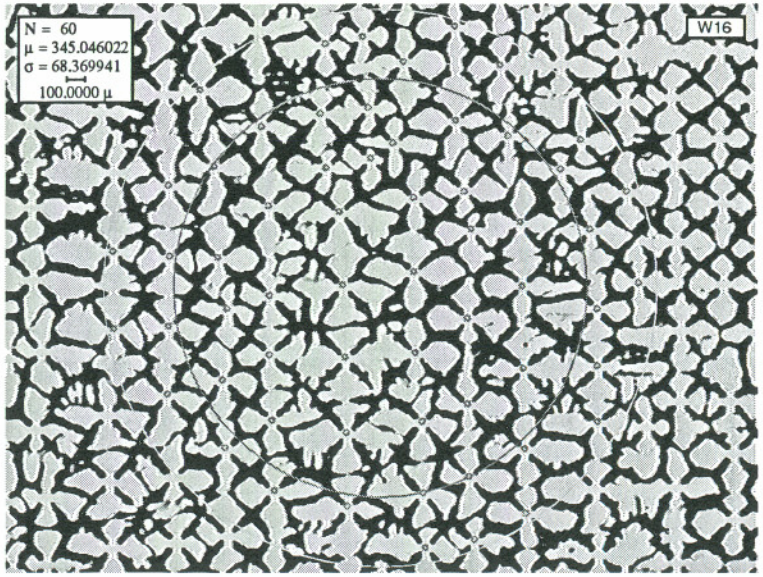
N = 60
μ = 345.046022
σ = 68.369941
100.0000 μ
W16

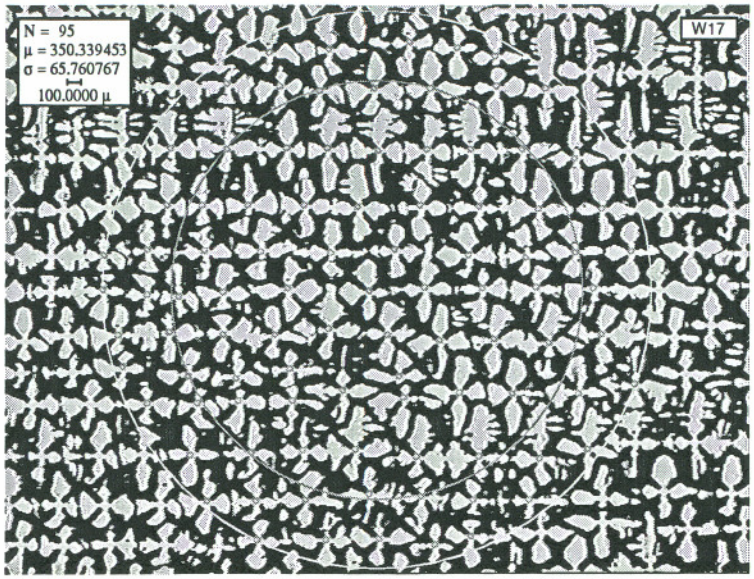
N = 95
μ = 350.339453
σ = 65.760767
100.0000 μ
W17

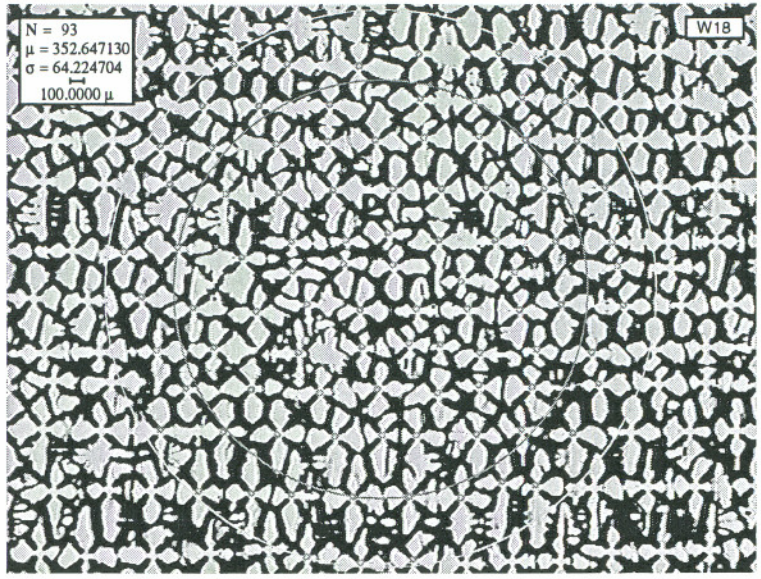
N = 93
μ = 352.647130
σ = 64.224704
100.0000 μ
W18

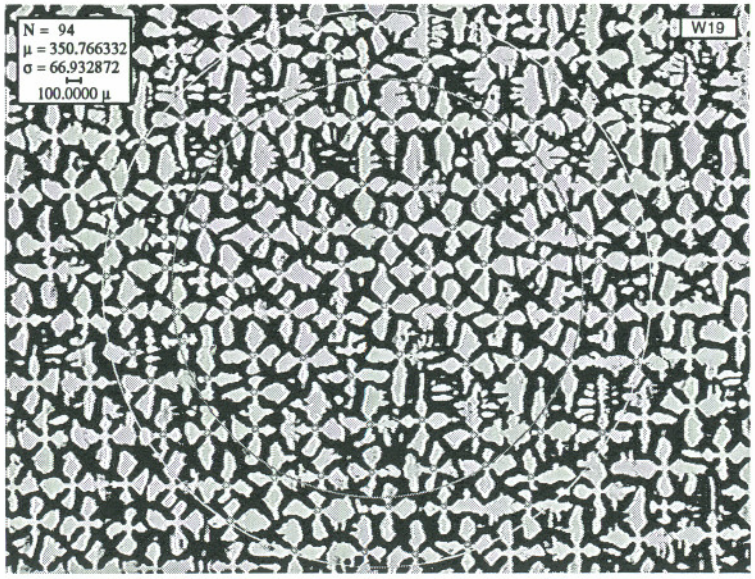
N = 94
μ = 350.766332
σ = 66.932872
100.0000 μ
W19

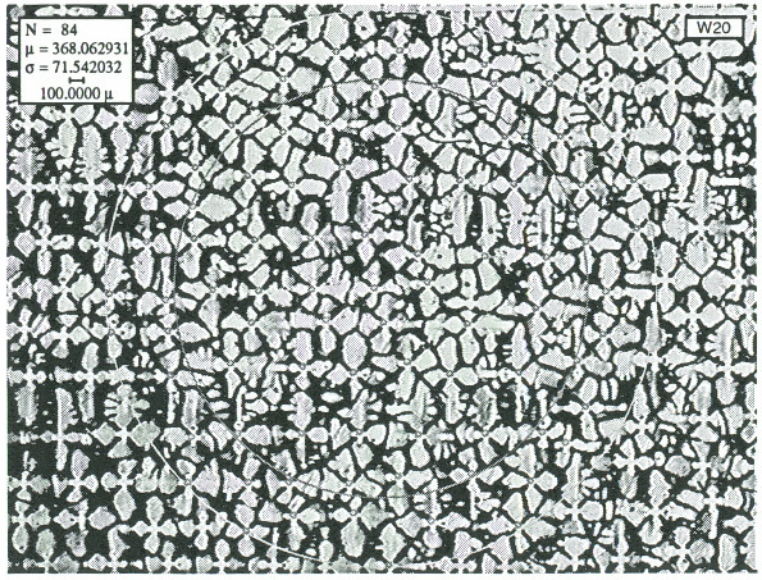
N = 84
μ = 368.062931
σ = 71.542032
100.0000 μ
W20

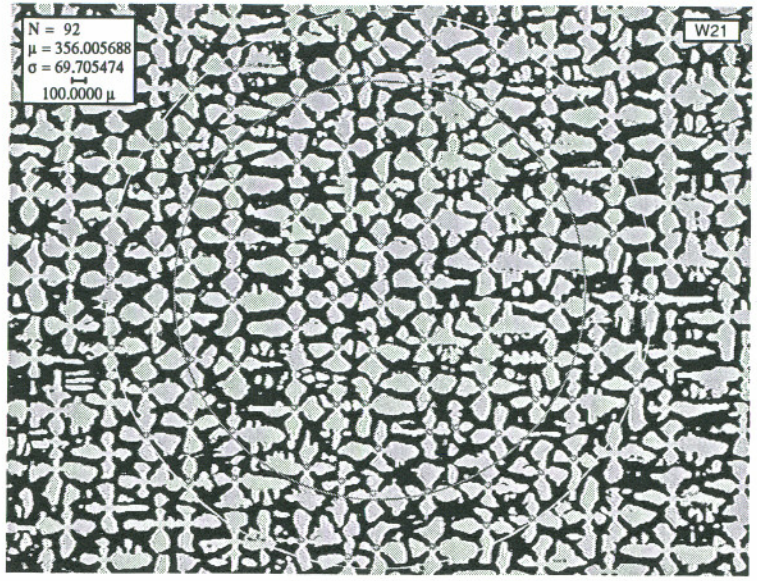
N = 92
μ = 356.005688
σ = 69.705474
100.0000 μ
W21

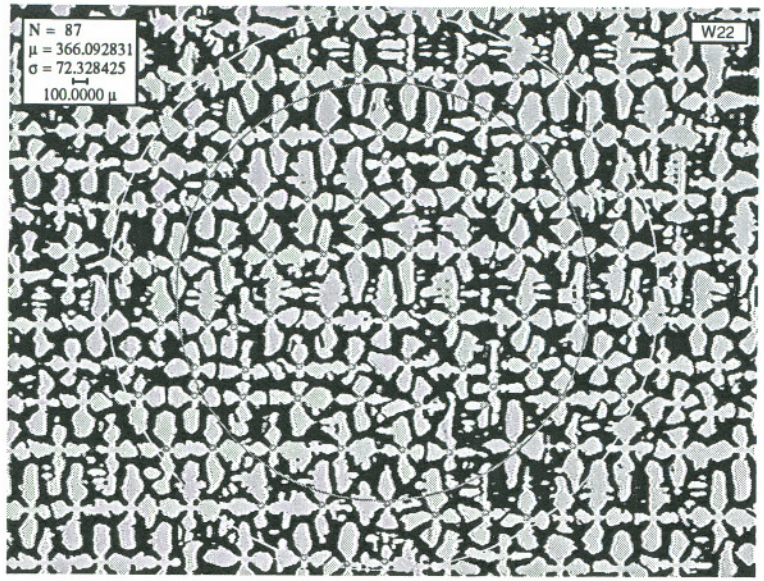
N = 87
μ = 366.092831
σ = 72.328425
100.0000 μ
W22

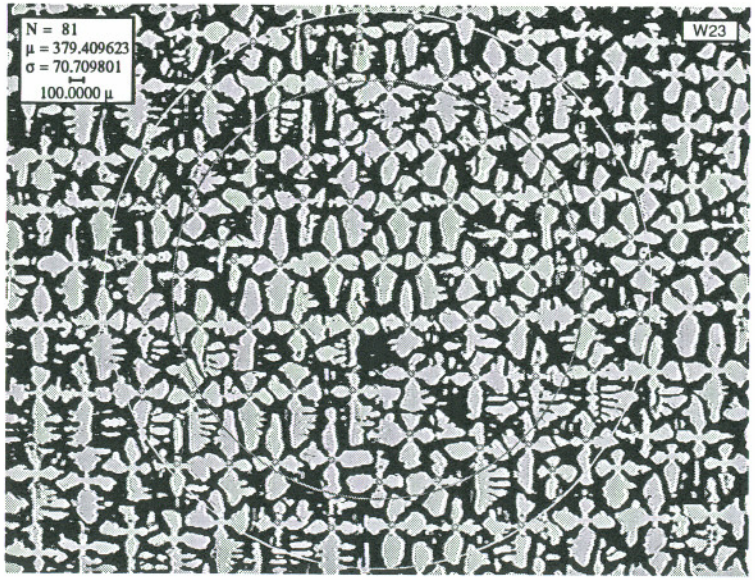
N = 81
μ = 379.409623
σ = 70.709801
100.0000 μ
W23

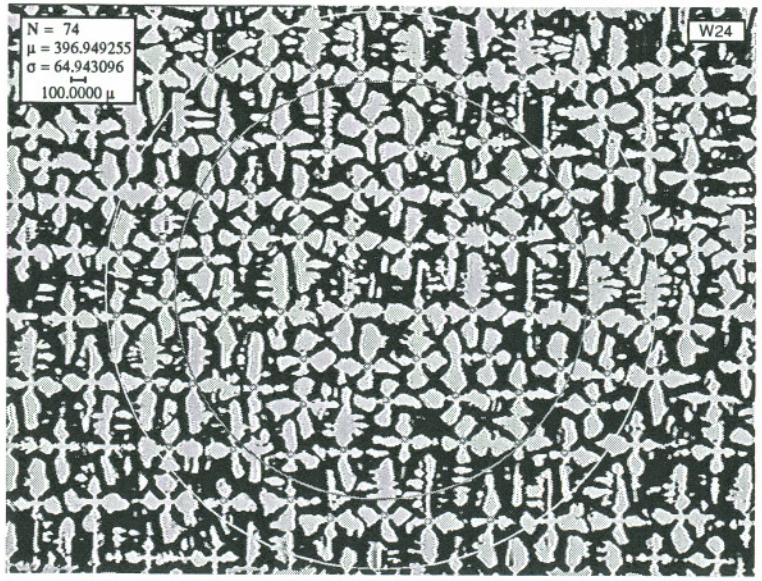
N = 74
μ = 396.949255
σ = 64.943096
100.0000 μ
W24


N = 89
μ = 361.956056
σ = 73.678937
100.0000 μ
W25

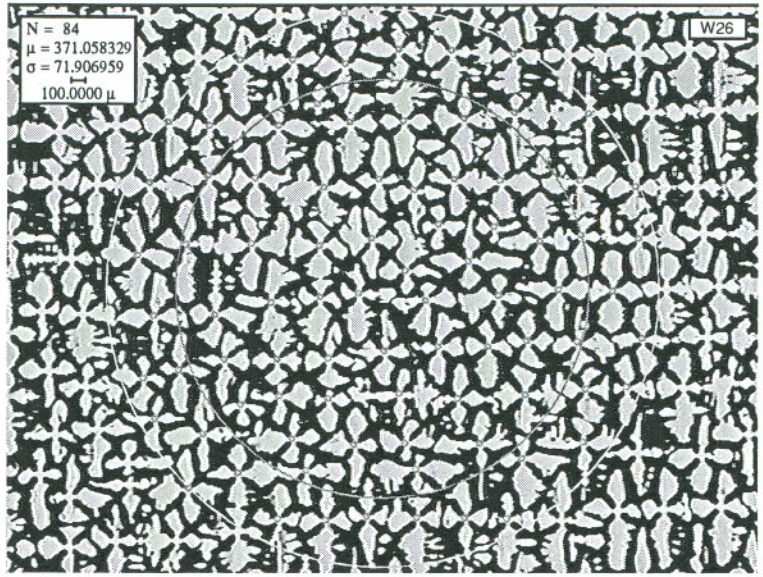
N = 84
μ = 371.058329
σ = 71.906959
100.0000 μ
W26

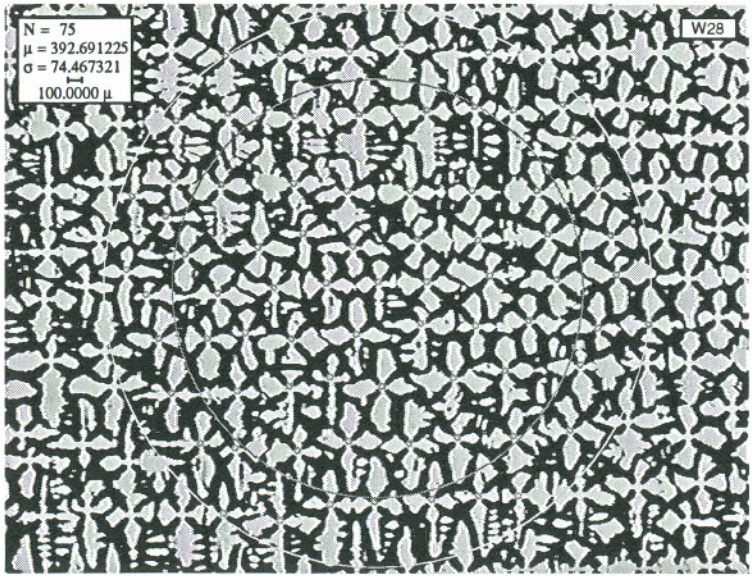
N = 75
μ = 392.691225
σ = 74.467321
100.0000 μ
W28

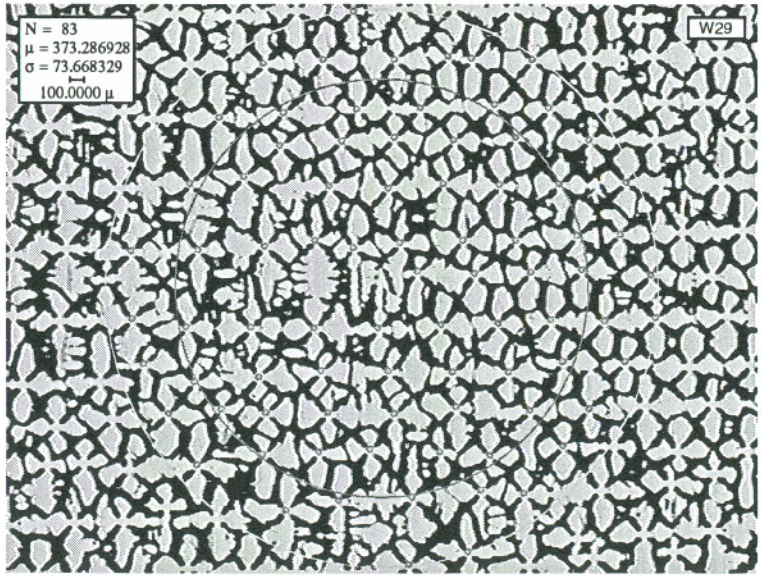
N = 83
μ = 373.286928
σ = 73.668329
100.0000 μ
W29


W30
N = 86
μ = 366.718317
σ = 74.320012
100.0000 μ

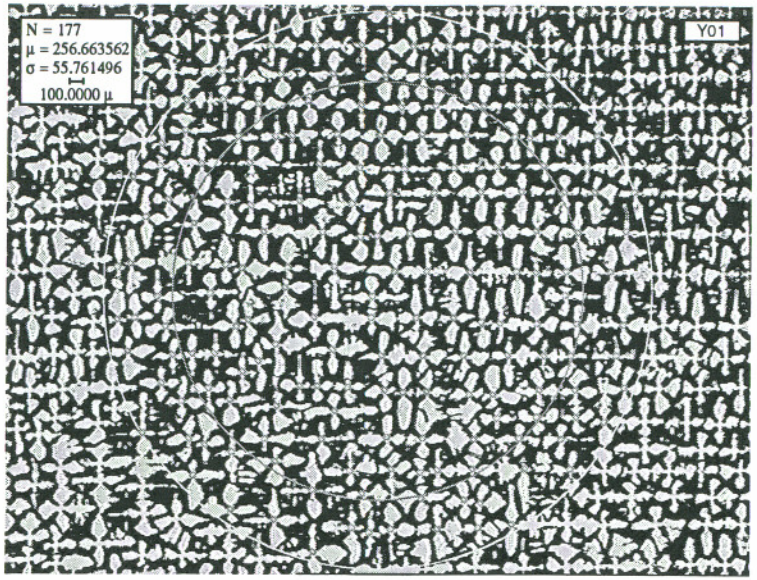
N = 177
μ = 256.663562
σ = 55.761496
100.0000 μ
Y01

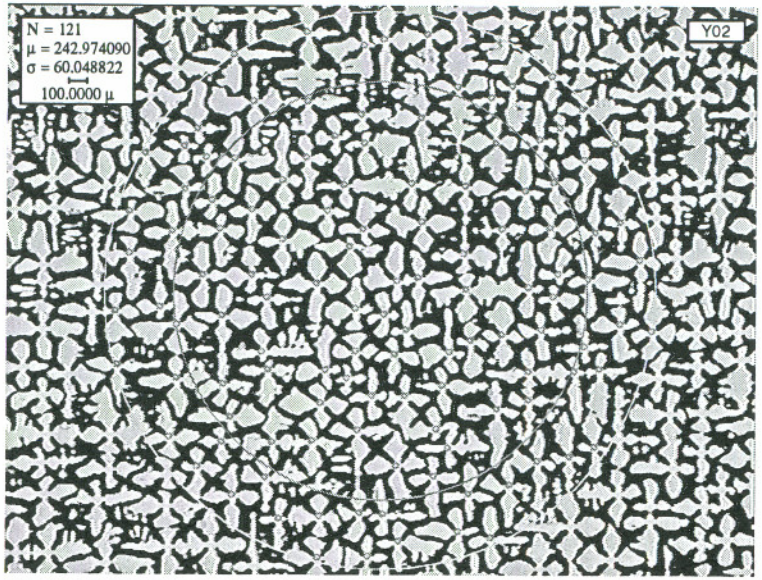
N = 121
μ = 242.974090
σ = 60.048822
100.0000 μ
Y02

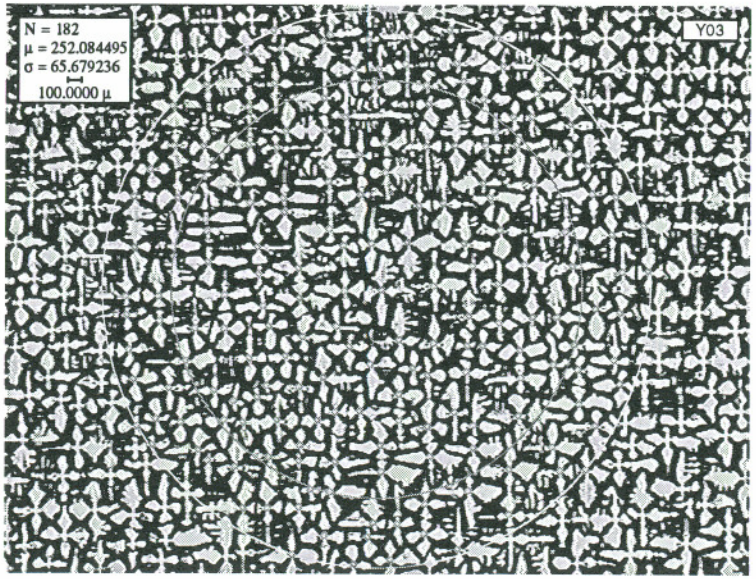
N = 182
μ = 252.084495
σ = 65.679236
100.0000 μ
Y03

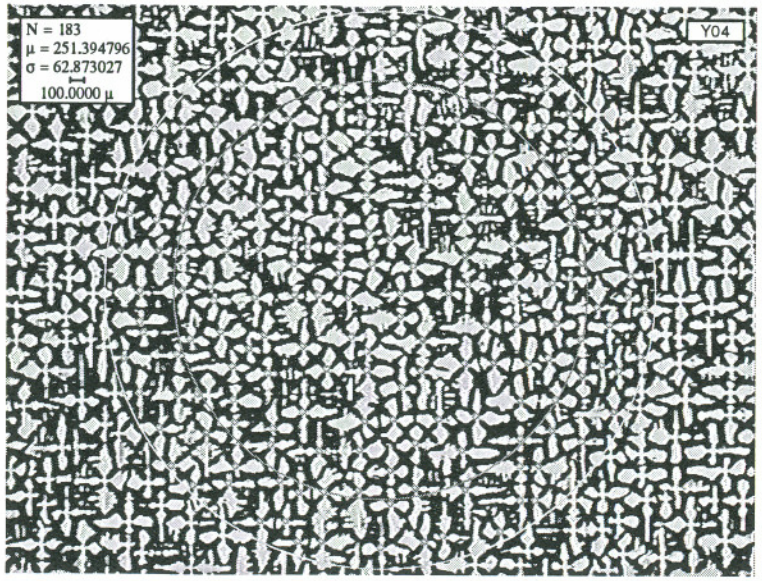
N = 183
μ = 251.394796
σ = 62.873027
100.0000 μ
Y04

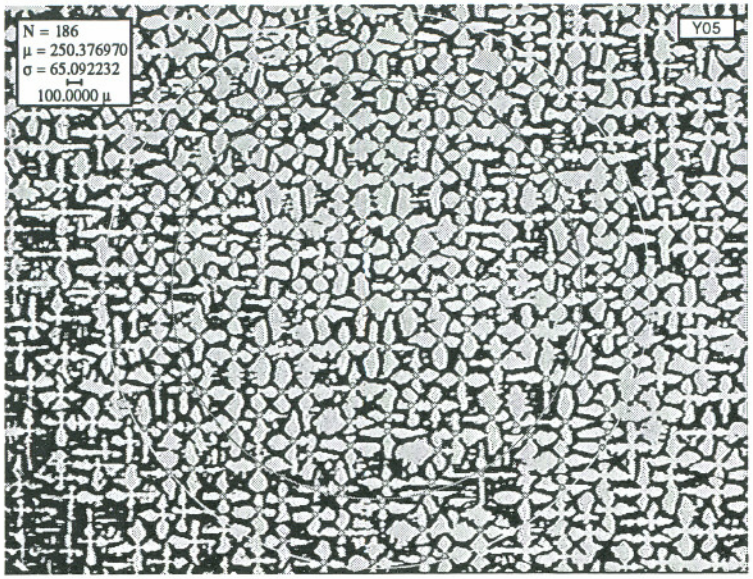
N = 186
μ = 250.376970
σ = 65.092232
100.0000 μ
Y05

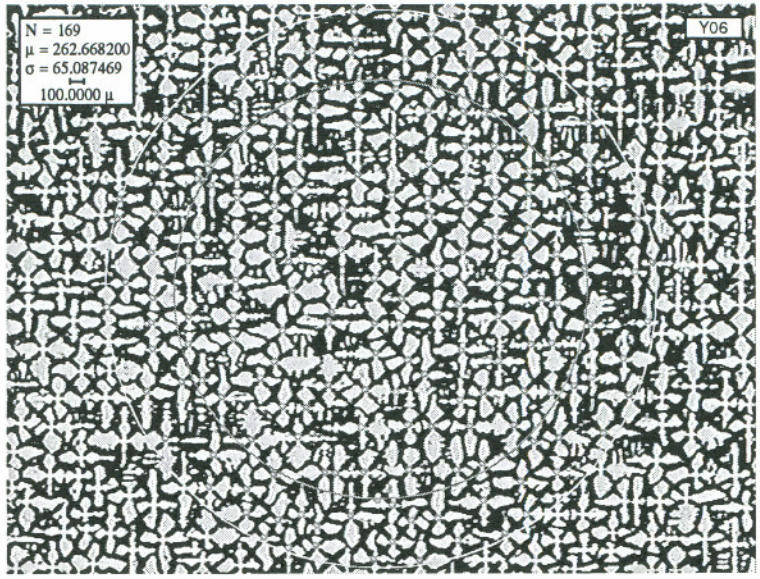
N = 169
μ = 262.668200
σ = 65.087469
100.0000 μ
Y06

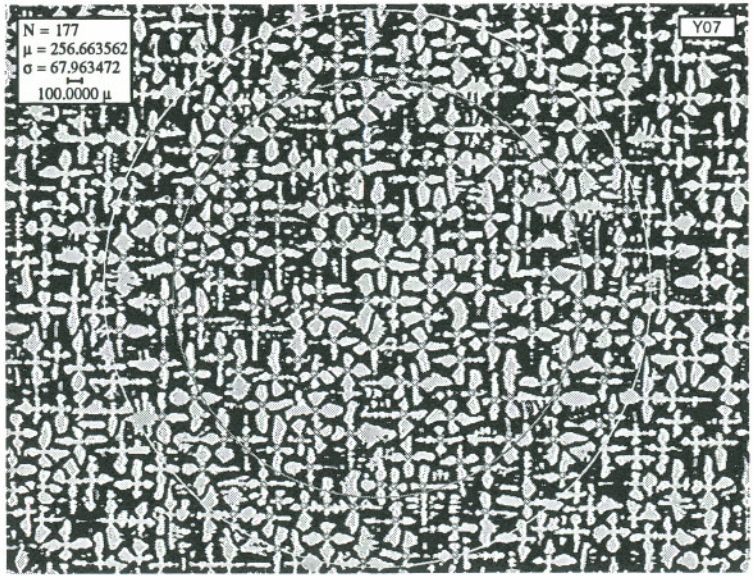
N = 177
μ = 256.663562
σ = 67.963472
100.0000 μ
Y07

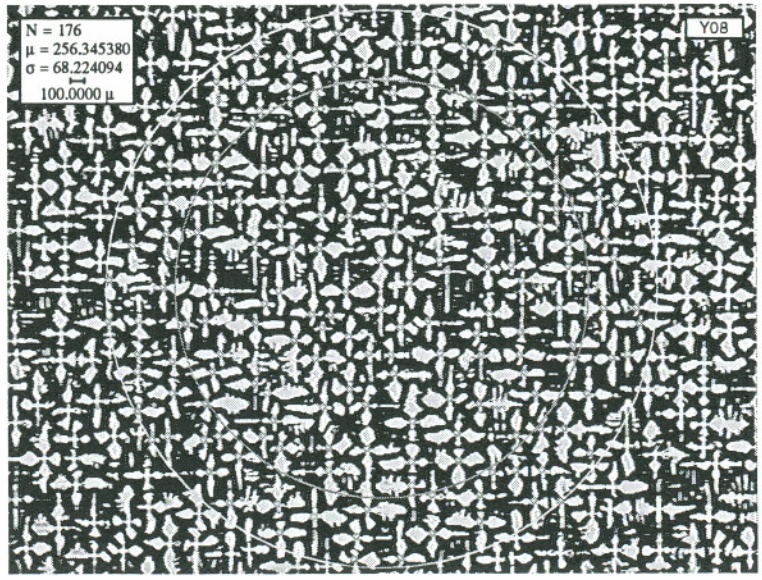
N = 176
μ = 256.345380
σ = 68.224094
100.0000 μ
Y08


Y10
N = 116
μ = 248.155357
σ = 60.883488
100.0000 μ

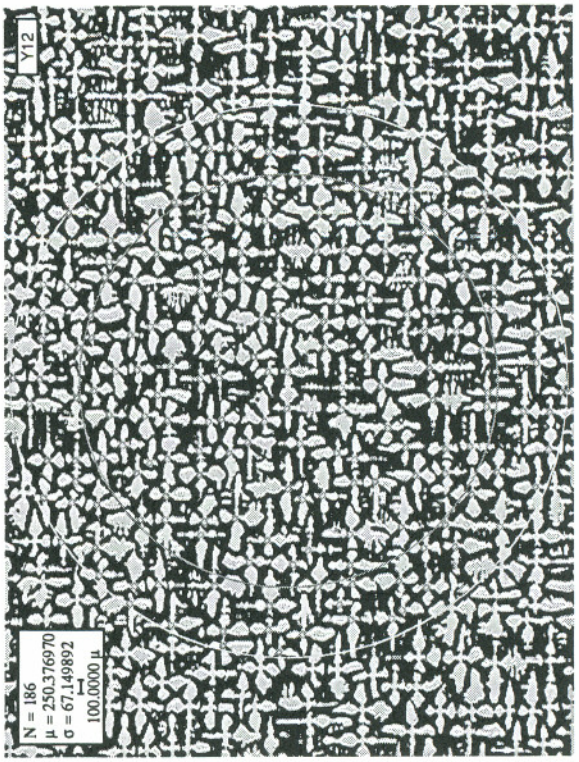
Y12
N = 186
μ = 250.376970
σ = 67.149892
100.0000 μ

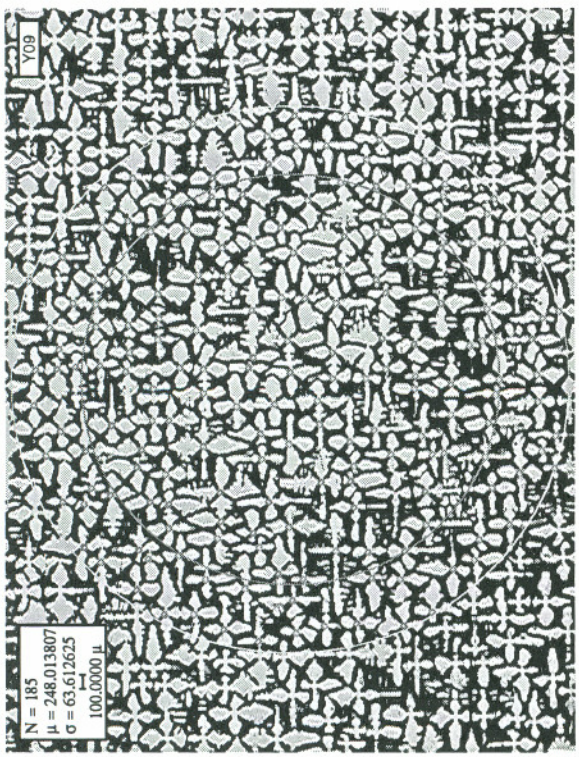
Y09
N = 185
μ = 248.013807
σ = 63.612625
100.0000 μ

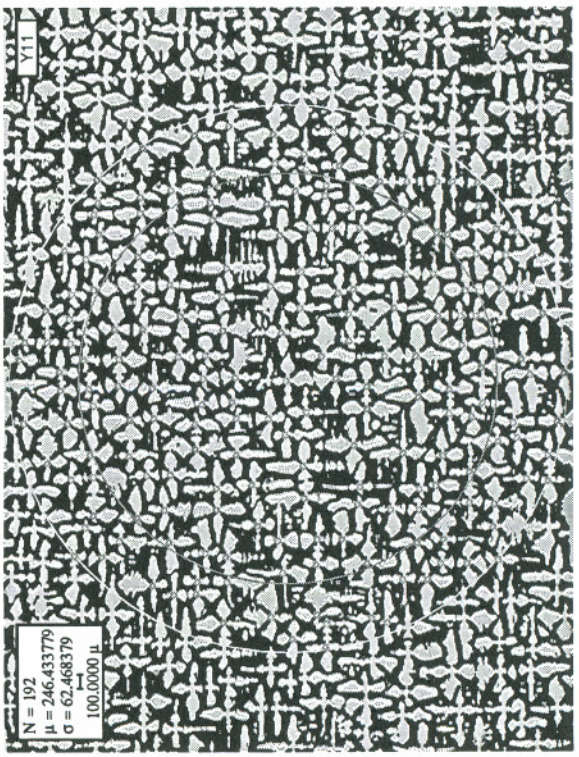
Y11
N = 192
μ = 246.433779
σ = 62.468379
100.0000 μ

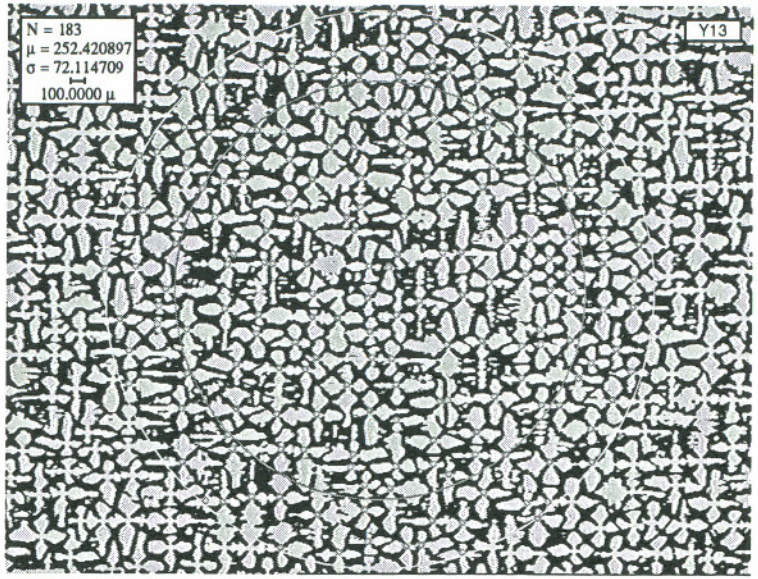
N = 183
μ = 252.420897
σ = 72.114709
100.0000 μ
Y13

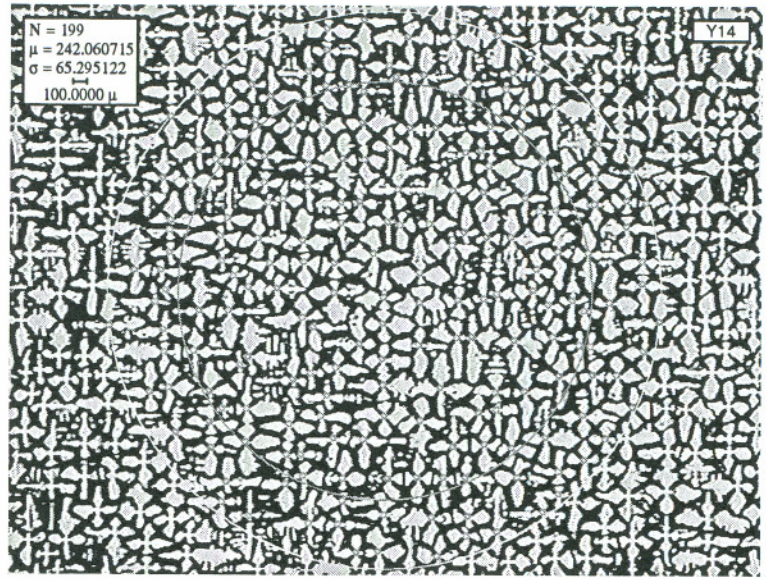
N = 199
μ = 242.060715
σ = 65.295122
100.0000 μ
Y14

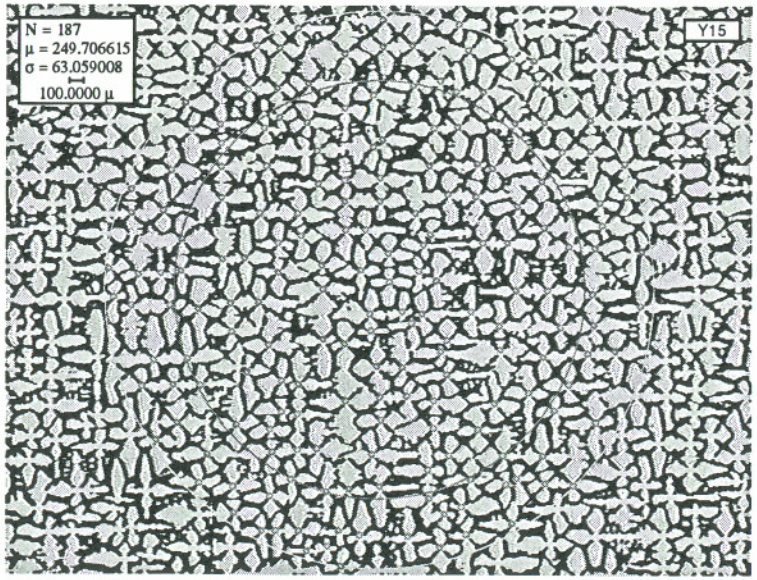
N = 187
μ = 249.706615
σ = 63.059008
100.0000 μ
Y15

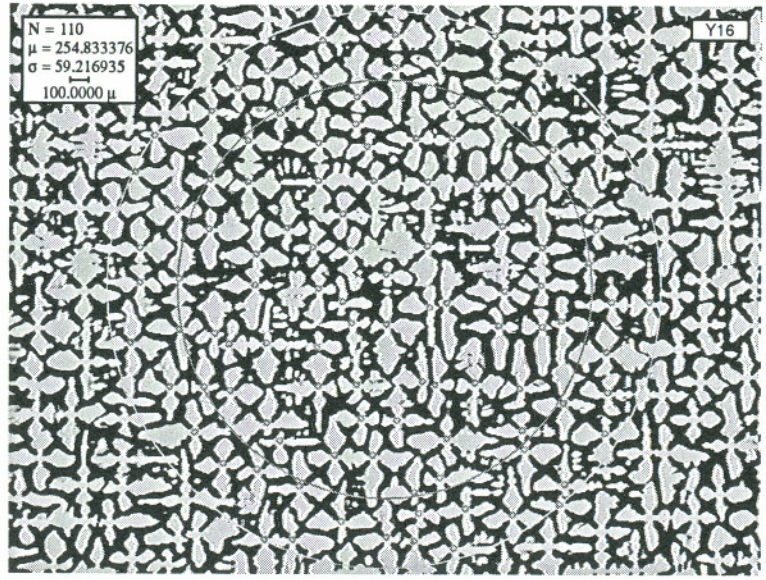
N = 110
μ = 254.833376
σ = 59.216935
100.0000 μ
Y16

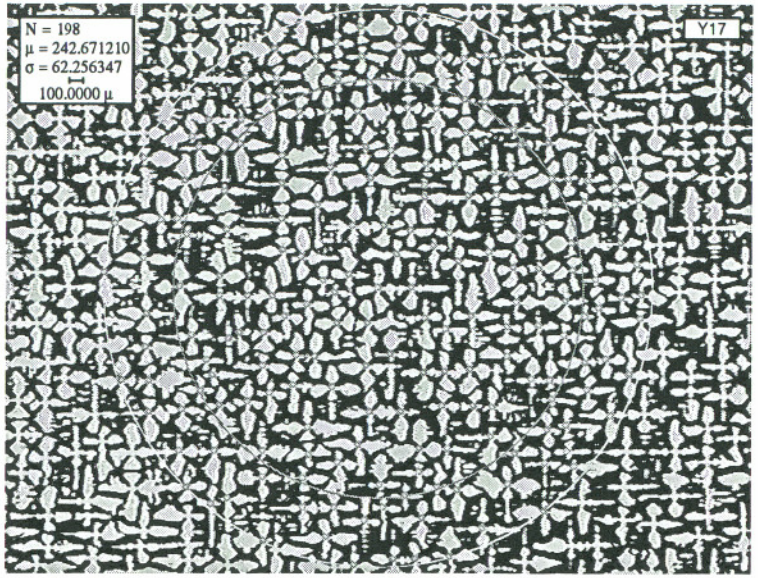
N = 198
μ = 242.671210
σ = 62.256347
100.0000 μ
Y17

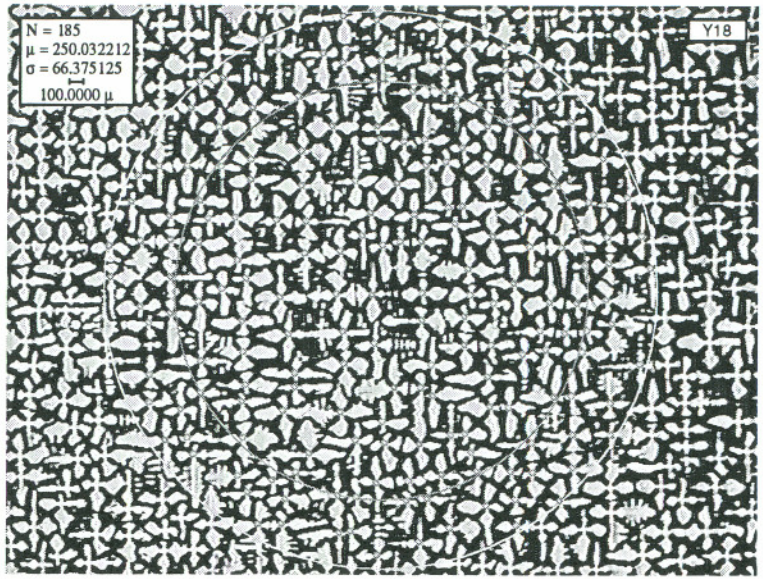
N = 185
μ = 250.032212
σ = 66.375125
100.0000 μ
Y18

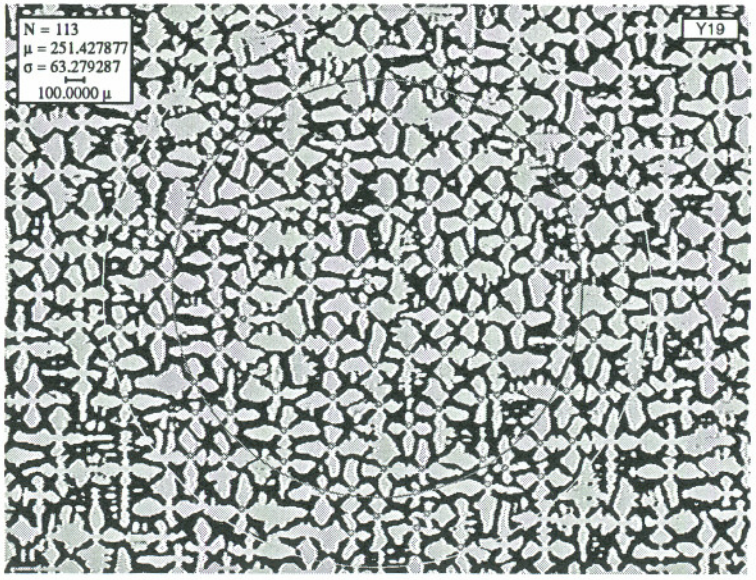
N = 113
μ = 251.427877
σ = 63.279287
100.0000 μ
Y19

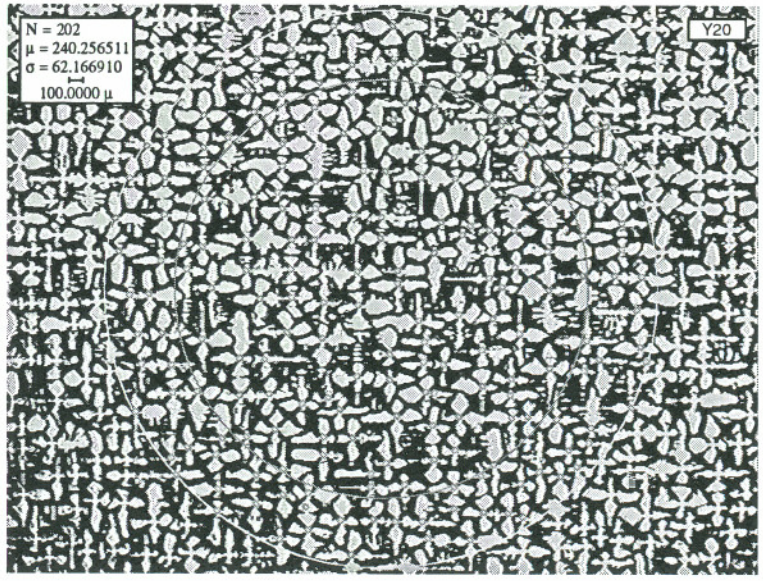
N = 202
μ = 240.256511
σ = 62.166910
100.0000 μ
Y20

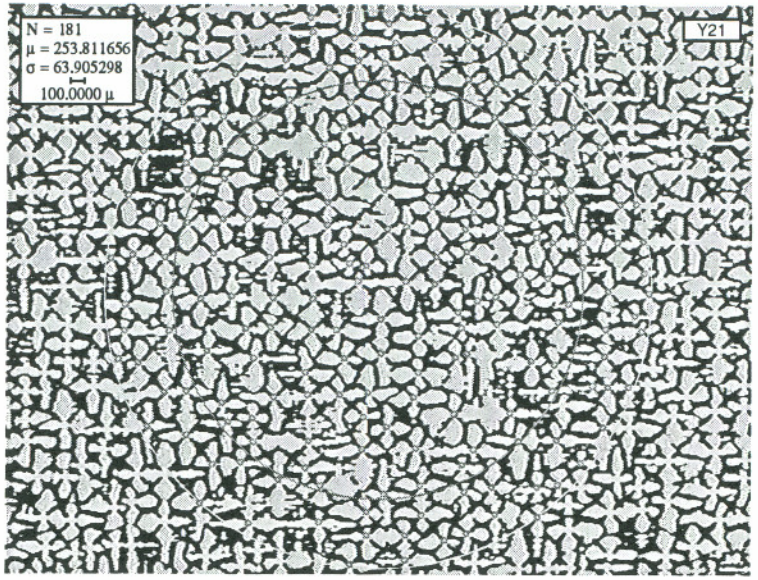
N = 181
μ = 253.811656
σ = 63.905298
100.0000 μ
Y21

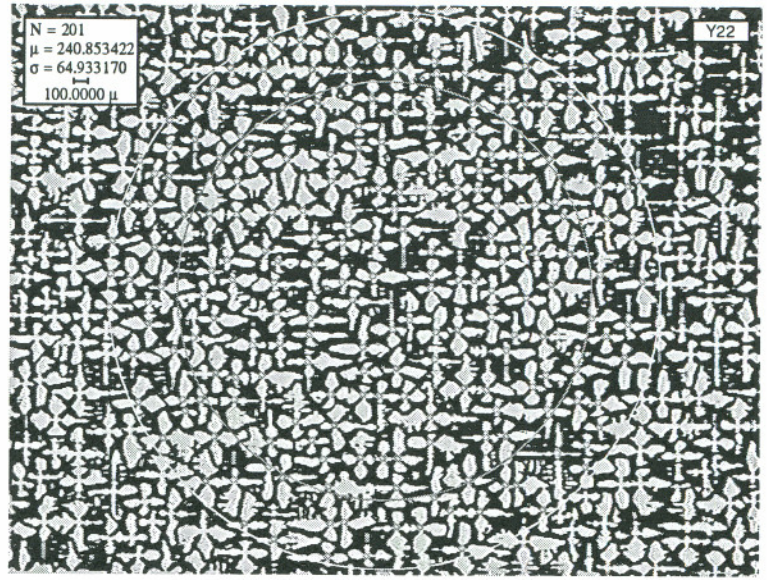
N = 201
μ = 240.853422
σ = 64.933170
100.0000 μ
Y22

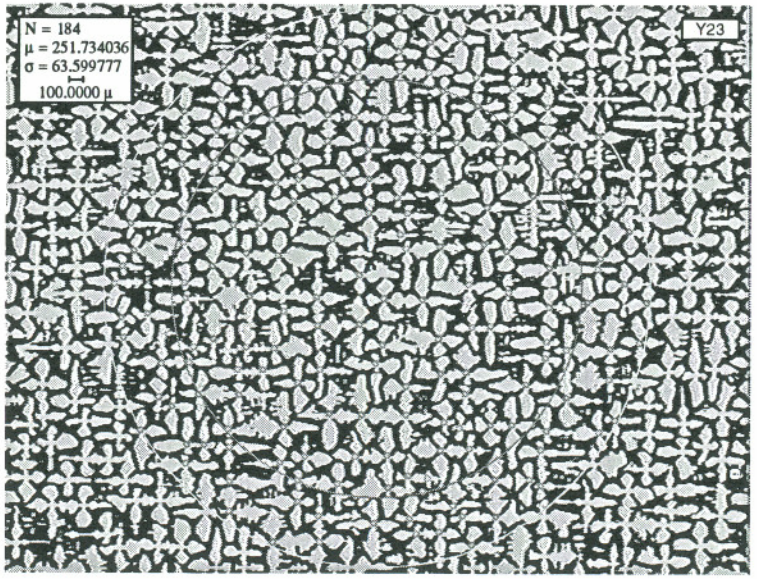
N = 184
μ = 251.734036
σ = 63.599777
100.0000 μ
Y23

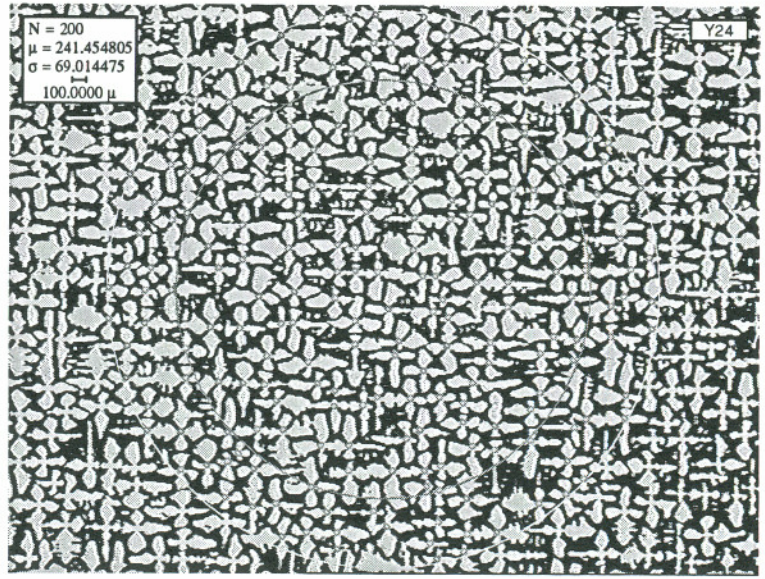
N = 200
μ = 241.454805
σ = 69.014475
100.0000 μ
Y24

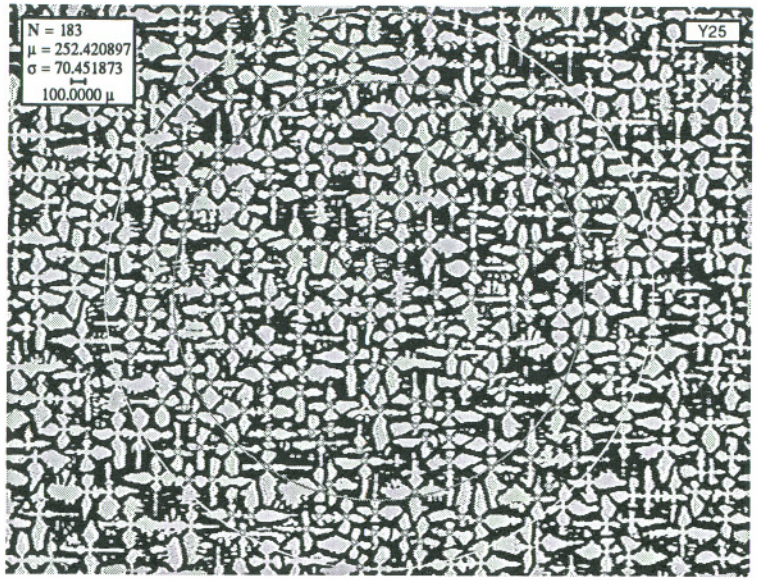
N = 183
μ = 252.420897
σ = 70.451873
100.0000 μ
Y25

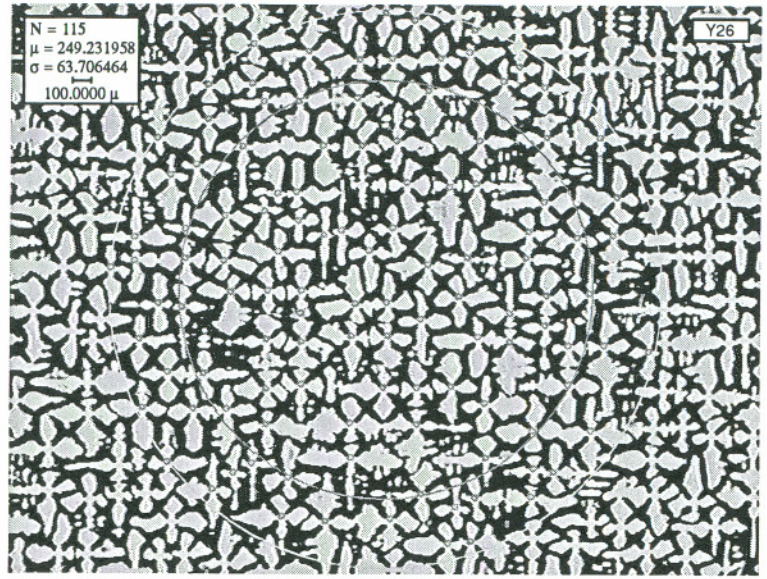
N = 115
μ = 249.231958
σ = 63.706464
100.0000 μ
Y26

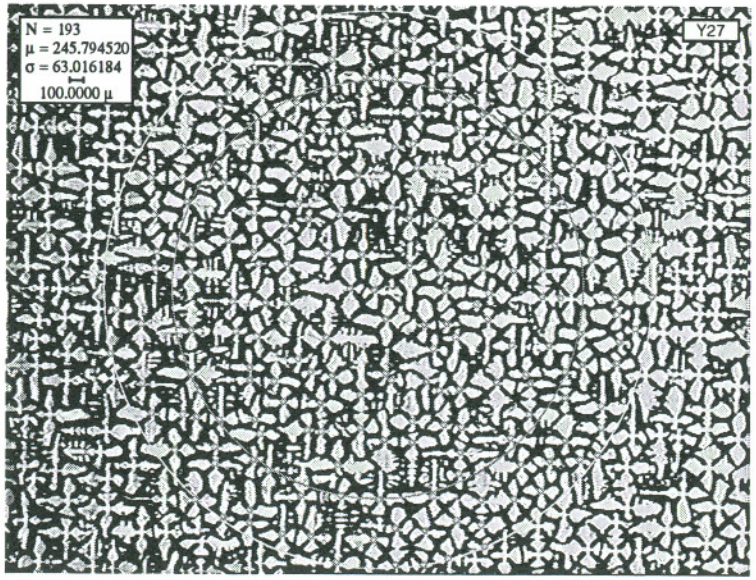
N = 193
μ = 245.794520
σ = 63.016184
100.0000 μ
Y27

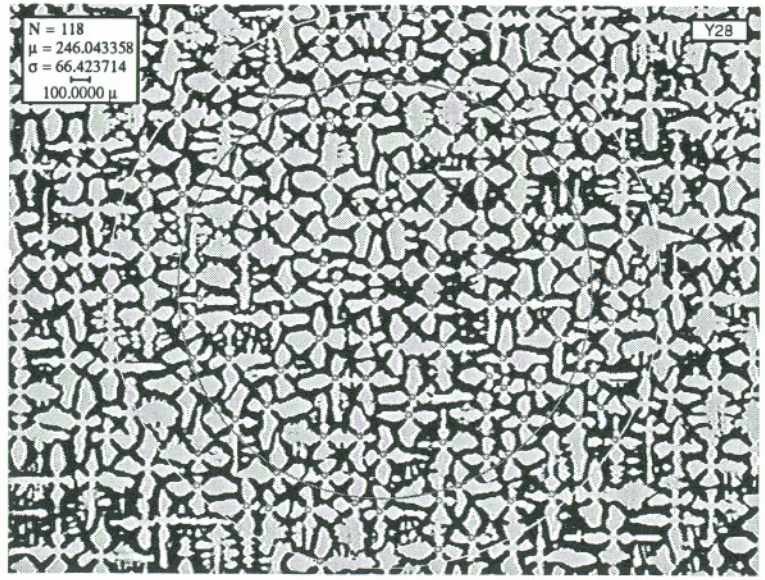
N = 118
μ = 246.043358
σ = 66.423714
100.0000 μ
Y28


Y30
N = 174
μ = 258.866723
σ = 69.052141
100.0000 μ


Y29
N = 166
μ = 261.822931
σ = 66.649586
100.0000 μ

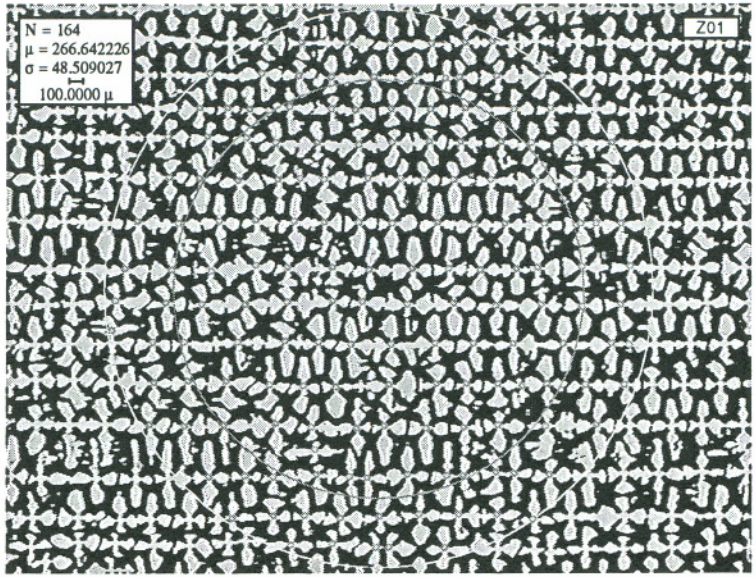
N = 164
μ = 266.642226
σ = 48.509027
100.0000 μ
Z01


N = 144
μ = 284.557217
σ = 67.431329
100.0000 μ
Z02

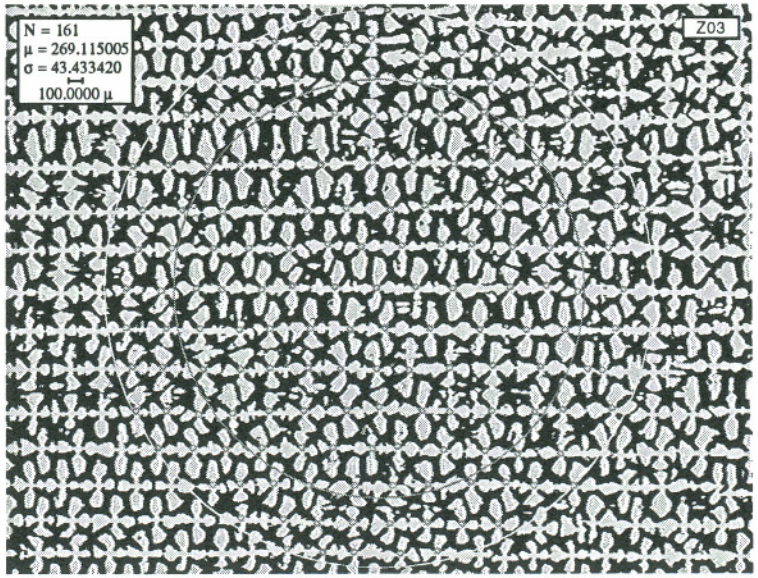
N = 161
μ = 269.115005
σ = 43.433420
100.0000 μ
Z03

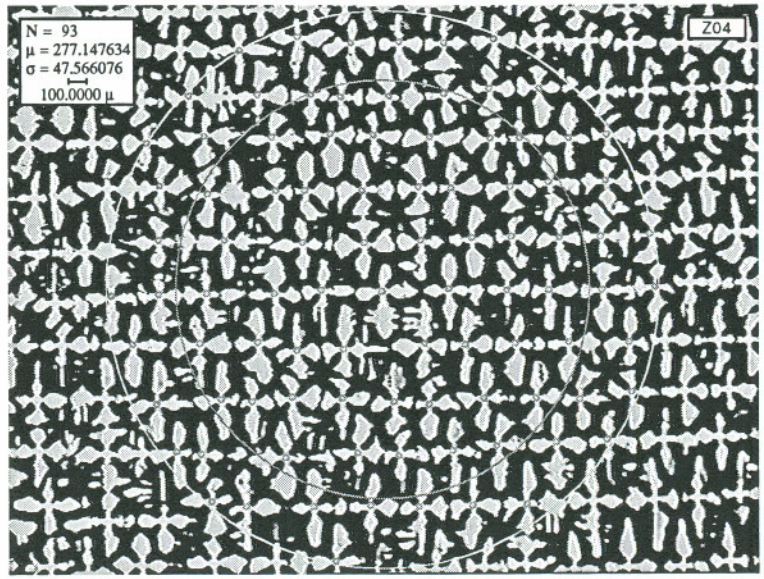
N = 93
μ = 277.147634
σ = 47.566076
100.0000 μ
Z04


N = 163
μ = 267.458897
σ = 55.689923
100.0000 μ
Z05

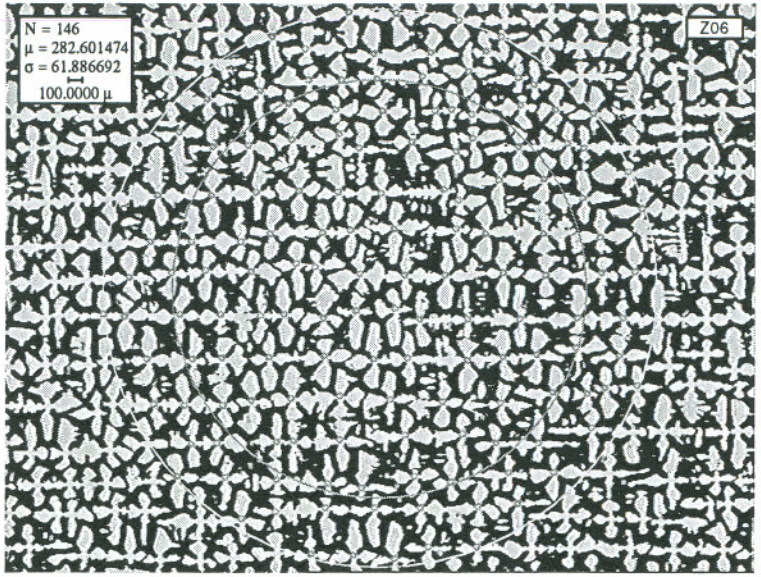
N = 146
μ = 282.601474
σ = 61.886692
100.0000 μ
Z06

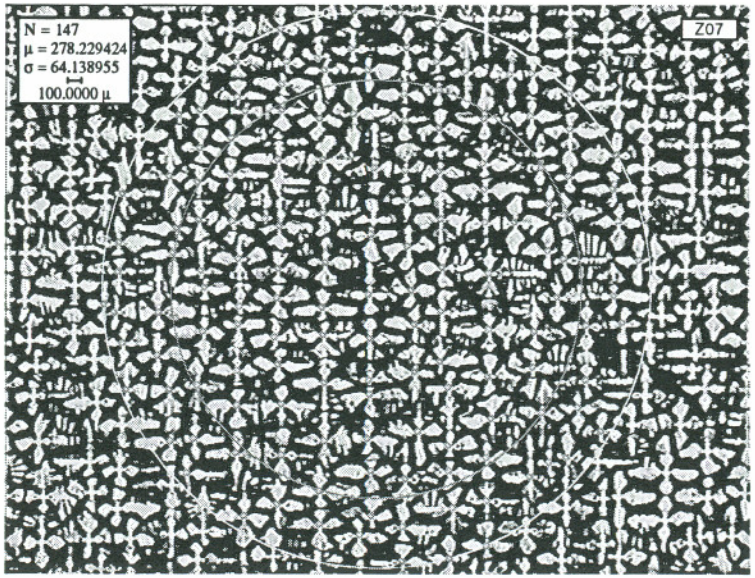
N = 147
μ = 278.229424
σ = 64.138955
100.0000 μ
Z07

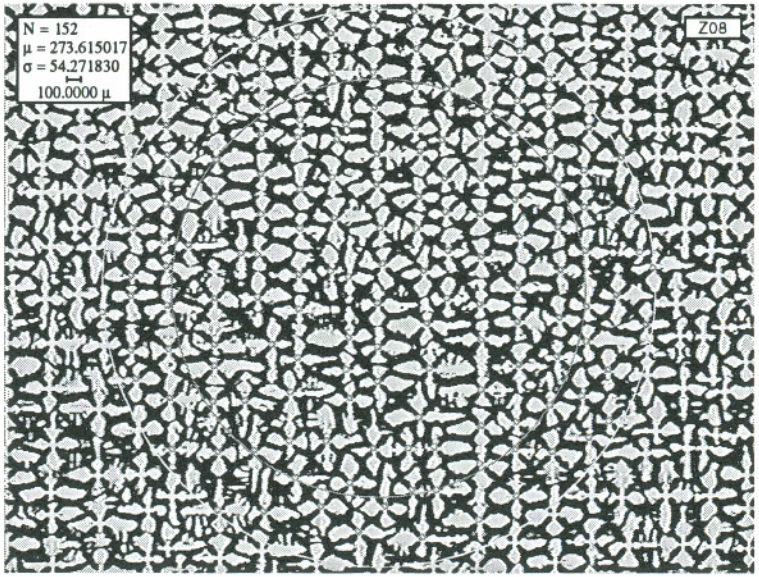
N = 152
μ = 273.615017
σ = 54.271830
100.0000 μ
Z08


Z10
N = 85
μ = 289.896644
σ = 66.124305
100.0000 μ


Z12
N = 94
μ = 275.669503
σ = 76.1311320
100.0000 μ


Z09
N = 89
μ = 283.307223
σ = 68.323398
100.0000 μ

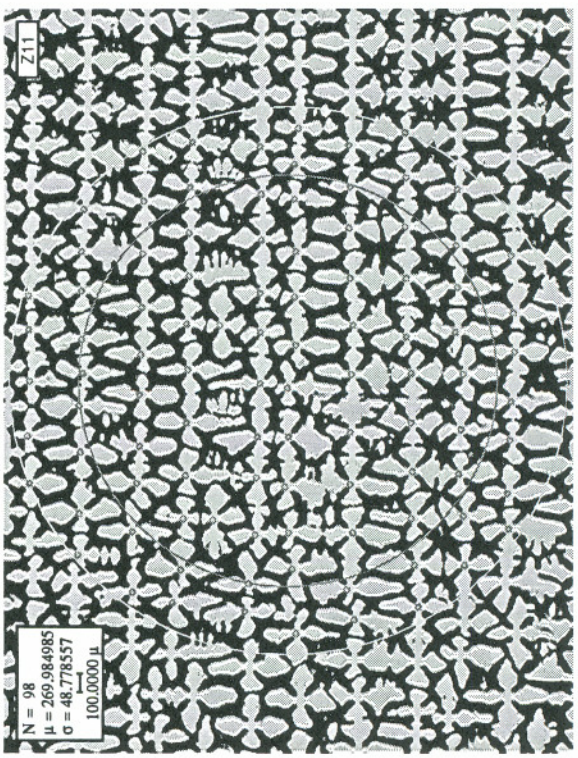
Z11
N = 98
μ = 269.984985
σ = 48.778557
100.0000 μ

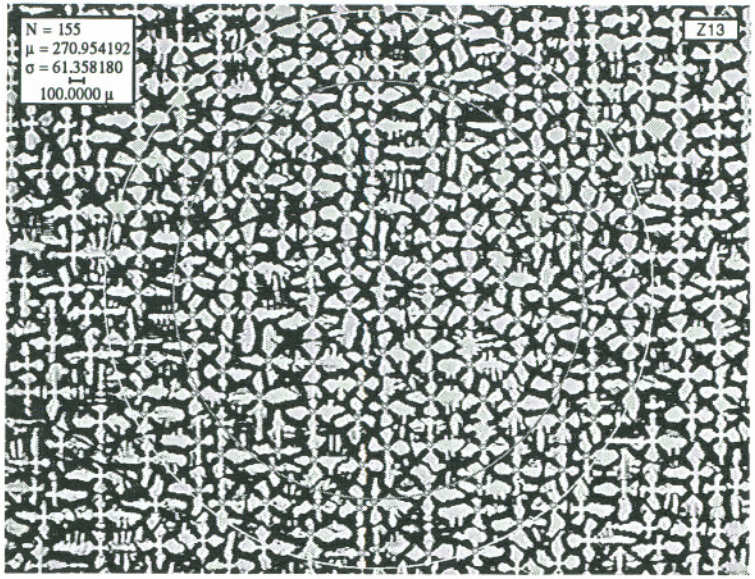
N = 155
μ = 270.954192
σ = 61.358180
100.0000 μ
Z13

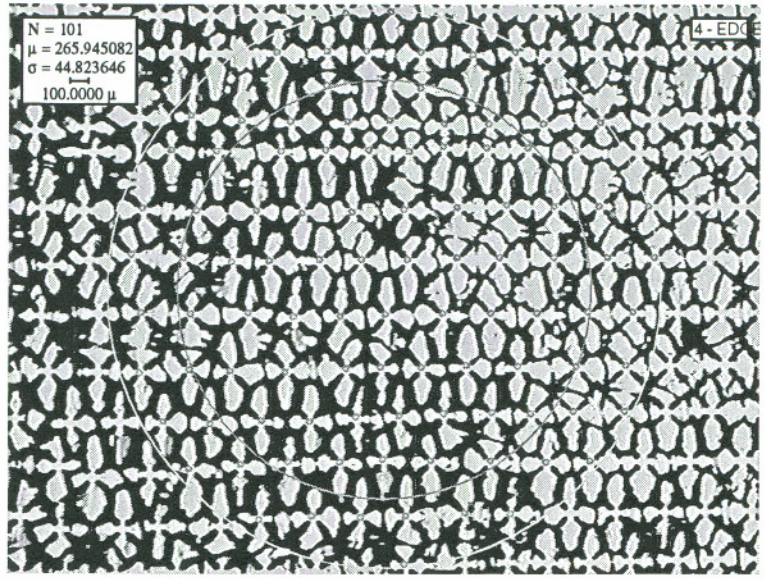
N = 101
μ = 265.945082
σ = 44.823646
100.0000 μ
4 - EDC

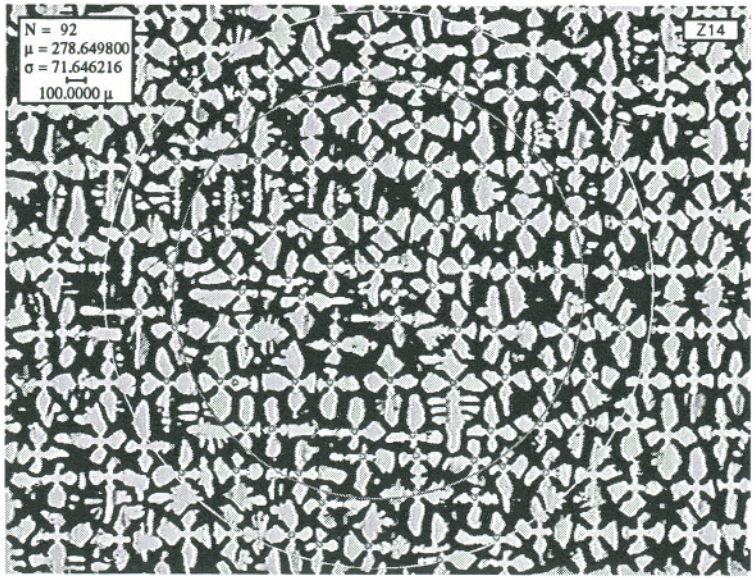
N = 92
μ = 278.649800
σ = 71.646216
100.0000 μ
Z14

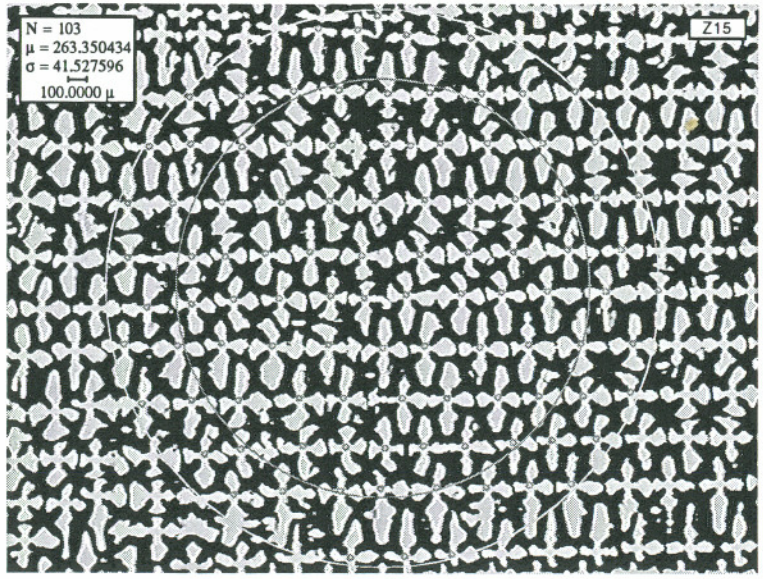
N = 103
μ = 263.350434
σ = 41.527596
100.0000 μ
Z15


Z17
N = 94
μ = 275.669503
σ = 62.634467
100.0000 μ

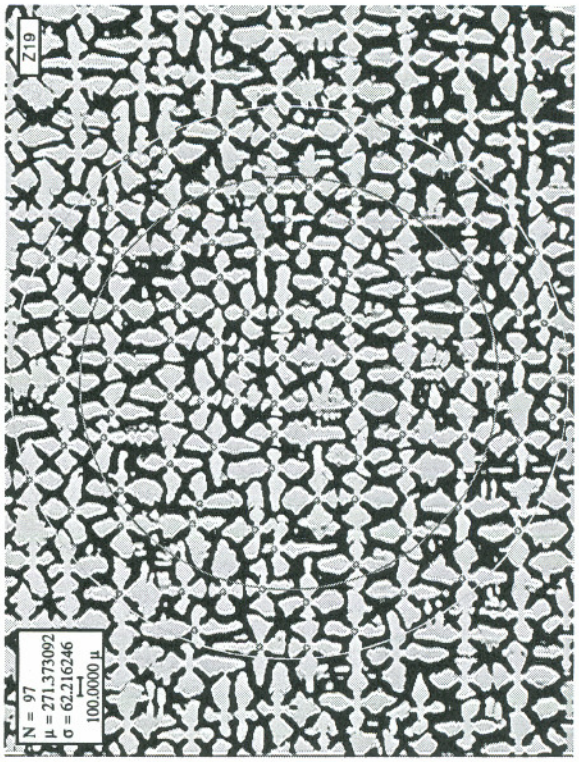
Z19
N = 97
μ = 271.373092
σ = 62.216246
100.0000 μ


Z16
N = 136
μ = 289.262589
σ = 71.689417
100.0000 μ


Z18
N = 94
μ = 276.543035
σ = 67.849103
100.0000 μ

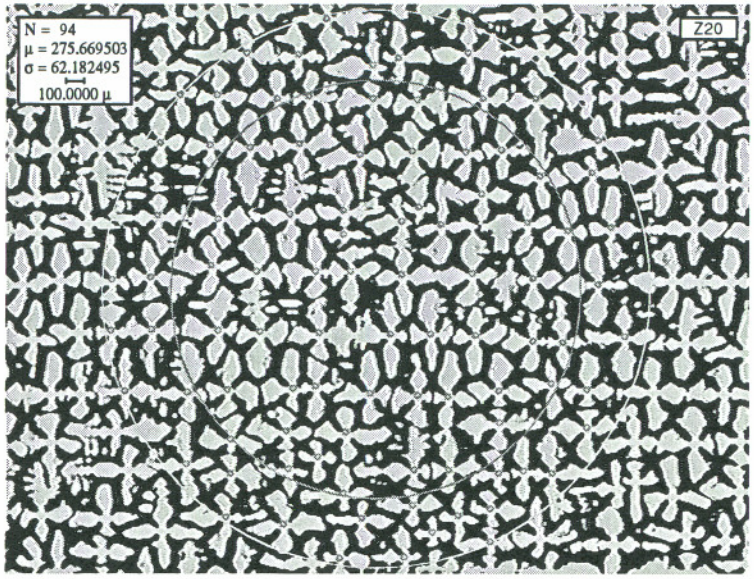
N = 94
μ = 275.669503
σ = 62.182495
100.0000 μ
Z20

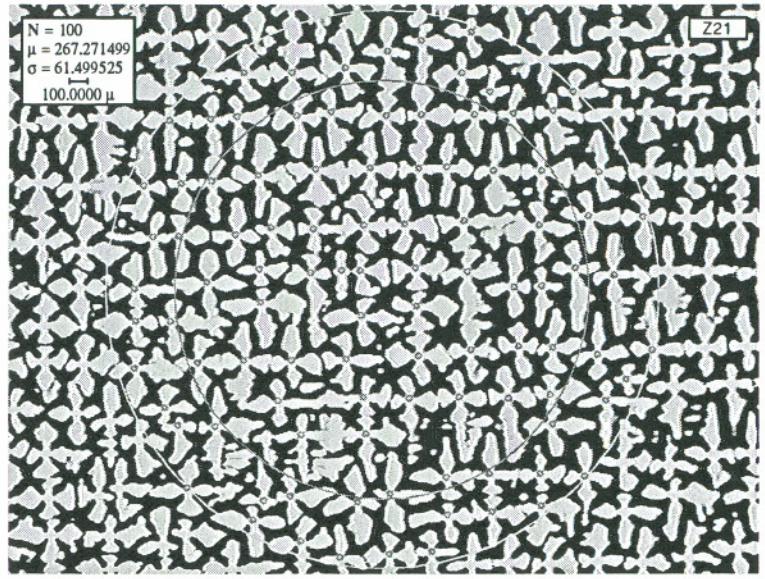
N = 100
μ = 267.271499
σ = 61.499525
100.0000 μ
Z21

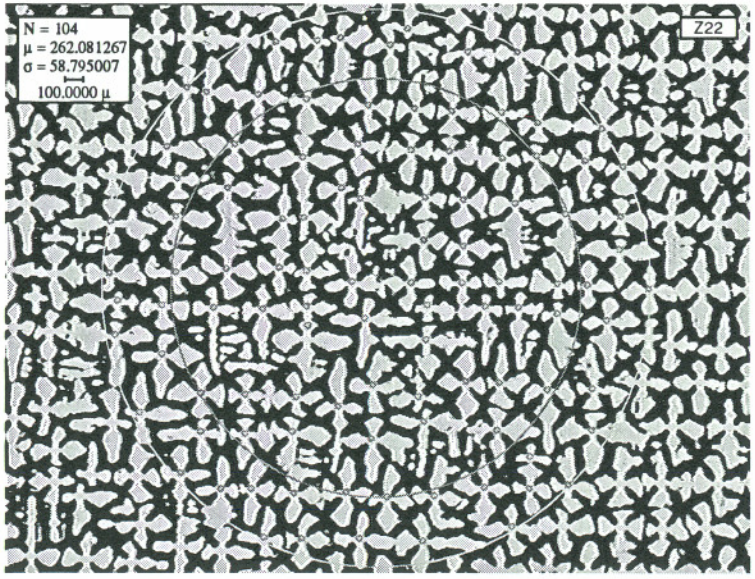
N = 104
μ = 262.081267
σ = 58.795007
100.0000 μ
Z22

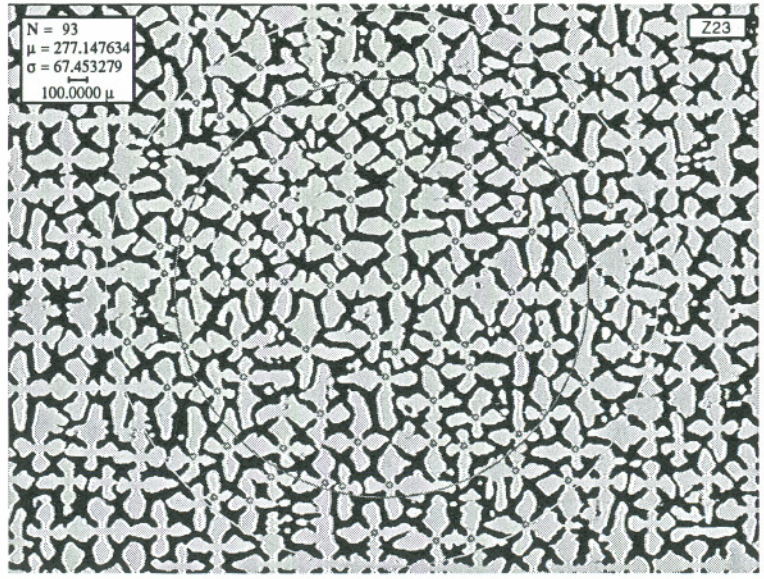
N = 93
μ = 277.147634
σ = 67.453279
100.0000 μ
Z23

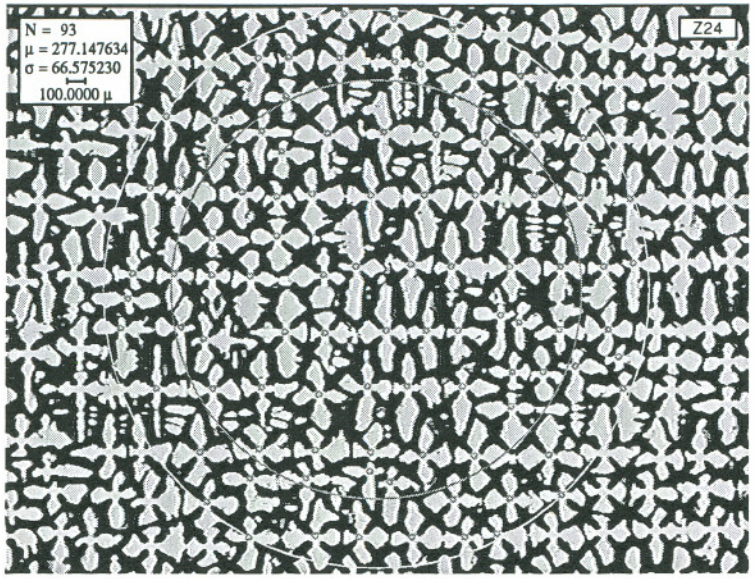
N = 93
μ = 277.147634
σ = 66.575230
100.0000 μ
Z24

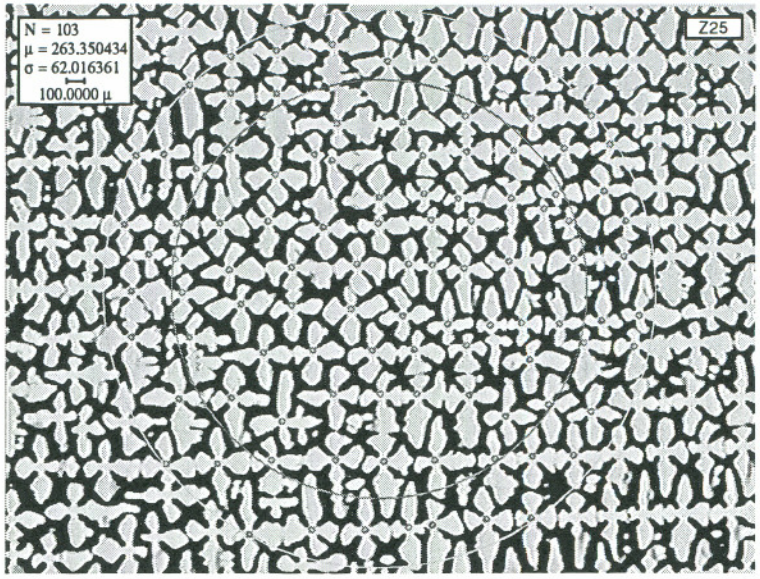
N = 103
μ = 263.350434
σ = 62.016361
100.0000 μ
Z25

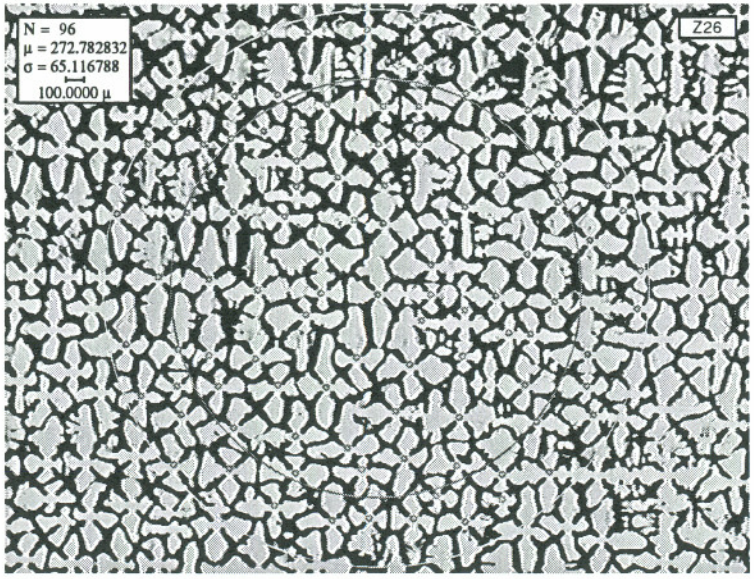
N = 96
μ = 272.782832
σ = 65.116788
100.0000 μ
Z26

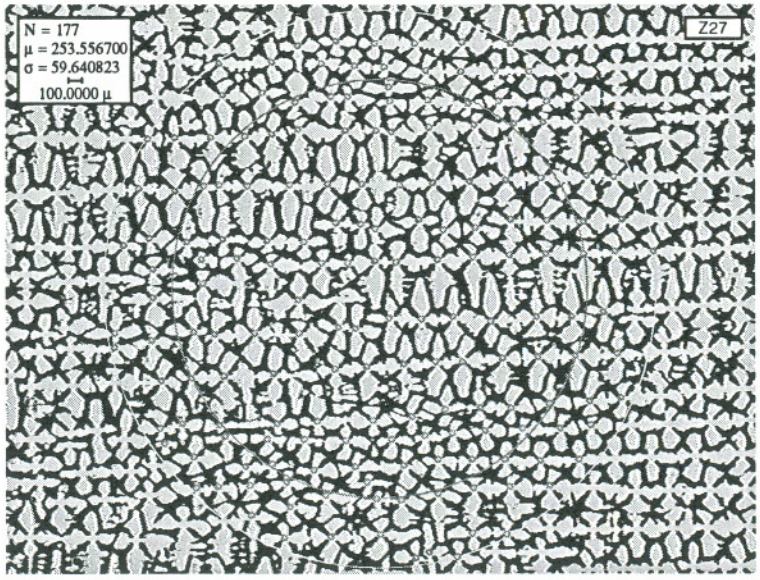
N = 177
μ = 253.556700
σ = 59.640823
100.0000 μ
Z27

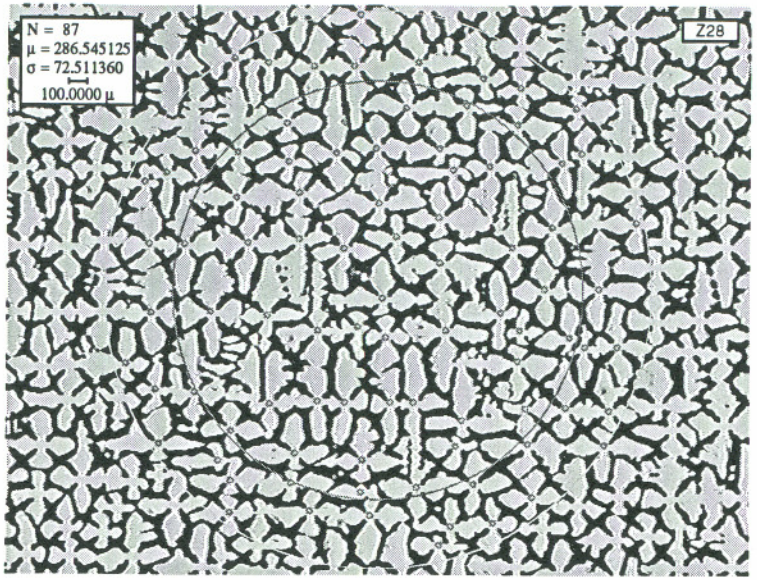
N = 87
μ = 286.545125
σ = 72.511360
100.0000 μ
Z28

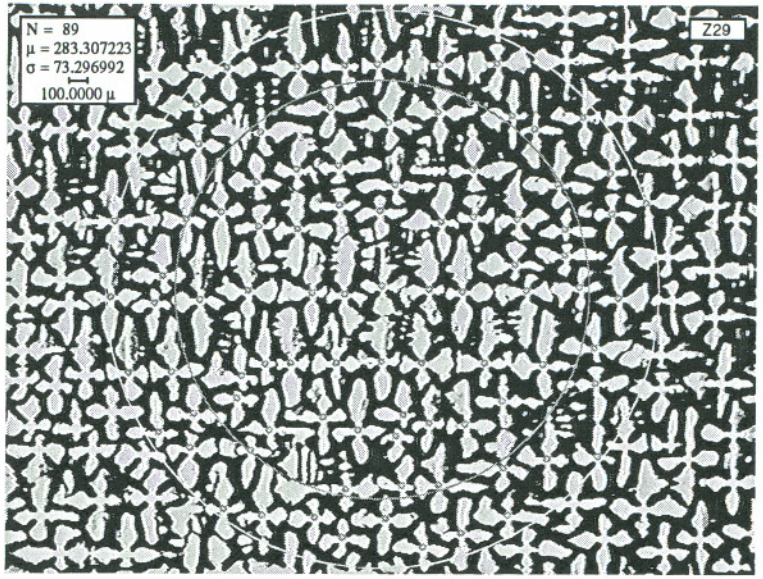
N = 89
μ = 283.307223
σ = 73.296992
100.0000 μ
Z29

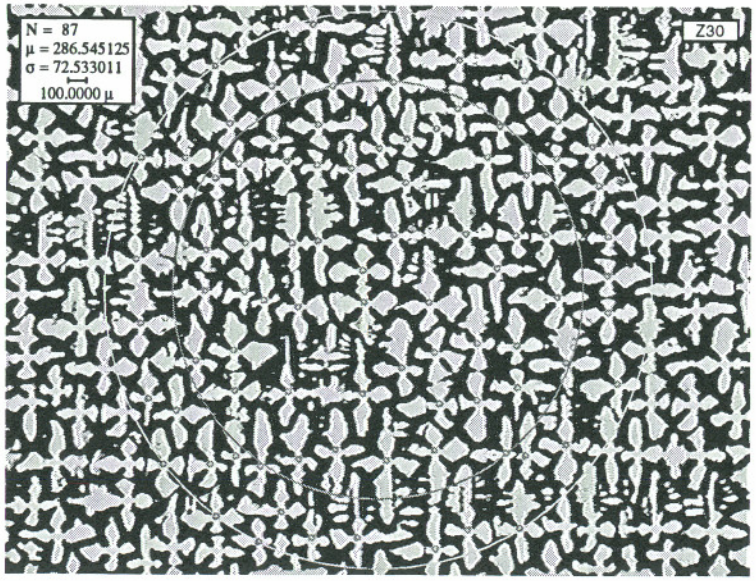
N = 87
μ = 286.545125
σ = 72.533011
100.0000 μ
Z30

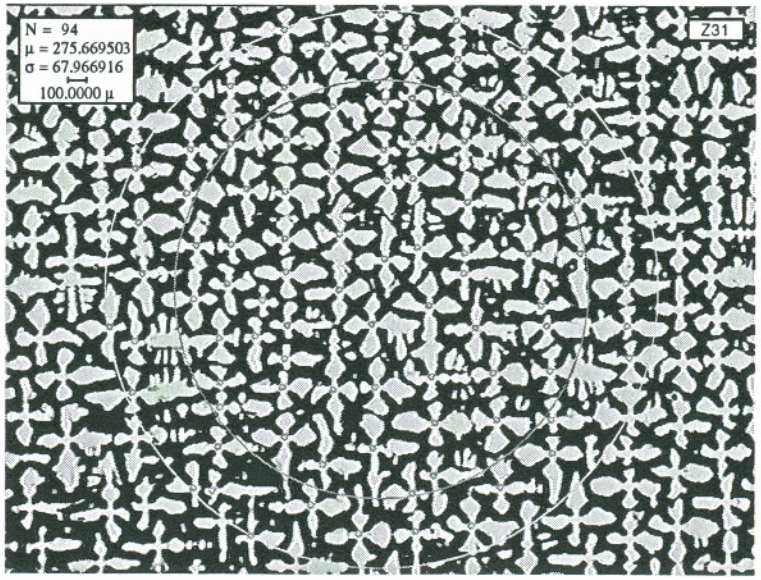
N = 94
μ = 275.669503
σ = 67.966916
100.0000 μ
Z31

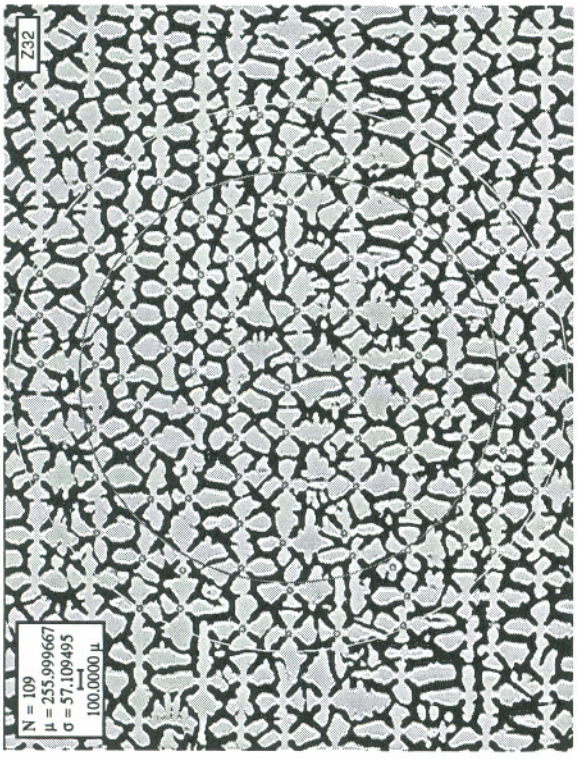
Z32
N = 109
μ = 255.999667
σ = 57.109495
100.0000 μm

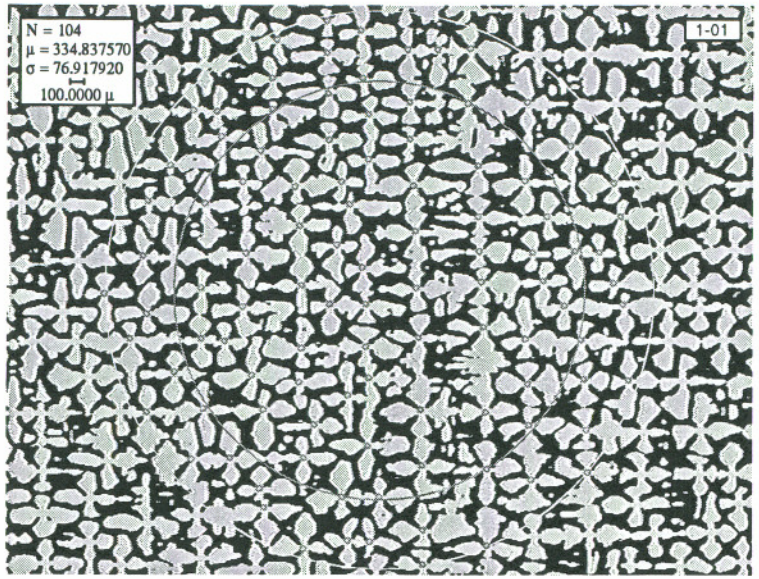
N = 104
μ = 334.837570
σ = 76.917920
100.0000 μ
1-01

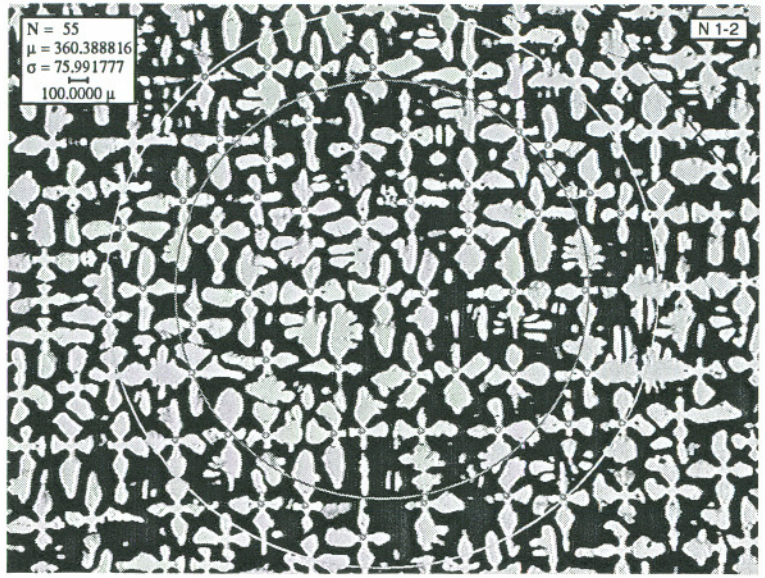
N = 55
μ = 360.388816
σ = 75.991777
100.0000 μ
N 1-2

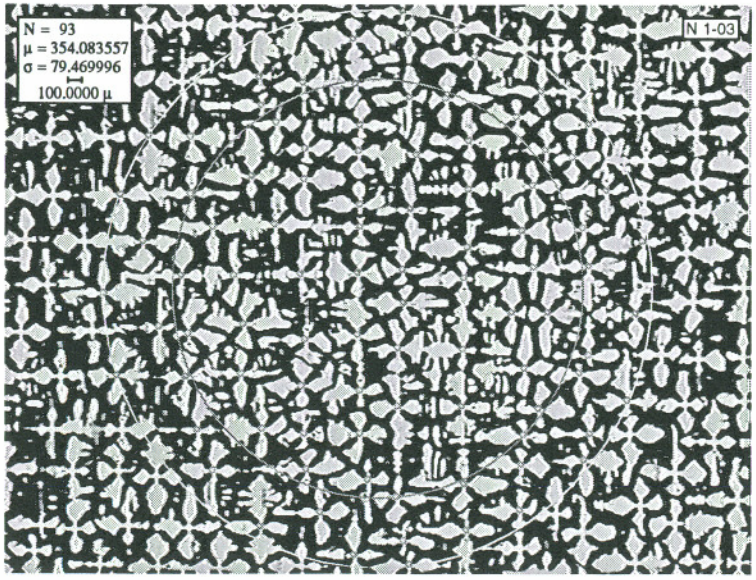
N = 93
μ = 354.083557
σ = 79.469996
100.0000 μ
N 1-03

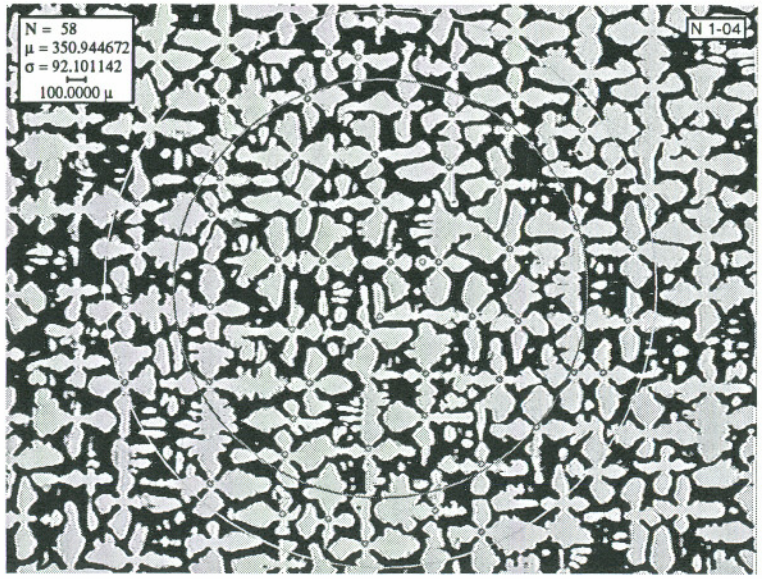
N = 58
μ = 350.944672
σ = 92.101142
100.0000 μ
N 1-04


N 1-06
N = 89
μ = 360.484690
σ = 70.181815
100.0000 μ


N 1-08
N = 88
μ = 362.527112
σ = 73.234955
100.0000 μ


N 1-05
N = 85
μ = 370.371679
σ = 88.474208
100.0000 μ


N 1-07
N = 86
μ = 366.718317
σ = 82.204213
100.0000 μ

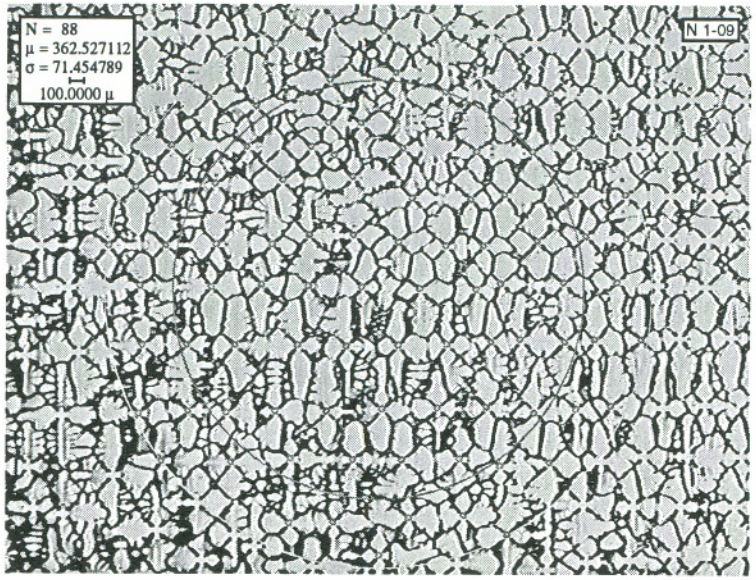
N = 88
μ = 362.527112
σ = 71.454789
100.0000 μ
N 1-09

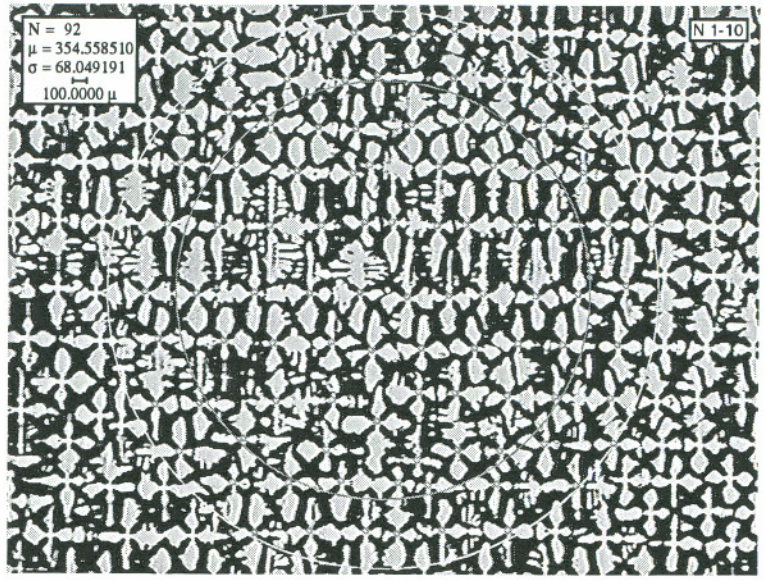
N = 92
μ = 354.558510
σ = 68.049191
100.0000 μ
N 1-10

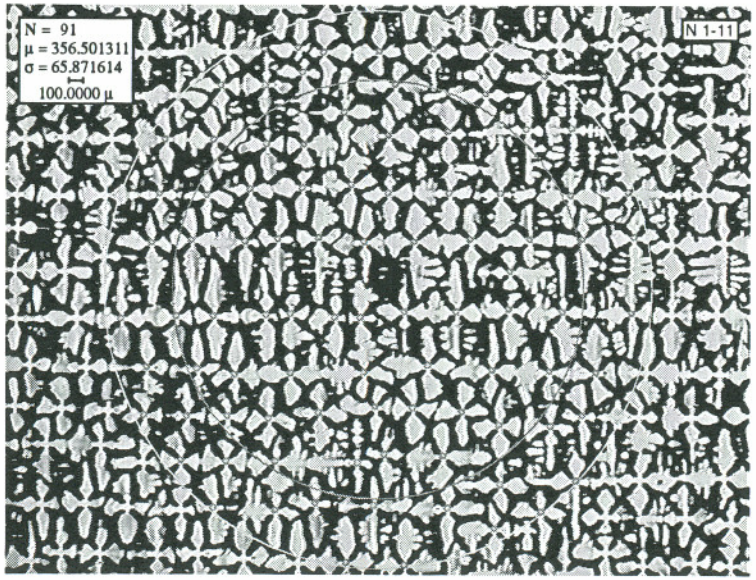
N = 91
μ = 356.501311
σ = 65.871614
100.0000 μ
N 1-11

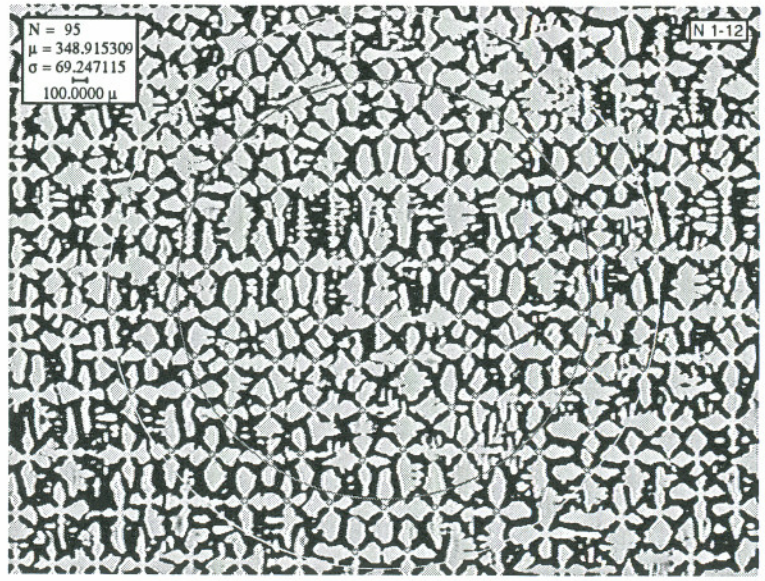
N = 95
μ = 348.915309
σ = 69.247115
100.0000 μ
N 1-12

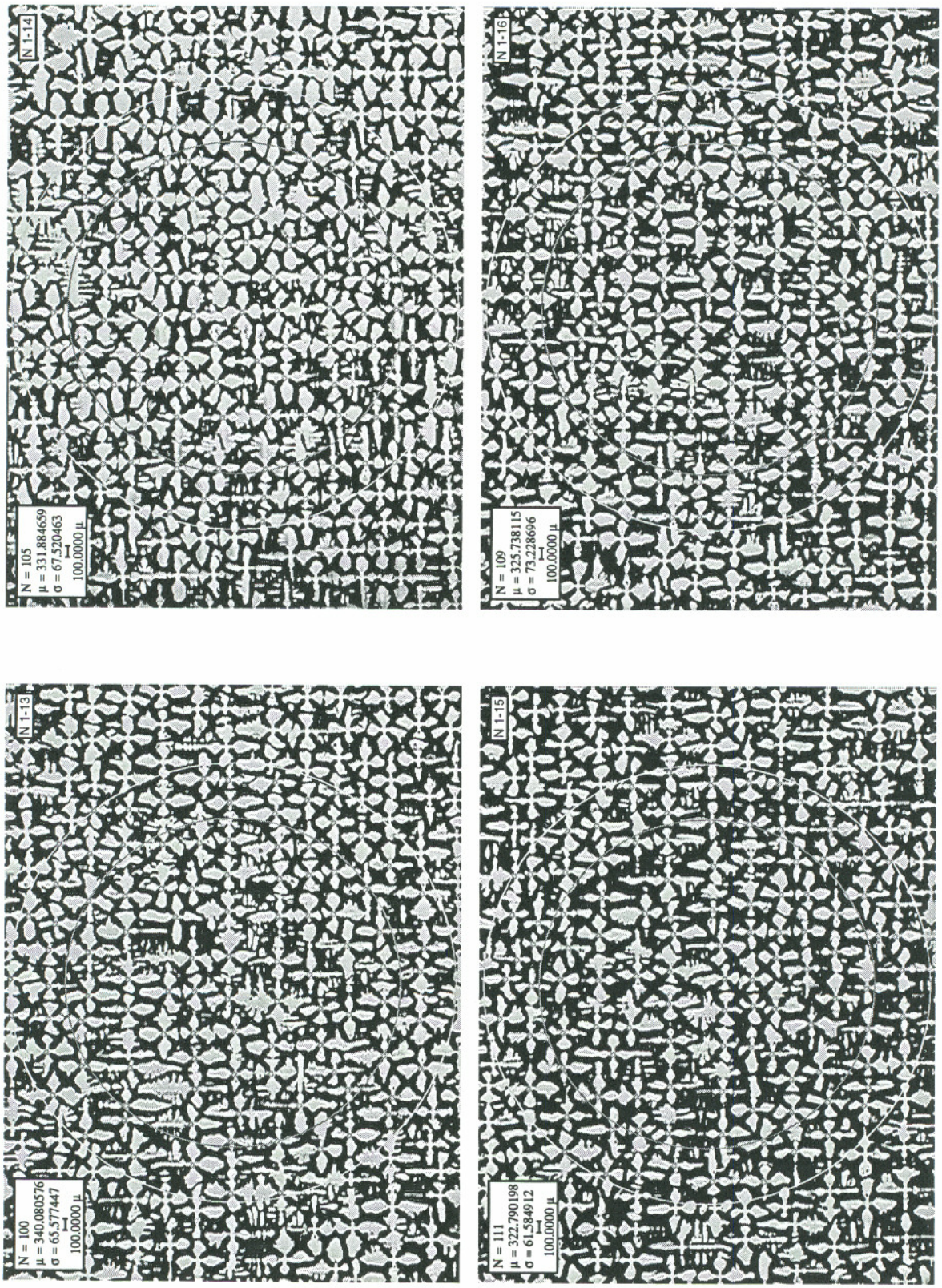
N 1-13
N = 100
μ = 340.080576
σ = 65.577447
100.0000 μ
N 1-14
N = 105
μ = 331.884659
σ = 67.520463
100.0000 μ
N 1-15
N = 111
μ = 322.790198
σ = 61.584912
100.0000 μ
N 1-16
N = 109
μ = 325.738115
σ = 73.228696
100.0000 μ

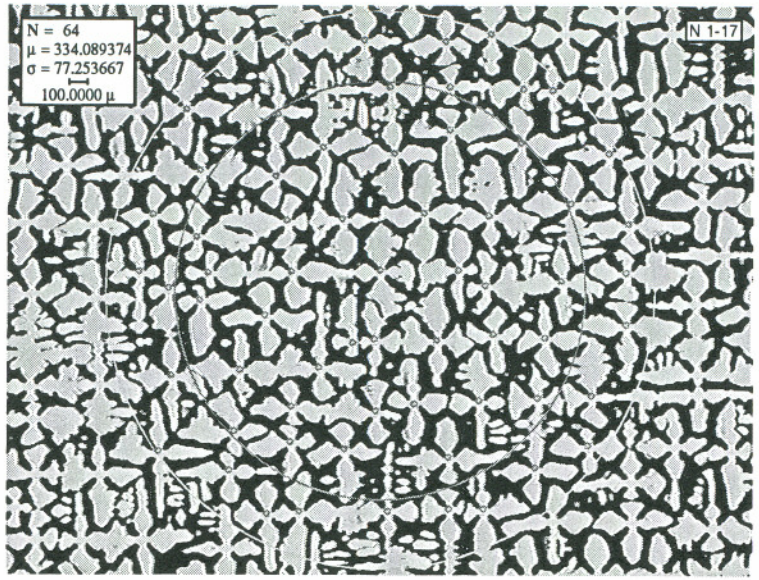
N = 64
μ = 334.089374
σ = 77.253667
100.0000 μ
N 1-17

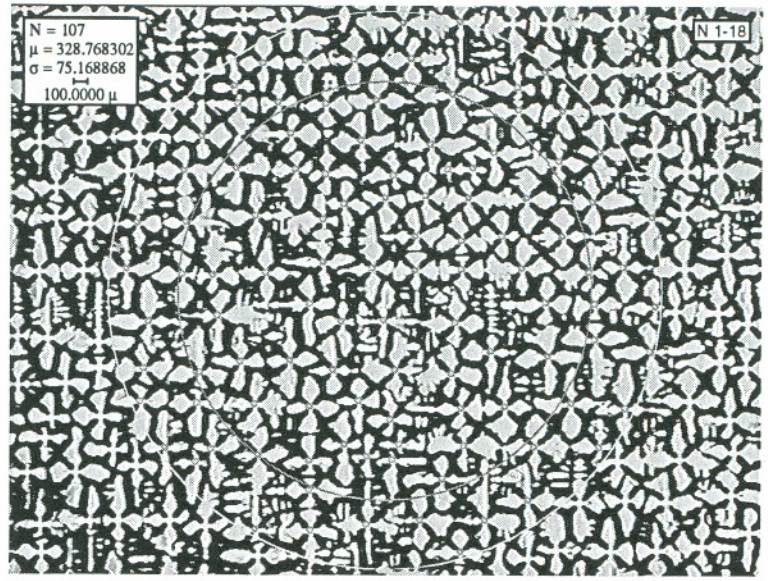
N = 107
μ = 328.768302
σ = 75.168868
100.0000 μ
N 1-18

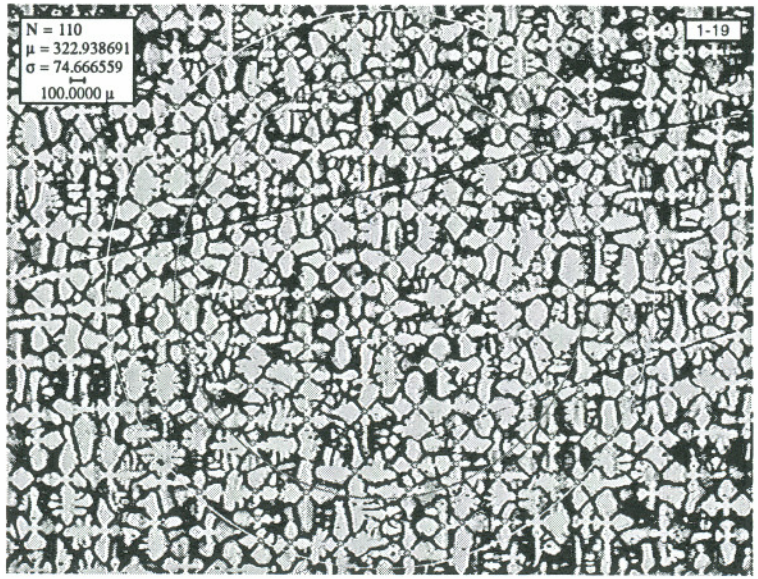
N = 110
μ = 322.938691
σ = 74.666559
100.0000 μ
1-19

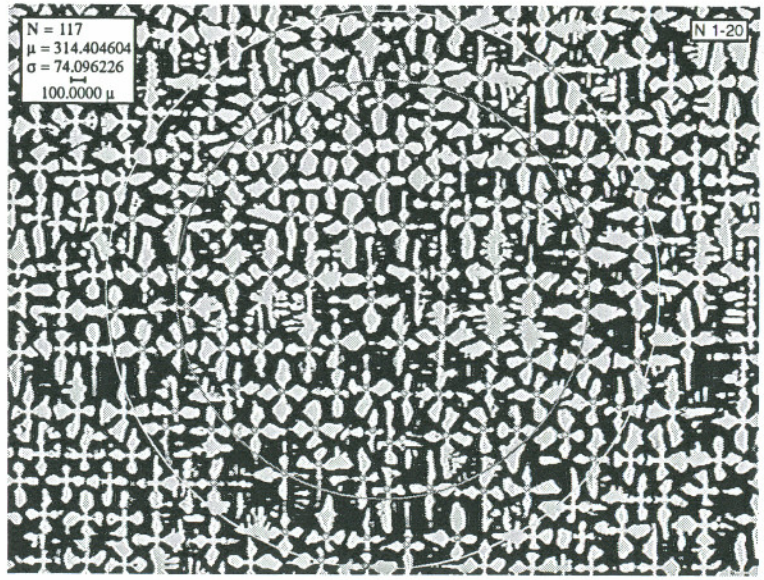
N = 117
μ = 314.404604
σ = 74.096226
100.0000 μ
N 1-20

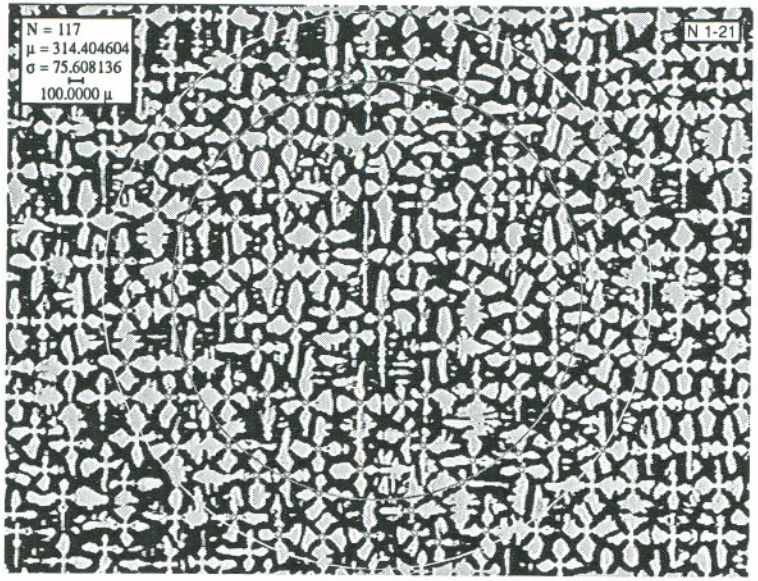
N = 117
μ = 314.404604
σ = 75.608136
100.0000 μ
N 1-21

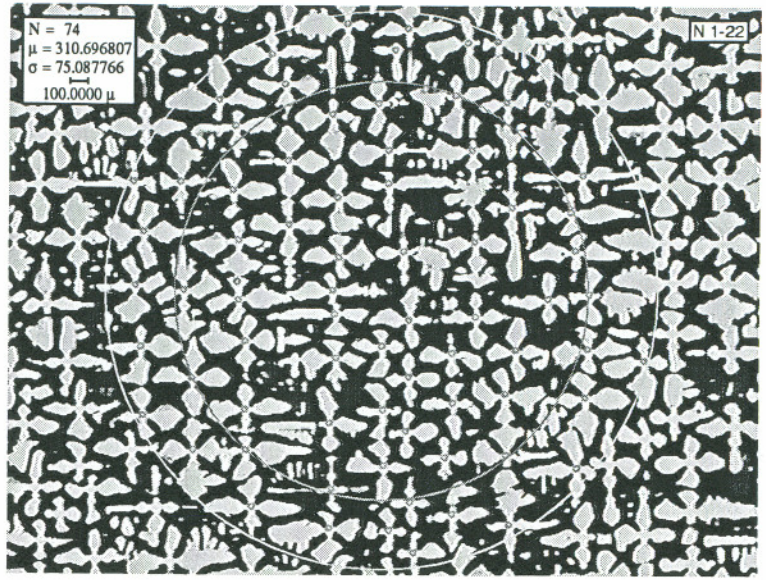
N = 74
μ = 310.696807
σ = 75.087766
100.0000 μ
N 1-22

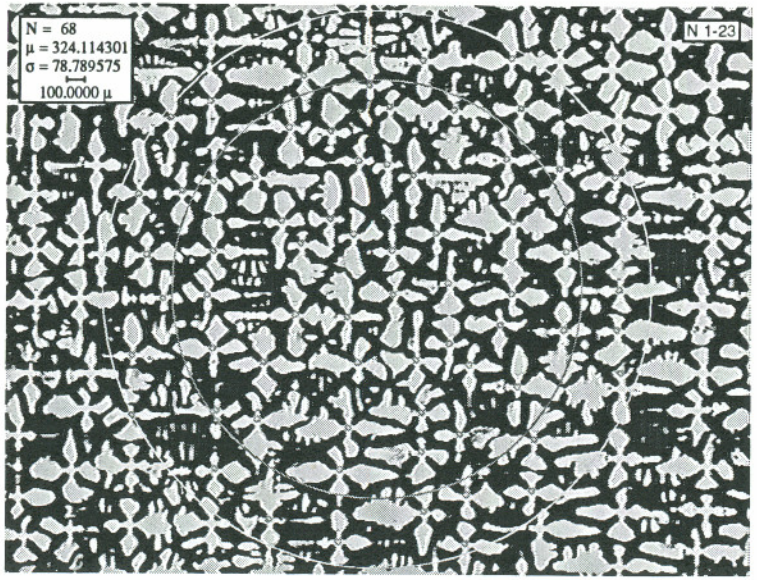
N = 68
μ = 324.114301
σ = 78.789575
100.0000 μ
N 1-23

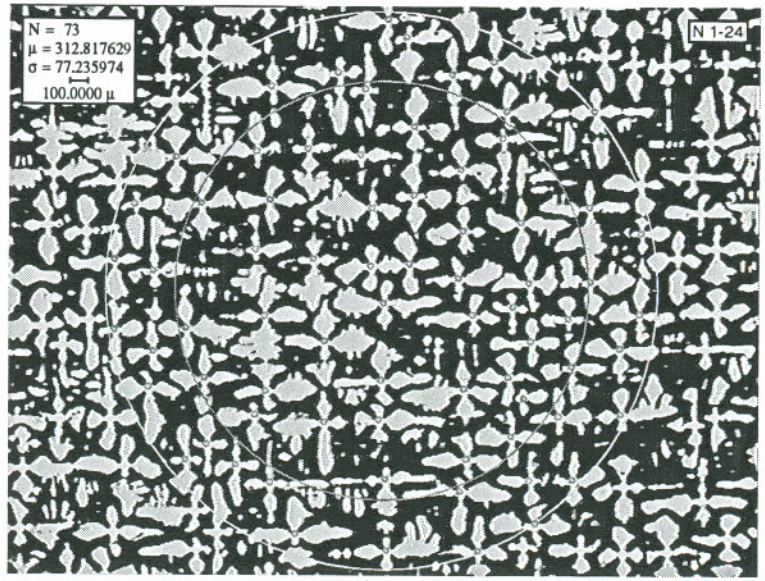
N = 73
μ = 312.817629
σ = 77.235974
100.0000 μ
N 1-24

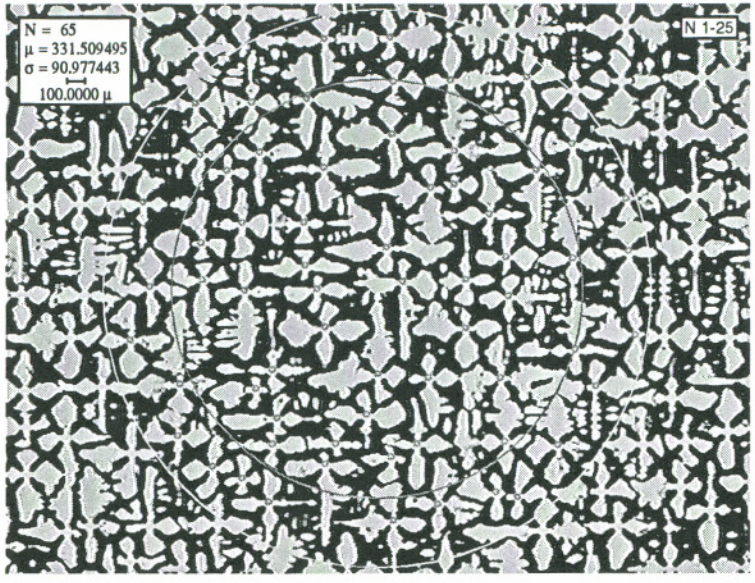
N = 65
μ = 331.509495
σ = 90.977443
100.0000 μ
N 1-25

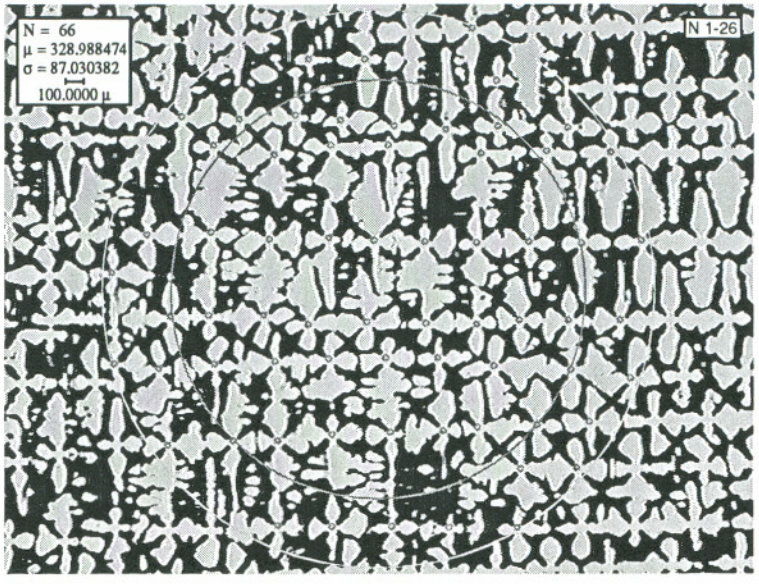
N = 66
μ = 328.988474
σ = 87.030382
100.0000 μ
N 1-26

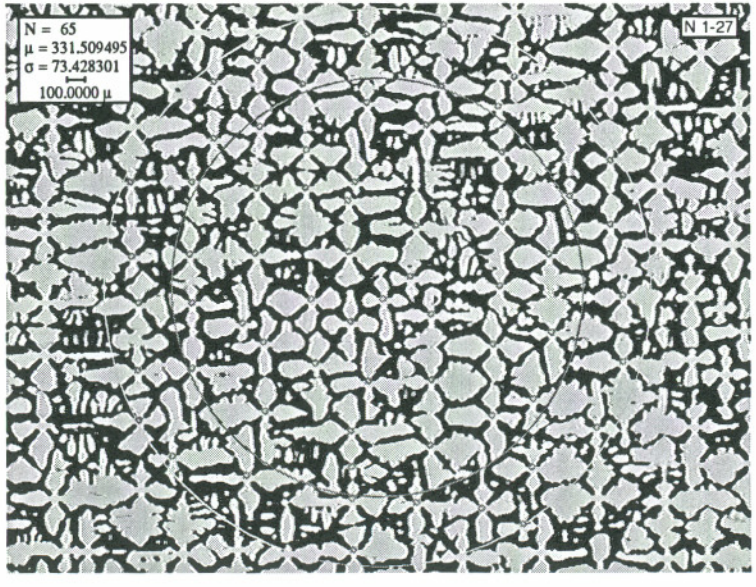
N = 65
μ = 331.509495
σ = 73.428301
100.0000 μ
N 1-27

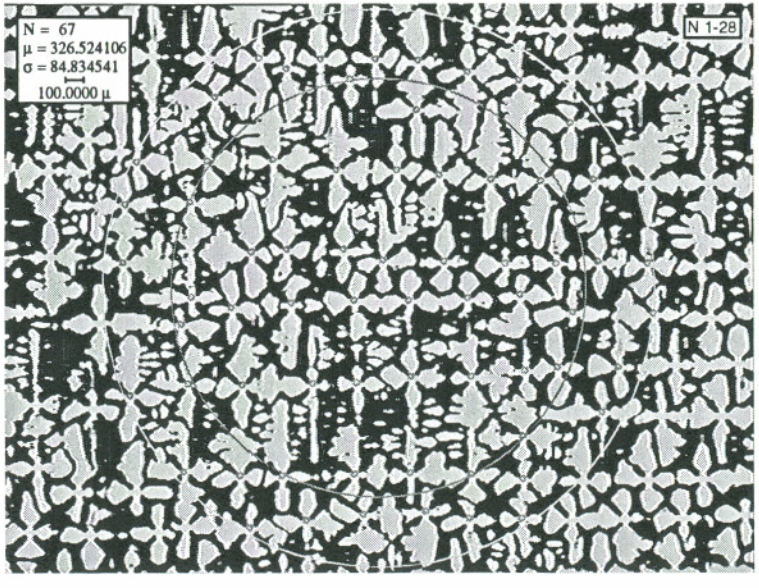
N = 67
μ = 326.524106
σ = 84.834541
100.0000 μ
N 1-28

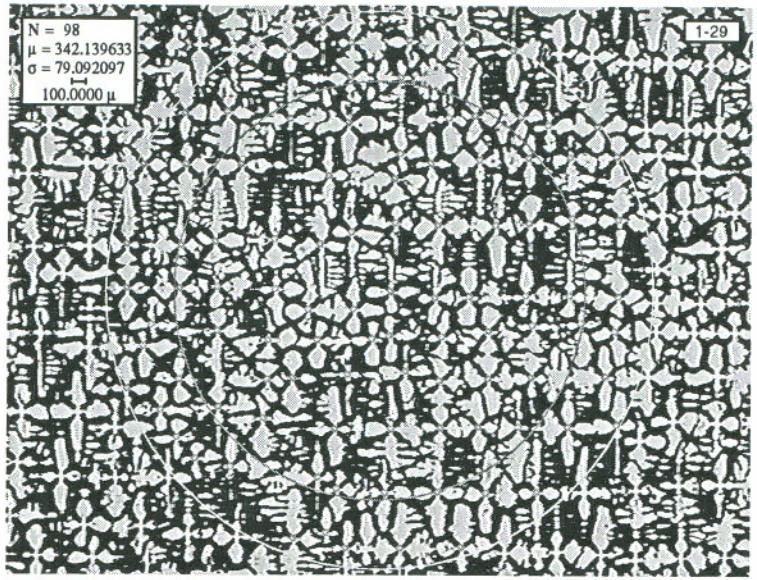
N = 98
μ = 342.139633
σ = 79.092097
100.0000 μ
1-29

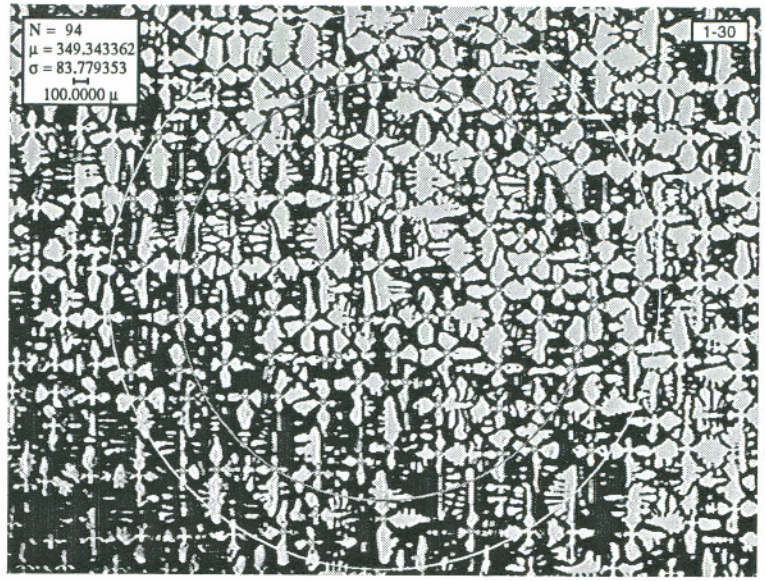
N = 94
μ = 349.343362
σ = 83.779353
100.0000 μ
1-30

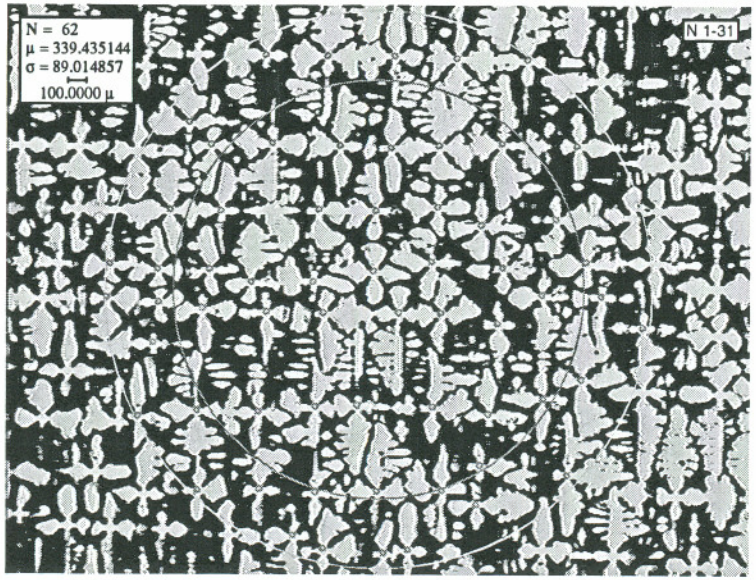
N = 62
μ = 339.435144
σ = 89.014857
100.0000 μ
N 1-31

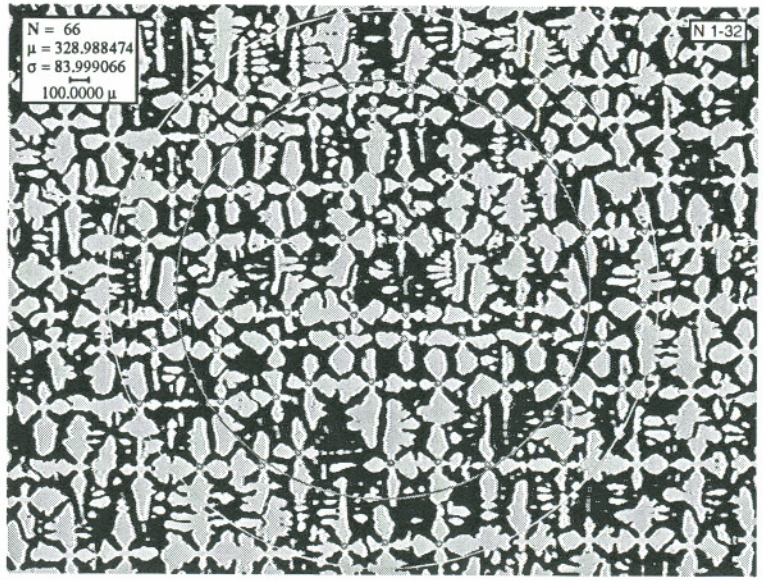
N = 66
μ = 328.988474
σ = 83.999066
100.0000 μ
N 1-32

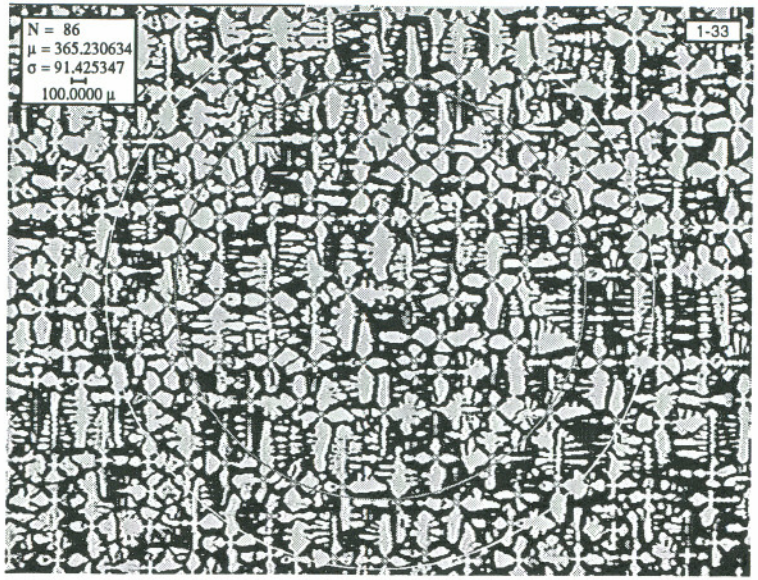
N = 86
μ = 365.230634
σ = 91.425347
100.0000 μ
1-33

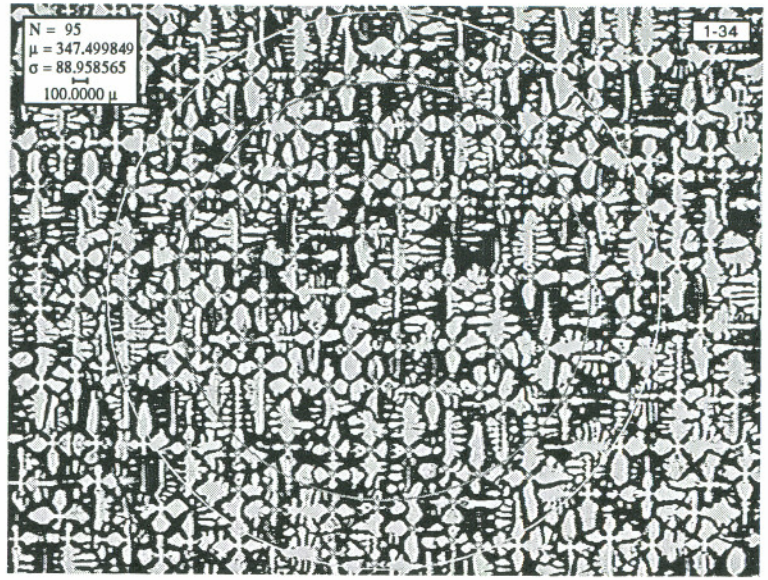
N = 95
μ = 347.499849
σ = 88.958565
100.0000 μ
1-34

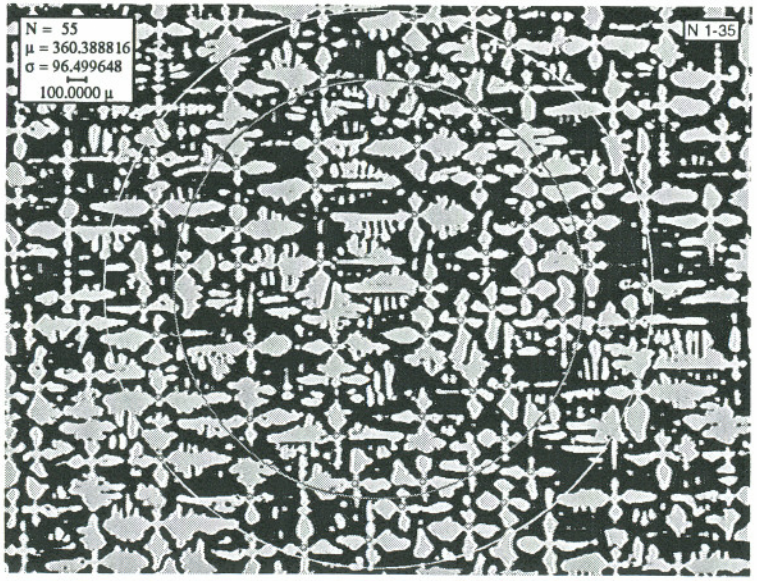
N = 55
μ = 360.388816
σ = 96.499648
100.0000 μ
N 1-35

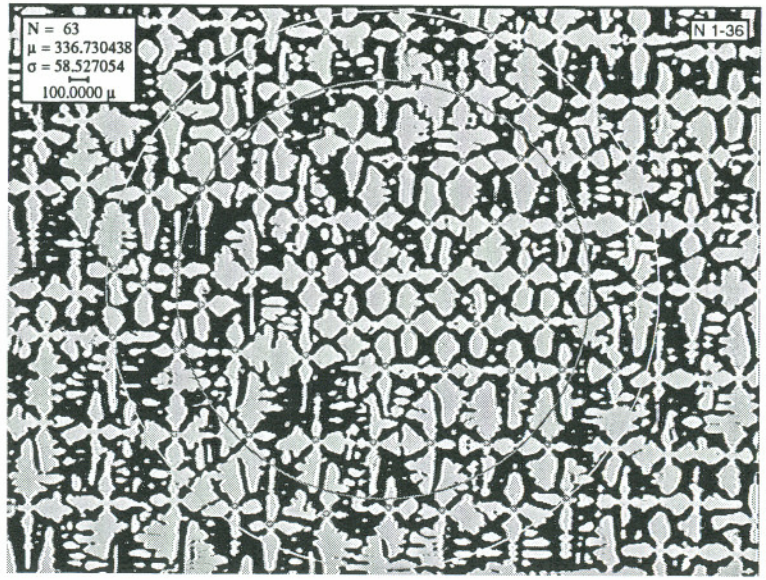
N = 63
μ = 336.730438
σ = 58.527054
100.0000 μ
N 1-36


N 1-38
N = 96
μ = 347.093285
σ = 72.113961
100.0000 μ

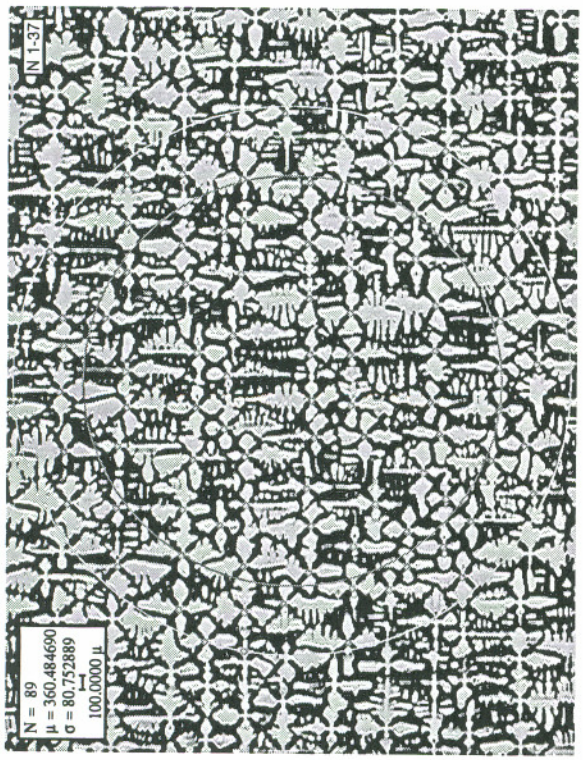
N 1-37
N = 89
μ = 360.484690
σ = 80.752889
100.0000 μ

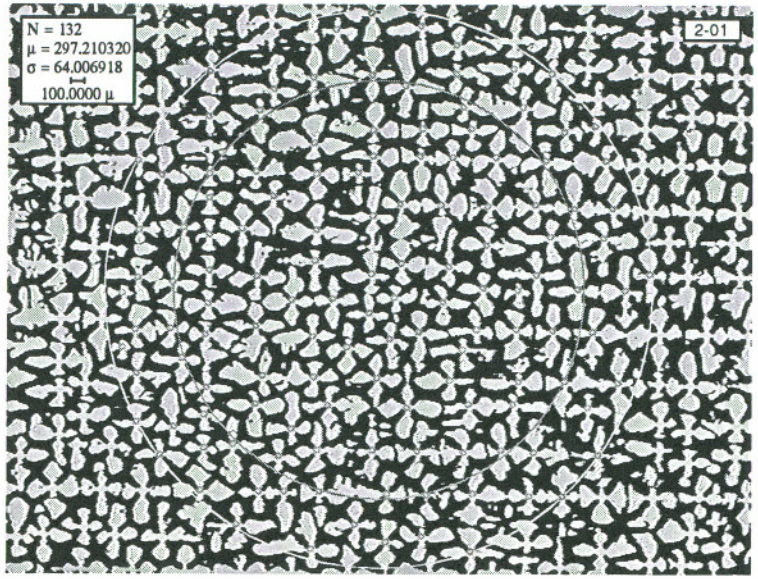
N = 132
μ = 297.210320
σ = 64.006918
100.0000 μ
2-01

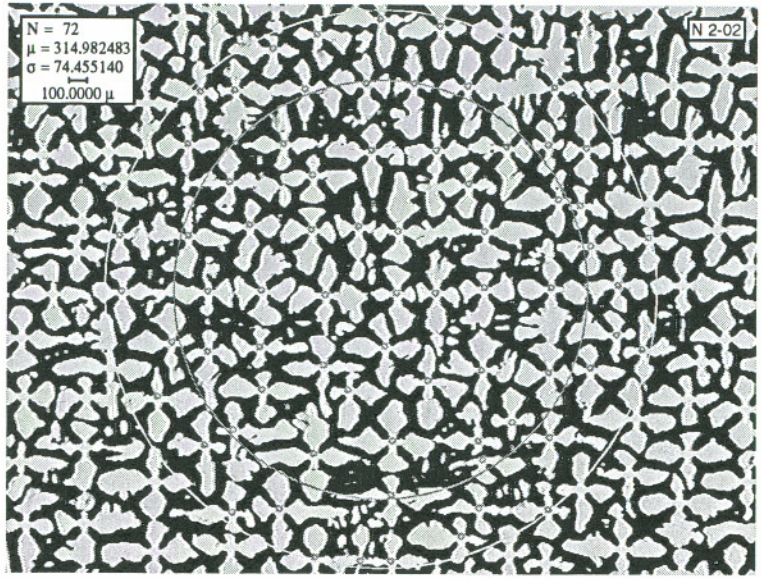
N = 72
μ = 314.982483
σ = 74.455140
100.0000 μ
N 2-02

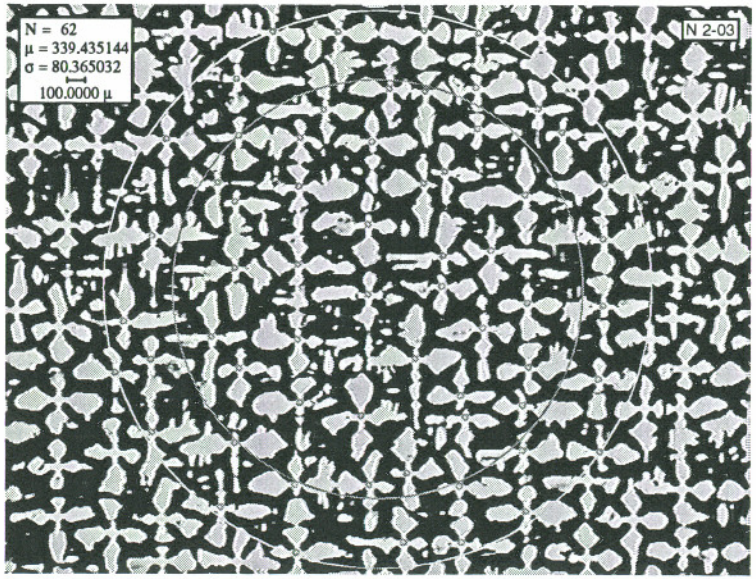
N = 62
μ = 339.435144
σ = 80.365032
100.0000 μ
N 2-03

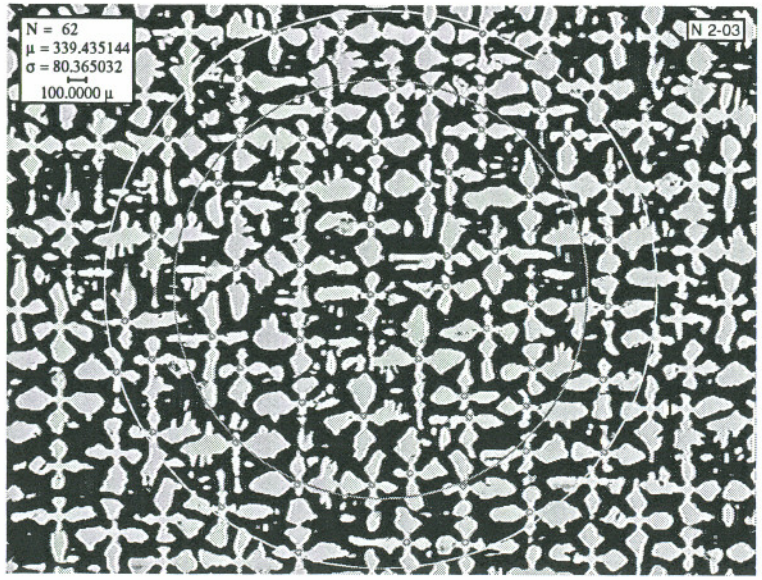
N = 62
μ = 339.435144
σ = 80.365032
100.0000 μ
N 2-03

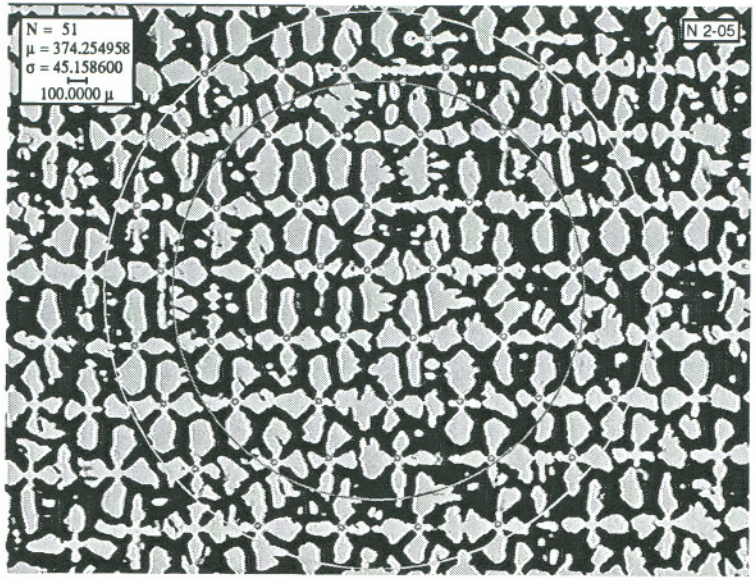
N = 51
μ = 374.254958
σ = 45.158600
100.0000 μ
N 2-05

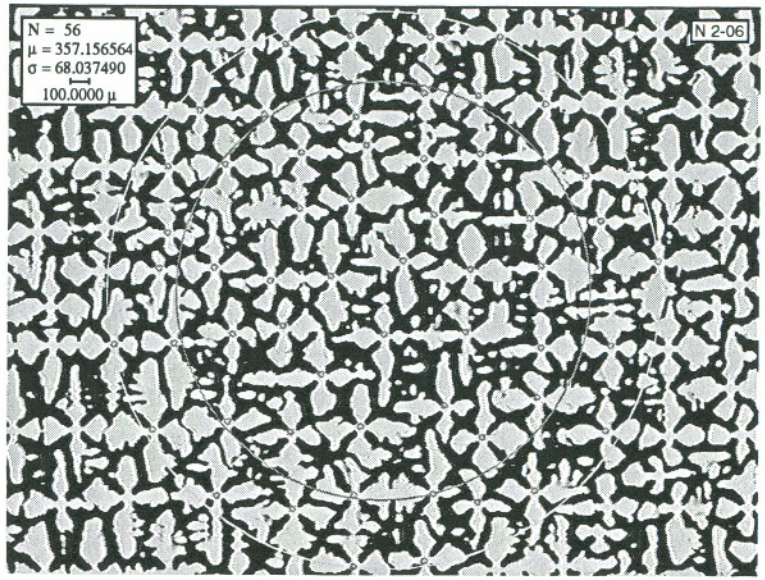
N = 56
μ = 357.156564
σ = 68.037490
100.0000 μ
N 2-06

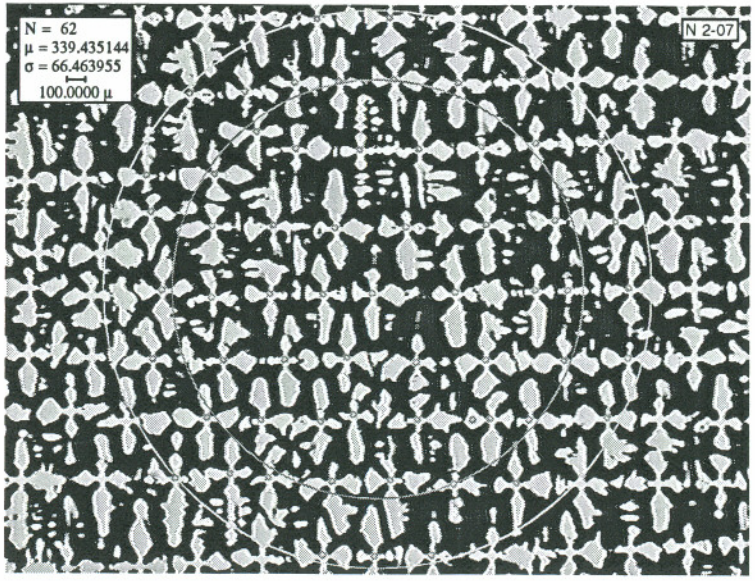
N = 62
μ = 339.435144
σ = 66.463955
100.0000 μ
N 2-07

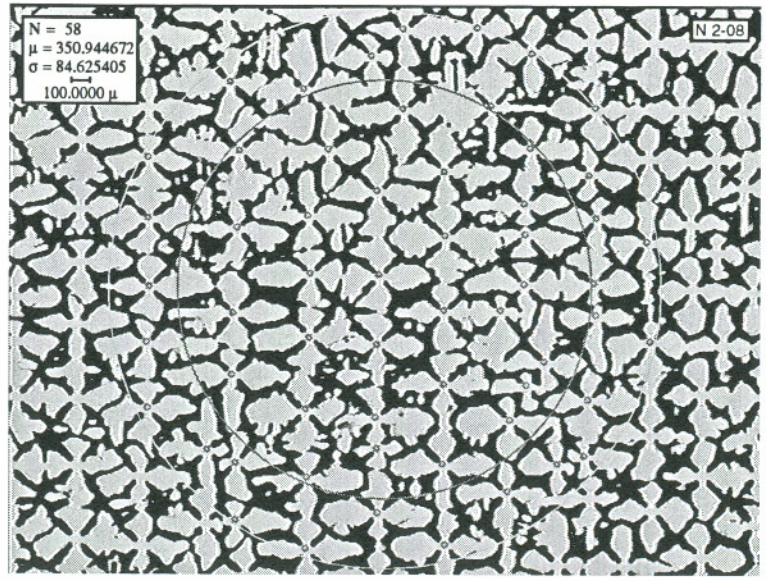
N = 58
μ = 350.944672
σ = 84.625405
100.0000 μ
N 2-08

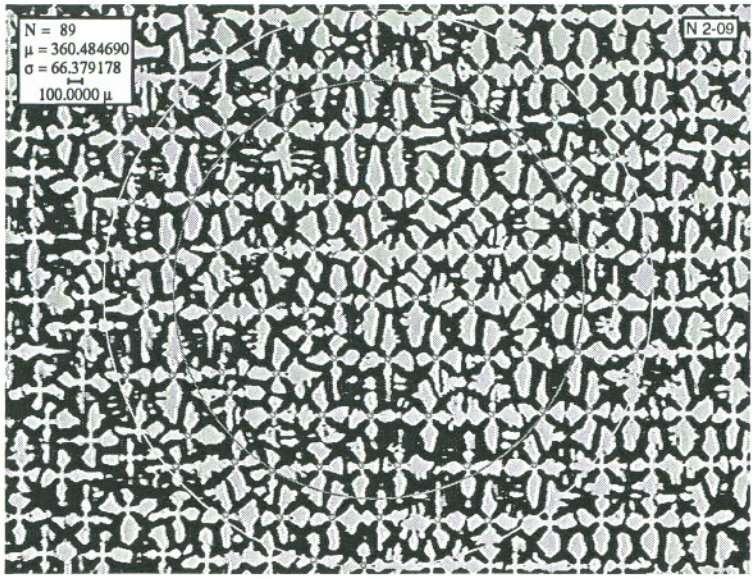
N = 89
μ = 360.484690
σ = 66.379178
100.0000 μ
N 2-09

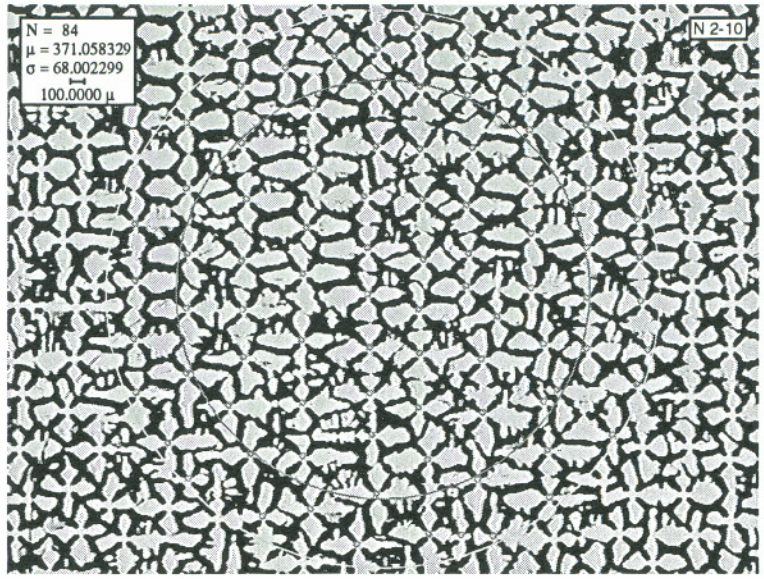
N = 84
μ = 371.058329
σ = 68.002299
100.0000 μ
N 2-10

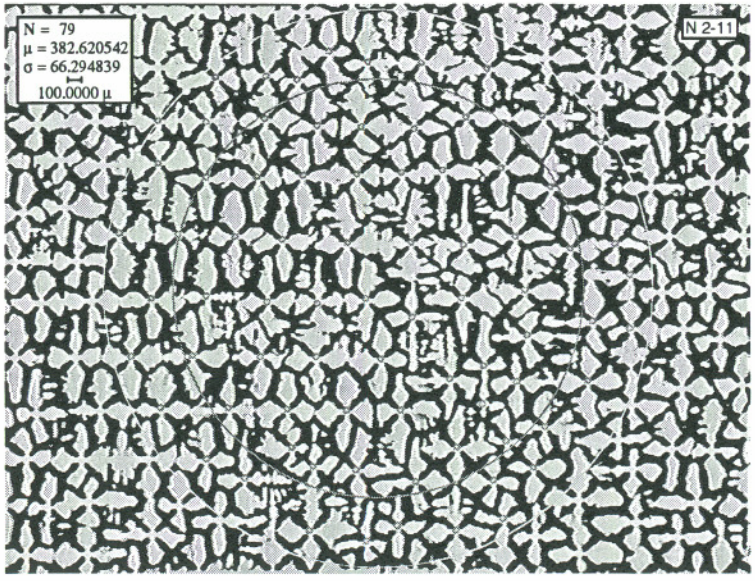
N = 79
μ = 382.620542
σ = 66.294839
100.0000 μ
N 2-11

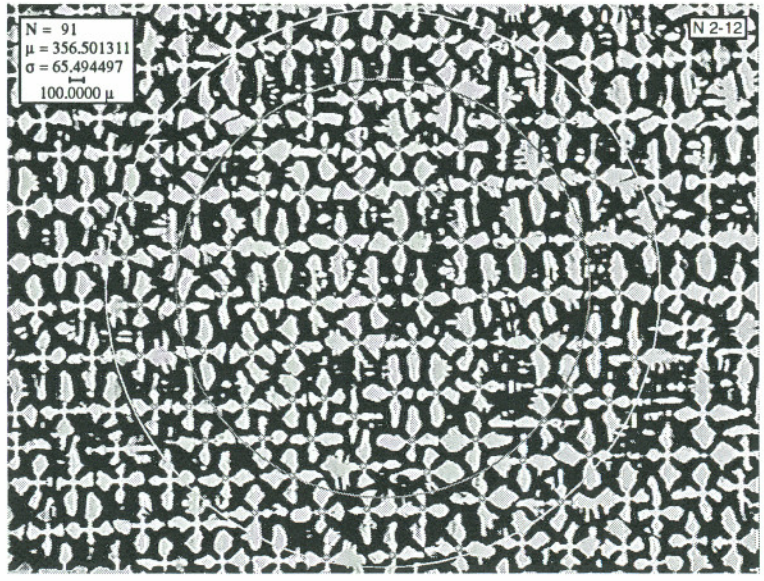
N = 91
μ = 356.501311
σ = 65.494497
100.0000 μ
N 2-12

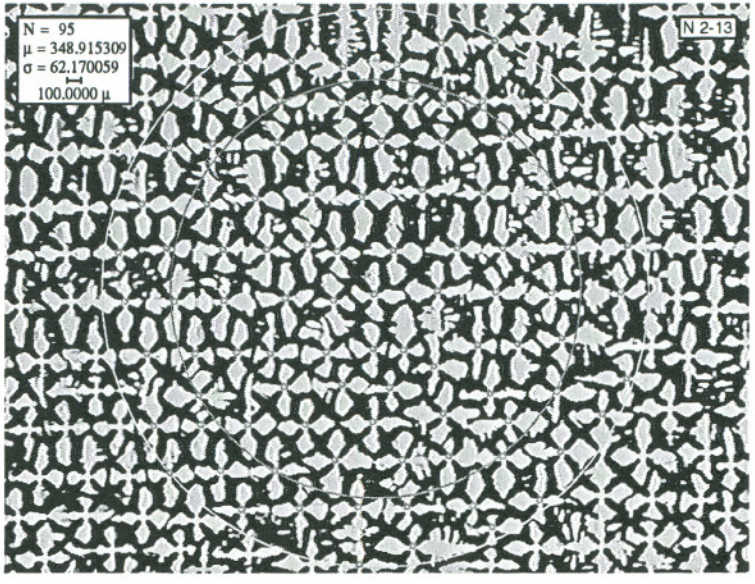
N = 95
μ = 348.915309
σ = 62.170059
100.0000 μ
N 2-13

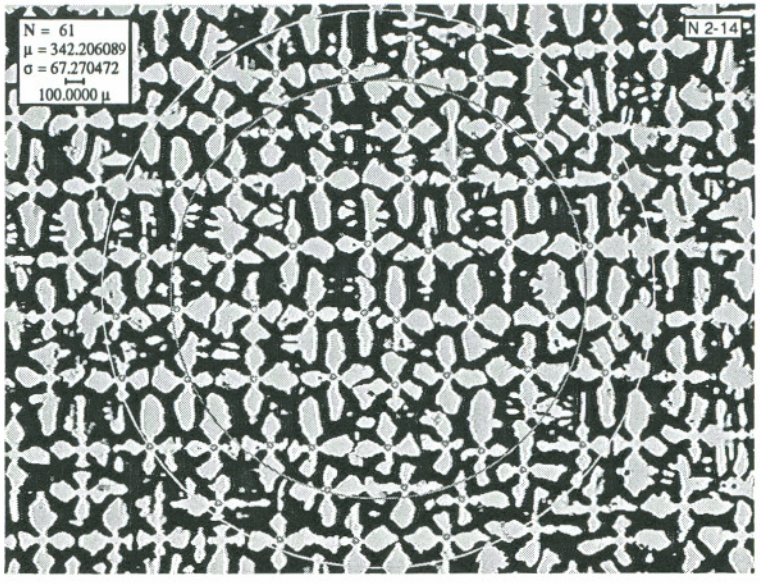
N = 61
μ = 342.206089
σ = 67.270472
100.0000 μ
N 2-14

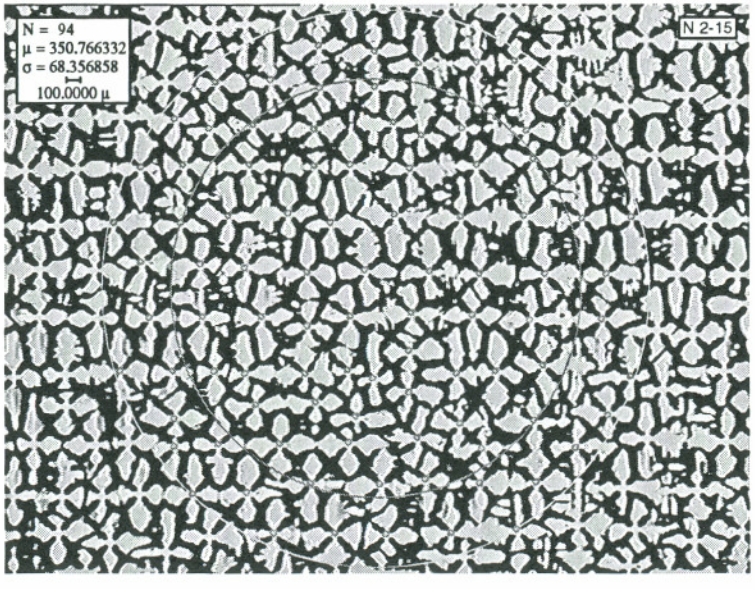
N = 94
μ = 350.766332
σ = 68.356858
100.0000 μ
N 2-15

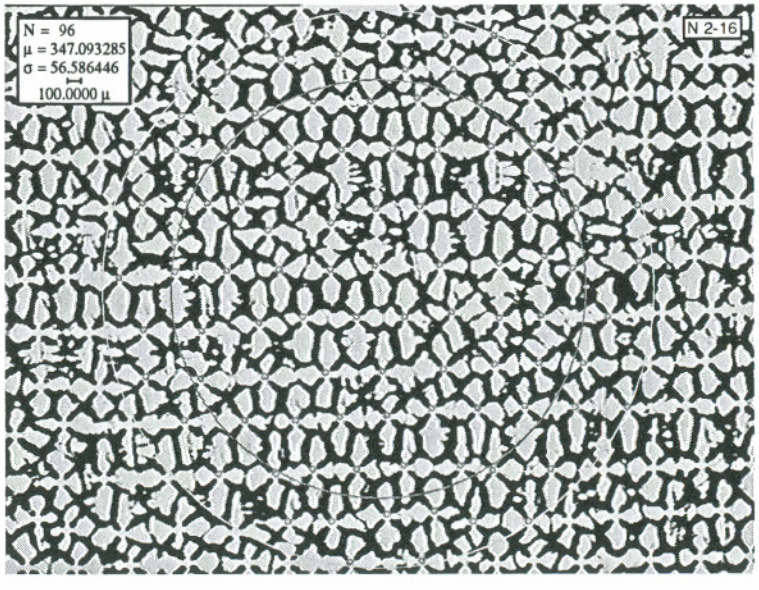
N = 96
μ = 347.093285
σ = 56.586446
100.0000 μ
N 2-16

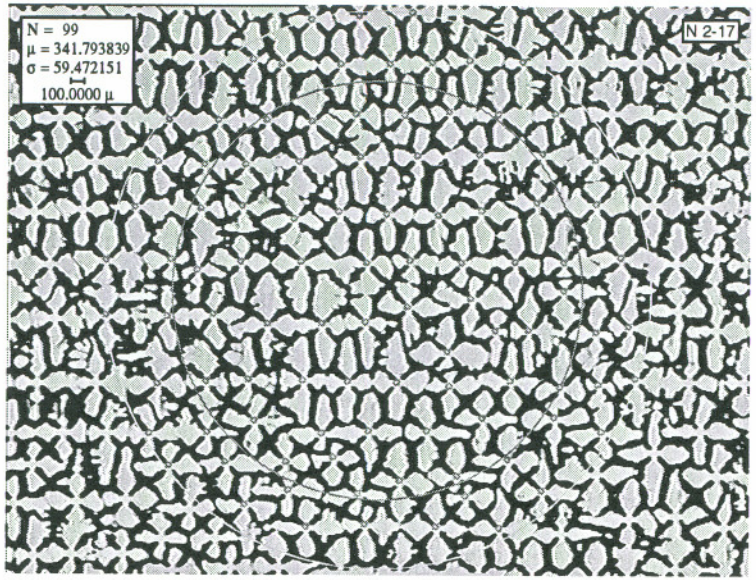
N = 99
μ = 341.793839
σ = 59.472151
100.0000 μ
N 2-17

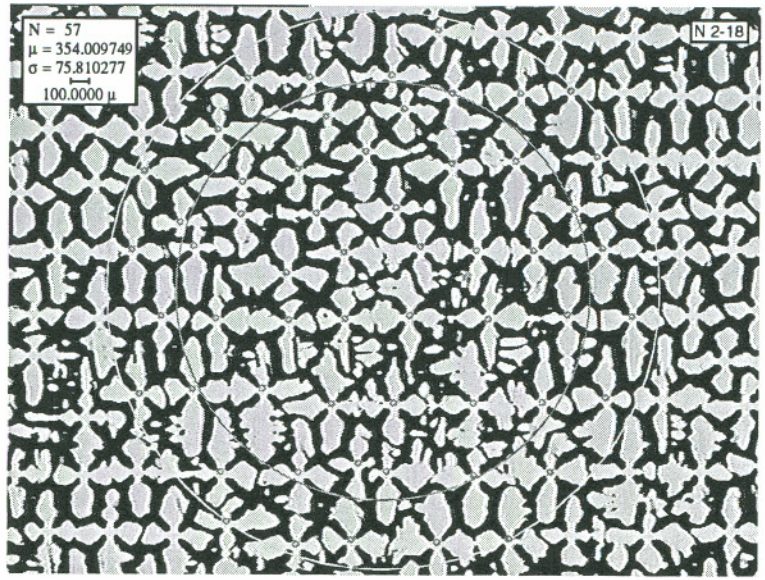
N = 57
μ = 354.009749
σ = 75.810277
100.0000 μ
N 2-18

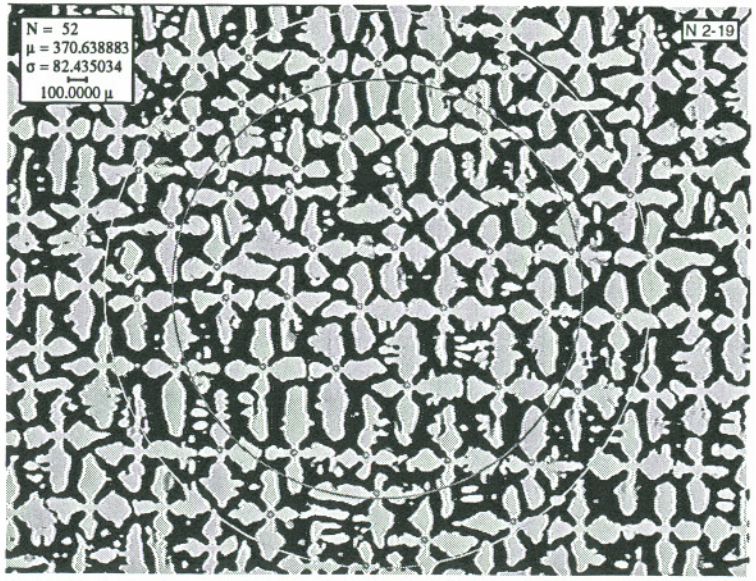
N = 52
μ = 370.638883
σ = 82.435034
100.0000 μ
N 2-19

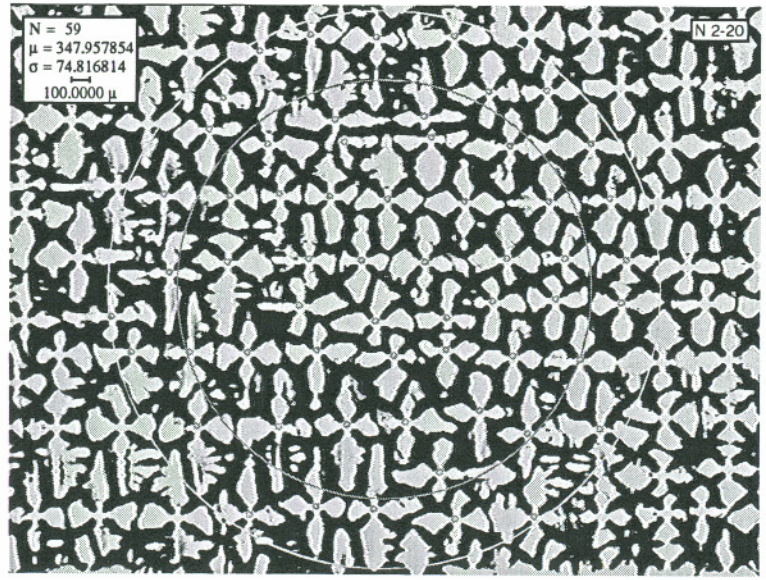
N = 59
μ = 347.957854
σ = 74.816814
100.0000 μ
N 2-20

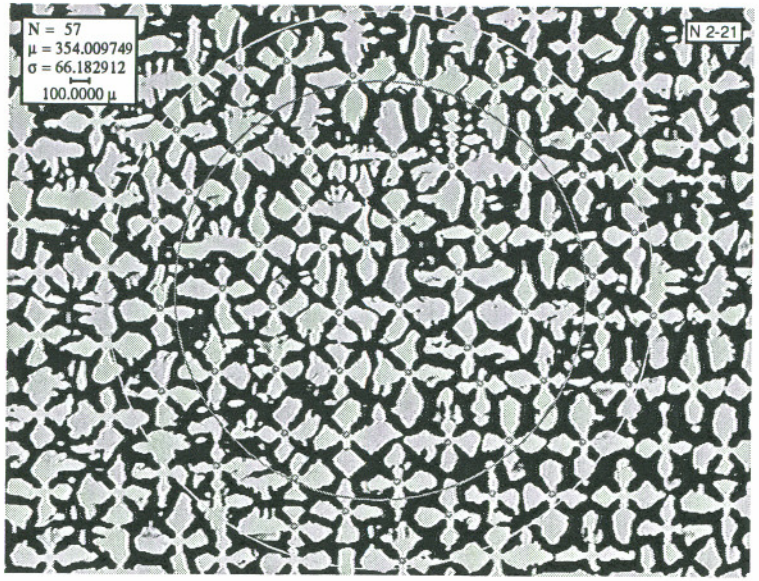
N = 57
μ = 354.009749
σ = 66.182912
100.0000 μ
N 2-21

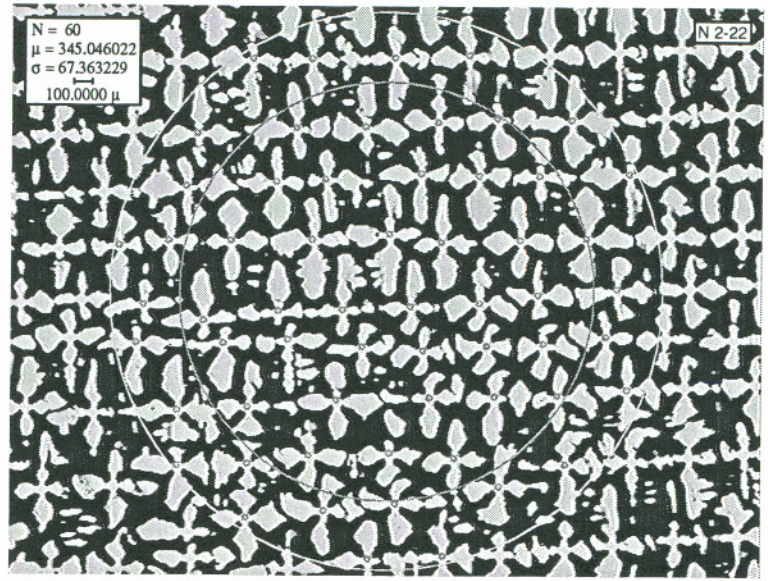
N = 60
μ = 345.046022
σ = 67.363229
100.0000 μ
N 2-22

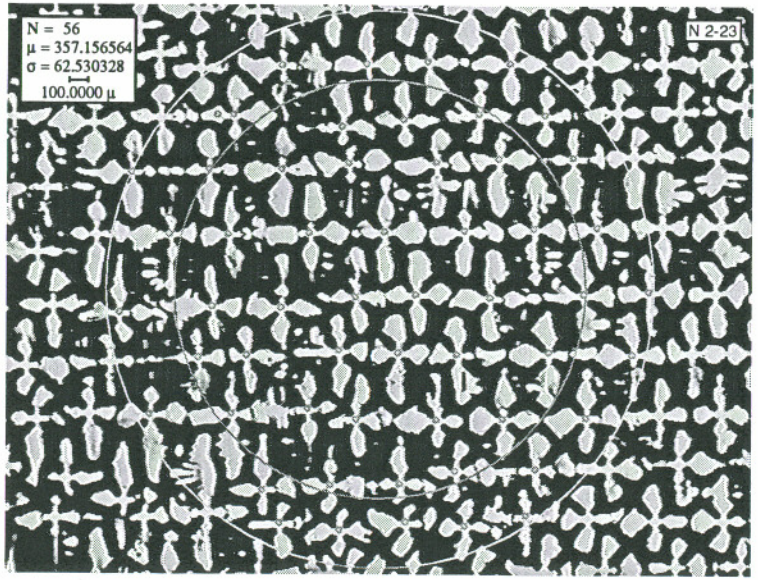
N = 56
μ = 357.156564
σ = 62.530328
100.0000 μ
N 2-23

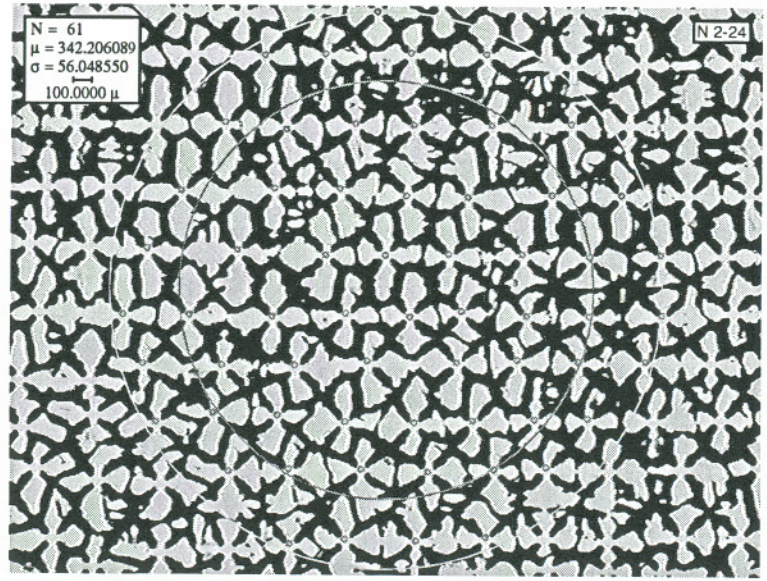
N = 61
μ = 342.206089
σ = 56.048550
100.0000 μ
N 2-24


N = 59
μ = 347.957854
σ = 82.177788
100.0000 μ
N 2-25

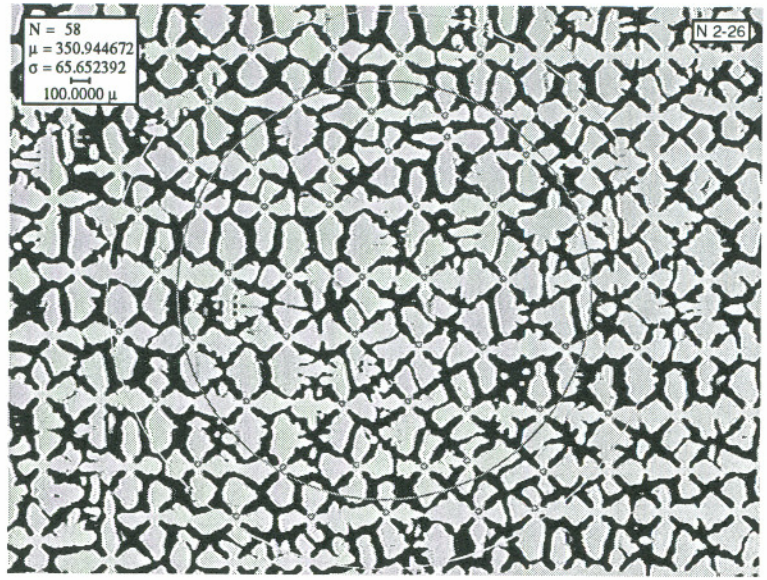
N = 58
μ = 350.944672
σ = 65.652392
100.0000 μ
N 2-26

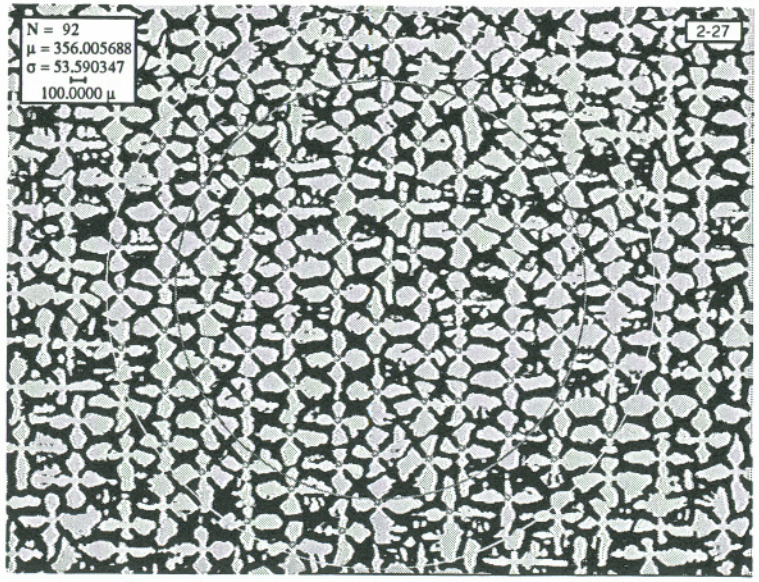
N = 92
μ = 356.005688
σ = 53.590347
100.0000 μ
2-27

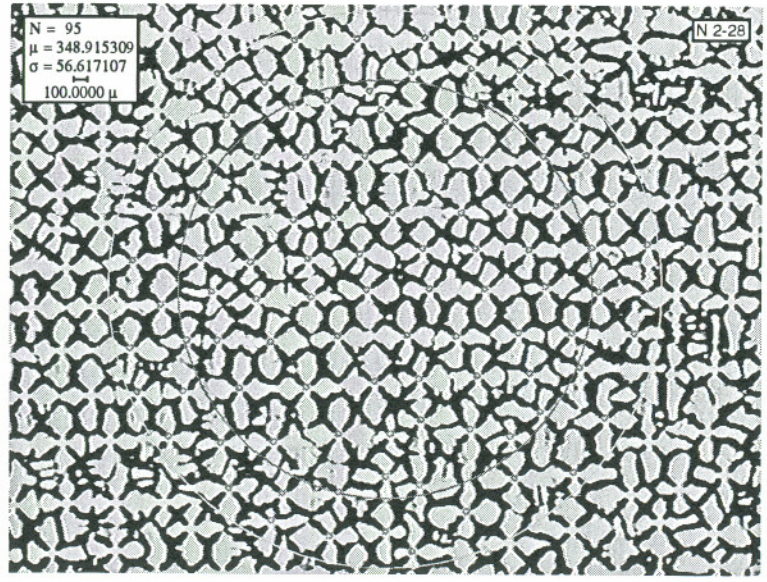
N = 95
μ = 348.915309
σ = 56.617107
100.0000 μ
N 2-28

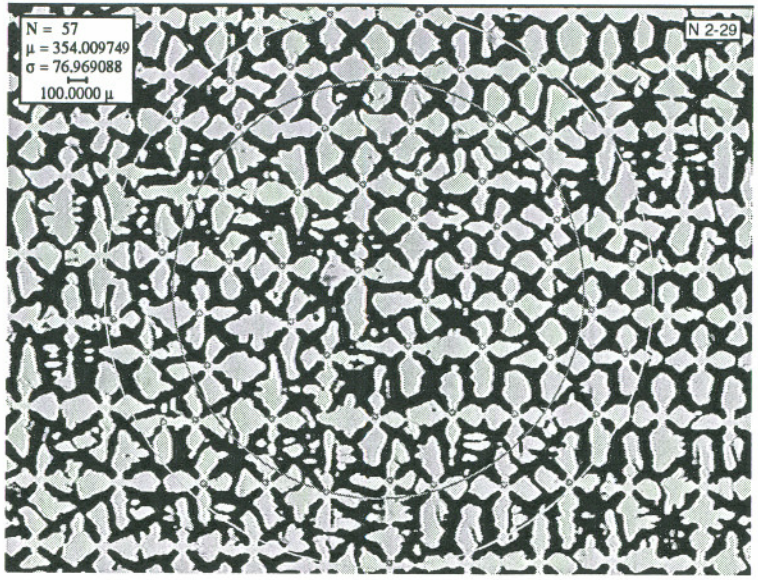
N = 57
μ = 354.009749
σ = 76.969088
100.0000 μ
N 2-29


N = 60
μ = 345.046022
σ = 74.131721
100.0000 μ
N 2-30

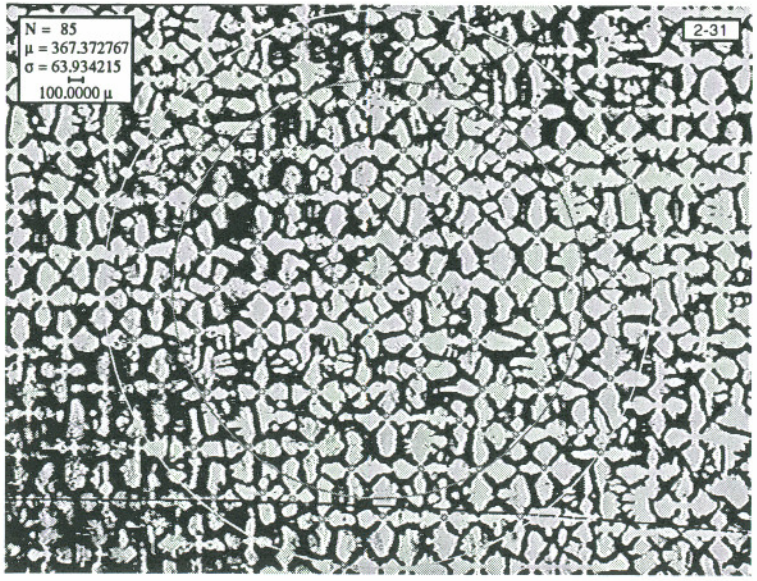
N = 85
μ = 367.372767
σ = 63.934215
100.0000 μ
2-31

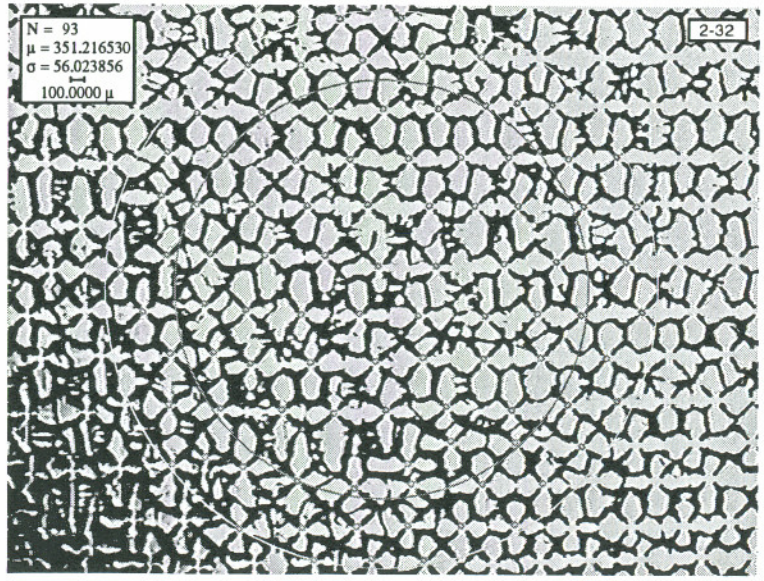
N = 93
μ = 351.216530
σ = 56.023856
100.0000 μ
2-32


N 2-34
N = 48
μ = 385.773180
σ = 71.297349
100.0000 μ

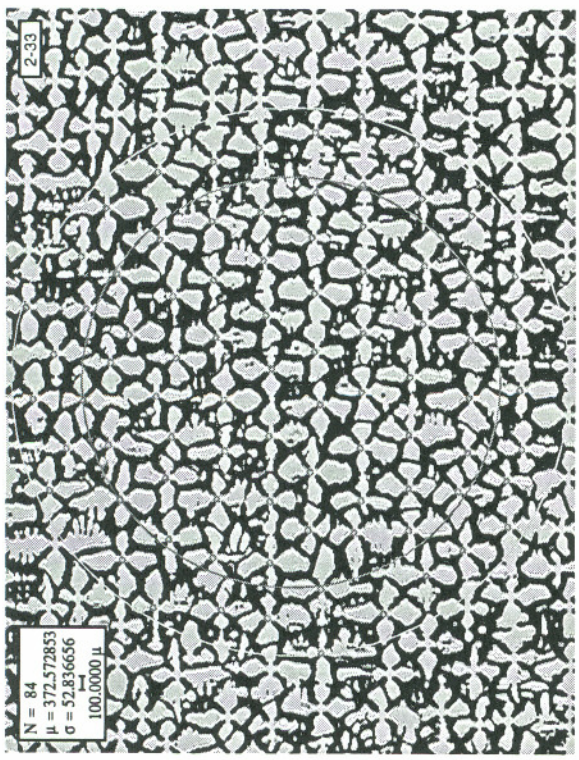
2-33
N = 84
μ = 372.572853
σ = 52.836656
100.0000 μ

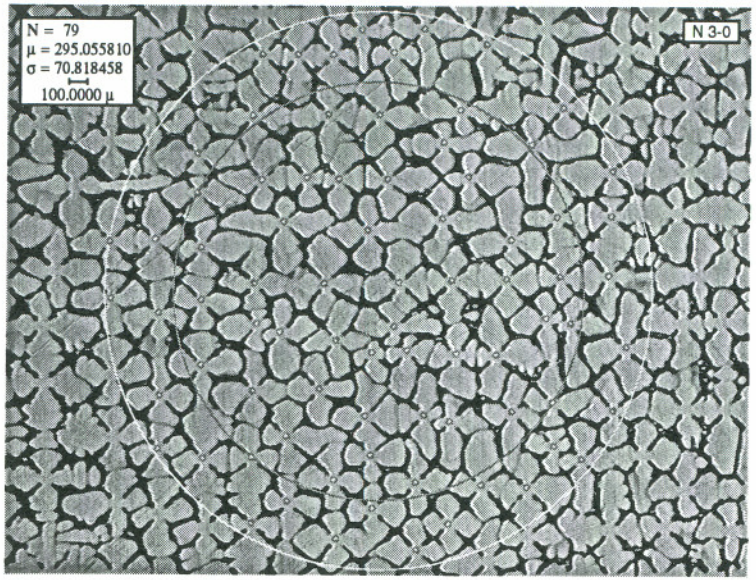
N = 79
μ = 295.055810
σ = 70.818458
100.0000 μ
N 3-0

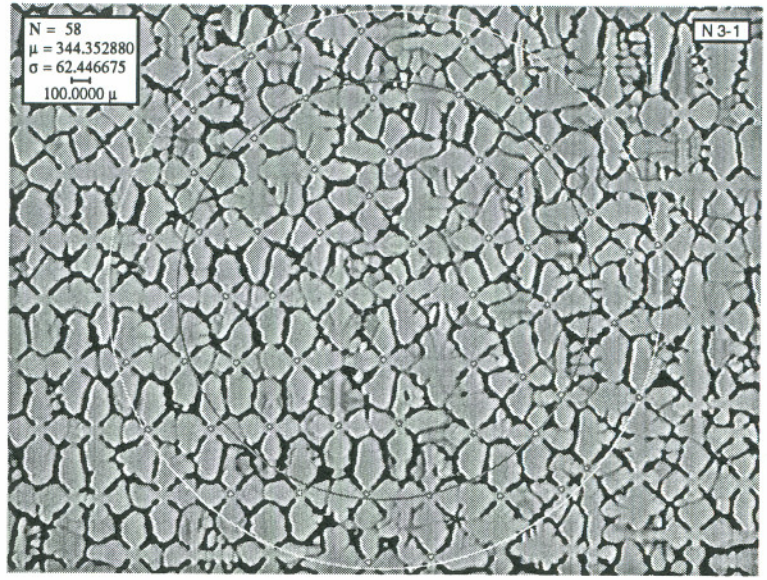
N = 58
μ = 344.352880
σ = 62.446675
100.0000 μ
N 3-1

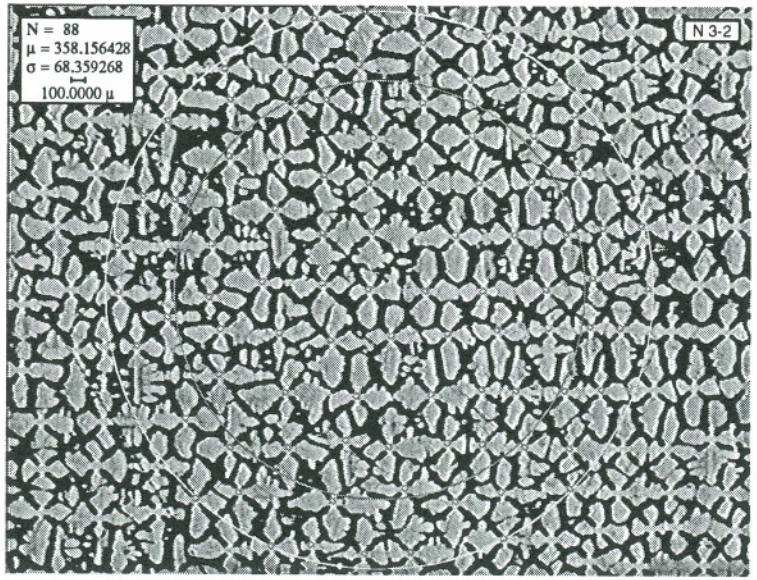
N = 88
μ = 358.156428
σ = 68.359268
100.0000 μ
N 3-2

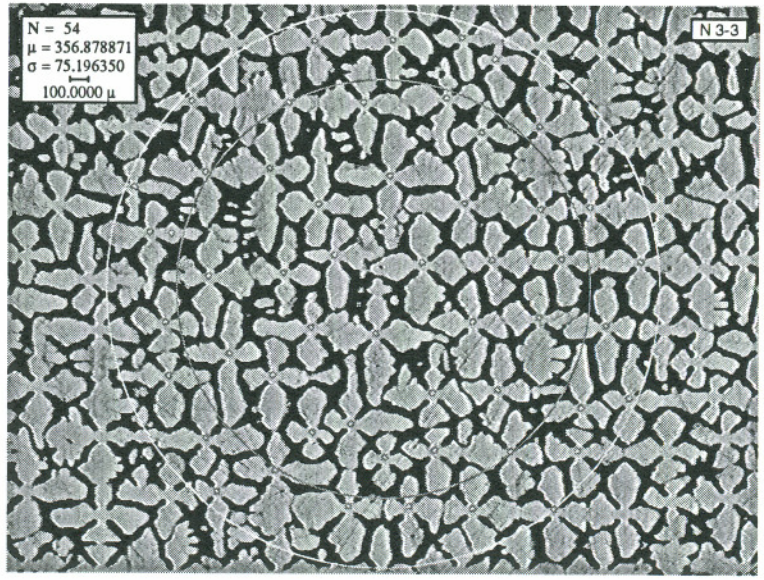
N = 54
μ = 356.878871
σ = 75.196350
100.0000 μ
N 3-3

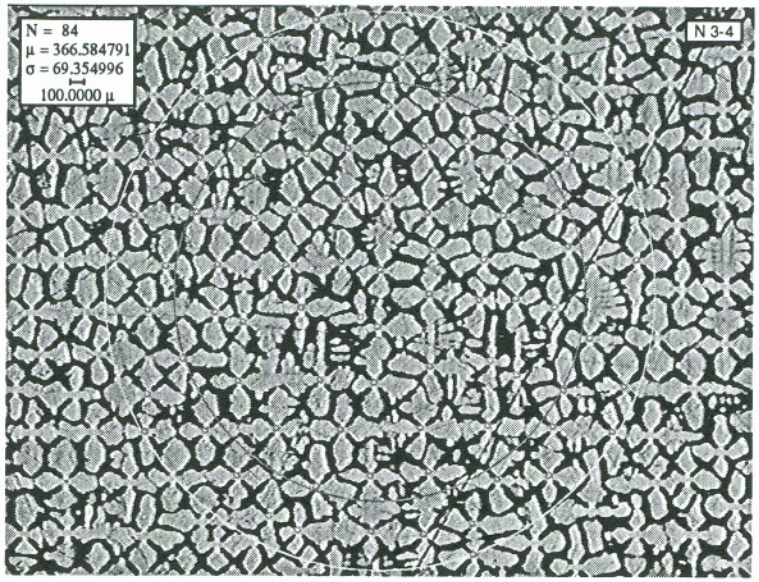
N = 84
μ = 366.584791
σ = 69.354996
100.0000 μ
N 3-4

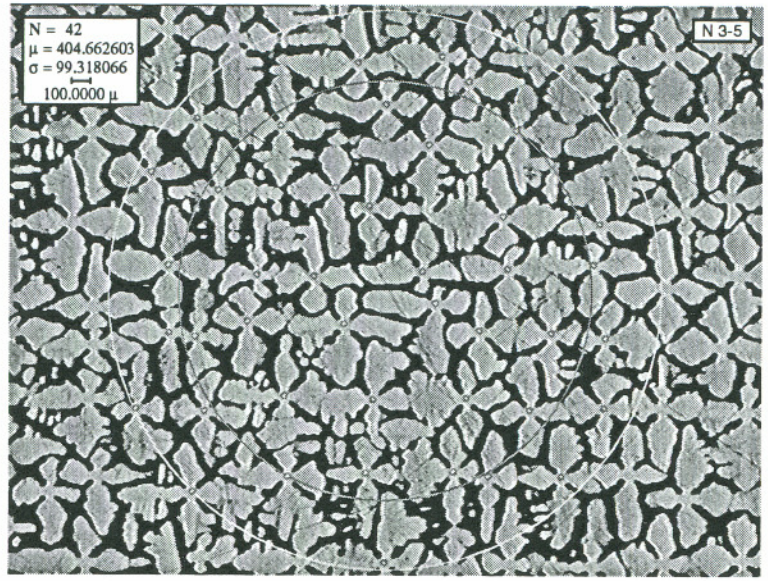
N = 42
μ = 404.662603
σ = 99.318066
100.0000 μ
N 3-5

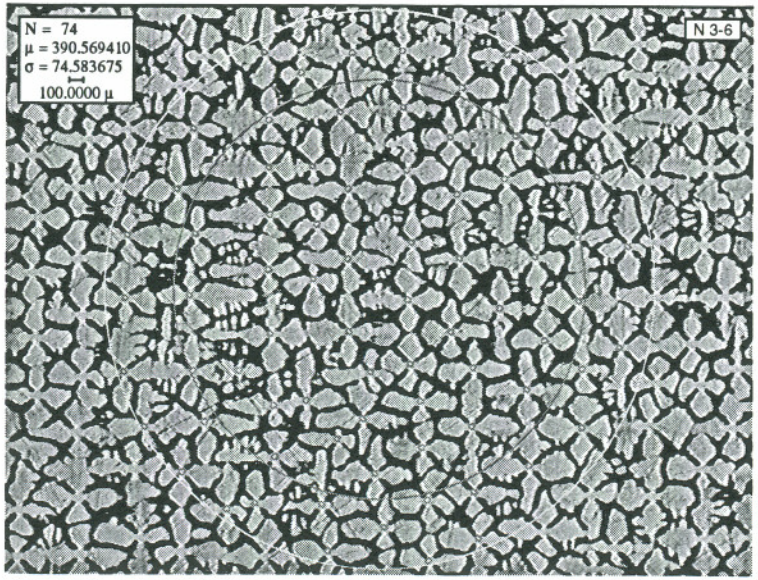
N = 74
μ = 390.569410
σ = 74.583675
100.0000 μ
N 3-6

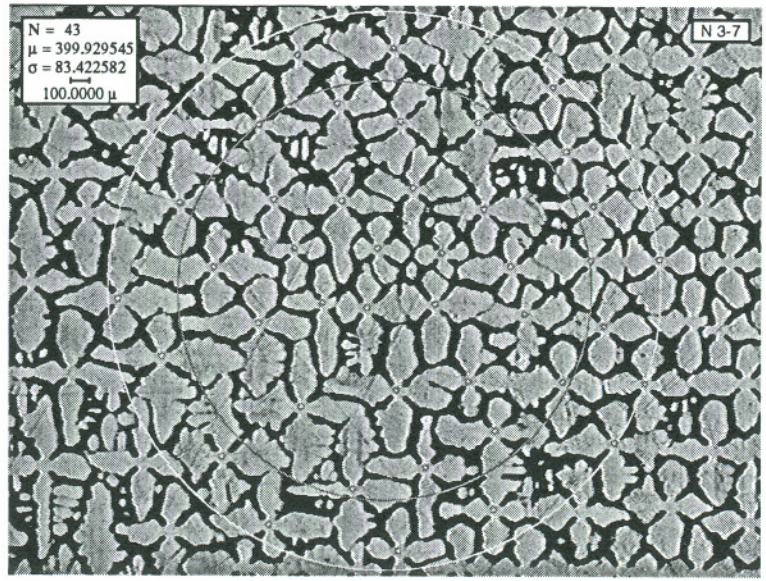
N = 43
μ = 399.929545
σ = 83.422582
100.0000 μ
N 3-7


N 3-8
N = 60
μ = 433.748974
σ = 91.861552
100.0000 μ

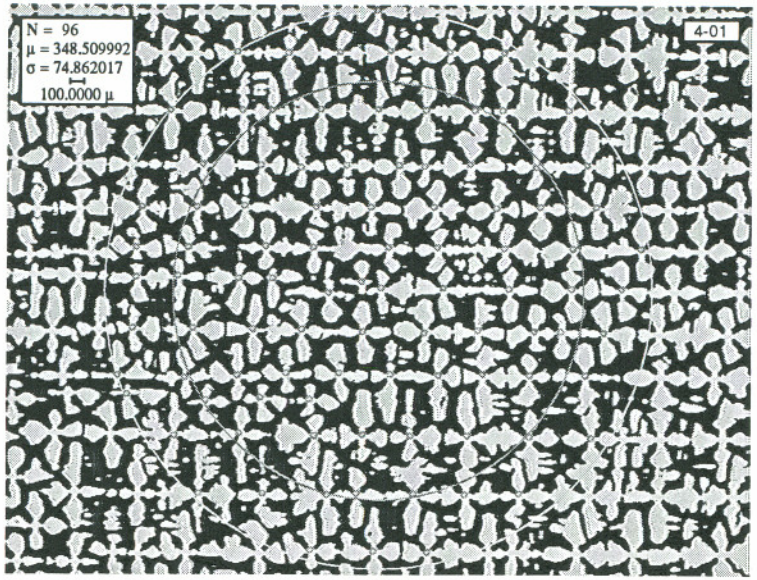
N = 96
μ = 348.509992
σ = 74.862017
100.0000 μ
4-01


N = 88
μ = 362.527112
σ = 66.539678
100.0000 μ
N 4-02

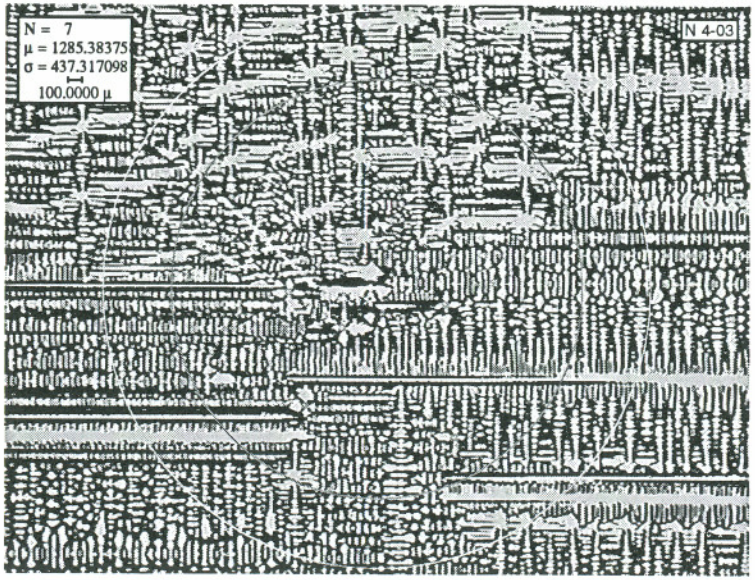
N = 7
μ = 1285.38375
σ = 437.317098
100.0000 μ
N 4-03

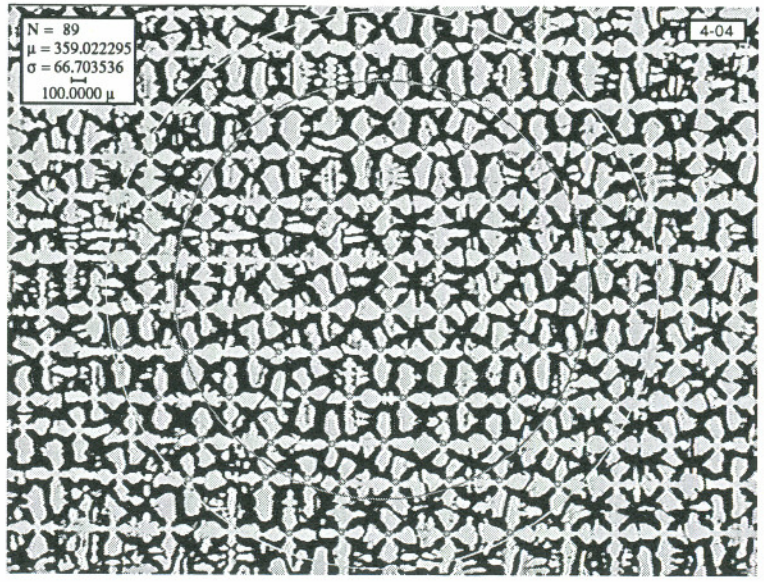
N = 89
μ = 359.022295
σ = 66.703536
100.0000 μ
4-04

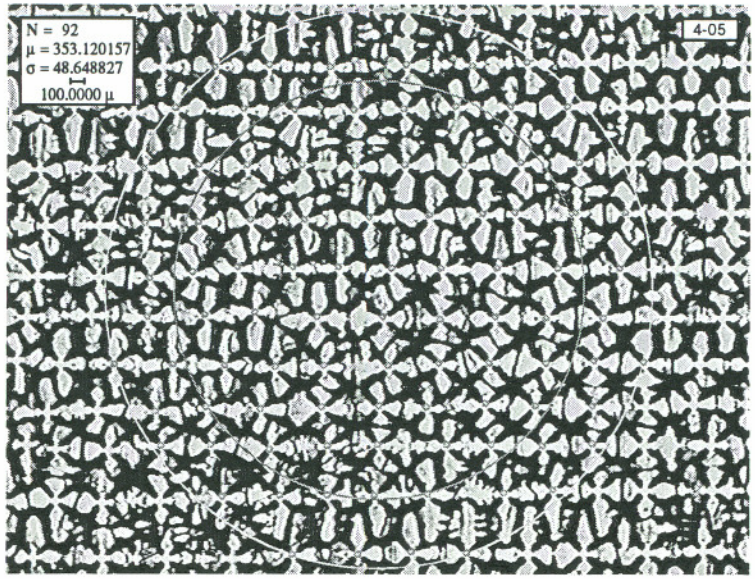
N = 92
μ = 353.120157
σ = 48.648827
100.0000 μ
4-05

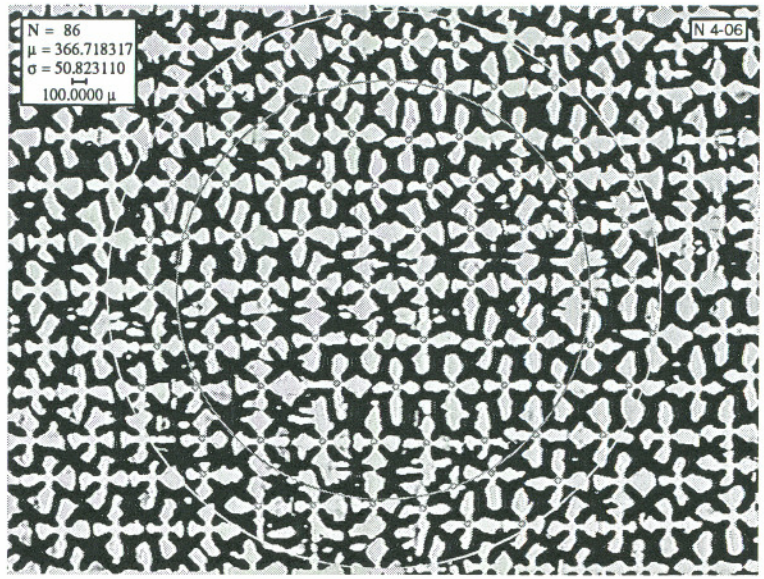
N = 86
μ = 366.718317
σ = 50.823110
100.0000 μ
N 4-06

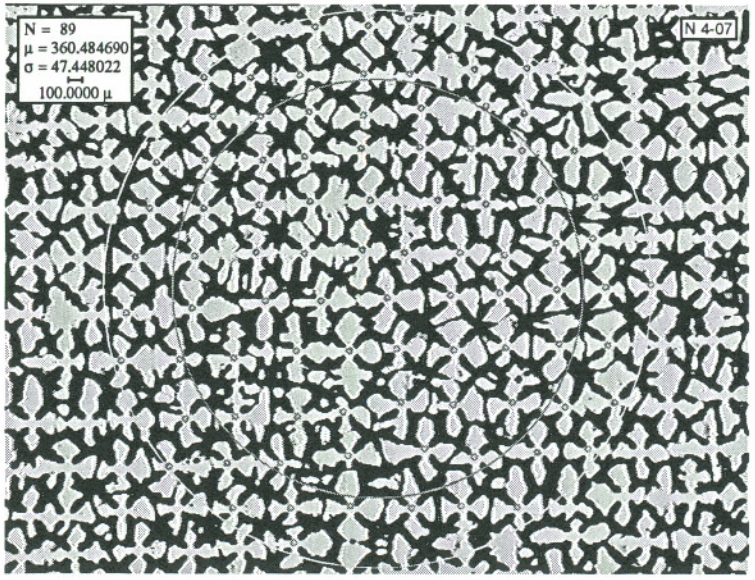
N = 89
μ = 360.484690
σ = 47.448022
100.0000 μ
N 4-07

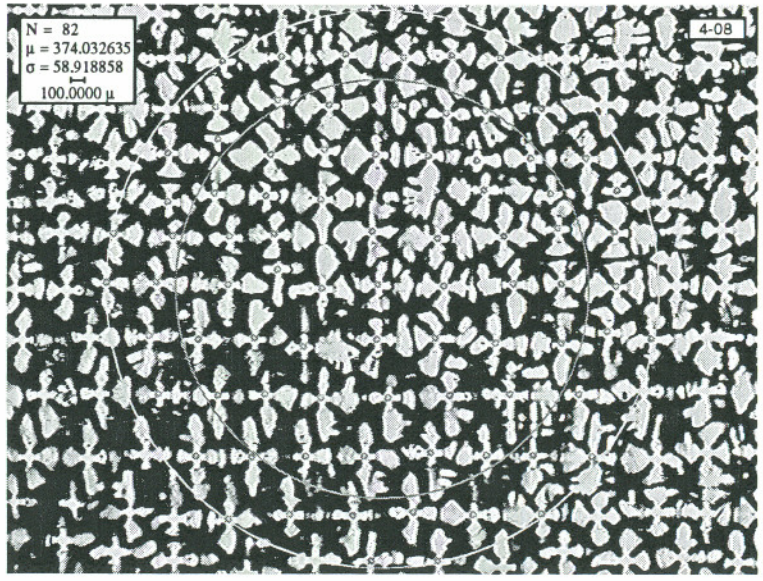
N = 82
μ = 374.032635
σ = 58.918858
100.0000 μ
4-08


N 4-10
N = 76
μ = 390.099175
σ = 64.186848
100.0000 μ


N 4-12
N = 79
μ = 382.620542
σ = 72.822836
100.0000 μ

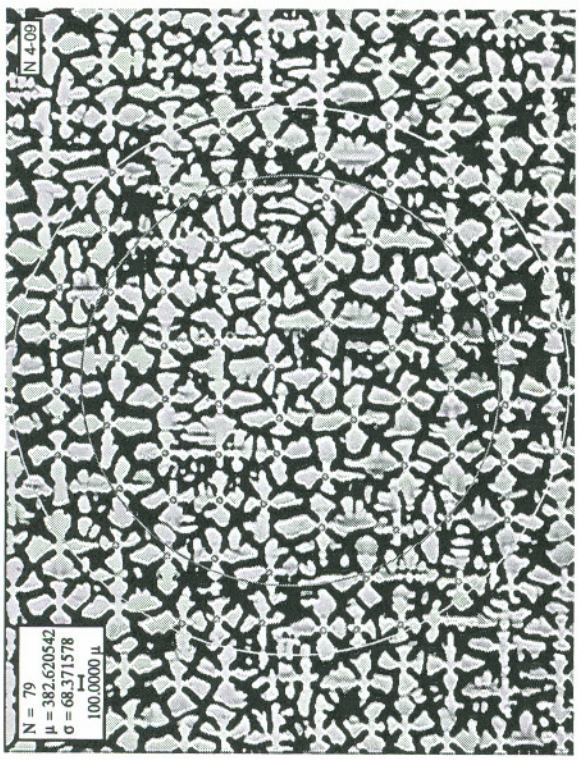
N 4-09
N = 79
μ = 382.620542
σ = 68.371578
100.0000 μ


N 4-11
N = 79
μ = 382.620542
σ = 73.628985
100.0000 μ

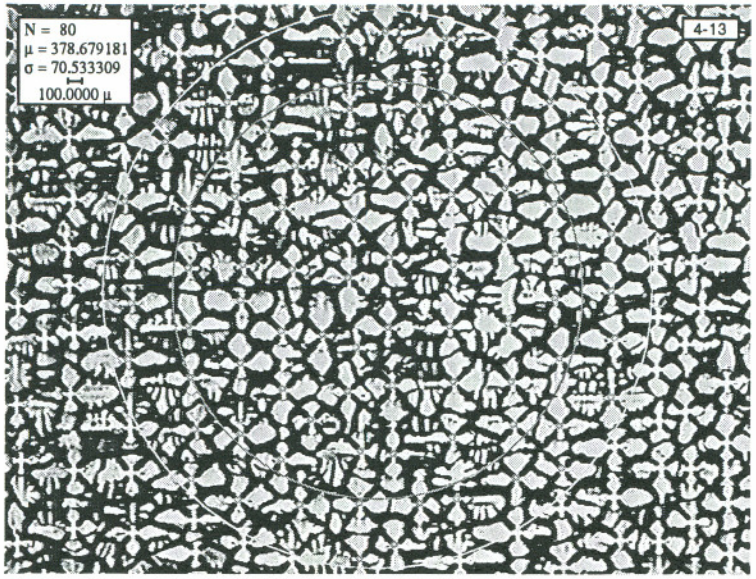
N = 80
μ = 378.679181
σ = 70.533309
100.0000 μ
4-13

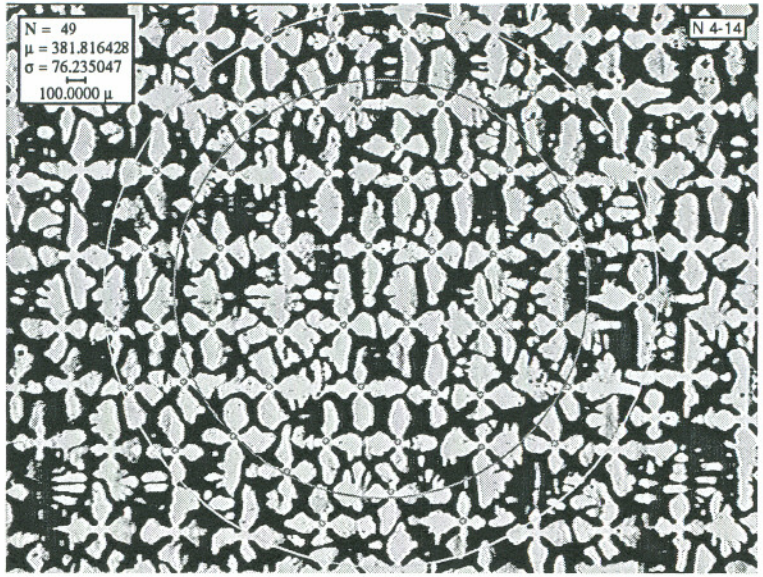
N = 49
μ = 381.816428
σ = 76.235047
100.0000 μ
N 4-14

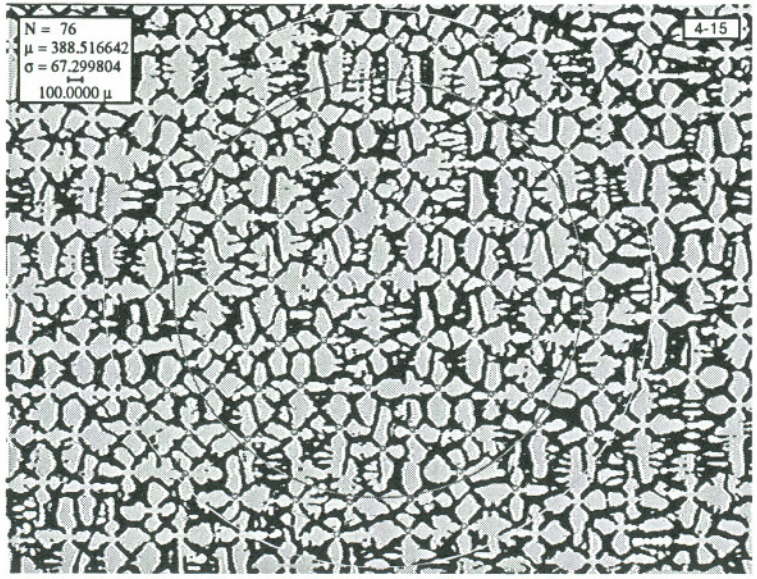
N = 76
μ = 388.516642
σ = 67.299804
100.0000 μ
4-15

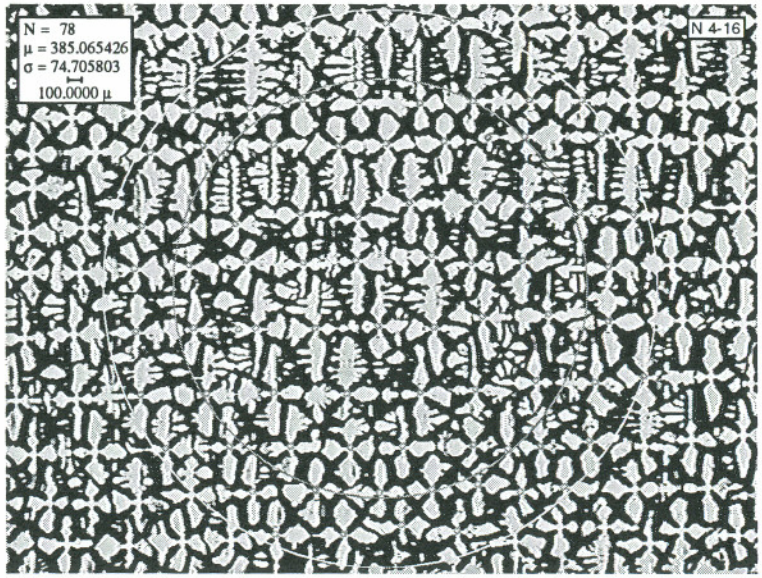
N = 78
μ = 385.065426
σ = 74.705803
100.0000 μ
N 4-16

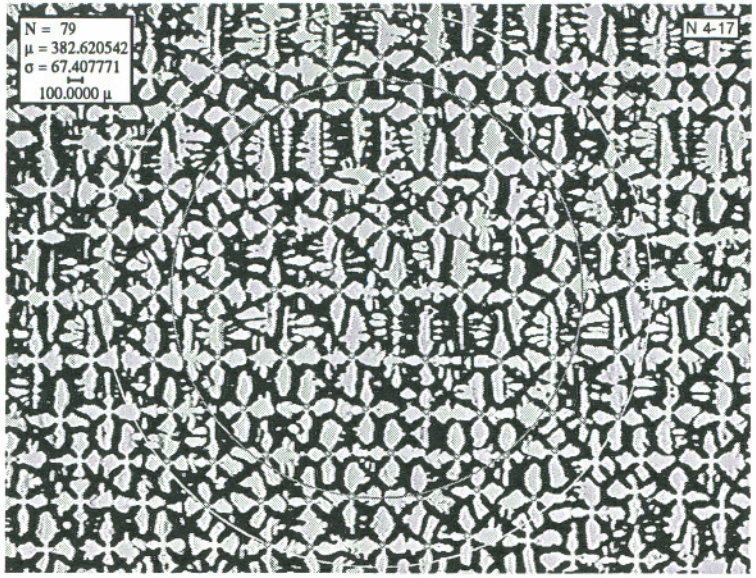
N = 79
μ = 382.620542
σ = 67.407771
100.0000 μ
N 4-17

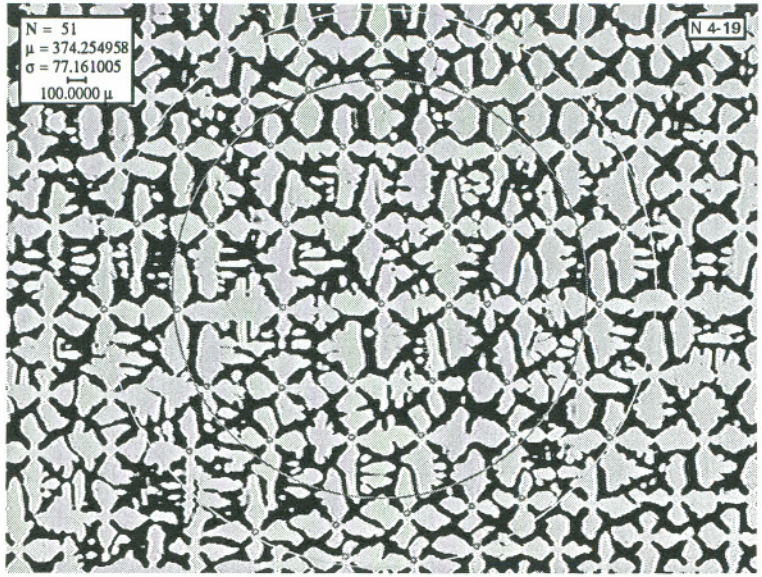
N = 51
μ = 374.254958
σ = 77.161005
100.0000 μ
N 4-19

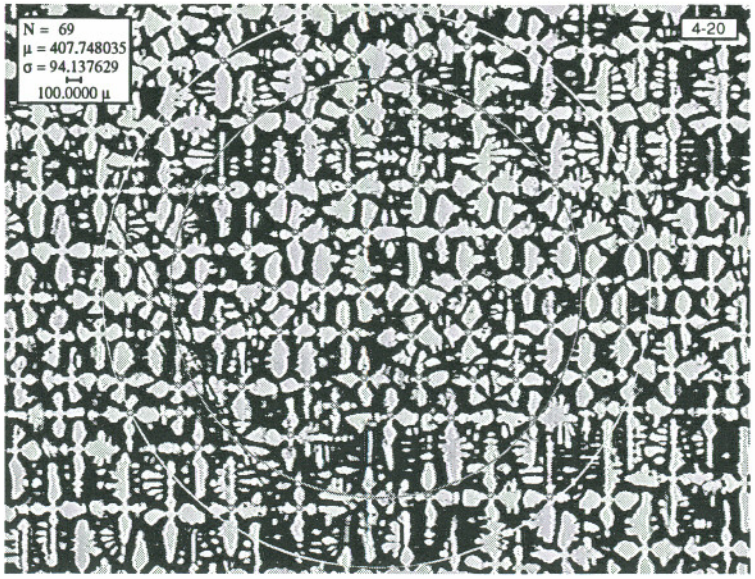
N = 69
μ = 407.748035
σ = 94.137629
100.0000 μ
4-20

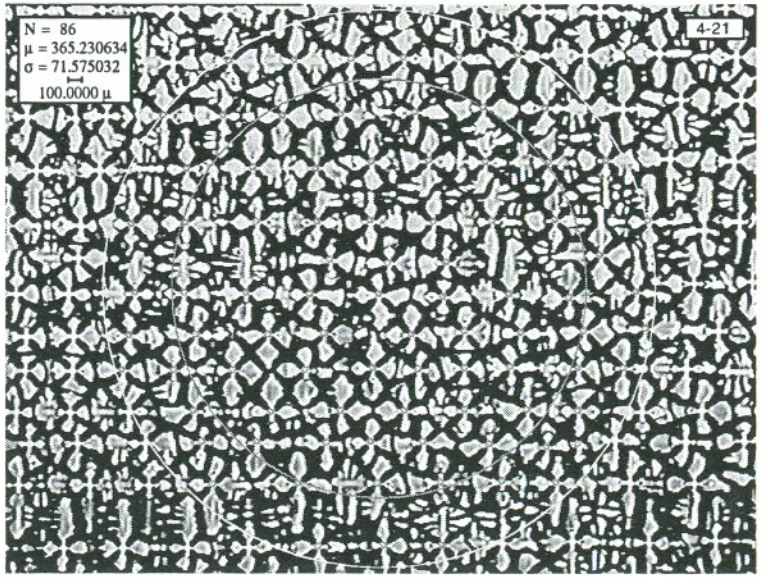
N = 86
μ = 365.230634
σ = 71.575032
100.0000 μ
4-21

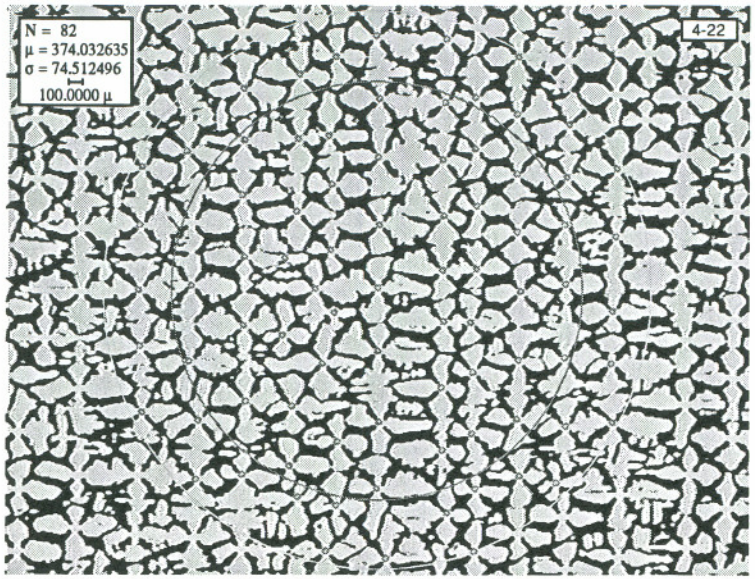
N = 82
μ = 374.032635
σ = 74.512496
100.0000 μ
4-22

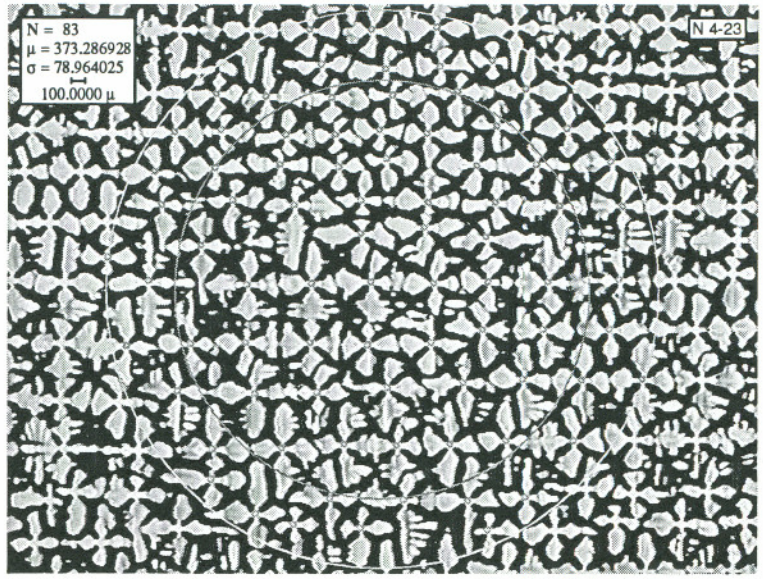
N = 83
μ = 373.286928
σ = 78.964025
100.0000 μ
N 4-23

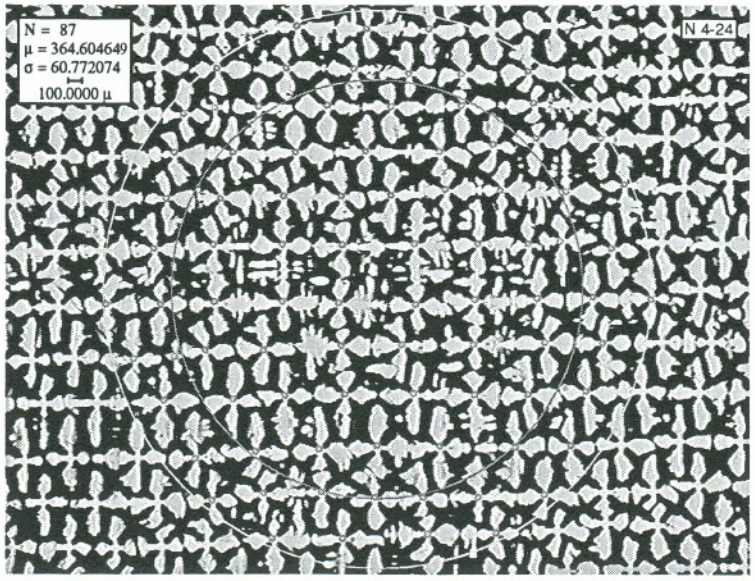
N = 87
μ = 364.604649
σ = 60.772074
100.0000 μ
N 4-24

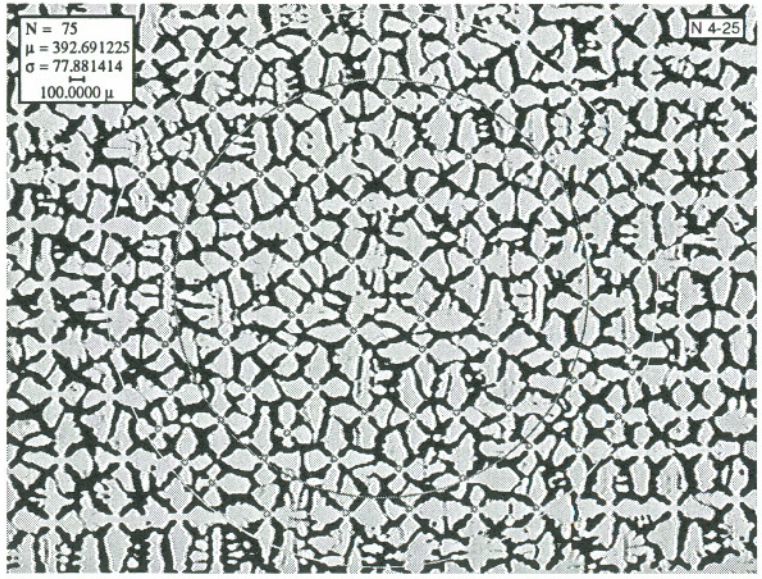
N = 75
μ = 392.691225
σ = 77.881414
100.0000 μ
N 4-25

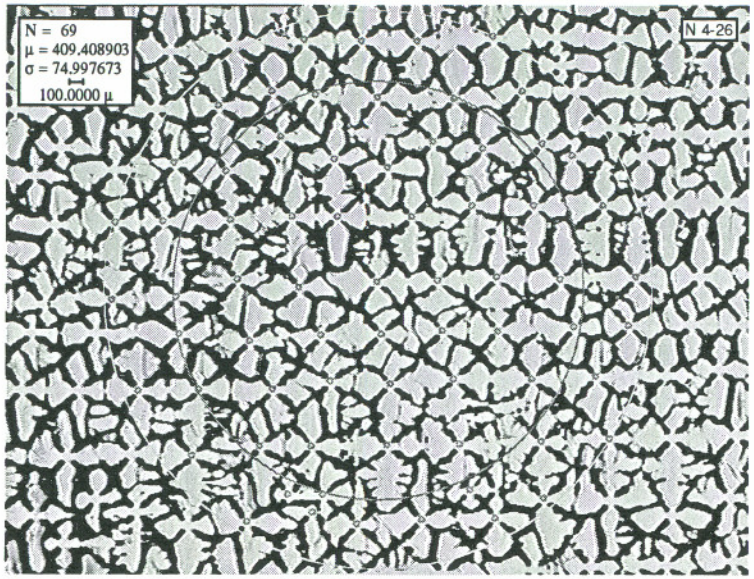
N = 69
μ = 409.408903
σ = 74.997673
100.0000 μ
N 4-26

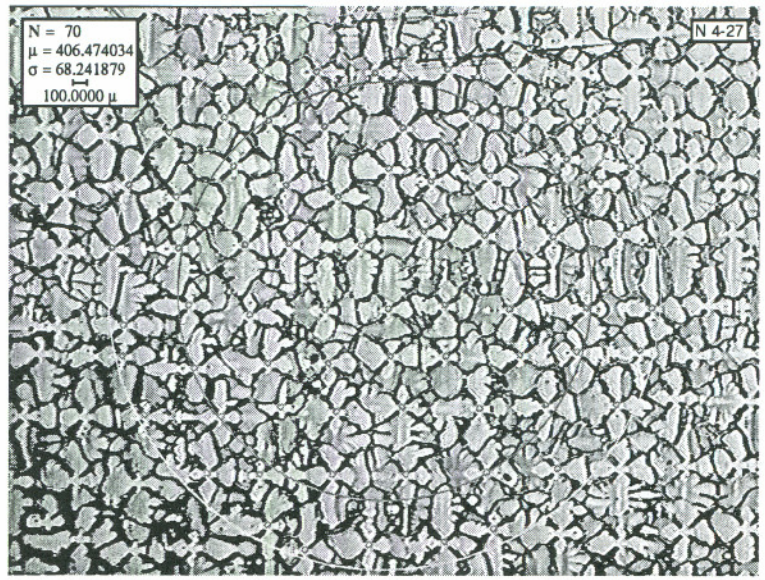
N = 70
μ = 406.474034
σ = 68.241879
100.0000 μ
N 4-27

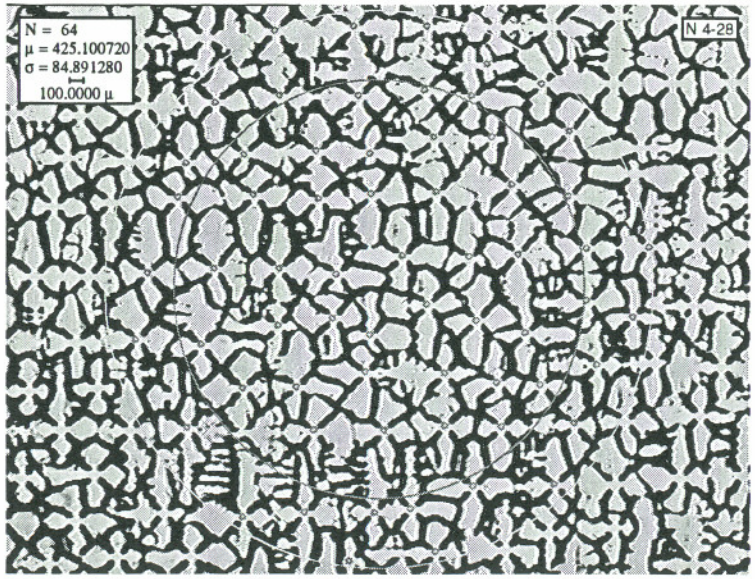
N = 64
μ = 425.100720
σ = 84.891280
100.0000 μ
N 4-28

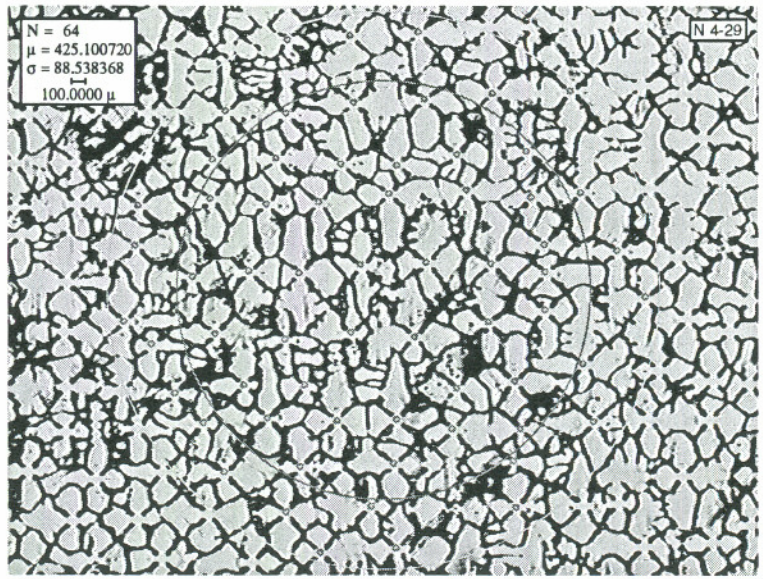
N = 64
μ = 425.100720
σ = 88.538368
100.0000 μ
N 4-29

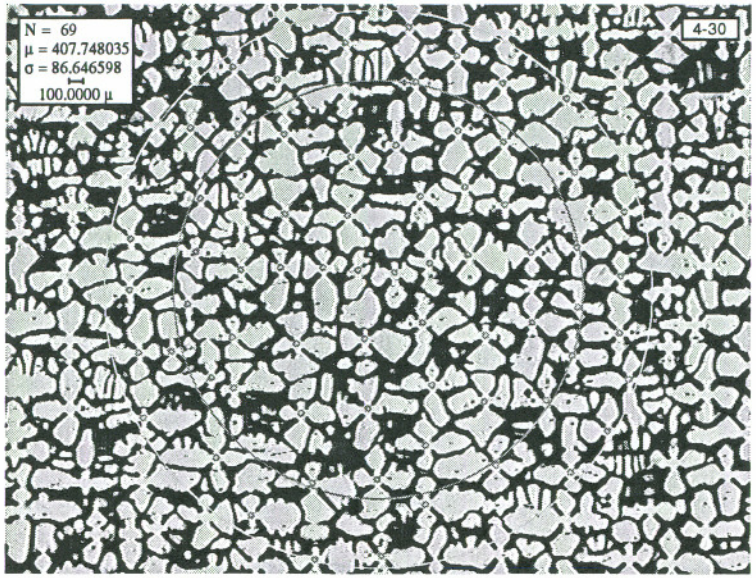
N = 69
μ = 407.748035
σ = 86.646598
100.0000 μ
4-30

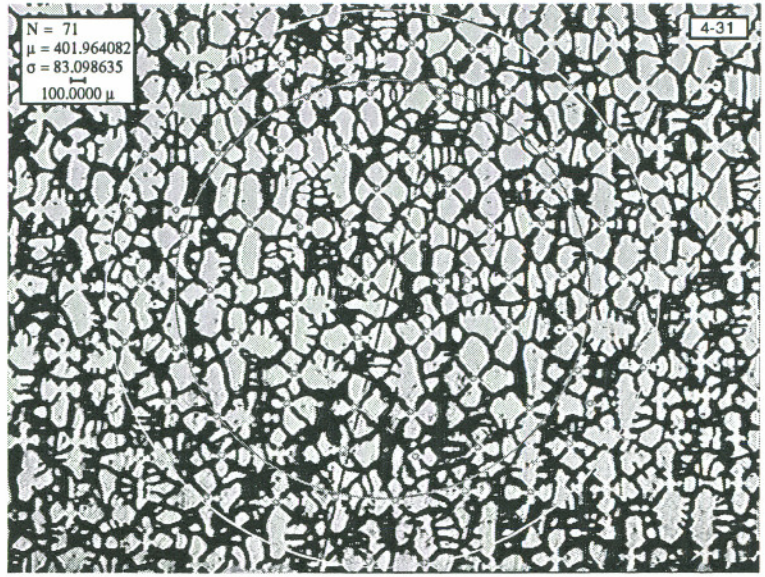
N = 71
μ = 401.964082
σ = 83.098635
100.0000 μ
4-31

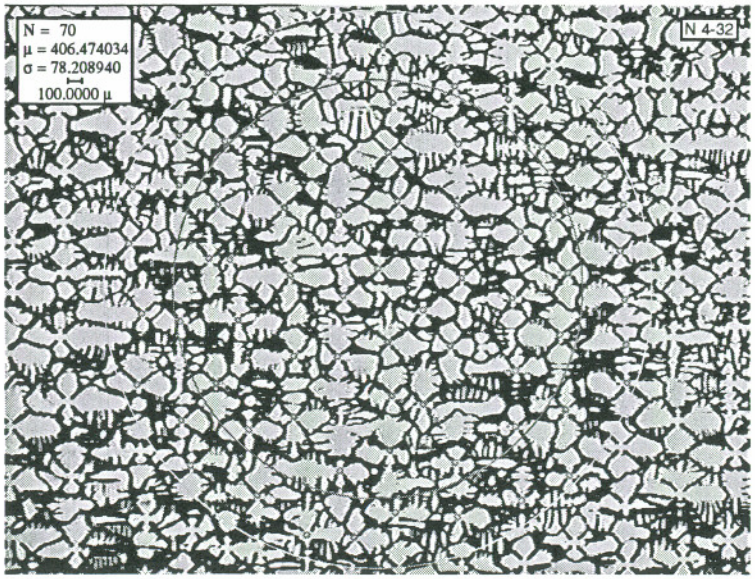
N = 70
μ = 406.474034
σ = 78.208940
100.0000 μ
N 4-32

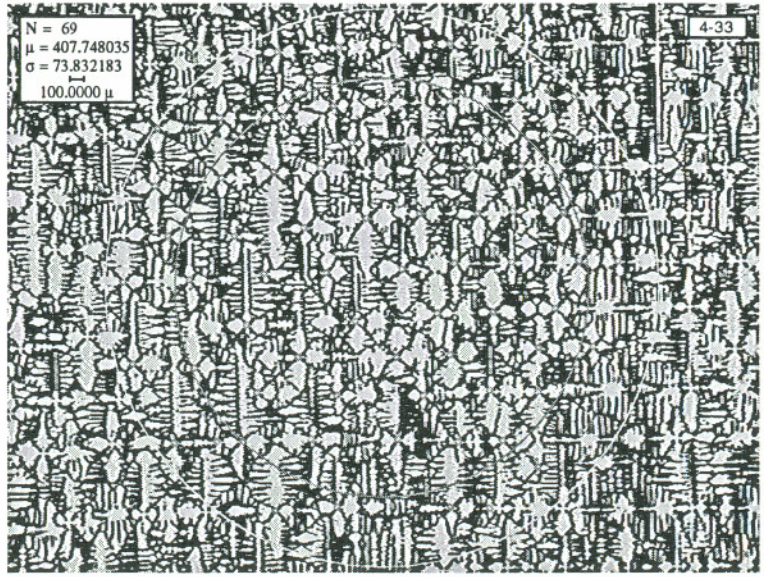
N = 69
μ = 407.748035
σ = 73.832183
100.0000 μ
4-33

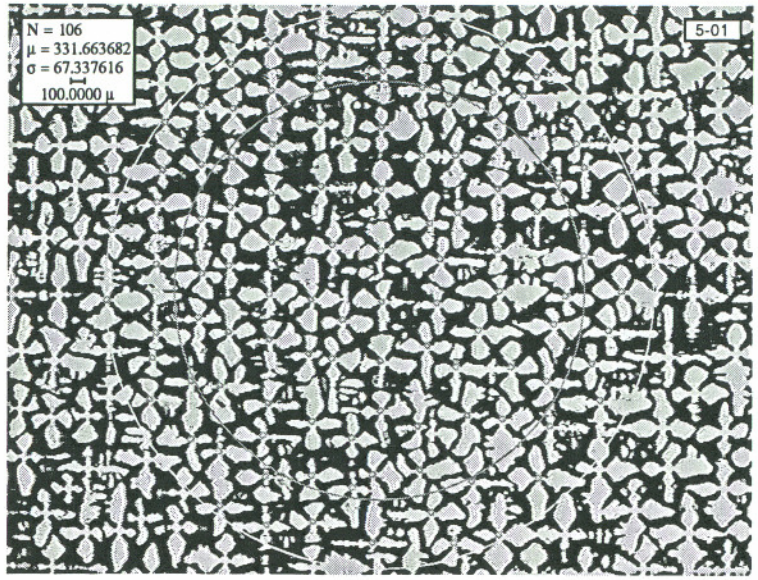
N = 106
μ = 331.663682
σ = 67.337616
100.0000 μ
5-01

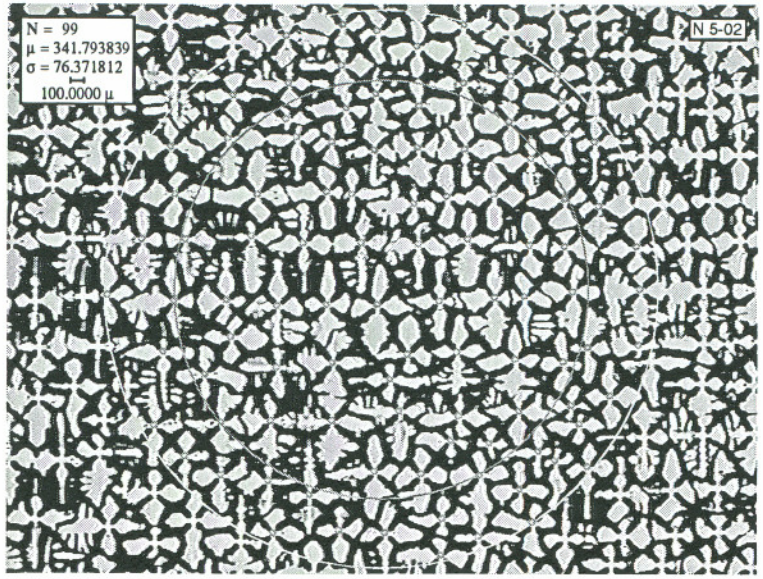
N = 99
μ = 341.793839
σ = 76.371812
100.0000 μ
N 5-02

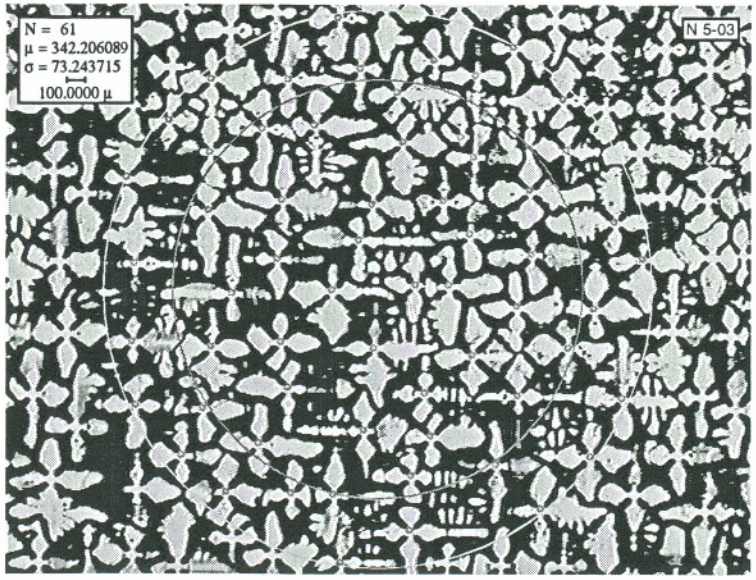
N = 61
μ = 342.206089
σ = 73.243715
100.0000 μ
N 5-03

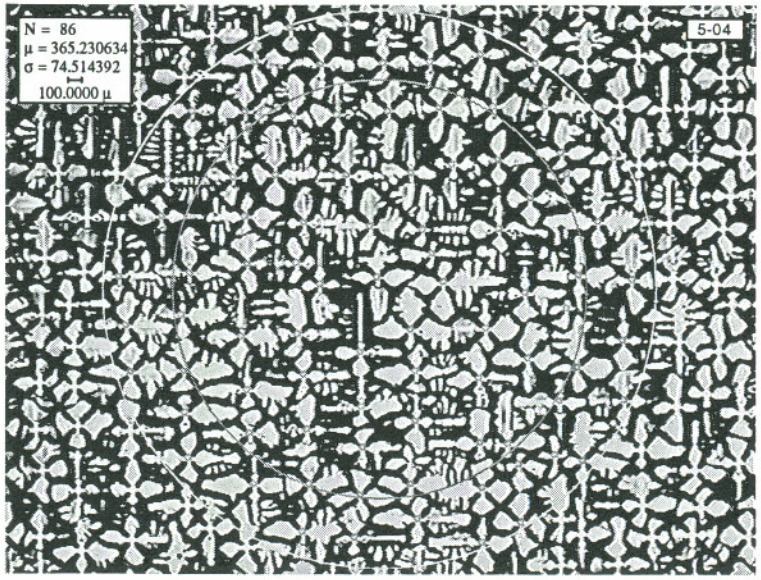
N = 86
μ = 365.230634
σ = 74.514392
100.0000 μ
5-04

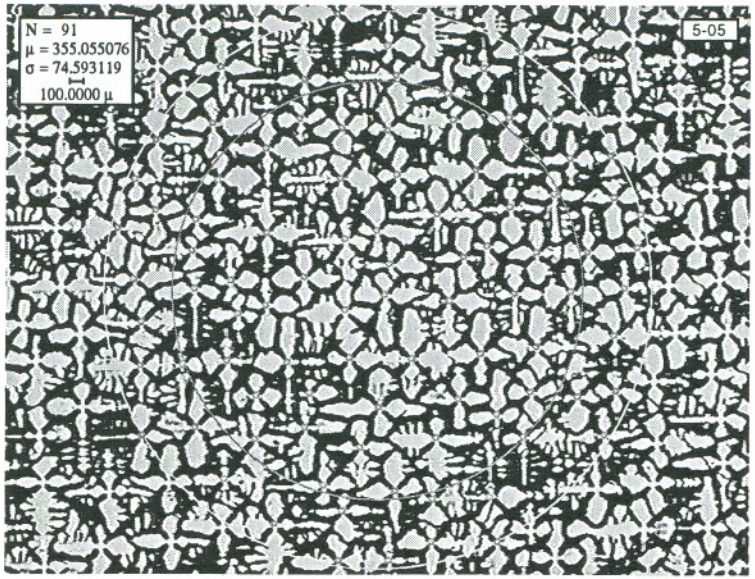
N = 91
μ = 355.055076
σ = 74.593119
100.0000 μ
5-05

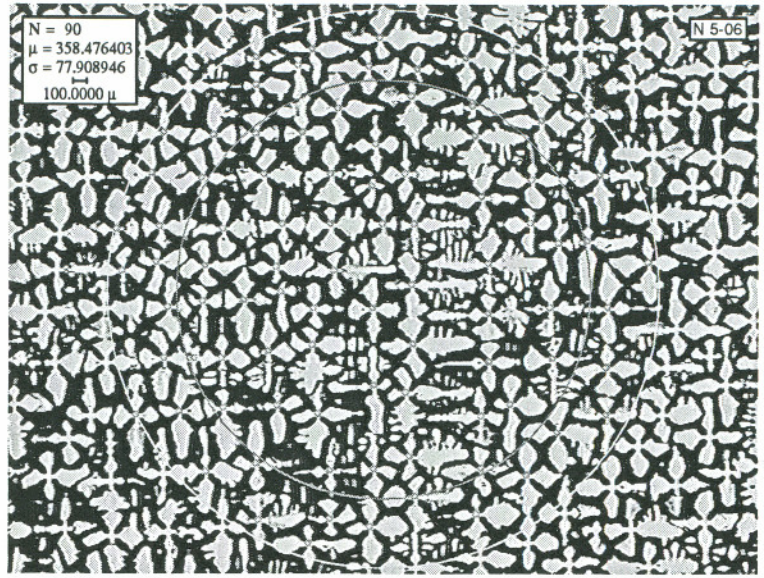
N = 90
μ = 358.476403
σ = 77.908946
100.0000 μ
N 5-06

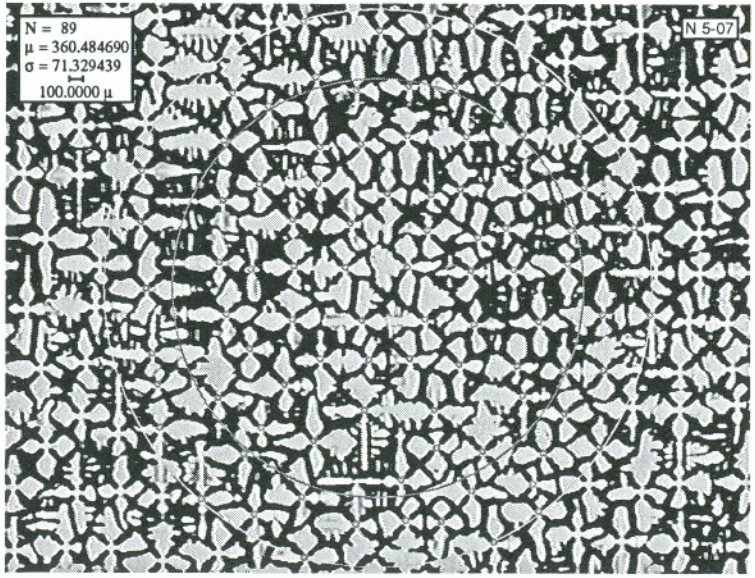
N = 89
μ = 360.484690
σ = 71.329439
100.0000 μ
N 5-07

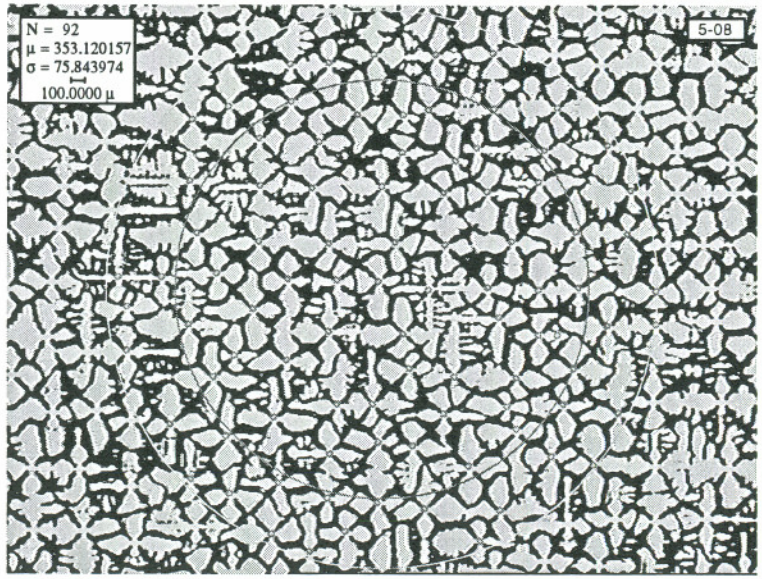
N = 92
μ = 353.120157
σ = 75.843974
100.0000 μ
5-08

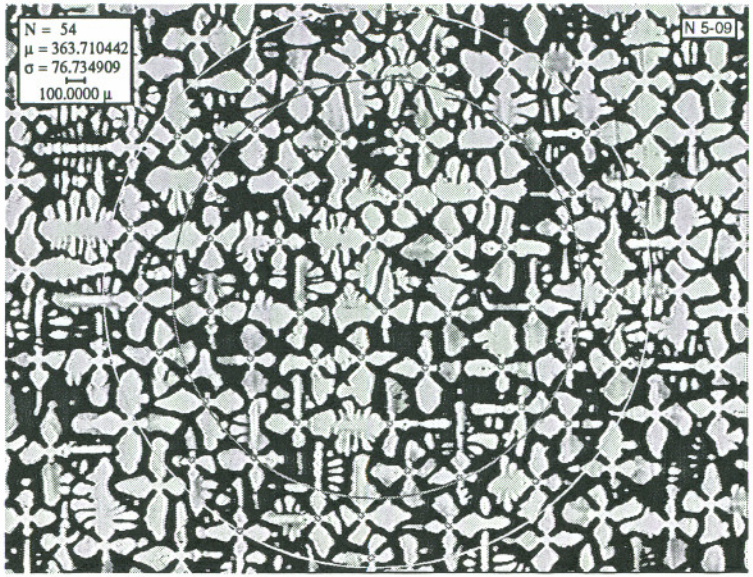
N = 54
μ = 363.710442
σ = 76.734909
100.0000 μ
N 5-09

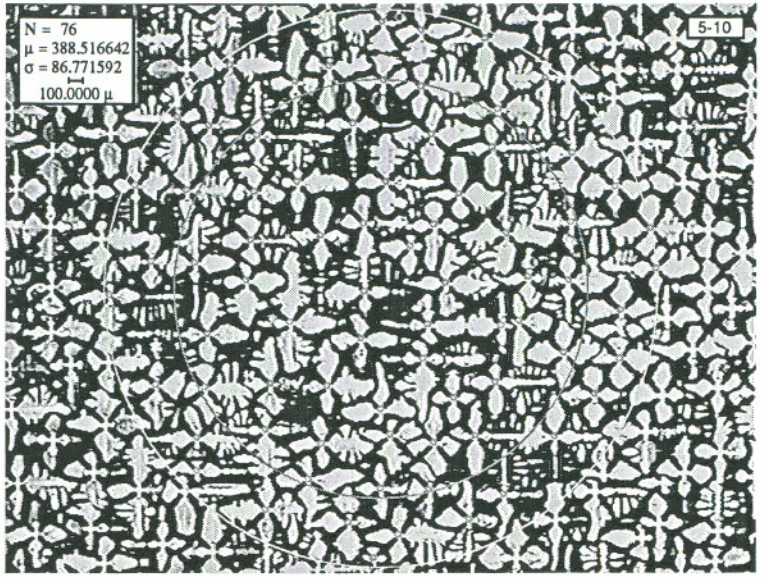
N = 76
μ = 388.516642
σ = 86.771592
100.0000 μ
5-10

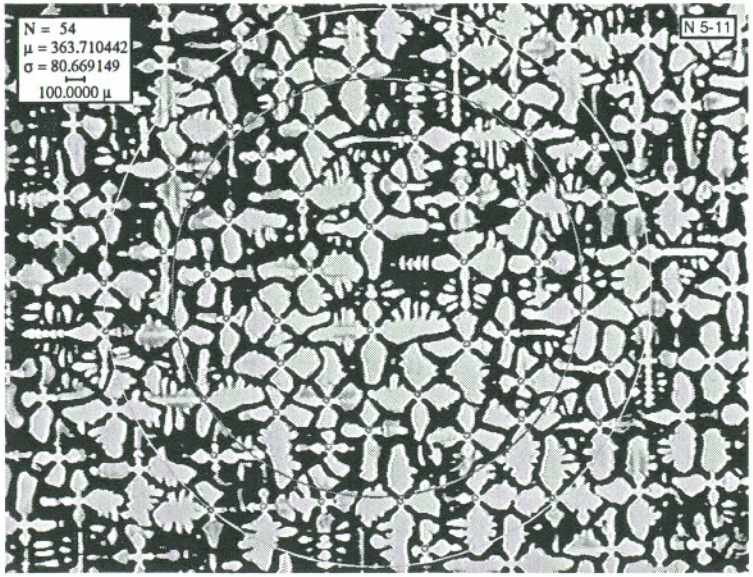
N = 54
μ = 363.710442
σ = 80.669149
100.0000 μ
N 5-11

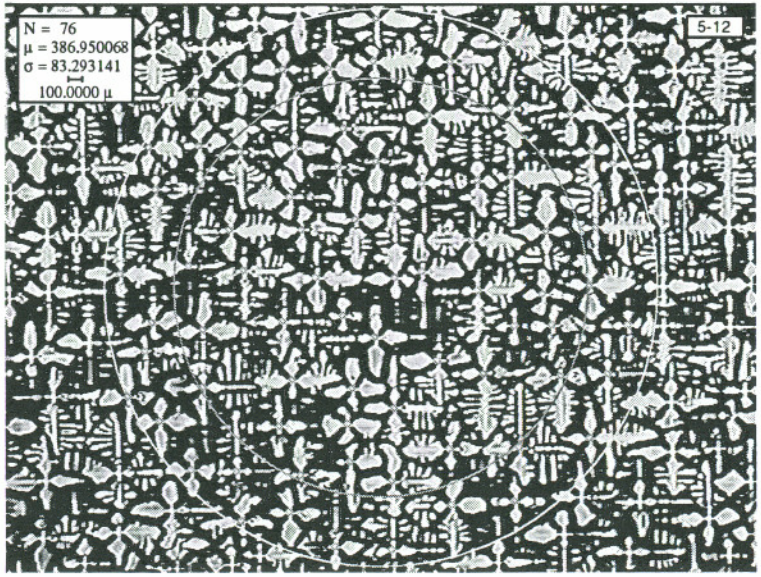
N = 76
μ = 386.950068
σ = 83.293141
100.0000 μ
5-12

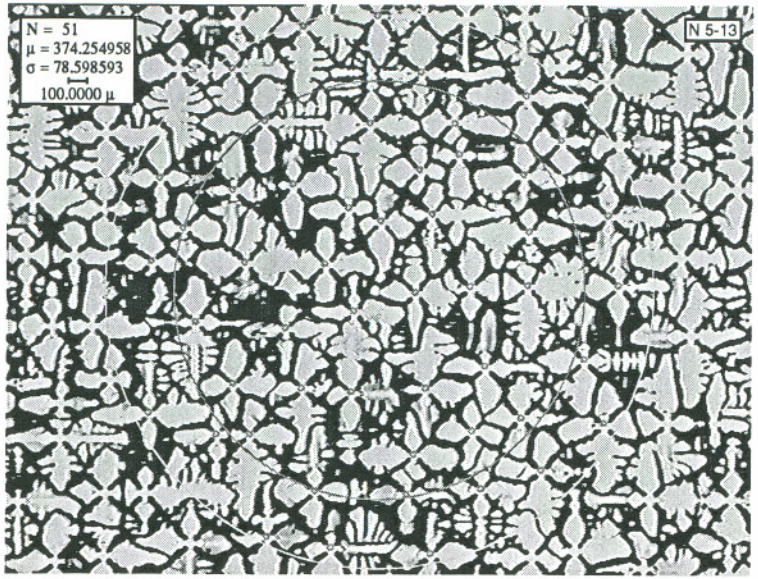
N = 51
μ = 374.254958
σ = 78.598593
100.0000 μ
N 5-13

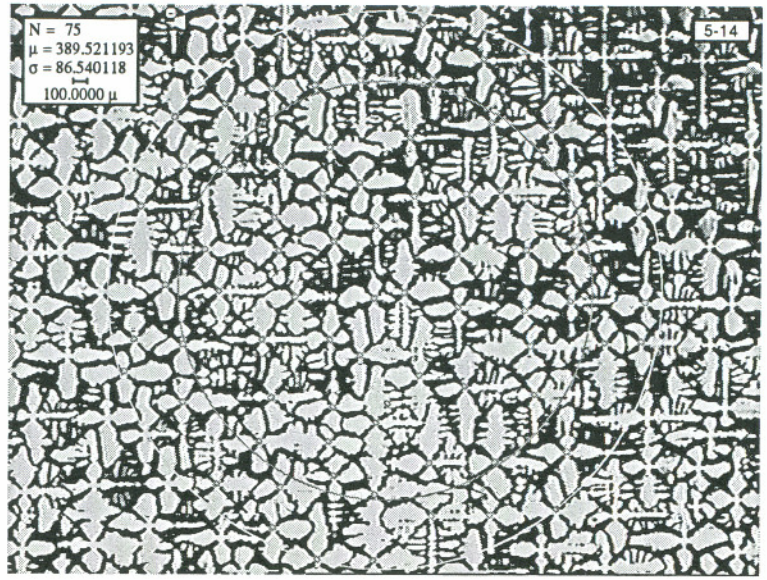
N = 75
μ = 389.521193
σ = 86.540118
100.0000 μ
5-14

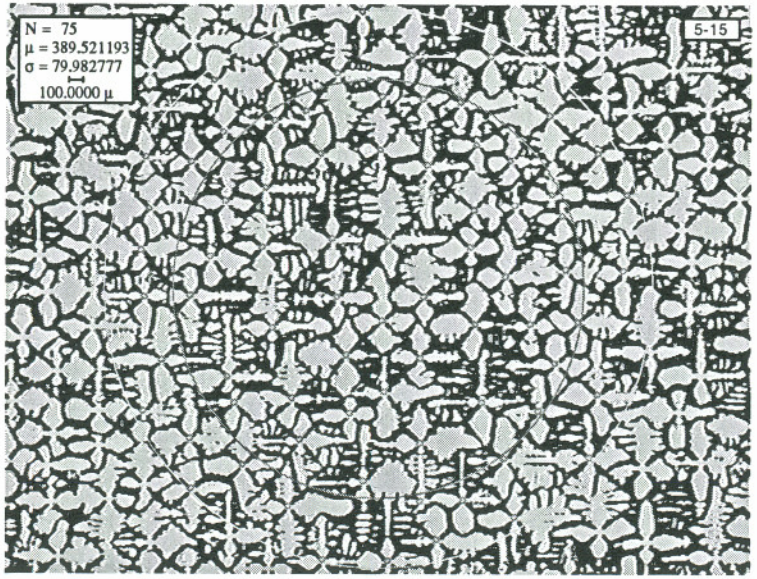
N = 75
μ = 389.521193
σ = 79.982777
100.0000 μ
5-15

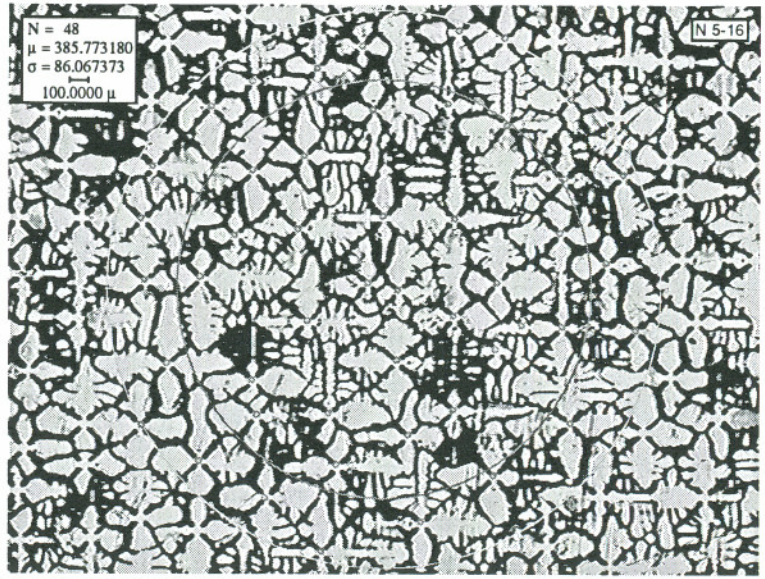
N = 48
μ = 385.773180
σ = 86.067373
100.0000 μ
N 5-16

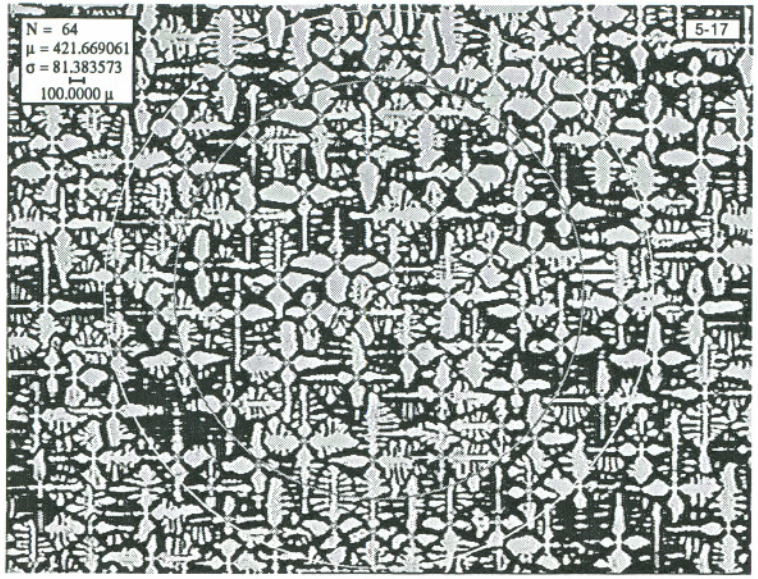
N = 64
μ = 421.669061
σ = 81.383573
100.0000 μ
5-17

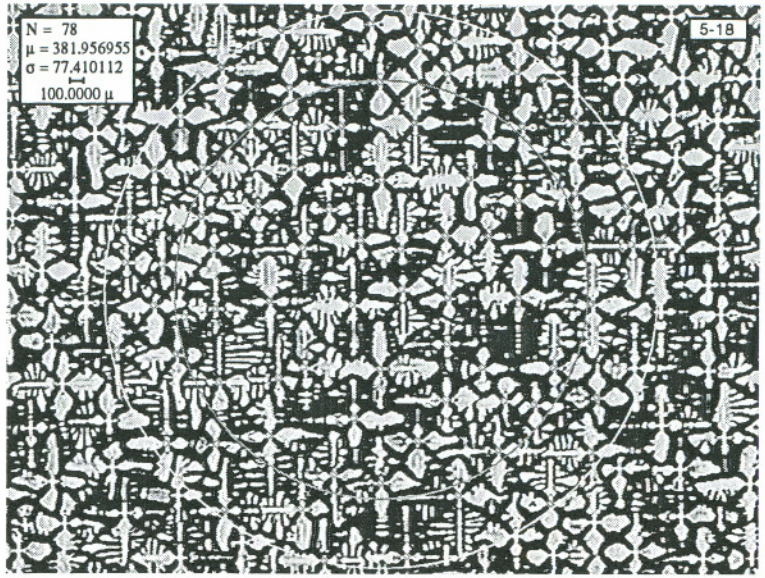
N = 78
μ = 381.956955
σ = 77.410112
100.0000 μ
5-18

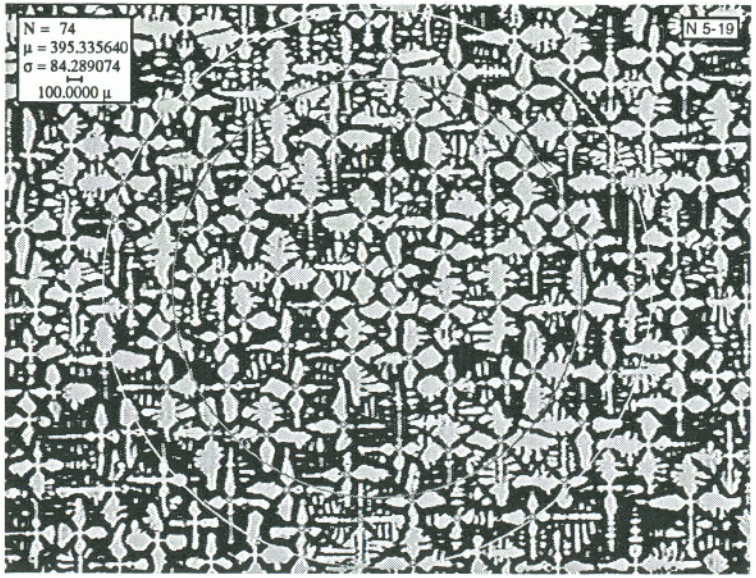
N = 74
μ = 395.335640
σ = 84.289074
100.0000 μ
N 5-19

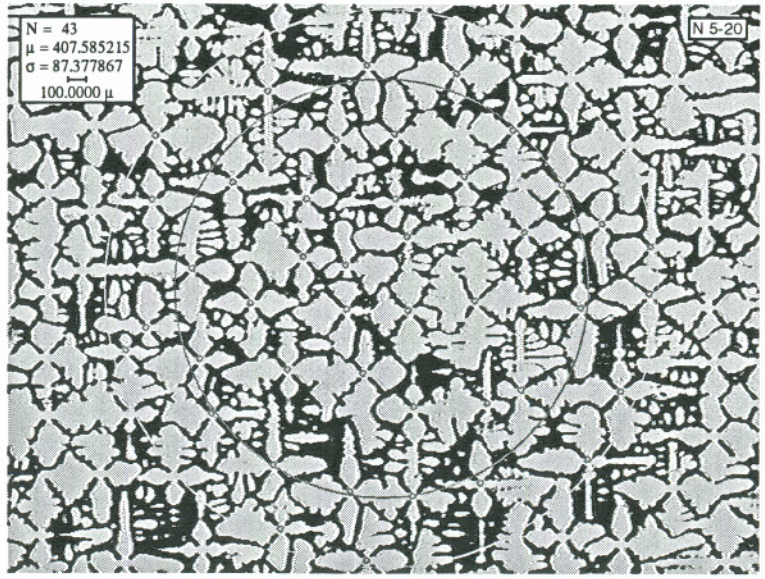
N = 43
μ = 407.585215
σ = 87.377867
100.0000 μ
N 5-20

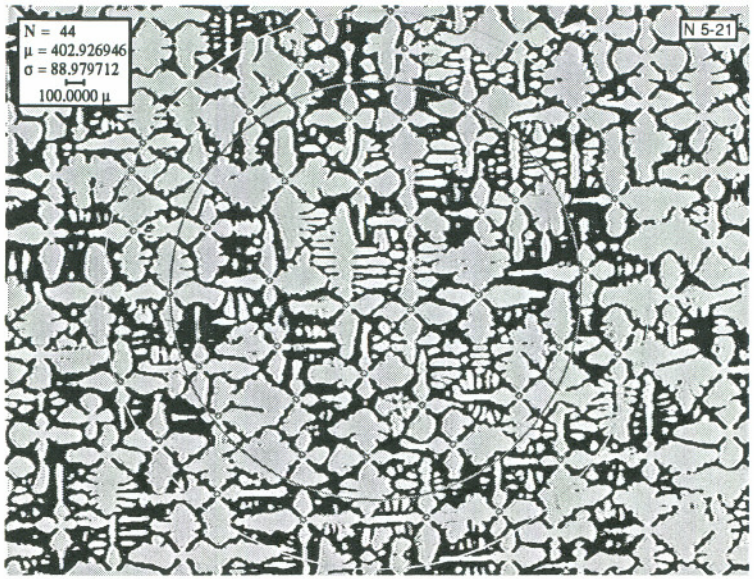
N = 44
μ = 402.926946
σ = 88.979712
100.0000 μ
N 5-21

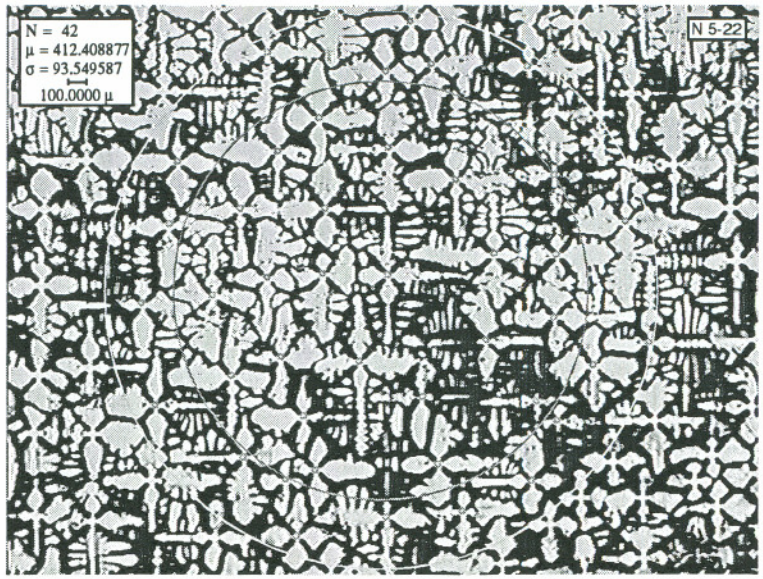
N = 42
μ = 412.408877
σ = 93.549587
100.0000 μ
N 5-22

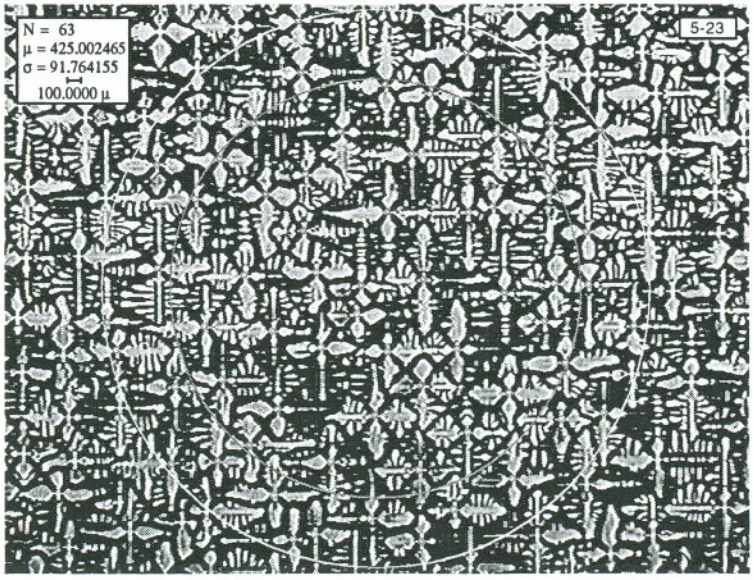
N = 63
μ = 425.002465
σ = 91.764155
100.0000 μ
5-23

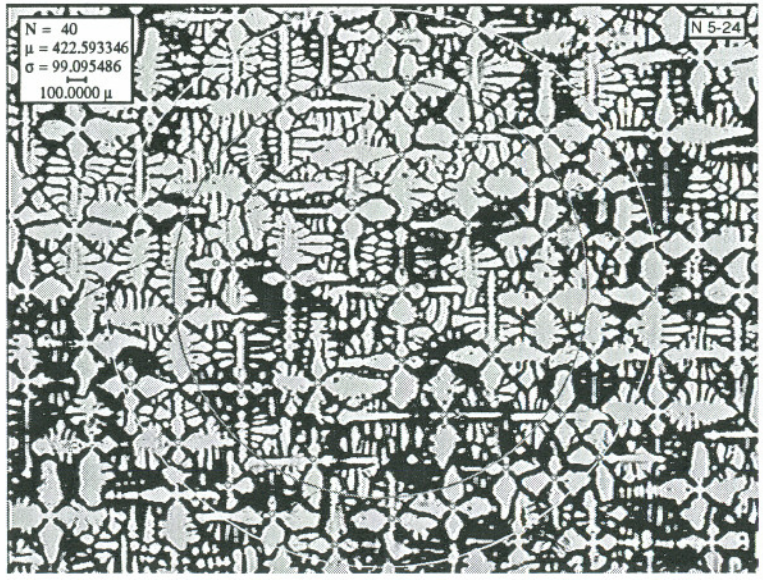
N = 40
μ = 422.593346
σ = 99.095486
100.0000 μ
N 5-24

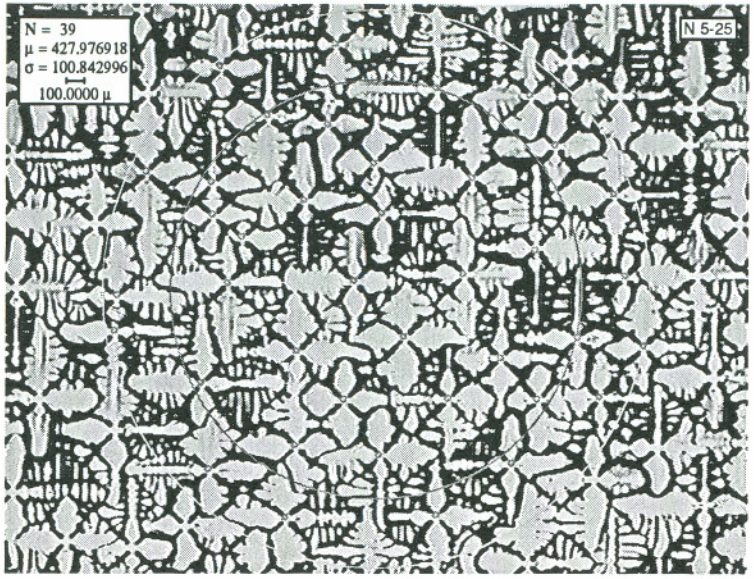
N = 39
μ = 427.976918
σ = 100.842996
100.0000 μ
N 5-25

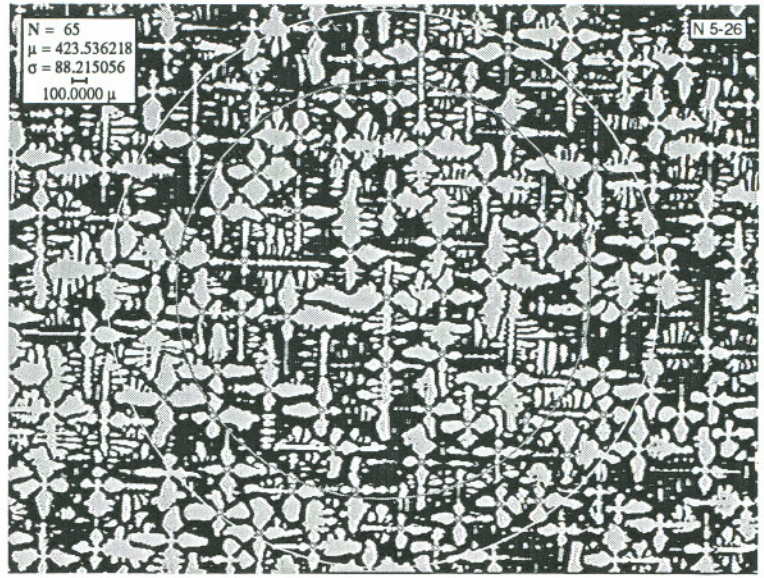
N = 65
μ = 423.536218
σ = 88.215056
100.0000 μ
N 5-26

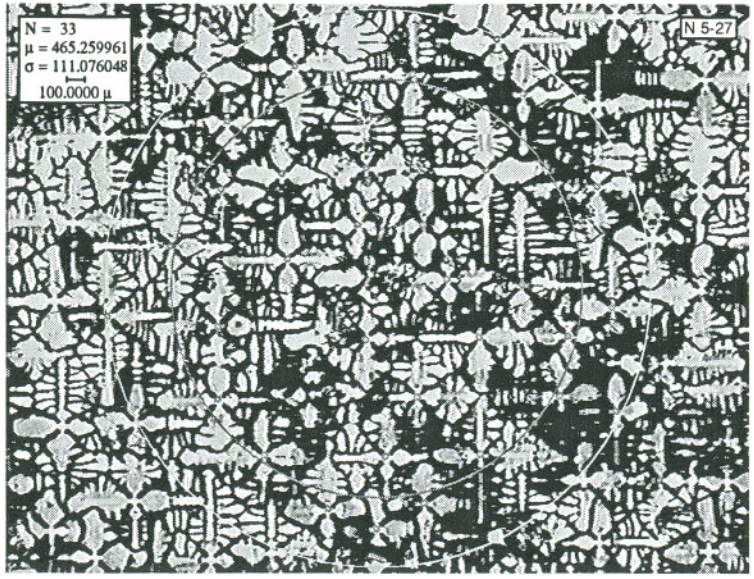
N = 33
μ = 465.259961
σ = 111.076048
100.0000 μ
N 5-27

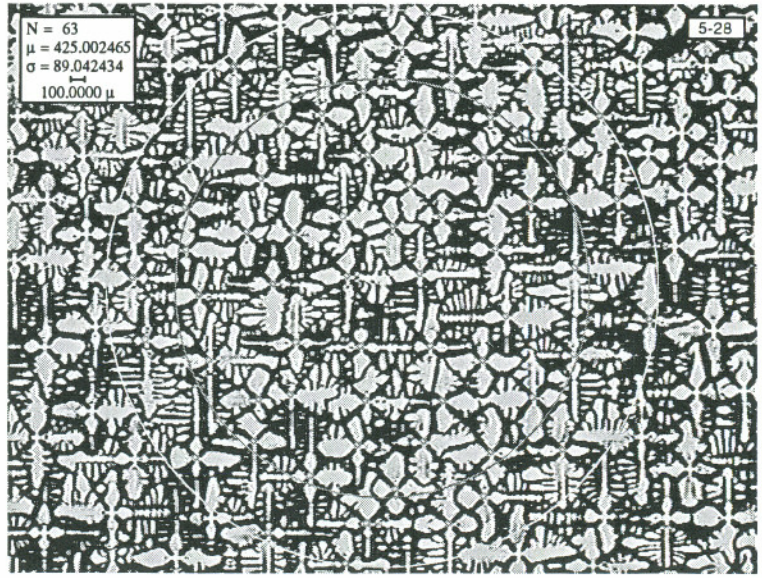
N = 63
μ = 425.002465
σ = 89.042434
100.0000 μ
5-28

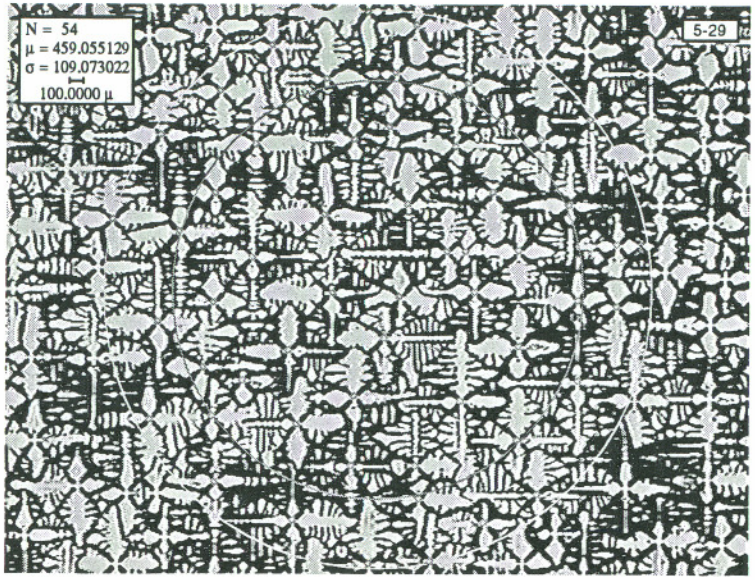
N = 54
μ = 459.055129
σ = 109.073022
100.0000 μ
5-29

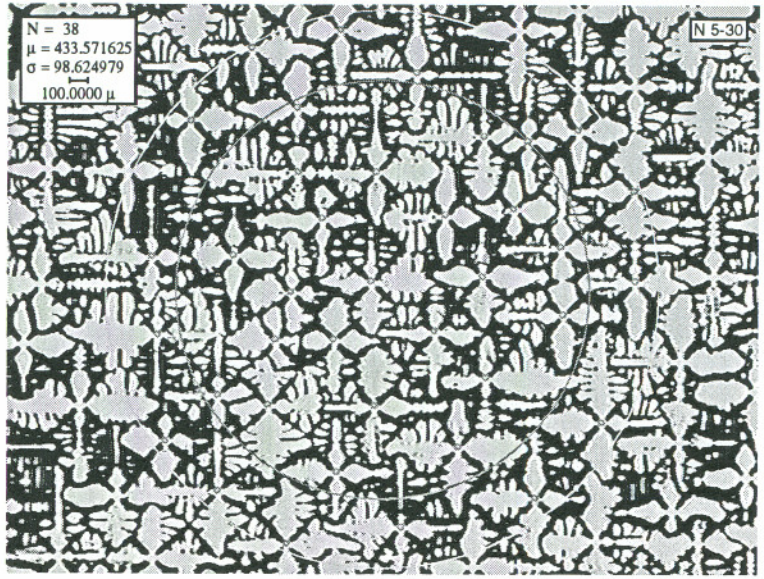
N = 38
μ = 433.571625
σ = 98.624979
100.0000 μ
N 5-30

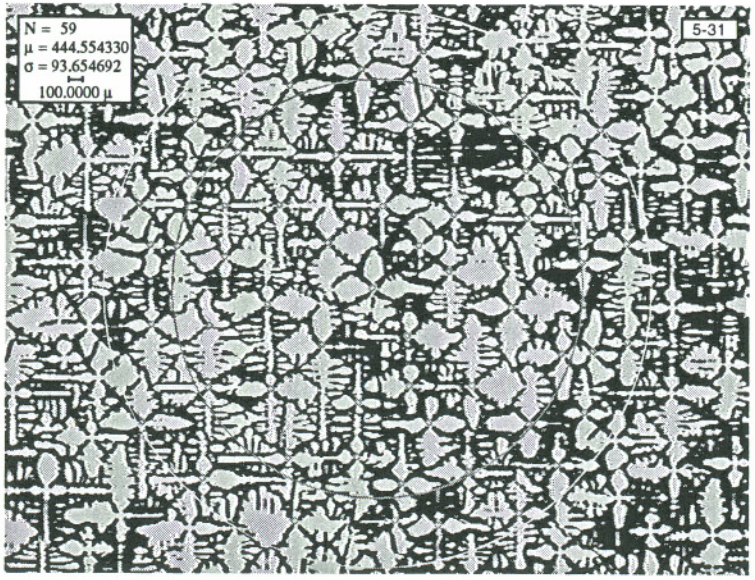
N = 59
μ = 444.554330
σ = 93.654692
100.0000 μ
5-31

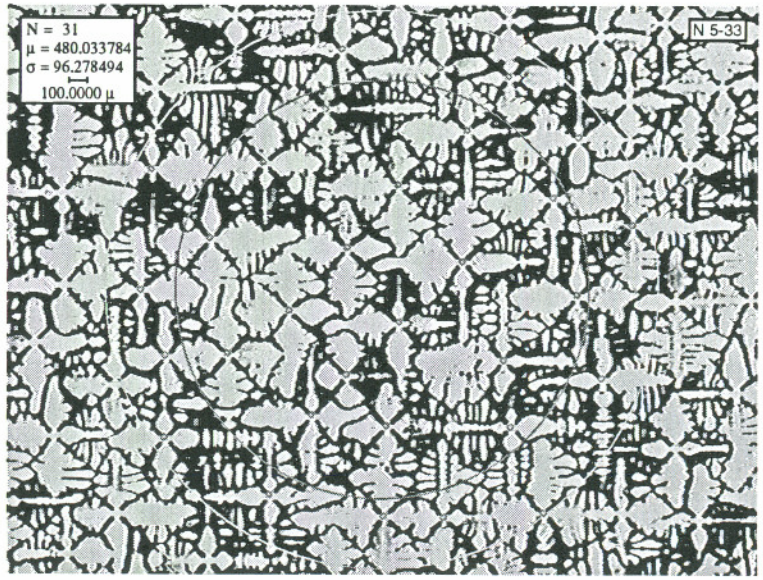
N = 31
μ = 480.033784
σ = 96.278494
100.0000 μ
N 5-33

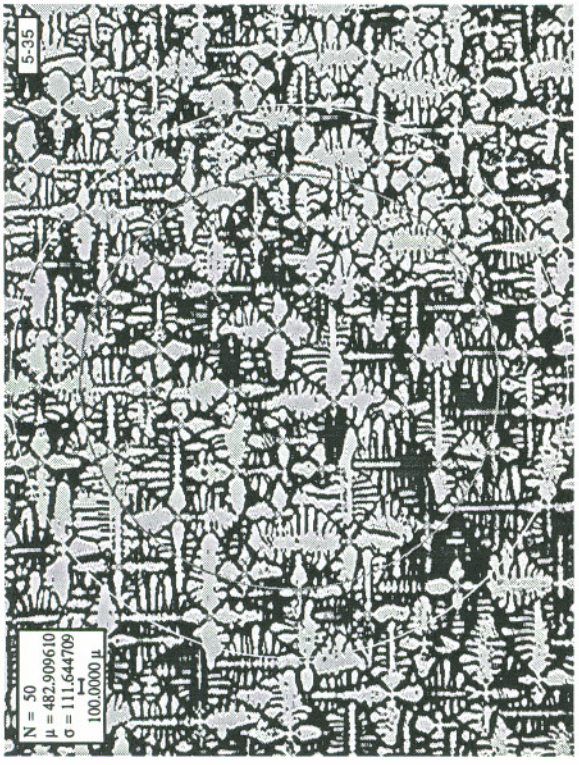
5-35
N = 50
μ = 482.909610
σ = 111.644709
100.0000 μ

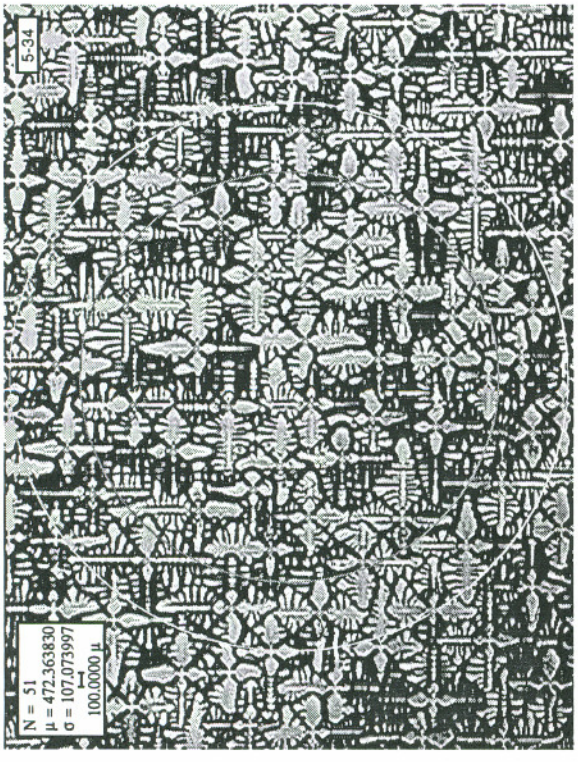
5-34
N = 51
μ = 472.363830
σ = 107.073997
100.0000 μ

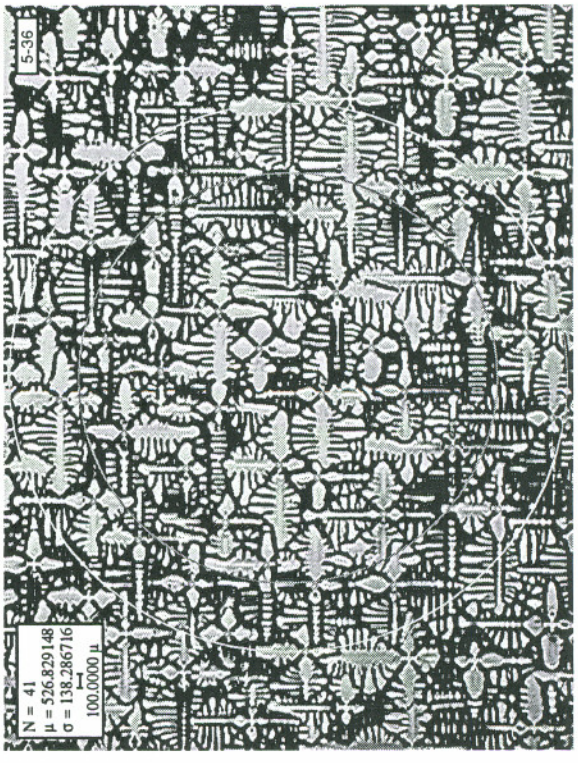
5-36
N = 41
μ = 526.829148
σ = 138.286716
100.0000 μ

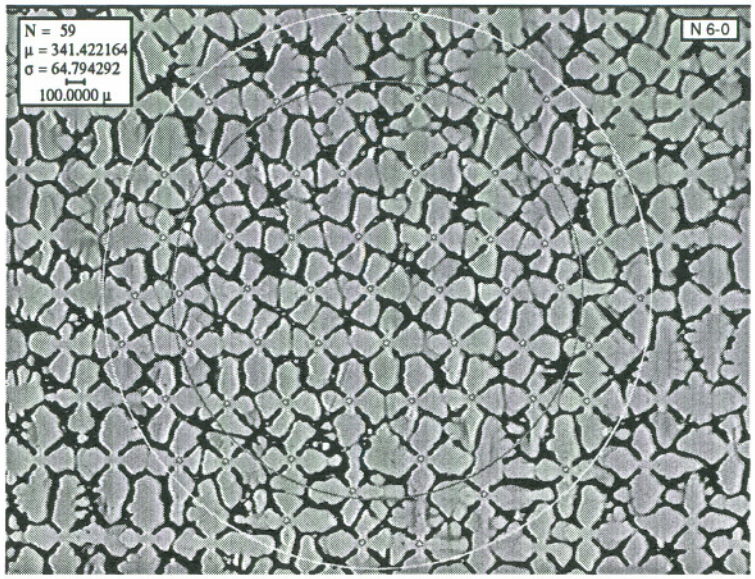
N = 59
μ = 341.422164
σ = 64.794292
100.0000 μ
N 6-0

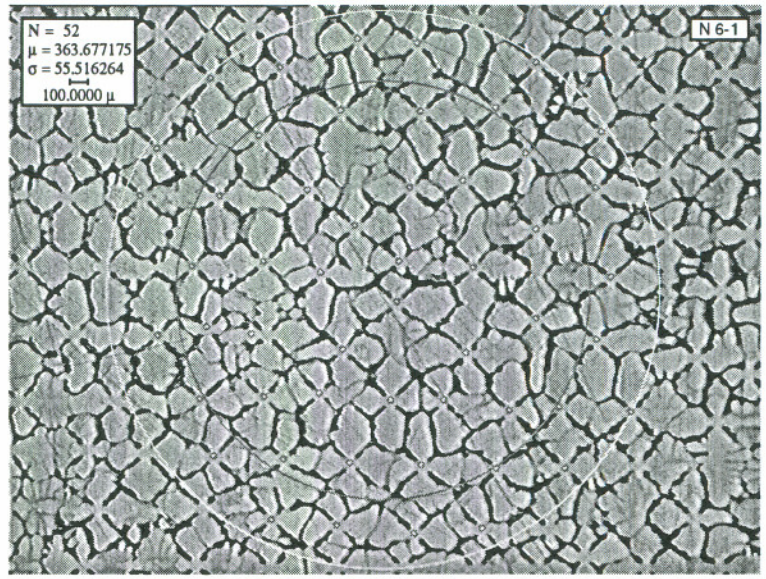
N = 52
μ = 363.677175
σ = 55.516264
100.0000 μ
N 6-1


N = 69
μ = 404.473004
σ = 63.192759
100.0000 μ
N 6-2

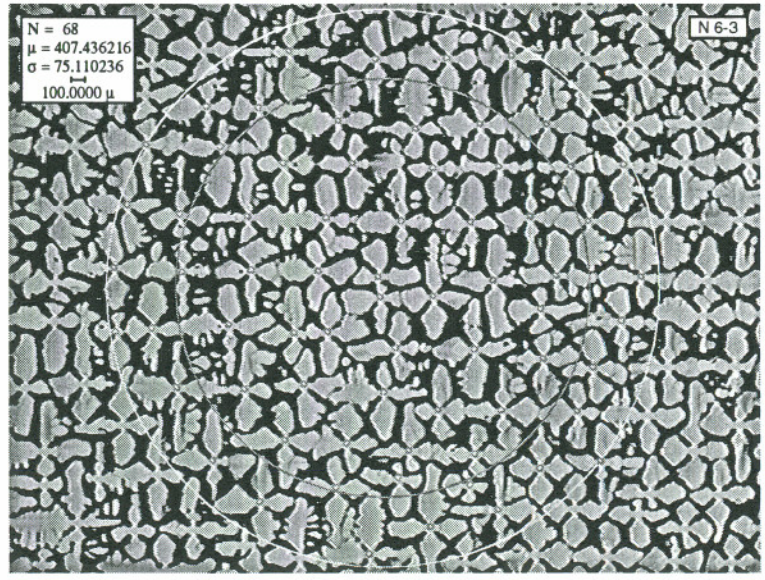
N = 68
μ = 407.436216
σ = 75.110236
100.0000 μ
N 6-3

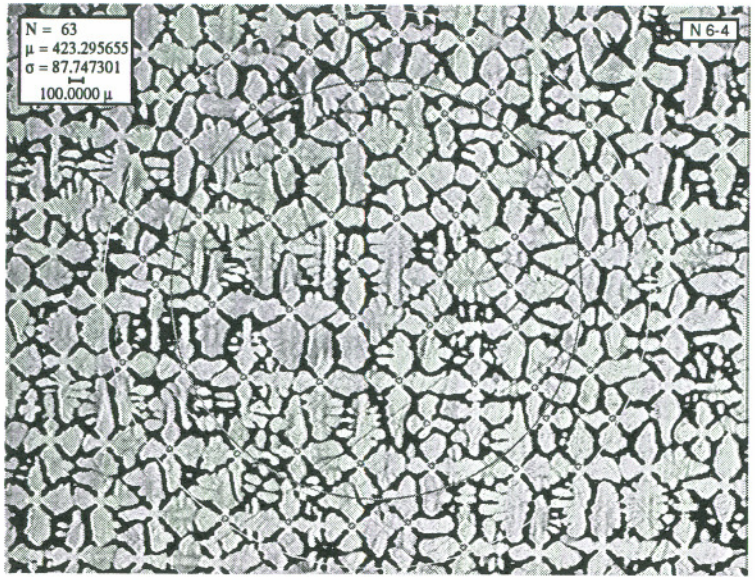
N = 63
μ = 423.295655
σ = 87.747301
100.0000 μ
N 6-4

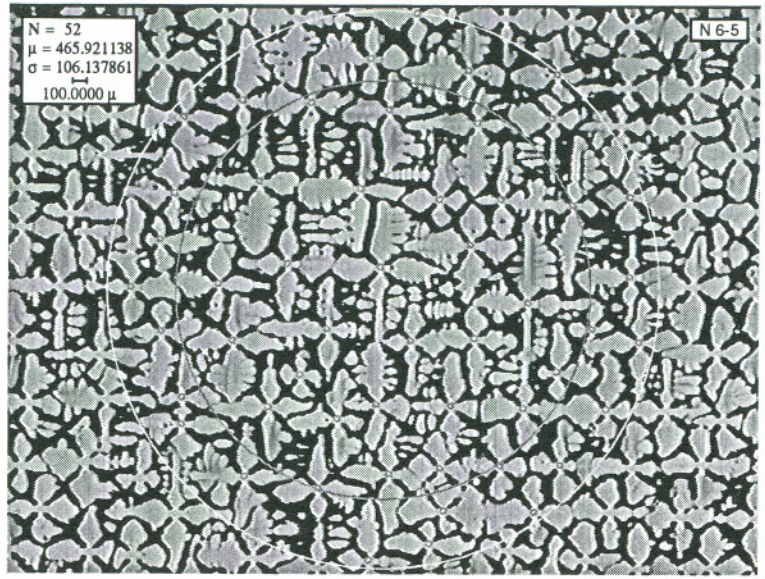
N = 52
μ = 465.921138
σ = 106.137861
100.0000 μ
N 6-5

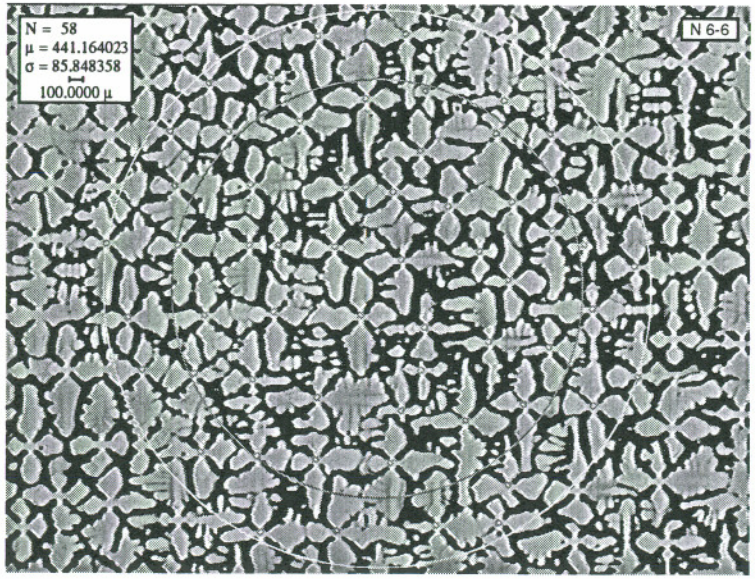
N = 58
μ = 441.164023
σ = 85.848358
100.0000 μ
N 6-6

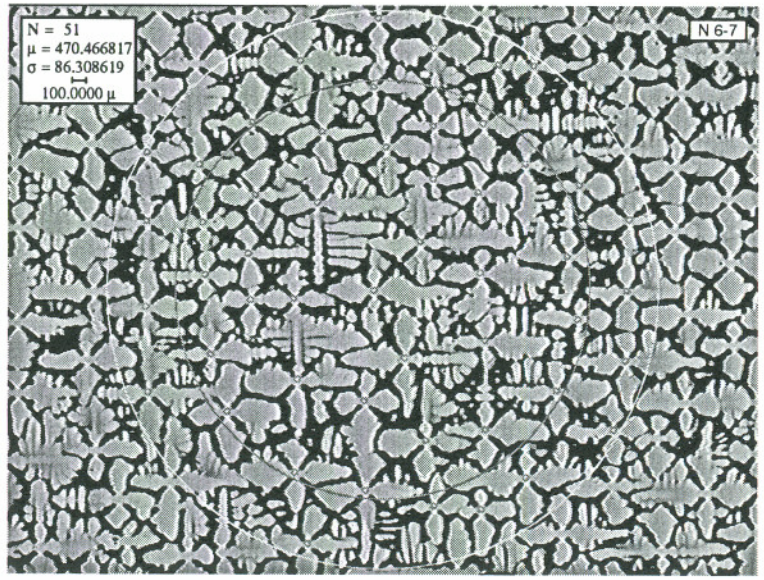
N = 51
μ = 470.466817
σ = 86.308619
100.0000 μ
N 6-7


N6-9
N = 45
μ = 500.850174
σ = 115.824525
100.0000 μ

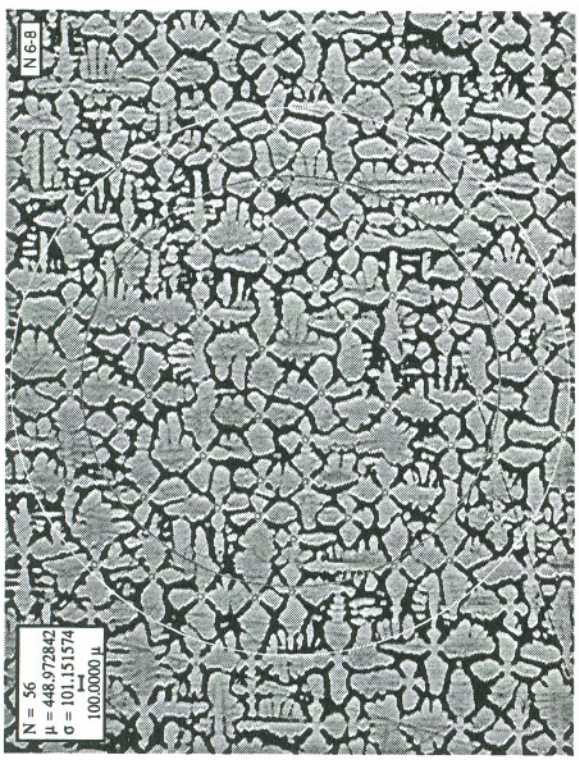
N6-8
N = 56
μ = 448.972842
σ = 101.151574
100.0000 μ

Appendix F...Dendrite Statistics

Sample Identifier	Thickness (mm)	Position (mm)	Number of Dendrites	Spacing (μ)	Standard Deviation
1-01	7.8740	7.7724	104	334.80	76.900
1-02	2.6670	12.040	55	360.40	76.000
1-03	2.5908	16.231	93	354.10	79.500
1-04	2.8702	20.701	58	350.90	92.100
1-05	2.4384	24.740	85	370.40	88.500
1-06	2.6416	28.981	89	360.50	70.200
1-07	2.6162	33.198	86	366.70	82.200
1-08	2.5654	37.363	88	362.50	73.200
1-09	2.4638	41.427	88	362.50	71.500
1-10	2.5146	45.542	92	354.60	68.000
1-11	2.5400	49.682	91	356.50	65.900
1-12	2.4384	53.721	95	348.90	69.200
1-13	2.4892	57.810	100	340.10	65.600
1-14	2.5146	61.925	105	331.90	67.500
1-15	2.6162	66.142	111	322.80	61.600
1-16	2.4384	70.180	109	325.70	73.200
1-17	2.1336	73.914	64	334.10	77.300
1-18	2.5908	78.105	107	328.80	75.200
1-19	2.3368	82.042	110	322.90	74.700
1-20	2.5654	86.208	117	314.40	74.100
1-21	2.4384	90.246	117	314.40	75.600
1-22	2.7432	94.590	74	310.70	75.100
1-23	2.7178	98.908	68	324.10	78.800
1-24	2.7686	103.28	73	312.80	77.200
1-25	2.6924	107.57	65	331.50	91.000
1-26	2.7432	111.91	66	329.00	87.000
1-27	2.7940	116.31	65	331.50	73.400
1-28	2.7432	120.65	67	326.50	84.800
1-29	2.7686	125.02	98	342.10	79.100
1-30	2.6670	129.29	94	349.30	83.800
1-31	2.7686	133.65	62	339.40	89.000
1-32	2.7686	138.02	66	329.00	84.000
1-33	2.7432	142.37	86	365.20	91.400
1-34	2.7686	146.74	95	347.50	89.000
1-35	2.8448	151.18	55	360.40	96.500
1-36	2.7178	155.50	63	336.70	58.500
1-37	2.6416	159.74	89	360.50	80.800
1-38	2.5400	163.88	96	347.10	72.100

Table 20-1
Statistics for Sample 1

Sample Identifier	Thickness (mm)	Position (mm)	Number of Dendrites	Spacing (μ)	Standard Deviation
2-01	8.9916	8.9916	132	297.2	64
2-02	2.9210	13.513	72	315	74.5
2-03	2.8702	17.983	62	339.4	80.4
2-04	2.7940	22.377	62	339.4	67.2
2-05	2.7432	26.721	51	374.3	45.2
2-06	2.7432	31.064	56	357.2	68
2-07	2.8702	35.535	62	339.4	66.5
2-08	2.0066	39.141	58	350.9	84.6
2-09	2.5400	43.282	89	360.5	66.4
2-10	2.7432	47.625	84	371.1	68
2-11	2.8194	52.045	79	382.6	66.3
2-12	2.8448	56.490	91	356.5	65.5
2-13	2.5908	60.681	95	348.9	62.2
2-14	2.6924	64.973	61	342.2	67.3
2-15	2.6162	69.190	94	350.8	68.4
2-16	2.6416	73.431	96	347.1	56.6
2-17	2.6162	77.648	99	341.8	59.5
2-18	2.8956	82.144	57	354	75.8
2-19	2.6924	86.436	52	370.6	82.4
2-20	2.7178	90.754	59	348	74.8
2-21	2.7432	95.098	57	354	66.2
2-22	2.7686	99.466	60	345	67.4
2-23	2.7432	103.81	56	357.2	62.5
2-24	2.8448	108.25	61	342.2	56
2-25	2.7432	112.60	59	348	82.2
2-26	2.8448	117.04	58	350.9	65.7
2-27	2.9210	121.56	92	356	53.6
2-28	2.6416	125.81	95	348.9	56.6
2-29	2.7686	130.18	57	354	77
2-30	2.8956	134.67	60	345	74.1
2-31	2.7178	138.99	85	367.4	63.9
2-32	2.7940	143.38	93	351.2	56
2-33	2.9210	147.90	84	372.6	52.8
2-34	2.7940	152.30	48	385.8	71.3

Table 20-2
Statistics for Sample 2

Sample Identifier	Thickness (mm)	Position (mm)	Number of Dendrites	Spacing (μ)	Standard Deviation
N 3-0	0.0000	0.0000	79.000	295.06	70.818
N 3-1	19.630	19.630	58.000	344.35	62.447
N 3-2	19.920	41.350	88.000	358.16	68.359
N 3-3	19.660	62.810	54.000	356.88	75.196
N 3-4	18.850	83.460	84.000	366.58	69.355
N 3-5	18.880	104.14	42.000	404.66	99.318
N 3-6	17.230	123.17	74.000	390.57	74.584
N 3-7	17.740	142.71	43.000	399.93	83.423
N 3-8	19.740	164.25	60.000	433.75	91.862

Table 20-3
Statistics for Sample 3

Sample Identifier	Thickness (mm)	Position (mm)	Number of Dendrites	Spacing (μ)	Standard Deviation
N 4-01	10.719	10.719	96	348.5	74.9
N 4-02	2.6162	14.935	88	362.5	66.5
N 4-03	2.5654	19.101	7	1285.4	437.3
N 4-04	2.6924	23.393	89	359	66.7
N 4-05	2.6670	27.661	92	353.1	48.6
N 4-06	2.6162	31.877	86	366.7	50.8
N 4-07	2.6416	36.119	89	360.5	47.4
N 4-08	2.6670	40.386	82	374	58.9
N 4-09	2.5908	44.577	79	382.6	68.4
N 4-10	2.6162	48.793	76	390.1	64.2
N 4-11	2.6162	53.010	79	382.6	73.6
N 4-12	2.6162	57.226	79	382.6	72.8
N 4-13	2.8194	61.646	80	378.7	70.5
N 4-14	2.6924	65.938	49	381.8	76.2
N 4-15	2.6924	70.231	76	388.5	67.3
N 4-16	2.5654	74.397	78	385.1	74.7
N 4-17	2.5146	78.511	79	382.6	67.4
N 4-18	2.4384	82.550	80	380.2	69.9
N 4-19	2.4384	86.589	51	374.3	77.2
N 4-20	2.3114	90.500	69	407.7	94.1
N 4-21	2.7178	94.818	86	365.2	71.6
N 4-22	2.7432	99.162	82	374	74.5
N 4-23	2.5400	103.30	83	373.3	79
N 4-24	2.4638	107.37	87	364.6	60.8
N 4-25	2.6162	111.58	75	392.7	77.9
N 4-26	2.5400	115.72	69	409.4	75
N 4-27	2.4130	119.74	70	406.5	68.2
N 4-28	2.5146	123.85	64	425.1	84.9
N 4-29	2.5654	128.02	64	425.1	88.5
N 4-30	2.2606	131.88	69	407.7	86.6
N 4-31	2.2352	135.71	71	402	83.1
N 4-32	2.4638	139.78	70	406.5	78.2
N 4-33	2.3622	143.74	69	407.7	73.8

Table 20-4
Statistics for Sample 4

Sample Identifier	Thickness (mm)	Position (mm)	Number of Dendrites	Spacing (μ)	Standard Deviation
N 5-01	10.516	10.516	106	331.7	67.3
N 5-02	2.5146	14.630	99	341.8	76.4
N 5-03	2.8448	19.075	61	342.2	73.2
N 5-04	2.6670	23.343	86	365.2	74.5
N 5-05	2.6670	27.610	91	355.1	74.6
N 5-06	2.6416	31.852	90	358.5	77.9
N 5-07	2.5908	36.043	89	360.5	71.3
N 5-08	2.7178	40.361	92	353.1	75.8
N 5-09	2.6670	44.628	54	363.7	76.7
N 5-10	2.7686	48.997	76	388.5	86.8
N 5-11	2.6924	53.289	54	363.7	80.7
N 5-12	2.7940	57.683	76	387	83.3
N 5-13	2.7686	62.052	51	374.3	78.6
N 5-14	2.7432	66.396	75	389.5	86.5
N 5-15	2.8702	70.866	75	389.5	80
N 5-16	2.8702	75.336	48	385.8	86.1
N 5-17	2.8194	79.756	64	421.7	81.3
N 5-18	2.7178	84.074	78	382	77.4
N 5-19	2.5908	88.265	74	395.3	84.3
N 5-20	2.7432	92.608	43	407.6	87.4
N 5-21	2.7178	96.926	44	402.9	89
N 5-22	2.8448	101.37	42	412.4	93.5
N 5-23	2.7178	105.69	63	425	91.8
N 5-24	2.8194	110.11	40	422.6	99.1
N 5-25	2.7432	114.45	39	428	100.8
N 5-26	2.9210	118.97	65	423.5	88.2
N 5-27	2.8194	123.39	33	465.3	110.9
N 5-28	2.8956	127.89	63	425	89
N 5-29	2.8194	132.31	54	459.1	109.1
N 5-30	2.8194	136.73	38	433.6	98.6
N 5-31	2.9464	141.27	59	444.6	93.7
N 5-32	2.6924	145.57	35	451.8	112
N 5-33	2.7178	149.89	31	480	96.3
N 5-34	2.8702	154.36	51	472.4	107.1
N 5-35	2.9210	158.88	50	482.9	111.6
N 5-36	2.6670	163.14	41	526.8	138.3

Table 20-5
Statistics for Sample 5

Sample Identifier	Thickness (mm)	Position (mm)	Number of Dendrites	Spacing (μ)	Standard Deviation
N 6-0	0.0000	0.0000	59	341.4	64.8
N 6-1	15.270	15.270	52	363.7	55.5
N 6-2	14.760	31.830	69	404.5	63.2
N 6-3	14.340	47.970	68	407.4	75.1
N 6-4	13.750	63.520	63	423.3	87.7
N 6-5	12.820	78.140	52	465.9	106.1
N 6-6	10.140	90.080	58	441.2	85.8
N 6-7	12.090	103.97	51	470.5	86.3
N 6-8	16.850	122.62	56	449	101.2
N 6-9	13.870	138.29	45	500.9	115.8

Table 20-6
Statistics for Sample 6

Sample Identifier	Thickness (mm)	Position (mm)	Number of Dendrites	Spacing (μ)	Standard Deviation
A01	3.3528	3.3528	77	389.1	78.3
A02	3.3528	8.3058	102	338.1	72.1
A03	2.7432	12.649	88	359.6	75.7
A04	3.2512	17.501	108	328.6	65.7
A05	2.1082	21.209	49	381.8	71.2
A06	2.6416	25.451	81	379.4	66.9
A07	2.9464	29.997	78	386.6	79.1
A08	3.5814	35.179	86	368.2	72
A09	2.8956	39.675	58	350.9	64.2
A10	2.4892	43.764	69	411.1	85.6
A11	2.3114	47.676	72	397.6	67.1
A12	3.4036	52.680	86	368.2	65.9
A13	3.5814	57.861	81	379.4	73.5
A14	3.1750	62.636	84	372.6	68.4
A15	3.0480	67.285	91	358	77
A16	2.7178	71.603	42	412.4	94.8
A17	2.5146	75.717	65	423.5	75
A18	3.7084	81.026	57	354	73
A19	3.1242	85.750	85	370.4	75.4
A20	2.7178	90.068	57	354	72.6
A21	3.6322	95.301	96	348.5	57.7
A22	2.2606	99.162	79	379.5	81.4
A23	2.7940	103.56	85	365.9	71.2
A24	3.3782	108.53	86	368.2	76.3
A25	2.4384	112.57	97	346.7	72.6
A26	2.6924	116.87	59	348	77.4
A27	2.6924	121.16	47	389.9	87.3
A28	2.6924	125.45	61	342.2	72.9
A29	1.2446	128.30	51	478.1	114.3
A30	3.2004	133.10	59	444.6	102
A31	2.4638	137.16	51	478.1	115.3
A32	2.1082	140.87	34	458.4	101.5
A33	1.7780	144.25	58	448.4	107.4
A34	3.2766	149.12	87	366.1	69.5
A35	3.0988	153.82	65	423.5	94.5
A36	9.9314	165.35	55	460.4	102.5
A37	2.7432	169.70	31	480	110.4

Table 20-7
Statistics for Sample A

Sample Identifier	Thickness (mm)	Position (mm)	Number of Dendrites	Spacing (μ)	Standard Deviation
W01	8.4836	8.4836	100	341.5	55.5
W02	2.9972	13.081	105	333.2	62.9
W03	4.3434	19.025	105	331.9	57.6
W04	4.1402	24.765	105	331.9	62
W05	3.9624	30.328	68	324.1	44.8
W06	2.8448	34.773	65	331.5	59.7
W07	11.100	47.473	97	346.7	62.1
W08	2.4130	51.486	94	350.8	65.8
W09	2.3622	55.448	92	351.7	60.8
W10	2.5146	59.563	93	352.6	59.3
W11	1.8542	63.017	58	350.9	58.4
W12	2.5908	67.208	92	354.6	66
W13	3.5306	72.339	95	350.3	79.1
W14	11.151	85.090	94	352.2	65.8
W15	2.8956	89.586	53	367.1	84.3
W16	1.8542	93.040	60	345	68.4
W17	3.1496	97.790	95	350.3	65.8
W18	2.6162	102.01	93	352.6	64.2
W19	2.4384	106.04	94	350.8	66.9
W20	2.2606	109.91	84	368.1	71.5
W21	3.0988	114.60	92	356	69.7
W22	3.1496	119.35	87	366.1	72.3
W23	3.4798	124.43	81	379.4	70.7
W24	3.0988	129.13	74	396.9	64.9
W25	3.4036	134.14	89	362	73.7
W26	2.6416	138.38	84	371.1	71.9
W27	2.1844	142.16	79	379.5	86.2
W28	2.6162	146.38	75	392.7	74.5
W29	4.3942	152.37	83	373.3	73.7
W30	2.4638	156.44	86	366.7	74.3

Table 20-8
Statistics for Sample W

Sample Identifier	Thickness (mm)	Position (mm)	Number of Dendrites	Spacing (μ)	Standard Deviation
Y01	12.548	12.548	177	256.7	55.8
Y02	2.6670	16.815	121	243	60
Y03	1.6510	20.066	182	252.1	65.7
Y04	2.5146	24.181	183	251.4	62.9
Y05	2.4130	28.194	186	250.4	65.1
Y06	3.2258	33.020	169	262.7	65.1
Y07	3.3274	37.948	177	256.7	68
Y08	3.4290	42.977	176	256.3	68.2
Y09	2.3876	46.965	185	248	63.6
Y10	2.8448	51.410	116	248.2	60.9
Y11	3.0480	56.058	192	246.4	62.5
Y12	3.1242	60.782	186	250.4	67.1
Y13	3.2512	65.634	183	252.4	72.1
Y14	2.9718	70.206	199	242.1	65.3
Y15	3.2004	75.006	187	249.7	63.1
Y16	3.7846	80.391	110	254.8	59.2
Y17	3.0480	85.039	198	242.7	62.3
Y18	4.0894	90.729	185	250	66.4
Y19	3.7592	96.088	113	251.4	63.3
Y20	3.4544	101.14	202	240.3	62.2
Y21	3.3528	106.10	181	253.8	63.9
Y22	3.0988	110.79	201	240.9	64.9
Y23	3.0988	115.49	184	251.7	63.6
Y24	2.9972	120.09	200	241.5	69
Y25	3.1496	124.84	183	252.4	70.5
Y26	3.7084	130.15	115	249.2	63.7
Y27	3.1750	134.92	193	245.8	63
Y28	3.8100	140.34	118	246	66.4
Y29	2.7686	144.70	166	261.8	66.6
Y30	3.5560	149.86	174	258.9	69.1

Table 20-9
Statistics for Sample Y

Sample Identifier	Thickness (mm)	Position (mm)	Number of Dendrites	Spacing (μ)	Standard Deviation
Z01	8.4582	8.4582	164	266.6	48.5
Z02	3.0226	13.081	144	284.6	67.4
Z03	2.9718	17.653	161	269.1	43.4
Z04	2.8448	22.098	93	277.1	47.6
Z05	2.9718	26.670	163	267.5	55.7
Z06	2.8194	31.090	146	282.6	61.9
Z07	2.8448	35.535	147	278.2	64.1
Z08	2.8194	39.954	152	273.6	54.3
Z09	2.7686	44.323	89	283.3	68.3
Z10	2.8702	48.793	85	289.9	66.1
Z11	2.8702	53.264	98	270	48.8
Z12	2.8194	57.683	94	275.7	76.1
Z13	2.7686	62.052	155	271	61.4
Z14	2.8448	66.497	92	278.6	71.6
Z15	2.8194	70.917	103	263.4	41.5
Z16	2.8448	75.362	136	289.3	71.7
Z17	2.8956	79.858	94	275.7	62.6
Z18	2.7432	84.201	94	276.5	67.8
Z19	2.8702	88.671	97	271.4	62.2
Z20	2.8448	93.116	94	275.7	62.2
Z21	2.8194	97.536	100	267.3	61.5
Z22	2.8448	101.98	104	262.1	58.8
Z23	2.7940	106.38	93	277.1	67.5
Z24	2.8702	110.85	93	277.1	66.6
Z25	2.7940	115.24	103	263.4	62
Z26	2.7432	119.58	96	272.8	65.1
Z27	2.7686	123.95	177	253.6	59.6
Z28	2.6924	128.24	87	286.5	72.5
Z29	2.6924	132.54	89	283.3	73.3
Z30	2.6670	136.80	87	286.5	72.5
Z31	2.6924	141.10	94	275.7	68
Z32	2.7178	145.41	109	256	57.1

Table 20-10
Statistics for Sample Z

Appendix G...PDAS Plots

The following plots represent the tabulated PDAS dat form Appendix F displayed as graphs. The graphs plot PDAS versus position along the bar. Scatter is due to measurement error that results from variations in the measurement location. Sample A was dropped and as such trends in the data are not meaningfull.

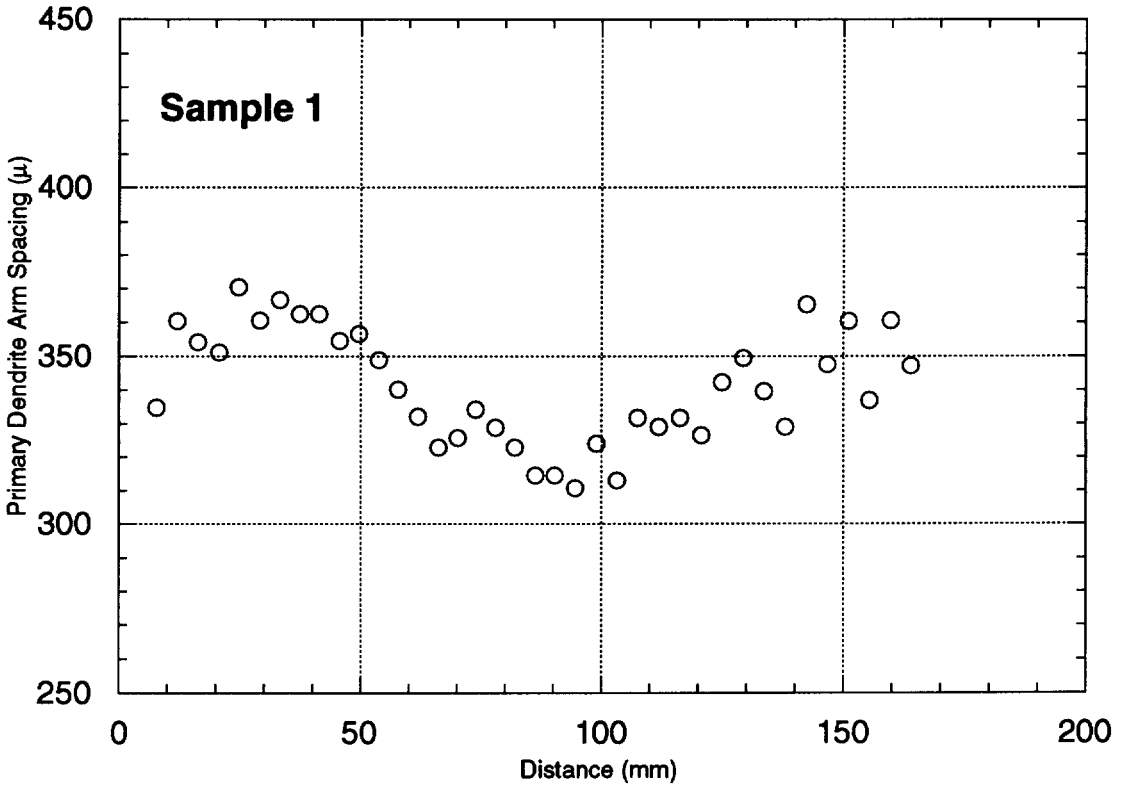
Sample 1
Primary Dendrite Arm Spacing (μ)
450
400
350
300
250
0
50
100
150
200
Distance (mm)

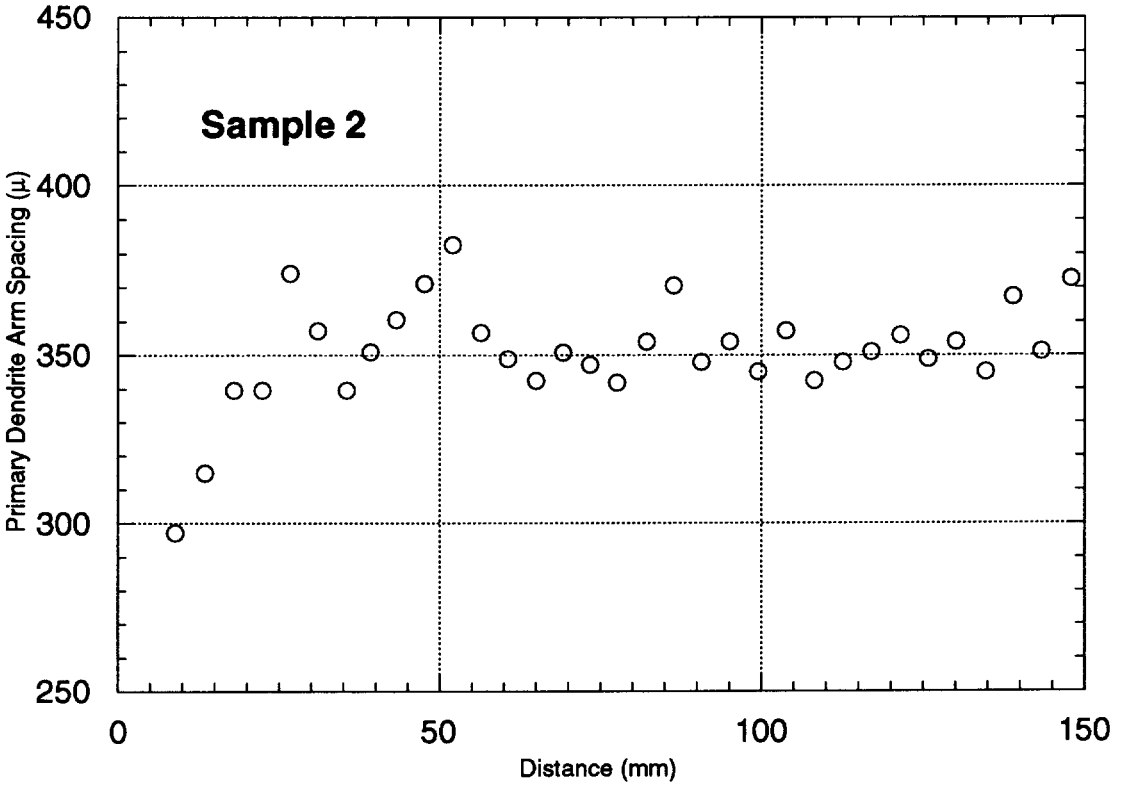
Sample 2
Primary Dendrite Arm Spacing (μ)
450
400
350
300
250
0
50
100
150
Distance (mm)

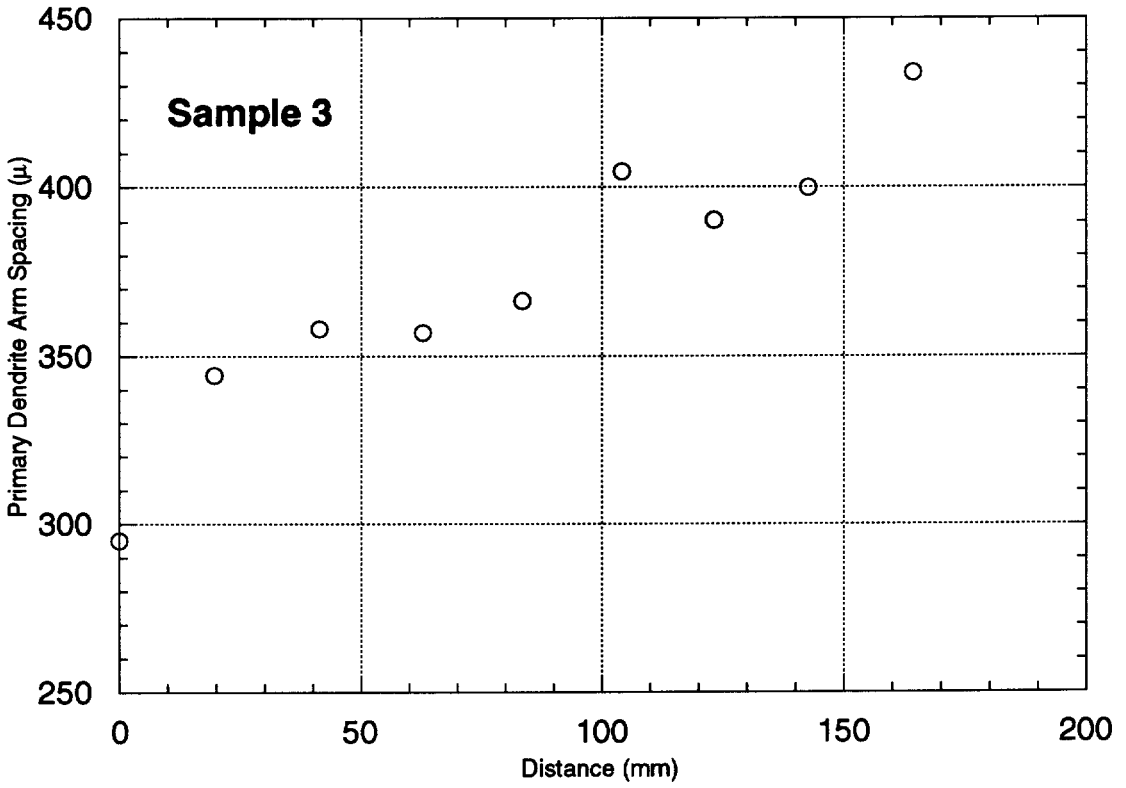
Sample 3
Primary Dendrite Arm Spacing (μ)
450
400
350
300
250
0
50
100
150
200
Distance (mm)

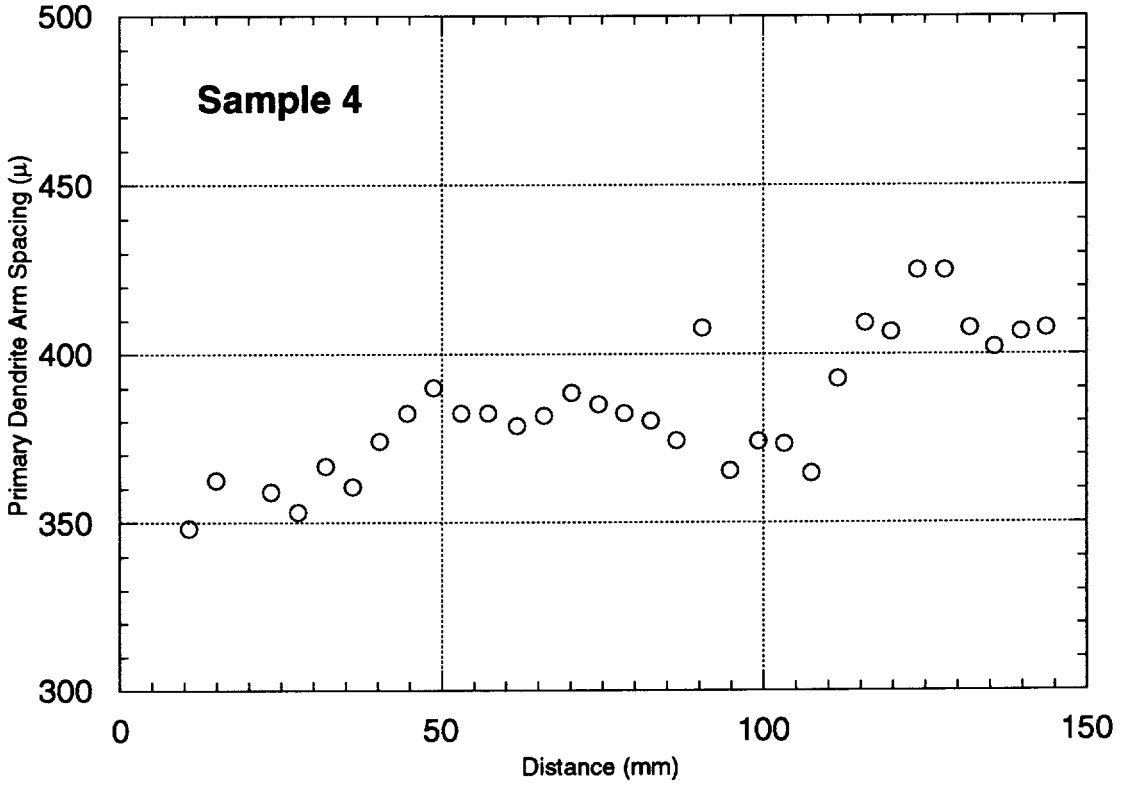
Sample 4
Primary Dendrite Arm Spacing (μ)
500
450
400
350
300
0
50
100
150
Distance (mm)

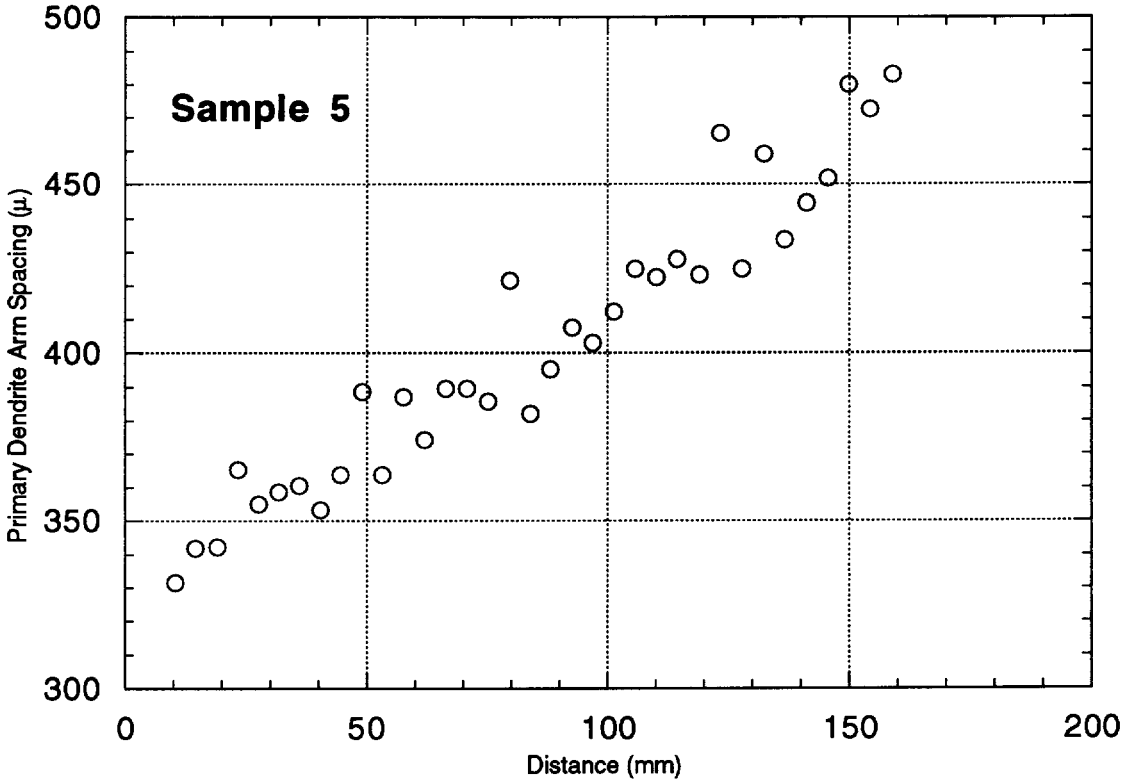
Sample 5
Primary Dendrite Arm Spacing (μ)
500
450
400
350
300
0
50
100
150
200
Distance (mm)

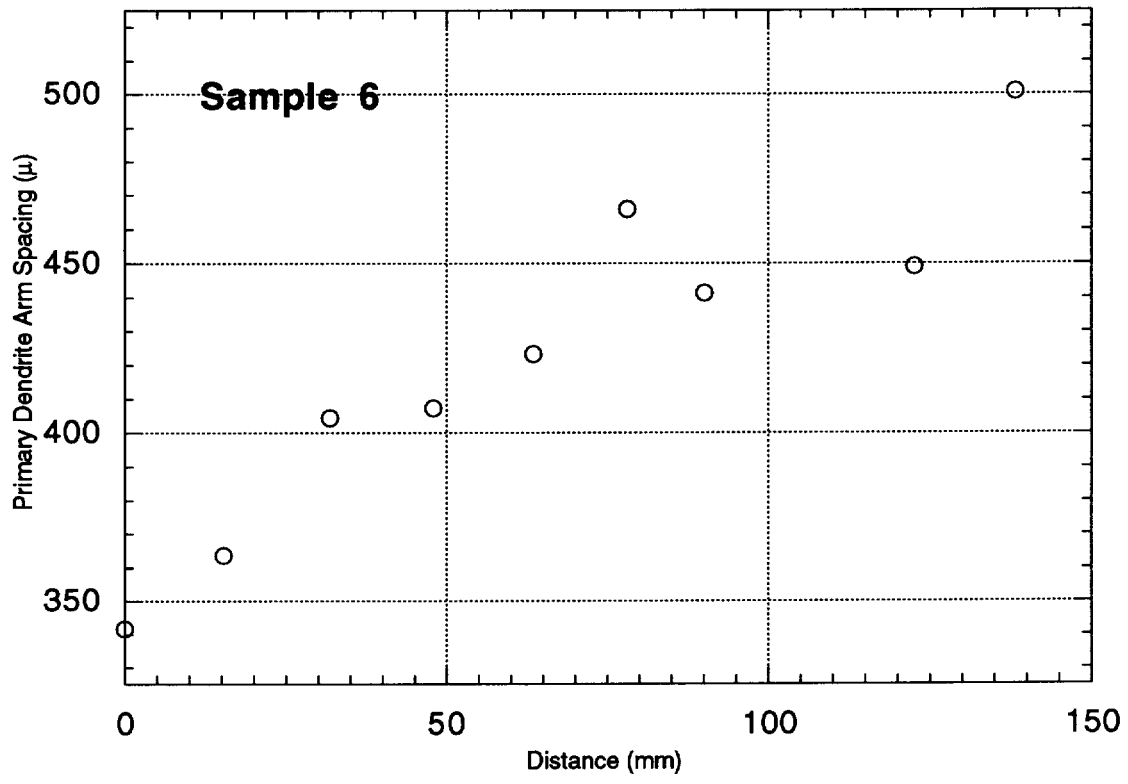
Sample 6
Primary Dendrite Arm Spacing (μ)
500
450
400
350
0
50
100
150
Distance (mm)

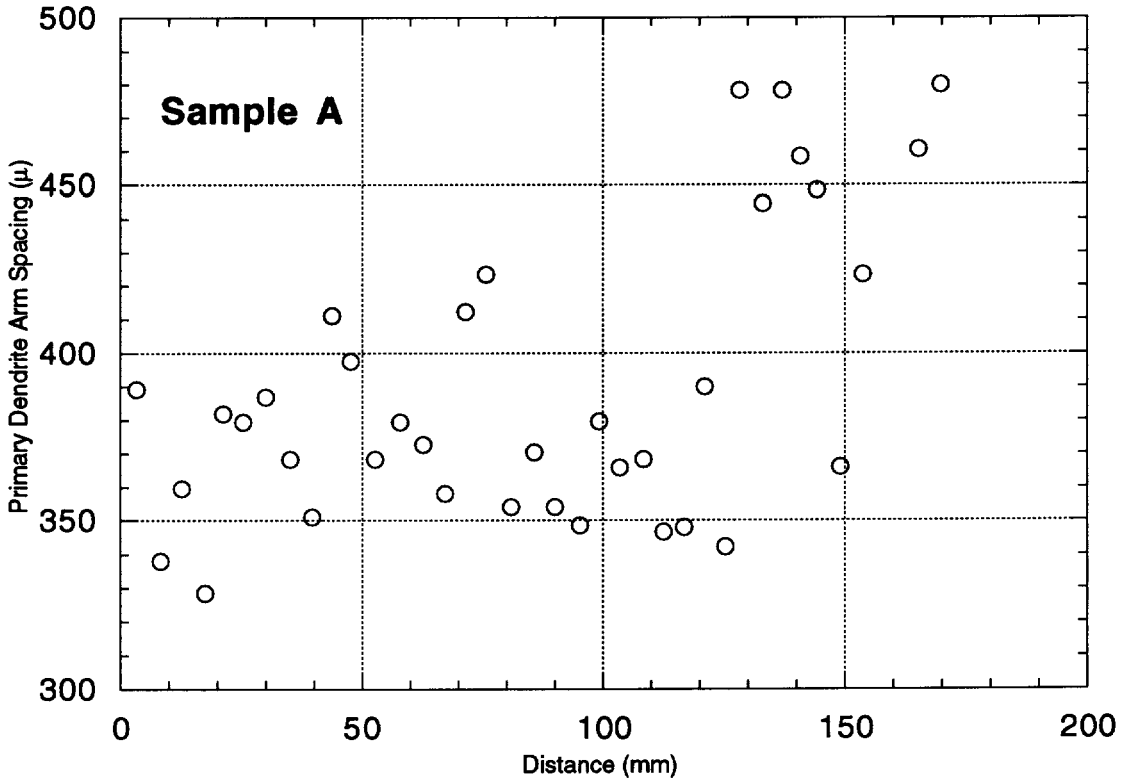
Sample A
Primary Dendrite Arm Spacing (μ)
500
450
400
350
300
0
50
100
150
200
Distance (mm)

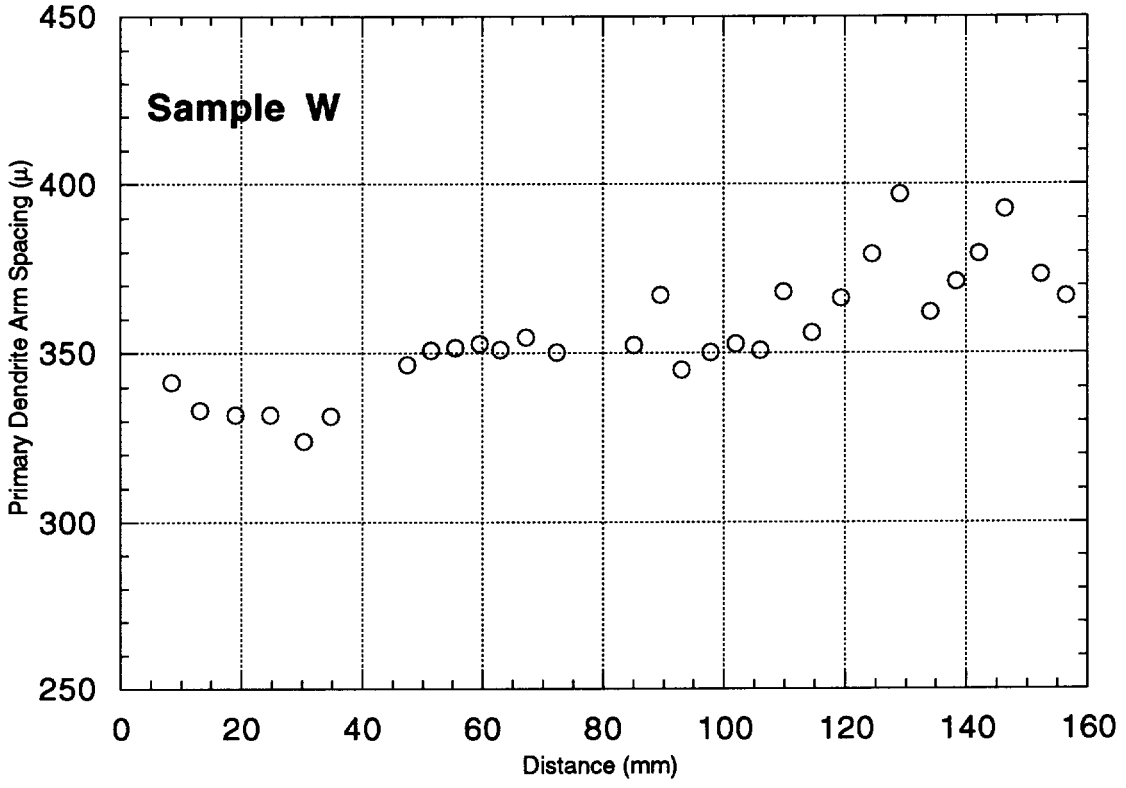
Sample W
Primary Dendrite Arm Spacing (μ)
450
400
350
300
250
0
20
40
60
80
100
120
140
160
Distance (mm)

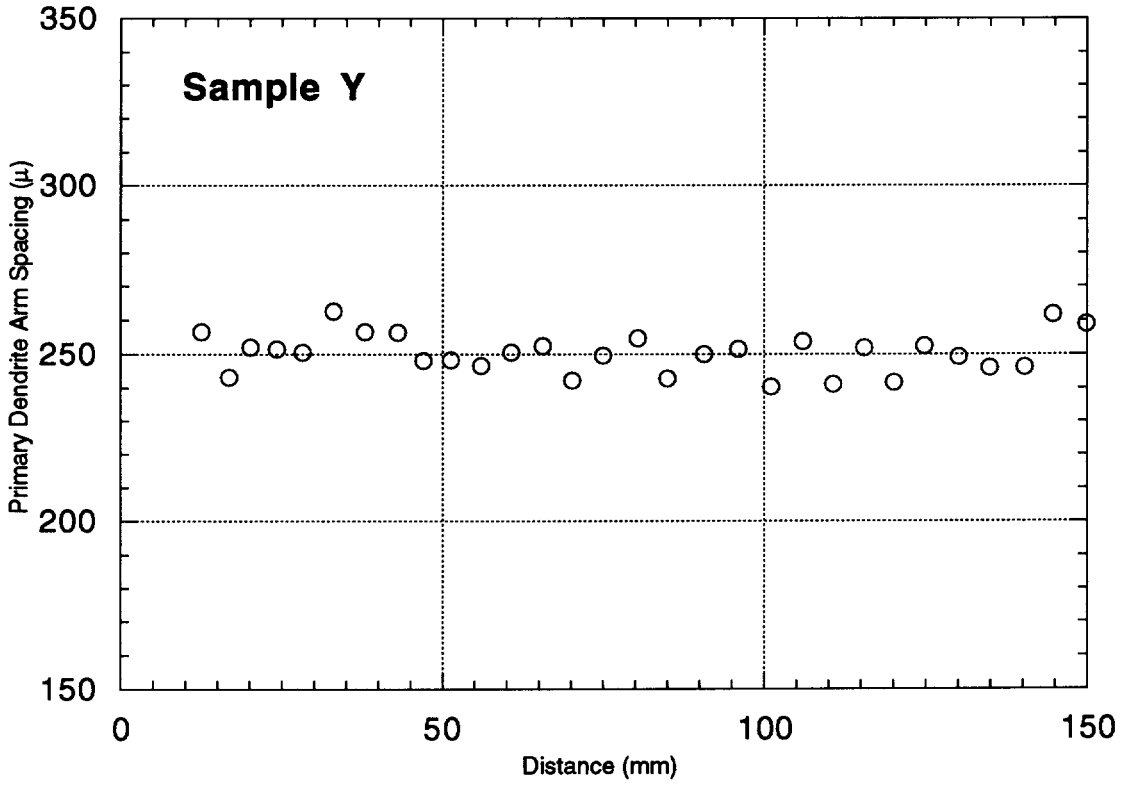
Sample Y
Primary Dendrite Arm Spacing (μ)
350
300
250
200
150
0
50
100
150
Distance (mm)

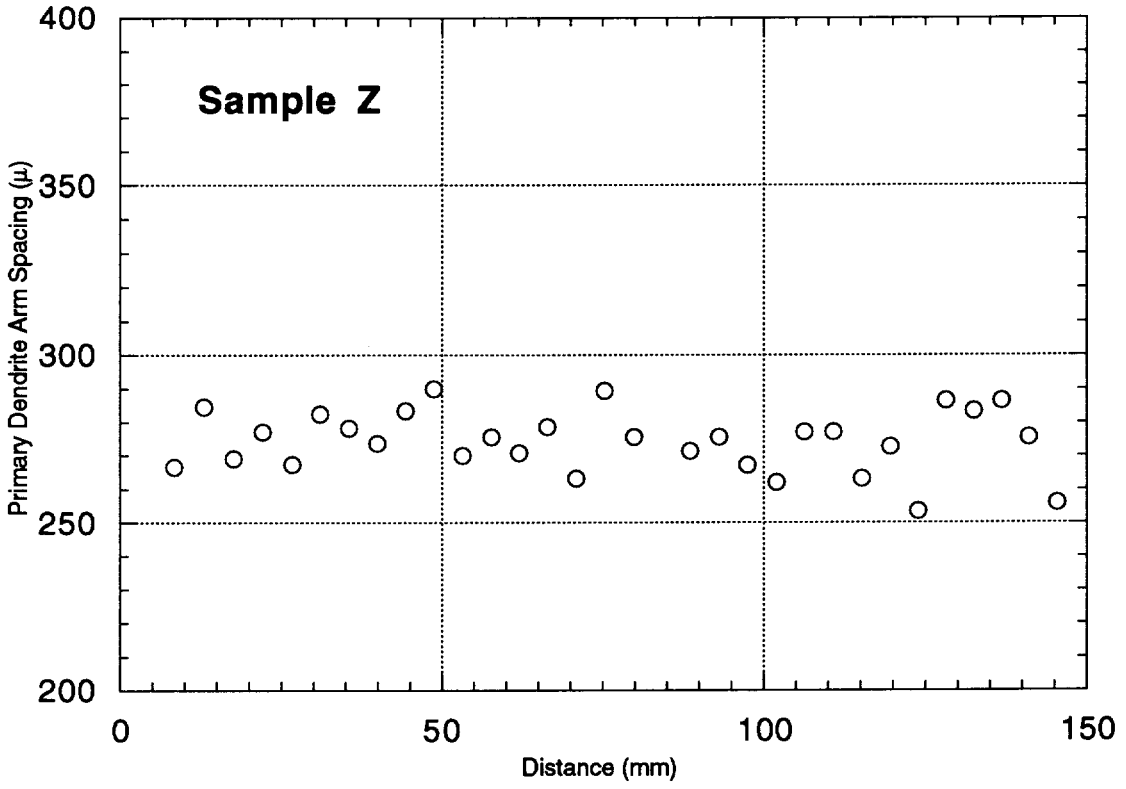
Sample Z
Primary Dendrite Arm Spacing (μ)
400
350
300
250
200
0
50
100
150
Distance (mm)

Appendix H...BEKP Images

The following eleven pages are the Backscattered Electron Kikuchi Patterns which were obtained for evaluation of the interface curvature.

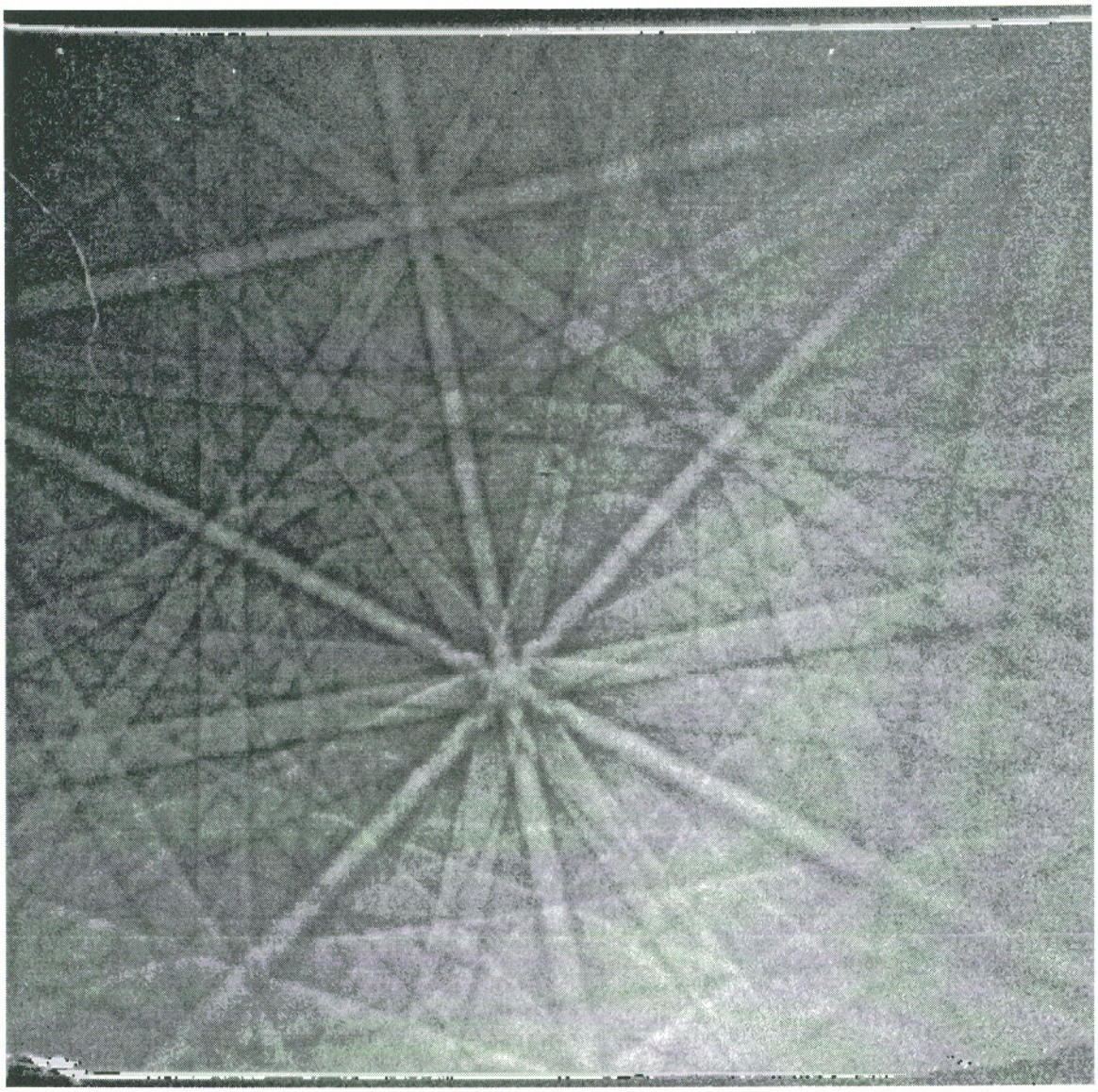

Figure 22.1
Sample 5, Slice 10, Position 1

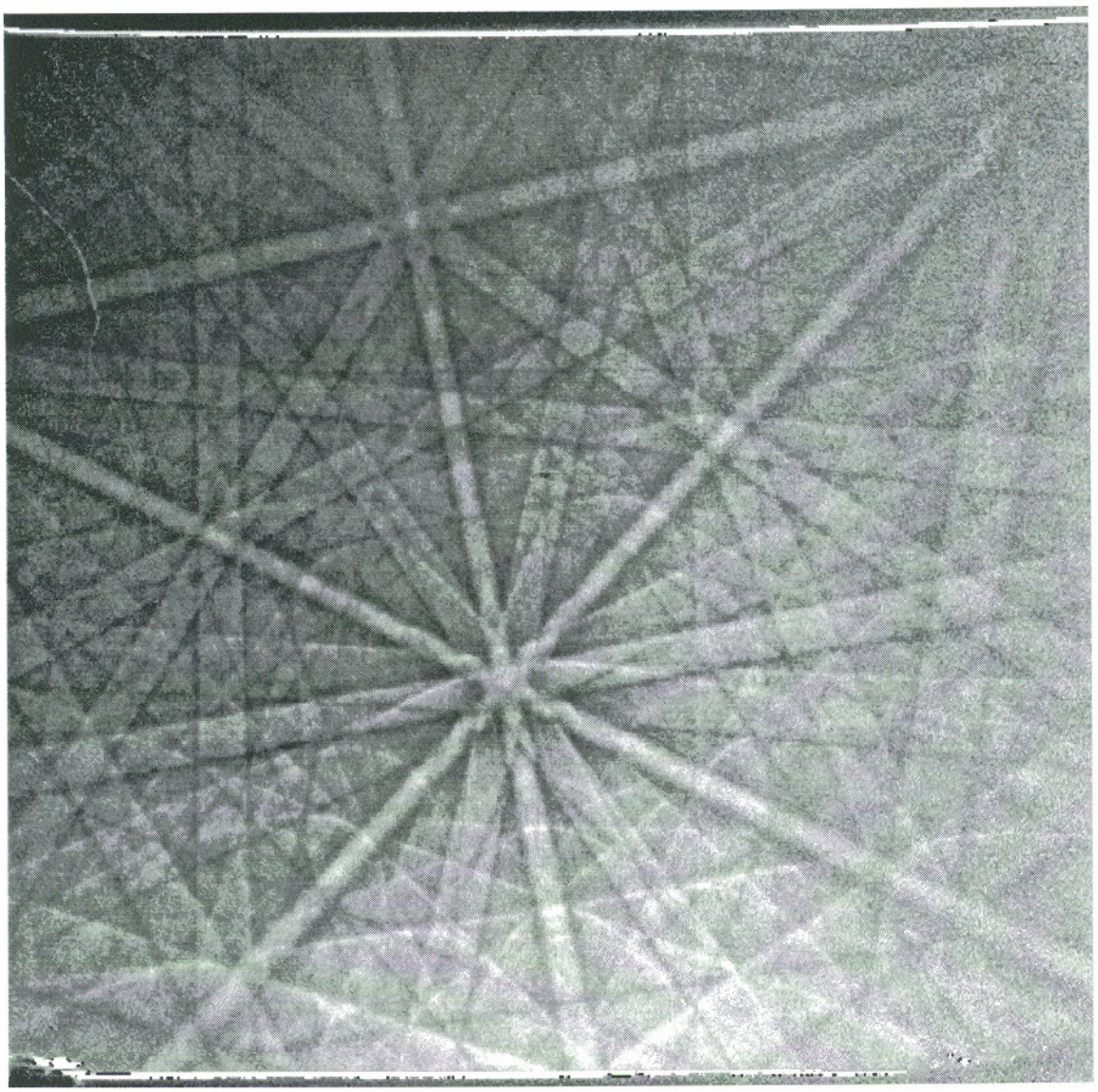

Figure 22.2
Sample 5, Slice 10, Position 2

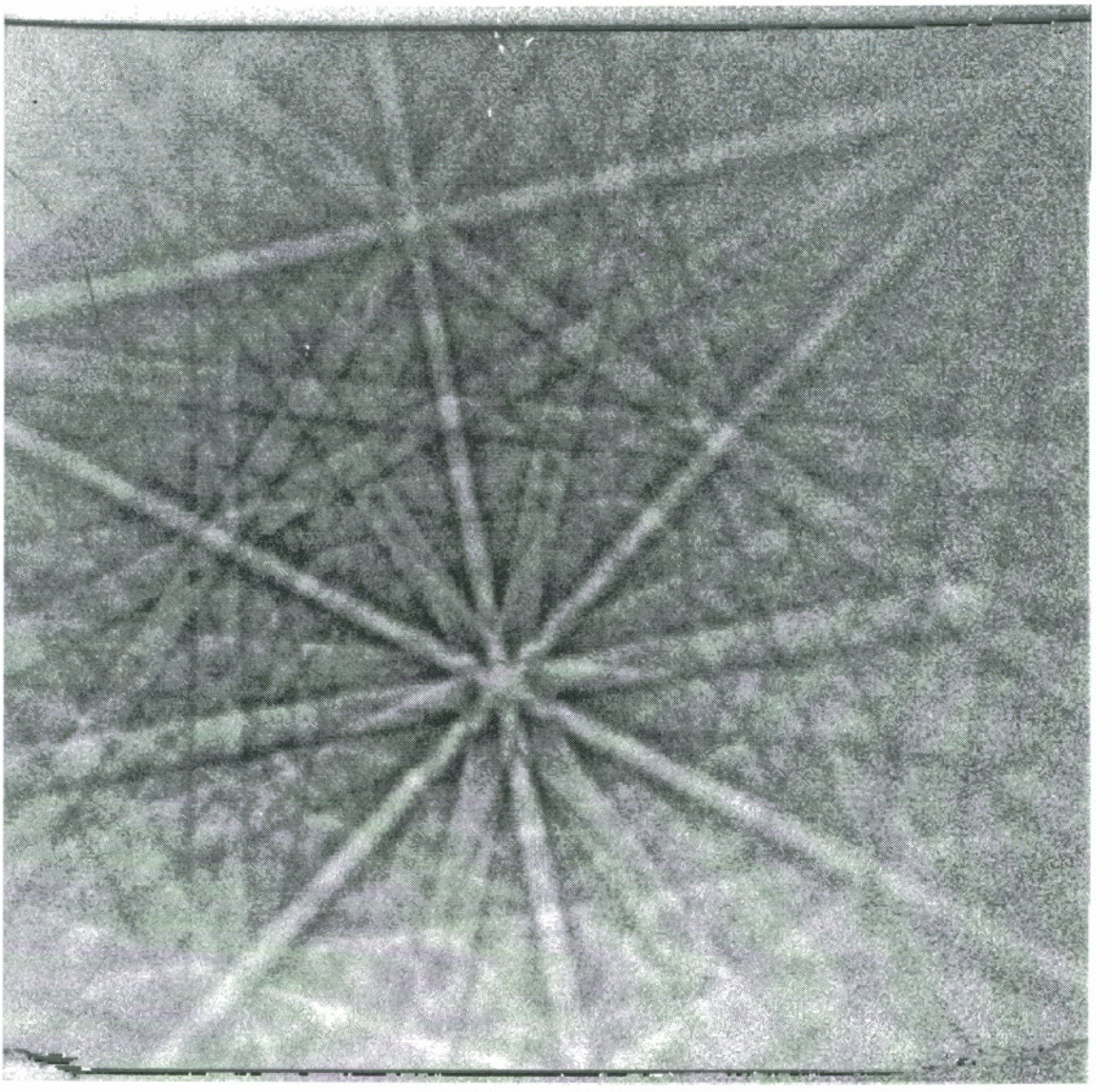

Figure 22.3
Sample 5, Slice 10, Position 3

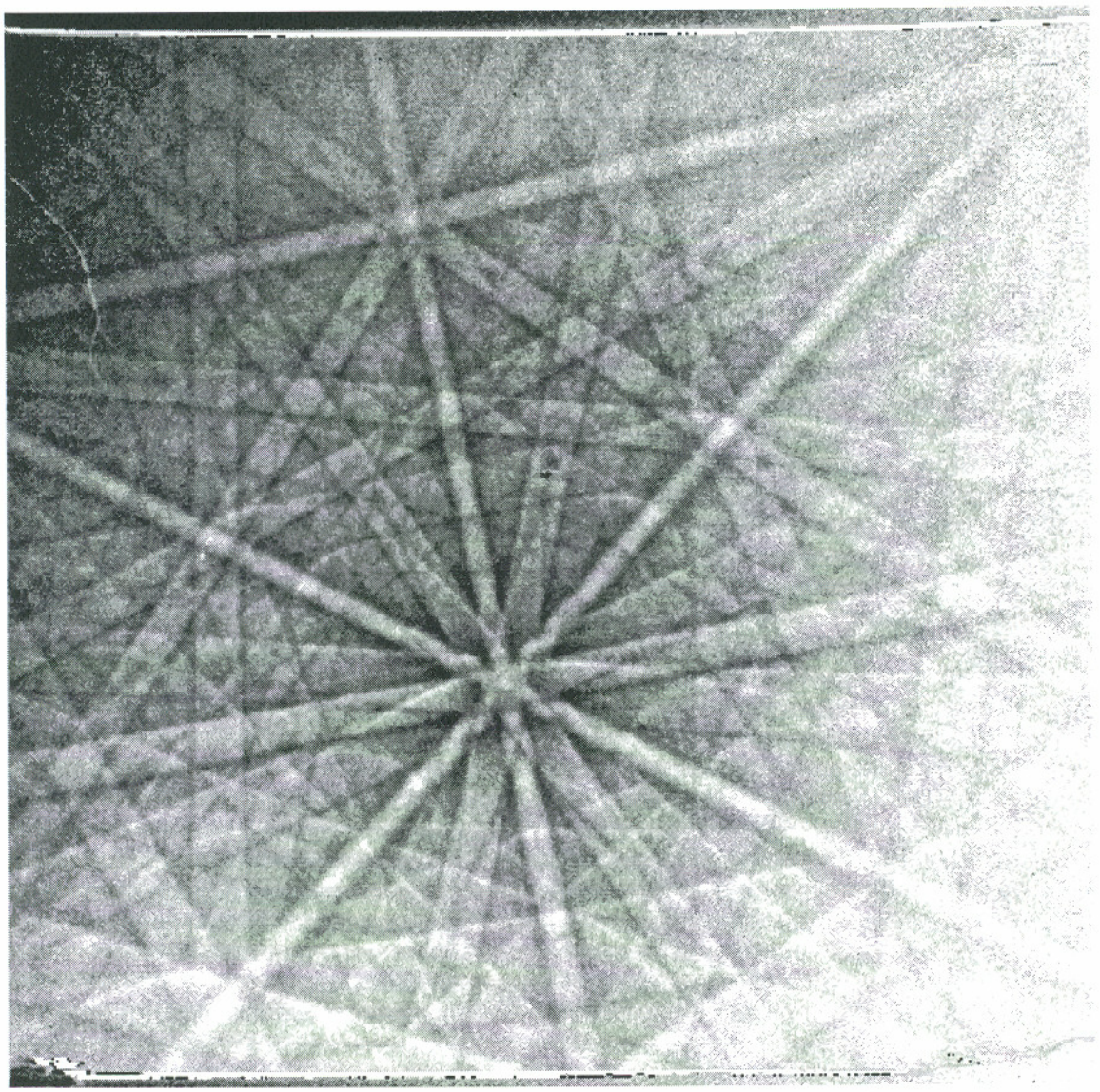

Figure 22.4
Sample 5, Slice 10, Position 4

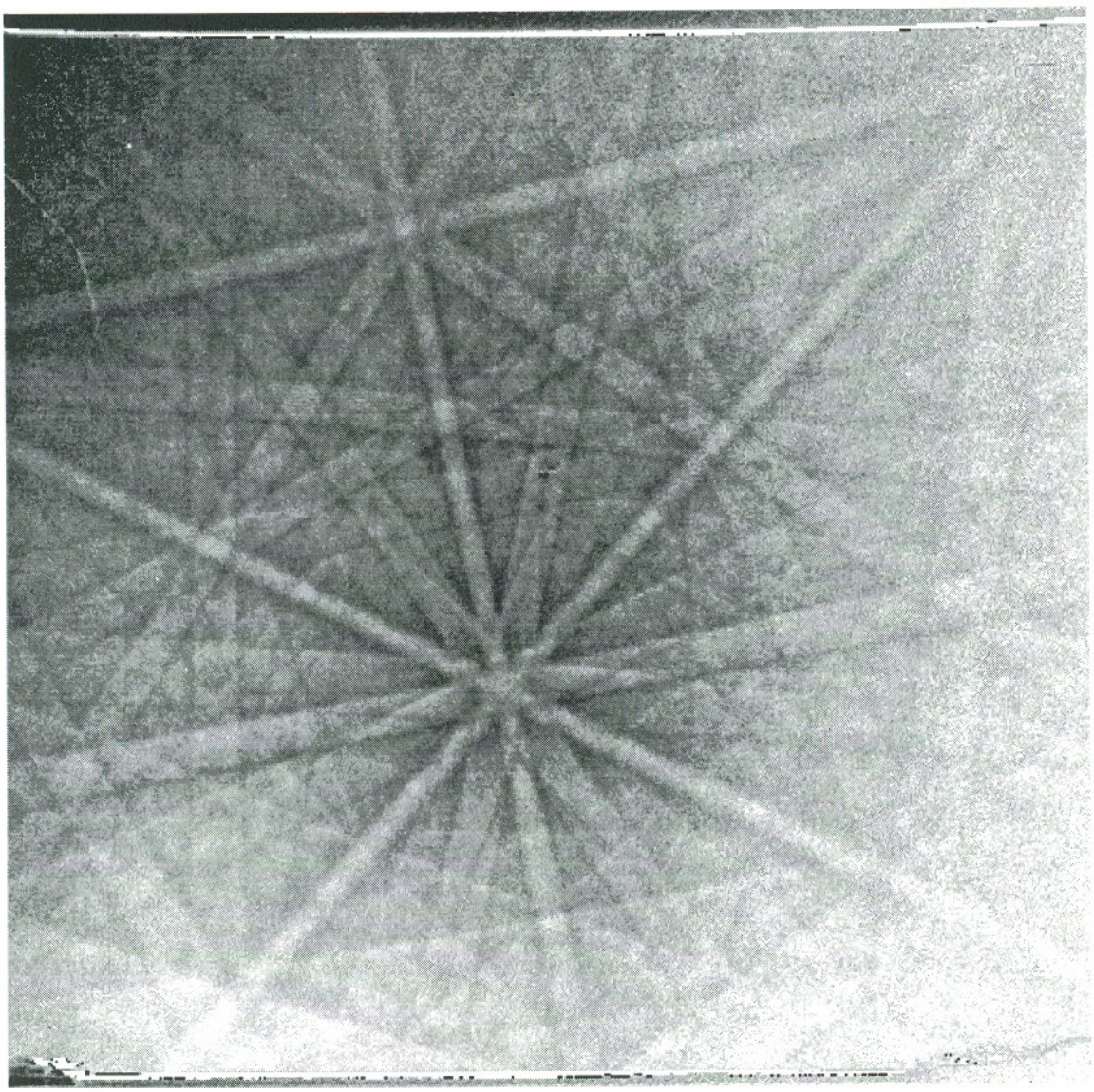

Figure 22.5
Sample 5, Slice 10, Position 5

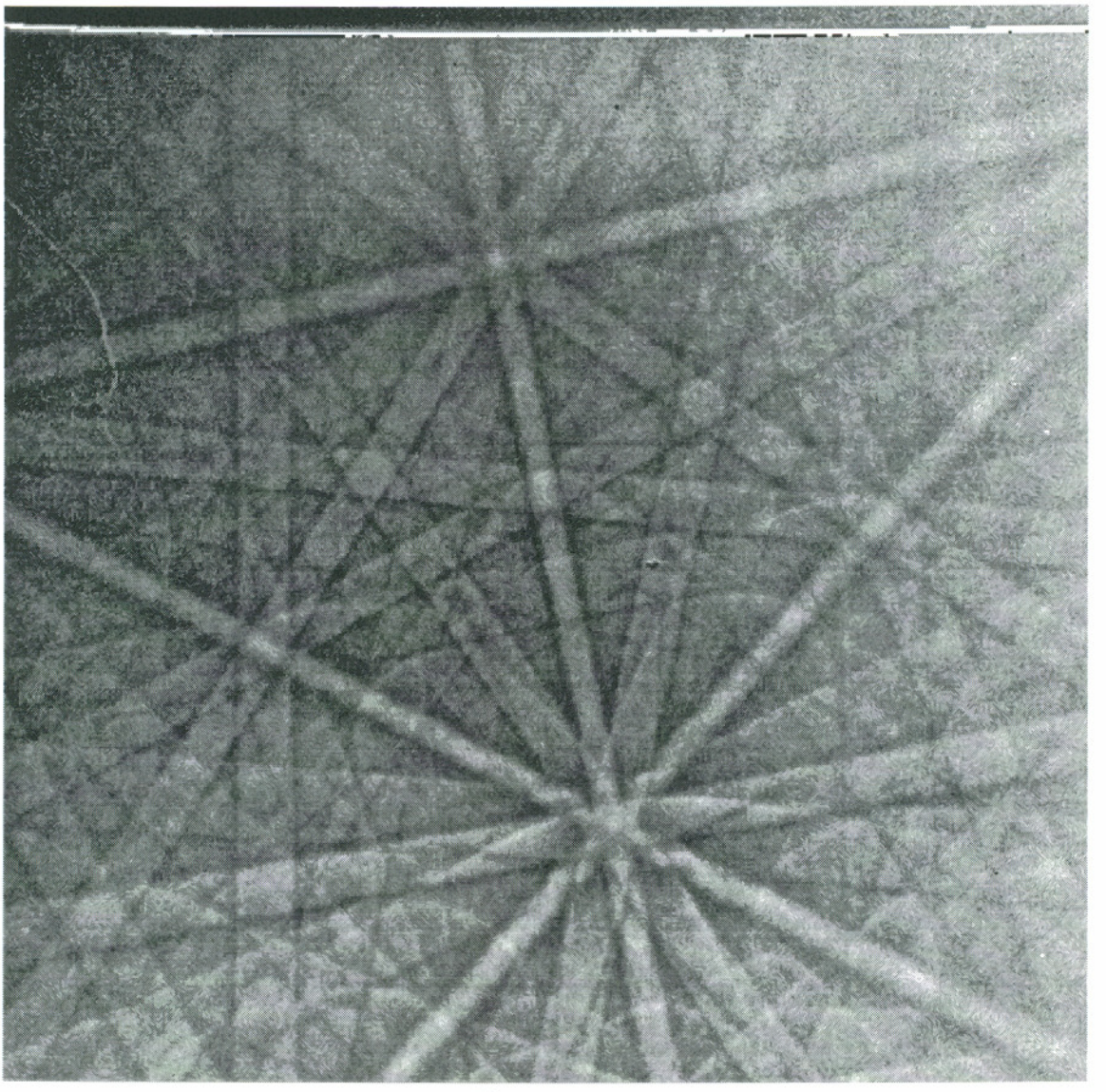

Figure 22.6
Sample 5, Slice 10, Position 6

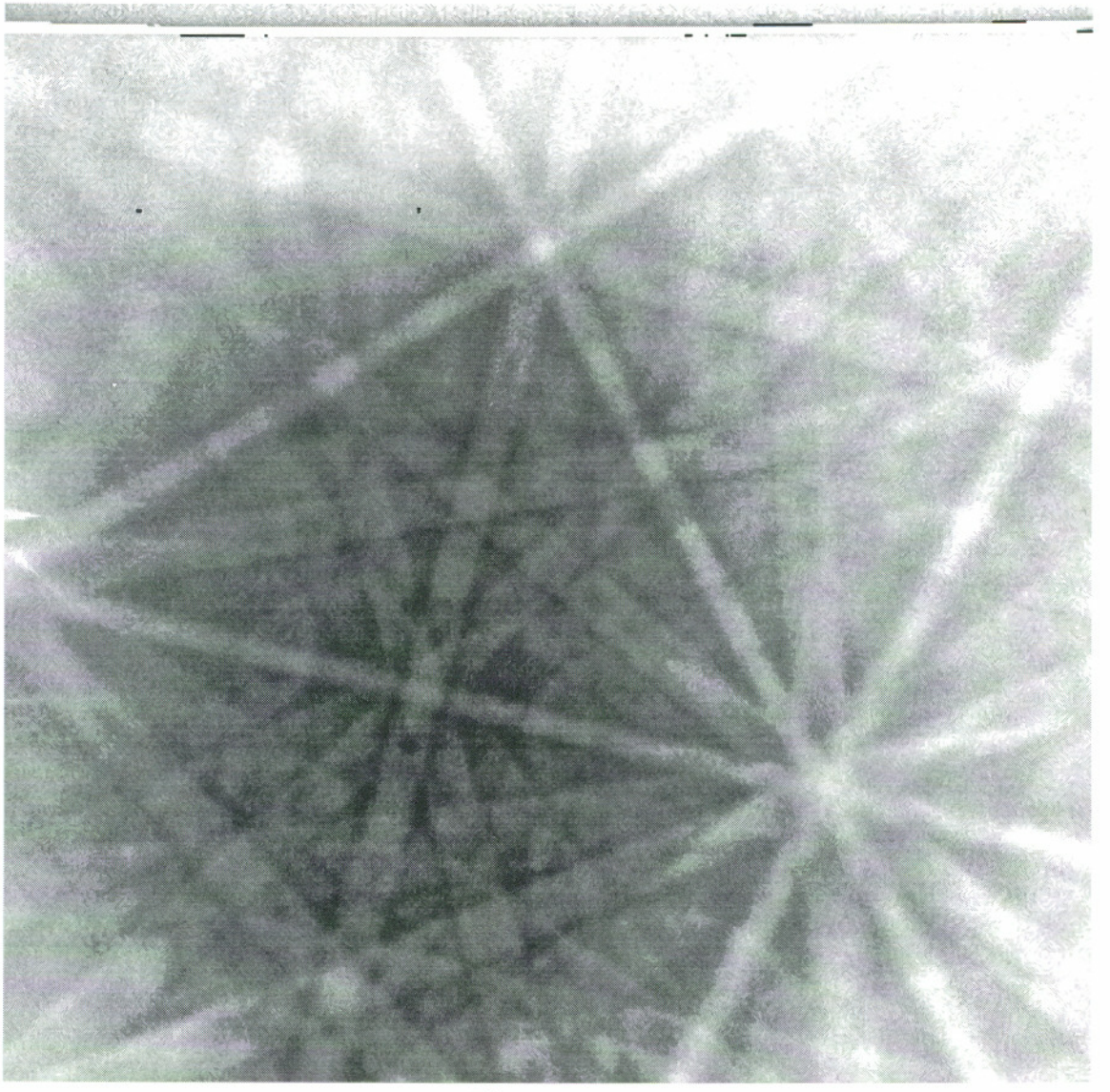

Figure 22.7
Sample 5, Slice 33, Position 1

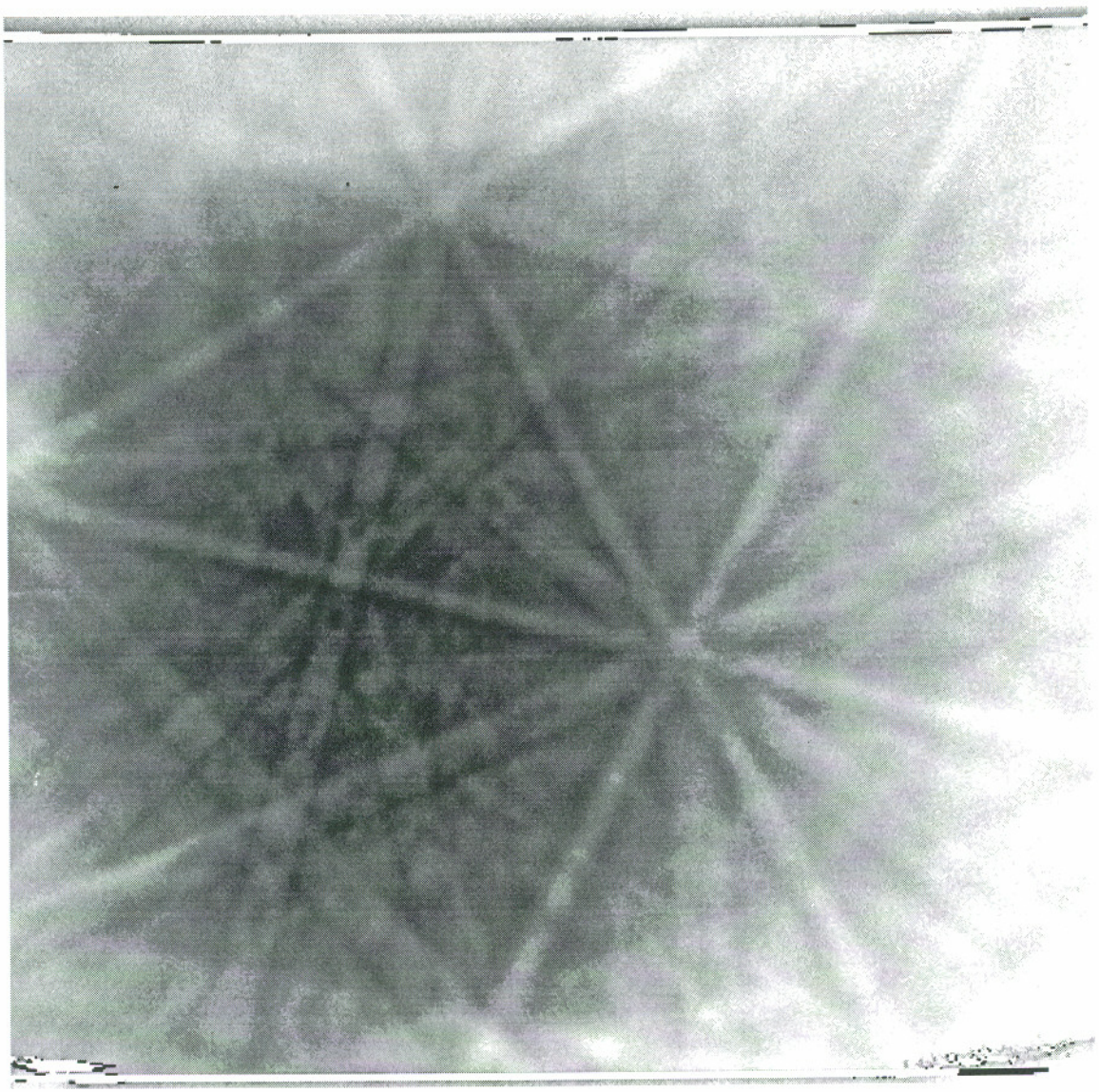

Figure 22.8
Sample 5, Slice 33, Position 2

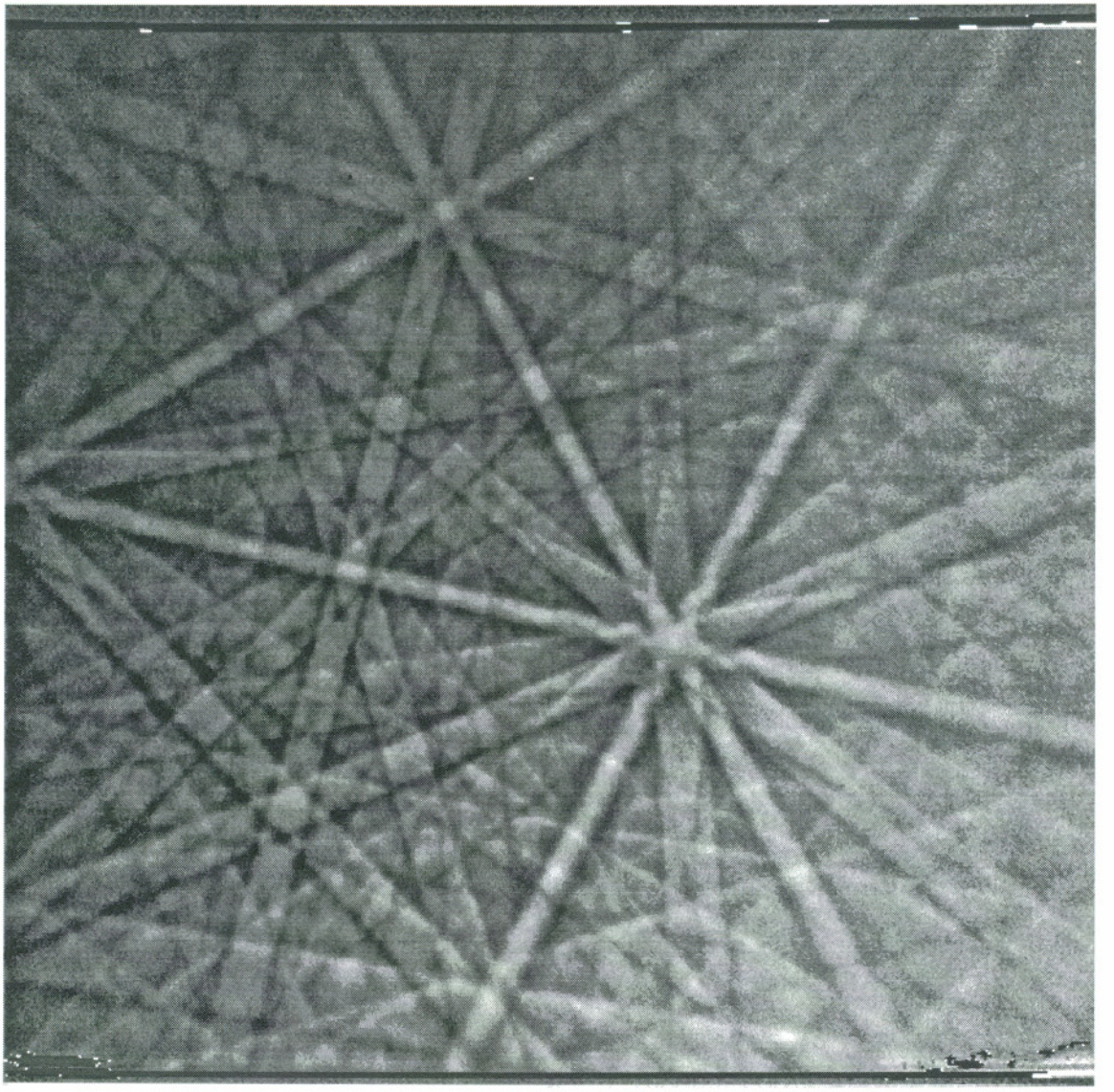

Figure 22.9
Sample 5, Slice 33, Position 3

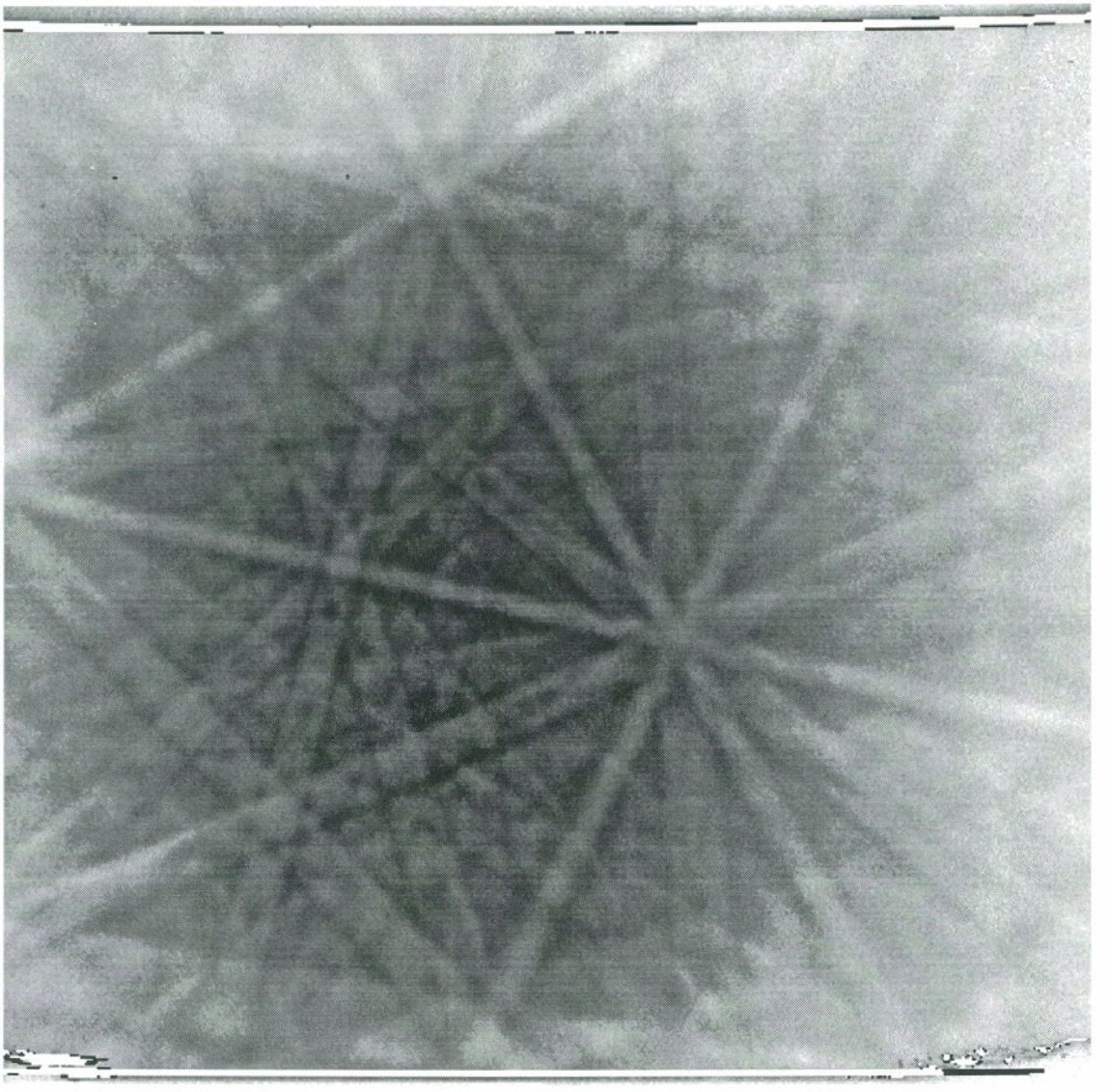

Figure 22.10
Sample 5, Slice 33, Position 4

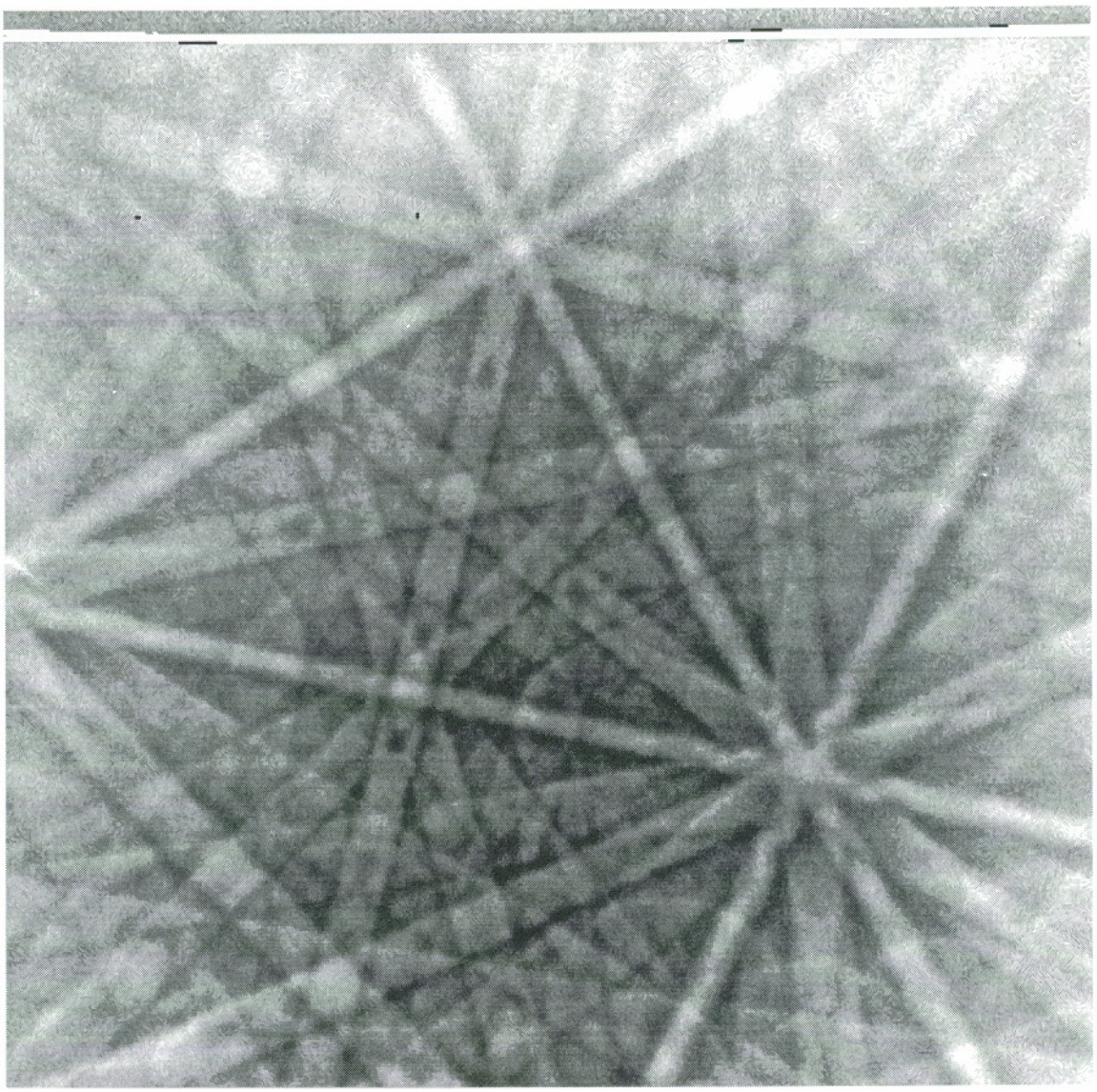

Figure 22.11
Sample 5, Slice 33, Position 5

Biographical Sketch

Max Eric Schlienger was born January 7, 1957 in Pittsburgh Pennsylvania. After completing high school in San Rafael California, he attended the University of Colorado at Boulder. In 1979 he received a Bachelor of Science degree in Electrical Engineering from this school. Subsequent to the receipt of this degree he went to work at Retech Inc. of Ukiah California. Eric worked at Retech in the field of liquid metal processing until 1986 when he began graduate in metallurgy at the University of Illinois at Champaign-Urbana. He returned to Retech in 1988 and received his Master of Science degree in Materials Science and Engineering from Illinois in 1992. Eric then enrolled at the Oregon Graduate Institute of Science and Technology in Beaverton Oregon. While working on his doctoral dissertation Eric continued his activities at Retech. In 1993 he left his position as Engineering Manager at Retech and began working for the Liquid Metal Processing Laboratory of Sandia National Laboratories in Albuquerque New Mexico. While at Sandia Eric was able to complete the requirements for the degree of Ph.D. in Materials Science.

Eric is past chairman of the Vacuum Metallurgy Division of the American Vacuum Society and continues working with the division as a member of the executive committee. He was publication chairman of the 1994 International Symposium on Liquid Metal Processing and casting and is the general chairman for the 1997 conference. Publications include:

"Computer control of a Production VAR", *Proceedings 1986 Vacuum Metallurgy Conference*, (1986).

"Computer Control of Plasma Torches in Plasma Melting", *Proceedings 1989 Vacuum Metallurgy Conference*, (1989).

"Control Considerations in Cold Hearth Withdrawal", *Electron Beam Melting and Refining, State of the Art 1989*, (1989).

"The Electrical Mac: Repairing the ADB", *MacTutor: The Macintosh Programming Journal*, 5 (11), (1989).

"Grain Size Effects in Plasma Cold Hearth Melting", *Proceedings 1990 MRS Spring Meeting*, (1990).

"Control of Plasma Hearth Melted Ingot Surfaces", *Proceedings 10th International Conference on Vacuum Melting*, (1990).

"Molten Pool Characteristics in Plasma Cold Hearth Melting", *Electron Beam Melting and Refining, State of the Art 1992*, (1992).

"Phenomenological Characteristics of Plasma Hearth Melting", *Symposium on Thermal Plasmas, 1992 TMS Annual Meeting*, (1992)

"Recent Improvements in the Economics of Plasma Melting", *7th TMS World Titanium Conference*, (1992).

"Plasma Cold Hearth Remelting of UDIMET® Alloy 718", *Superalloys 1992*, (1992).

"Evaluation of Hearth Melted UDIMET® 718", *Electron Beam Melting and Refining, State of the Art 1993*, (1993).

"Waste Minimization with Plasma Processing", *Proceedings Waste Management 1993, (1993).*

"The Mobile PCF2", *Proceedings Waste Management 1993, (1993).*

"The Influence of VAR Processes and Parameters on White Spot Formation in Alloy 718", *Proceedings 1994 TMS International Symposium on Superalloys 718, 625, 706 and Various Derivatives*, (1994).

"Popcorn, Diffraction and the Computer Revolution", *Microscopy Today*, **94**, (9), (1994)

Bibliography

1 Fawley, R. W., The Superalloys, John Wiley & Sons, New York NY , (1972).

2 Gell, M., Duhl, D. N. and Giamei, A. F., Superalloys 1980, ASM, Metals Park, OH, (1980), 205-214.

3 Westbrook, J. H., Ordered Alloys; Structural Applications and Physical Metallurgy, Claitors Publishing Division, Baton Rouge LA, (1970), 1-21.

4 Grant, N. J., Transactions of the ASM, 39, (1947), 335-367.

5 Gell, M., Sullivan, C. P. and VerSnyder, F. L., Solidification Technology, Brook Hill Publishing Company, Chestnut Hill MA, (1974), 141-164.

6 VerSnyder, F. L. and Guard, R. W., Transactions of the ASM, 52, (1960), 485-493.

7 VerSnyder, F. L. and Shank, M. E., Materials Science and Engineering, 6, ASM, Metals Park OH, (1970), 213-247.

8 Northwood, J. E., Metallurgia July 1979, (1979).

9 Strutt, P. R. and Dodd, R. A., Ordered Alloys; Structural Applications and Physical Metallurgy, Claitors Publishing Division, Baton Rouge LA, (1970), 475-504.

10 Leverant, G. R. and Duhl, D. N., Met Trans., 2 (3), (1971).

11 Gell, M., Sullivan, C. P. and VerSnyder, F. L., Solidification Technology, Brook Hill Publishing Company, Chestnut Hill MA., (1974), 141-164

12 Duhl, D. N. and Sullivan, C. P., Journal of Metals, July 1971, (1971), 38-40.

13 Gell, M. and Leverant, G. R., Ordered Alloys; Structural Applications and Physical Metallurgy, Claitors Publishing Division, Baton Rouge LA, (1970), 505-523.

14 Varin, J. D., The Superalloys, John Wiley & Sons, New York NY, (1972).

15 Higginbothom, G. J. S., Materials and Design, 8 (1), (1987).

16 Copley, S. M., Giamei, A. F., Johnson, S. M. and Hornbecker, M. F., Met Trans., 1 (8), (1970), 2193.

17 Decker, R. F and Sims, C. T., The Superalloys, John Wiley & Sons, New York NY, (1972), 33-77.

18 Davies, R. G. and Johnston, T. L., Ordered Alloys: Structural Applications and Physical Metallurgy, Claitors Publishing Division, Baton Rouge LA, (1970), 447-474.

19 Wilcox, R. and Clauer, A. H., Ordered Alloys: Structural Applications and Physical Metallurgy, Claitors Publishing Division, Baton Rouge LA, (1970), 197-231.

20 Ham, R. K., Ordered Alloys: Structural Applications and Physical Metallurgy, Claitors Publishing Division, Baton Rouge LA, (1970), 365-374.

21 Popov, L. E., Golosov, N. S., Ginzburg, A. E., Kodzemyakin, N. V. and Kozlov, E. V., Ordered Alloys: Structural Applications and Physical Metallurgy, Claitors Publishing Division, Baton Rouge LA, (1970), 307-319.

22 Cole, G. S. and Cremisio, R. S., The Superalloys, John Wiley & Sons, New York NY, (1972).

23 Erickson, J. S., Owczarski, W. A. and Curran, P. M., Metal Progress, March 1971 (1971).

24 Staub, F., Walser, B. and Wortman, J., Sulzer Technical Review (3/ 1988).

25 Staub, F., Walser, B. and Wortman, J., Proceedings of the First ASM Europe Technical Conference, Paris France, Sept 7-9, 1987, ASM, Metals Park OH, (1987).

26 Stanescu, J., Sahm, P. R., Schädlich-Stubenrauch, J., and Ludwig, A., Proceedings of the 40th Annual Technical Meeting: Investment Casting Institute, (1992), 29:1-29:13.

27 Gell, M., Sullivan, C. P. and VerSnyder, F. L., Solidification Technology, Proceedings of the First Army Materials Technology Conference, Brook Hill Publishing Company, Chestnut Hill MA, (1974), 141-164.

28 Kats, E. L., Koriakin, S. V., Amelyanohik, A. V., and Spiridinov, S. V., Heat-Resistant Materials, Proceedings of the First International Conference, Fontana, Wisconsin, USA (Sept 23-26,1991).

29 Erickson, J. S., Owczarski, W. A. and Curran, P. M., Metal Progress, March 1971, (1971).

30 Yoshinari, A., Morimoto, S. and Kodama, H., Proceedings 1st Intl SAMPE Symposium, (Nov 28, - Dec 1, 1989).

31 Nakagawa, Y. G., Superalloys Japan-US Seminar, TMS Publications, Warrendale PA, (1985).

32 Pollock, T. M., Murphy, W. H., Goodman, E. H., Uram, D. L. and Tu, J. S., Superalloys 1992, TMS Publications, Warrendale PA, (1992), 125.

33 Strang, G., Introduction to Applied Mathematics, Wellesley-Cambridge Press, (1986), 35.

34 Heubner, U., Köhler, M. and Prinz, B., Superalloys 1988, TMS Publications, Warrendale PA, (1988), 437-447.

35 Kurz, W. and Fisher, D., Fundamentals of Solidification, Trans Tech Publications - Karl Distributors, Rockport MA, (1986), 157.

36 Rabenstein, A. L., Elementary Differential Equations with Linear Algebra, 2nd Ed., Academic Press, New York NY, (1975)

37 Kurz, W. and Fisher, D., Fundamentals of Solidification, Trans Tech Publications - Karl Distributors, Rockport MA, (1986), 47-61.

38 Langer, J. S., Müller-Krumbhaar, H., Acta Metallurgica, 42 (11), (1977).

39 Kurz, W. and Fisher, D., Fundamentals of Solidification, Trans Tech Publications, Aedermannsdorf, (1986), 86.

40 Wills, V. A. and McCartney, D. G., Materials Science and Engineering, A145, (1991), 223-232.

41 Heubner, U., Köhler, M. and Prinz, B., Superalloys 1988, TMS Publications, Warrendale PA, (1988), 437-447.

42 Kikuchi, S., Japanese Journal of Physics, 5 (83), (1928).

43 Alam, M. N., Blackman, M. and Pashley, D. W., Proc. Roy. Soc., 221, (1954), 224-242.

44 Meibom, R. von and Rupp, E., Z. Tech. Phys., 82., (1933), 690.

45 Boersch, H., Z. Tech. Phys., 18, (1937), 574.

46 Venables, J. A., and Harland, C.J, Phil. Mag., 27, (1973), 1193-1200.

47 Dingley, D.J, and Baba-Kishi, K., Scanning Electron Microscopy, II, (1986), 383-391.

48 Baba-Kishi, K., Ultramicroscopy, 36, (1991), 355-360.

49 Venables, J. A., and Bin-Jaya, R., Phil. Mag., 27, (1977), 1317-1332.

50 Schmidt, N. H., Bilde-Sorensen, J. B. and Juul-Jensen, D., Scanning Microscopy, 5 (3), (1991), 637 - 643.

51 Kunze, K., Wright, S. I., Adams, B. L. and Dingley, D. J., Textures and Microstructures, preprint, (Submitted Jan. 1992).

52 Wright, S. I. and Adams, B. L., Met. Trans. A, 23A, (1992), 759-767.

53 Adams, B. L., Wright, S. I. and Kunze, K., Met. Trans. A, 24A, (1993), 819-831.

54 Adams, B. L., and Kunze, K., Materials Science and Engineering, A160, ASM, Metals Park OH, (1993), 229-240.

55 Dingley, D. J., and Wilkinson, A. J., Acta Metall. Mater., 39 (12), (1991), 3047-3055.

56 Dingley, D. J., Proceedings, Microscopy Society of America 52nd Annual Meeting, San Francisco Press, (1994), 602-603.

57 Dingley, D. J., Mackenzie, R. and Baba-Kishi, K., Microbeam Analysis, San Francisco Press, (1989).

58 Michael, J. R. and Goehner, R. P., Proceedings, Microscopy Society of America 52nd Annual Meeting, San Francisco Press, (1994), 596-597.

59 Randle, V., Microtexture Determination and its Applications, The Institute of Materials, London England, (1992).

60 Venables, J. A., and Bin-Jaya, R., Phil. Mag., 27, (1977), 1317-1332.

61 Quested, P. N. and McLean, M., Materials Science and Engineering, 65, ASM, Metals Park OH, (1984), 171.

62 Pollock, T. M. and Murphy, W. H., Met. Trans., (pre-publication 1993).